

Springer Series in Computational Neuroscience

Maurizio De Pittà
Hugues Berry *Editors*

Computational Glioscience

Springer Series in Computational Neuroscience

Series editors

Alain Destexhe, Computationnelles, UNIC, Gif-sur-Yvette, France
Romain Brette, Institut de la Vision, Paris, France

Computational Neuroscience gathers monographs and edited volumes on all aspects of computational neuroscience, including theoretical and mathematical neuroscience, biophysics of the brain, models of neurons and neural networks, and methods of data analysis (e.g. information theory). The editors welcome suggestions and projects for inclusion in the series.

About the Editors

Alain Destexhe is Research Director at the Centre National de la Recherche Scientifique (CNRS), France, and Romain Brette is Research Director at the Institut National de la Santé et de la Recherche Médicale (INSERM), France.

More information about this series at <http://www.springer.com/series/8164>

Maurizio De Pittà · Hugues Berry
Editors

Computational Glioscience



Springer

Editors

Maurizio De Pittà
Group of Mathematical, Computational
and Experimental Neuroscience
Basque Center for Applied Mathematics
Bilbao, Biscay, Spain

Hugues Berry
INRIA Rhône-Alpes
Université de Lyon
Villeurbanne, Lyon, France

ISSN 2197-1900

ISSN 2197-1919 (electronic)

Springer Series in Computational Neuroscience

ISBN 978-3-030-00815-4

ISBN 978-3-030-00817-8 (eBook)

<https://doi.org/10.1007/978-3-030-00817-8>

Library of Congress Control Number: 2018954856

© Springer Nature Switzerland AG 2019

This work is subject to copyright. All rights are reserved by the Publisher, whether the whole or part of the material is concerned, specifically the rights of translation, reprinting, reuse of illustrations, recitation, broadcasting, reproduction on microfilms or in any other physical way, and transmission or information storage and retrieval, electronic adaptation, computer software, or by similar or dissimilar methodology now known or hereafter developed.

The use of general descriptive names, registered names, trademarks, service marks, etc. in this publication does not imply, even in the absence of a specific statement, that such names are exempt from the relevant protective laws and regulations and therefore free for general use.

The publisher, the authors and the editors are safe to assume that the advice and information in this book are believed to be true and accurate at the date of publication. Neither the publisher nor the authors or the editors give a warranty, express or implied, with respect to the material contained herein or for any errors or omissions that may have been made. The publisher remains neutral with regard to jurisdictional claims in published maps and institutional affiliations.

This Springer imprint is published by the registered company Springer Nature Switzerland AG
The registered company address is: Gewerbestrasse 11, 6330 Cham, Switzerland

Preface

The past 30 years have witnessed an appraisal of the role of glial cells, from passive bystanders of neurons to active players in information processing and storage of the brain. This possibility has spurred an increasing number of experimental and technological advances to harness the complexity of glial cells, whose large variety is suggested to reflect an equally large diversity of functions. If experimental excitement surfs this new wave of glial research, theoretical efforts to characterize what glia do lag behind. Both the novice and the experienced theoretician may indeed be jeopardized by the morphological and functional complexity of glial cells which encompass a whole richness of dynamical interactions with neurons, ranging from molecular and cellular signaling to network activity and behavior. The overwhelming experimental details often make difficult to identify the appropriate level of modeling for a particular problem. On the other hand, anyone who approaches the field may also be baffled to find out that some of the most fundamental questions that we can ask for neurons, for example, what is the input–output characteristic of a neuron, not only remain to be answered for glial cells, but may even not be properly posed in the case of these cells. In this book, we consider some of these open questions and present along possible modeling approaches that could yield insight into the function of glial cells in the brain.

In a panorama where most of the theoretical analysis and computational approaches in neuroscience are oriented to study what neurons do or we could do with them, we emblematically entitled this book *Computational Glioscience*. Clearly, there is not such a thing as “glioscience” inasmuch as the study of glia is just a field of neuroscience, be it either experimental or computational. Moreover, the very concept of glioscience may be detrimental for the advancement of the field, given the recognition of the important functions played by glial cells *in association with* neurons. Yet, we purportedly argue that “glioscience,” as a possible subdiscipline of neuroscience, has its own reason to be defined, for the challenges that it bears, to the experimentalist and to the theoretician, in unraveling glia complexity. In this perspective, we refer to “computational glioscience” as to the whole spectrum of theoretical approaches and computational methods put forth to model and

simulate glial signaling in the brain, at its multiple spatial and temporal scales of interaction, be they either among other glial cells or with neurons.

Organization and Approach

With the exception of the initial chapter in the introductory Part I that aims at providing a general overview of some of the key debated aspects in current research on glia, the other chapters of the book mostly focus on astrocytes, the main type of cortical glial cells that have been behind the momentum gained by modern glia research in the past three decades. Accordingly, the book is organized into four parts. Part II, Calcium Dynamics, (Chaps. 2–7) is devoted to modeling of calcium signaling in astrocytes, both at the subcellular level of individual astrocytes (Chaps. 2–6) and the intercellular level of networks of astrocytes (Chaps. 6 and 7). Focus is on the mechanism of calcium-induced calcium release from the cell's endoplasmic reticulum mediated by inositol trisphosphate, whose deterministic (Chaps. 3 and 5) and stochastic aspects (Chap. 4) are both considered in detail. Emphasis is then given on possible mechanisms of stimulus encoding of astrocytes by means of their intracellular calcium dynamics (Chaps. 5 and 6) and how these mechanisms could account for lateral information transfer in neuron–glial networks (Chap. 7). The interaction between astrocytes and synapses is considered in Part III with Chaps. 8 and 9 providing a detailed overview of the mechanisms of interaction by glutamatergic and purinergic gliotransmission. Chapter 10 then presents a general framework to model gliotransmission and discusses some of the potential functional implications of gliotransmitter-mediated regulation of synaptic plasticity. Chapter 11 instead reviews some modeling approaches to study the effect of dysfunctional astrocytic regulation of synaptic transmission in the onset of brain disorders. In Part IV, further mechanisms of interaction of astrocytes with neurons other than gliotransmission are considered. These include uptake of neurotransmitters by astrocytes (Chaps. 12 and 13), astrocyte-mediated regulation of extracellular potassium homeostasis (Chap. 14), and metabolic coupling between astrocytes and neurons (Chap. 15). Finally, Part V provides an overview of computational models (Chap. 16) and practical techniques (Chaps. 17 and 18) to analyze and simulate astrocytic calcium signaling and neuron–glial interactions in general.

In an attempt to ease the approach to modeling glia, both to the reader without previous exposure to glial biology and the one without a computational background, we attempted, whenever possible, to narrow biological information down to concise mechanistic details. At the same time, while we do not hesitate to employ the level of analysis needed to be precise and rigorous, we review technical aspects and mathematical details on the derivation of model presented in the book in dedicated appendices at the end of individual chapters. In these appendices, the reader may also find details on the derivation and estimation of parameters used in the simulations of the models presented in the book. The code for simulations presented in Chaps. 3, 5, 7, 10, and 18 is made freely available on the online repository associated with this book: <https://github.com/mdepitta/comp-glia-book>.

Acknowledgements

A substantial part of this book was originally conceived during a workshop on “Computational Methods and Modeling of Astrocyte Physiology and Neuron-Glia Interactions” organized by the editors within the framework of the annual meeting of the Organization for Computational Neurosciences in the summer of 2014. Some of the contributing authors of the book were also speakers at the workshop, and others instead were invited later to join. To all of them, we express our sincere gratitude for investing their time, effort, and patience that ultimately made possible the ambitious project of this book to turn into reality. We are also extremely grateful to a large number of colleagues at many institutions who have painstakingly read, commented on, and critically reviewed numerous versions of all the chapters. We particularly thank Benjamin Auffart, Maxwell Gillett, Joules Lallouette, Marja-Leena Linne, Roger Min, David Ropers, Mirko Santello, Mark Sherwood, Alexander Skupin, James Sneyd, Rüdiger Thul, Yulia Tomifeeva, and Vladislav Volman.

We received also significant additional advice from Alfonso Araque, David Attwell, Nicolas Brunel, Renaud Jolivet, Stéphane Oliet, Aude Panatier, Vladimir Parpura, Misha Tsodyks, and Andrea Volterra. We would like to dedicate this book to the memory of Eshel Ben-Jacob whose excitement for glia ignited our interest on the topic. MDP wishes to acknowledge the support of the Junior Leader Fellowship Program by “la Caixa” Banking Foundation (LCF/BQ/LI18/11630006), as well as the support by the Basque Government through the BERC 2018–2021 program and by the Spanish Ministry of Science, Innovation and Universities: BCAM Severo Ochoa accreditation SEV-2017-0718. During the writing of this book MDP was also supported by the European Commission by an Alain Bensoussan Fellowship from the European Research Consortium for Informatics and Mathematics, and by an International Outgoing Fellowship from the Marie Skłodowska-Curie Actions. Finally, we apologize to anyone we have inadvertently omitted from these lists.

Bilbao, Bizkaia, Spain
Lyon, France
November 2018

Maurizio De Pittà
Hugues Berry

Contents

Part I Introduction

- 1 A Neuron–Glial Perspective for Computational Neuroscience 3
Maurizio De Pittà and Hugues Berry

Part II Calcium Dynamics

- 2 Data-Driven Modelling of the Inositol Trisphosphate Receptor (IP₃R) and its Role in Calcium-Induced Calcium Release (CICR) 39
Ivo Siekmann, Pengxing Cao, James Sneyd and Edmund J. Crampin
- 3 Intracellular Calcium Dynamics: Biophysical and Simplified Models 69
Yulia Timofeeva
- 4 Modeling of Stochastic Ca²⁺ Signals 91
Sten Rüdiger and Jianwei Shuai
- 5 G Protein-Coupled Receptor-Mediated Calcium Signaling in Astrocytes 115
Maurizio De Pittà, Eshel Ben-Jacob and Hugues Berry
- 6 Emergence of Regular and Complex Calcium Oscillations by Inositol 1,4,5-Trisphosphate Signaling in Astrocytes 151
Valeri Matrosov, Susan Gordleeva, Natalia Boldyreva,
Eshel Ben-Jacob, Victor Kazantsev and Maurizio De Pittà

- 7 Astrocyte Networks and Intercellular Calcium Propagation** 177
Jules Lallouette, Maurizio De Pittà and Hugues Berry

Part III Tripartite Synapse and Regulation of Network Activity

- 8 Gliotransmission at Tripartite Synapses** 213
Candela González-Arias and Gertrudis Perea
- 9 Purinergic Signaling at Tripartite Synapses** 227
Anup Pillai and Suhita Nadkarni
- 10 Gliotransmitter Exocytosis and Its Consequences
on Synaptic Transmission** 245
Maurizio De Pittà
- 11 Computational Models of Pathophysiological Glial Activation
in CNS Disorders** 289
Vladislav Volman and Maxim Bazhenov

Part IV Homeostasis and Metabolic Coupling

- 12 The Role of Astrocytes in Neurotransmitter Uptake
and Brain Metabolism** 309
Annalisa Scimemi
- 13 Glutamate Uptake by Astrocytic Transporters** 329
Konstantin Mergenthaler, Franziska Oschmann and Klaus Obermeyer
- 14 Astrocytic Ion Dynamics: Implications for Potassium
Buffering and Liquid Flow** 363
Geir Halnes, Klas H. Pettersen, Leiv Øyehaug, Marie E. Rognes
and Gaute T. Einevoll
- 15 Constraint-Based Modeling of Metabolic Interactions
in and Between Astrocytes and Neurons** 393
Tunahan Çakır

**Part V Computational Tools to Analyze and Model Astrocyte
Experiments**

- 16 Computational Models of Astrocytes and Astrocyte–Neuron
Interactions: Characterization, Reproducibility, and Future
Perspectives** 423
Tiina Manninen, Riikka Havela and Marja-Leena Linne

17 GECIquant: Semi-automated Detection and Quantification of Astrocyte Intracellular Ca^{2+} Signals Monitored with GCaMP6f	455
Sharmila Venugopal, Rahul Srinivasan and Baljit S. Khakh	
18 Modeling Neuron–Glia Interactions with the <i>Brian 2 Simulator</i>	471
Marcel Stimberg, Dan F. M. Goodman, Romain Brette and Maurizio De Pittà	

Contributors

Maxim Bazhenov Department of Medicine, University of California, San Diego, CA, USA

Eshel Ben-Jacob School of Physics and Astronomy, Tel Aviv University, Ramat Aviv, Israel

Hugues Berry EPI BEAGLE, INRIA Rhône-Alpes, Villeurbanne, France

Natalia Boldyreva N.I. Lobachevsky State University of Nizhni Novgorod, Nizhny Novgorod, Russia

Romain Brette Sorbonne Universités, INSERM, CNRS, Institut de la Vision, Paris, France

Tunahan Çakır Department of Bioengineering, Gebze Technical University, Kocaeli, Turkey

Pengxing Cao Department of Mathematics and Statistics, University of Melbourne, VIC, Australia

Edmund J. Crampin Systems Biology Laboratory, Department of Mathematics and Statistics, Melbourne School of Engineering, School of Medicine, University of Melbourne, Melbourne, VIC, Australia

Maurizio De Pittà Group of Mathematical, Computational and Experimental Neuroscience, Basque Center for Applied Mathematics, Bilbao, Biscay, Spain; Department of Neurobiology, The University of Chicago, Chicago, IL, USA; EPI BEAGLE, INRIA Rhône-Alpes, Villeurbanne, France

Gaute T. Einevoll Faculty of Science and Technology, Norwegian University of Life Sciences, Ås, Norway; Department of Physics, University of Oslo, Oslo, Norway

Candela González-Arias Functional and Systems Neurobiology, Cajal Institute (CSIC), Madrid, Spain

Dan F. M. Goodman Department of Electrical and Electronic Engineering, Imperial College London, London, UK

Susan Gordleeva N.I. Lobachevsky State University of Nizhni Novgorod, Nizhny, Novgorod, Russia

Geir Halnes Faculty of Science and Technology, Norwegian University of Life Sciences, Ås, Norway

Riikka Havela Computational Neuroscience Group, Faculty of Biomedical Sciences and Engineering, BioMediTech Institute, Tampere University of Technology, Tampere, Finland

Victor Kazantsev N.I. Lobachevsky State University of Nizhni Novgorod, Nizhny, Novgorod, Russia

Baljit S. Khakh Department of Physiology, David Geffen School of Medicine, University of California, Los Angeles, Los Angeles, CA, USA; Department of Neurobiology, David Geffen School of Medicine, Los Angeles, CA, USA

Jules Lallouette EPI BEAGLE, INRIA Rhône-Alpes, Villeurbanne, France

Marja-Leena Linne Computational Neuroscience Group, Faculty of Biomedical Sciences and Engineering, BioMediTech Institute, Tampere University of Technology, Tampere, Finland

Tiina Manninen Computational Neuroscience Group, Faculty of Biomedical Sciences and Engineering, BioMediTech Institute, Tampere University of Technology, Tampere, Finland

Valeri Matrosov N.I. Lobachevsky State University of Nizhni Novgorod, Nizhny, Novgorod, Russia

Konstantin Mergenthaler Neural Information Processing, Electrical Engineering and Computer Science, Bernstein Center for Computational Neuroscience, Technische Universität Berlin, Berlin, Germany

Suhita Nadkarni Indian Institute of Science Education and Research, Pune, India

Klaus Obermeyer Neural Information Processing, Electrical Engineering & Computer Science and Bernstein Center for Computational Neuroscience, Technische Universität Berlin, Berlin, Germany

Franziska Oschmann Neural Information Processing, Electrical Engineering & Computer Science and Bernstein Center for Computational Neuroscience, Technische Universität Berlin, Berlin, Germany

Leiv Øyehaug Faculty of Technology, Art and Design, OsloMet - Oslo Metropolitan University, Oslo, Norway

Gertrudis Perea Functional and Systems Neurobiology, Cajal Institute (CSIC), Madrid, Spain

Klas H. Pettersen Letten Centre and GliaLab, Centre for Molecular Medicine, University of Oslo, Oslo, Norway

Anup Pillai Indian Institute of Science Education and Research, Pune, India

Marie E. Rognes Simula Research Laboratory, Fornebu, Norway; Department of Mathematics, University of Oslo, Oslo, Norway

Sten Rüdiger Institute of Physics, Humboldt-Universität zu Berlin, Berlin, Germany

Annalisa Scimemi Department of Biology, SUNY Albany, Albany, NY, USA

Jianwei Shuai Department of Physics, State Key Laboratory of Cellular Stress Biology, Innovation Center for Cell Signaling Network, Xiamen University, Xiamen, China

Ivo Siekmann Department of Applied Mathematics, James Parsons Building, Liverpool, Merseyside, UK

James Sneyd Department of Mathematics, University of Auckland, Auckland, New Zealand

Rahul Srinivasan Department of Neuroscience and Experimental Therapeutics, Texas A&M University College of Medicine, Bryan, TX, USA

Marcel Stimberg Sorbonne Universités, INSERM, CNRS, Institut de la Vision, Paris, France; BCAM - Basque Center for Applied Mathematics, Bilbao, Spain

Yulia Timofeeva Department of Computer Science, Centre for Complexity Science, University of Warwick, Coventry, UK

Sharmila Venugopal Department of Integrative Biology and Physiology, Division of Life Sciences, University of California, Los Angeles, Los Angeles, CA, USA

Vladislav Volman Progenity Inc., San Diego, CA, USA

Part I

Introduction

Chapter 1

A Neuron–Glial Perspective for Computational Neuroscience



Maurizio De Pittà and Hugues Berry

Abstract There is growing excitement around glial cells, as compelling evidence point to new, previously unimaginable roles for these cells in information processing of the brain, with the potential to affect behavior and higher cognitive functions. Among their many possible functions, glial cells could be involved in practically every aspect of the brain physiology in health and disease. As a result, many investigators in the field welcome the notion of a neuron–glial paradigm of brain function, as opposed to Ramon y Cajal’s more classical neuronal doctrine which identifies neurons as the prominent, if not the only, cells capable of a signaling role in the brain. The demonstration of a brain-wide neuron–glial paradigm however remains elusive and so does the notion of what neuron–glial interactions could be functionally relevant for the brain computational tasks. In this perspective, we present a selection of arguments inspired by available experimental and modeling studies with the aim to computational neuroscience that no longer is a mere prerogative of neuronal signaling but rather it is the outcome of complex interaction between neurons and glial cells.

Keywords Neuron–glia paradigm · Calcium coding · Neuron–glial systems
Oligodendrocytes · Microglia

Abbreviations

Ado	Adenosine
AMPA (AMPAR)	α -Amino-3-hydroxy-5-methyl-4-isoxazolepropionic acid (receptor)
ANLS	Astrocyte-to-neuron lactate shuttle

M. De Pittà (✉)

Group of Mathematical, Computational and Experimental Neuroscience, Basque Center for Applied Mathematics, Bilbao, Biscay, Spain
e-mail: maurizio.depitta@gmail.com

M. De Pittà · H. Berry

EPI BEAGLE, INRIA Rhône-Alpes, Villeurbanne, France

AP	Action potential
AQP4	Aquaporin channel type 4
cAMP	Cyclic adenosine monophosphate
CICR	Calcium-induced calcium release
CNS	Central nervous system
ECS	Extracellular space
GABA	γ -Aminobutyric acid
GGC	Glutamate–glutamine cycle
GPCR	G protein–coupled receptor
IP ₃	Inositol 1,4,5-trisphosphate
Kir	Inwardly rectifying K ⁺ channel
LTD	Long-term depression
LTP	Long-term potentiation
MCT	Monocarboxylate transporter
NA	Noradrenaline
NBC	Na ⁺ -HCO ₃ ⁻ cotransporter
NKP	Na ⁺ /K ⁺ -ATPase pump
NMDA (NMDAR)	<i>N</i> -Methyl-D-aspartate (receptor)
SIC (SOC)	Slow inward (outward) current
SON	Supraoptic nucleus
SSR	Steady-state synaptic release
TNF α	Tumor necrosis factor alpha
V1	Primary visual cortex

1.1 Introduction

A decade ago, Ben Barres began his famous review on “The Mystery and Magic of Glia” recalling how he first became interested in the function of glial cells as a young neurologist in training. As he looked at brain sections from various neurological diseases under the microscope, not only he came to realize that at least a half of the brain cells are glial cells—astrocytes, oligodendrocytes, and microglial cells—but also that glial cell phenotypes are radically altered in many brain injuries and diseases (Barres 2008). These early observations grew in him the wonder of what glial cells normally do, and what their role in the disease is—a question that still lingers, beyond his lifetime achievements and the many other findings by his peers.

It is almost 30 years since the seminal discovery by Anne Cornell-Bell and colleagues that glutamate evokes calcium concentration rises in astrocytes (Cornell-Bell et al. 1990)—a phenomenon later confirmed in slices (Dani et al. 1992; Porter and McCarthy 1996; Newman and Zahs 1997) and in vivo (Wang et al. 2006), which could also occur in other glia types (Biber et al. 1999; Alberdi et al. 2002; Butt et al. 2004)—and yet our understanding of the functional role of glial calcium signaling is still very limited. As Ca²⁺ signaling can propagate along astrocytic processes and even between glial cells as waves (Cornell-Bell et al. 1990; Dani et al. 1992; Newman and Zahs 1997; Hirase et al. 2004; Nimmerjahn et al. 2004), the possibility that

glial Ca^{2+} waves might constitute an extraneuronal signaling system in the CNS was raised (Newman and Zahs 1997). The next step was reached with the demonstration that increases in cytosolic Ca^{2+} concentration of astrocytes could regulate the release of neuroactive molecules (Parpura et al. 1994; Nedergaard 1994; Jeftinija et al. 1996; Coco et al. 2003; Benz et al. 2004) and hormones (Krzan et al. 2003) or influence ion homeostasis (Price et al. 2002). The possibility that these astrocytic Ca^{2+} transients could influence neurons (Parpura et al. 1994; Nedergaard 1994) and vascular smooth muscles (Zonta et al. 2003; Mulligan and MacVicar 2004; Gordon et al. 2007), led to the idea that astrocytes are powerful regulators of neuronal spiking, synaptic plasticity, and cerebral blood flow (Nedergaard et al. 2003; Haydon and Carmignoto 2006).

The current consensus is that neuronal spiking, synaptic plasticity, and the coupling between neurons and the vasculature underpin higher brain functions (Laughlin and Sejnowski 2003). The recognition that glial cells could be much more than passive bystanders of neurons and their synapses has therefore been welcomed as a revolution of the classical neuron paradigm of the brain in favor of a more comprehensive neuron–glial paradigm (Haydon 2001). Nonetheless, few topics in neuroscience are as controversial as the idea that glia could be an active partner in information processing, and cognitive and behavioral tasks elaborated by neurons. In part, this is due to a lack of definite experimental evidence. But in our opinion, much of the controversy originates from the lack of a theoretical platform whereupon to elaborate the neuron–glial paradigm. This perhaps comes without surprise in a context where theoretical studies in neuroscience claim they are able to account for many of the computational tasks performed by our brain by the sole consideration of neurons (Abbott et al. 2016). However, understanding the activity patterns of neural activity that support sensory processing (Ganmor et al. 2015), memory (Buzsáki 2010), decision-making (Beck et al. 2008), and cognition (Rigotti et al. 2013) remains a major challenge for neuroscience theories. In the following, we argue that such theories should also take into account a glial component, as we point out to key mechanisms of computational value that are mediated by glia.

1.2 Glial Codes

When talking about neurons, the term “neural code” refers to the properties of a single sequence of action potentials (spike trains) or a spike train ensemble to encode, decode, and process sensory and/or cognitive information (Perkel and Bullock 1968). Experimental and theoretical approaches to investigate the neural code are often based on presenting different inputs (stimuli) to an animal, and quantifying various properties of the generated spike patterns (Bialek and Rieke 1992). Is it possible to think of an analogous code for glial cells?

Because glial cells are notoriously electrically passive (Tasaki and Chang 1958; Steinhäuser et al. 1992), their code (if any) must rely on mechanisms that are different from the membrane potential, and these mechanisms are likely to be found among

the many intracellular signaling pathways occurring within glial cells. Supported by modeling arguments (Kummer et al. 2000; Violin et al. 2008; De Pittà et al. 2009), signals originating from receptors in the glial plasma membrane could all be potential candidates, as long as they bear strong correlation between the triggering extracellular stimulus and the downstream intracellular events, so as not to loose information about the former. This could be the case, for example, of second messengers like inositol 1,4,5-trisphosphate (IP_3), intracellular calcium, or cyclic adenosine monophosphate (cAMP) which result from the activation of a rich panoply of G protein–coupled receptors (GPCRs) expressed by glial cells (Porter and McCarthy 1997; Káradóttir and Attwell 2007; Pocock and Kettenmann 2007). However, the diversity of these receptors, and the fact that they are linked to different signaling cascades— G_q -PCRs to IP_3/Ca^{2+} signaling, and G_s - and $G_{i/o}$ -PCRs, respectively, to stimulation and inhibition of cAMP (Gilman 1987)—suggest that there might be multiple glial codes at play.

Among the possible glial codes, calcium signaling is the most studied one, arguably because of the availability of indicators to monitor intracellular Ca^{2+} (Rusakov 2015), as well as for its recognized function as intracellular messenger in a multitude of other cells (Berridge et al. 2000). There are nonetheless further reasons why Ca^{2+} signaling could be an effective code for glial cells. In particular, Ca^{2+} signaling could serve all the four key functions originally proposed by Perkel and Bullock for a candidate neural code: stimulus representation, interpretation, transformation, and transmission (Perkel and Bullock 1968).

Stimulus representation is broadly defined as the capability to reflect (or encode) extracellular stimuli by detectable changes in the cell activity. Stimulus representation is clearly carried out by Ca^{2+} signaling, which is at the core of our current notion of glial excitability (Zorec et al. 2012). By such notion, we refer to the ability of glial cells to respond to extracellular stimuli by transient increases of their intracellular Ca^{2+} concentration (Butt 2006; Agulhon et al. 2008; Kettenmann et al. 2011). And accordingly, we dub a glial cell as “activated” when its intracellular Ca^{2+} dynamics departs from a baseline concentration (Verkhratsky and Kettenmann 1996; Hoffmann et al. 2003). Because intracellular Ca^{2+} is a simple ion, one expects the associated signal should be encoded in temporal and spatial patterns of intracellular Ca^{2+} concentration (Fig. 1.1, *yellow pathways*), very similar to the use of electric voltage or current signals in information technology (Jaffe 1993). The ways by which a stimulus could be represented by glial calcium are multiple. **The arguably simplest way possibly is that the concentration of the extracellular agonist is encoded in the frequency, or amplitude, or a combination thereof, of the sequence of Ca^{2+} elevations ensuing from stimulation (Schuster et al. 2002; De Pittà et al. 2008).**

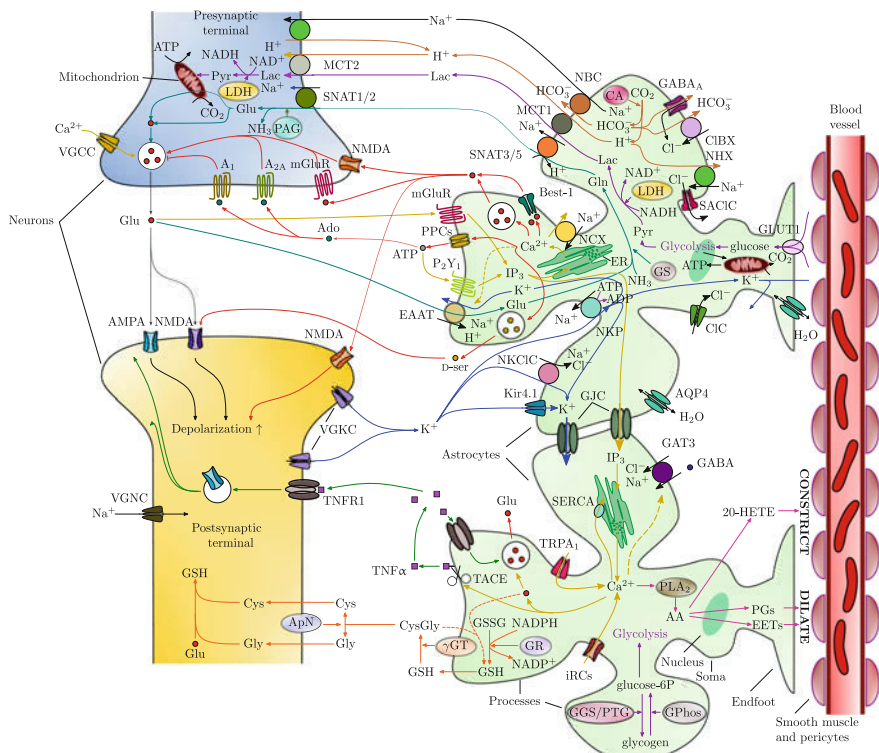
Interpretation refers to the possibility to reliably decode the information on the stimulus carried by the candidate code. In the case of glial Ca^{2+} signaling, decoding is a necessary readout step for any mechanism that uses intracellular Ca^{2+} to perform a downstream action, be it, for example, the release of neuroactive molecules (Liu et al. 2006; Frühbeis et al. 2013; Imura et al. 2013; Araque et al. 2014) and myelin-related proteins (Krämer-Albers et al. 2007), the regulation of the blood flow (Haydon and Carmignoto 2006; Attwell et al. 2010) or the transcription of cellular factors (O’Neill and Kaltschmidt 1997). All these processes seem to be strongly constrained by intracellular Ca^{2+} dynamics: some of them require intracellular Ca^{2+} concentration to overcome a threshold value in order to occur (Dolmetsch et al. 1997; Parpura and Haydon 2000; Pasti et al. 2001; Liu et al. 2006), while others depend, in magnitude, on intracellular Ca^{2+} concentration (Zonta et al. 2003; Krämer-Albers et al. 2007). **Gliotransmitter exocytosis from astrocytes appears to occur preferentially during rising phases of Ca^{2+} elevations** (Pasti et al. 1997; Marchaland et al. 2008), hinting a preferential dependence on the frequency rather than the duration of these elevations (De Pittà et al. 2011). Conversely, the activation of transcription factors positively correlates with the amplitude and duration of Ca^{2+} increases (Dolmetsch et al. 1997). Taken together, these observations hint the existence of readout mechanisms that are finely tuned to extract selective features of the Ca^{2+} signal.

Transformation. The Ca^{2+} signal that is generated within glial cells must be manipulated (i.e., transformed) in a controlled way to allow computations of some sort in order to be effectively regarded as a code. Consider, for example, the formation of a Ca^{2+} wave, that is a range of Ca^{2+} concentration transients traveling through the cytoplasm of a glial cell or a group of glial cells (Leybaert and Sanderson 2012). One hypothesis states that these waves result from the spatiotemporal summation of short-lived, spatially confined Ca^{2+} puffs (Marchant and Parker 2001) whose coordination is possible by inherent cellular properties, like the characteristic distance between Ca^{2+} puff sites and their spatial coupling set by local Ca^{2+} buffers (Skupin et al. 2008). In this example, the generation of the wave is a transformation of the local Ca^{2+} signal. The growing recognition of a compartmentation of Ca^{2+} signals within glial cells, like astrocytes in the cortex (Bindocci et al. 2017) or Bergman cells in the cerebellum (Grosche et al. 1999), also supports the hypothesis of a transformation on Ca^{2+} signals by the cellular architecture, based on control by this latter of the genesis, dynamics and extension of Ca^{2+} waves.

Transmission. The candidate code must also enable transmission of information between different cells, allowing for the exchange and propagation of information across cell networks. The propagation of intercellular Ca^{2+} waves in astrocyte networks has been observed in the cortex (Nimmerjahn et al. 2004), the hippocampus (Kuga et al. 2011), the retina (Newman 2001), or the cerebellum (Hoogland et al. 2009). Ca^{2+} waves could as well occur in microglia and oligodendrocytes either independently (Takeda et al. 1995; Wu et al. 2013; Jiang et al. 2017) or in interaction with astrocytes (Verderio and Matteoli 2001; Schipke et al. 2002; Parys et al. 2010).

Taken together, Ca^{2+} signaling seems to match the four key functions above. There are however several obstacles on the path of the identification of Ca^{2+} signaling as a glial code. First of all, Ca^{2+} signaling is stochastic, a property that has mostly been

studied with Ca^{2+} spikes in cultured astrocytes and microglia (Skupin et al. 2008; Thurley and Falcke 2011; Thurley et al. 2012, 2014). This stochasticity largely complicates the analysis of glial Ca^{2+} signaling. Moreover, at the molecular level, there might be more than a single Ca^{2+} signaling system at play in glia cells, and those different systems might be segregated to distinct regions of the cell (Volterra et al. 2014). The best-known example of this anisotropy is provided by astrocytes, where the main mechanism of Ca^{2+} transients is believed to be Ca^{2+} exchange between the endoplasmic reticulum and the cytosol (Scemes and Giaume 2006; Leybaert and Sanderson 2012). However, knockout of $\text{IP}_3\text{R}2$ receptors—generally considered the main channels responsible of this exchange (Zhang et al. 2014)—indeed abolished nearly all Ca^{2+} transients in astrocytic somata, but spared roughly half of those transients in the processes (Srinivasan et al. 2015). The molecular mechanisms for those $\text{IP}_3\text{R}2$ -independent Ca^{2+} transients in the processes could rely on additional extracellular calcium fluxes from plasma membrane channels (Srinivasan et al. 2015) or on type-1 or type-3 IP_3R (Sherwood et al. 2017), or a combination thereof.



◀Fig. 1.1 Interaction of astrocytes with neuropil and vasculature. Simplified illustration of the main pathways of interaction of astrocytes with neurons at glutamatergic synapses. (*yellow pathway*) **Calcium signaling**. Glutamate (Glu) spillover from the synaptic cleft targets metabotropic receptors (mGluR) on perisynaptic astrocytic processes which trigger inositol 1,4,5-trisphosphate (IP₃)-mediated calcium (Ca²⁺) release from the cell's endoplasmic reticulum (ER). IP₃ can also diffuse intra- and intercellularly by gap junction channels (GJCs), allowing regenerative propagation of Ca²⁺ signaling to other regions of the cell or neighboring astrocytes. Intracellular Ca²⁺ transients in astrocytic processes can also occur by spontaneous opening of transient receptor potential channels TRPA₁ (Shigetomi et al. 2013), or by neurotransmitter-gated ionotropic receptor channels (iRCs) such as AMPA and NMDA channels and purine-bound P2X channels (Newman 2005; Suadicani et al. 2006; Hamilton et al. 2008; Palygin et al. 2010; Lind et al. 2013). Excess Ca²⁺ is pumped out of the cell by the sodium Na⁺/Ca²⁺ exchanger (NCX) or into the ER by (sarco)endoplasmic reticulum Ca²⁺/ATPase (SERCA) pumps. (*red pathway*) **Gliotransmission**. Transient cytosolic Ca²⁺ increases may trigger release of neuroactive molecules (or “gliotransmitters”) from astrocytes by multiple pathways. These pathways include glutamate release by exocytosis or by bestrophin-1 (Best-1) ion channels (Sahler et al. 2014), and release of ATP by vesicular exocytosis (not shown) or by purine-permeable channels (PPCs) (Stout et al. 2002; Suadicani et al. 2006; Bowser and Khakh 2007). Extracellular ATP is rapidly degraded into adenosine (Ado) which, along with glutamate of astrocytic origin, can target different receptors on presynaptic and postsynaptic elements, thereby modulating synaptic transmission and neuronal excitability (Savtchouk and Volterra 2018). Either with glutamate (not shown) or independently, astrocytes can also release D-serine (D-ser), which is the main co-agonist (with glutamate) of postsynaptic NMDA receptors at many synapses (Mothet et al. 2000; Henneberger et al. 2010; Papouin et al. 2012). (*green pathway*) **Cytokine signaling**. Among possible signals mediated by astrocytes is also the release of cytokine tumor necrosis factor alpha (TNF α) by Ca²⁺-dependent TNF α -converting enzyme (TACE) (Bezzi et al. 2001). This cytokine—which is also present in the extracellular milieu at constitutive concentrations <100 to 200 pM—may target both astrocytic and synaptic TNF receptors (TNFR1). In the astrocyte, this modulates glutamatergic gliotransmission via a yet-unresolved pathway (Santello and Volterra 2012); at synapses it modulates instead insertion (endocytosis) of postsynaptic AMPA (GABA) receptors (not shown) (Stellwagen et al. 2005; Pribiag and Stellwagen 2013; Lewitus et al. 2014). (*turquoise pathway*) **Glutamate–glutamine cycle**. Astrocytic excitatory amino acid transporters (EAATs) are responsible for the uptake of a large fraction of glutamate at the synapse. Glutamate is converted into glutamine by glutamine synthetase (GS) and shuttled back to neurons by Na⁺-coupled neutral amino acid transporters (SNATs) (Mackenzie and Erickson 2004). Once in the neuron, glutamine is reconverted to glutamate by phosphate-activate glutaminase (PAG), and the ensuing glutamate may either be (transiently) consumed by oxidative metabolism of mitochondria, or be used to refill synaptic vesicles. The whole process is coupled with ammonia (NH₃) homeostasis and also accounts for GABA synthesis from glutamate at inhibitory synapses (not shown), possibly in association with astrocytic uptake by GABA transporter 3 (GAT3) (Rothman et al. 2003; Hertz 2013). Significantly, expression of astrocytic EAATs and GATs may be modulated by intracellular Ca²⁺ (*dashed yellow pathways*) (Mashimo et al. 2010; Shigetomi et al. 2012; Devaraju et al. 2013). (*blue pathway*) **Potassium buffering**. Astrocytes buffer excess potassium (K⁺) released into the extracellular space as a result of neuronal activity. Excess extracellular K⁺ is taken up mostly by inwardly rectifying K⁺ channels (Kir4.1) in conjunction with Na⁺/K⁺-ATPase (NKP) pumps and Na⁺-K⁺-2Cl⁻ cotransporters (NKCIC), all of which are richly expressed on perisynaptic astrocytic processes. Potassium ions then travel down their concentration gradient through the astrocyte's cytoplasm, or through gap junction channels to other cells, where they are released at sites of lower extracellular K⁺ concentration or shunted to the vascular system (Kofuji and Newman 2004; Simard and Nedergaard 2004). The pathway is coupled with the cell's water homeostasis by aquaporin channels (AQP4), as well as with glutamate uptake, since intracellular K⁺ controls astrocytic transporters' stoichiometry together with extracellular Na⁺ and H⁺ (Sect. 1.5). (*purple pathway*) **Lactate shuttle**. Glutamate uptake is accompanied

◀Fig. 1.1 (continued)

by Na^+ influx into the astrocyte which is counteracted by the action of NKPs. The resulting increase in ADP/ATP ratio triggers anaerobic glucose utilization in astrocytes by glycolysis which may be associated with glycogenolysis and/or with glucose uptake from the circulation by glucose transporter GLUT1. Lactate dehydrogenase (LDH) catalyzes the interconversion of pyruvate (Pyr) from glycolysis into lactate (and vice versa) with concomitant interconversion of NADH and NAD^+ . Lactate (Lac) is then shuttled to neurons through monocarboxylate transporters (mainly MCT1 in astrocytes and MCT2 in neurons), where it can be used as an energy substrate after its re-conversion to pyruvate (Allaman et al. 2011). (*brown pathway*) *pH buffering*. Abundant carbonic anhydrase (CA) in astrocytes converts CO_2 resulting from cellular metabolism (plus H_2O) into H^+ and HCO_3^- . Two HCO_3^- are transported into the extracellular space along with one Na^+ via the Na^+ -coupled bicarbonate transporter (NBC), thereby increasing the extracellular buffering power. The efflux of HCO_3^- induces extracellular alkalinization and also occurs by activation of GABA_A channels as well as by $\text{Cl}^-/\text{HCO}_3^-$ exchanger (CIBX). Excess H^+ in astrocytes is extruded via Na^+/H^+ exchanger (NHX). Chloride and bicarbonate homeostasis are also intimately related to cell volume regulation (Sect. 1.5). (*orange pathway*) *Glutathione metabolism*. Astrocytes release glutathione (GSH) in the extracellular space where it is cleaved by the astrocytic ectoenzyme γ -glutamyl transpeptidase (γ GT) to produce cysteinylglycine (CysGly). In turn, CysGly is cleaved by neuronal ectoaminopeptidase N (ApN), forming cysteine (Cys) and glycine (Gly), which serve as precursors for neuronal GSH synthesis (Aoyama et al. 2008). In the astrocyte the reduced form of glutathione (i.e., GSH) is obtained by multiple pathways including recycling of extracellular CysGly, *de novo* synthesis from intracellular glutamate, or precursors of it like glutamine (*dashed orange arrow*), or by oxidized glutathione (GSSG) via NADPH-dependent glutathione reductase (GR) (Dringen 2000). Astrocytic GSSG ensues from oxidative metabolism but may also be linked with the ANLS via NADP^+ -dependent ascorbic acid/vitamin C recycling (not shown, see Castro et al. (2009)). NADPH/NADP⁺ can instead be modulated by NADH/NAD⁺ either in the cytoplasm or in mitochondria (Ying 2008), although astrocytic NADPH production seems strongly dependent on pentose phosphate pathway-mediated metabolism of glucose 6-phosphate (glucose-6P) (Dringen 2000)—the main available form of intracellular glucose obtained from uptake from blood and by glycogenolysis. Shuttling of GSH between astrocytes and neurons is essential in providing precursors for neuronal GSH synthesis and makes astrocytes key players in neuroprotection against oxidative stress. (*magenta pathway*) *Vascular coupling*. Ca^{2+} rise in the astrocyte may also stimulate generation of arachidonic acid (AA) from phospholipase A₂ (PLA₂), which is converted to prostaglandins (PGs) and epoxyeicosatrienoic acids (EETs) (by cyclooxygenases) to dilate blood vessels through astrocytic endfeet—which are specialized astrocytic processes contacting blood vessels. Alternatively, astrocytic AA passes via endfoot to the smooth muscle surrounding capillaries, and there it is converted into 20-hydroxy-eicosatetraenoic acid (20-HETE) (by ω -hydroxylase) which constricts vessels (Attwell et al. 2010). CIC: chloride channel; NAD^+ (NADH): oxidized (reduced) nicotinamide adenine dinucleotide; NADP^+ (NADPH): oxidized (reduced) nicotinamide adenine dinucleotide phosphate; GPhos: glycogen phosphorylase; GGS/PTG: glycogen synthase/UTP-glycogen-phosphate uridylyltransferase; SACIC: swell-activated chloride channel; VGCC: voltage-gated Ca^{2+} channel; VGKC: voltage-gated K^+ channel

The presence of different mechanisms of Ca^{2+} spiking has also been suggested to account for the variety of the spatiotemporal scales of Ca^{2+} signals that include fast Ca^{2+} events (move values in parentheses here), locally confined in astrocytic processes (Di Castro et al. 2011; Bindocci et al. 2017), as well as large and longer Ca^{2+} signals (move value in parentheses here) spanning whole processes and that can invade (Volterra et al. 2014; Bindocci et al. 2017). This is reminiscent of the hierarchy of Ca^{2+} induced- Ca^{2+} release (CICR)-mediated Ca^{2+} events that, from blips and puffs—respectively, associated with the opening of individual IP₃R receptors or

a cluster thereof—can ultimately lead to the generation of cell-wide Ca^{2+} spikes (Skupin et al. 2008; Thurley and Falcke 2011).

There is however evidence that the distribution of intervals between consecutive Ca^{2+} blips or puffs at the astrocyte periphery may be different from those reported for CICR-mediated Ca^{2+} events in primary processes and somata (Bindocci et al. 2017). Therefore, a key question is whether the different Ca^{2+} signals observed in astrocytes are the result of spatiotemporal summation of an underlying unique microscopic mechanism or, rather, they ensue from different microscopic mechanisms, each possibly associated to a specific location in the cell.

- can we link small local w/ large

1.3 Oligodendrocytes and Regulation of Axonal Electric Conduction

A unique specialization of glia in vertebrates is myelination, that is the ensheathing of axons by myelin (Waehneldt et al. 1986; Zalc et al. 2008). Myelination provides at least two advantages. First, compact lipid-rich myelin provides high membrane electrical resistance and low capacitance, which prevents current loss and enables rapid and efficient action potential (AP) conduction. Second, increased conduction velocity allows for computational complexity within a compact nervous system such as that of vertebrates (Fields 2008).

Oligodendrocytes are the specialized glial cells responsible both for axon myelination, and for the formation and maintenance of nodal structures and lifelong integrity of axons in the CNS (Nave 2010). By controlling the structural properties that characterize myelinated axons, oligodendrocytes likely participate to the fine-tuning of action potential shape and conduction velocity (Kimura and Itami 2009; Tomassy et al. 2014; Ford et al. 2015; Hughes et al. 2018). This could be achieved either by changes of myelin thickness or internode length or node geometry, or by a combination thereof (Ullén 2009; Fields 2008; Arancibia-Carcamo et al. 2017). For instance, adjustments of conduction speed of myelinated axons can tune propagation times to mediate sound localization (Carr and Konishi 1990; McAlpine and Grothe 2003; Seidl et al. 2010; Ford et al. 2015) or promote synchronous neuronal firing (Sugihara et al. 1993; Lang and Rosenbluth 2003). Together with delays induced by the AP-generation dynamics (Fourcaud-Trocmé et al. 2003) and those rising from synaptic processing (Markram et al. 1997), axonal conduction delays are an important property of neural interactions, which may induce a wealth of dynamical states with different spatiotemporal properties and domains of multistability which could serve different computational purposes (Roxin et al. 2005; Roxin and Montbrió 2011).

The observation that the tuning of conduction delays by oligodendrocytes continues during adulthood (Dimou et al. 2008; Young et al. 2013) suggests the thought-provoking possibility that these different states could change in an experience-dependent way, i.e., in a manner that depends on neuronal electrical activity (Fields 2009b). The potential functional and computational implications of this two-way regulation of oligodendrocyte-mediated transmission delays and neuronal activity

remain to be investigated, but we note that the active control of conduction delays of axon ensembles by oligodendrocytes may lead to time-locked patterns of activation of the neurons—a concept known as polychronization which could be of great computational significance (Izhikevich 2006).

1.4 Glia Morphology and Functional Specialization

The factors underpinning morphogenesis of neuronal structures remain poorly understood, in particular when one includes neuron–glia interactions into the framework. Experimental studies have identified a combination of transcriptional programs and a battery of molecular signals that seem to be regulated both developmentally and regionally, in a cell-specific manner (Jadhav et al. 2009; Eroglu and Barres 2010; Götz 2013; Stassart et al. 2013). A paramount example of this complex combination of factors is provided by astrocytes, the glial cells recognized as key regulators of the neuronal connectome in the cortex and hippocampus (Fields et al. 2015). In the postnatal developing brain, astrocytes are found in spatially distinct domains and express domain-specific genes that are needed to support formation of specific neural circuits and neuronal subtypes (Molofsky et al. 2014). Astrocytes also secrete a variety of molecules that regulate with spatiotemporal specificity all stages of the genesis of functional neural circuits (Allen 2013; Clarke and Barres 2013). This intimate relationship between astrocytes and synapses continues in the adult brain, with the processes of the astrocytes that wrap themselves around synapses (Reichenbach et al. 2010), engaging in a multitude of signals (Fig. 1.1). Eventually, a single astrocyte contacts approximately 20–150 thousand synapses in the rodent (Bushong et al. 2002), and ~300 thousand to 2 million synapses in the human brain (Oberheim et al. 2009). What are the possible functional impacts of this ensheathing?

One obvious possibility is that astrocytic processes are strategically positioned at synaptic loci to act as physical barriers that constrain and regulate extracellular diffusion of neurotransmitters (Ventura and Harris 1999). A realistic reconstruction of the extracellular space (ECS) between astrocytic processes and glutamatergic synapses of the hippocampus revealed a strong impact of astrocyte arrangements on glutamate diffusivity (Kinney et al. 2013). The degree of astrocytic ensheathing at glutamatergic synapses also directly dictates the rate of glutamate uptake by glial transporters—the main mechanism of glutamate uptake in the adult brain (Clements 1996; Danbolt 2001). Moreover, the degree of ensheathing seems inversely correlated with the size of dendritic spines (Medvedev et al. 2014). This suggests that, in agreement with independent theoretical arguments (Barbour 2001), smaller synapses are strongly sealed by astrocytic processes, whereas larger synapses might exhibit more glutamate spillover (Ventura and Harris 1999).

An additional element of complexity is that astrocytic processes are highly motile and may undergo structural changes in response to neural activity (Heller and Rusakov 2015). Activity-dependent plasticity of perisynaptic glial processes has been reported in the rat supraoptic nucleus in relation with parturition (Oliet et al.

2001; Piet et al. 2004), in the hypothalamic suprachiasmatic nucleus in association with circadian light/dark cycles (Becquet et al. 2008), in the hippocampus (Haber et al. 2006; Verbich et al. 2012) and the cerebellum in correlation with neural activity (Lippman et al. 2008, 2010) and in the somatosensory cortex *in vivo* by sensory stimulation (Bernardinelli et al. 2014b; Perez-Alvarez et al. 2014). Those results suggest that activity-dependent plasticity of perisynaptic glial processes is a brain-wide phenomenon, although its functional consequences are likely region-specific (Khakh and Sofroniew 2015). At hippocampal excitatory synapses, for example, astrocyte processes preferentially colocalize with the postsynaptic element (Rusakov 2001; Lehre and Rusakov 2002). Simulations of glutamate diffusion at those synapses suggest that this arrangement favors glutamate spillover to the presynaptic elements (Rusakov 2001; Lehre and Rusakov 2002). This could promote activation of presynaptic metabotropic receptors and account for feedback inhibition mediated by these receptors at mossy fiber-to-pyramidal cell synapses (Lehre and Rusakov 2002; Nicoll and Schmitz 2005; Omrani et al. 2009).

Glial transporters and the degree of glial coverage of synapses have also been implicated in the control of long-term plasticity at excitatory synapses. Astrocytic glutamate transporters gate spike-timing-dependent plasticity in the striatum *ex-vivo* (Valtcheva and Venance 2016), as well as rate-coded long-term potentiation (LTP) in the amygdala (Tsvetkov et al. 2004) and in the hippocampus (Katagiri et al. 2001; Lushnikova et al. 2009). LTP induction in the hippocampus correlates with dynamical changes of astrocytic processes at the stimulated synapses (Lushnikova et al. 2009; Bernardinelli et al. 2014b; Perez-Alvarez et al. 2014), and these changes could associate with long-lasting spine formation and remodeling (Lushnikova et al. 2009; Verbich et al. 2012; Bernardinelli et al. 2014b). Taken together, these results pinpoint a key role for activity-dependent, dynamical reshaping of glial ensheathing in the control of synapse morphology, extracellular glutamate homeostasis, and the functionality of neural circuits (Bernardinelli et al. 2014a).

1.5 Ion Homeostasis and Volume Regulation

Glial cells express a vast cassette of ion channels, transporters, and pumps, whereby they can sense and regulate extracellular ion concentrations with important functional consequences on neural activity (Kettenmann and Ransom 2013; Simard and Nedergaard 2004). One of the first recognized possible functions of astrocytes was their importance in the maintenance of extracellular K⁺ (Fig. 1.1, *blue pathway*) (Hertz 1965; Orkand et al. 1966). Although traditionally considered in a pathological context including epilepsy and spreading depression (Somjen 2002), electrophysiological recordings *in vivo* also implicate modulations of extracellular K⁺ by astrocytes in the regional control of neuronal excitability in the healthy brain (Amzica et al. 2002; Djukic et al. 2007; Chever et al. 2010). The resting membrane potential of neurons depends on intra- and extracellular concentrations of different ions (by the Goldman-Hodgkin-Katz equation) (Johnston and Wu 1995), so changes of extracellular K⁺

concentration can alter neuronal excitability. Theoretical investigations suggest that the interplay of astrocytic Na^+/K^+ pumps (NKP_s) and Kir4.1 channels (Walz 2000) can promote AP generation in conditions of low neuronal firing (Somjen et al. 2008), thus potentially contributing to the brain basal level of spontaneous neural activity (Deco et al. 2011). Alternatively, depending on the activity level, this could translate into a non-trivial positive feedback on neuronal firing, turning regular spiking dynamics into bursting (Somjen et al. 2008; Øyehaug et al. 2012; Cui et al. 2018).

Astrocyte-mediated regulation of extracellular K^+ also affects neuronal excitability by modulating the time course of glutamate at excitatory synapses (Djukic et al. 2007). For each glutamate molecule transported, glial glutamate transporters co-transport 3 Na^+ , 1 H^+ in exchange of 1 K^+ (Levy et al. 1998). Therefore, alteration of extracellular K^+ concentration is expected to change the rate of glutamate uptake, thus modulating the excitatory drive of a neuron and its firing dynamics.

Astrocytes also express a number of transporters involved in pH regulation (Deitmer and Rose 1996, see also Fig. 1.1, *brown pathway*) that may be affected by alterations of K^+ concentration and glutamate transport rate. The impact of these glial transport/uptake systems on neuronal computation would strongly depend on the stoichiometry of individual transporters and their spatial organization on the glial plasma membrane along with that of ion channels and pumps. All this can vary depending on the brain region (Kofuji and Newman 2004; Rose and Chatton 2016). In the rat optic nerve, for example, extracellular K^+ buffering seems more dependent on NKP_s than on Kir channels (Ransom et al. 2000). Similarly, glial K^+ spatial buffering, which ensues from the electrotonic propagation of a K^+ current in glial cells from ECS regions where K^+ is high to others where the concentration of this ion is low (Orkand et al. 1966), may be carried out differently in astrocytes vs. Müller glia, possibly because of the different expression and distribution of Kir channels in these cells (Kofuji and Newman 2004).

Another specificity of astrocytes in connection with extracellular ion homeostasis is that their volume can change by activity-dependent modulations of extracellular K^+ (Florence et al. 2012; Larsen et al. 2014). Although the molecular mechanisms of astrocytic swelling remain to be elucidated, colocalization of astrocytic Kir4.1 with aquaporin water channels AQP4 strongly supports a role for these channels in this phenomenon (Nagelhus et al. 2004). Compartmental modeling supports a mechanism, whereby K^+ influx into astrocytes through Kir4.1 channels, resulting from K^+ buffering of neuronal activity, sets an osmolarity gradient across the astrocyte membrane which drives extracellular water into the astrocyte by AQP4 channels, thus increasing the cell volume (Østby et al. 2009). Bicarbonate (HCO_3^-) homeostasis also plays a crucial role in physiological astrocyte swelling (Florence et al. 2012), presumably by improving the steepness of the osmolarity gradient (Østby et al. 2009).

1.6 Gliotransmission

Gliotransmission, that is the active information transfer from astrocytes to neurons (Bezzi and Volterra 2001), probably bears the widest implications in information processing. There is arguably no other concept that epitomizes the neuron–glia paradigm better than the “tripartite synapse,” whereby the astrocyte is the third active element in synaptic information transfer besides pre- and postsynaptic terminals, sensing synaptically released neurotransmitters by a variety of mechanisms, and signaling back to synaptic terminals by gliotransmission (Fig. 1.1, *red pathway*) (Araque et al. 1999, 2014). An emerging view is that gliotransmission is probably not a global, stereotyped on–off phenomenon, but rather a multifaceted one, dependent on age, circuit, stimulation, and the considered synapse (Savtchouk and Volterra 2018). Indeed, not all synapses are tripartite: ~10 to 50% of cortical and hippocampal synapses are not adjacent to any astrocytic process (Ventura and Harris 1999; Witcher et al. 2007; Kasthuri et al. 2015), and proximity of glial processes to dendritic spines varies depending on the brain area (Ventura and Harris 1999; Grosche et al. 2002) and on the considered synapse in a given area (Chao et al. 2002). The existence of such bidirectional communication between astrocytes and synapses in physiological conditions is therefore still lively debated (see, e.g., Fiacco and McCarthy (2018) and Savtchouk and Volterra (2018)). However, consideration of this possibility opens to profound functional implications as it puts astrocytes in the position to actively control synaptic transmission.

Although astrocytes can release a range of gliotransmitters, including glutamate, ATP, GABA, and D-serine (Sahleender et al. 2014), the effects of these gliotransmitters can be generalized in terms of modifications of short- and long-term properties of synapses. Consider first short-term synaptic dynamics. An important consequence of this dynamics is that synapses can act as filters of the AP sequence they transmit (Fortune and Rose 2001). However, the filtering characteristics of a given synapse is not fixed but can be adjusted through modulation of the initial release probability p_0 (Dittman et al. 2000). Depending on receptor type, gliotransmitters may either increase or decrease the value of p_0 at both excitatory and inhibitory synapses (Araque et al. 2014; Angulo et al. 2008), thereby turning high-pass filtering synapses into band-pass filtering ones, or band-pass filtering synapses into low-pass filtering ones, and vice versa (De Pittà et al. 2015). Low-pass filtering synaptic characteristics associate with derivative synaptic coding that is the transmission of variations (i.e., the derivative) of AP sequences, as opposed to high-pass filtering, which results instead in integrative synaptic coding and carries information on the count of incoming APs (Tsodyks 2005). Hence, modulation of synaptic filtering by gliotransmitters could make a synapse alternate between these different coding modes (De Pittà and Brunel 2016).

The modulation of synaptic release probability by gliotransmitters may also occur on multiple timescales (reviewed by De Pittà et al. 2015). It may last for tens of seconds up to few minutes, thus affecting synaptic transmission and network computations merely for a transient period of time. But it can become persistent and last for

tens of minutes that is on timescales that could promote long-term plastic changes of the synapse (Bear and Malenka 1994). This possibility was showed to account for long-term depression (LTD) at glutamatergic synapses between neurons in layers 4 and 2/3 of the barrel cortex (Min and Nevian 2012). Long-term modulations of synaptic release are expected to substantially alter the recruitment of postsynaptic NMDA receptors, thereby modulating the influx of Ca^{2+} ions (Froemke and Dan 2002; Froemke et al. 2006, 2010). Because the time course of postsynaptic Ca^{2+} is believed to control the outcome of spike-timing-dependent plasticity (STDP)—namely whether LTP or LTD is observed (Ismailov et al. 2004; Nevian and Sakmann 2006; Graupner and Brunel 2010), the above arguments predict that persistent alterations of synaptic release by gliotransmitters modulate STDP. Computational arguments however hint that this modulation is not straightforward and depends on the timing of gliotransmitter release from perisynaptic astrocytic processes with respect to pre- and postsynaptic APs (De Pittà and Brunel 2016).

Gliotransmitters may also modulate the probability of activation of postsynaptic receptors, either by the release of D-serine from astrocytes, which is a co-agonist for NMDA receptors with synaptically released glutamate (Oliet and Mothet 2009), or by slow depolarizing and hyperpolarizing currents (De Pittà and Brunel 2016), respectively, mediated by extrasynaptic NMDA and GABA receptors (Kozlov et al. 2006; Jiménez-González et al. 2011; Chen et al. 2012; Le Meur et al. 2012; Martín et al. 2015). How could gliotransmission affect learning via modulation of synaptic plasticity? Although this topic remains to be investigated, few theoretical studies offer some enticing insights into the question. Porto-Pazos and collaborators investigated the performance of an astrocyte-inspired learning rule to train deep learning networks in data classification and found that the trained neuron–glial networks were able to outperform identical networks without astrocytes in all discrimination tasks they implemented (Porto-Pazos et al. 2011; Alvarellos-González et al. 2012; Mesejo et al. 2015). Although those investigators do not provide any explanation for the possible mechanism whereby astrocyte-mediated plasticity could improve network learning and performance, a significant feature of their learning rule is that, for successful training, potentiation by astrocytes must be weaker than depression resulting from astrocyte inactivity (Alvarellos-González et al. 2012; Mesejo et al. 2015). In their model, this amounts to putting the threshold between LTP and LTD under the control of astrocyte activity. There is circumstantial evidence that astrocytes could modify the threshold for LTD vs. LTP induction, such as in the supraoptic nucleus—where astrocytic coverage of synapse is reduced during lactation (Panatier et al. 2006).

Philips et al. (2017) devised a modified version of the BCM rule (Bienenstock et al. 1982; Gerstner and Kistler 2002) where the threshold rate of postsynaptic firing for induction of LTD vs. LTP varies proportionally with astrocyte activation, and investigated how this rule affects development of orientation preference maps (OPMs) in a self-organizing network model of the primary visual cortex (V1) (Stevens et al. 2013). This choice not only allows reproducing map orientation experimentally observed in V1, but also reveals that, upon reduction of astrocytic radius, the periodicity of OPMs increases, while the width of individual hypercolumns decreases (Philips et al. 2017).

Since astrocyte size varies across species (Oberheim et al. 2009; López-Hidalgo et al. 2016), these results predict a causal link between astrocytic radius and the different hypercolumn widths observed in different species (Kaschube et al. 2010).

1.7 Resource Management

Glucose is the almost exclusive energetic fuel of the mammalian brain and can completely sustain neural activity acting as a substrate for the synthesis of lipids and amino acids, as well as of neurotransmitters like glutamate, GABA, or acetylcholine (Dienel 2012; Mergenthaler et al. 2013). Cerebral glucose fuels neural activity by glycolysis which converts glucose into pyruvate by the concomitant production of two molecules of ATP. Pyruvate may then either enter mitochondria, where it is oxidized by Krebs cycle, or be temporarily converted to lactate in the cytoplasm for later use. Moreover, lactate produced in one cell can also be released into the ECS and be used by other cells (Simpson et al. 2007). Glucose supply to the brain is mainly either through the interstitial fluid by blood circulation or by metabolism of intracellular glycogen—the only glucose store in the cell. Multiple mechanisms ensure neurovascular coupling, whereby local energy supply, together with the cerebral blood flow, is finely adjusted to variations of the neuronal activity to allow normal neuronal function (Magistretti and Allaman 2015). Astrocytes have been implicated in all aspects of this coupling. They can regulate cerebral blood flow, by dilating or constricting blood vessels through multiple Ca^{2+} -dependent pathways (Fig. 1.1, *magenta pathway*) (Iadecola and Nedergaard 2007; Attwell et al. 2010). In parallel, they can actively supply glucose through glycogen and by production of lactate—possibly triggered by the energy demand of excitatory synaptic activity (Magistretti and Allaman 2015).

The proposal of an astrocyte-to-neuron lactate shuttle (ANLS) was originally formulated by Pellerin and Magistretti (1994) and envisaged the generation of lactate at excitatory synapses by astrocytes, and its export to neurons where it is converted to pyruvate for ATP generation in mitochondria (Pellerin and Magistretti 2012). This scheme could regulate the energy supplied to neurons in response to their activity, since glutamate released by active neurons could promote lactate production in astrocytes by stimulating glycolytic ATP generation to power astrocytic uptake of glutamate in a positive feedback loop (Fig. 1.1, *purple pathway*). However, it is not clear under what circumstances of neuronal activation the ANLS could occur, as well as if it could be a brain-wide signaling pathway, or rather depend on the architecture of local neuron–glial circuits (Vaishnavi et al. 2010; Bélanger et al. 2011; Magistretti and Allaman 2015). At present, the only evidence *in vivo* for the ANLS sees it implicated in hippocampal LTP maintenance (Suzuki et al. 2011) and spatial working memory (Newman et al. 2011).

Astrocytes are also mediators of the glutamate–glutamine cycle (GGC) (Danbolt 2001; Hertz 2013), whereby synaptically released glutamate is taken up by astrocytic transporters and converted to glutamine by glutamine synthase—an enzyme exclu-

sively found in astrocytes (Fig. 1.1, *turquoise pathway*). Glutamine is then released to the ECS, where it is sequestered by neurons and reconverted to glutamate, and by this latter, possibly to GABA too (Rothman et al. 2003; Hertz 2013). The GGC can continuously supply neurotransmitters to neurons to sustain synaptic transmission, both at excitatory and at inhibitory synapses. At cortical and hippocampal excitatory synapses however, neurotransmitter supply by GGC was proven necessary to sustain synaptic release for prolonged, high-frequency stimulations, but appeared dispensable in conditions of low synaptic activity (Tani et al. 2014).

1.8 Microglia in Neuronal and Astrocytic Signaling

Microglial cells roughly constitute 5–15% of the brain’s cellular elements, representing the most numerous glial population in the brain after astrocytes and oligodendrocytes (Lawson et al. 1990; Pelvig et al. 2008). Although they are traditionally described to comprise the main component of the brain’s innate immune system by responding to any pathological insult, experimental observations over the past two decades also suggest an involvement of these cells in the genesis and function of neural circuits in the healthy brain (Kettenmann et al. 2013).

Microglial processes in the somatosensory and visual cortex make brief, repetitive contacts with synapses at a frequency of about once per hour (Nimmerjahn et al. 2005; Wake et al. 2009). The nature of these contacts is synapse-specific and varies with neuronal activity and brain region. Visual deprivation shifts the preferential association of V1 microglial processes to small dendritic spines that transiently grow, to a subset of bigger spines that persistently shrink (Tremblay et al. 2010). Reduction of spontaneous neuronal activity correlates with retraction of microglial processes in the visual cortex (Wake et al. 2009), but not in the somatosensory cortex (Nimmerjahn et al. 2005).

Besides a role in structural synaptic plasticity (Stevens et al. 2007; Schafer et al. 2012; Kettenmann et al. 2013), microglia could also participate in several forms of functional synaptic plasticity (Kettenmann et al. 2013; Wake et al. 2013). This could be achieved either directly, by release from microglia of plasticity-inducing molecules, or indirectly, through the modulation of gliotransmission-mediated pathways of plasticity (Sect. 1.6). In the latter scenario in particular, microglia could either promote (Pascual et al. 2011) or amplify glutamate release from astrocytes (Bezzi et al. 2001), with the potential to modulate excitatory synaptic transmission and neuronal excitability in a variegated fashion.

The proinflammatory cytokine tumor necrosis factor alpha (TNF α) is tightly related to microglia. Brain TNF α production can be stimulated by neuronal activity (Churchill et al. 2008), and the cytokine can be released into the ECS both by astrocytes and by microglia (Habbas et al. 2015; Lewitus et al. 2016). TNF α is found in low concentrations in the ECS in physiological conditions (Santello and Volterra 2012), where it seems necessary for normal glutamatergic gliotransmission (Bezzi et al. 2001; Stellwagen et al. 2005; Domercq et al. 2006; Santello et al. 2011;

Pribeag and Stellwagen 2013) and regulation of homeostatic synaptic plasticity mechanisms, like synaptic scaling (Steinmetz and Turrigiano 2010). The implication of TNF α in synaptic scaling may be important during competition with Hebbian plasticity, for instance for ocular dominance plasticity (Kaneko et al. 2008).

1.9 Glia in Higher Brain Functions

A popular argument, often raised to wow the audience, is that Albert Einstein’s brain, when first inspected, did not look statistically significantly different from that of other individuals with normal cognitive ability, except for a higher glia-to-neuron ratio, leading to speculate that the larger number of glial cells could partly have accounted for Einstein’s exceptional intelligence (Diamond et al. 1985). The further observation that Einstein’s corpus callosum—the largest bundle of myelinated fibers in the brain that connects the two cerebral hemispheres—was thicker in several subregions than in elderly and younger individuals certainly added to the popularity of the argument (Men et al. 2014). Although the studies at the origin of those sensational results have been strongly opposed because of methodological issues or interpretation biases (Fields 2009a), the implication of glia in higher brain functions is still an hypothesis that cannot be rejected.

From an evolutionary point of view, glia emergence coincides with the appearance of the centralized nervous systems (Hartline 2011), and later on, with the birth of radial glial cells which hallmark the development of nervous systems of chordates and vertebrates and are precursors of astrocytes in the adult brain of these animals (Sild and Ruthazer 2011). In parallel, the evolution of myelin reduced the energy required for neuronal communication and boosted the speed of impulse propagation, allowing complex nervous systems to operate quickly and efficiently (Zalc and Colman 2000). Oligodendrocytes also provide trophic support for the axons they myelinate, thus allowing for longer axons and, ultimately, greater vertebrate size (Nave 2010). As nervous systems increase in complexity, a trend in increased complexity is also observed for astrocytes (Verkhratsky and Nedergaard 2016). Human and primate astrocytes are larger and more branched than rodent ones, with humans astrocytes generally being the largest (Oberheim et al. 2009). Moreover, human astrocytes morphologies are more diverse, with some morphologies that are not observed in other species (Colombo and Reisin 2004; Oberheim et al. 2009). A landmark study by Maiken Nedergaard’s group considered the injection of human glial progenitor cells into the ventricles of newborn mice (Han et al. 2013). As those progenitors cells differentiated into mature astrocytes and oligodendrocytes, the adult engrafted animals were found to outperform their littermates that did not receive human glial progenitor grafts, on multiple cognition tests, including novel object recognition and fear conditioning. Overall, these observations provide direct evidence that human astrocytes boost cognitive abilities of mice, possibly by increasing neural plasticity (Han et al. 2013).

Several lines of evidence in humans and in other animal models link glia function with the development and maturation of multiple cognitive and motor skills (Fields 2008; Oliveira et al. 2015). Beyond motor performance, sensory processing is of great importance for appropriate evaluation of behavior. The development and function of cortical maps seem coupled with astrocytic signaling (López-Hidalgo and Schummers 2014). In the primary visual cortex, for example, astrocytes are integral components of OPMs, as they are both visually responsive and capable of modulating visually driven responses in close register with receptive fields of individual neurons (Schummers et al. 2008). In addition, astrocytes, either individually or in association with microglia, could control OPM formation during developmental plasticity (Sects. 1.6 and 1.8), as well as during adulthood (López-Hidalgo and Schummers 2014). Gliotransmission has also been implicated in the sensory modulation of rhythmic activity of the central pattern generators responsible for breathing and chewing (Kadala et al. 2015; Del Negro et al. 2018). Stimulation of glutamatergic sensory fibers that project onto the trigeminal sensory-motor circuit for mastication can indeed activate astrocytes, triggering Ca^{2+} -dependent release of the astrocyte-specific Ca^{2+} -binding protein S100 β . In turn, this results in a reduction of Ca^{2+} in the ECS which promotes rhythmic bursting at frequencies that are compatible with those observed for voluntary chewing (Morquette et al. 2015; Condamine et al. 2018). In addition, medial basal hypothalamic astrocytes can control feeding behavior bidirectionally by purinergic gliotransmission, regulating appetite under both favorable and unfavorable conditions (Yang et al. 2015). Thus, astrocytes critically regulate food intake which is a crucial behavior for energy homeostasis, preventing energy deficits or surfeit.

In the general framework of neuronal network theory, glia-mediated variations of network activity may ultimately be linked to modulations of the balance between excitation (E) and inhibition (I). This possibility arises by the analysis of the few currently available models of neuron–glia network dynamics which come in different flavors, as a result of the combination of different E–I network configurations with different choices of neuronal (and synaptic) models and astrocytic signaling pathways (Savin et al. 2009; Ullah et al. 2009; Volman et al. 2013; Savtchenko and Rusakov 2014; Garnier et al. 2016). Nonetheless, all these models eventually envisage an effect of glial signaling in terms of a modulation of synaptic drive, either at excitatory (Savin et al. 2009; Savtchenko and Rusakov 2014) or at excitatory and inhibitory synapses (Ullah et al. 2009; Volman et al. 2013; Garnier et al. 2016), which accounts for emergence of a variety of network activities. Similar observations may also be made by other models which consider different scenarios of gliotransmission, such as short-term modulation of E-to-I synaptic connections by glutamatergic or purinergic gliotransmission (Savtchenko and Rusakov 2014), or homeostatic upregulation of excitation by glial TNF α , although the latter scenario could also account for emergence of paroxysmal activity in various pathological conditions (Volman et al. 2013). Significantly, these models identify the spatial extent of gliotransmission as a key factor for the regulation of glia-mediated episodes of increased network activity (Volman et al. 2013; Savtchenko and Rusakov 2014). In these models, the transient depression of synapses within an astrocytic anatomical domain correlates

with a decrease of neuronal firing and synchronization, which is larger for larger astrocytic domains (Savchenko and Rusakov 2014). In the context of oscillatory network dynamics, this could then account for reductions of specific frequencies of oscillation with possibly multiple functional and behavioral consequences (Buzsáki and Draguhn 2004). For example, selective, inducible inhibition of vesicular release from brain-wide astrocytic domains was shown to reduce the power spectrum of gamma frequency oscillations (\sim 25 to 80 Hz) in living mice and in correlation with performance deficit in novel object recognition tasks (Lee et al. 2014) (Lee et al. 2014). Another possible pathway that has indeed been linked with memory consolidation during fear conditioning is gliotransmitter release by connexin 43 (Cx43) hemichannels (Stehberg et al. 2012).

Another illustration is the putative involvement of glia in sleep regulation. Many factors involved in the regulation of sleep are still unknown, yet mounting evidence indicate glia as integral component of the neurobiological substrate underpinning circadian and homeostatic mechanisms believed to regulate sleep (Halassa and Haydon 2010; Jackson 2011; Petit and Magistretti 2016). In the suprachiasmatic nucleus of the hypothalamus where the main circadian clock resides, neuron–glial networks undergo rhythmic structural reorganization during the 24 h light/day cycle, which is deemed necessary for appropriate adjustment of the circadian clock to this cycle (Becquet et al. 2008). Gene transcription analysis revealed that several genes that control diverse aspects of glial morphology and function are differentially expressed during sleep vs. wakefulness, independently of the behavioral state (Cirelli et al. 2004; Bellesi et al. 2013, 2015). In parallel, compelling evidence also links astrocytes with homeostatic mechanisms of sleep. Extracellular accumulation during wakefulness of adenosine originating from astrocytic ATP has been implicated in the progressive need of sleep (also dubbed “sleep pressure”) (Pascual et al. 2005; Schmitt et al. 2012; Bjorness et al. 2016), as well as in cognitive impairment associated with prolonged periods of sleep deprivation (Halassa et al. 2009; Florian et al. 2011). Spatially confined extracellular glutamate increases that correlate with astrocytic Ca^{2+} activation could also promote putative sleep states at the level of individual brain regions, triggering there slow wave activity characteristic of non-random eye movement (NREM) sleep (Nir et al. 2011; Vyazovskiy et al. 2011; Poskanzer and Yuste 2016).

1.10 Conclusions

The variety of experimental and theoretical arguments presented in the previous sections outlines a role for glial cells in the control of multiple mechanisms underpinning information processing by the brain. Although this role can in principle extend to the whole brain in its many spatial and temporal scales of activity, the biophysical considerations made here also support the idea of a strong regional specialization for neuron–glial interactions and function, ensuing from evolutionary, developmental, and environmental (activity-dependent) factors (Sects. 1.2 and 1.4). The multiplicity

of chemical signals that glial cells can sense and generate in response to neuronal activity also makes these cells potential signaling hubs in the neuropil. Accordingly, glial cells could sense different aspects of neuronal activity, such as electrical signals, synaptic neurotransmitters, structural changes, energy demands, and vascular metabolites, thanks to a rich cassette of membrane receptors, channels, transporters, and pumps (Sects. 1.4 and 1.5). In turn, they can release multiple molecules with different, and potentially multiple signaling, roles. Gliotransmitters like ATP and glutamate could also be involved both in metabolic (Sect. 1.7) and in inflammatory processes (Sect. 1.8). Conversely, glial release of the proinflammatory cytokine TNF α could be permissive toward gliotransmission and homeostatic mechanisms of plasticity (Sect. 1.8). While signaling multiplexing may be guaranteed by spatially and temporally distinct scales of action of different signals impinging on and mediated by glial cells, it should be emphasized that these different signals could also be interdependent, with potential for emergence of non-trivial correlations in the neural code.

It may be objected that the majority of the arguments exposed here link glial signaling to neurobiological mechanisms that are generally regarded to underpin computations performed by the brain but for which a definitive experimental connection with higher brain functions is still missing (Sect. 1.9). This however does not weaken the original motivation of our hitherto discussion, that is the conceptualization of a neuron–glial paradigm of the brain; rather, it should prompt readers to revise our knowledge of the literature from a different, potentially deeper perspective, inclusive of glial signaling. We indeed predict that many contradicting results in neuroscience and poorly understood signaling pathways of the brain could benefit from novel investigations driven by a theoretical understanding of the possible functional relevance of neuron–glial interactions in brain physiology.

Acknowledgements MDP acknowledges the support of Pôle emploi Rhône-Alpes and of the Junior Leader Postdoctoral Fellowship Program by “la Caixa” Banking Foundation (LCF/BQ/LI18/11630 006). Completion of this chapter was also possible thank to the support of the Basque Government by the BERC 2018–2021 program and by the Spanish Ministry of Science, Innovation and Universities: BCAM Severo Ochoa accreditation SEV-2017-0718.

References

- Abbott LF, DePasquale B, Memmesheimer R-M (2016) Building functional networks of spiking model neurons. *Nat Neurosci* 19(3):350
- Agulhon C, Petracic J, McMullen AB, Sweger EJ, Minton SK, Taves SR, Casper KB, Fiacco TA, McCarthy KD (2008) What is the role of astrocyte calcium in neurophysiology? *Neuron* 59:932–946
- Alberdi E, Sánchez-Gómez MV, Marino A, Matute C (2002) Ca^{2+} influx through AMPA or kainate receptors alone is sufficient to initiate excitotoxicity in cultured oligodendrocytes. *Neurobiol Dis* 9(2):234–243
- Allaman I, Belanger M, Magistretti PJ (2011) Astrocyte-neuron metabolic relationships: for better and for worse. *Trends Neurosci* 34(2):76–87

- Allen NJ (2013) Role of glia in developmental synapse formation. *Curr Opin Neurobiol* 23(6):1027–1033
- Alvarellos-González A, Pazos A, Porto-Pazos AB (2012) Computational models of neuron-astrocyte interactions lead to improved efficacy in the performance of neural networks. *Comput Math Methods Med* 2012:476324
- Amzica F, Massimini M, Manfridi A (2002) Spatial buffering during slow and paroxysmal sleep oscillations in cortical networks of glial cells in vivo. *J Neurosci* 22(3):1042–1053
- Angulo MC, Le Meur K, Kozlov AS, Charpak S, Audinat E (2008) GABA, a forgotten gliotransmitter. *Prog Neurobiol* 86(3):297–303
- Aoyama K, Watabe M, Nakaki T (2008) Regulation of neuronal glutathione synthesis. *J Pharmacol Sci* 108(3):227–238
- Arancibia-Carcamo IL, Ford MC, Cossell L, Ishida K, Tohyama K, Attwell D (2017) Node of Ranvier length as a potential regulator of myelinated axon conduction speed. *eLife* 6:e23329
- Araque A, Carmignoto G, Haydon PG, Oliet SHR, Robitaille R, Volterra A (2014) Gliotransmitters travel in time and space. *Neuron* 81(4):728–739
- Araque A, Parpura V, Sanzgiri RP, Haydon PG (1999) Tripartite synapses: glia, the unacknowledged partner. *Trends Neurosci* 23(5):208–215
- Attwell D, Buchan AM, Charpak S, Lauritzen M, MacVicar BA, Newman EA (2010) Glial and neuronal control of brain blood flow. *Nature* 468(7321):232–243
- Barbour B (2001) An evaluation of synapse independence. *J Neurosci* 21(20):7969–7984
- Barres B (2008) The mystery and magic of glia: a perspective on their roles in health and disease. *Neuron* 60(3):430–440
- Bear MF, Malenka RC (1994) Synaptic plasticity: LTP and LTD. *Curr Opin Neurobiol* 4(3):389–399
- Beck JM, Ma WJ, Kiani R, Hanks T, Churchland AK, Roitman J, Shadlen MN, Latham PE, Pouget A (2008) Probabilistic population codes for Bayesian decision making. *Neuron* 60(6):1142–1152
- Becquet D, Girardet C, Guillaumond F, François-Bellan A-M, Bosler O (2008) Ultrastructural plasticity in the rat suprachiasmatic nucleus. Possible involvement in clock entrainment. *Glia* 56(3):294–305
- Bélanger M, Allaman I, Magistretti PJ (2011) Brain energy metabolism: focus on astrocyte-neuron metabolic cooperation. *Cell Metab* 14(6):724–738
- Bellesia M, de Vivo L, Tononi G, Cirelli C (2015) Effects of sleep and wake on astrocytes: clues from molecular and ultrastructural studies. *BMC Biol* 13(1):66
- Bellesia M, Pfister-Genskow M, Maret S, Keles S, Tononi G, Cirelli C (2013) Effects of sleep and wake on oligodendrocytes and their precursors. *J Neurosci* 33(36):14288–14300
- Benz B, Grima G, Do KQ (2004) Glutamate-induced homocysteic acid release from astrocytes: possible implication in glia-neuron signaling. *Neuroscience* 124(2):377–386
- Bernardinelli Y, Muller D, Nikonenko I (2014a) Astrocyte-synapse structural plasticity. *Neural Plast* 2014:23215
- Bernardinelli Y, Randall J, Janett E, Nikonenko I, König S, Jones EV, Flores CE, Murai KK, Bochet CG, Holtmaat A, Muller D (2014b) Activity-dependent structural plasticity of perisynaptic astrocytic domains promotes excitatory synapse stability. *Curr Biol* 24(15):1679–1688
- Berridge MJ, Lipp P, Bootman MD (2000) The versatility and universality of calcium signalling. *Nat Rev Mol Cell Biol* 1:11–21
- Bezzi P, Domercq M, Brambilla L, Galli R, Schols D, De Clercq E, Vescovi A, Bagetta G, Kollias G, Meldolesi J, Volterra A (2001) CXCR4-activated astrocyte glutamate release via TNF α : amplification by microglia triggers neurotoxicity. *Nat Neurosci* 4(7):702–710
- Bezzi P, Volterra A (2001) A neuron-glia signalling network in the active brain. *Curr Opin Neurobiol* 11:387–394
- Bialek W, Rieke F (1992) Reliability and information transmission in spiking neurons. *Trends Neurosci* 15(11):428–434
- Biber K, Laurie DJ, Berthele A, Sommer B, Tölle TR, Gebicke-Härter P-J, Van Calker D, Boddeke HWGM (1999) Expression and signaling of group I metabotropic glutamate receptors in astrocytes and microglia. *J Neurochem* 72(4):1671–1680

- Bienstock E, Cooper L, Munro P (1982) Theory for the development of neuron selectivity: orientation specificity and binocular interaction in visual cortex. *J Neurosci* 2(1):32–48
- Bindocci E, Savtchouk I, Liaudet N, Becker D, Carriero G, Volterra A (2017) Three-dimensional Ca^{2+} imaging advances understanding of astrocyte biology. *Science* 356:6339
- Bjorness TE, Dale N, Mettlach G, Sonneborn A, Sahin B, Fienberg AA, Yanagisawa M, Bibb JA, Greene RW (2016) An adenosine-mediated glial-neuronal circuit for homeostatic sleep. *J Neurosci* 36(13):3709–3721
- Bowser DN, Khakh BS (2007) Vesicular ATP is the predominant cause of intercellular calcium waves in astrocytes. *J Gen Physiol* 129(6):485–491
- Bushong EA, Martone ME, Jones YZ, Ellisman MH (2002) Protoplasmic astrocyte in CA1 stratum radiatum occupy separate anatomical domains. *J Neurosci* 22(1):183–192
- Butt AM (2006) Neurotransmitter-mediated calcium signalling in oligodendrocyte physiology and pathology. *Glia* 54(7):666–675
- Butt AM, Pugh M, Hubbard P, James G (2004) Functions of optic nerve glia: axoglial signalling in physiology and pathology. *Eye* 18(11):1110
- Buzsáki G (2010) Neural syntax: cell assemblies, synapsesembles, and readers. *Neuron* 68(3):362–385
- Buzsáki G, Draguhn A (2004) Neuronal oscillations in cortical networks. *Science* 304(5679):1926–1929
- Carr CE, Konishi M (1990) A circuit for detection of interaural time differences in the brain stem of the barn owl. *J Neurosci* 10(10):3227–3246
- Castro MA, Beltrán FA, Brauchi S, Concha II (2009) A metabolic switch in brain: glucose and lactate metabolism modulation by ascorbic acid. *J Neurochem* 110(2):423–440
- Chao TI, Rickmann M, Wolff JR (2002) The synapse-astrocyte boundary: an anatomical basis for an integrative role of glia in synaptic transmission. In: Volterra A, Magistretti PJ, Haydon PG (eds) *The tripartite synapse: glia in synaptic transmission* (Chap. 1). Oxford University Press, New York, pp 3–23
- Chen N, Sugihara H, Sharma J, Perea G, Petracic J, Le C, Sur M (2012) Nucleus basalis enabled stimulus specific plasticity in the visual cortex is mediated by astrocytes. *Proc Natl Acad Sci USA* 109(41):E2832–E2841
- Chever O, Djukic B, McCarthy KD, Amzica F (2010) Implication of Kir4.1 channel in excess potassium clearance: an *in vivo* study on anesthetized glial-conditional Kir4.1 knock-out mice. *J Neurosci* 30(47):15769–15777
- Churchill L, Rector DM, Yasuda K, Fix C, Rojas MJ, Yasuda T, Krueger JM (2008) Tumor necrosis factor α : activity dependent expression and promotion of cortical column sleep in rats. *Neuroscience* 156(1):71–80
- Cirelli C, Gutierrez CM, Tononi G (2004) Extensive and divergent effects of sleep and wakefulness on brain gene expression. *Neuron* 41(1):35–43
- Clarke LE, Barres BA (2013) Emerging roles of astrocytes in neural circuit development. *Nat Rev Neurosci* 14(5):311–321
- Clements JD (1996) Transmitter timecourse in the synaptic cleft: its role in central synaptic function. *Trends Neurosci* 19(5):163–171
- Coco S, Calegari F, Pravettoni E, Pozzi D, Taverna E, Rosa P, Matteoli M, Verderio C (2003) Storage and release of ATP from astrocytes in culture. *J Biol Chem* 278(2):1354–1362
- Colombo JA, Reisin HD (2004) Interlaminar astroglia of the cerebral cortex: a marker of the primate brain. *Brain Res* 1006(1):126–131
- Condamine S, Lavoie R, Verdier D, Kolta A (2018) Functional rhythmicogenic domains defined by astrocytic networks in the trigeminal main sensory nucleus. *Glia* 66(2):311–326
- Cornell-Bell AH, Finkbeiner SM, Cooper MS, Smith SJ (1990) Glutamate induces calcium waves in cultured astrocytes: long-range glial signaling. *Science* 247(4941):470–473
- Cui Y, Yang Y, Ni Z, Dong Y, Cai G, Foncalle A, Ma S, Sang K, Tang S, Li Y, Berry H, Shengzi W, Hailan H (2018) Astroglial Kir4.1 in the lateral habenula drives neuronal bursts in depression. *Nature* 554(7692):323

- Danbolt NC (2001) Glutamate uptake. *Prog Neurobiol* 65:1–105
- Dani JW, Chernjavsky A, Smith SJ (1992) Neuronal activity triggers calcium waves in hippocampal astrocyte networks. *Neuron* 8:429–440
- De Pittà M, Brunel N (2016) Modulation of synaptic plasticity by glutamatergic gliotransmission: a modeling study. *Neural Plast* p 7607924
- De Pittà M, Brunel N, Volterra A (2015) Astrocytes: orchestrating synaptic plasticity? *Neuroscience*
- De Pittà M, Goldberg M, Volman V, Berry H, Ben-Jacob E (2009) Glutamate-dependent intracellular calcium and IP₃ oscillating and pulsating dynamics in astrocytes. *J Biol Phys* 35:383–411
- De Pittà M, Volman V, Berry H, Ben-Jacob E (2011) A tale of two stories: astrocyte regulation of synaptic depression and facilitation. *PLoS Comput Biol* 7(12):e1002293
- De Pittà M, Volman V, Levine H, Pioggia G, De Rossi D, Ben-Jacob E (2008) Coexistence of amplitude and frequency modulations in intracellular calcium dynamics. *Phys Rev E* 77(3):030903(R)
- Deco G, Jirsa VK, McIntosh AR (2011) Emerging concepts for the dynamical organization of resting-state activity in the brain. *Nat Rev Neurosci* 12(1):43
- Deitmer JW, Rose CR (1996) pH regulation and proton signalling by glial cells. *Prog Neurobiol* 48(2):73–103
- Del Negro CA, Funk GD, Feldman JL (2018) Breathing matters. *Nat Rev Neurosci* 19(6):351–367
- Devaraju P, Sun M-Y, Myers TL, Lauderdale K, Fiacco TA (2013) Astrocytic group I mGluR-dependent potentiation of astrocytic glutamate and potassium uptake. *J Neurophysiol* 109(9):2404–2414
- Di Castro M, Chuquet J, Liaudet N, Bhaukaurally K, Santello M, Bouvier D, Tiret P, Volterra A (2011) Local Ca²⁺ detection and modulation of synaptic release by astrocytes. *Nat Neurosci* 14:1276–1284
- Diamond MC, Scheibel AB, Murphy GM Jr, Harvey T (1985) On the brain of a scientist: Albert Einstein. *Exp Neurol* 88(1):198–204
- Dienel GA (2012) Fueling and imaging brain activation. *ASN Neuro* 4(AN20120021):5
- Dimou L, Simon C, Kirchhoff F, Takebayashi H, Götz M (2008) Progeny of Olig2-expressing progenitors in the gray and white matter of the adult mouse cerebral cortex. *J Neurosci* 28(41):10434–10442
- Dittman JS, Kreitzer AC, Regehr WG (2000) Interplay between facilitation, depression, and residual calcium at three presynaptic terminals. *J Neurosci* 20(4):1374–1385
- Djukic B, Casper KB, Philpot BD, Chin L-S, McCarthy KD (2007) Conditional knock-out of Kir4.1 leads to glial membrane depolarization, inhibition of potassium and glutamate uptake, and enhanced short-term synaptic potentiation. *J Neurosci* 27(42):11354–11365
- Dolmetsch RE, Lewis RS, Goodnow CC, Healy JI (1997) Differential activation of transcription factors induced by Ca²⁺ response amplitude and duration. *Nature* 386(24):855–858
- Domercq M, Brambilla L, Pilati E, Marchaland J, Volterra A, Bezzi P (2006) P2Y1 receptor-evoked glutamate exocytosis from astrocytes: control by tumor necrosis factor- α and prostaglandins. *J Biol Chem* 281:30684–30696
- Dringen R (2000) Metabolism and functions of glutathione in brain. *Prog Neurobiol* 62(6):649–671
- Eroglu C, Barres BA (2010) Regulation of synaptic connectivity by glia. *Nature* 468(7321):223–231
- Fiacco TA, McCarthy KD (2018) Multiple lines of evidence indicate that gliotransmission does not occur under physiological conditions. *J Neurosci* 38(1):3–13
- Fields RD (2008) White matter in learning, cognition and psychiatric disorders. *Trends Neurosci* 31(7):361–370
- Fields RD (2009a) The other brain: From dementia to schizophrenia, how new discoveries about the brain are revolutionizing medicine and science (1st ed). Simon and Schuster
- Fields RD (2009b) Regulation of myelination by functional activity. In: Kettenmann H, Ransom BR (eds) *Neuroglia* (3rd ed) (Chap. 45). Oxford University Press, Oxford, pp 573–586
- Fields RD, Woo DH, Bassar PJ (2015) Glial regulation of the neuronal connectome through local and long-distant communication. *Neuron* 86(2):374–386
- Florence CM, Baillie LD, Mulligan SJ (2012) Dynamic volume changes in astrocytes are an intrinsic phenomenon mediated by bicarbonate ion flux. *PLoS One* 7(11):e51124

- Florian C, Vecsey CG, Halassa MM, Haydon PG, Abel T (2011) Astrocyte-derived adenosine and A1 receptor activity contribute to sleep loss-induced deficits in hippocampal synaptic plasticity and memory in mice. *J Neurosci* 31(19):6956–6962
- Ford MC, Alexandrova O, Cossell L, Stange-Marten A, Sinclair J, Kopp-Scheinpflug C, Pecka M, Attwell D, Grothe B (2015) Tuning of Ranvier node and internode properties in myelinated axons to adjust action potential timing. *Nat Commun* 6:8073
- Fortune ES, Rose GJ (2001) Short-term synaptic plasticity as a temporal filter. *Trends Neurosci* 24(7):381–385
- Fourcaud-Trocmé N, Hansel D, van Vreeswijk C, Brunel N (2003) How spike generation mechanisms determine the neuronal response to fluctuating inputs. *J Neurosci* 23(37):11628–11640
- Froemke RC, Dan Y (2002) Spike-timing-dependent synaptic modification induced by natural spike trains. *Nature* 416(6879):433–438
- Froemke RC, Debanne D, Bi G (2010) Temporal modulation of spike-timing-dependent plasticity. *Frontiers Synaptic Neurosci* 2(19):1–16
- Froemke RC, Tsay IA, Raad M, Long JD, Dan Y (2006) Contribution of individual spikes in burst-induced long-term synaptic modification. *J Neurophysiol* 95(3):1620–1629
- Fröhbeis C, Fröhlich D, Kuo WP, Amphornrat J, Thilemann S, Saab AS, Kirchhoff F, Möbius W, Goebels S, Nave K (2013) Neurotransmitter-triggered transfer of exosomes mediates oligodendrocyte-neuron communication. *PLoS Biol* 11(7):e1001604
- Ganmor E, Segev R, Schneidman E (2015) A thesaurus for a neural population code. *eLife* 4:e06134
- Garnier A, Vidal A, Benali H (2016) A theoretical study on the role of astrocytic activity in neuronal hyperexcitability by a novel neuron-glia mass model. *J Math Neurosci* 6(1):10
- Gerstner W, Kistler WM (2002) Mathematical formulations of Hebbian learning. *Biol Cybern* 87(5–6):404–415
- Gilman AG (1987) G proteins: transducers of receptor-generated signals. *Annu Rev Biochem* 56(1):615–649
- Gordon GRJ, Mulligan SJ, MacVicar BA (2007) Astrocyte control of the cerebrovasculature. *Glia* 55(12):1214–1221
- Götz M (2013) Neuroglia, chapter Radial glial cells. Oxford University Press, Oxford, pp 50–61
- Graupner M, Brunel N (2010) Mechanisms of induction and maintenance of spike-timing dependent plasticity in biophysical synapse models. *Frontiers Comput Neurosci* 4(136):1–19
- Grosche J, Kettenmann H, Reichenbach A (2002) Bergmann glial cells form distinct morphological structures to interact with cerebellar neurons. *J Neurosci Res* 68:128–149
- Grosche J, Matyash V, Möller T, Verkhratsky A, Reichenbach A, Kettenmann H (1999) Microdomains for neuron-glia interaction: parallel fiber signaling to Bergmann glial cells. *Nature* 2(2):139–143
- Habbas S, Santello M, Becker D, Stubbe H, Zappia G, Liaudet N, Klaus FR, Kollias G, Fontana A, Pryce CR, Suter T, Volterra A (2015) Neuroinflammatory TNF α impairs memory via astrocyte signaling. *Cell* 163(7):1730–1741
- Haber M, Zhou L, Murai KK (2006) Cooperative astrocyte and dendritic spine dynamics at hippocampal excitatory synapses. *J Neurosci* 26(35):8881–8891
- Halassa M, Haydon P (2010) Integrated brain circuits: astrocytic networks modulate neuronal activity and behavior. *Annu Rev Physiol* 72:335–355
- Halassa MM, Florian C, Fellin T, Munoz JR, Lee SY, Abel T, Haydon PG, Frank MG (2009) Astrocytic modulation of sleep homeostasis and cognitive consequences of sleep loss. *Neuron* 61(2):213–219
- Hamilton N, Vayro S, Kirchhoff F, Verkhratsky A, Robbins J, Gorecki DC, Butt AM (2008) Mechanisms of ATP- and glutamate-mediated calcium signaling in white matter astrocytes. *Glia* 56(7):734–749
- Han X, Chen M, Wang F, Windrem M, Wang S, Shanz S, Xu Q, Oberheim NA, Bekar L, Betstadt S, Silva AJ, Takano T, Goldman SA, Nedergaard M (2013) Forebrain engraftment by human glial progenitor cells enhances synaptic plasticity and learning in adult mice. *Cell Stem Cell* 12(3):342–353

- Hartline DK (2011) The evolutionary origins of glia. *Glia* 59(9):1215–1236
- Haydon PG (2001) Glia: listening and talking to the synapse. *Nat Rev Neurosci* 2:185–193
- Haydon PG, Carmignoto G (2006) Astrocyte control of synaptic transmission and neurovascular coupling. *Physiol Rev* 86:1009–1031
- Heller JP, Rusakov DA (2015) Morphological plasticity of astroglia: understanding synaptic microenvironment. *Glia* 63(12):2133–2151
- Henneberger C, Papouin T, Oliet SHR, Rusakov DA (2010) Long-term potentiation depends on release of D-serine from astrocytes. *Nature* 463:232–237
- Hertz L (1965) Possible role of neuroglia: a potassium-mediated neuronal-neuroglial-neuronal impulse transmission system. *Nature* 206(4989):1091
- Hertz L (2013) The glutamate-glutamine (GABA) cycle: importance of late postnatal development and potential reciprocal interactions between biosynthesis and degradation. *Frontiers Endocrinol* 4:59
- Hirase H, Qian L, Barthó P, Buzsáki G (2004) Calcium dynamics of cortical astrocytic networks in vivo. *PLoS Biol* 2(4):0494–0496
- Hoffmann A, Kann O, Ohlemeyer C, Hanisch U-K, Kettenmann H (2003) Elevation of basal intracellular calcium as a central element in the activation of brain macrophages (microglia): suppression of receptor-evoked calcium signaling and control of release function. *J Neurosci* 23(11):4410–4419
- Hoogland TM, Kuhn B, Göbel W, Huang W, Nakai J, Helmchen F, Flint J, Wang SS (2009) Radially expanding transglial calcium waves in the intact cerebellum. *Proc Nat Acad Sci* 106(9):3496–3501
- Hughes EG, Orthmann-Murphy JL, Langseth AJ, Bergles DE (2018) Myelin remodeling through experience-dependent oligodendrogenesis in the adult somatosensory cortex. *Nat Neurosci* 21:696–706
- Iadecola C, Nedergaard M (2007) Glial regulation of the cerebral microvasculature. *Nat Neurosci* 10(11):1369–1376
- Imura Y, Morizawa Y, Komatsu R, Shibata K, Shinozaki Y, Kasai H, Moriishi K, Moriyama Y, Koizumi S (2013) Microglia release ATP by exocytosis. *Glia* 61(8):1320–1330
- Ismailov I, Kalikulov D, Inoue T, Friedlander MJ (2004) The kinetic profile of intracellular calcium predicts long-term potentiation and long-term depression. *J Neurosci* 24(44):9847–9861
- Izhikevich EM (2006) Polychronization: computation with spikes. *Neural Comput* 18(2):245–282
- Jackson FR (2011) Glial cell modulation of circadian rhythms. *Glia* 59(9):1341–1350
- Jadhav AP, Roesch K, Cepko CL (2009) Development and neurogenic potential of Müller glial cells in the vertebrate retina. *Prog Retinal Eye Res* 28(4):249–262
- Jaffe LF (1993) Classes and mechanisms of calcium waves. *Cell Calcium* 14(10):736–745
- Jeftinija SD, Jeftinija KV, Stefanovic G, Liu F (1996) Neuropil ligand-evoked calcium-dependent release of excitatory amino acids from cultured astrocytes. *J Neurochem* 66:676–684
- Jiang P, Xing F, Guo B, Yang J, Li Z, Wei W, Hu F, Lee I, Zhang X, Pan L, Xu J (2017) Nucleotide transmitters ATP and ADP mediate intercellular calcium wave communication via P2Y_{12/13} receptors among BV-2 microglia. *PLoS One* 12(8):e0183114
- Jiménez-González C, Pirttimäki T, Cope DW, Parri HR (2011) Non-neuronal, slow GABA signalling in the ventrobasal thalamus targets δ -subunit-containing GABA_A receptors. *Eur J Neurosci* 33(8):1471–1482
- Johnston D, Wu SM-S (1995) Foundations of cellular neurophysiology. MIT Press, Cambridge, MA
- Kadala A, Verdier D, Morquette P, Kolta A (2015) Ion homeostasis in rhythmogenesis: the interplay between neurons and astroglia. *Physiology* 30(5):371–388
- Kaneko M, Stellwagen D, Malenka RC, Stryker MP (2008) Tumor necrosis factor-alpha mediates one component of competitive, experience-dependent plasticity in developing visual cortex. *Neuron* 58:673–680
- Káradóttir R, Attwell D (2007) Neurotransmitter receptors in the life and death of oligodendrocytes. *Neuroscience* 145(4):1426–1438

- Kaschube M, Schnabel M, Löwel S, Coppola DM, White LE, Wolf F (2010) Universality in the evolution of orientation columns in the visual cortex. *Science* 330(6007):1113–1116
- Kasthuri N, Hayworth K, Berger DR, Schalek RL, Conchello JA, Knowles-Barley S, Lee D, Vázquez-Reina A, Kaynig V, Jones TR, Roberts M, Lyskowski JM, Tapia JC, Seung HS, Roncal WG, Vogelstein JT, Burns R, Sussman DL, Priebe CE, Pfister H, Lichtman JW (2015) Saturated reconstruction of a volume of neocortex. *Cell* 162(3):648–661
- Katagiri H, Tanaka K, Manabe T (2001) Requirement of appropriate glutamate concentrations in the synaptic cleft for hippocampal LTP induction. *Eur J Neurosci* 14(3):547–553
- Kettenmann H, Hanisch U-K, Noda M, Verkhratsky A (2011) Physiology of microglia. *Physiol Rev* 91(2):461–553
- Kettenmann H, Kirchhoff F, Verkhratsky A (2013) Microglia: new roles for the synaptic stripper. *Neuron* 77(1):10–18
- Kettenmann H, Ransom BR (2013) Neuroglia, 3rd edn. Oxford University Press, Oxford
- Khakh BS, Sofroniew MV (2015) Diversity of astrocyte functions and phenotypes in neural circuits. *Nat Neurosci* 18(7):942
- Kimura F, Itami C (2009) Myelination and isochronicity in neural networks. *Frontiers Neuroanat* 3:12
- Kinney JP, Spacek J, Bartol TM, Bajaj CL, Harris KM, Sejnowski TJ (2013) Extracellular sheets and tunnels modulate glutamate diffusion in hippocampal neuropil. *J Comp Neurol* 521(2):448–464
- Kofuji P, Newman EA (2004) Potassium buffering in the central nervous system. *Neuroscience* 129(4):1043–1054
- Kozlov AS, Angulo MC, Audinat E, Charpak S (2006) Target cell-specific modulation of neuronal activity by astrocytes. *Proc Natl Acad Sci USA* 103(26):10058–10063
- Krämer-Albers E-M, Bretz N, Tenzer S, Winterstein C, Möbius W, Berger H, Nave K-A, Schild H, Trotter J (2007) Oligodendrocytes secrete exosomes containing major myelin and stress-protective proteins: trophic support for axons? *Proteomics-Clin Appl* 1(11):1446–1461
- Krzan M, Stenovec N, Kreft M, Pangrsic T, Grilc S, Haydon PG, Zorec R (2003) Calcium-dependent exocytosis of atrial natriuretic peptide from astrocytes. *J Neurosci* 23:1580–1583
- Kuga N, Sasaki T, Takahara Y, Matsuki N, Ikegaya Y (2011) Large-scale calcium waves traveling through astrocytic networks in vivo. *J Neurosci* 31(7):2607–2614
- Kummer U, Olsen LF, Green AK, Bomberg-Bauer E, Baier G (2000) Switching from simple to complex oscillations in calcium signaling. *Biophys J* 79:1188–1199
- Lang EJ, Rosenbluth J (2003) Role of myelination in the development of a uniform olivocerebellar conduction time. *J Neurophysiol* 89(4):2259–2270
- Larsen BR, Assentoft M, Cotrina ML, Hua SZ, Nedergaard M, Kaila K, Voipio J, MacAulay N (2014) Contributions of the Na⁺/K⁺-ATPase, NKCC1, and Kir4.1 to hippocampal K⁺ clearance and volume responses. *Glia* 62(4):608–622
- Laughlin SB, Sejnowski TJ (2003) Communication in neuronal networks. *Science* 301(5641):1870–1874
- Lawson LJ, Perry VH, Dri P, Gordon S (1990) Heterogeneity in the distribution and morphology of microglia in the normal adult mouse brain. *Neuroscience* 39(1):151–170
- Le Meur K, Mendizabal-Zubiaga J, Grandes P, Audinat E (2012) GABA release by hippocampal astrocytes. *Front Comp Neurosci* p 6
- Lee HS, Ghetti A, Pinto-Duarte A, Wang X, Dziewczapolski G, Galimi F, Huitron-Resendiz S, Piñá-Crespo JC, Roberts AJ, Verma IM, Sejnowski TJ, Heinemann SF (2014) Astrocytes contribute to gamma oscillations and recognition memory. *Proc Nat Acad Sci USA* pp E3343–E3352
- Lehre KP, Rusakov DA (2002) Asymmetry of glia near central synapses favors presynaptically directed glutamate escape. *Biophys J* 83(1):125–134
- Levy LM, Warr O, Attwell D (1998) Stoichiometry of the glial glutamate transporter GLT-1 expressed inducibly in a chinese hamster ovary cell line selected for low endogenous Na⁺-dependent glutamate uptake. *J Neurosci* 18(23):9620–9628

- Lewitus GM, Konefal SC, Greenhalgh AD, Pribiag H, Augereau K, Stellwagen D (2016) Microglial TNF- α suppresses cocaine-induced plasticity and behavioral sensitization. *Neuron* 90(3):483–491
- Lewitus GM, Pribiag H, Duseja R, St-Hilaire M, Stellwagen D (2014) An adaptive role of TNF α in the regulation of striatal synapses. *J Neurosci* 34(18):6146–6155
- Leybaert L, Sanderson MJ (2012) Intercellular Ca²⁺ waves: mechanisms and function. *Physiol Rev* 92(3):1359–1392
- Lind BL, Brazhe AR, Jessen SB, Tan FCC, Lauritzen MJ (2013) Rapid stimulus-evoked astrocyte Ca²⁺ elevations and hemodynamic responses in mouse somatosensory cortex *in vivo*. *Proc Nat Acad Sci* 110(48):E4678–E4687
- Lippman JJ, Lordkipanidze T, Buell ME, Yoon SO, Dunaevsky A (2008) Morphogenesis and regulation of Bergmann glial processes during Purkinje cell dendritic spine ensheathment and synaptogenesis. *Glia* 56(13):1463–1477
- Lippman JJ, Lordkipanidze T, Cobb N, Dunaevsky A (2010) Bergmann glial ensheathment of dendritic spines regulates synapse number without affecting spine motility. *Neuron Glia Biol* 6(3):193–200
- Liu GJ, Kalous A, Werry EL, Bennett MR (2006) Purine release from spinal cord microglia after elevation of calcium by glutamate. *Mol Pharmacol* 70(3):851–859
- López-Hidalgo M, Hoover WB, Schummers J (2016) Spatial organization of astrocytes in ferret visual cortex. *J Comp Neurol* 524(17):3561–3576
- López-Hidalgo M, Schummers J (2014) Cortical maps: a role for astrocytes? *Curr Opin Neurobiol* 24:176–189
- Lushnikova I, Skibo G, Muller D, Nikonenko I (2009) Synaptic potentiation induces increased glial coverage of excitatory synapses in CA1 hippocampus. *Hippocampus* 19(8):753–762
- Mackenzie B, Erickson JD (2004) Sodium-coupled neutral amino acid (System N/A) transporters of the SLC38 gene family. *Pflügers Archiv - Eur J Physiol* 447(5):784–795
- Magistretti PJ, Allaman I (2015) A cellular perspective on brain energy metabolism and functional imaging. *Neuron* 86(4):883–901
- Marchaland J, Cali C, Voglmaier SM, Li H, Regazzi R, Edwards RH, Bezzi P (2008) Fast subplasma membrane Ca²⁺ transients control exo-endocytosis of synaptic-like microvesicles in astrocytes. *J Neurosci* 28(37):9122–9132
- Marchant JS, Parker I (2001) Role of elementary Ca²⁺ puffs in generating repetitive Ca²⁺ oscillations. *EMBO J* 20(1–2):65–76
- Markram H, Lübke J, Frotscher M, Roth A, Sakmann B (1997) Physiology and anatomy of synaptic connections between thick tufted pyramidal neurones in the developing rat neocortex. *J Physiol* 500(2):409–440
- Martín R, Bajo-Grañeras R, Moratalla R, Perea G, Araque A (2015) Circuit-specific signaling in astrocyte-neuron networks in basal ganglia pathways. *Science* 349(6249):730–734
- Mashimo M, Okubo Y, Yamazawa T, Yamasaki M, Watanabe M, Murayama T, Iino M (2010) Inositol 1,4,5-trisphosphate signaling maintains the activity of glutamate uptake in Bergmann glia. *Eur J Neurosci* 32(10):1668–1677
- McAlpine D, Grothe B (2003) Sound localization and delay lines—do mammals fit the model? *Trends Neurosci* 26(7):347–350
- Medvedev N, Popov V, Henneberger C, Kraev I, Rusakov DA, Stewart MG (2014) Glia selectively approach synapses on thin dendritic spines. *Phil Trans R Soc B* 369(1654):20140047
- Men W, Falk D, Sun T, Chen W, Li J, Yin D, Zang L, Fan M (2014) The corpus callosum of Albert Einstein's brain: another clue to his high intelligence? *Brain* 137(4):e268–e268
- Mergenthaler P, Lindauer U, Dienel GA, Meisel A (2013) Sugar for the brain: the role of glucose in physiological and pathological brain function. *Trends Neurosci* 36(10):587–597
- Mesejo P, Ibáñez O, Fernández-Blanco E, Cedrón F, Pazos A, Porto-Pazos AB (2015) Artificial neuron–glia networks learning approach based on cooperative coevolution. *Int J Neural Syst* 25(04):1550012

- Min R, Nevian T (2012) Astrocyte signaling controls spike timing-dependent depression at neocortical synapses. *Nat Neurosci* 15(5):746–753
- Molofsky AV, Kelley KW, Tsai H-H, Redmond SA, Chang SM, Madireddy L, Chan JR, Baranzini SE, Ullian EM, Rowitch DH (2014) Astrocyte-encoded positional cues maintain sensorimotor circuit integrity. *Nature* 509(7499):189
- Morquette P, Verdier D, Kadala A, Féthière J, Philippe AG, Robitaille R, Kolta A (2015) An astrocyte-dependent mechanism for neuronal rhythrogenesis. *Nat Neurosci* 18(6):844
- Mothet J-P, Parent AT, Wolosker H, Brady RO, Linden DJ, Ferris CD, Rogawski MA, Snyder SH (2000) D-serine is an endogenous ligand for the glycine site of the N-methyl-D-aspartate receptor. *Proc Nat Acad Sci* 97(9):4926–4931
- Mulligan S, MacVicar B (2004) Calcium transients in astrocyte endfeet cause cerebrovascular constrictions. *Nature* 431(7005):195–199
- Nagelhus EA, Mathiisen TM, Ottersen OP (2004) Aquaporin-4 in the central nervous system: cellular and subcellular distribution and coexpression with KIR4.1. *Neuroscience* 129(4):905–913
- Nave K-A (2010) Myelination and support of axonal integrity by glia. *Nature* 468(7321):244
- Nedergaard M (1994) Direct signaling from astrocytes to neurons in cultures of mammalian brain cells. *Science* 263(5154):1768
- Nedergaard M, Ransom BR, Goldman SA (2003) New roles for astrocytes: redefining the functional architecture of the brain. *Trends Neurosci* 26(10):523–530
- Nevian T, Sakmann B (2006) Spine Ca²⁺ signaling in spike-timing-dependent plasticity. *J Neurosci* 26(43):11001–11013
- Newman E (2005) Calcium increases in retinal glial cells evoked by light-induced neuronal activity. *J Neurosci* 25(23):5502–5510
- Newman EA (2001) Propagation of intercellular calcium waves in retinal astrocytes and Müller cells. *J Neurosci* 21:2215–2223
- Newman EA, Zahs KR (1997) Calcium waves in retinal glial cells. *Science* 275:844–847
- Newman LA, Korol DL, Gold PE (2011) Lactate produced by glycogenolysis in astrocytes regulates memory processing. *PloS One* 6(12):e28427
- Nicoll RA, Schmitz D (2005) Synaptic plasticity at hippocampal mossy fibre synapses. *Nat Rev Neurosci* 6(11):863
- Nimmerjahn A, Kirchhoff F, Helmchen F (2005) Resting microglial cells are highly dynamic surveillants of brain parenchyma in vivo. *Science* 308(5726):1314–1318
- Nimmerjahn A, Kirchhoff F, Kerr JND, Helmchen F (2004) Sulforhodamine 101 as a specific marker of astroglia in the neocortex in vivo. *Nat Methods* 1:31–37
- Nir Y, Staba RJ, Andrillon T, Vyzavotskiy VV, Cirelli C, Fried I, Tononi G (2011) Regional slow waves and spindles in human sleep. *Neuron* 70(1):153–169
- Oberheim NA, Takano T, Han X, He W, Lin JHC, Wang F, Xu Q, Wyatt JD, Pilcher W, Ojemann JG, Ransom BR, Goldman SA, Nedergaard M (2009) Uniquely hominid features of adult human astrocytes. *J Neurosci* 29(10):3276–3287
- Oliet SHR, Mothet J (2009) Regulation of N-methyl-D-aspartate receptors by astrocytic D-serine. *Neuroscience* 158(1):275–283
- Oliet SHR, Piet R, Poulain DA (2001) Control of glutamate clearance and synaptic efficacy by glial coverage of neurons. *Science* 292:923–926
- Oliveira JF, Sardinha VM, Guerra-Gomes S, Araque A, Sousa N (2015) Do stars govern our actions? Astrocyte involvement in rodent behavior. *Trends Neurosci* 38(9):535–549
- Omroni A, Melone M, Bellesi M, Safiulina V, Aida T, Tanaka K, Cherubini E, Conti F (2009) Up-regulation of GLT-1 severely impairs LTD at mossy fibre-CA3 synapses. *J Physiol* 587(19):4575–4588
- O'Neill LAJ, Kaltschmidt C (1997) NF- κ B: a crucial transcription factor for glial and neuronal cell function. *Trends Neurosci* 20(6):252–258
- Orkand RK, Nicholls JG, Kuffler SW (1966) Effect of nerve impulses on the membrane potential of glial cells in the central nervous system of amphibia. *J Neurophysiol* 29(4):788–806

- Østby I, Øyehaug L, Einevoll GT, Nagelhus EA, Plahte E, Zeuthen T, Lloyd CM, Ottersen OP, Omholt SW (2009) Astrocytic mechanisms explaining neural-activity-induced shrinkage of extraneuronal space. *PLoS Comput Biol* 5(1):e1000272
- Øyehaug L, Østby I, Lloyd CM, Omholt SW, Einevoll GT (2012) Dependence of spontaneous neuronal firing and depolarisation block on astroglial membrane transport mechanisms. *J Comput Neurosci* 32(1):147–165
- Palygin O, Lalo U, Verkhratsky A, Pankratov Y (2010) Ionotropic NMDA and P2X_{1/5} receptors mediate synaptically induced Ca²⁺ signalling in cortical astrocytes. *Cell Calcium* 48(4):225–231
- Panatier A, Theodosis DT, Mothet JP, Touquet B, Pollegioni L, Poulaire DA, Oliet SH (2006) Glia-derived D-serine controls NMDA receptor activity and synaptic memory. *Cell* 125:775–784
- Papouin T, Ladépêche L, Ruel J, Sacchi S, Labasque M, Hanini M, Groc L, Pollegioni L, Mothet J, Oliet S (2012) Synaptic and extrasynaptic NMDA receptors are gated by different endogenous coagonists. *Cell* 150(3):633–646
- Parpura V, Basarsky TA, Liu F, Jeftinija K, Jeftinija S, Haydon PG (1994) Glutamate-mediated astrocyte-neuron signalling. *Nature* 369:744–747
- Parpura V, Haydon PG (2000) Physiological astrocytic calcium levels stimulate glutamate release to modulate adjacent neurons. *Proc Natl Acad Sci USA* 97(15):8629–8634
- Parys B, Côté A, Gallo V, De Koninck P, Sik A (2010) Intercellular calcium signaling between astrocytes and oligodendrocytes via gap junctions in culture. *Neuroscience* 167(4):1032–1043
- Pascual O, Ben Achour S, Rostaing P, Triller A, Bessis A (2011) Microglia activation triggers astrocyte-mediated modulation of excitatory neurotransmission. *Proc Natl Acad Sci* pp 1–9
- Pascual O, Casper KB, Kubera C, Zhang J, Revilla-Sanchez R, Sul JY, Takano H, Moss SJ, McCarthy K, Haydon PG (2005) Astrocytic purinergic signaling coordinates synaptic networks. *Science* 310:113–116
- Pasti L, Volterra A, Pozzan T, Carmignoto G (1997) Intracellular calcium oscillations in astrocytes: a highly plastic, bidirectional form of communication between neurons and astrocytes in situ. *J Neurosci* 17(20):7817–7830
- Pasti L, Zonta M, Pozzan T, Vicini S, Carmignoto G (2001) Cytosolic calcium oscillations in astrocytes may regulate exocytotic release of glutamate. *J Neurosci* 21(2):477–484
- Pellerin L, Magistretti PJ (1994) Glutamate uptake into astrocytes stimulates aerobic glycolysis: a mechanism coupling neuronal activity to glucose utilization. *Proc Natl Acad Sci* 91(22):10625–10629
- Pellerin L, Magistretti PJ (2012) Sweet sixteen for ANLS. *J Cereb Blood Flow Metab* 32(7):1152–1166
- Pelvig DP, Pakkenberg H, Stark AK, Pakkenberg B (2008) Neocortical glial cell numbers in human brains. *Neurobiol Aging* 29(11):1754–1762
- Perez-Alvarez A, Navarrete M, Covelo A, Martin ED, Araque A (2014) Structural and functional plasticity of astrocyte processes and dendritic spine interactions. *J Neurosci* 34(38):12738–12744
- Perkel DH, Bullock TH (1968) Neural coding: a report based on an NRP work session. *Neurosci Res Program Bull* 6:219–349
- Petit J-M, Magistretti PJ (2016) Regulation of neuron-astrocyte metabolic coupling across the sleep-wake cycle. *Neuroscience* 323:135–156
- Philips RT, Sur M, Chakravarthy VS (2017) The influence of astrocytes on the width of orientation hypercolumns in visual cortex: A computational perspective. *PLoS Comput Biol* 13(10):e1005785
- Piet R, Vargová L, Syková E, Poulaire D, Oliet S (2004) Physiological contribution of the astrocytic environment of neurons to intersynaptic crosstalk. *Proc Natl Acad Sci USA* 101(7):2151–2155
- Pocock JM, Kettenmann H (2007) Neurotransmitter receptors on microglia. *Trends Neurosci* 30(10):527–535
- Porter JT, McCarthy KD (1996) Hippocampal astrocytes in situ respond to glutamate released from synaptic terminals. *J Neurosci* 16(16):5073–5081
- Porter JT, McCarthy KD (1997) Astrocytic neurotransmitter receptors in situ and in vivo. *Prog Neurobiol* 51(4):439–455

- Porto-Pazos AB, Veiguela N, Mesejo P, Navarrete M, Alvarellos A, Ibáñez O, Pazos A, Araque A (2011) Artificial astrocytes improve neural network performance. *PLoS One* 6(4):e19109
- Poskanzer KE, Yuste R (2016) Astrocytes regulate cortical state switching in vivo. *Proc Nat Acad Sci* 113(19):E2675–E2684
- Pribiag H, Stellwagen D (2013) TNF- α downregulates inhibitory neurotransmission through protein phosphatase 1-dependent trafficking of GABA_A receptors. *J Neurosci* 33(40):15879–15893
- Price DL, Ludwig JW, Mi H, Schwarz TL, Ellisman MH (2002) Distribution of rSlo Ca²⁺-activated K⁺ channels in rat astrocyte perivascular endfeet. *Brain Res* 956(2):183–193
- Ransom CB, Ransom BR, Sontheimer H (2000) Activity-dependent extracellular K⁺ accumulation in rat optic nerve: the role of glial and axonal Na⁺ pumps. *J Physiol* 522(3):427–442
- Reichenbach A, Derouiche A, Kirchhoff F (2010) Morphology and dynamics of perisynaptic glia. *Brain Res Rev* 63(1):11–25
- Rigotti M, Barak O, Warden MR, Wang X-J, Daw ND, Miller EK, Fusi S (2013) The importance of mixed selectivity in complex cognitive tasks. *Nature* 497(7451):585
- Rose CR, Chatton J-Y (2016) Astrocyte sodium signaling and neuro-metabolic coupling in the brain. *Neuroscience* 323:121–134
- Rothman DL, Behar KL, Hyder F, Shulman RG (2003) In vivo NMR studies of the glutamate neurotransmitter flux and neuroenergetics: implications for brain function. *Annu Rev Physiol* 65(1):401–427
- Roxin A, Brunel N, Hansel D (2005) Role of delays in shaping spatiotemporal dynamics of neuronal activity in large networks. *Phys Rev Lett* 94(23):238103
- Roxin A, Montbrió E (2011) How effective delays shape oscillatory dynamics in neuronal networks. *Phys D* 240(3):323–345
- Rusakov DA (2001) The role of perisynaptic glial sheaths in glutamate spillover and extracellular Ca²⁺ depletion. *Biophys J* 81(4):1947–1959
- Rusakov DA (2015) Disentangling calcium-driven astrocyte physiology. *Nat Rev Neurosci* 16:226–233
- Sahlender DA, Savtchouk I, Volterra A (2014) What do we know about gliotransmitter release from astrocytes? *Phil Trans Royal Soc B* 369:20130592
- Santello M, Bezzi P, Volterra A (2011) TNF α controls glutamatergic gliotransmission in the hippocampal dentate gyrus. *Neuron* 69:988–1001
- Santello M, Volterra A (2012) TNF α in synaptic function: switching gears. *Trends Neurosci* 35(10):638–647
- Savin C, Triesch J, Meyer-Hermann M (2009) Epileptogenesis due to glia-mediated synaptic scaling. *J R Soc Interface* 6(37):655–668
- Savtchenko LP, Rusakov DA (2014) Regulation of rhythm genesis by volume-limited, astroglia-like signals in neural networks. *Phil Trans Royal Soc B: Biol Sci* 369(1654):20130614
- Savtchouk I, Volterra A (2018) Gliotransmission: beyond black-and-white. *J Neurosci* 38(1):14–25
- Scemes E, Giaume C (2006) Astrocyte calcium waves: What they are and what they do. *Glia* 54:716–725
- Schafer DP, Lehrman EK, Kautzman AG, Koyama R, Mardinly AR, Yamasaki R, Ransohoff RM, Greenberg ME, Barres BA, Stevens B (2012) Microglia sculpt postnatal neural circuits in an activity and complement-dependent manner. *Neuron* 74(4):691–705
- Schipke CG, Boucsein C, Ohlemeyer C, Kirchhoff F, Kettenmann H (2002) Astrocyte Ca²⁺ waves trigger responses in microglial cells in brain slices. *FASEB J* 16(2):255–257
- Schmitt L, Sims R, Dale N, Haydon P (2012) Wakefulness affects synaptic and network activity by increasing extracellular astrocyte-derived adenosine. *J Neurosci* 32(13):4417–4425
- Schummers J, Yu H, Sur M (2008) Tuned responses of astrocytes and their influence on hemodynamic signals in the visual cortex. *Sci STKE* 320(5883):1638
- Schuster S, Marhl M, Höfer T (2002) Modelling of simple and complex calcium oscillations from single-cell responses to intercellular signalling. *Eur J Biochem* 269:1333–1355
- Seidl AH, Rubel EW, Harris DM (2010) Mechanisms for adjusting interaural time differences to achieve binaural coincidence detection. *J Neurosci* 30(1):70–80

- Sherwood MW, Arizono M, Hisatsune C, Bannai H, Ebisui E, Sherwood JL, Panatier A, Oliet SHR, Mikoshiba K (2017) Astrocytic IP₃Rs: Contribution to Ca²⁺ signalling and hippocampal ltp. *Glia* 65(3):502–513
- Shigetomi E, Jackson-Weaver O, Huckstepp RT, O'Dell TJ, Khakh BS (2013) TRPA1 channels are regulators of astrocyte basal calcium levels and long-term potentiation via constitutive D-serine release. *J Neurosci* 33(24):10143–10153
- Shigetomi E, Tong X, Kwan K, Corey D, Khakh B (2012) TRPA1 channels regulate astrocyte resting calcium levels and inhibitory synapse efficacy via GAT-3. *Nat Neurosci* 15(1):70–80
- Sild M, Ruthazer ES (2011) Radial glia: progenitor, pathway, and partner. *Neuroscientist* 17(3):288–302
- Simard M, Nedergaard M (2004) The neurobiology of glia in the context of water and ion homeostasis. *Neuroscience* 129(4):877–896
- Simpson IA, Carruthers A, Vannucci SJ (2007) Supply and demand in cerebral energy metabolism: the role of nutrient transporters. *J Cereb Blood Flow Metab* 27(11):1766–1791
- Skupin A, Kettenmann H, Winkler U, Wartenberg M, Sauer H, Tovey SC, Taylor CW, Falcke M (2008) How does intracellular Ca²⁺ oscillate: by chance or by clock? *Biophys J* 94:2404–2411
- Somjen GG (2002) Ion regulation in the brain: implications for pathophysiology. *Neuroscientist* 8(3):254–267
- Somjen GG, Kager H, Wadman WJ (2008) Computer simulations of neuron–glia interactions mediated by ion flux. *J Comput Neurosci* 25(2):349–365
- Srinivasan R, Huang BS, Venugopal S, Johnston AD, Chai H, Zeng H, Golshani P, Khakh BS (2015) Ca²⁺ signaling in astrocytes from Ip3r2^{-/-} mice in brain slice and during startle responses in vivo. *Nat Neurosci* 18:708–717
- Stassart R, Goebels S, Nave K-A (2013) Factors controlling myelin formation. In: Kettenmann H, Ransom BR (eds) *Neuroglia* (3rd ed) (Chap. 44). Oxford University Press, Oxford, pp 555–572
- Stehberg J, Moraga-Amaro R, Salazar C, Becerra A, Echeverría C, Orellana JA, Bultynck G, Ponzaerts R, Leybaert L, Simon F, Simon F, Sáez JC, Retamal MA (2012) Release of gliotransmitters through astroglial connexin 43 hemichannels is necessary for fear memory consolidation in the basolateral amygdala. *FASEB J* 26(9):3649–3657
- Steinhausen C, Berger T, Frotscher M, Kettenmann H (1992) Heterogeneity in the membrane current pattern of identified glial cells in the hippocampal slice. *Eur J Neurosci* 4(6):472–484
- Steinmetz CC, Turrigiano GG (2010) Tumor necrosis factor- α signaling maintains the ability of cortical synapses to express synaptic scaling. *J Neurosci* 30(44):14685–14690
- Stellwagen D, Beattie EC, Seo JY, Malenka RC (2005) Differential regulation of AMPA receptor and GABA receptor trafficking by tumor necrosis factor- α . *J Neurosci* 25(12):3219–3228
- Stevens B, Allen NJ, Vazquez LE, Howell GR, Christopherson KS, Nouri N, Micheva KD, Mehalow AK, Huberman AD, Stafford B, Sher A, Litke AM, Lambris JD, Smith SJ, John SWM, Barres BA (2007) The classical complement cascade mediates CNS synapse elimination. *Cell* 131(6):1164–1178
- Stevens J-LR, Law JS, Antolik J, Bednar JA (2013) Mechanisms for stable, robust, and adaptive development of orientation maps in the primary visual cortex. *J Neurosci* 33(40):15747–15766
- Stout CE, Costantin JL, Naus CCG, Charles AC (2002) Intercellular calcium signaling in astrocytes via ATP release through connexin hemichannels. *J Biol Chem* 277(12):10482–10488
- Suadicani SO, Brosnan CF, Scemes E (2006) P2X₇ receptors mediate ATP release and amplification of astrocytic intercellular Ca²⁺ signaling. *J Neurosci* 26(5):1378–1385
- Sugihara I, Lang EJ, Llinás R (1993) Uniform olivocerebellar conduction time underlies purkinje cell complex spike synchronicity in the rat cerebellum. *J Physiol* 470(1):243–271
- Suzuki A, Stern SA, Bozdagi O, Huntley G, Wlaker RH, Magistretti PJ, Alberini CM (2011) Astrocyte–neuron lactate transport is required for long-term memory formation. *Cell* 144:810–823
- Takeda M, Nelson DJ, Soliven B (1995) Calcium signaling in cultured rat oligodendrocytes. *Glia* 14(3):225–236

- Tani H, Dulla CG, Farzampour Z, Taylor-Weiner A, Huguenard JR, Reimer RJ (2014) A local glutamate-glutamine cycle sustains synaptic excitatory transmitter release. *Neuron* 81(4):888–900
- Tasaki I, Chang JJ (1958) Electric response of glia cells in cat brain. *Science* 128(3333):1209–1210
- Thurley K, Falcke M (2011) Derivation of Ca^{2+} signals from puff properties reveals that pathway function is robust against cell variability but sensitive for control. *Proc Nat Acad Sci USA* 108(1):427–432
- Thurley K, Skupin A, Thul R, Falcke M (2012) Fundamental properties of Ca^{2+} signals. *Biochim Biophys Acta* 1820:1185–1194
- Thurley K, Tovey SC, Moenke G, Prince VL, Meena A, Thomas AP, Skupin A, Taylor CW, Falcke M (2014) Reliable encoding of stimulus intensities within random sequences of intracellular Ca^{2+} spikes. *Sci Signaling* 7(331):ra59
- Tomassy GS, Berger DR, Chen H, Kasthuri N, Hayworth KJ, Vercelli A, Seung HS, Lichtman JW, Arlotta P (2014) Distinct profiles of myelin distribution along single axons of pyramidal neurons in the neocortex. *Science* 344(6181):319–324
- Tremblay M-È, Lowery RL, Majewska AK (2010) Microglial interactions with synapses are modulated by visual experience. *PLoS Biol* 8(11):e1000527
- Tsodyks M (2005) Activity-dependent transmission in neocortical synapses. In: Chow C, Gutkin B, Hansel D, Meunier C, Dalibard J (eds) *Methods and models in neurophysics* (Chap. 7). Elsevier, Amsterdam, pp 245–265
- Tsvetkov E, Shin R-M, Bolshakov VY (2004) Glutamate uptake determines pathway specificity of long-term potentiation in the neural circuitry of fear conditioning. *Neuron* 41(1):139–151
- Ullah G, Cressman JR Jr, Barreto E, Schiff SJ (2009) The influence of sodium and potassium dynamics on excitability, seizures, and the stability of persistent states: II. Network and glial dynamics. *J Comput Neurosci* 26(2):171–183
- Ullén F (2009) Is activity regulation of late myelination a plastic mechanism in the human nervous system? *Neuron Glia Biol* 5(1–2):29–34
- Vaishnavi SN, Vlassenko AG, Rundle MM, Snyder AZ, Mintun MA, Raichle ME (2010) Regional aerobic glycolysis in the human brain. *Proc Nat Acad Sci* 107(41):17757–17762
- Valtcheva S, Venance L (2016) Astrocytes gate Hebbian synaptic plasticity in the striatum. *Nat Commun* 7:13845
- Ventura R, Harris KM (1999) Three-dimensional relationships between hippocampal synapses and astrocytes. *J Neurosci* 19(16):6897–6906
- Verbich D, Prenosil GA, Chang PK-Y, Murai KK, McKinney RA (2012) Glial glutamate transport modulates dendritic spine head protrusions in the hippocampus. *Glia* 60(7):1067–1077
- Verderio C, Matteoli M (2001) ATP mediates calcium signaling between astrocytes and microglial cells: modulation by IFN- γ . *J Immunol* 166(10):6383–6391
- Verkhratsky A, Kettenmann H (1996) Calcium signaling in glial cells. *Trends Neurosci* 19:346–352
- Verkhratsky A, Nedergaard M (2016) The homeostatic astroglia emerges from evolutionary specialization of neural cells. *Phil Trans R Soc B* 371(1700):20150428
- Violin JD, DiPilato LM, Yildirim N, Elston TC, Zhang J, Lefkowitz RJ (2008) β 2-adrenergic receptor signaling and desensitization elucidated by quantitative modeling of real time cAMP dynamics. *J Biol Chem* 283(5):2949–2961
- Volman V, Bazhenov M, Sejnowski TJ (2013) Divide and conquer: functional segregation of synaptic inputs by astrocytic microdomains could alleviate paroxysmal activity following brain trauma. *PLoS Comput Biol* 9(1):e1002856
- Volterra A, Liaudet N, Savtchouk I (2014) Astrocyte Ca^{2+} signalling: an unexpected complexity. *Nat Rev Neurosci* 15:327–334
- Vyazovskiy VV, Olcese U, Hanlon EC, Nir Y, Cirelli C, Tononi G (2011) Local sleep in awake rats. *Nature* 472(7344):443
- Waehneldt TV, Matthieu J-M, Jeserich G (1986) Appearance of myelin proteins during vertebrate evolution. *Neurochem Int* 9(4):463–474

- Wake H, Moorhouse AJ, Jinno S, Kohsaka S, Nabekura J (2009) Resting microglia directly monitor the functional state of synapses in vivo and determine the fate of ischemic terminals. *J Neurosci* 29(13):3974–3980
- Wake H, Moorhouse AJ, Miyamoto A, Nabekura J (2013) Microglia: actively surveying and shaping neuronal circuit structure and function. *Trends Neurosci* 36(4):209–217
- Walz W (2000) Role of astrocytes in the clearance of excess extracellular potassium. *Neurochem Int* 36(4–5):291–300
- Wang X, Lou N, Xu Q, Tian G-F, Peng WG, Han X, Kang J, Takano T, Nedergaard M (2006) Astrocytic Ca^{2+} signaling evoked by sensory stimulation in vivo. *Nat Neurosci* 9(6):816–823
- Witcher M, Kirov S, Harris K (2007) Plasticity of perisynaptic astroglia during synaptogenesis in the mature rat hippocampus. *Glia* 55(1):13–23
- Wu X, Pan L, Liu Y, Jiang P, Lee I, Drevensek-Olenik I, Zhang X, Xu J (2013) Cell-cell communication induces random spikes of spontaneous calcium oscillations in multi-BV-2 microglial cells. *Biochem Biophys Res Commun* 431(4):664–669
- Yang L, Qi Y, Yang Y (2015) Astrocytes control food intake by inhibiting AGRP neuron activity via adenosine A1 receptors. *Cell Rep* 11(5):798–807
- Ying W (2008) NAD $^+$ /NADH and NADP $^+$ /NADPH in cellular functions and cell death: regulation and biological consequences. *Antioxid Redox Signal* 10(2):179–206
- Young KM, Psachoulia K, Tripathi RB, Dunn S, Cossell L, Attwell D, Tohyama K, Richardson WD (2013) Oligodendrocyte dynamics in the healthy adult CNS: evidence for myelin remodeling. *Neuron* 77(5):873–885
- Zalc B, Colman DR (2000) Origins of vertebrate success. *Science* 288(5464):271–271
- Zalc B, Goujet D, Colman D (2008) The origin of the myelination program in vertebrates. *Curr Biol* 18(12):R511–R512
- Zhang Y, Chen K, Sloan SA, Bennett ML, Scholze AR, O'Keeffe S, Phatnani HP, Guarneri P, Caneda C, Ruderisch N, Deng S, Liddelow SA, Zhang C, Daneman R, Maniatis T, Barres BA, Wu JQ (2014) An RNA-sequencing transcriptome and splicing database of glia, neurons, and vascular cells of the cerebral cortex. *J Neurosci* 34(36):11929–11947
- Zonta M, Angulo MC, Gobbo S, Rosengarten B, Hossmann KA, Pozzan T, Carmignoto G (2003) Neuron-to-astrocyte signaling is central to the dynamic control of brain microcirculation. *Nat Neurosci* 6:43–40
- Zorec R, Araque A, Carmignoto G, Haydon P, Verkhratsky A, Parpura V (2012) Astroglial excitability and gliotransmission: An appraisal of Ca^{2+} as a signaling route. *ASN Neuro* 4(2):e00080

Part II

Calcium Dynamics

Chapter 2

Data-Driven Modelling of the Inositol Trisphosphate Receptor (IP₃R) and its Role in Calcium-Induced Calcium Release (CICR)



Ivo Siekmann, Pengxing Cao, James Sneyd and Edmund J. Crampin

Abstract We review the current state of the art of data-driven modelling of the inositol trisphosphate receptor (IP₃R). After explaining that the IP₃R plays a crucial role as a central regulator in calcium dynamics, several sources of relevant experimental data are introduced. Single ion channels are best studied by recording single-channel currents under different ligand concentrations via the patch-clamp technique. The particular relevance of modal gating, the spontaneous switching between different levels of channel activity that occur even at constant ligand concentrations, is highlighted. In order to investigate the interactions of IP₃Rs, calcium release from small clusters of channels, so-called calcium puffs, can be used. We then present the mathematical framework common to all models based on single-channel data, aggregated continuous-time Markov models, and give a short review of statistical approaches for parameterising these models with experimental data. The process of building a Markov model that integrates various sources of experimental data is illustrated using two recent examples, the model by Ullah et al. and the “Park–Drive” model by Siekmann et al. (Biophys. J. 2012), the only models that account for all sources of data currently available. Finally, it is demonstrated that the essential features of the Park–Drive model in different models of calcium dynamics are preserved after reducing it to a two-state model that only accounts for the switching between the inactive “park” and the active “drive” modes. This highlights the fact that modal

I. Siekmann (✉)

Department of Applied Mathematics, James Parsons Building, 3 Byrom Street,
Liverpool, Merseyside L3 3AF, UK
e-mail: i.siekmann@ljmu.ac.uk

E. J. Crampin

Systems Biology Laboratory, Melbourne School of Engineering,
University of Melbourne, Melbourne, VIC, Australia

P. Cao · E. J. Crampin

Department of Mathematics and Statistics, University of Melbourne,
Melbourne, VIC, Australia

J. Sneyd

Department of Mathematics, University of Auckland, Auckland, New Zealand

E. J. Crampin

School of Medicine, University of Melbourne, Melbourne, VIC, Australia

gating is the most important mechanism of ligand regulation in the IP₃R. It also emphasises that data-driven models of ion channels do not necessarily have to lead to detailed models but can be constructed so that relevant data is selected to represent ion channels at the appropriate level of complexity for a given application.

Keywords Inositol trisphosphate receptor (IPR) · Single-channel data · Calcium puffs · Calcium dynamics · Modal gating

2.1 Introduction

A number of models have been published that relate different physiological processes involving glial cells to calcium dynamics. De Pittà et al. (2012) give an overview of current problems in the modelling of astrocytes. One area of continuing interest is the propagation of signals between astrocytes via intercellular calcium waves. Höfer et al. (2002) investigated the spreading of signals between astrocytes via calcium waves based on a model by Sneyd et al. (1994). Bennett et al. (2005, 2006) developed a more detailed model of calcium waves that combines underlying calcium dynamics with ATP release by purinergic receptors in order to demonstrate that calcium waves depend on ATP release rather than on IP₃ diffusion through gap junctions as in the model by Höfer et al. (2002). Edwards and Gibson (2010) later published a model that included both modes of signal propagation and concluded that both were necessary to account for data collected from the retina. Recently, the study of calcium waves has been extended from one- or two-dimensional to three-dimensional spatial domains (Lallouette et al. 2014). Macdonald and Silva (2013) model wave propagation on an astrocyte network derived from experimental data. The Bennett et al. model was used for investigating spreading depression, a wave of electrical silence that propagates through the cortex and depolarises neurons and glial cells (Bennett et al. 2008).

A fundamental problem in calcium dynamics in general is the question how multiple signals can be encoded by the dynamics of a single quantity, the concentration of calcium. De Pittà et al. (2008, 2009a,b) investigated how a stimulus could be encoded via the frequency or the amplitude or both frequency and amplitude which demonstrates that two different signals can be represented independently in an individual calcium signal. Dupont et al. (2011) showed in a detailed model how the signal received by a particular glutamate receptor is encoded via calcium oscillations.

Lavrentovich and Hemkin (2008), Zeng et al. (2009), Riera et al. (2011a,b) investigated spontaneous calcium oscillations in astrocytes and Li et al. (2012) explored their role in spreading depression.

Also the coupling of the astrocyte network with the neural network has been investigated. At the single-cell level, De Pittà et al. (2011) modelled the interaction of an astrocyte with a synapse. Allegrini et al. (2009), Postnov et al. (2009) study the influence of a network of astrocytes on a neural network.

Most recently, Barrack et al. (2014, 2015) explored the role of calcium signalling in neural development. By coupling calcium dynamics with a model of the cell cycle,

they examine how glial progenitors differentiate to neurons triggered by a calcium signal.

This review of the modelling literature on glial cells clearly demonstrates that the importance of calcium dynamics is well recognised—the majority of studies in the literature accounts for calcium signalling and often models are used to find a link of physiological processes with calcium signalling. In many cell types including glial cells, the inositol trisphosphate receptor (IP₃R) plays a crucial role in inducing oscillatory Ca²⁺ signals. In the presence of IP₃, opening of IP₃R channels leads to Ca²⁺ release from the endoplasmic reticulum (ER), an intracellular compartment with a very high Ca²⁺ concentration a few orders of magnitude higher than that of the cytoplasm. The IP₃R is activated by Ca²⁺ so that such a release event dramatically increases the open probability of the IP₃R which induces further release of Ca²⁺ (henceforth called calcium-induced-calcium release, or CICR) until a high Ca²⁺ concentration in the channel environment eventually inhibits the IP₃R.

The Li–Rinzel model (Li and Rinzel 1994), an approximation of the classical De Young–Keizer model (De Young and Keizer 1992), is by far the most commonly used representation of the IP₃R in models of glial cells. Only Allegri et al. (2009) and Lavrentovich and Hemkin (2008) chose different models based on Atri et al. (1993) or Tu et al. (2005), respectively. Dupont et al. (2011) use the model by Swillens et al. (1994) that explicitly accounts for the effect of interactions in a cluster of IP₃R channels. Early models of the IP₃R were designed to account for the bell-shaped Ca²⁺ dependency of the open probability p_O of the channel described by Bezprozvanny et al. (1991). Since then the dynamics of IP₃R in response to varying concentrations of IP₃, Ca²⁺ and ATP have been characterised much more comprehensively as well as the differences between the different isoforms of the IP₃R (among the models mentioned above, in fact, only Tu et al. (2005) account for the fact that astrocytes predominantly express type II IP₃R).

The scope of current data-driven models of ion channels has advanced beyond representing the average open probability p_O . Recent models capture the stochastic opening or closing of single IP₃Rs in aggregated Markov models; i.e., instead of only modelling the stationary behaviour of the channel, they represent the dynamics of the IP₃R (Sect. 2.3.4). Accurate representation of IP₃R dynamics depends on various sources of experimental data (Sects. 2.3.1 and 2.3.2) as well as appropriate statistical methods for fitting Markov models to these data (Sect. 2.3.5). Statistical methods automate the process of estimating parameters for a given Markov model. Thus, the main challenge of data-driven ion channel modelling is to define the structure of a Markov model which allows the integration of various sources of experimental data. We illustrate this process with two recent examples of models for the IP₃R (Sects. 2.3.6 and 2.3.7).

Once a model for a single channel has been developed, data from small clusters of channels can be used to determine how well the behaviour of a cluster is represented by an ensemble of single-channel models (Sect. 2.4.1). Studying the influence of an IP₃R model on calcium dynamics allows us to evaluate the relative importance of different aspects of single-channel dynamics. Cao et al. (2014) showed that the essential features of calcium dynamics in airway smooth muscle could be preserved

after iteratively simplifying the IP₃R model by Siekmann et al. (2012b) to a two-state model that only accounted for the switching between the inactive “park” and the active “drive” mode. In Sect. 2.4.2, it is shown that this also applies to the puff distribution. This demonstrates that modal gating is the most important regulatory mechanism of the IP₃R. It also emphasises that data-driven modelling of ion channels does not necessarily have to lead to detailed models based on complicated model structures but rather can be used so that relevant data is selected to represent ion channels at the appropriate level of complexity for a given application.

2.2 Mathematical Models of Calcium Dynamics/CICR

The purpose of a mathematical model of CICR is to explain the emergence of complex intracellular calcium dynamics such as oscillations as the result of interdependent calcium fluxes. This comprises both fluxes into and out of the cell as well as the exchange between the cytosol and intracellular stores (Fig. 2.1).

The dynamics of cytosolic (c) and stored calcium (c_{ER}) resulting from these fluxes can be represented by a system of differential equations:

$$\frac{dc}{dt} = J_{\text{IP}_3\text{R}} + J_{\text{RyR}} + J_{\text{in}} - J_{\text{pm}} - J_{\text{SERCA}} \quad (2.1)$$

$$\frac{dc_{\text{ER}}}{dt} = \gamma(J_{\text{SERCA}} - J_{\text{IP}_3\text{R}} - J_{\text{RyR}}) \quad (2.2)$$

Here, J_{in} is calcium influx from the extracellular space via calcium channels located in the cell membrane, and J_{pm} accounts for calcium removed from the cell by the plasma membrane pump. $J_{\text{IP}_3\text{R}}$ and J_{RyR} represent calcium release from the endoplasmic reticulum (ER) through the IP₃R and the RyR, respectively, and J_{SERCA} stands for reuptake of calcium into the ER by the SERCA pump. The conversion factor γ , the ratio of the cytoplasmic volume to the ER volume, is necessary because calcium concentrations are calculated with respect to the different volumes of these two compartments. The model (2.1), (2.2) provides a description of Ca²⁺ concentrations across the whole cell. This means that we cannot account for spatial effects due to heterogeneities of the spatial distribution of IP₃R, SERCA and other relevant components of the system. By using a deterministic model, we further assume that the various Ca²⁺ fluxes can be described as deterministic after averaging over a large number of channels and transporters. In Sect. 2.4, we will consider a stochastic model over a small spatial domain for a cluster of interacting IP₃Rs.

In a whole-cell model of calcium dynamics such as (2.1), (2.2), a representation of the IP₃R must, in principle, just provide a functional expression for

$$J_{\text{IP}_3\text{R}}([\text{IP}_3], [\text{Ca}^{2+}], [\text{ATP}]), \quad (2.3)$$

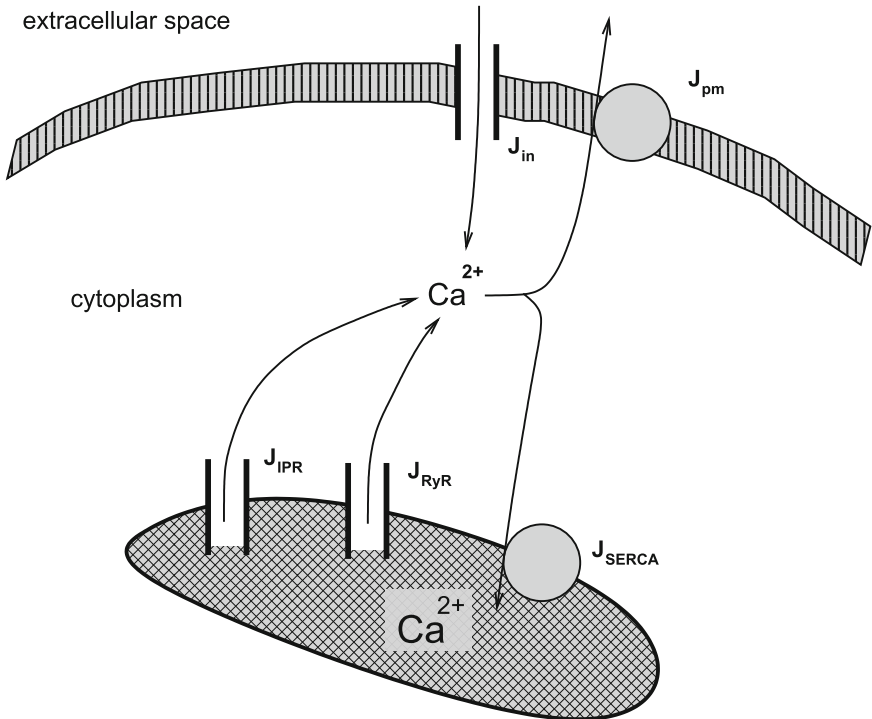


Fig. 2.1 General structure of calcium fluxes in glial (and other non-excitatory) cells. The central component is the flux J_{IPR} through the inositol trisphosphate receptor (IP₃R). The IP₃R is activated by binding of IP₃ which is generated upon stimulation of the cell by an agonist. This causes the release of Ca²⁺ from the endoplasmic reticulum (ER) to the cytoplasm. The resulting elevated Ca²⁺ concentration increases the open probability of the IP₃R and the ryanodine receptor (RyR) which stimulates further Ca²⁺ release. This mechanism is known as calcium-induced calcium release (CICR). At high concentrations, Ca²⁺ inhibits the IP₃R, i.e. the open probability of the IP₃R decreases. In consequence, J_{SERCA} influx into the ER through the SERCA pump dominates the efflux through IP₃R and RyR so that Ca²⁺ is reabsorbed by the ER. Ca²⁺ exchange with the extracellular space is controlled by uptake through various channels (J_{in}) and by extrusion via pumps (J_{pm})

the ligand-dependent flux through IP₃R channels present in a cell. Because the calcium concentration [Ca²⁺] is time-dependent, $J_{\text{IP}_3\text{R}}$ varies over time. In the early days of modelling of the IP₃R, phenomenological models were used for representing the IP₃R flux. A good example is the model by Atri et al. (1993):

$$J_{\text{IP}_3\text{R}}(p, c) = N_{\text{open}}k \left(\mu_0 + \frac{\mu_1}{k_\mu + p} \right) \left(b + \frac{V_1c}{k_1 + c} \right) \quad (2.4)$$

where $p = [\text{IP}_3]$, $c = [\text{Ca}^{2+}]$ and N_{open} is the number of open channels. The model by De Young and Keizer (1992) is derived from more detailed assumptions on chemical

interactions of the channel with its ligands. In Sect. 2.3.6, we present a more recent model (Ullah et al. 2012b) that is representative for this approach. The Hill function-type terms in (2.4) enabled Atri et al. to interpret their model in terms of a physical process but the main motivation of the model was to obtain a fit of the calcium-dependent whole-cell flux $J_{\text{IP}_3\text{R}}$ to data collected by Parys et al. (1992). From a purely mathematical point of view, phenomenological models seem to be the ideal approach for investigating the role of IP₃R in calcium dynamics—restriction to minimal models that generate the desired behaviour ensures that model behaviour can be analysed to a great extent. This allows us to test hypotheses on IP₃R regulation in an elegant way.

But the capability of simple mathematical expressions for the macroscopic flux $J_{\text{IP}_3\text{R}}$ to perform the appropriate functional role in calcium dynamics is only a relatively indirect test for IP₃R models. By following a phenomenological approach, we mostly ignore data that gives more direct information on the IP₃R, such as the molecular structure of the channel protein which can be obtained from crystallography and time series of opening and closing of a single channel from patch-clamp recordings. Taking into account these data may allow us to restrict the set of theoretically possible mathematical expressions and, in this way, also the set of possible mechanism.

2.3 Data-Driven Modelling of Single IP₃Rs

Because most biophysical data relate to single channels, data-driven modelling involves an important conceptual step—instead of directly specifying the whole-cell flux $J_{\text{IP}_3\text{R}}$, we first construct a model for the flux through a single channel. Whereas for the macroscopic flux $J_{\text{IP}_3\text{R}}$, which is averaged spatially over many channels distributed across the whole cell, the deterministic model (2.3) is appropriate, representing the flux through a single channel requires a stochastic model. In a second step, $J_{\text{IP}_3\text{R}}$ is then derived by appropriately averaging over the stochastic fluxes through individual channels.

In Sects. 2.3.1 and 2.3.2, we describe two sources of data that are commonly used for the construction of ion channel models. Ca²⁺ release data from small clusters of IP₃R, so-called calcium puffs (Sect. 2.3.3), can be used for validating models of single channels. In Sect. 2.3.4 aggregated continuous-time Markov models, the mathematical framework common to all models based on single-channel data is introduced. A short review of statistical approaches for fitting Markov models to single-channel data is given in Sect. 2.3.5. In Sects. 2.3.6 and 2.3.7, examples of two recent models of the IP₃R are given in order to illustrate different modelling approaches. Earlier models have been reviewed by Gin et al. (2009c) and Sneyd and Falcke (2005). Model comparisons (Sneyd et al. 2004; Hituri and Linne 2013) generally show that models not parameterised by fitting to experimental data may not do a very good job at reproducing the statistical properties of ion channel kinetics.

2.3.1 Molecular Structure

The mathematical structure of many ion channel models is designed to mimic the chemical structure of the channel protein. The motivation for this approach is to link molecular structure of the ion channel to its function.

In vertebrates, there exist three different genes encoding three different types of the IP₃R. In mammals, type I IP₃R is ubiquitously expressed but most cells express more than one isoform. The predominant isoform in astrocytes is type II IP₃R (Sharp et al. 1999; Holtzclaw et al. 2002). For each isoform, there are several splice variants.

Imaging the three-dimensional structure of the complete IP₃R and RyR channel proteins is challenging and only recently have accurate 3D visualisations of complete IP₃Rs using electron cryomicroscopy (cryo-EM) become available (Ludtke and Serysheva 2013). Parts of the channel can be imaged at higher resolution by crystallography and be superimposed on cryo-EM images (Fedorenko et al. 2014). These studies have revealed that IP₃R channels are tetramers i.e. they consist of four IP₃R proteins. These tetramers may consist of different IP₃R subtypes but experimental studies have so far concentrated on investigating homotetramers formed by four copies of the same subtype (but see Alzayady et al. 2013). The classical description by De Young and Keizer (1992) took into account this information by building a model from identical subunits that all had to be in an open state for the channel to open, although the model assumed three instead of four subunits.

Analysis of the amino acid sequence by mutation experiments has assigned functional roles to various segments; e.g., the IP₃ binding core (IBC), which contains an IP₃ binding site has been identified. There is less information on the number and localisation of Ca²⁺ binding sites. Because localisation of Ca²⁺ binding sites by mutation studies has been difficult, Foskett et al. (2007) infer various Ca²⁺ binding sensors from the observed co-regulation by IP₃ and Ca²⁺; see Foskett and Mak (2010) for a summary. Often models assume a certain number of IP₃ and Ca²⁺ binding sites and represent binding and unbinding of these ligands as transitions between states regulated by mass action kinetics. This modelling approach will be described in more detail in Sect. 2.3.6.

2.3.2 Patch-Clamp Recordings

Detailed studies of individual ion channels became possible due to the development of the patch-clamp technique. Neher and Sakmann (1976) were the first to detect the flow of ions through a single ion channel by measuring the resulting current at constant voltage. The time course of opening and closing can be inferred from the detected current which stochastically jumps between zero (closed) and one or more small nonzero current levels in the pA range (open) whose sign depends on the valence of the ion and the direction of the current.

Mak and Foskett (2015) recently reviewed the single-channel literature of IP₃R channels. An important experimental development that they highlight relates to the difficulty that IP₃Rs are naturally localised within cells rather than in the cell membrane. Whereas in earlier patch-clamp experiments, IP₃R channels were studied in artificial lipid bilayers, more recently investigating IP₃R in isolated nuclei is favoured because it is assumed that nuclei provide an environment similar to the endoplasmic reticulum (ER), the native domain of the IP₃R.

2.3.2.1 Stationary Data

If ligand concentrations (such as IP₃, Ca²⁺ and ATP) are kept constant for the whole duration of the experiment, we obtain stationary data. These data allow us to observe the “typical” channel dynamics for a given combination of ligands. The reason that we refer to these data as “stationary” is that we assume that the channel has fully adjusted to the concentration of ligands—the term stationary suggests that the channel has reached its stationary probability distribution; see Sect. 2.3.4. Because the stationary solution is only reached asymptotically, we can, in theory, never be sure that our ion channel has actually reached equilibrium. Instead, we can check if a data set is *not* stationary by using indicators such as the open probability. If the open probability averaged over a sufficient number of data points spontaneously changes (which indicates the switching of the channel to a different activity level), the channel may exhibit modal gating.

2.3.2.2 Modal Gating

Spontaneous switching between different levels of channel activity at constant ligand concentrations has been observed for a long time. The earliest example is perhaps from a classical study of the large-conductance potassium channel (BK) (Magleby and Pallotta 1983a, b). In IP₃R channels, modal gating was discovered only relatively recently (Ionescu et al. 2007). The authors found three different modes characterised by high (H), intermediate (I) and low (L) levels of open probabilities, p_O^H , p_O^I and p_O^L . They also realised the importance of modal gating for IP₃R regulation: they observed that the same three modes seemed to exist for different combinations of ligand concentrations. Because the IP₃R mostly seemed to adjust the time spent in each of the three modes, they proposed that modal gating is the major mechanism of ligand regulation in IP₃R channels.

One reason that the significance of modal gating has not been appreciated until recently is due to the fact that switching between different modes cannot always be recognised easily without statistical analysis. Recently, Siekmann et al. (2014) developed a statistical method which for a given set of single-channel data detects switching between an arbitrary number of modes M^i characterised by their respective open probabilities $p_O^{M^i}$. A software implementation which is publicly available under <https://github.com/merlinthemagician/icmestat.git> was applied to a large data set

from Wagner and Yule (2012). Siekmann et al. (2014) found that the same two modes, an inactive “park” ($p_O^{\text{park}} \approx 0$) and an active “drive” mode ($p_O^{\text{drive}} \approx 0.7$), were found across all combinations of ligands. There may be various reasons why two modes were observed rather than the three modes found in the earlier study (Ionescu et al. 2007); see Siekmann et al. (2014) for more details. But more importantly, a detailed study of a bacterial potassium channel (KscA) (Chakrapani et al. 2007a, b, 2011) strongly suggests that the stochastic dynamics characteristic for each mode may be closely related to distinct three-dimensional configurations (conformations) of the channel. Thus, whereas it is often difficult to relate individual open or closed states in ion channel models to distinct conformations of the channel protein, the set of model states that represents a particular mode may, in fact, have a biophysical counterpart (Siekmann et al. 2014). In order to confirm this hypothesis, more studies of modal gating for a variety of channels are needed.

Independent from its biophysical significance, appropriately accounting for modal gating is crucial from a modelling point of view. As we will see in Sect. 2.3.4, the phenomenon of modal gating demonstrates that a Markov process must be observed for a sufficiently long time in order to infer the correct stationary distribution; otherwise, we observe a “quasi-steady state”. For example, a channel whose kinetics is restricted to an active and an inactive mode can produce intermediate activity only by switching between both modes. Thus, a model that is not capable of switching between different levels of activity is misleading because it produces a constant open probability instead of alternating between highly different open probabilities. In their recent review, Mak and Foskett (2015) explicitly recognise the importance of modal gating which so far has only been represented in the most recent models (Ullah et al. 2012b; Siekmann et al. 2012b).

2.3.2.3 Response to Rapid Changes of Ligand Concentrations

Modal gating is an aspect of stationary data collected at constant concentrations of ligands. In contrast, Mak et al. (2007) designed an experiment where IP₃ and/or Ca²⁺ concentrations in the channel environment were rapidly altered in order to simulate an instantaneous change of ligand concentrations. Switching from ligand concentration where the IP₃R is inactive to conditions where the channel is maximally activated (and vice versa) enabled Mak et al. (2007) to investigate the question how fast the IP₃R responds to varying ligand concentrations. To illustrate the experiment, let us consider the change from inhibitory to activating conditions. At an inhibitory condition, the open probability of the channel is very close to zero ($p_O \approx 0$) so that initially the IP₃R is most likely closed. When changing from an inhibitory to an activating condition, the channel will activate but it needs a certain time to respond to the change. In order to measure this latency, Mak et al. (2007) recorded the time the channel took from when they altered the ligand concentration until the first opening. For the opposite change from activating to inhibitory conditions, they analogously detected the time the channel needed to switch from a high to a low level

of activity. This experiment was repeated multiple times for switching between the same conditions which enabled the authors to investigate the latency statistics. It was not only discovered that for some conditions the latencies were surprisingly long but interestingly, they also found that for some conditions the latency distributions were multi-modal which shows that multiple timescales may be observed for the same latency.

Due to the substantial effort required to perform these experiments (which have to be repeated multiple times for each condition where each repeat only gives a single data point rather than a time course), it is unsurprising that these data are very rare. In fact, to date, Mak et al. (2007) is the only data set of this kind currently available. Mak and Foskett (2015) explain that their data suggests that there may be long refractory periods between release events from the same IP₃R which makes these results particularly relevant for the modelling of Ca²⁺ puffs.

2.3.3 Calcium Puffs

So far we have only considered data recorded from single IP₃Rs. In order to understand how the macroscopic flux $J_{\text{IP}_3\text{R}}$ arises from the release of many individual channels, we have to consider the hierarchical nature of Ca²⁺ release. As reviewed by Parker et al. (1996), Falcke (2004) and Thurley et al. (2012), stochastic opening of a single IP₃R channel leads to a localised Ca²⁺ release event (a Ca²⁺ blip). Such a release further sensitises neighbouring IP₃R to induce more Ca²⁺ release through a few tightly clustered IP₃Rs by CICR (a Ca²⁺ puff). Sufficiently many puffs could eventually trigger a global elevation of [Ca²⁺]_i that is able to propagate through the entire cell (a Ca²⁺ wave) (Marchant et al. 1999). Thus, Ca²⁺ puffs play a crucial role: not only are they essential for the formation of functional global Ca²⁺ signals (Callamaras et al. 1998) but they also reflect the quantal Ca²⁺ releases by stochastic openings of IP₃R in vivo (Smith and Parker 2009).

Experimentally, Ca²⁺ release at a specific spatial position can be initiated by triggering release of caged IP₃ using a laser. A relative measure for the local Ca²⁺ concentration is obtained by detecting fluorescent dye bound to Ca²⁺ using a light microscope. For a given point within the cell the resulting time series is characterised by a sequence of stochastic spikes that are highly variable as far as the spike amplitude, the frequency and the time interval between subsequent spikes, the interpuff interval, are concerned. From a modelling point of view, these data can be used to test whether the single-channel behaviour represented in a model is able to account for the release from a cluster of interacting IP₃Rs. As explained in Sect. 2.4.1, Cao et al. (2013) found that the original model by Siekmann et al. (2012b) was incapable of generating the correct stochastic puff distribution as long as the adaptation to different ligand concentrations was assumed to occur instantaneously. After augmenting the model so that it accounted for the latency data by Mak et al. (2007) presented in the previous section, the puff statistics could be reproduced accurately.

The only other model that accounts for latency data is the model by Ullah et al. (2012b). Because the models by Siekmann et al. (2012b), Cao et al. (2013) and by Ullah et al. (2012b) are the only models that account for all aspects of single-channel data assumed to be necessary for an understanding of the IP₃R we focus on these models and the alternative modelling approaches that they represent in Sects. 2.3.6 and 2.3.7.

2.3.4 Aggregated Continuous-Time Markov Models

The most natural model for the stochastic process of opening and closing of a single ion channel is the aggregated continuous-time Markov model. A good introduction to the theory reviewed here is the classical paper by Colquhoun and Hawkes (1981) which also gives some simple but illustrative examples.

An aggregated continuous-time Markov model is a graph on a set of n_C closed and n_O open states $S = \{C_1, \dots, C_{n_C}, O_{n_C+1}, \dots, O_{n_C+n_O}\}$ (Fig. 2.2).

Between adjacent states S_i and S_j , the transition rate (from S_i to S_j) is given by $q_{ij} > 0$ so that the whole model is represented by a matrix with constant coefficients, the infinitesimal generator $\mathbf{Q} = (q_{ij})$. The time-dependent probability distribution $\mathbf{p}(t)$ over the state set S is the solution of the differential equation

$$\frac{d\mathbf{p}(t)}{dt} = \mathbf{p}(t)\mathbf{Q}, \quad \mathbf{p}(0) = \mathbf{p}_0. \quad (2.5)$$

The stochastic interpretation of (2.5) is as follows: for a given point in time, one particular state S_i of the model is “active”. But how long it will take until the current state S_i is vacated and which state S_j will be active after a time t cannot be answered with certainty (i.e. deterministically) due to the stochastic transitions between states.

For the model defined by (2.5), the Markov property holds both for the stochastic sequence of active states as well as for the time that it takes until the active state is left. In fact:

- (1) which state S_j will be the next active state only depends on the currently active state S_i , not on previously active states.
- (2) the time t_{S_i} it takes until the model exits from the state S_i , also called the *sojourn time* in S_i , does not depend on the time already spent in S_i .

The second point implies that sojourn times t_{S_i} must be exponentially distributed because the exponential distribution is the only continuous probability distribution with this property. This explains why multiple open and closed states may be needed for accurately representing the opening and closing of ion channels.

In order to ensure that $\mathbf{p}(t)$ is a stochastic vector i.e. $\sum_{i=1}^{n_S} p_i$, $p_i \geq 0$ for all $t \geq 0$, the matrix \mathbf{Q} must be conservative; i.e., for the diagonal elements q_{ii} , we have

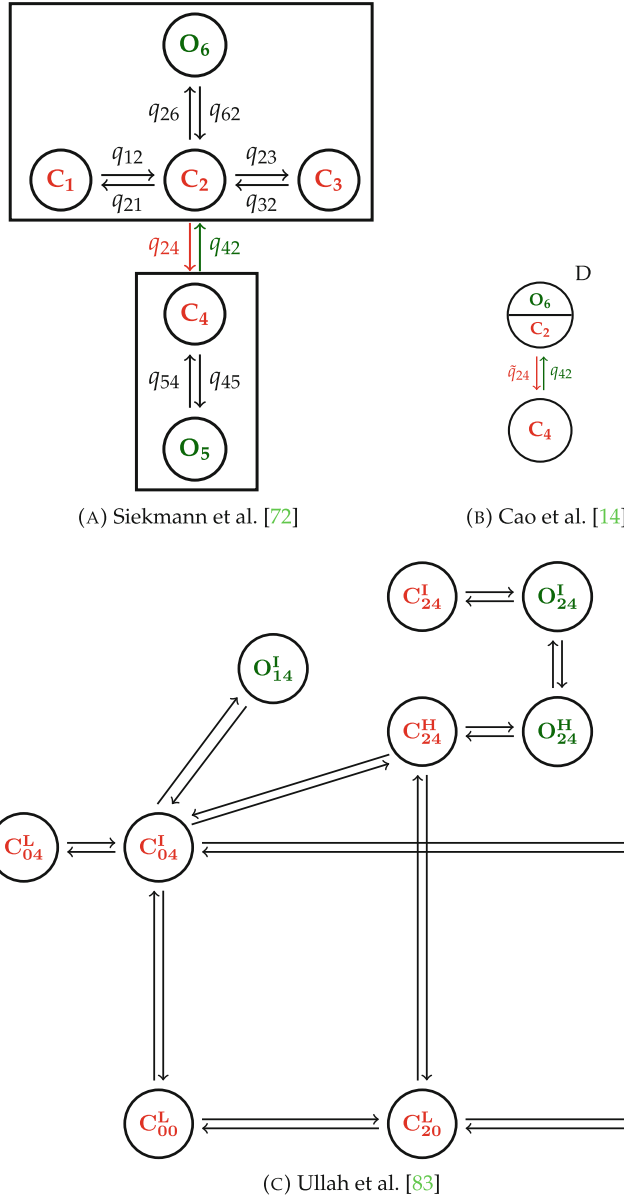


Fig. 2.2 Two examples of recent Markov models of the IP₃R. Two versions of the Park–Drive model are shown in (a) and (b), whereas the model by Ullah et al. (2012b) is shown in (c). The original six-state Park–Drive model (a) by Siekmann et al. (2012b) has been simplified by Cao et al. (2014) to a two-state model (b). As described in more detail in the main text, C_1 , C_3 and O_5 were omitted due to their low occupancy. The two states C_2 and O_6 of the Drive mode were approximated by a partially open state D which releases a ratio of $\frac{q_{26}}{q_{26}+q_{62}}$ of the flux J_r assumed to flow through a single channel. Due to the altered occupancy of the state D , the rate q_{24} must be corrected by the scaling factor so that we obtain $\bar{q}_{24} = q_{24} \frac{q_{62}}{q_{26}+q_{62}}$

$$q_{ii} = - \sum_{j \neq i} q_{ij}, \quad i, j = 1, \dots, n_S. \quad (2.6)$$

Provided that (2.6) holds, the solution

$$\mathbf{p}(t) = \mathbf{p}_0 \exp(\mathbf{Q}t), \quad (2.7)$$

is a stochastic vector for all $t > 0$ if and only if the initial distribution \mathbf{p}_0 is a stochastic vector. From (2.7), the time-dependent open probability $p_O(t)$ of the channel can be calculated by summing over the individual probabilities of all open states.

For large times t , the solution $\mathbf{p}(t)$ approaches a stochastic vector $\boldsymbol{\pi}$ which is known as the stationary distribution. This means that provided we wait sufficiently long, the expected frequency of observing a state S_i approaches a probability π_i . Because $\mathbf{p}(t)$ is the solution of a differential equation, $\boldsymbol{\pi}$ is, in fact, a stationary solution of (2.5) i.e. can be obtained by solving the equation

$$\boldsymbol{\pi} \mathbf{Q} = 0. \quad (2.8)$$

This homogeneous linear equation has non-trivial solutions because the matrix \mathbf{Q} is singular by (2.6). An argument based on Perron–Frobenius theory for nonnegative matrices ensures that $\boldsymbol{\pi}$ is a unique strictly positive stochastic vector. Moreover, $\boldsymbol{\pi}$ is stable so that for $t \rightarrow \infty$ indeed $\mathbf{p}(t)$ approaches $\boldsymbol{\pi}$, i.e. we have $\lim_{t \rightarrow \infty} \mathbf{p}(t) = \boldsymbol{\pi}$ (Seneta 1981).

2.3.5 Estimation of Markov Models from Experimental Data

Whereas the mathematical framework of aggregated Markov models was developed a short time after single-channel data became available, the statistical estimation of these models is a topic of current research. Most commonly used are approaches based on Bayesian statistics. For a given time series Y of open and closed events recorded from an ion channel, the conditional probability density $f(\mathbf{Q}|Y)$, known as the posterior density in the Bayesian framework, is used for determining a suitable Markov model with infinitesimal generator \mathbf{Q} . Note that both Y and \mathbf{Q} are considered as random variables; thus, the posterior distribution quantifies how likely a model \mathbf{Q} is under the condition that data Y have been observed. Direct calculation of the posterior distribution $f(\mathbf{Q}|Y)$ is analytically intractable and computationally prohibitive but efficient approaches for maximum likelihood estimation (MLE) i.e. estimating

$$\hat{\mathbf{Q}} = \operatorname{argmax}_{\mathbf{Q}} f(\mathbf{Q}|Y) \quad (2.9)$$

were published in the 1990s (Qin et al. 1996, 1997; Colquhoun et al. 1996). Software implementations of these methods have been made available freely for academic use.

Currently, the methods by Qin et al. (1996, 1997) can be obtained under the name QUB as stand-alone GUI applications at <http://www.qub.buffalo.edu/>. DCPROGS based on Colquhoun et al. (1996) is still under active development and the source code of the most recent version has been published on github: <https://github.com/DCPROGS>.

An alternative approach to maximum likelihood estimation has been pursued since the late 1990s. The aim of Markov chain Monte Carlo (MCMC) is to approximate the posterior density $f(\mathbf{Q}|Y)$ by sampling. MCMC enables us to randomly generate a sequence $(\mathbf{Q}^k)_{k=1}^N$ of models such that the expected frequency of a model \mathbf{Q}^k within this sequence is as large as the density $f(\mathbf{Q}^k|Y)$. Thus, by generating a sufficient number of samples, the posterior $f(\mathbf{Q}|Y)$ is approximated.

The early method by Ball et al. (1999) for estimation of a Markov model \mathbf{Q} depends on a suitable idealisation of discretely sampled measurements to continuous open and closed times. This leads to a difficult statistical problem that has been discussed widely in the ion channel literature as the “missed events” problem. Rosales and colleagues were the first to propose a method that directly uses the discrete measurements and thus does not require further idealisation of the data (Rosales et al. 2001; Rosales 2004). Their algorithm estimates a discrete-time Markov model which describes the transition probabilities between states during a sampling interval rather than the so-called infinitesimal generator \mathbf{Q} . Gin et al. (2009a) were the first to propose a method for estimating \mathbf{Q} from discretely sampled data, their method was extended to models with arbitrary numbers of open and closed states by Siekmann et al. (2011) and Siekmann et al. (2012a). The current version of the software implementation of this method is available on github: <https://github.com/merlinthemagician/ahmm.git>. For an overview of various approaches to statistical modelling based on single-channel data, see Gin et al. (2009c).

The crucial advantage of MCMC methods over MLE approaches is that uncertainties can be comprehensively understood by analysing the posterior $f(\mathbf{Q}|Y)$. Already marginal distributions for individual rate constants (Fig. 2.3) are helpful for localising and quantifying uncertainties within a model \mathbf{Q} .

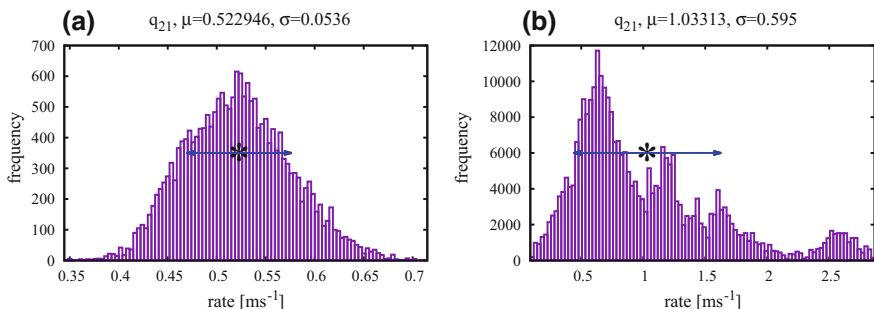


Fig. 2.3 Two examples for marginal distributions of rate constants. **a** Shows a histogram with a well-defined mean μ and a low standard deviation σ which indicates a low level of parameter uncertainty, whereas the histogram in **b** shows a complex multi-modal distribution which shows that multiple values of the rate constants are capable of representing the data

But even more can be gained by analysing statistical relationships between combinations of model parameters as, for example, demonstrated by Siekmann et al. (2012a). An important drawback of aggregated Markov models is non-identifiability i.e. model structures whose parameters cannot be inferred unambiguously from experimental data. Unfortunately, non-identifiable aggregated Markov models have not been completely classified (Fredkin et al. 1985; Fredkin and Rice 1986; Bruno et al. 2005). But non-identifiability can at least be detected by analysing the posterior distribution $f(\mathbf{Q}|Y)$ (Siekmann et al. 2012a). Thus, MCMC allows us to disentangle different causes of model uncertainty because it enables us to distinguish between parameter uncertainties due to insufficient or noisy data from pathologies in the structure of the model itself.

2.3.6 *The Ullah et al. Model*

A common approach for selecting a model structure for an ion channel model (which goes back at least to the classical model by De Young and Keizer (1992)) is to identify the states of the Markov model with different chemical states of the channel protein. As explained in Sect. 2.3.1, the IP₃R has various binding sites that allow specific ligands such as Ca²⁺ and IP₃ to bind to the channel protein and induce conformational changes of its three-dimensional structure. To account for this, model states are distinguished by how many particles of each ligand are bound to the channel. This assumption not only determines the state set of the model but also the possible transitions between states—in each state, we can either bind a ligand to a free binding site or remove a ligand from an occupied binding site. The dynamics of binding and unbinding of ligands is modelled by the law of mass action so that, in principle, the model is completely specified by the number of binding sites for each ligand. However, in practice, such a model would be heavily overparameterised when fitted to experimental data, so it is necessary to simplify the model.

To illustrate this with an example, consider the recent model by Ullah et al. (2012b) which is representative for this approach. The model states in Fig. 2.2c are arranged in a grid whose coordinates are mapped by a two-digit subscript. The horizontal axis of the grid (left digit) shows how many Ca²⁺ molecules are bound to the channel, whereas the vertical axis of the grid (right digit) indicates how many IP₃ binding sites are occupied, and whose columns. Thus, the position within the grid of a specific model state reflects how many Ca²⁺ ions and how many IP₃ molecules, respectively, are bound to the channel. For example, neither Ca²⁺ nor IP₃ are bound to the state C₀₀^L in the lower left corner, whereas two Ca²⁺ and four IP₃ binding sites are occupied for the states C₂₄^I, O₂₄^I, C₂₄^H and O₂₄^H. This is also indicated by the subscript indices—the first digit stands for the number of Ca²⁺ ions, whereas the second digit accounts for the number of IP₃ molecules bound to the channel. Figure 2.2c shows that only a subset of eight combinations, out of twenty possible combinations of occupying Ca²⁺, ATP and IP₃ binding sites, appears in the model. This considerable reduction is due to the removal of “low occupancy states”—Ullah

et al. (2012a) developed a perturbation theory approach that allows them to omit states with low stationary probabilities while at the same time accounting for the delays caused by passing through these states.

The model is constructed in an iterative four-step process integrating several sources of data. In a first step, Ullah et al. (2012b) use Ca^{2+} and IP_3 dependency of the average open probability p_O in order to determine a minimal set of model states. By optimising an Akaike information criterion (AIC) score function, a model with five closed, C_{00} , C_{04} , C_{24} , C_{32} and C_{34} , and one open state, O_{24} , was selected as the best fit for the p_O data.

In a second step, the ligand-dependent average probabilities π^L , π^I and π^H of being in modes characterised by three different levels of activity as well as the open probabilities in each mode (p_O^L , p_O^I and p_O^H) are used for assigning each of the six model states with a mode. At this step, some additional states are added because, for example, the state C_{04} must exist both in the low (C_{04}^L) as well as the intermediate mode (C_{04}^I) in order to get a good fit to the data. To properly account for the Ca^{2+} dependency of p_O^I , the open probability in the intermediate mode, an additional state O_{14}^I had to be introduced.

In the first two steps, Ullah et al. (2012b) use stationary probabilities in order to determine which states should appear in the model without considering transitions between states. In step 3, the authors infer the transitions that are needed to account for the average sojourn times τ^L , τ^I and τ^H in the three modes, whereas in step 4, data on the IP_3R response to rapid changes in Ca^{2+} and IP_3 (latencies) is used for determining the remaining transitions. Two additional states, C_{20}^L and C_{30}^L , are introduced in order to account for the latency data.

Until this point, data is only used for determining the model structure but not for parameter estimation. The model is finally parameterised using the latency data from Mak et al. (2007) or a combination of these data and single-channel time series obtained at three different constant Ca^{2+} concentrations.

2.3.7 Siekmann et al. “Park–Drive” Model

The main aims of the modelling study by Siekmann et al. (2012b) were first to account for switching between an inactive “park” and an active “drive” mode observed in the data set by Wagner and Yule (2012). As mentioned by Mak et al. (2007), Foskett and Mak (2010) and Mak and Foskett (2015), the importance of modal gating is well recognised and the implications for not appropriately capturing the timescale separation of fast opening and closing and slower switching between different activity levels is obviously unsatisfactory from a modelling point of view.

Second, these data provided the possibility to build a model of two different mammalian isoforms of the IP_3R , type I and type II IP_3R . In addition to a comparative study of type I and type II IP_3R , these data also include ligand dependency of ATP in addition to IP_3 and Ca^{2+} .

Third, Siekmann et al. (2012b) followed a primarily statistical approach to inference, rather than deriving the model from a binding scheme as the model by Ullah et al. (2012b) discussed above. Based on the experience of the earlier study by Gin et al. (2009b) where similar data could be fitted satisfactorily by a model with four states and only one ligand-dependent pair of rate constants, the number of parameters required to account for binding of IP₃, Ca²⁺ and ATP was likely to lead to a highly overparameterised model.

Due to these considerations, Siekmann et al. (2012b) made the inactive “park” and the active “drive” mode the construction principle of their model. In a first step, Markov models representing the stochastic dynamics for these two modes were constructed based on representative segments of the time series data that were characteristic for one of the two modes. Models with different numbers of states and model structures were fitted to these segments using the method by Siekmann et al. (2011, 2012a). It was observed that the best fits for either of the two modes across all combinations of ligands available in the large data set by Wagner and Yule (2012) were quantitatively similar. In agreement with Ionescu et al. (2007), this strongly suggested that the dynamics within park and drive modes are ligand-independent and that ligand-dependent regulation of IP₃R activity is achieved by varying the prevalence of park or drive mode.

In a second step after both park and drive mode had been modelled separately, a model of the ligand-dependent switching between the ligand-independent modes was constructed. The structure for the full Park–Drive model (Fig. 2.3a) was found by connecting the Markov models of park and drive mode obtained previously with a pair of transition rates. Due to the infrequent switching between park and drive mode observed in the data, it was decided that adding more than a single pair of transition rates was statistically unwarranted. The full Park–Drive model was then fitted to time series for all combinations of ligands of the study by Wagner and Yule (2012). The results of these fits established the ligand dependency of modal gating by the IP₃-, Ca²⁺- and ATP-dependent variation of the two transition rates.

Probably, the most important result of this study is that only models that take into account modal gating are able to accurately capture IP₃R kinetics. A channel whose kinetics is restricted to an active and an inactive mode can produce intermediate activity only by switching between both modes. Thus, a model that is not capable of switching between different levels of activity is misleading because it produces a constant open probability instead of alternating between highly different open probabilities. However, Cao et al. (2013) showed that accounting for modal gating alone was insufficient for modelling stochastic Ca²⁺ release events (puffs) that arise from the interactions of a few IP₃R channels. This study showed that the Park–Drive model has to be augmented by latency data (Mak et al. 2007) in order to account for the delayed response of individual channels to changes in ligand concentrations.

Constructing the Park–Drive model based on the two modes proved very useful in the study by Cao et al. (2014). The authors iteratively reduced the Park–Drive model to a two-state model that only approximates the dynamics of opening and closing within the modes and focuses on the level of activity determined by the relative prevalence of the modes. This further emphasises that switching between park and

drive mode rather than stochastic dynamics within the modes is the most important mechanism of IP₃R regulation.

2.3.8 Comparison of Type I and Type II IP₃R

The experimental study by Wagner and Yule (2012) not only investigated the IP₃R under a wide range of ligand conditions but also contrasted the behaviour of type I and type II IP₃R. In the models for type I and type II IP₃R constructed by Siekmann et al. (2012b) at a first glance, the similarities between both subtypes are probably more obvious than the differences. First of all, it is striking that both IP₃R subtypes can not only be represented in the same model structure but that active and inactive modes in both channels are nearly identical. This indicates that both subtypes have the same modes and that their differences are entirely due to differences in modal gating.

One difference is that type II IP₃R responds more sensitively to IP₃, in contrast to type I IP₃R. The most important differences between both subtypes was found to be ATP regulation; see Wagner and Yule (2012), Siekmann et al. (2012b) for details.

2.4 Using Data-Driven IP₃R Models in Calcium Dynamics

So far we have focused on the dynamics of individual IP₃Rs. In order to investigate the role of IP₃Rs in calcium dynamics, we will now consider the interaction of IP₃Rs within a cluster.

2.4.1 Modelling Calcium Puffs Using the Park–Drive IP₃R Model

There is a large literature on stochastic models of calcium puffs for which we refer to the recent review by Rüdiger (2014). Here, we present a simple model based on the Park–Drive model (Siekmann et al. 2012b) which is based on the following assumptions:

- The ER contains sufficiently high [Ca²⁺]_i to keep a nearly constant Ca²⁺ release rate through a cluster of IP₃R (Ullah et al. 2012c). Thus, ER [Ca²⁺]_i dynamics is not explicitly modelled.
- Ca²⁺ fluxes through the cell membrane have little effect on the very localised Ca²⁺ puffs far from cell membrane.
- We compartmentalise our model to capture heterogeneity within a cluster of IP₃Rs. We assume that sufficiently far away from individual channels we have a

homogeneous basal Ca²⁺ concentration $c = [\text{Ca}^{2+}]_i$ that slowly responds to the total Ca²⁺ flux $J_{\text{IP}_3\text{R}}$ through all IP₃R channels. In the vicinity of an open IP₃R channel, this basal concentration c is elevated by a constant c_h ; once the channel closes, it instantaneously equilibrates to the basal concentration c .

Furthermore, Ca²⁺ buffers are not considered except for a Ca²⁺ fluorescence dye. With these assumptions, the model is given as follows,

$$\frac{dc}{dt} = J_{\text{IP}_3\text{R}} + J_{\text{leak}} - \frac{V_d c}{c + K_d} - k_{\text{on}}(B - b)c + k_{\text{off}}b \quad (2.10)$$

$$\frac{db}{dt} = k_{\text{on}}(B - b)c - k_{\text{off}}b \quad (2.11)$$

where $V_d c / (c + K_d)$ models the flux (mainly via diffusion and SERCA) removing Ca²⁺ from the puff site. J_{leak} represents Ca²⁺ leak current from the ER for stabilising the resting $[\text{Ca}^{2+}]_i$ of $0.1 \mu\text{M}$ (a typical value). B and b represent the total dye buffer concentration and Ca²⁺-bound dye buffer concentration, respectively, and the buffering process follows the mass action kinetics. $J_{\text{IP}_3\text{R}}$ is the Ca²⁺ flux through open IP₃R, which is modelled by the production of a constant release flux rate (J_r) and number of open IP₃R channels (N_o), i.e. $J_{\text{IP}_3\text{R}} = J_r N_o$. Each open IP₃R will equally contribute to the elevation of cluster $[\text{Ca}^{2+}]_i$, c . Note that the actual $[\text{Ca}^{2+}]_i$ modulating each IP₃R is either c , when the receptor is in closed states, or $c + c_h$, when it is in open states. Parameters values are $J_r = 200 \mu\text{M}$, $V_d = 4000 \mu\text{M s}^{-1}$, $K_d = 12 \mu\text{M}$, $J_{\text{leak}} = 33 \mu\text{M s}^{-1}$, $B = 20 \mu\text{M}$, $k_{\text{on}} = 150 \mu\text{M s}^{-1}$, $k_{\text{off}} = 300 \text{s}^{-1}$ and $c_h = 120 \mu\text{M}$ (Cao et al. 2013). The cluster is assumed to contain 10 IP₃R channels.

The Park–Drive IP₃R model is used to simulate IP₃R state and coupled to the deterministic equations via a hybrid-Gillespie method (Rüdiger et al. 2007). However, the puff model based on the Park–Drive model fails to reproduce nonexponential interpuff interval (IPI) distribution due to the sole use of stationary single-channel data (i.e. Ca²⁺ is fixed during measurement) in IP₃R model construction. This does not allow the model to capture the transient single-channel behaviour when Ca²⁺ experiences a rapid change (Mak et al. 2007; Cao et al. 2013). Thus, the Park–Drive model is modified by incorporating time-dependent intermode transitions so that the transient single-channel behaviour is captured. In detail, the transition rates q_{24} and q_{42} are changed from constants to functions of four newly introduced gating variables,

$$q_{24} = a_{24} + V_{24}(1 - m_{24}h_{24}) \quad (2.12)$$

$$q_{42} = a_{42} + V_{42}m_{42}h_{42} \quad (2.13)$$

where m_{24} , h_{24} , m_{42} and h_{42} are gating variables obeying

$$\frac{dG}{dt} = \lambda_G(G_\infty - G), \quad G = m_{24}, h_{24}, m_{42}, h_{42}. \quad (2.14)$$

G_∞ is the steady state which is a function of channel-sensed Ca^{2+} and IP_3 concentrations and is determined by stationary single-channel data (i.e. the Park–Drive model). λ_G is the rate at which the steady state is approached. This is based on the fact that a IP_3R channel cannot immediately reach its steady state upon a transient change in Ca^{2+} concentration (Mak et al. 2007). The values of λ_G for m_{24} , h_{24} and m_{42} are found to be large so that the three gating variables could be approximated by their steady states i.e. $G = G_\infty$, a method called quasi-steady-state approximation. However, $\lambda_{h_{42}}$ at low $[\text{Ca}^{2+}]_i$ should be very small, reflecting a very slow recovery of IP_3R from high Ca^{2+} inhibition (Mak et al. 2007). Note that when $\lambda_{h_{42}}$ is sufficiently large, quasi-steady-state approximation applies and the modified IP_3R model reduces to the original Park–Drive model. Details about the functions and parameters can be seen in (Cao et al. 2013).

An example of simulation results using the modified Park–Drive model is given in Fig. 2.4. The waiting time between two successive puffs (or interpuff interval, IPI) is a key statistics to quantify the underlying process governing the emergence of puffs. Figure 2.5 shows that as $\lambda_{h_{42}}$ at low $[\text{Ca}^{2+}]_i$ increases, the IPI distribution changes from nonexponential to exponential, demonstrating that the missing slow timescale in the original Park–Drive model is very crucial to explain the inhomogeneous Poisson process governing puff emergence found by Thurley et al. (2011). The IPI distributions were generated by fitting the probability density function proposed by Thurley et al. (2011) to the simulated IPI histograms (Cao et al. 2013). The proposed IPI distribution is

$$P = \lambda(1 - e^{-\xi t})e^{[-\lambda t + \lambda(1 - e^{-\xi t})/\xi]}, \quad (2.15)$$

where t represents IPI. λ is the puff rate, a measure of the typical IPI (similar to average puff frequency), and ξ is the recovery rate.

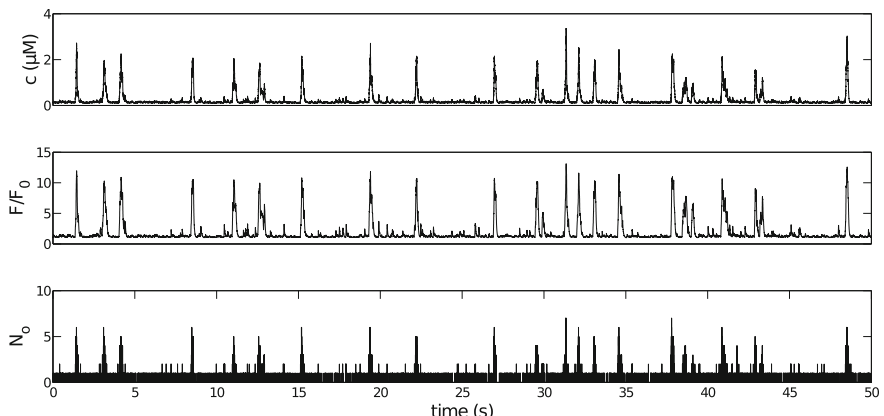
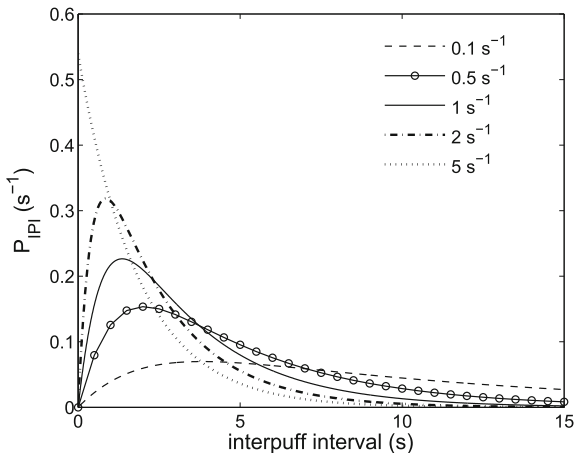


Fig. 2.4 A simulation result of calcium puffs. F/F_0 represents the ratio of Ca^{2+} -bound dye buffer b to its resting value. IP_3 concentration is $0.1 \mu\text{M}$. Adapted from Cao et al. (2013)

Fig. 2.5 Dependence of IPI distribution on λ_{h42} (indicated in the legend) at low $[Ca^{2+}]_i$. IP₃ concentration is 0.1 μM . Adopted from Cao et al. (2013)



Hence, this example shows the particular importance of considering both stationary and nonstationary data when constructing an IP₃R model. However, even if a model is constructed based on both data sets, it could also fail to reproduce Ca²⁺ puffs. One example is the Ullah model (Ullah et al. 2012b) as introduced in Sect. 2.3.6. A model simulation using the same puff model (2.10), (2.11) with the Ullah model is given in Fig. 2.6, where the Ca²⁺ signal behaves very irregularly and no puffs are clearly detected.

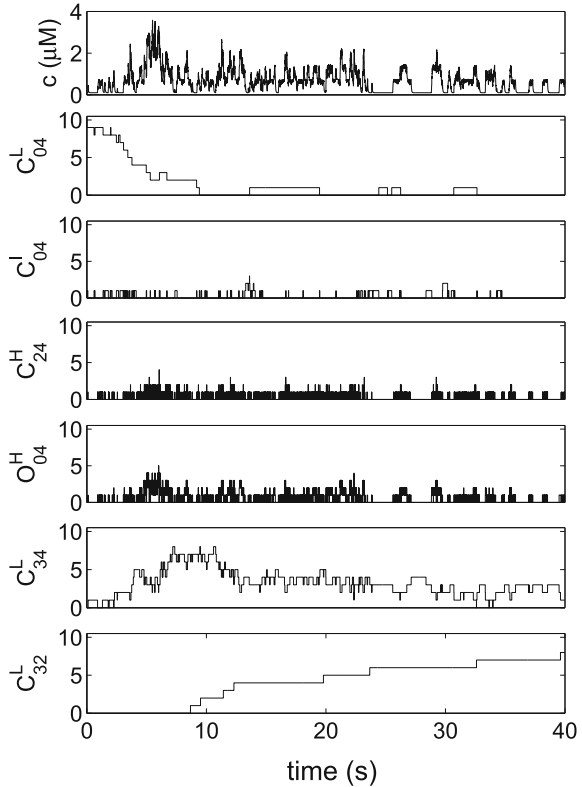
2.4.2 The Role of Modal Gating of IP₃R in Modulating Calcium Signals

The Park–Drive model (and its modified version) has the feature that IP₃R exists in two different modes, each of which contains multiple states, some open, some closed. Intermode transitions are important for modulating Ca²⁺ signals because of their ligand- and time-dependent property. However, structure within each mode may also have substantial contribution to the formation of different Ca²⁺ signals. Here, we examine the relative importance of intermode and intramode transitions using model reduction methods. By reducing the six-state IP₃R model to a two-state open/closed model, we will remove the intramodal structure, and a direct comparison between the statistics generated by the two IP₃R models will show the importance of intramodal structure.

The model reduction takes the following steps:

- The low probabilities of C_1 , C_3 and O_5 (sum of which is less than 0.03 for any $[Ca^{2+}]_i$) mean that the IP₃R either rarely visit those states or have very short dwell time in those states. This allows to completely remove the three states from the six-state model.

Fig. 2.6 A simulation result of calcium puffs using the Ullah IP₃R model. IP₃ concentration is 0.1 μM. y-axis values indicate the number of IP₃R channels in corresponding states. Parameter values for the puff model remain the same



- Transitions q_{26} and q_{62} are far larger (about two orders of magnitude) than q_{24} and q_{42} . By taking a quasi-steady-state approximation to the transition between C_2 and O_6 , we have $O_6 = C_2 q_{26}/q_{62}$. Combining C_2 and O_6 to be a new state D , i.e. $D = C_2 + O_6$, the six-state model becomes a two-state model, where D represents a partially open state with Ca²⁺ flux through the channel decreased by a factor of $q_{26}/(q_{62} + q_{26})$. Moreover, q_{24} needs to be rescaled by $q_{62}/(q_{62} + q_{26})$ due to the quasi-steady-state approximation so that the effective closing rate is $q_{24}q_{62}/(q_{62} + q_{26})$.

For model simulations, the state of each IP₃R is determined by the reduced IP₃R model and the equations governing the cytoplasmic calcium concentration and the calcium dye buffer remain Eqs. (2.10) and (2.11) except that calcium flux J_r is replaced by $q_{26}/(q_{26} + q_{62}) \cdot J_r$. Parameter values remain unchanged (Table 2.1).

Figure 2.7 shows the distributions of interpuff interval, puff duration and amplitude generated by using the 6-state IP₃R model (the Park–Drive model) and the reduced 2-state model. Reducing the intramodal structure does not qualitatively change the distributions but may lead to quantitative difference, which could be caused by missing open state O_5 that significantly contributes to the fluctuations of basal level of

Table 2.1 Model parameters. IP₃-dependent parameters are evaluated at a concentration of 0.1 μM as indicated by subscripts. Full model details are given in Cao et al. (2013)

Symbol	Description	Value	Units
<i>Gating kinetics</i>			
a_{24}	Basal level of q_{24}	$29.85_{p=0.1\mu M}$	s ⁻¹
V_{24}	Gating-dependent part of q_{24}	$312.85_{p=0.1\mu M}$	s ⁻¹
a_{42}	Basal level of q_{42}	$0.05_{p=0.1\mu M}$	s ⁻¹
V_{42}	Gating-dependent part of q_{42}	100	s ⁻¹
λ_{h24}	Rate of approach to steady state of h_{24}	40	s ⁻¹
n_{-24}	Hill coefficient for Ca ²⁺ dependency of $h_{24\infty}$	$0.04_{p=0.1\mu M}$	
k_{-24}	Half-saturation constant for Ca ²⁺ dependency of $h_{24\infty}$	$97.00_{p=0.1\mu M}$	
$h_{24\infty}$	Steady state of h_{24}	$\frac{k_{-24}^{n_{-24}}}{c^{n_{-24}} + k_{-24}^{n_{-24}}}$	
a_{h42}	Basal level of λ_{h42} (tuning parameter)	0.5	s ⁻¹
V_{h42}	Ca ²⁺ -dependent part of λ_{h42}	100	s ⁻¹
K_{h42}	Half-saturation constant for Ca ²⁺ -dependency of λ_{h42}	20	μM
λ_{h42}	Rate of approach to steady state of h_{42}	$a_{h42} + \frac{V_{h42} c^7}{c^7 + K_{h42}^7}$	s ⁻¹
n_{-42}	Hill coefficient for Ca ²⁺ dependency of $h_{42\infty}$	$3.23_{p=0.1\mu M}$	
k_{-42}	Half-saturation constant for Ca ²⁺ dependency of $h_{42\infty}$	$0.17_{p=0.1\mu M}$	
$h_{42\infty}$	Steady state of h_{42}	$\frac{k_{-42}^{n_{-42}}}{c^{n_{-42}} + k_{-42}^{n_{-42}}}$	
λ_{m24}	Rate of approach to steady state of m_{24}	100	s ⁻¹
n_{24}	Hill coefficient for Ca ²⁺ dependency of $m_{24\infty}$	$6.31_{p=0.1\mu M}$	
k_{24}	Half-saturation constant for Ca ²⁺ dependency of $m_{24\infty}$	$0.549_{p=0.1\mu M}$	
$m_{24\infty}$	Steady state of m_{24}	$\frac{c^{n_{24}}}{c^{n_{24}} + k_{24}^{n_{24}}}$	
λ_{m42}	Rate of approach to steady state of m_{42}	100	s ⁻¹
n_{42}	Hill coefficient for Ca ²⁺ dependency of $m_{42\infty}$	$11.16_{p=0.1\mu M}$	
k_{42}	Half-saturation constant for Ca ²⁺ dependency of $m_{42\infty}$	$0.40_{p=0.1\mu M}$	
$m_{42\infty}$	Steady state of m_{42}	$\frac{c^{n_{42}}}{c^{n_{42}} + k_{42}^{n_{42}}}$	
<i>Ca²⁺balance</i>			
c_h	Elevated Ca ²⁺ in vicinity of open IP ₃ R channel	120	μM
B	Total buffer concentration	20	μM
k_{on}	Binding of fluo4 buffer to Ca ²⁺	150	μMs ⁻¹
k_{off}	Unbinding of fluo4 buffer from Ca ²⁺	300	s ⁻¹
J_r	Flux of Ca ²⁺ through single channel	200	μMs ⁻¹
J_{leak}	Ca ²⁺ influx from cluster environment	33	μMs ⁻¹
V_d	Rate of cytoplasmic Ca ²⁺ removal from the cluster	4000	μMs ⁻¹
K_d	Half-saturation constant for cytoplasmic Ca ²⁺ removal	12	μM

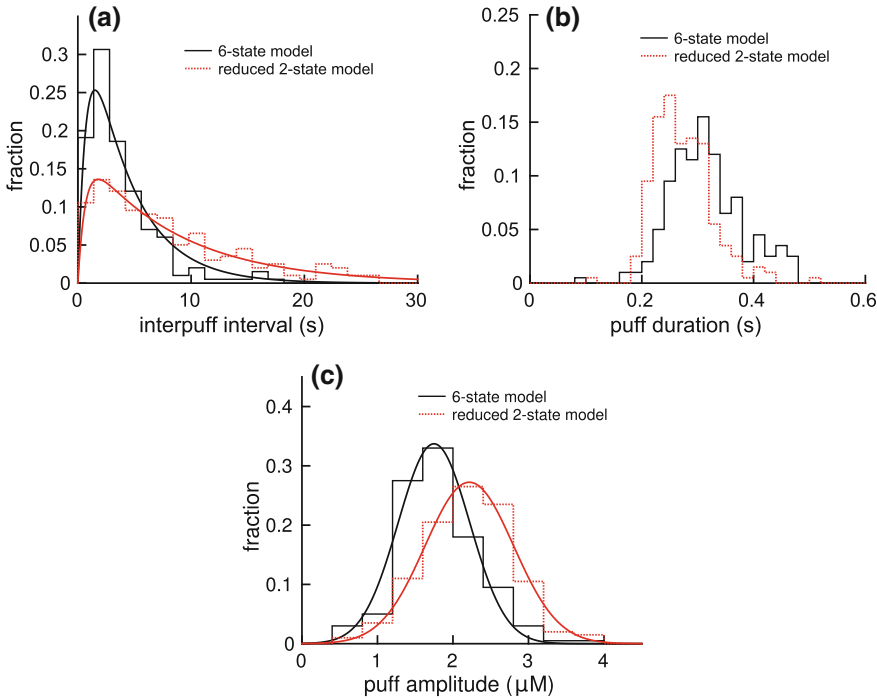


Fig. 2.7 Comparison of interpuff interval, puff duration and amplitude between the six-state IP₃R model (the Park–Drive model) and the reduced two-state model. 199 samples for each model were used to generate **a** and 200 samples for **b** and **c**. Interpuff interval distributions were fit by using Eq. 2.15 proposed by Thurley et al. (2011). Puff amplitude distributions were fit by normal distribution

$[\text{Ca}^{2+}]_i$. However, if the IP₃R channel is not very sensitive to small fluctuations of basal $[\text{Ca}^{2+}]_i$, the quantitative difference is significantly reduced (Cao et al. 2014). Thus, the fundamental process governing the generation of Ca^{2+} puffs and oscillations is primarily controlled by the modal structure but not the intramodal structure which improves the model fitting to the single-channel data.

2.5 Conclusions

The IP₃R plays a major role in CICR. For this reason, more and more aspects of its behaviour have been investigated by experiments. It usually turned out that new types of data had to be explicitly included in a model to account for them. For example, in early models such as the De Young–Keizer model (De Young and Keizer 1992), the rate constants were determined by fitting to the p_O observed at different calcium concentrations. But it soon became obvious that models parameterised with p_O data

could not be used for extrapolating the channel kinetics, i.e. the stochastic opening and closing. See Sneyd and Falcke (2005) or Ullah et al. (2012b) for a more detailed explanation why it is impossible to infer kinetics from the ligand dependency of the open probability p_O .

Just as kinetics cannot be inferred from p_O , it turned out that the response of the IP₃R to varying ligand concentrations cannot be predicted from data collected at constant ligand concentrations. This was demonstrated by the next generation of models that were directly fitted to single-channel data, taking into account the stochastic process of opening and closing. The simplest assumption for integrating models for different ligand concentration is that the IP₃R adjusts instantaneously. If this were true in practice, we could represent the channel kinetics appropriately by simply replacing the model for the kinetics at 0.05 μM with the model for the kinetics at 0.2 μM calcium as we increase the calcium concentration. But Cao et al. (2013) showed that only after taking into account rapid-perfusion data generated by Mak et al. (2007) was the model of Siekmann et al. (2012b) capable of generating the correct puff distribution.

It is important to note that taking into account, more data does not necessarily have to lead to more complicated models. Instead, after taking into account that the simpler kinetics of modal gating should capture the part of the channel dynamics that is most important for the functional role of the IP₃R in CICR, Cao et al. (2014) were able to reduce the six-state model by Siekmann et al. (2012b) to a two-state model. Thus, after interpreting experimental data in the right way, we are able to build models for the functional role of IP₃R that are nearly as simple as the early phenomenological models.

2.6 Future Work

After reviewing the current state of data-driven approaches to investigating the IP₃R we would like to take a look at promising future directions. In order to address the particular importance of modal gating, Siekmann et al. (2016) develop a novel hierarchical model structure that enables us to combine Markov models that represent the stochastic switching between modes with models that account for the characteristic opening and closing within different modes. Thus, models for both processes can be fitted separately (e.g. using the method by Siekmann et al. (2011, 2012a)) after analysing the data with statistical method presented by Siekmann et al. (2014). This allows us to build models for modal gating following a completely data-driven approach.

More generally, we have compared two current models as representative examples for different modelling approaches, Ullah et al. (Ullah et al. 2012b) and the Park–Drive model (Siekmann et al. 2012b; Cao et al. 2013, 2014). Although both approaches ultimately meet in the middle, their different construction principles impose different requirements for future progress. From a statistical point of view, representation of ligand interactions with a channel by mass action kinetics as in

Ullah et al. (2012b) defines a sufficiently large search space of models. It is crucial to select from this search space an appropriately simplified model that is obtained by removing states of the full model in a consistent way. A method for model reduction is provided by Ullah et al. (2012a,b) who demonstrate how data can be used to statistically select from all possible simplified models. A central principle of the biophysical approach is to design models in a way that closely follows physical principles. In this context, the bond graph approach to modelling ion channels by Gawthrop et al. (2017), Gawthrop and Crampin (2014) is highly relevant because it ensures that physical principles are enforced when choosing a model structure.

For models that primarily focus on a statistically satisfying representation in a first instance, the model selection problem arises again but in the other direction. Rather than starting from a model structure determined by an underlying mass action model, Gin et al. (2009b) and Siekmann et al. (2012b) iteratively increased the number of states in their model structure until further increasing the number of parameters appears statistically unwarranted. This process is time-consuming and may be computationally prohibitive if models exceed a certain number of states. Developing a method that is able to automatically compare models with an increasing number of states has proven to be difficult, as indicated by the few number of studies that have appeared on this subject after an early article on comparison of a finite number of models (Hodgson and Green 1999). A promising new direction is the nonparametric Bayesian method developed by Hines et al. (2015) which allows the authors to estimate the number of states within an ion channel data set. Determining the required number of open and closed states in a first step may increase efficiency because it restricts the class of models which have to be compared in a second step.

Acknowledgements Funding from NIH grant R01-DE19245 is gratefully acknowledged.

References

- Allegrini P, Fronzoni L, Pirino D (2009) The influence of the astrocyte field on neuronal dynamics and synchronization. *J Biol Phys* 35(4):413–423
- Alzayady KJ, Wagner LE, Chandrasekhar R, Monteagudo A, Godiska R, Tall GG, Joseph SK, Yule DI (2013) Functional inositol 1,4,5-trisphosphate receptors assembled from concatenated homo- and heteromeric subunits. *J Biol Chem* 288(41):29772–29784
- Atri A, Amundson J, Clapham D, Sneyd J (1993) A single-pool model for intracellular calcium oscillations and waves in the *Xenopus laevis* oocyte. *Biophys J* 65(4):1727–1739
- Ball FG, Cai Y, Kadane JB, O'Hagan A (1999) Bayesian inference for ion-channel gating mechanisms directly from single-channel recordings, using Markov chain Monte Carlo. *Proc R Soc Lond A* 455:2879–2932
- Barrack DS, Thul R, Owen MR (2014) Modelling the coupling between intracellular calcium release and the cell cycle during cortical brain development. *J Theor Biol* 347:17–32
- Barrack DS, Thul R, Owen MR (2015) Modelling cell cycle synchronisation in networks of coupled radial glial cells. *J Theor Biol* 377:85–97
- Bennett MR, Buljan V, Farnell L, Gibson WG (2006) Purinergic junctional transmission and propagation of calcium waves in spinal cord astrocyte networks. *Biophys J* 91:3560–3571

- Bennett MR, Farnell L, Gibson WG (2005) A quantitative model of purinergic junctional transmission of calcium waves in astrocyte networks. *Biophys J* 89:2235–2250
- Bennett MR, Farnell L, Gibson WG (2008) A quantitative model of cortical spreading depression due to purinergic and gap-junction transmission in astrocyte networks. *Biophys J* 95:5648–5660
- Bezprozvanny I, Watras J, Ehrlich BE (1991) Bell-shaped calcium-response curves of Ins(1,4,5)P₃-gated and calcium-gated channels from endoplasmic-reticulum of cerebellum. *Nature* 351(6329):751–754
- Bruno WJ, Yang J, Pearson JE (2005) Using independent open-to-closed transitions to simplify aggregated Markov models for ion channel gating kinetics. *Proc Nat Acad Sci USA* 102(16):6326–6331
- Callamaras N, Marchant JS, Sun XP, Parker I (1998) Activation and coordination of InsP₃-mediated elementary Ca²⁺ events during global Ca²⁺ signals in Xenopus oocytes. *J Physiol* 509:81–91
- Cao P, Donovan G, Falcke M, Sneyd J (2013) A stochastic model of calcium puffs based on single-channel data. *Biophys J* 105:1133–1142
- Cao P, Tan X, Donovan G, Sanderson MJ, Sneyd J (2014) A deterministic model predicts the properties of stochastic calcium oscillations in airway smooth muscle cells. *PLoS Comput Biol* 10(8):e1003783
- Chakrapani S, Cordero-Morales JF, Jogini V, Pan AC, Cortes DM, Roux B, Perozo E (2011) On the structural basis of modal gating behaviour in K⁺ channels. *Nat Struct Mol Biol* 18(1):67–75
- Chakrapani S, Cordero-Morales JF, Perozo E (2007a) A quantitative description of KscA gating II: single-channel currents. *J Gen Physiol* 130(5):479–496
- Chakrapani S, Cordero-Morales JF, Perozo E (2007b) A quantitative description of KscA gating I: macroscopic currents. *J Gen Physiol* 130(5):465–478
- Colquhoun D, Hawkes AG (1981) On the stochastic properties of single ion channels. *Proc R Soc Lond B* 211:205–235
- Colquhoun D, Hawkes AG, Srodzinski K (1996) Joint distributions of apparent open and shut times of single-ion channels and maximum likelihood fitting of mechanisms. *Philos Trans R Soc Lond A* 354:2555–2590
- De Pittà M, Volman V, Levine H, Pioggia G, De Rossi D, Ben-Jacob E (2008) Coexistence of amplitude and frequency modulations in intracellular calcium dynamics. *Phys Rev E - Stat Nonlin Soft Matter Phys* 77(3):030903
- De Pittà M, Goldberg M, Volman V, Berry H, Ben-Jacob E (2009a) Glutamate regulation of calcium and IP₃ oscillating and pulsating dynamics in astrocytes. *J Biol Phys* 35(4):383–411
- De Pittà M, Volman V, Levine H, Ben-Jacob E (2009b) Multimodal encoding in a simplified model of intracellular calcium signaling. *Cogn Process* 10(1):55–70
- De Pittà M, Volman V, Berry H, Ben-Jacob E (2011) A tale of two stories: astrocyte regulation of synaptic depression and facilitation. *PLoS Comput Biol* 7(12):e1002293
- De Pittà M, Volman V, Berry H, Parpura V, Volterra A, Ben-Jacob E (2012) Computational quest for understanding the role of astrocyte signaling in synaptic transmission and plasticity. *Front Comput Neurosci* 6
- De Young GW, Keizer J (1992) A single-pool inositol 1,4,5-trisphosphate-receptor-based model for agonist-stimulated oscillations in Ca²⁺ concentration. *Proc Nat Acad Sci* 89(20):9895–9899
- Dupont G, Lokenye EFL, Challiss RJ (2011) A model for Ca²⁺ oscillations stimulated by the type 5 metabotropic glutamate receptor: an unusual mechanism based on repetitive, reversible phosphorylation of the receptor. *Biochimie* 93(12):2132–2138
- Edwards J, Gibson W (2010) A model for Ca²⁺ waves in networks of glial cells incorporating both intercellular and extracellular communication pathways. *J Theor Biol* 263(1):45–58
- Falcke M (2004) Reading the patterns in living cells - the physics of Ca²⁺ signaling. *Adv Phys* 53(3):255–440
- Fedorenko OA, Popugaeva E, Enomoto M, Stathopoulos PB, Ikura M, Bezprozvanny I (2014) Intracellular calcium channels: inositol-1,4,5-trisphosphate receptors. *Eur J Pharmacol* 739:39–48 (Special Issue on Calcium Channels)

- Foskett JK, Mak D-OD (2010) Regulation of IP₃r channel gating by Ca²⁺ and Ca²⁺ binding proteins. In: Serysheva II (ed) Structure and function of calcium release channels, vol 66. current topics in membranes. Academic Press, New York, pp 235–272
- Foskett JK, White C, Cheung K, Mak D (2007) Inositol trisphosphate receptor Ca²⁺ release channels. *Physiol Rev* 87:593–568
- Fredkin DR, Montal M, Rice JA (1985) Identification of aggregated Markovian models: application to the nicotinic acetylcholine receptor. In: Cam LML, Olshen RA (eds) Proceedings of the Berkeley conference in Honor of Jerzy Neyman and Jack Kiefer, volume 1. Wadsworth, Belmont, CA, pp 269–289
- Fredkin DR, Rice JA (1986) On aggregated Markov processes. *J Appl Probab* 23(1):208–214
- Gawthrop PJ, Crampin EJ (2014) Energy-based analysis of biochemical cycles using bond graphs. *Proc Royal Soc Lond A: Math Phys Eng Sci* 470(2171):
- Gawthrop PJ, Siekmann I, Kameneva T, Saha S, Ibbotson MR, Crampin EJ (2017) Bond graph modelling of chemoelectrical energy transduction, *IET Sys Bio* 11(5):127–138. <https://doi.org/10.1049/iet-syb.2017.0006>, IET digital library, <http://digital-library.theiet.org/content/journals/10.1049/iet-syb.2017.0006>
- Gin E, Falcke M, Wagner LE, Yule DI, Sneyd J (2009a) Markov chain Monte Carlo fitting of single-channel data from inositol trisphosphate receptors. *J Theor Biol* 257:460–474
- Gin E, Falcke M, Wagner LE II, Yule DI, Sneyd J (2009b) A kinetic model of the inositol trisphosphate receptor based on single-channel data. *Biophys J* 96(10):4053–4062
- Gin E, Wagner LE II, Yule DI, Sneyd J (2009c) Inositol trisphosphate receptor and ion channel models based on single-channel data. *Chaos: an interdisciplinary J Nonlinear Sci* 19(3):037104
- Hines KE, Bankston JR, Aldrich RW (2015) Analyzing single-molecule time series via nonparametric Bayesian inference. *Biophys J* 108(3):540–556
- Hituri K, Linne M-L (2013) Comparison of models for IP₃ receptor kinetics using stochastic simulations. *PLoS ONE* 8(4):e59618
- Hodgson MEA, Green PJ (1999) Bayesian choice among Markov models of ion channels using Markov chain Monte Carlo. *Proc Royal Soc Lond Ser A-Math Phys Eng Sci* 455(1989):3425–3448
- Höfer T, Venance L, Giaume C (2002) Control and plasticity of intercellular calcium waves in astrocytes: a modeling approach. *J Neurosci* 22(12):4850–4859
- Holtzclaw L, Pandhit S, Bare D, Mignery G, Russell J (2002) Astrocytes in adult rat brain express type 2 inositol 1,4,5-trisphosphate receptors. *GLIA* 39(1):69–84
- Ionescu L, White C, Cheung K-H, Shuai J, Parker I, Pearson JE, Foskett JK, Mak D-OD (2007) Mode switching is the major mechanism of ligand regulation of InsP₃ receptor calcium release channels. *J Gen Physiol* 130(6):631–645
- Lallouette J, De Pittà M, Ben-Jacob E, Berry H (2014) Sparse short-distance connections enhance calcium wave propagation in a 3D model of astrocyte networks. *Frontiers Comput Neurosci* 8:45
- Lavrentovich M, Hemkin S (2008) A mathematical model of spontaneous calcium(II) oscillations in astrocytes. *J Theor Biol* 251(4):553–560
- Li B, Chen S, Zeng S, Luo Q, Li P (2012) Modeling the contributions of Ca²⁺ flows to spontaneous Ca²⁺ oscillations and cortical spreading depression-triggered Ca²⁺ waves in astrocyte networks. *PLoS ONE* 7(10)
- Li Y-X, Rinzel J (1994) Equations for InsP₃ receptor-mediated [Ca²⁺]_i oscillations derived from a detailed kinetic model: a Hodgkin-Huxley like formalism. *J Theor Biol* 166(4):461–473
- Ludtke SJ, Serysheva II (2013) Single-particle cryo-EM of calcium release channels: structural validation. *Curr Opin Struct Biol* 23:755–762
- Macdonald C, Silva G (2013) A positive feedback cell signaling nucleation model of astrocyte dynamics. *Frontiers Neuroeng* 6:4
- Magleby KL, Pallotta BS (1983a) Burst kinetics of single calcium-activated potassium channels in cultured rat muscle. *J Physiol-Lond* 344:605–623
- Magleby KL, Pallotta BS (1983b) Calcium dependence of open and shut interval distributions from calcium-activated potassium channels in cultured rat muscle. *J Physiol-Lond* 344:585–604

- Mak D-OD, Foskett JK (2015) Inositol 1,4,5-trisphosphate receptors in the endoplasmic reticulum: a single-channel point of view. *Cell Calcium* 58(1):67–78
- Mak D-OD, Pearson JE, Loong KPC, Datta S, Fernández-Mongil M, Foskett JK (2007) Rapid ligand-regulated gating kinetics of single inositol 1,4,5-trisphosphate receptor Ca²⁺ release channels. *EMBO Rep* 8(11):1044–1051
- Marchant J, Callamaras N, Parker I (1999) Initiation of IP₃-mediated Ca²⁺ waves in Xenopus oocytes. *EMBO J* 18:5285–5299
- Neher E, Sakmann B (1976) Single-channel currents recorded from membrane of denervated frog muscle fibres. *Nature* 260(5554):799–802
- Parker I, Choi J, Yao Y (1996) Elementary events of InsP₃-induced Ca²⁺ liberation in Xenopus oocytes: hot spots, puffs and blips. *Cell Calcium* 20(2):105–121
- Parry JB, Sernett SW, DeLisle S, Snyder PM, Welsh MJ, Campbell KP (1992) Isolation, characterization, and localization of the inositol 1,4,5-trisphosphate receptor protein in *Xenopus laevis* oocytes. *J Biol Chem* 267(26):18776–18782
- Postnov D, Koreshkov R, Brazhe N, Brazhe A, Sosnovtseva O (2009) Dynamical patterns of calcium signaling in a functional model of neuron-astrocyte networks. *J Biol Phys* 35(4):425–445
- Qin F, Auerbach A, Sachs F (1996) Idealization of single-channel currents using the segmental K-means method. *Biophys J* 70(2, Part 2):MP432
- Qin F, Auerbach A, Sachs F (1997) Maximum likelihood estimation of aggregated Markov processes. *Proc R Soc Lond Ser B-Biol Sci* 264:375–383
- Riera J, Hatanaka R, Ozaki T, Kawashima R (2011a) Modeling the spontaneous Ca²⁺ oscillations in astrocytes: inconsistencies and usefulness. *J Integr Neurosci* 10(04):439–473
- Riera J, Hatanaka R, Uchida T, Ozaki T, Kawashima R (2011b) Quantifying the uncertainty of spontaneous Ca²⁺ oscillations in astrocytes: particulars of Alzheimer's disease. *Biophys J* 101(3):554–564
- Rosales R (2004) MCMC for hidden Markov models incorporating aggregation of states and filtering. *Bull Math Biol* 66:1173–1199
- Rosales R, Stark JA, Fitzgerald WJ, Hladky SB (2001) Bayesian restoration of ion channel records using hidden Markov models. *Biophys J* 80(3):1088–1103
- Rüdiger S (2014) Stochastic models of intracellular calcium signals. *Phys Rep* 534(2):39–87
- Rüdiger S, Shuai J, Huisenga W, Nagaiah C, Warnecke G, Parker I, Falcke M (2007) Hybrid stochastic and deterministic simulations of calcium blips. *Biophys J* 93(6):1847–1857
- Seneta E (1981) Non-negative Matrices and Markov Chains, 2nd edn. Springer Series in Statistics, Springer, New York
- Sharp AH, Nucifora FC Jr, Blondel O, Sheppard CA, Zhang C, Snyder SH, Russell JT, Ryugo DK, Ross CA (1999) Differential cellular expression of isoforms of inositol 1,4,5-triphosphate receptors in neurons and glia in brain. *J Comp Neurol* 406(2):207–220
- Siekmann I, Crampin EJ, Sneyd J (2012a) MCMC can detect non-identifiable models. *Biophys J* 103(11):1275–1286
- Siekmann I, Fackrell M, Crampin EJ, Taylor P (2016) Modelling modal gating of ion channels with hierarchical Markov models. *Proceedings of the Royal Society of London A* 472, 20160122
- Siekmann I, Sneyd J, Crampin EJ (2014) Statistical analysis of modal gating in ion channels. *Proc R Soc Lond A* 470(2166):20140030
- Siekmann I, Wagner LE II, Yule D, Crampin EJ, Sneyd J (2012b) A kinetic model of type I and type II IP₃R accounting for mode changes. *Biophys J* 103(4):658–668
- Siekmann I, Wagner LE II, Yule D, Fox C, Bryant D, Crampin EJ, Sneyd J (2011) MCMC estimation of Markov models for ion channels. *Biophys J* 100:1919–1929
- Smith IF, Parker I (2009) Imaging the quantal substructure of single IP₃R channel activity during Ca²⁺ puffs in intact mammalian cells. *Proc Nat Acad Sci USA* 106(15):6404–6409
- Sneyd J, Charles A, Sanderson M (1994) A model for the propagation of intercellular calcium waves. *Am J Physiol - Cell Physiol* 266:C293–C302
- Sneyd J, Falcke M (2005) Models of the inositol trisphosphate receptor. *Prog Biophys Mol Biol* 89:207–245

- Sneyd J, Falcke M, Dufour JF, Fox C (2004) A comparison of three models of the inositol trisphosphate receptor. *Prog Biophys Mol Biol* 85:121–140
- Swillens S, Combettes L, Champeil P (1994) Transient inositol 1,4,5-trisphosphate-induced Ca^{2+} release: a model based on regulatory $\text{Ca}^{(2+)}$ -binding sites along the permeation pathway. *Proc Nat Acad Sci* 91(21):10074–10078
- Thurley K, Skupin A, Thul R, Falcke M (2012) Fundamental properties of Ca^{2+} signals. *Biochim Biophys Acta* 8:1185–1194
- Thurley K, Smith IF, Tovey SC, Taylor CW, Parker I, Falcke M (2011) Timescales of IP_3 -evoked Ca^{2+} spikes emerge from Ca^{2+} puffs only at the cellular level. *Biophys J* 101:2638–2644
- Tu H, Wang Z, Bezprozvanny I (2005) Modulation of mammalian inositol 1,4,5-trisphosphate receptor isoforms by calcium: a role of calcium sensor region. *Biophys J* 88(2):1056–1069
- Ullah G, Bruno WJ, Pearson JE (2012a) Simplification of reversible Markov chains by removal of states with low equilibrium occupancy. *J Theor Biol* 311:117–129
- Ullah G, Mak D-OD, Pearson JE (2012b) A data-driven model of a modal gated ion channel: the inositol 1,4,5-trisphosphate receptor in insect Sf9 cells. *J Gen Physiol* 140(2):159–173
- Ullah G, Parker I, Mak DOD, Pearson JE (2012c) Multi-scale data-driven modeling and observation of calcium puffs. *Cell Calcium* 52:152–160
- Wagner LE, Yule DI (2012) Differential regulation of the InsP_3 receptor type-1 and -2 single channel properties by InsP_3 , Ca^{2+} and ATP. *J Physiol* 590(14):3245–3259
- Zeng S, Li B, Zeng S, Chen S (2009) Simulation of spontaneous Ca^{2+} oscillations in astrocytes mediated by voltage-gated calcium channels. *Biophys J* 97(9):2429–2437

Chapter 3

Intracellular Calcium Dynamics: Biophysical and Simplified Models



Yulia Timofeeva

Abstract Calcium ions are an important second messenger in living cells. A fundamental approach for studying calcium signalling is the combination of state-of-the-art experimental techniques with spatiotemporal mathematical models of calcium regulation. Extensive modelling work on calcium oscillations and waves consists of a variety of theoretical/computational methods and models of different complexity. Some models can be assigned to a category of biologically realistic, detailed models, analysis of which is restricted to numerical methods. Other models can be placed in a category of simplified, minimal models susceptible to mathematical analysis. In this chapter, we provide an overview of a number of models for intracellular calcium dynamics belonging to both categories. Both types of models complement each other nicely and are vital for a better understanding of the complex mechanisms involved in cellular calcium signalling.

3.1 Introduction

Biological rhythms occur at all levels of biological organisation, and besides quite obvious examples such as the beating of the heart, the sleep-wake and hormonal cycles, lung respiration and central pattern generation of locomotion in animals, there are many instances of biological oscillations at the cellular level (Goldbeter 1996; Goldbeter et al. 2012). The discovery of calcium (Ca^{2+}) oscillations within the last three decades can be viewed as one of the most significant findings in the field of intracellular signalling. These oscillations occur in a large number of cell types, either spontaneously or as a result of an external stimulus (by a hormone or a neurotransmitter), and they represent the most widespread oscillatory phenomenon at the cellular level, besides the electrical rhythms in neuronal and muscle cells (see, for example, reviews by Carafoli (2002) and Petersen et al. (2005) for a historical perspective on major developments in Ca^{2+} signalling). Moreover, Ca^{2+} oscillations

Y. Timofeeva (✉)

Department of Computer Science and Centre for Complexity Science,
University of Warwick, Coventry CV4 7AL, UK

e-mail: y.timofeeva@warwick.ac.uk

are often associated with the propagation of Ca^{2+} waves within the cytosol (an area within the entire cell membrane exclusive of organelles) and also between adjacent cells, leading to one of the major examples of spatiotemporal organisation at the cellular level (Dupont et al. 2007).

The progress of the experimental results on cytosolic Ca^{2+} signalling that has taken place over the years has been examined in a series of recent reviews and books, for example, in Berridge et al. (2000, 2003), Combettes et al. (2004), Berridge (2005), Rizzuto and Pozzan (2006), Miyazaki (2006), Krebs and Michalak (2007) and Bootman et al. (2011). Here we briefly recall the main properties of Ca^{2+} oscillations and waves as determined from a large number of experimental studies. Period of Ca^{2+} oscillations ranges from nearly one second to tens of minutes, depending on the cell type. The shape of the oscillations is also highly variable; some of them are quasi-sinusoidal, whilst others take the form of abrupt spikes which are often preceded by a gradual increase reminiscent of the pacemaker depolarising potential in oscillatory neurons or cardiac cells. It has been repeatedly observed that oscillations occur only in a certain range of stimulation and that the frequency of Ca^{2+} spikes increases with the intensity of the stimulus. In addition to this encoding of agonist concentration in the frequency, these oscillatory patterns might also encode the type of the involved agonist (Falcke 2004). Signalling information is also known to be encoded in the amplitude of the Ca^{2+} spikes. This combination of frequency and amplitude modulation provides oscillatory Ca^{2+} patterns with an effective mechanism for selective recruitment of downstream targets (Parekh 2011). Besides the direct induction of oscillations by activating Ca^{2+} channels at the surface of the cell membrane, it is often possible to elicit a train of Ca^{2+} spikes by increasing the level of extracellular or intracellular Ca^{2+} or the level of inositol 1,4,5-trisphosphate (IP_3). The latter messenger is synthesised in response to the binding of an extracellular agonist to a receptor in the surface cell membrane and is known to raise the level of cytosolic Ca^{2+} through mobilisation from intracellular stores (Berridge 2009).

Ca^{2+} signalling in the form of oscillations is closely related to signalling in the form of the wave-like propagations mediated by diffusive transport of Ca^{2+} ions, see, for example, (Røttingen and Iversen 2000; Dupont et al. 2007; Leybaert and Sanderson 2012). The velocity of Ca^{2+} waves varies in different cells; the wave propagates at a rate of the order of $10\text{ }\mu\text{m/s}$ on the surface of oocytes (Jaffe 1993), $30\text{ }\mu\text{m/s}$ in hepatocytes (Thomas et al. 1991) and at a rate close to $100\text{ }\mu\text{m/s}$ in the cytoplasm of cardiac cells (Takamatsu and Wier 1990). High-resolution imaging in a variety of cell types shows that Ca^{2+} travelling waves can vary in their appearance by propagating in either a continuous manner or as a sequence of bursts. Another interesting aspect of intracellular Ca^{2+} regulation is the generation of global events built up from elemental local events called *puffs* or *sparks* (which, respectively, reflect the opening of a group of either the inositol 1,4,5-trisphosphate receptors or the ryanodine receptors discussed below). These local events are simple examples of the stochastic nature of intracellular Ca^{2+} dynamics due to the individual gating of Ca^{2+} channels. Some large cells (particularly, *Xenopus* oocytes, but also, for example, larger cardiac cells and networks of astrocytes and glia) can demonstrate highly complex wave patterns, exhibiting hot spots, spherical, spiral and planar waves, for example (Lechleiter et al. 1991; Lipp and Niggli 1993; Kaneko et al. 2000).

Moreover, some cell types support propagation of intercellular Ca^{2+} waves, which are believed to be mediated by the passage of IP_3 molecules and Ca^{2+} ions through gap junctions connecting neighbouring cells, although extracellular messengers such as ATP may also be involved [see Boitano et al. (1992), Dupont et al. (2000), Paemeleire et al. (2000), Scemes and Giaume (2006), Leybaert and Sanderson (2012)]. Highly versatile intra and intercellular Ca^{2+} signals operating over a wide range of spatial and temporal scales are known to regulate a large number of cellular functions, such as synaptic plasticity, muscle contraction, gene transcription, cell proliferation, bursting oscillations, cardiac rhythms (Berridge et al. 2000; Clapham 2007; Bootman et al. 2011).

Before discussing ways of modelling Ca^{2+} oscillations and waves, we first overview the regulatory mechanisms involved in the control of Ca^{2+} concentration ($[\text{Ca}^{2+}]$) within a cell. Two classes of Ca^{2+} oscillations can be recognised; those that depend primarily on the influx of Ca^{2+} through channels located on the cell membrane, and those that depend primarily on Ca^{2+} release from internal stores. In this latter class, distinctions can be made on the basis of whether the release of Ca^{2+} is dominated by the ryanodine receptors (RyRs), the inositol 1,4,5-trisphosphate receptors (IP_3 Rs) or a combination of both types (see schematic diagram in Fig. 3.1). In response to signals at the cell membrane, Ca^{2+} is released from the endoplasmic reticulum (ER) into the cytosol in the form of global or spatially localised puffs/sparks (Berridge 2005). The surface cell membrane consists of several different types of Ca^{2+} channels: voltage-gated Ca^{2+} channels that open in response to depolarisation of the cell membrane; receptor-operated channels that open in response to the binding of an external ligand; second messenger-operated channels that open in response to the binding of a cellular second messenger; and mechanically operated channels that open in response to mechanical stimulation. The mechanism of transduction of the signal at the cell membrane to the ER depends on the nature of the initial stimulus. In all cell types, external ligand binding to its receptor channel initiates a cascade

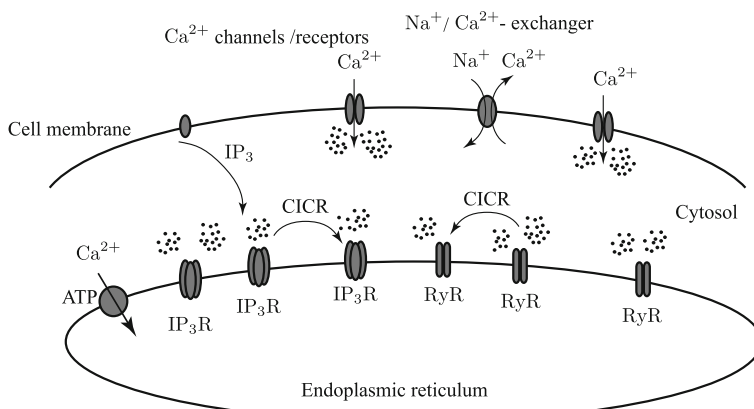


Fig. 3.1 Schematic diagram of the pathways involved in the control of cytosolic Ca^{2+} oscillations

of signals which ultimately leads to the release of Ca^{2+} from the ER. In the case of the second messenger IP_3 , its diffusion into the cell and subsequent binding to IP_3Rs located on the ER results in Ca^{2+} release (Berridge 2009). In excitable cells, an action potential or activation of receptor-operated channels results in influx of Ca^{2+} across the cell membrane which subsequently acts as the messenger to stimulate the RyRs, and also IP_3Rs , to release Ca^{2+} through an autocatalytic process referred to as Ca^{2+} -induced Ca^{2+} release (CICR) (Endo et al. 1970). Both the RyRs and IP_3Rs are subject to several levels of regulation on the cytosolic side where Ca^{2+} can both promote and inhibit its release from either channel. At low $[\text{Ca}^{2+}]$ release is stimulated by Ca^{2+} , whereas at high $[\text{Ca}^{2+}]$ it is inhibited. Thus, Ca^{2+} potentiates its own release and can stimulate release from neighbouring receptors resulting in propagation of Ca^{2+} waves by the triggering of the CICR mechanism. Of equal importance to the regulation of Ca^{2+} release from the ER are the mechanisms of Ca^{2+} clearance from the cytosol. This function is performed by a number of transporters located in the cell membrane and the ER. One such transporter is the ER calcium ATPase which is a Ca^{2+} pump located in the membrane of the ER whose function is to accumulate Ca^{2+} into the internal stores using ATP as an energy source (Stokes and Green 2003). Another mechanism of Ca^{2+} removal is a $\text{Na}^+/\text{Ca}^{2+}$ -exchanger in the cell membrane that uses the energy of the Na^+ electrochemical gradient to remove Ca^{2+} from the cell at the expense of Na^+ entry.

Modelling of Ca^{2+} oscillations and waves has contributed and continues to contribute significantly to our better understanding of the complex Ca^{2+} signalling machinery in living cells [see, for example, Schuster et al. (2002), Falcke (2004) and a recently published book (Dupont et al. 2016)]. This chapter provides an overview of a number of theoretical models for intracellular Ca^{2+} oscillations and waves. In Sect. 3.2, the general principles of modelling Ca^{2+} oscillations are described, together with a biophysically realistic model for an IP_3R proposed by De Young and Keizer (1992). Due to its nonlinear form, this model as well as its reduced version (Li and Rinzel 1994) can only be analysed by the use of numerical methods. In Sect. 3.3, we discuss spatial models of Ca^{2+} dynamics, firstly a model based on the detailed biophysical model of De Young and Keizer (1992) and then a simplified, but mathematically tractable, model for Ca^{2+} wave propagation in one- and two-dimensional cases. Finally, in Sect. 3.4, we give some concluding remarks.

3.2 Single-Compartment Ca^{2+} Models

The mechanism of Ca^{2+} oscillations relies on feedback processes that regulate cytosolic $[\text{Ca}^{2+}]$. Whilst extracellular $[\text{Ca}^{2+}]$ varies between 1 and 2 mM, cytosolic $[\text{Ca}^{2+}]$ at a resting level fluctuates between 50 and 100 nM. In response to cellular stimulation, the cytosolic $[\text{Ca}^{2+}]$ can transiently rise to between 1 and 10 μM (Berridge et al. 2000). The cell has to regulate any changes in $[\text{Ca}^{2+}]$ strictly within defined limits, as although increases in cytosolic $[\text{Ca}^{2+}]$ are necessary for many cellular functions, excessive sustained elevations can be cytotoxic and may lead to cell

death. In order to achieve this, the cell is equipped with a repertoire of Ca^{2+} channels, binding proteins, pumps and exchangers discussed in Sect. 3.1.

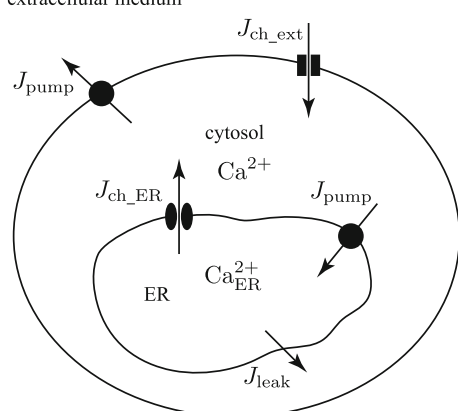
Many models of Ca^{2+} oscillations are based on the interpretation of essential fluxes and described using the language of differential equations. The rate of change of $[\text{Ca}^{2+}]$ in the cytosol, $C(t)$, depends on a combination of fluxes contributing positively and negatively towards $[\text{Ca}^{2+}]$:

$$\frac{dC}{dt} = J_{\text{in}} - J_{\text{out}}. \quad (3.1)$$

Ca^{2+} influx (J_{in}) usually occurs via two principal pathways: inflow from the extracellular medium through Ca^{2+} channels located in the cell membrane and release from internal stores via IP_3 Rs or RyR s (see Fig. 3.2). Removal of Ca^{2+} from the cytosol (J_{out}) also occurs in two principal ways: it is pumped out of a cell and is sequestered back into the ER. Ca^{2+} ions can also passively leak from the ER into the cytosol. Described by systems of nonlinear ordinary differential equations (ODEs) capable to support self-sustained oscillations, the deterministic models of Ca^{2+} signalling typically demonstrate excitable, oscillatory or bistable local dynamics. Excitable dynamical systems respond to reasonably small perturbations of a linearly stable stationary state with a large amplitude excursion that ultimately returns the system to rest. Oscillatory dynamical systems are different in that they exhibit sustained oscillations, typically around an unstable fixed point. Finally, bistability refers to systems with two stable stationary states, perhaps separated by an unstable state.

One of the earliest models for IP_3 -dependent Ca^{2+} release is the so-called two-pool model. It assumes the existence of two distinct internal stores (pools), one of which is sensitive to IP_3 , whereas the other one is sensitive to Ca^{2+} (Goldbeter et al. 1990; Goldbeter 1996). The IP_3 produced in response to the agonist stimulation leads to a release of Ca^{2+} from the IP_3 -sensitive pool through IP_3 Rs. This released Ca^{2+} can then stimulate additional release from the Ca^{2+} -sensitive pool. A crucial

Fig. 3.2 Schematic diagram of the main fluxes involved in intracellular Ca^{2+} dynamics



assumption of this model is that $[Ca^{2+}]$ in the IP_3 -sensitive pool remains constant, as the pool is quickly refilled from the extracellular medium. The model is described by two nonlinear ODEs and can be put into the form of a generalised FitzHugh–Nagumo model initially proposed for describing excitable nerve membrane (FitzHugh 1961; Nagumo et al. 1962). The FitzHugh–Nagumo model is a minimal model capable of supporting self-sustained oscillations, and its characteristics are common to many models describing excitable biological systems at the cellular level. In the two-pool model, Ca^{2+} stimulates its own release which is terminated when $[Ca^{2+}]$ in the Ca^{2+} -sensitive pool becomes too low. However, subsequent experimental evidence has indicated that the cytosolic Ca^{2+} can both stimulate and inhibit its own release on two different time scales, fast and slow, respectively (Parker and Ivorra 1990). This sequential activation and inactivation of the IP_3R by Ca^{2+} is believed to be the fundamental mechanism underlying IP_3 -dependent Ca^{2+} oscillations, and a number of models incorporating this mechanism have been proposed since (see, for example, Falcke (2004); Sneyd and Falcke (2005) for reviews).

One of the classical models for a biophysically realistic IP_3R was developed by De Young and Keizer (1992). It mimics the molecular subunit configuration of the IP_3R to reflect the activation/inactivation sequence of the channel resulting from the binding of Ca^{2+} and IP_3 to the IP_3R . Here we will consider this model in more detail together with its reduction.

3.2.1 The De Young–Keizer Model

The De Young–Keizer (DYK) model assumes that the IP_3R is composed of three independent and identical subunits. This simplifies the actual tetrameric structure of the IP_3R , which has four identical subunits (Mikoshiba 2007), but can be easily extended to account for it through a straightforward modification. Each of the three subunits includes a binding site activated by IP_3 , activated by Ca^{2+} and inactivated by Ca^{2+} (see Fig. 3.3). Only when IP_3 and Ca^{2+} bind to the IP_3 -activated and Ca^{2+} -activated sites, does the receptor open for a Ca^{2+} flux. Each state of the subunit is given by X_{ikj} , $i, k, j \in \{0, 1\}$, where the first index refers to the IP_3 binding site, the second to the Ca^{2+} -activated site and the third to the Ca^{2+} -inactivated site. If the binding site is occupied, the corresponding index is equal 1; otherwise it is 0. The model generates eight possible receptor states with correlated transitions between them as shown in Fig. 3.3, where I and C denote $[IP_3]$ and $[Ca^{2+}]$, respectively. The ODEs for the receptor states are based on mass-action kinetics, for example:

$$\frac{dX_{000}}{dt} = [k_{-1}X_{100} - k_1IX_{000}] + [k_{-4}X_{001} - k_4CX_{000}] + [k_{-5}X_{010} - k_5CX_{000}]. \quad (3.2)$$

Experimental data indicates that the receptor subunits act in a cooperative fashion, and therefore the receptor is assumed to be open only when all three subunits are in the

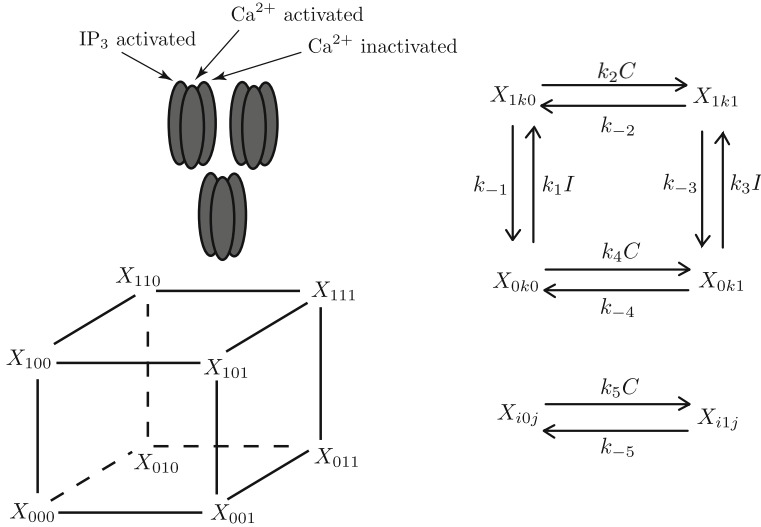


Fig. 3.3 Schematic diagram of the IP_3 receptor in the De Young–Keizer model

state X_{110} , leading to the open probability of the receptor to be X_{110}^3 . The DYK model consists of seven ODEs for the receptor states (with the constraint $\sum_{i,k,j} X_{ikj} = 1$, expressing conservation of probability) and with the following equation for Ca^{2+} dynamics:

$$\frac{dC}{dt} = \underbrace{(\Omega_C X_{110}^3 + \Omega_L)(C_T - (1 + \rho_A)C)}_{J_{\text{receptor}} + J_{\text{leak}}} - \underbrace{O_P \mathcal{H}_2(C, K_P)}_{J_{\text{pump}}} \\ = \rho_A (\Omega_C X_{110}^3 + \Omega_L)(C_{\text{ER}} - C) - O_P \mathcal{H}_2(C, K_P), \quad (3.3)$$

where $C_{\text{ER}} = (C_T - C)/\rho_a$ denotes $[\text{Ca}^{2+}]$ in the ER, ρ_A is the volume ratio between the ER and the cytosol, and C_T is the total $[\text{Ca}^{2+}]$. The Ca^{2+} flux through the IP_3 R controlled by the receptor permeability coefficient Ω_C as well as an IP_3 -independent leak from the ER into the cytosol characterised by a constant Ω_L are proportional to the concentration difference between the ER and the cytosol. Here the model disregards depletion of Ca^{2+} in the ER and therefore C_{ER} is considered to be a constant. The last term in (3.3) describes the action of Ca^{2+} ATPases that pump Ca^{2+} from the cytosol into the ER and is modelled by the Hill function $\mathcal{H}_n(x, K) = x^n/(x^n + K^n)$ with the maximal Ca^{2+} uptake rate O_P .

Parameters in the model are usually chosen to obtain agreement with the steady-state (equilibrium) data, showing that the receptor open probability is a bell-shaped function of the cytosolic $[\text{Ca}^{2+}]$ (Bezprozvanny et al. 1991). Behaviour of the DYK model can be summarised by a bifurcation diagram widely used in dynamical systems and showing the possible long-term behaviour (fixed points, periodic orbits, quasi-periodic orbits, etc) of a system as a function of a chosen parameter. The bifurcation

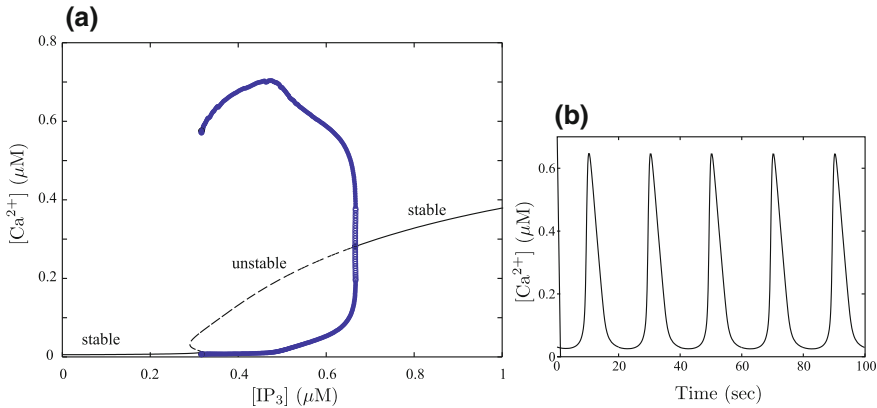


Fig. 3.4 **a** Bifurcation diagram of the DYK model. Dark blue circles denote maximal and minimal amplitudes of periodic orbits giving Ca^{2+} oscillations. **b** An example of Ca^{2+} oscillations in the DYK model for $I = 0.53 \mu M$

Table 3.1 Parameters of the De Young–Keizer model used in Timofeeva and Coombes (2003)

$k_1 400 \mu M^{-1} s^{-1}$	$k_{-1} 52 s^{-1}$	$\rho_A \Omega_C 20 s^{-1}$
$k_2 0.2 \mu M^{-1} s^{-1}$	$k_{-2} 0.21 s^{-1}$	$\rho_A \Omega_L 0.004 s^{-1}$
$k_3 400 \mu M^{-1} s^{-1}$	$k_{-3} 377.36 s^{-1}$	$O_P 1.2 \mu M \cdot s^{-1}$
$k_4 0.2 \mu M^{-1} s^{-1}$	$k_{-4} 0.029 s^{-1}$	$K_P 0.1 \mu M$
$k_5 20 \mu M^{-1} s^{-1}$	$k_{-5} 1.65 s^{-1}$	$C_{ER} 1 \mu M$

diagram of the DYK model as a function of the main bifurcation parameter I is shown in Fig. 3.4a. Other parameters are given in Table 3.1.

The diagram demonstrates that there is only one stable fixed point for low and high $[IP_3]$. For a small window of I values, three steady-state solutions exist as the curve of steady states folds up. When the system has an unstable fixed point, periodic oscillations occur and the figure shows the maximum and minimum of the periodic oscillations. Here the kinetic parameters of the IP_3R are as in the original work of De Young and Keizer (1992), whereas some of the other parameters, particularly Ω_C and Ω_L , are modified. These modified parameters lead to the bifurcation diagram with a homoclinic bifurcation at low $[IP_3]$, and therefore a larger range of periods for frequency encoding, whilst remaining within biologically constrained bounds. More details about such bifurcation structure can be found in Timofeeva and Coombes (2003). A typical example of Ca^{2+} oscillations in the DYK model is shown in Fig. 3.4b.

3.2.2 Reduction of the De Young–Keizer Model

The complexity of the DYK model consisting of eight ODEs provides motivation to simplify the model with the retention of its essential properties. One simplification of it was suggested by Li and Rinzel (1994) who have shown that the original full

model can be reduced to just two ODEs having the form of a Hodgkin–Huxley type model initially proposed for an excitable membrane (Hodgkin and Huxley 1952). Experiments indicate that IP_3 and Ca^{2+} bind quickly to the activating sites giving rise to the assumption that the receptor is in a quasi-steady-state with respect to IP_3 binding and Ca^{2+} activation. This is implied by the parameter values for the detailed receptor model shown in Table 3.1, where k_i and k_{-i} , $i = 1, 3, 5$ are significantly larger than k_i and k_{-i} , $i = 2, 4$. Thus, the receptor states can be arranged into two groups: those without Ca^{2+} bound to the inactivating site ($X_{000}, X_{010}, X_{100}$ and X_{110}) called group I states, and those with Ca^{2+} bound to the inactivating site ($X_{001}, X_{011}, X_{101}$ and X_{111}) called group II states. Within each group the binding states are assumed to be at a quasi-steady-state with respect to transitions within the group. Introducing the inactivation variable $h = X_{000} + X_{100} + X_{010} + X_{110}$ (a linear combination of group I states), assuming that the group I binding sites are all in quasi-steady-state ($dX_{ik0}/dt = 0$) and neglecting slow terms allows one to find the group I state probabilities as

$$X_{000} = \frac{d_1 d_5 h}{(I + d_1)(C + d_5)}, \quad X_{100} = \frac{d_5 I h}{(I + d_1)(C + d_5)}, \quad (3.4)$$

$$X_{010} = \frac{d_1 C h}{(I + d_1)(C + d_5)}, \quad X_{110} = \frac{I C h}{(I + d_1)(C + d_5)}, \quad (3.5)$$

where $d_i = k_{-i}/k_i$. An identical procedure can be applied to the group II receptor states to obtain:

$$X_{001} = \frac{d_3 d_5 (1 - h)}{(I + d_3)(C + d_5)}, \quad X_{101} = \frac{d_5 I (1 - h)}{(I + d_3)(C + d_5)}, \quad (3.6)$$

$$X_{011} = \frac{d_3 C (1 - h)}{(I + d_3)(C + d_5)}, \quad X_{111} = \frac{I C (1 - h)}{(I + d_3)(C + d_5)}. \quad (3.7)$$

A differential equation for h can be derived by adding the ODEs for the group I states with the inclusion of transitions between the group I and group II states and using the obtained quasi-steady-state expressions (3.4)–(3.7). It gives

$$\frac{dh}{dt} = \left[\frac{k_{-2} I + k_{-4} d_3}{I + d_3} \right] (1 - h) - \left[\frac{(k_{-4} d_1 d_2 + k_{-2} d_4 I) C}{d_2 d_4 (I + d_1)} \right] h. \quad (3.8)$$

This leads to the reduced DYK model described by only two ODEs, Eq.(3.3) for the Ca^{2+} dynamics and Eq.(3.8) for the inactivation variable, combined with the algebraic equation for X_{110} given in (3.5). The dynamics of the inactivation variable h is reminiscent of that of the gating variables in the Hodgkin-Huxley model of nerve membrane (Hodgkin and Huxley 1952), and the Li–Rinzel model can be written as

$$\frac{dC}{dt} = \rho_A(\Omega_C m_\infty^3 h^3 + \Omega_L)(C_{\text{ER}} - C) - O_P \mathcal{H}_2(C, K_P), \quad (3.9)$$

$$\frac{dh}{dt} = \frac{h_\infty - h}{\tau_h}, \quad (3.10)$$

where

$$m_\infty = \mathcal{H}_1(I, d_1) \mathcal{H}_1(C, d_5), \quad h_\infty = \frac{Q_2}{Q_2 + C}, \quad (3.11)$$

$$\tau_h = \frac{1}{O_2(Q_2 + C)}, \quad Q_2 = d_2 \frac{I + d_1}{I + d_3}. \quad (3.12)$$

Here $O_2 = k_2 = k_4$. The bifurcation diagram of the reduced DYK model (not shown here, but can be found in (Li and Rinzel, 1994)) is in good qualitative agreement with that of the full DYK model, see (Timofeeva and Coombes, 2003) for a bifurcation diagram of the reduced DYK model with parameters given in Table 3.1. Importantly, the reduced model captures the essential features of the full model suggesting that the assumptions used in the mathematical reduction are both realistic and effective for simplification of the original DYK model.

3.3 Spatiotemporal Ca²⁺ Models

As we discussed in Introduction section, oscillations of intracellular Ca²⁺ do not often occur uniformly throughout the cell, but are organised into repetitive intracellular Ca²⁺ waves (Røttingen and Iversen 2000; Dupont et al. 2007; Leybaert and Sanderson 2012). The observed Ca²⁺ waves in many types of cells are believed to be the result of Ca²⁺ diffusion between Ca²⁺ release sites. Although travelling waves cannot be explained by diffusion in all cell types, e.g. (Cornell-Bell et al. 1990; Wang et al. 2000; Toma et al. 2008), it is a reasonable assumption for modelling intracellular Ca²⁺ waves. According to this hypothesis, the cell cytosol forms either an excitable or an oscillatory system. In either of these cases, the linking of release sites by diffusion can lead to coordinated waves of high [Ca²⁺].

In actual physiological systems, cytosolic Ca²⁺ is strongly buffered in the cell, and buffer-bound Ca²⁺ is at least an order of magnitude less mobile than free Ca²⁺ (Kupferman et al. 1997). If Ca²⁺ buffering is included in a model for Ca²⁺ dynamics and the buffer has fast kinetics, the analysis of such a model demonstrates that Ca²⁺ obeys a nonlinear diffusion-advection equation (Wagner and Keizer 1994; Sneyd et al. 1998). The effective diffusion coefficient in this equation is a linear combination of the two diffusion coefficients D_c and D_b of free Ca²⁺ and buffer, respectively. If the buffer is immobile, i.e. $D_b = 0$, it can be included implicitly in the Ca²⁺ model by considering a reduced diffusion coefficient for Ca²⁺. It is also possible to show that inclusion of mobile buffers does not tend to eliminate an existing wave (Sneyd et al. 1998), although it can cause the appearance of two stable waves in some cases (Slepchenko et al. 2000). It had also been shown that buffer mobility has only a limited effect on wave properties (Sneyd and Tsaneva-Atanasova 2003), and therefore we ignore the

explicit inclusion of Ca^{2+} buffers here and assume that Ca^{2+} buffering is included implicitly in the models by treating all fluxes as effective fluxes.

3.3.1 Waves in the De Young–Keizer Model

Travelling waves in the DYK model can be studied by adding a term $D\nabla^2 C$ to the right hand side of Eq. (3.3), where D is an *effective* diffusion coefficient. We consider a one-dimensional model and ignore any effects of heterogeneity within a single cell. One common approach in analysing such types of models is to assume an unbounded cell domain, so travelling waves propagate with fixed velocity s , and to rewrite the model in the comoving reference frame $\xi = x - st$. In the case of the reduced DYK model, a transformation into this frame yields

$$\partial_t C = D\partial_\xi^2 C + s\partial_\xi C + f_1(C, h) \quad (3.13)$$

$$\partial_t h = s\partial_\xi h + f_2(C, h), \quad (3.14)$$

where

$$f_1(C, h) = \rho_A(\Omega_C m_\infty^3 h^3 + \Omega_L)(C_{\text{ER}} - C) - O_P \mathcal{H}_2(C, K_P), \quad (3.15)$$

$$f_2(C, h) = \frac{h_\infty - h}{\tau_h}. \quad (3.16)$$

In the comoving frame, travelling waves with speed s correspond to stationary solutions defined by $\partial_t C = \partial_t h = 0$. Hence, they can be found by studying solutions to the travelling wave ODEs

$$\frac{dC}{d\xi} = w, \quad D \frac{dw}{d\xi} = -sw - f_1(C, h), \quad s \frac{dh}{d\xi} = -f_2(C, h). \quad (3.17)$$

As this is a nonlinear system of ODEs, the model's behaviour can be analysed only by numerical methods. For any fixed value of s , it is possible to construct the bifurcation diagram similar to that in Fig. 3.4 and find a window of I values when periodic oscillations occur. These periodic oscillations in the transformed ODE system (3.17) correspond to periodic Ca^{2+} travelling waves in the spatial model. Varying values of s we can trace how this window of I values for existence of periodic Ca^{2+} waves changes. This is shown in a two-parameter bifurcation diagram in Fig. 3.5. It is important to notice that this model can support periodic travelling waves as well as solitary travelling pulses which can be computed as periodic solutions with periods tending to infinity. This two-parameter bifurcation demonstrates complex dynamics for some values of the parameter I , and we refer the reader to Sneyd et al. (2000), Timofeeva and Coombes (2003) for a more detailed discussion on it.

The analysis of travelling waves, even in the reduced, but still nonlinear, models of Ca^{2+} dynamics is typically only possible with the use of numerical techniques. Now we consider a much simpler, so-called Fire-Diffuse-Fire (FDF) type model of Ca^{2+} release that exhibits many of the waves observed in the DYK type models. The

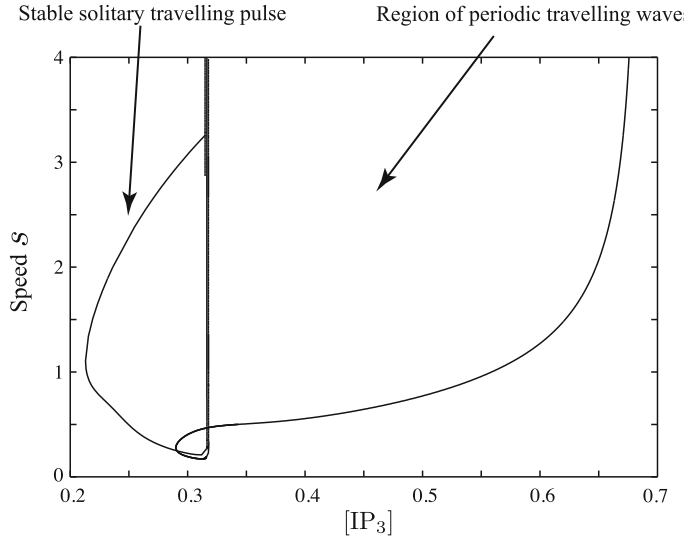


Fig. 3.5 Two-parameter bifurcation diagram of Ca^{2+} travelling waves in the reduced DYK model. Parameters as in Table 3.1, $D = 1$

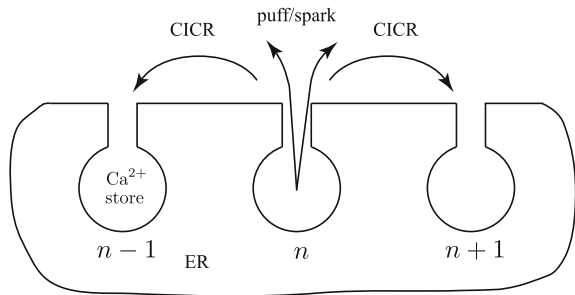
major advantages of the FDF model are that it can be analysed both in the discrete and continuous limits for Ca^{2+} release sites, and that it allows for exact mathematical analysis.

3.3.2 Waves in the Fire-Diffuse-Fire Type Model

The FDF model of Keizer et al. (1998) was originally introduced as a minimal model of spark-mediated Ca^{2+} waves. The generalised version of the model sustains both solitary and periodic travelling wave propagation. The Ca^{2+} signal is generated by the mechanism of CICR, i.e. the receptor channel is activated at low cytosolic $[\text{Ca}^{2+}]$ and inhibited after completion of the release. Thus, for low $[\text{Ca}^{2+}]$, an increase in $[\text{Ca}^{2+}]$ stimulates a further increase. At higher levels the receptor inactivates and cannot reopen for some time during which it is in a refractory state. Thus, the release of Ca^{2+} by intracellular stores is self-regulating. The release events (Ca^{2+} puffs or sparks) lead to the propagation of travelling waves via diffusion of Ca^{2+} . A schematic diagram of the model is given in Fig. 3.6. In one dimension the FDF model may be written in the form

$$\frac{\partial c}{\partial t} = D \frac{\partial^2 c}{\partial x^2} + \underbrace{\rho(x) \sum_m \eta(t - T^m(x))}_{J_{\text{receptor}}} - \underbrace{\frac{c}{\tau_d}}_{J_{\text{pump}}}, \quad x \in \mathbb{R}, \quad t > 0, \quad (3.18)$$

Fig. 3.6 Schematic representation of the FDF model



where $c(x, t)$ denotes $[\text{Ca}^{2+}]$ in the cytosol. The decay time τ_d describes the action of Ca^{2+} pumps that resequester Ca^{2+} back into the stores. Note that in comparison with the DYK model, the model of a pump is linear which is required for mathematical tractability. In addition, the model does not explicitly include receptor dynamics. Instead, Ca^{2+} puffs are triggered from the release site at position x at times $T^m(x)$, $m \in \mathbb{Z}$. These release times are defined in terms of a threshold process according to

$$T^m(x) = \inf\{t \mid c(x, t) > c_{\text{th}}, \frac{\partial c(x, t)}{\partial t} > 0; t \geq T^{m-1}(x)\}. \quad (3.19)$$

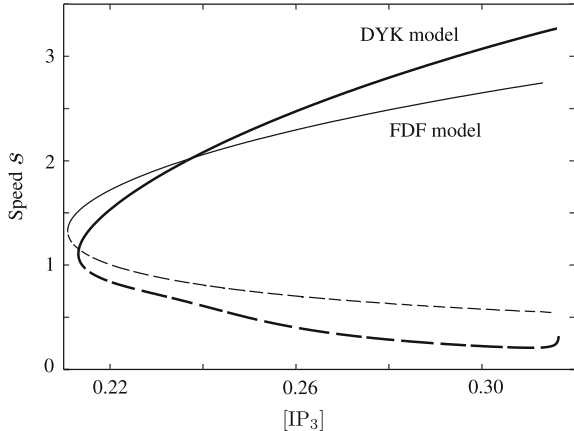
The function $\eta(t)$ describes the shape of the puff and is often considered to be a simple rectangle:

$$\eta(t) = \frac{\sigma}{\tau} \Theta(t) \Theta(\tau - t), \quad (3.20)$$

where $\Theta(t)$ is a step function, σ is the strength of the puff and τ its duration. The function $\rho(x)$ models the density distribution of Ca^{2+} release sites. A model in continuous limit can be studied by considering $\rho(x) = 1$. The discrete approximation in the FDF model may be obtained by modelling Ca^{2+} release sites as point sources so that the function $\rho(x)$ is given by $\rho(x) = \sum_n \delta(x - x_n)$, where x_n is the spatial position of the n th release site and $\delta(x)$ is the Dirac delta function.

To study periodic travelling waves in this model, a process of refractoriness needs to be included. For retaining analytical tractability, it can be mimicked by a time-dependent threshold, $c_{\text{th}} = c_{\text{th}}(t)$, which is high just after a release event, but gradually decays back to some low level. We refer the reader to Coombes (2001), Timofeeva and Coombes (2003) for explicit construction of solitary and periodic travelling wave solutions in the FDF framework. Also in its current form, the FDF model is independent of $[\text{IP}_3]$, which is an important parameter of the DYK model. To include a notion of IP_3 sensitivity within the FDF framework, it is natural to modify the threshold parameter c_{th} , such that release events are easier to generate in the presence of high $[\text{IP}_3]$. The inclusion of an IP_3 -dependent threshold, $c_{\text{th}} = c_{\text{th}}(I)$, in the FDF model allows then a more direct comparison with results from the DYK model. In Fig. 3.7, we plot the wave speed of a pulse as a function of the $[\text{IP}_3]$ in both the continuous FDF and the reduced DYK models.

Fig. 3.7 Speed of the solitary travelling wave as a function of $[IP_3]$ in the continuous FDF model and in the reduced DYK model. Parameters of the FDF model: $\tau_d = 0.29$, $D = 1$, $\tau = 0.5$, $\sigma = 10$, $c_{\text{th}}(I) = c_0 + Ae^{-BI}/(I - C)$, where $c_0 = 0.48$, $A = 0.1627$, $B = 0.5583$, $C = 0.055$. Parameters of the DYK model as in Fig. 3.5. Solid (dashed) curves indicate stable (unstable) travelling waves



The simplicity of the underlying deterministic FDF model can lead to further computational improvements. When considering a discrete distribution of release sites the model can be simplified further by making the assumption that release events occur on a regular temporal lattice. Thus, under this assumption, the model may be re-written in the language of binary *release events*, and it does not have to be evolved as a discontinuous partial differential equation with a self-consistent search for the times of threshold crossing. We consider that the release sites are located at positions $x_n = nd$ and can trigger Ca^{2+} puffs at times T_n^m . Release events are separated by at least a time $\tau_R = R\tau$ for some $R \in \mathbb{Z}$, i.e. $T_n^m \geq T_n^{m-1} + \tau_R$. We define a *release function* $a_n(k)$, where $a_n(k) = 1$ if $T_n^m = k\tau$ and is zero otherwise. Then we may write

$$a_n(k) = \Theta(c_n(k) - c_{\text{th}}) \prod_{m=1}^{\min(R,k)} \Theta(c_{\text{th}} - c_n(k-m)), \quad (3.21)$$

where $c_n(k) \equiv c(nd, k\tau)$. The first term on the right in Eq. (3.21) is a simple threshold condition for the determination of a release event whilst the second term ensures that release events are separated by at least τ_R . This restriction of the model eliminates the need for the precise determination of release times. The FDF model then takes the particularly simple form

$$\frac{\partial c}{\partial t} + \frac{c}{\tau_d} - D \frac{\partial^2 c}{\partial x^2} = \frac{\sigma}{\tau} \sum_n a_n(k) \delta(x - nd), \quad k\tau < t < (k+1)\tau, \quad (3.22)$$

with the Green's function

$$G(x, t) = \exp[-t/\tau_d - x^2/4Dt]/\sqrt{4\pi Dt}\Theta(t). \quad (3.23)$$

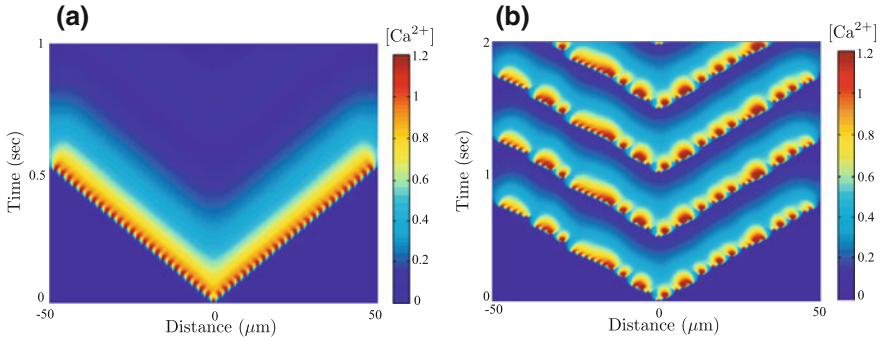


Fig. 3.8 **a** An example of two saltatory pulses in a one-dimensional discrete-time FDF model with 50 regularly spaced release sites. Parameters: $d = 2 \mu\text{m}$, $D = 30 \mu\text{m}^2/\text{s}$, $\tau = 10 \text{ ms}$, $\tau_d = 0.2 \text{ s}$, $\sigma = 1 \mu\text{M} \cdot \mu\text{m}$, $R = 50$, $c_{\text{th}} = 0.1$. **b** An example of periodic travelling wave in a one-dimensional discrete-time FDF model with irregularly spaced release sites. Parameters as in a except $R = 48$

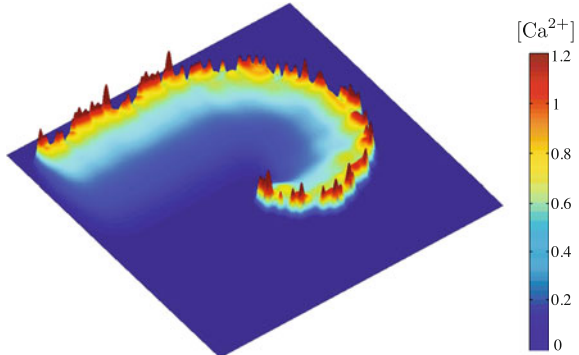
The dynamics for $k\tau < t < (k + 1)\tau$ may then be determined in terms of initial data $c_k(x) = c(x, k\tau)$ as

$$c(x, t) = \frac{\sigma}{\tau} \sum_n a_n(k) H(x - nd, t - k\tau) + (G \otimes c_k)(x, t), \quad (3.24)$$

where $H(x, t) = \int_0^t G(x, t - s) ds$ and $(G \otimes c_k)(x, t) = \int_{-\infty}^{\infty} G(x - y, t - k\tau) c_k(y) dy$. A closed form expression for $H(x, t)$ is given in Coombes (2001), Coombes and Timofeeva (2003). Compared to the original FDF model, this discrete-time FDF model is computationally cheap to solve. The solution $c(x, (k + 1)\tau)$ is a sum of two terms that are both amenable to fast numerical evaluation. In particular, the first term in Eq. (3.24) with $t = (k + 1)\tau$ depends on the basis functions $H_n(x) = \sigma H(x - nd, \tau)/\tau$ which are fixed for all time. Hence, they need only be computed once. The convolution operation arising in the second term may be performed efficiently using fast Fourier transform techniques. In Fig. 3.8, we plot solitary and periodic travelling waves in the discrete-time FDF model with regular (a) and irregular (b) distributions of Ca^{2+} release channels.

The generalisation of the discrete-time FDF model to two dimensions is both natural and straightforward by introducing a continuous spatial coordinate $\mathbf{r} \in \mathbb{R}^2$ and a discrete set of vectors $\mathbf{r}_n \in \mathbb{R}^2$, $n \in \mathbb{Z}$, indicating the positions of release sites (Coombes and Timofeeva 2003; Coombes et al. 2004). Analytical progress for function H in (3.24) is still possible in a few limiting cases, in particular, for small τ we have that $H(\mathbf{r}, t) \rightarrow G(\mathbf{r}, t)$, where $G(\mathbf{r}, t) = G(|\mathbf{r}|, t)$ given by (3.23). Since the puff duration is very small compared to the refractory time τ_R , this is a very accurate approximation used here in two-dimensional simulations. An example of a spiral Ca^{2+} wave in the model with a two-dimensional irregular square lattice is shown in Fig. 3.9. Such complex patterns can be observed in larger cells, for example, in Xenopus oocytes (Lechleiter et al. 1991) or cardiac myocytes (Lipp and Niggli 1993).

Fig. 3.9 Snapshot of a spiral wave in the deterministic two-dimensional FDF model on the irregular square lattice cell of size $120\text{ }\mu\text{m} \times 120\text{ }\mu\text{m}$. Other parameters as in Fig. 3.8



Recently, the FDF framework has been also generalised to a three-dimensional cell model and used for studying the initiation and propagation of subcellular Ca^{2+} waves in an atrial myocyte (Thul et al. 2012).

3.3.3 Stochastic Ca^{2+} Waves

It is important to recognise that the release of Ca^{2+} is controlled by the stochastic opening and closing of Ca^{2+} channels, and Ca^{2+} waves are composed of elementary stochastic release events (Ca^{2+} puffs/sparks) through single channels or several channels in a cluster (Cheng and Lederer 2008). For example, Keizer and Smith (1998), Falcke et al. (2000), Falcke (2003), Dupont et al. (2007) have emphasised the importance of modelling stochastic release kinetics when considering initiation and subsequent propagation of waves. The study of stochastic calcium signaling is addressed more in detail in the next chapter (Chap. 4). In what follows we restrict our analysis instead to a stochastic version of the FDF model.

The discrete-time FDF threshold model defined by Eqs.(3.21) and (3.24) is in an ideal form to be generalised to incorporate stochastic effects. We consider the stochastic gating of receptor channels to give rise to an effective threshold that can be modelled under the replacement $c_{\text{th}} \rightarrow c_{\text{th}} + \xi$, where ξ is an additive noise term with distribution $\rho(\xi)$. The probability that $a_n(p) = 1$ is then given by

$$P(a_n(p) = 1) = P(c_n(p) > c_{\text{th}}) \prod_{m=1}^{\min(R,p)} P(c_n(p-m) < c_{\text{th}}), \quad (3.25)$$

where

$$P(c > c_{\text{th}}) = \int \rho(\xi) \Theta(c - c_{\text{th}} - \xi) d\xi. \quad (3.26)$$

For convenience we choose $\rho(\xi) = f'(\xi)$ so that

$$P(c > c_{\text{th}}) = f(c - c_{\text{th}}). \quad (3.27)$$

In work by Izu et al. (2001), it has been argued that the probability of release per unit time follows a functional form given by $c^n/(K^n + c^n)$ with the Hill coefficient $n = 1.6$ and Ca^{2+} sensitivity parameter $K = 15 \mu\text{M}$. Moreover, work described in Coombes et al. (2004) shows that such functional forms can be derived from stochastic models of channel clusters. This suggests that natural choices for $f(c)$ are sigmoidal functions, and therefore the following choice for $f(c)$ can be made:

$$f(c) = \left\{ \frac{1}{1 + e^{-\beta c}} - \frac{1}{1 + e^{\beta c_{\text{th}}}} \right\} (1 + e^{-\beta c_{\text{th}}}), \quad (3.28)$$

so that the probability of release is zero when $c = 0$ and tends to one as $c \rightarrow \infty$. In summary, the stochastic FDF model is defined by Eq. (3.24) with the $a_n(p) \in \{0, 1\}$ treated as random variables such that $P(a = 1)$ is given by (3.25). Note, that in the limit $\beta \rightarrow \infty$, the function $f(c)$ in (3.28) approaches a step function so that $P(c > c_{\text{th}}) = \Theta(c - c_{\text{th}})$, and we recover our original deterministic model. Thus, we interpret β as a parameter describing the level of noise. For sigmoidal forms of f , the noise distribution $\rho = f'$ is bell-shaped with the width of the bell controlled by β . In this framework, the refractory time scale can also be thought of as being drawn from some distribution, since release events are no longer bound by the constraint that they are separated by at least τ_R . Figure 3.10 demonstrates two examples of stochastic Ca^{2+} waves with different levels of threshold noise. These results demonstrate that this model can capture the main qualitative features of the experimentally observed calcium puff/sparks and waves in a variety of cell types. In the two-dimensional case, the stochastic FDF model may also generate Ca^{2+} sparks and waves in the fashion similar to that seen in experiments. This is illustrated in Fig. 3.11.

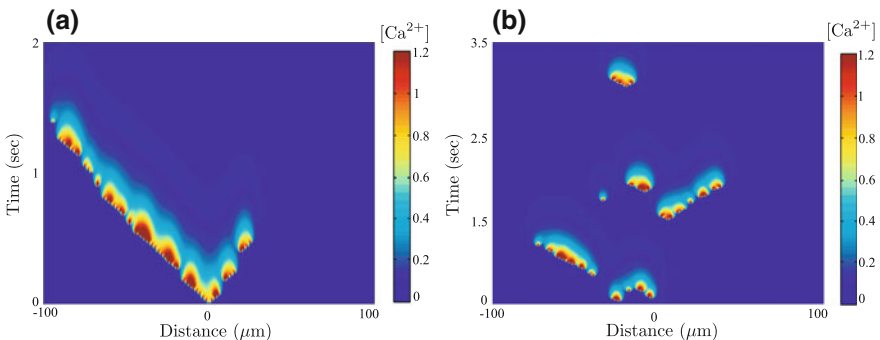


Fig. 3.10 Examples of stochastic travelling waves in the FDF framework with a finite amount of noise, where $\beta = 70$ (a) and $\beta = 10$ (b). Other parameters as in Fig. 3.8

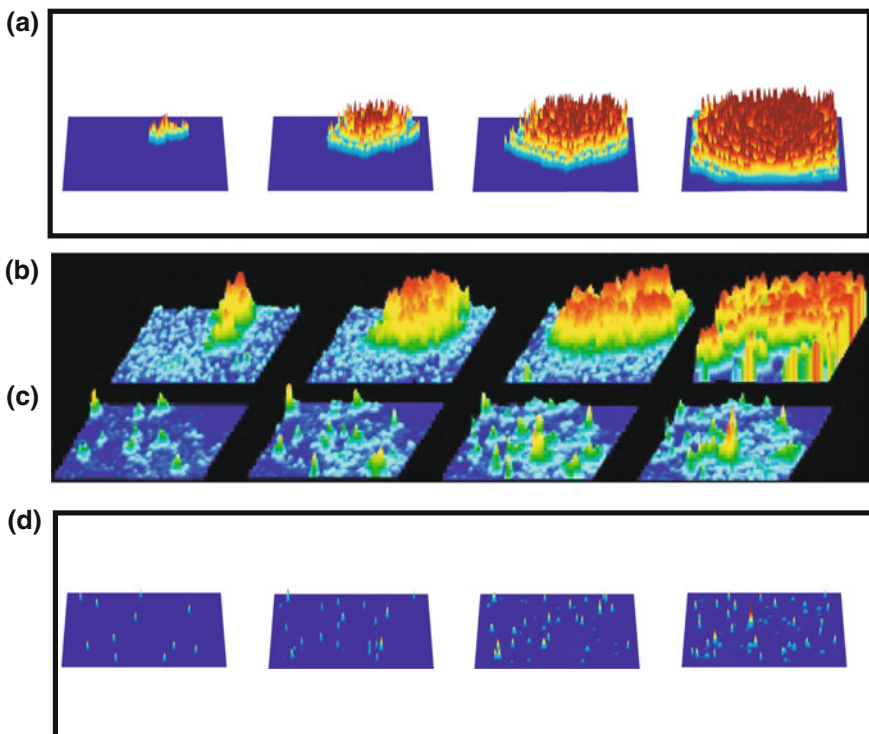


Fig. 3.11 **b** and **c** Image sequences illustrating the patterns of Ca^{2+} liberation evoked in immature Xenopus oocytes by a photolysis flash of IP_3 (Marchant and Parker 2001). Each image sequence was captured at intervals of 0.1 s. **a** and **d** An example of generated Ca^{2+} puffs/sparks and propagating waves in the stochastic two-dimensional FDF model of Ca^{2+} release for $\beta = 70$, $R = 5$ and $\beta = 5$, $R = 50$ respectively. Frames are presented every 0.25 s

3.4 Conclusions

In this chapter, we have discussed a number of models for studying oscillations and waves of cytosolic Ca^{2+} in single cells. We have focused on two models of Ca^{2+} release, a biophysically realistic DYK model and a much simpler minimal FDF model. The latter model is motivated by numerical bifurcation analysis of the DYK model and is capable of exhibiting qualitatively similar behaviour. The generalised version of the FDF framework can support more general choices of the distribution of release sites and the stochastic triggering of release and can be studied in one, two or three dimensions.

As discussed, in many cell types an initiated wave of increased intracellular $[\text{Ca}^{2+}]$ can spread from cell to cell to form an intercellular wave. Models of intercellular Ca^{2+} signalling are often based on a gap-junctional diffusion hypothesis (for either IP_3 or Ca^{2+} or both). Both models presented in this chapter can be extended to

support intercellular Ca^{2+} waves. It has been shown that within the FDF framework, some analytical progress is still possible when only Ca^{2+} ions can diffuse through gap junctions (Harris and Timofeeva 2010). To incorporate IP_3 dependence to this model, a further extension can be made by considering the FDF model with the IP_3 -sensitive threshold and including additional equations describing the dynamics of cytosolic $[\text{IP}_3]$ in each cell and at the cells' boundaries. If IP_3 is assumed to move through individual cells and gap junction channels by passive diffusion, the mathematical tractability of the FDF framework can be retained.

For both intracellular and intercellular Ca^{2+} signalling, future progress may depend to a substantial extent on 3D modelling, which has thus far received much less attention than 1D and 2D work. In all cases, a good balance has to be struck between the complexity and reductive requirements of such models.

Supplementary Online Material

Bifurcation diagrams for the DYK and the reduced DYK models were computed in the XPPAUT tool developed by Bard Ermentrout (Ermentrout 2002). This is an interactive package for numerically solving and analysing differential equations. XPPAUT codes used for Fig. 3.4 (the full DYK model, file DYK.ode) and for Fig. 3.5 (the reduced DYK model, file reducedDYK.ode) are provided online (<https://github.com/mdepitta/compglia-book/tree/master/Ch3.Timofeeva>). The discrete-time FDF model was implemented in MATLAB. Files for the 1D case are also available online together with an animation of a spiral wave simulation, a snapshot of which is shown in Fig. 3.9 (file irregular_spiral.avi).

References

- Berridge MJ (2005) Unlocking the secrets of cell signalling. *Ann Rev Physiol* 67:1–21
- Berridge MJ (2009) Inositol trisphosphate and calcium signalling mechanisms. *Biochimica et Biophysica Acta* 1793:933–940
- Berridge MJ, Lipp P, Bootman MD (2000) The versatility and universality of calcium signalling. *Nat Rev Mol Cell Biol* 1:11–21
- Berridge MJ, Bootman MD, Roderick HL (2003) Calcium signalling: dynamics, homeostasis and remodelling. *Nat Rev Mol Cell Biol* 4:517–529
- Bezprozvanny I, Watras J, Ehrlich BE (1991) Bell-shaped calcium-response curves of $\text{Ins}(1,4,5)\text{P}_3$ - and calcium-gated channels from endoplasmic reticulum of cerebellum. *Nature* 351:751–754
- Boitano S, Dirksen ER, Sanderson MJ (1992) Intercellular propagation of calcium waves mediated by inositol trisphosphate. *Science* 258:292–294
- Bootman MD, Berridge MJ, Putney JW, Roderick HL (eds) (2011) Calcium signaling. Cold Spring Harbor Laboratory Press, New York
- Carafoli E (2002) Calcium signaling: a tale for all seasons. *Proc Natl Acad Sci USA* 99(3):1115–1122
- Cheng H, Lederer WJ (2008) Calcium sparks. *Physiol Rev* 88:1491–1545

- Clapham DE (2007) Calcium signaling. *Cell* 131:1047–1058
- Combettes L, Dupont G, Parys JB (2004) New mechanisms and functions in Ca^{2+} signalling. *Biol Cell* 96:1–2
- Coombes S (2001) The effect of ion pumps on the speed of travelling waves in the fire-diffuse-fire model of Ca^{2+} release. *Bull Math Biol* 63:1–20
- Coombes S, Timofeeva Y (2003) Sparks and waves in a stochastic fire-diffuse-fire model of calcium release. *Phys Rev E* 68(021):915
- Coombes S, Hinch R, Timofeeva Y (2004) Receptors, sparks and waves in a fire-diffuse-fire framework for calcium release. *Prog Biophys Mol Biol* 85:197–216
- Cornell-Bell AH, Finkbeiner SM, Cooper MS, Smith SJ (1990) Glutamate induces calcium waves in cultured astrocytes: long-range glial signaling. *Science* 247(4941):470–473
- Dupont G, Tordjmann T, Clair C, Swillens S, Claret M, Combettes L (2000) Mechanism of receptor-oriented intercellular calcium wave propagation in hepatocytes. *FASEB J* 14(2):279–289
- Dupont G, Combettes L, Leybaert L (2007) Calcium dynamics: spatio-temporal organization from the subcellular to the organ level. *Int Rev Cytol* 261:193–245
- Dupont G, Falcke M, Kirk V, Sneyd J (2016) Models of calcium signalling. Springer, Interdisciplinary Applied Mathematics
- Endo M, Tanaka M, Ogawa Y (1970) Calcium induced release of calcium from the sarcoplasmic reticulum of skinned skeletal muscle fibres. *Nature* 228:34–36
- Ermentrout GB (2002) Simulating, analysing, and animating dynamical systems: a guide to XPPAUT for researchers and students. SIAM, Philadelphia
- Falcke M (2003) Deterministic and stochastic models of intracellular Ca^{2+} waves. *New J Phys* 5:96.1–96.28
- Falcke M (2004) Reading the patterns in living cells - the physics of Ca^{2+} signaling. *Adv Phys* 53(3):255–440
- Falcke M, Tsimring L, Levine H (2000) Stochastic spreading of intracellular Ca^{2+} release. *Phys Rev E* 62:2636–2643
- FitzHugh R (1961) Impulses and physiological states in models of nerve membrane. *Biophys J* 1:445–466
- Goldbeter A (1996) Biochemical oscillations and cellular rhythms: the molecular bases of periodic and chaotic behaviour. Cambridge University Press, Cambridge
- Goldbeter A, Dupont G, Berridge MJ (1990) Minimal model for signal-induced Ca^{2+} oscillations and for their frequency encoding through protein phosphorylation. *Proc Natl Acad Sci USA* 87:1461–1465
- Goldbeter A, Gérard C, Gonze D, Leloup J, Dupont G (2012) Systems biology of cellular rhythms. *FEBS Lett* 586:2955–2965
- Harris J, Timofeeva Y (2010) Intercellular calcium waves in the fire-diffuse-fire framework: green's function for gap-junctional coupling. *Phys Rev E* 82(051):910
- Hodgkin AL, Huxley AF (1952) A quantitative description of membrane current and its application to conduction and excitation in nerve. *J Physiol* 117:500–544
- Izu LT, Wier WG, Balke CW (2001) Evolution of cardiac waves from stochastic calcium sparks. *Biophys J* 80:103–120
- Jaffe LF (1993) Classes and mechanisms of calcium waves. *Cell Calcium* 14:736–745
- Kaneko T, Tanaka H, Oyamada M, Kawata S, Takamatsu T (2000) Three distinct types of Ca^{2+} waves in Langendorff-perfused rat heart revealed by real-time confocal microscopy. *Circ Res* 86:1093–1099
- Keizer JE, Smith GD (1998) Spark-to-wave transition: saltatory transmission of calcium waves in cardiac myocytes. *Biophys Chem* 72:87–100
- Keizer JE, Smith GD, Dawson SP, Pearson J (1998) Saltatory propagation of Ca^{2+} waves by Ca^{2+} sparks. *Biophys J* 75:595–600
- Krebs J, Michalak M (eds) (2007) Calcium: a matter of life or death, New comprehensive biochemistry, vol 41. Elsevier Science

- Kupferman R, Mitra PP, Hohenberg PC, Wang SSH (1997) Analytical calculation of intracellular calcium wave characteristics. *Biophys J* 72:2430–2444
- Lechleiter J, Girard S, Peralta E, Clapham D (1991) Spiral calcium wave propagation and annihilation in *Xenopus laevis* oocytes. *Science* 252:123–126
- Leybaert L, Sanderson MJ (2012) Intercellular Ca^{2+} waves: mechanisms and function. *Physiol Rev* 92:1359–1392
- Li YX, Rinzel J (1994) Equations for InsP_3 receptor-mediated $[\text{Ca}^{2+}]$ oscillations derived from a detailed kinetic model: a Hodgkin-Huxley like formalism. *J Theor Biol* 166:461–473
- Lipp P, Niggli E (1993) Microscopic spiral waves reveal positive feedback in subcellular calcium signaling. *Biophys J* 65:2272–2276
- Marchant JS, Parker I (2001) Role of elementary Ca^{2+} puffs in generating repetitive Ca^{2+} oscillations. *EMBO J* 20:65–76
- Mikoshiba K (2007) IP_3 receptor/ Ca^{2+} channel: from discovery to new signaling concepts. *J Neurochem* 102:1426–1446
- Miyazaki S (2006) Thirty years of calcium signals at fertilization. *Semin Cell Dev Biol* 17:233–243
- Nagumo J, Arimoto S, Yoshizawa S (1962) An active pulse transmission line simulation nerve axon. *Proc IRE* 50:2061–2070
- Paemeleire K, Martin PEM, Coleman SL, Fogarty KE, Carrington WA, Leybaert L, Tuft RA, Evans WH, Sanderson MJ (2000) Intercellular calcium waves in HeLa cells expressing GFP-labeled connexin 43, 32, or 26. *Mol Biol Cell* 11(5):1815–1827
- Parekh AB (2011) Decoding cytosolic Ca^{2+} oscillations. *Trends Biochem Sci* 36(2):78–87
- Parker I, Ivorra I (1990) Inhibition by Ca^{2+} of inositol trisphosphate-mediated Ca^{2+} liberation: a possible mechanism for oscillatory release of Ca^{2+} . *Proc Natl Acad Sci USA* 87:260–264
- Petersen OH, Michalak M, Verkhratsky A (2005) Calcium signalling: past, present and future. *Cell Calcium* 38:161–169
- Rizzuto R, Pozzan T (2006) Microdomains of intracellular Ca^{2+} : molecular determinants and functional consequences. *Physiol Rev* 86:369–408
- Røttingen JA, Iversen JG (2000) Ruled by waves? Intracellular and intercellular calcium signalling. *Acta Physiol Scand* 169:203–219
- Scemes E, Giaume C (2006) Astrocyte calcium waves: what they are and what they do. *Glia* 54:716–725
- Schuster S, Marhl M, Höfer T (2002) Modelling of simple and complex calcium oscillations. From single-cell responses to intercellular signalling. *Eur J Biochem* 269:1333–1355
- Slepchenko BM, Schaff JC, Choi YS (2000) Numerical approach to fast reactions in reaction-diffusion systems: application to buffered calcium waves in bistable models. *J Comput Phys* 162:186–218
- Sneyd J, Falcke M (2005) Models of the inositol trisphosphate receptor. *Prog Biophys Mol Biol* 89:207–245
- Sneyd J, Tsaneva-Atanasova K (2003) Understanding calcium dynamics: experiments and theory, Springer, chap Modeling calcium waves, pp 179–199
- Sneyd J, Dale P, Duffy A (1998) Traveling waves in buffered systems: applications to calcium waves. *SIAM J Appl Math* 58:1178–1192
- Sneyd J, LeBeau A, Yule D (2000) Traveling waves of calcium in pancreatic acinar cells: model construction and bifurcation analysis. *Phys D* 145:158–179
- Stokes DL, Green NM (2003) Structure and function of the calcium pump. *Ann Rev Biophys Biomol Struct* 32:445–468
- Takamatsu T, Wier WG (1990) Calcium waves in mammalian heart: quantification of origin, magnitude, waveform, and velocity. *FASEB J* 4:1519–1525
- Thomas AP, Renard DC, Rooney TA (1991) Spatial and temporal organization of calcium signalling in hepatocytes. *Cell Calcium* 12:111–126
- Thul R, Coombes S, Roderick HL, Bootman MD (2012) Subcellular calcium dynamics in a whole-cell model of an atrial myocyte. *Proc Natl Acad Sci USA* 109(6):2150–2155

- Timofeeva Y, Coombes S (2003) Wave bifurcation and propagation failure in a model of calcium release. *J Math Biol* 47:249–269
- Toma I, Bansal E, Meer EJ, Kang JJ, Vargas SL, Peti-Peterdi J (2008) Connexin 40 and ATP-dependent intercellular calcium wave in renal glomerular endothelial cells. *Am J Physiol - Regul Integr Comp Physiol* 294(6):R1769–R1776
- Wagner J, Keizer J (1994) Effects of rapid buffers on Ca^{2+} diffusion and Ca^{2+} oscillations. *Biophys J* 67:447–456
- Wang Z, Haydon PG, Yeung ES (2000) Direct observation of calcium-independent intercellular ATP signaling in astrocytes. *Anal Chem* 72(9):2001–2007
- Young GD, Keizer J (1992) A single pool IP_3 -receptor based model for agonist-stimulated Ca^{2+} oscillations. *Proc Natl Acad Sci USA* 89:9895–9899

Chapter 4

Modeling of Stochastic Ca^{2+} Signals



Sten Rüdiger and Jianwei Shuai

Abstract It has been shown that IP_3R channels are distributed in clusters on the membrane of the endoplasmic reticulum, generating Ca^{2+} signals on multiple scales, from local puffs to global intra- and intercellular waves. Local Ca^{2+} puffs released from a cluster of IP_3R s are strongly stochastic. The most obvious source of noise for puffs is the small number of channels within a cluster. In this chapter we discuss the simulation of stochastic Ca^{2+} signals. Various simulation methods such as the Gillespie algorithm, a two-state Markovian chain, and gate-based and channel-based Langevin approaches have been introduced for use in the study of stochastic gating dynamics of IP_3R channels. Combining the stochastic channel dynamics with the deterministic simulation the Ca^{2+} diffusion process, the fluctuating Ca^{2+} signals, including puffs and both intra- and intercellular waves, can be investigated by hybrid models.

Keywords Stochastic processes · Calcium signaling · Channel gating dynamics
Inositol 1,4,5-trisphosphate receptor · Calcium puffs · Calcium sparks · Calcium waves · Intracellular waves · Intercellular waves

4.1 Introduction

Calcium is a ubiquitous mediator of cellular responses to external stimuli including neurotransmitters, hormones and mechanical stresses. The stimulus is represented by transient or repetitive increases of cytosolic Ca^{2+} concentrations. In astrocytes, for example, oscillations of $[\text{Ca}^{2+}]$ enable intercellular communication and are linked to the plasticity of neuronal synapses (Volterra et al. 2014; Rusakov 2015). Ca^{2+} was shown to regulate gene expression by involving a number of transcription factors

S. Rüdiger (✉)

Institute of Physics, Humboldt-Universität zu Berlin, Berlin, Germany

e-mail: sten.ruediger@physik.hu-berlin.de

J. Shuai

Department of Physics and State Key Laboratory of Cellular Stress Biology,
Innovation Center for Cell Signaling Network, Xiamen University, Xiamen 361005, China
e-mail: jianweishuai@xmu.edu.cn

(Dolmetsch et al. 1998; Di Capite et al. 2009). The regulation of a multitude of such processes emerges from the tuning of Ca^{2+} levels in space and time.

Cytosolic Ca^{2+} levels are structured by coordinated release from intracellular stores located in cell organelles, particularly the endoplasmic reticulum (ER). The release from stores occurs through two related types of receptor channels in the membrane of the ER: inositol trisphosphate receptors (IP_3Rs) and ryanodine receptors (RyRs). The receptor channels regulate Ca^{2+} release in response to the binding of specific ligands, including Ca^{2+} , to binding sites on the cytosolic side of the channels. Ca^{2+} released by a channel diffuses into the cytosol and increases the probability of neighboring channels being open by binding to their activating binding sites. This provides a self-amplifying mechanism called Ca^{2+} -induced Ca^{2+} release (CICR), which is the basis of all Ca^{2+} signals discussed here.

We focus on two properties of Ca^{2+} signals that have been studied recently:

- *Subcellular organization.* The multiple intracellular spatial scales and a related hierarchy of collective behavior (Berridge et al. 2003) shape the signals of Ca^{2+} (Fig. 4.1). This fact becomes apparent since release events at the different scales can be associated with different functional roles in cellular communication. The smallest events in the Ca^{2+} signal hierarchy are short-lived openings of single channels called blips. Experimental observation of larger, yet still localized release events called puffs (Parker and Yao 1996) indicates that functioning IP_3R channels are grouped into clusters on the ER membrane containing at most tens of channels. Their opening is the result of local diffusion of Ca^{2+} and CICR between adjacent channels. Ca^{2+} signals therefore often exhibit spatial gradients, which have been shown to be important in the signaling content of Ca^{2+} signals for gene expression (Di Capite et al. 2009). The significance of the nanodomain distribution for Ca^{2+} function has also been shown recently in dendritic spines, where it was found that RyR channels are present in the postsynaptic dendritic spine (Johenning et al. 2015). Here, the channels play a role in synaptic plasticity but can do so only if a local concentration is raised above the Ca^{2+} elevation in the spine. Finally, the largest scale of Ca^{2+} signals is produced by whole-cell oscillations and waves, which are observed in many cell types. These signals are believed to comprise release from many clusters and possibly from further isolated channels situated between the clusters (Smith et al. 2009).
- *Stochasticity.* It was found that puffs, lasting from 50 to a few hundreds milliseconds, are strongly stochastic events (Marchant and Parker 2001). The most obvious source of noise for puffs is the small number of channels within a cluster (around 3–30). Several mathematical models have been put forward that reproduce the stochastic and dynamic features of puffs based on the single channel gating noise (e.g. Shuai and Jung 2003; DeRemigio et al. 2008; Rüdiger et al. 2010a). Furthermore, experiments have shown that global oscillations also have a strong stochastic component. Attributing this noise again to intrinsic stochastic behavior, fluctuations in the interwave interval have been associated with single channel noise in a number of computational models (Falcke 2003; Skupin et al. 2010; Rückl et al. 2015).

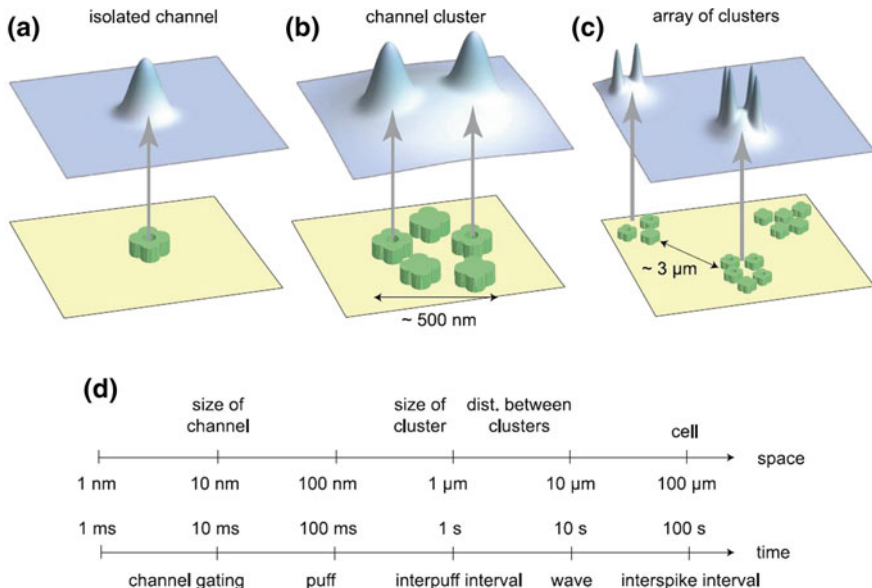


Fig. 4.1 The multiple spatial and time scales of Ca^{2+} signals (Rüdiger 2014a). **a** Ca^{2+} blips released from a single channel, **b** Ca^{2+} puffs released from several channels in a cluster, **c** Ca^{2+} signals released from an array of clusters. **d** An overview of the relevant scales in space and time

In early modeling studies, time-dependent Ca^{2+} elevations were described using deterministic ordinary differential equations (ODEs). These were based on a small number of feedback processes, the combination of which can indeed guarantee the existence of a limit cycle behavior. However, the two properties that we have mentioned, spatial localization and noise, require more complex spatial, nonlinear and stochastic equations, of the kind not usually studied in standard systems biology. Studies have resulted in evidence that the Ca^{2+} oscillator belongs to the class of stochastic excitable systems and not to the limit cycle class. In the following section we review a number of approaches to the problem, including partial differential equations (PDEs), Markovian modeling and numerical methods. In each case, we discuss the links to recent experimental results.

4.2 Stochastic Simulation of IP3R Gating Dynamics

4.2.1 Master Equations of the Stochastic Process

First, we discuss a toy model of a channel with the following open and close processes only



with the open rate α and the closing rate β . Given a large ensemble of channels, the differential equations for the state fractions x_i of channels ($i = o$ or c) can be given. For example, the open fraction x_o is written as,

$$\frac{dx_o}{dt} = \alpha(1 - x_o) - \beta x_o \quad (4.2)$$

Equation 4.2 is suitable for a large numbers of channels with continuous state fractions. However, when the channel number is small, the state fractions become discrete. The fluctuations of the channel number in the states i around its mean values become large, and the standard deviation around the mean value is of the order $1/\sqrt{N}$ with N the total channel number. As a result, the above differential equation based on the law of mass action needs to be replaced by the corresponding master equations, where the reactions are treated as Markovian birth-death processes. Taking M to be the number of open channels, one has the following master equation:

$$\begin{aligned} \frac{dP(M, t)}{dt} = & \alpha((N - M + 1)P(M - 1, t) - (N - M)P(M, t)) \\ & + \beta((M + 1)P(M + 1, t) - MP(M, t)), \end{aligned} \quad (4.3)$$

where $P(M, t)$ is the probability of having M open channels at time t .

The master equations can be solved in an analytical way only for simple cases. This is not practical in the case of more complex master equations involving many channels or many different receptor states. Thus, numerical methods are usually required to solve the master equations for complex gating states. For instance, a widely discussed IP₃R channel model based on the microscopic kinetics of IP₃ and Ca²⁺ gating was proposed by DeYoung and Keizer (1992). The model assumes that three equivalent and independent subunits are involved in conduction of an IP₃R. Each subunit has one binding site for IP₃ (gate m) and two binding sites for Ca²⁺: one Ca²⁺-binding site for activation (gate n), the other for inhibition (gate h). The subunit conducts only when the IP₃ site and activation Ca²⁺ site are bound. Thus, as shown in Fig. 4.2a, each subunit may exist in eight states with transitions governed by the first- or second-order rate constants. For such a subunit-based model with three types of binding sites, we need to determine the evolution of a probability density $P(M_m, M_n, M_h, t)$ in a three-dimensional occupation number space. For the channel-based model, the probability density in an even larger space must be tracked. In this case, solutions can be obtained by Monte Carlo methods, where exemplary trajectories are calculated using random numbers in a way appropriate to the transition rates. Single trajectories can then be collected to obtain statistical features of the system.

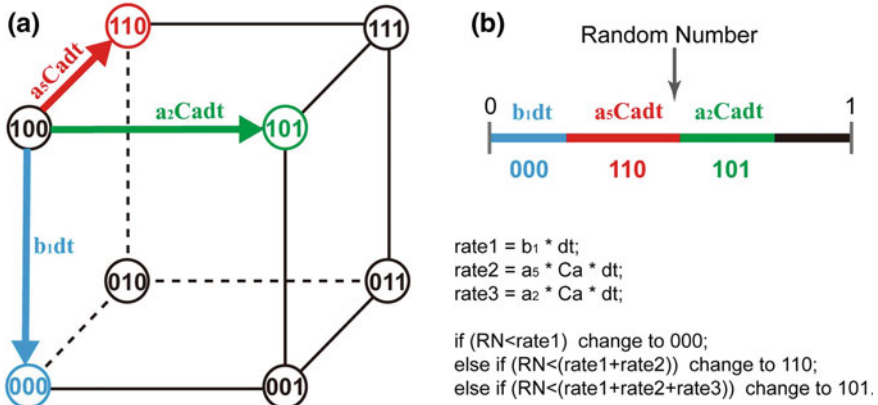


Fig. 4.2 **a** The eight IP₃R subunit states proposed by DeYoung and Keizer (1992). **b** An example to show how the two-state Markovian method simulates the stochastic gating dynamics from the current (100)-state to the three other possible states of (000), (110), or (101) (see also Chap. 3)

4.2.2 Gillespie Simulation

A mathematically precise basis for stochastic simulation algorithms was derived by Gillespie (1976, 1977). The approach relies on the notion of a propensity a_i for each microscopic transition or reaction R_i . Then

$$a_i dt = h_i c_i dt \quad (4.4)$$

is the probability that reaction R_i occurs during the next infinitesimal time step dt . Here c_i denotes the reaction constant of R_i (the probability density that a combination of molecules reacts) and h_i is the number of particle combinations of that particular reaction. For instance, in the case of a mono-molecular reaction, $A \rightarrow B$, h equals X_A , where X_A is the number of A -molecules in a certain well-mixed volume V , and c equals the macroscopic rate k of the transition. Similarly, for $A + B \rightarrow 2A$, $h = X_A X_B$ and the macroscopic $k = cV$. If a reaction is called, the corresponding numbers of participating molecule species, X_j , $j = 1, \dots, K$, are updated according to the stoichiometric factors, which are conveniently placed into a matrix, v_{ij} , defined as

$$v_{ij} \equiv \text{change in the number of } X_j \text{ molecules produced by one } R_i \text{ reaction.} \quad (4.5)$$

The stochastic algorithm determines the time of the next reaction and which reaction it will be, given the state $\mathbf{X} = (X_A, X_B, \dots)$ at the starting time t . Let

$P_0(\tau)$ be the probability that no reaction will occur in $(t, t + \tau)$ and $a_i = a_i(X)$ the propensity at time t . Since $1 - \sum_i a_i d\tau$ is the probability that no reaction will occur in $d\tau$, where the sum's index runs over all reactions, we find that

$$P_0(\tau + d\tau) = P_0(\tau) \left(1 - \sum_i a_i d\tau\right) \quad (4.6)$$

is the probability that no reaction has occurred in $(t, t + \tau + d\tau)$. The last equation implies that $P_0(\tau) = \exp(-\sum_i a_i \tau)$. On the other hand, the probability that the next reaction is R_i and it occurs in $(t + \tau, t + \tau + dt)$ is $P(\tau, i)dt = P_0(\tau)a_i dt$, i.e.,

$$P(\tau, i) = a_i \exp(-a_0 \tau), \quad (4.7)$$

where $a_0 = \sum_i a_i$ is the sum of all propensities. The probability density $P(\tau, i)$ can be implemented by drawing two random numbers r_1 and r_2 from a uniform distribution in the interval $[0, 1]$, and choosing τ and i such that

$$a_0 \cdot \tau = \ln(1/r_1), \quad \sum_{j=1}^i a_j \leq a_0 \cdot r_2 < \sum_{j=1}^{i+1} a_j. \quad (4.8)$$

This algorithm determines which reaction R_i is executed in the next step and when it will occur (time τ). This method is the so-called Direct Method (Gillespie 1976). Variants, which differ in the application of random numbers, are the First (Gillespie 1976) and Next Reaction Methods (Gibson and Bruck 2000).

The numerical effort can be substantially reduced if there is a strong disparity in the amplitude of noise in various parts of the reaction system. If some of the reactants are strongly fluctuating in their number, while others evolve more regularly, the system can be split into a stochastic part simulated with one of the methods described above, and a deterministic part solved by numerical schemes for differential equations. Both parts then need to be linked in an appropriate way. Previous research followed a strategy where fast reactions are represented by the deterministic rate equation, while slow reactions are treated with the exact stochastic algorithm. An example is the stochastic simulation of the Li-Rinzel Ca²⁺ model (Li and Rinzel 1994), as discussed below.

In a similar manner, the evolution of calcium concentration can be treated deterministically, while the gating transitions of ion channels need to be simulated stochastically. However, when combining a deterministic evolution with a stochastic solver, one may encounter the following problem. Gillespie's method rests on the assumption that during successive stochastic events, the propensities a_i do not change (Gillespie 1976, 1977; Gibson and Bruck 2000). However, when linking the stochastic reaction dynamics to the deterministic dynamics, we expect the propensity of a_i to change over time due to its dependence on deterministic variables. This effect, as seen below, will be particularly strong for the opening and closing of channels, since after such events the local calcium concentration changes dramatically by three or four orders of magnitude.

One way to resolve this problem was introduced by Alfonsi et al. (2005) and applied to the Ca^{2+} system (Rüdiger et al. 2007). Within this setting, the time τ to the next stochastic event is determined by solving

$$\int_t^{t+\tau} a_0(s, c) \, ds = \chi, \quad (4.9)$$

with $\chi = \ln(1/r_1)$, where the sum of propensities a_0 may depend explicitly on both time s and deterministic variables, here denoted by c . The above equation simplifies to the equation determining τ in (4.8) for a constant a_0 . To determine the time τ of the next reaction, condition (4.9) is conveniently rewritten in differential form by introducing a variable $g(\tau)$ and solving

$$\dot{g}(s) = a_0(s, c) \quad (4.10)$$

with initial condition $g(t) = 0$, along with the differential equations for deterministic variables. A reaction occurs whenever $g(s)$ reaches the random number χ . As before, the specific event R_i is determined based on a second random number r_2 satisfying the second condition in Eq. (4.8) with propensities evaluated at the event time $t + \tau$.

4.2.3 Two-State Markovian Method

As an alternative, solutions can be obtained by a simple two-state Markovian method. By expanding the transition probabilities at the linear order for the small time step δt , one can obtain the transition probability P of hopping from i -state to j -state within δt

$$P(i|j, \delta t) = \delta t \times \gamma_{ji} \quad (4.11)$$

with the rate γ_{ji} from i -state to j -state, and the probability to remain in the same state

$$P(i|i, \delta t) = 1 - \delta t \times \sum_j \gamma_{ji} \quad (4.12)$$

This scheme can be expressed directly in terms of a computer algorithm. In detail, the channel state is updated for every small time step δt . For the toy model (4.1), if the channel is closed at time t , the probability that it becomes open at time $t + \delta t$ is $\alpha \cdot \delta t$. If it is open at time t , then the probability that it becomes closed at time $t + \delta t$ is $\beta \cdot \delta t$.

Such a two-state Markovian method can be applied easily to the complex DeYoung-Keizer IP₃R model (DeYoung and Keizer 1992). Generally, to determine the state of a channel, random numbers from a uniform distribution on the unit interval [0, 1] are drawn. Each transition represents a subinterval on the unit interval proportional to the value of its transition probability where the sum of all subintervals

represents possible transitions. The transition that corresponds to the subinterval into which the random number falls is actually performed in simulation. An example is how the two-state Markovian method simulates the stochastic gating dynamics from the current (100)-state to the three other possible states of (000), (110), or (101) is explained in Fig. 4.2b.

4.2.4 Gate-Based Langevin Approach

For a large number of channels N , the master equation can be approximated by a Fokker-Planck equation, which is a linear partial differential equation. For every Fokker-Planck equation there is a statistically equivalent set of Langevin equations, i.e., a set of stochastic differential equations (Fox and Lu 1994).

As an example, we discuss the Langevin approach of the Li-Rinzel Ca^{2+} model (Li and Rinzel 1994) which is a simplified DeYoung-Keizer model (DeYoung and Keizer 1992) with two variables only (Chap. 3):

$$\frac{dC}{dt} = J_r(C, h, I) + J_l(C) - J_p(C), \quad (4.13)$$

$$\frac{dh}{dt} = \frac{h - h_\infty}{\tau_h} = \alpha_h(1 - h) - \beta_h h, \quad (4.14)$$

with C the intracellular Ca^{2+} concentration, I the IP_3 concentration, and h the fraction of deinactivated IP_3 Rs. The first term J_r in Eq. (4.13) denotes the channel flux density from the ER into the intracellular space, the second term J_l is the leak flux density and the third term J_p is the pump flux density from the intracellular space into the ER (Fig. 4.3). Equation (4.14) for h defines the fractions of the subunits in deinhibited states.

The expressions for the fluxes are given by

$$J_r = \Omega_C m_\infty^3 h^3 (C_T - (1 + \rho_A)C), \quad (4.15)$$

$$J_p = O_P \mathcal{H}_2(C, K_P), \quad (4.16)$$

$$J_l = \Omega_L (C_T - (1 + \rho_A)C), \quad (4.17)$$

with the parameters given as

$$\begin{aligned} m_\infty &= \mathcal{H}_1(I, d_1) \cdot \mathcal{H}_1(C, d_5), \\ \alpha_h &= \frac{h_\infty}{\tau_h} = O_2 Q_2, \\ \beta_h &= \frac{1 - h_\infty}{\tau_h} = O_2 C, \\ Q_2 &= d_2 \frac{I + d_1}{I + d_3}. \end{aligned} \quad (4.18)$$

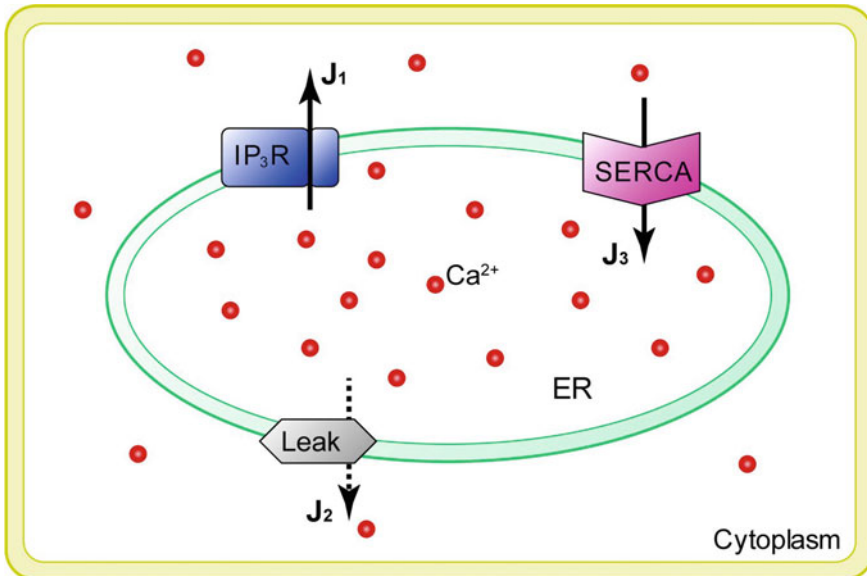


Fig. 4.3 The scheme of the Ca^{2+} oscillation model. Intracellular Ca^{2+} is controlled by channel flux as well as a leak flux from the ER into the intracellular space and the pump flux from the intracellular space into the ER

The parameters of the model are $\rho_A = 0.185$, $\Omega_C = 1.11 \text{ s}^{-1}$, $\Omega_L = 0.02035 \text{ s}^{-1}$, $O_P = 0.9 \mu\text{M s}^{-1}$, $K_P = 0.1 \mu\text{M}$, $d_1 = 0.13 \mu\text{M}$, $d_2 = 1.049 \mu\text{M}$, $d_3 = 0.9434 \mu\text{M}$, $d_5 = 0.08234 \mu\text{M}$, and $O_2 = 0.2 \mu\text{M}^{-1} \text{ s}^{-1}$ (Li and Rinzel 1994). Conservation of Ca^{2+} implies the constraint of Ca^{2+} concentration in ER $C_E = C_T - \rho C$ with $C_T = 2\rho \mu\text{M}$. The concentration I is a control parameter.

Equations (4.13) and (4.14) describe the deterministic behavior averaged for a large number of channels. The small number of IP_3R s in a single cluster suggests that a stochastic formulation of these equations is necessary if calcium release from a single cluster should be considered.

Following the deterministic Li-Rinzel model, one can consider the stochastic opening and closing process only for the gate h . Each gate h is an inactive binding site for Ca^{2+} which is occupied (closing) or non-occupied (opening). We describe the binding and unbinding of these three sites using an independent two-state Markov processes with opening and closing rates α_h and β_h , respectively.

One can simply assume that the stochastic dynamics of the IP_3R channels can be reflected by the fluctuation of the open fraction of channel subunit h . As a result, the Langevin equation for the fraction of the h -open subunit is expressed as (Shuai and Jung 2002)

$$\frac{dh}{dt} = \alpha_h(1-h) - \beta_h h + G_h(t) \quad (4.19)$$

where $G_h(t)$ are zero mean, uncorrelated, Gaussian white-noise terms with

$$\langle G_h(t)G_h(t') \rangle = \frac{\alpha_h(1-h) + \beta_h h}{N} \delta(t - t'), \quad (4.20)$$

Such a gate-based Langevin approach indicates that the stochastic dynamics of the IP₃R open fraction can be treated as a deterministic dynamics disturbed by a Gaussian white noise.

In the simulation, the Gaussian noise sources are generated at each integration step by the Box-Muller algorithm. For example, we can simply use the Euler integration to solve the deterministic terms. Let the time step be δt , and γ_1 and γ_2 be two uniformly distributed random numbers in (0, 1]. The Box-Muller algorithm requires that one should add the following noise term into the Euler integration (Fox 1997)

$$g_h = \sqrt{-2 \frac{\alpha_h(1-h) + \beta_h h}{N} \log(\gamma_1)} \sin(2\pi\gamma_2) \quad (4.21)$$

As a result, the Euler integration of the Langevin equation for the Li-Rinzel model is given as

$$h(t + \delta t) = h(t) + \delta t(\alpha_h(1-h) - \beta_h h) + g_h(t)\sqrt{\delta t} \quad (4.22)$$

Since h has to be bound between 0 and 1, it is necessary to verify this condition after each iteration step. The approximate nature of Eq. 4.19 does not automatically maintain h in the required interval. One can simply put the value of h as 0 or 1 when it is out of [0, 1]. Simulation shows that the results are insensitive to the choice of strategy used to keep h in [0, 1].

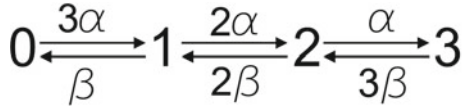
Instead of applying three identical h -gates with h^3 in Eq. (4.15), one can also consider three independent h -gates with $h_1h_2h_3$ in Eq. (4.15) which are disturbed individually by different Gaussian white noises (Shuai and Jung 2002; Huang et al. 2011).

4.2.5 Channel-Based Langevin Approach

Consisting of three subunits for IP₃R of the Li-Rinzel model, each channel has four possible h -uninhibited states, as shown in Fig. 4.4. Define state fraction x_i as the rate of the channel number in i h -uninhibited state among the total channel number with $i = 0, 1, 2, 3$. The stochastic channel kinetics can be modeled as a four-state Markov chain dynamics. Applying a vector $\mathbf{X} = \{x_i\}$ to represent the four state fractions, the evolution of channel state fractions can be traced by the following channel-based Langevin equation (Fox 1997; Huang et al. 2011)

$$\frac{d\mathbf{X}}{dt} = A\mathbf{X} + \frac{S}{\sqrt{N}}\xi, \quad (4.23)$$

Fig. 4.4 Transition diagram of IP₃R channel state. The number indicates how many subunits in the channel are in the *h*-uninhibited state



where A is the transition matrix representing the transition dynamics between different channel states. Based on the Markovian chain shown in Fig. 4.4, one has

$$A = \begin{pmatrix} -3\alpha & \beta & 0 & 0 \\ 3\alpha & -2\alpha - \beta & 2\beta & 0 \\ 0 & 2\alpha & -\alpha - 2\beta & 3\beta \\ 0 & 0 & \alpha & -3\beta \end{pmatrix} \quad (4.24)$$

In Eq. (4.23), the matrix S is the square root matrix of diffusion matrix $D = SS^T$ which is given by

$$D = \begin{pmatrix} 3\alpha x_0 + \beta x_1 & -3\alpha x_0 - \beta x_1 & 0 & 0 \\ -3\alpha x_0 - \beta x_1 & 3\alpha x_0 + (\beta + 2\alpha)x_1 + 2\beta x_2 & -2\alpha x_1 - 2\beta x_2 & 0 \\ 0 & -2\alpha x_1 - 2\beta x_2 & 2\alpha x_1 + (\alpha + 2\beta)x_2 + 3\beta x_3 & -\alpha x_2 - 3\beta x_3 \\ 0 & 0 & -\alpha x_2 - 3\beta x_3 & \alpha x_2 + 3\beta x_3 \end{pmatrix} \quad (4.25)$$

The vector ξ in Eq. (4.23) is a noise term with four elements. Each noise element is a Gaussian white noise with zero means and unit variances.

As a result, instead of Eq. (4.15) for channel flux, we have the following expressions for channel flux

$$J_r = \Omega_C m_\infty^3 x_3 (C_T - (1 + \rho_A)C) \quad (4.26)$$

in which x_3 is the *h*-open fraction of channels. Due to the Gaussian noise terms added, channel state fractions are no longer guaranteed to lie on the bounded domain, but have a probability to violate the meaningful interval [0, 1]. One can allow for the means of simplicity that fractions evolve unboundedly, and for values outside [0, 1] the positive semidefiniteness of the diffusion matrix may not be given thus hindering the computations of the matrix square roots. One can also keep the boundary limitation of [0, 1] by simply putting $x_i = 0$ or 1 once they are out of the bound and calculate $x_0 = 1 - \sum_{i>0} x_i$ to ensure $\sum x_i = 1$. Some better but complex constraining methods have also been proposed (Huang et al. 2013).

Orio et al. proposed a simple structure of the square root matrix to solve the stochastic differential equations of the Hodgkin-Huxley neuronal model (Orio and Soudry 2012), which can also be applied here to the Li-Rinzel Ca^{2+} model. In this approach, the Cholesky decomposition was extended to solve the stochastic terms of complex kinetic schemes of the four-state channel. In detail, the random term for i is equal to the square root of the sum of the forward ($i \rightarrow j$) and backward

$(i \leftarrow j)$ transition probabilities for the transition pair $i \leftarrow j$, scaled by the inverse of the channel number. As a result, one has

$$\frac{d\mathbf{X}}{dt} = A\mathbf{X} + S^O \xi, \quad (4.27)$$

Here, the square root matrix S^O in Eq. (4.27) is directly given by

$$S^O = \frac{KF}{\sqrt{N}} \quad (4.28)$$

where K is a 4×3 matrix given by

$$K = \begin{pmatrix} 1 & 0 & 0 \\ -1 & 1 & 0 \\ 0 & -1 & 1 \\ 0 & 0 & -1 \end{pmatrix} \quad (4.29)$$

and F is a 3×3 diagonal matrix with the diagonal elements given by

$$\text{diag}(F) = \begin{pmatrix} 3\alpha x_0 + \beta x_1 \\ 2\alpha x_1 + 2\beta x_2 \\ \alpha x_2 + 3\beta x_3 \end{pmatrix}$$

Such a simple expression for the square root matrix naturally fulfills the requirement of $SS^T = D$. Note that \mathbf{X} is a vector with four elements, but ξ here it is a noise vector with only three elements and S^O is a 3×4 matrix. With the method proposed by Orio and Soudry (2012), the expensive matrix square root calculation is avoided, largely reducing the total computational cost during the numerical simulation.

4.3 Stochastic Ca²⁺ Puff Dynamics

4.3.1 Limitation of Modeling with Homogeneous Ca²⁺ Concentration Within IP₃R Clusters

One can simply use the Markov version of the Li-Rinzel model (Li and Rinzel 1994) to study the statistical properties of Ca²⁺ puffs released from a cluster of IP₃Rs with stochastic gating dynamics. In this simple stochastic Li-Rinzel model, spatial aspects of the formation and collapse of localized Ca²⁺ elevations are ignored. The Ca²⁺ diffusion between the cluster and the environment is ignored so that an isolated cluster can be discussed. On the other hand, the channels are assumed to be close enough and the instantaneous Ca²⁺ diffusion within a cluster to be so fast that the

calcium concentration within a cluster is assumed to be always homogeneous. The small size of the IP_3R clusters introduces strong stochasticity for puffs, resulting in a distribution of puff amplitude, lifetime and inter-puff interval (Shuai and Jung 2002).

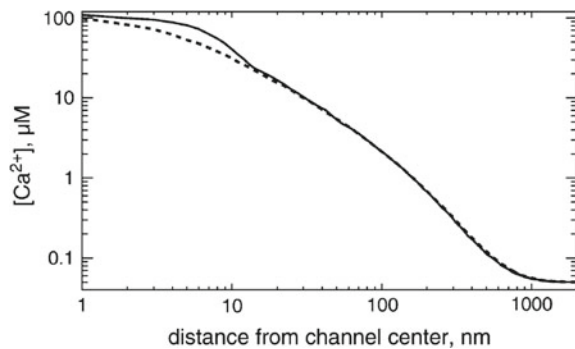
However, experimental and theoretical work (Roberts 1994; Rüdiger et al. 2007) suggests that even at steady state the Ca^{2+} diffusion at a Ca^{2+} release site may lead to inhomogeneous profiles even in a very small region. Simply assuming that the ER membrane acts as a flat boundary to limit the Ca^{2+} diffusion in a half three-dimensional space and Ca^{2+} ions diffuse from a point release source of IP_3Rs , a solution of the linearized reaction-diffusion equation indicates that a sharp distribution around the release point can be established (Smith 1996; Neher 1998),

$$c(r) = \frac{I_{\text{IP}_3\text{R}}}{4\pi r FD_{\text{Ca}}} \exp(-r/\lambda) + c_0, \quad (4.30)$$

where $I_{\text{IP}_3\text{R}}$ is the current of IP_3R , D_{Ca} is the diffusion coefficient for free Ca^{2+} , and c_0 is the Ca^{2+} concentration at resting state. The parameter λ is an important factor which accounts for the Ca^{2+} diffusion and binding to buffers. The term $\exp(-r/\lambda)/r$ indicates that the decay of Ca^{2+} concentration with distance is even sharper than the exponential function.

As shown in Fig. 4.5, a numerical simulation with the finite element method shows a sharp decay of the stationary Ca^{2+} concentration against distance from the channel center. The Ca^{2+} concentration at the channel pore is about $110 \mu\text{M}$. It decreases to about $20 \mu\text{M}$ at a distance of 15 nm which is about the size of the IP_3R channel, and decreases to about $0.7 \mu\text{M}$ at a distance of 200 nm , which is about the size of the IP_3R cluster. These data indicate that the homogeneous Ca^{2+} concentration for clustered IP_3Rs is not a suitable assumption, for a puff simulation with a cluster size of a few hundred nanometers.

Fig. 4.5 The stationary Ca^{2+} concentration against distance for an open channel directly along the ER membrane (solid) and perpendicular to the membrane (dashed) as calculated with finite element discretization (Rüdiger et al. 2010b)



4.3.2 Two-Scale Modeling of Ca^{2+} Concentration Within IP_3R Clusters

Considering the sharp decay around the open channel, a puff model with two-scale Ca^{2+} concentration was proposed (Rüdiger et al. 2010a). In fact, if a channel is open, the local Ca^{2+} concentrations reach values above 100 μM , while closed channels in a cluster are subjected to much lower concentrations. For simplicity, one may introduce a domain Ca^{2+} concentration for all the closed channels in a cluster. As shown in Fig. 4.6b, it can be seen that the domain Ca^{2+} , c_d , can be well described by a linear relationship with the number of open channels, n as

$$c_d(n) = c_0 + c_1 n, \quad (4.31)$$

where c_0 is the rest level concentration and c_1 is a coupling constant (Rüdiger et al. 2010a).

The dynamics for N channels in a cluster can then be simulated by using discrete Markovian gating transitions and using equations for the Ca^{2+} concentration such as Eq. (4.31). Various schemes have been studied and have been shown to produce Ca^{2+} dynamics resembling experimentally observed Ca^{2+} puffs (DeRemigio et al. 2008; Rüdiger et al. 2010a; Cao et al. 2013; Rüdiger 2014b).

When a channel switches from the open state to the closed state, the domain Ca^{2+} concentration will be influenced by its diffusion and binding and unbinding with various buffers before it reaches the equilibrium value c_d . To incorporate the collapsing dynamics, one can consider the following differential equation for c_d around the closed channels (Rüdiger et al. 2014)

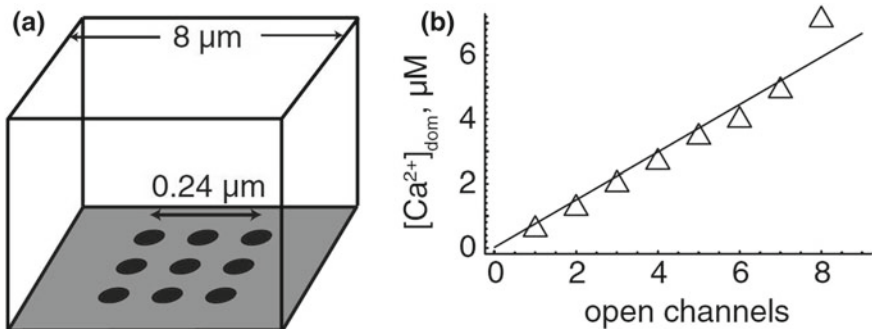


Fig. 4.6 FEM simulation of Ca^{2+} release from nine channels in a cluster (Rüdiger et al. 2010a). **a** The box of dimension $8 \times 8 \times 5 \mu\text{m}^3$ represents the cytosolic space. Channels are located on the ER membrane. **b** The domain calcium concentrations are obtained by averaging the closed channels for a given total number of open ones

$$\frac{dc_d}{dt} = \gamma(c_0 + c_1 n - c_d). \quad (4.32)$$

Here γ is the decay rate for the domain Ca^{2+} collapse, which in general depends on many factors such as cluster size and buffer content. As an example, the temporal evolution of the open channel number and the corresponding cluster domain Ca^{2+} is given in Fig. 4.7. The stochastic channel opening and closing in the cluster causes the occurrence of puffs and blips.

To further address the possible equivalence within a differential equation approach, one needs to replace n in Eq. (4.31) with the product of the total number of channels, N , and the fraction of channels in the open state a . Substituting the discrete number of channels for its continuous counterpart, Na , entails that c_d can be larger than c_0 even if less than one channel is open. This misrepresentation is a source of inadequate continuous modeling and in Rüdiger (2014b) a function that possesses a step at the crucial transition from zero to one open channel was introduced:

$$c_d(a) = c_0 + c_1 Na \frac{1}{2}[1 + \tanh((Na - 1)/\epsilon)]. \quad (4.33)$$

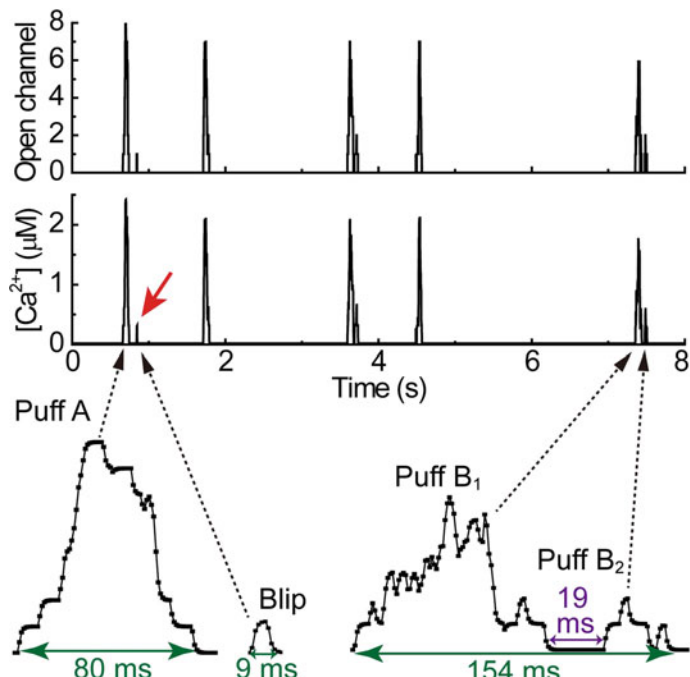


Fig. 4.7 The temporal evolution of open channel number (top) and the corresponding cluster domain Ca^{2+} (middle). The arrow marks a blip. Two puffs (Puff A and Puff B) and a blip are depicted in the enlarged drawing (bottom) (Qi et al. 2015)

Here, the parameter ϵ characterizes the “discreteness” of the 0-1 step and was chosen as 0.1 in Rüdiger (2014b).

4.3.3 Puff Dynamics in a Langevin Model

In Rüdiger et al. (2010a) a Markov chain of four states was used, which basically represent the four states obtained from activation and inhibition, see Fig. 4.8. The simulations based on this scheme and other schemes suggested a dynamics similar to the excitable behavior well known from models for neuronal action potentials including the Hodgkin-Huxley equations (Hodgkin and Huxley 1952).

Rate equations with Langevin noise for each gating state can be derived from the reaction scheme in the standard way (Shuai and Jung 2003). For example, the fraction of channels in the state a is given by

$$\frac{da}{dt} = k_a^+ c z - k_a^- a + k_i^- g - k_i^+ c_s a + G_{za} + G_{ag}. \quad (4.34)$$

The $G_{..}$ terms are Langevin noises representing stochasticity of channel opening/closing. Following the approach of Fox and Lu (1994) one obtains, for instance, for $G_{za}(t)$ a zero mean, Gaussian white noise term with $\langle G_{za}(t)G_{za}(t') \rangle = (k_a^+ c_d z + k_a^- a)\delta(t - t')/N$. In Rüdiger (2014b) these equations were simulated together with ODEs for the cluster domain Ca^{2+} concentration. It was found that an excitable trajectory, similar to those in other systems such as action potentials in the FitzHugh-Nagumo system, underlies the puff dynamics, see Fig. 4.8b.

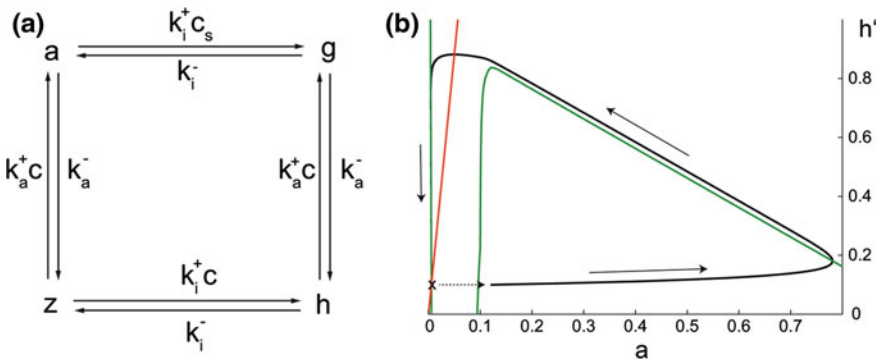


Fig. 4.8 **a** Four-state model based on single channel activation and inhibition. The rest state is denoted by z. Activation of the channel by Ca^{2+} binding corresponds to its opening (state a). Further Ca^{2+} binding results in the closing of the channel (states g and h). **b** Excitable trajectory (solid black line) in a two-dimensional ODE based on the model shown in (a) and Eq. (4.33). Here the green and red lines show the nullclines of the activator and inhibitor variables, respectively. Adapted from Rüdiger (2014b)

4.3.4 Ca²⁺ Dynamics with Clustered Channels in a 3D Model

Ca²⁺ release from a group of IP₃R channels has also been studied in three-dimensional models of the cytosolic space. The main problem encountered here is the strongly localized distribution of Ca²⁺ within the cell, which requires a very high spatial resolution in numerical modeling. Related to the clustering of IP₃R channels, there are two basic domain sizes to be considered. It was first recognized that the clustering of channels and release of Ca²⁺ produces a local elevation of Ca²⁺ to values between 1 and 10 μM. The spatial extent of these domains roughly follows that of the cluster (less than or close to 1 μM) and hence the domains are called microdomains. It was therefore suspected that the microdomain provides a homogenous local reaction space, so that all Ca²⁺ channels within the domain "feel" equal Ca²⁺ concentrations. Later, however, using more advanced methods of numerical spatial discretization, it appeared that Ca²⁺ is distributed very unevenly within a microdomain. This follows from the evidence that channels within a cluster are distanced at a few tens or hundreds of nm, so that after the opening of channels, gradients of [Ca²⁺] (roughly 1/r, where r is the radial distance from the channel pore) result. Thus, around an open channel, values of concentration of up to hundreds of μM result, while the concentrations at adjacent channels due to the open channel are much lower. Hence for a realistic modeling of local Ca²⁺ signals the assumption of a common reaction space for all channels is not valid (Rüdiger et al. 2010a).

An accurate description of intracellular Ca²⁺ dynamics takes into account Ca²⁺ diffusion and binding to buffers as well as transport to and from the intracellular storage compartments, mainly in the ER. Diffusion of Ca²⁺ and binding of Ca²⁺ to buffer proteins or endogenous buffers is modeled by reaction-diffusion equations, while transport through the ER membrane is given by influx conditions on the ER surface. In the following we consider the sample case of one buffer only, where *c* and *b* respectively denote the free cytosolic and bound buffer Ca²⁺ concentrations. Assuming simple reaction kinetics this leads to the following system of PDEs:

$$\frac{\partial c}{\partial t} = D_c \nabla^2 c + b k^- - c k^+ (B - b) \quad (4.35)$$

$$\frac{\partial b}{\partial t} = D_b \nabla^2 b - b k^- + c k^+ (B - b). \quad (4.36)$$

D_c, *D_b* and *B* denote the diffusion coefficients of free Ca²⁺, bound buffer and the total buffer concentration, respectively.

The equations are solved within a domain denoted Ω as shown below. Influx through the channels is given by boundary conditions on the domain boundary $\partial\Omega_M$ that represents the ER membrane:

$$D_c \vec{n} \cdot \vec{\nabla} c = \begin{cases} J, & \text{at } \partial\Omega_M \\ 0, & \text{at } \partial\Omega \setminus \partial\Omega_M \end{cases} \quad (4.37)$$

$$D_b \vec{n} \cdot \vec{\nabla} b = 0, \text{ at } \partial\Omega. \quad (4.38)$$

Here, \vec{n} denotes the outer normal vector of the boundary of the domain denoted by $\partial\Omega$. J describes the flux through the ER membrane and comprises three contributions:

$$J = P_c S(\vec{r}, t) (E - c) - P_p \frac{c^2}{K_d^2 + c^2} + P_l (E - c), \quad (4.39)$$

where $\vec{r} = (x, y, z)$ denotes the spatial position on the membrane and E is the $[Ca^{2+}]$ in the ER lumen. Since the ER was estimated to not be depleted during puffs (Ullah et al. 2012), one often assumes E to be constant.

The first term on the rhs of Eq. (4.39) models current through the IP₃R channels from the ER to the cytosol. This term is controlled by the channel state through the factor $S(\vec{r}, t)$, which is non-zero in small areas representing the open channels. The source areas should be chosen to be small to realistically model pore regions and the large Ca^{2+} gradients around open channels.

The second term in Eq. (4.39) models SERCA pumps. Standard models such as the one in Eq. (4.39) are of the Hill equation type with Hill coefficient 2 (Lytton et al. 1992). K_d is the dissociation constant of the pumps. The maximal pump current, V_p , was estimated to be 10–16 $\mu M s^{-1}$ (Falcke 2004). This number is based on a volume source and needs to be cast into a flux through a boundary by multiplying the volume current by the domain extension d_z . This results in units of moles per surface area and time, as is required for the boundary flux.

The last term in Eq. (4.39) models a small leakage of Ca^{2+} from the luminal to the cytosolic domain. Besides its physiological relevance, it also serves to balance the system in the rest state, i.e., it compensates the SERCA pumps when there are no open channels. To achieve a resting $[Ca^{2+}]$ of a few tens of nM (c_0) in the cytosolic domain and a few hundreds of μM in the ER (E), equating the two last terms of Eq. (4.39) provides a dependence of P_l on P_p :

$$P_l = \frac{P_p c_0^2}{(E - c_0)(K_d^2 + c_0^2)}. \quad (4.40)$$

Due to the multiple spatial scales, special care has to be given to spatial discretization in the numerical schemes. In one line of research, three-dimensional simulation software (Rüdiger et al. 2007, 2010b; Rückl et al. 2015) was established using the finite element method. The PDE-solver is based on locally grid-adapted finite elements in space that resolve the extreme spatial gradients of Ca^{2+} concentrations around an open channel. Typically, a spatial grid of less than 1 nm is needed in the close neighborhood of a channel, while the grid distance relaxes to around 500 nm further from the channels.

The stochastic gating transitions are described by schemes defining the states, the transitions and transition rates. As described above, the standard method to numerically time-advance such states' variables is the Gillespie method. The Gillespie method needs to be coupled to the time stepping of a reaction-diffusion equation using a hybrid method such as that given by Eq. (4.10).

The three-dimensional simulation tool permitted investigation of the interior Ca^{2+} distribution of clustered channels by taking into account the spatial separation of channels (Rüdiger et al. 2010a,b; Rückl et al. 2015). Previous publications had assumed all the channels of a cluster form a shared disk-shaped source area without allowing passive space between the channels. It was found that Ca^{2+} distributions around open channels are non-homogeneous at the scale of a cluster for realistic channel distances. This leads to a separation of Ca^{2+} scale into a large self-coupling value (concentration at the channel pore of an open channel), and the much smaller cluster domain values, defined as an appropriate average Ca^{2+} concentration at closed channels while others are open. It is then clear that incorporating spatial separation (as opposed to a tight cluster model) leads to models which allow a much better description of experimentally observed puffs see Sect. 4.3.2.

4.3.5 *Simulations with Discrete Ca^{2+} Ions*

The modeling approaches described above recognized the importance of number fluctuations in the binding to the channels and formulated hybrid models where the deterministic Ca^{2+} concentration is coupled to stochastic channel binding models (Rüdiger et al. 2007). More recently, however, it was found that local fluctuations stemming from diffusive noise of Ca^{2+} ions may also have a crucial influence in Ca^{2+} dynamics. Diffusive noise of Ca^{2+} regards the fluctuating number of ions that are in the neighborhood of the receptors and are available for binding to them. This noise source is similar to the noise in the diffusion of a chemoattractant that was considered in the classic work of Berg and Purcell (Berg and Purcell 1977).

A straightforward method to take diffusive noise into account involves tracking the exact diffusive paths of each individual ion in the computational domain. Doing so in the complete domain is computationally very intensive and, therefore, Flegg et al. applied spatial stochastic multiscale modeling in order to accurately incorporate diffusive noise (Flegg et al. 2013). In the two-regime method (Flegg et al. 2011), Brownian trajectories of the particles and binding events are followed in a small space surrounding the receptor cluster, while further away from the cluster the fluctuating numbers of ions in larger three-dimensional compartments are calculated. This method saves a considerable amount of simulation time while not compromising the microscopic detail needed for the binding dynamics close to the receptors. Flegg et al. showed that this approach can be used to calculate interpuff intervals for a cluster of nine channels.

A compartment-based approach was also used in the simulation of Wieder et al. (2015). There the influence of fluctuations in Ca^{2+} ion number on the equilibrium behavior of a single channel was studied and it was found that those fluctuations increase the open probability compared to the standard deterministic model. In an investigation of fluctuations in the number of Ca^{2+} ions in a single compartment in contact with the bulk, Weinberg and Smith found that mobile Ca^{2+} buffers may increase the size of fluctuations of $[\text{Ca}^{2+}]$ around its equilibrium value

(Weinberg and Smith 2014). Together, these studies hint at the presence of discrete Ca^{2+} noise, but further research is needed to draw clear conclusions regarding their relevance to Ca^{2+} release models.

4.4 Stochastic Intracellular Ca^{2+} Signals

Global synchronization of release results in cell-wide oscillations or waves (Berridge 1990; Lechleiter et al. 1991; Camacho and Lechleiter 1993) that can last up to several tens of seconds. Despite the ubiquity of Ca^{2+} oscillations in many cell types and many years of experimental and modeling research, there is still no consensus on the basic mechanism of the regenerative discharges. Here we would like to briefly look at the most widely discussed models and a few aspects in computational modeling that have been in focus recently. For a thorough discussion of the possible physiological mechanisms, we refer readers to the excellent review by Dupont et al. (2011).

Models of Ca^{2+} oscillations, just as any other kind of oscillation in biology, including cell cycle and circadian rhythms, rely on a number of nonlinear feedback processes (Nov'ak and Tyson 2008). Limiting the present discussion to intracellular IP_3 -controlled oscillations, two groups of mechanisms have been put forward. One group is based on the observation that IP_3R is biphasically regulated by Ca^{2+} . In its essence, oscillations are obtained by an alternation of activating and inhibiting binding to the receptor, which is obtained by various channel gating schemes such as for instance the DeYoung-Keizer scheme. This way, the global oscillations build on the same processes as the local signals discussed above and this suggests viewing the global signals as synchronized local signals. However, the times between the Ca^{2+} puffs are much shorter than those of the Ca^{2+} oscillations. In particular, recovery of the receptor from inhibition takes a few seconds at most, whereas oscillation periods can be longer than one minute. This and the very different durations of puffs and waves point to a shortcoming of this family of models.

A further group of models take into account the fact that in many cell types the concentration of IP_3 is also variable and may therefore drive Ca^{2+} oscillations. Several possibilities have been proposed including stimulation of IP_3 synthesis by released Ca^{2+} (Meyer and Stryer 1988) and Ca^{2+} -activated down-regulation of G-protein-coupled IP_3 production (Cuthbertson and Chay 1991). Other studies featured passive IP_3 variability (Dupont and Erneux 1997) or included several types of the mentioned mechanisms to allow a detailed quantitative comparison (De Pitt'a et al. 2009).

More recently a detailed study of release from a receptor cluster has been used to explain the dichotomy of puffs and waves observed in many cell types including *Xenopus* oocytes. Rückl et al. analyzed the modified DeYoung-Keizer model previously used to study the Ca^{2+} puffs and found that it is capable of producing both short-lived release as well as wave-like release that lasts for several seconds (Rückl et al. 2015). In the model, long-lasting events are accompanied by unbinding of IP_3

from the receptor. Since these long events have a much larger total Ca^{2+} release, they are more likely to stimulate neighboring clusters and thus tend to synchronize release as observed during a wave. Since the large events are less frequent than the short events, the model produces periods of global events in the order of the experimentally observed inter-spike intervals. Interestingly, the unbinding of IP_3 occurs with a short delay compared to the peak position, resulting in a delayed peak of free IP_3 concentration that has also been observed experimentally (Tanimura et al. 2009; Gaspers et al. 2014).

The mechanisms described above can in principle be used within a deterministic differential equation model. This has frequently been done to analyze whole-cell oscillations. However, with the increasing spatial resolution and characterization of local Ca^{2+} release in experiments, the role of noise in the appearance and generation of global Ca^{2+} signals has been recognized. This has prompted a way of modeling in accord with noise-driven, excitable local release, which thus shares similarities to the behavior found in the propagation of neuronal action potentials.

A number of experimental studies characterized puffs as the basic building blocks of global signals (Parker et al. 1996; Smith and Parker 2009). Since puffs are noise-driven as discussed above, Falcke and co-workers postulated that their inherent randomness carries over to waves (Skupin et al. 2010). According to this picture, a random opening of channels in one or several clusters triggers the activation of adjacent clusters, thus facilitating the spreading of a wave through the cell. These ideas also provide an explanation of the inherent randomness of Ca^{2+} oscillations, which is apparent most clearly in their fluctuating inter-spike period.

Besides the duration of an event, stochastic modeling addresses the different inter-puff times (a few seconds) and inter-wave times (several tens of seconds to minutes). In the approach by Falcke and co-workers the long periods of global oscillations are created by the waiting time for a sufficiently large local event encompassing several clusters (a nucleation event) (Thurley and Falcke 2011). Alternatively, it has also been suggested that the amplitude of elementary release events is distributed randomly. Accordingly, only the largest events would have sufficient potency to spread to adjacent clusters (Rückl et al. 2015). The latter model also explains why a cluster stays refractory after a wave for several seconds while it admits puffs shortly after termination of a prior puff (Marchant and Parker 2001).

4.5 Outlook of Intercellular Ca^{2+} Waves with Stochastic IP_3R Dynamics

Intercellular Ca^{2+} waves (ICWs) can be induced in response to bath application of glutamate or ATP in glial cells. Mechanical or electrical stimulation can also generate ICWs. Experimental data showed that the permeability of intracellular IP_3 messenger or Ca^{2+} ions through gap junctions and the spreading of extracellular ATP messengers are important mechanisms for ICWs.

Currently, many simulation models discussed for ICWs are based on deterministic signal dynamics. The biologically realistic features, such as the clustering distribution of IP₃R and the stochastic channel dynamics have been paid less attention. It has been found that the application of stochastic methods is necessary and useful to describe intracellular Ca²⁺ signaling. In this chapter we have presented how various theoretical concepts such as Markov chains, the Gillespie algorithm, the Langevin approach and hybrid modeling can be applied to the study of intracellular Ca²⁺ dynamics. Thus it is necessary to discuss the intercellular Ca²⁺ waves with stochastic dynamics of clustered IP₃R channels.

One can expect that the stochastic dynamics of clustered IP₃R channels can affect not only the intracellular Ca²⁺ signals, but also the intercellular Ca²⁺ waves. The ICWs model with stochastic and clustered IP₃R channels will be considerably closer to experimental observations and provide more quantitative insights into ICWs. For the coupled glial cells, it raises the model's complexity by integration of grouped-cell processes which span many scales, from single IP₃R channel dynamics and clustered channels, to intracellular cells and intercellular cells. Thus, a challenge is to develop an ICW model which is complex enough to account for the stochastic and clustered IP₃R channel dynamics, and at the same time is simple enough to be computationally efficient for numerical modeling. We believe that such an ICW model can lead to a deeper understanding of the ICW mechanisms of glial cells.

Acknowledgements Shuai acknowledges support from the China National Funds for Distinguished Young Scholars under grant 11125419, the National Natural Science Foundation of China under grants 31370830 and 11675134, and the Fujian Province Funds for Leading Scientist in Universities. S.R. acknowledges support from the Deutsche Forschungsgemeinschaft (RU 1660 and IRTG 1740).

References

- Alfonsi A, Cances E, Turinici G, Di Ventura B, Huisings W (2005) Exact simulation of hybrid stochastic and deterministic models for biochemical systems. *ESAIM: Proc* 14:1–13
- Berg HC, Purcell EM (1977) Physics of chemoreception. *Biophys J* 20(2):193–219
- Berridge MJ (1990) Calcium oscillations. *J Biol Chem* 265(17):9583–9586
- Berridge MJ, Bootman MD, Roderick HL et al (2003) Calcium signalling: dynamics, homeostasis and remodelling. *Nat Rev Mol Cell Biol* 4:517–529
- Camacho P, Lechleiter JD (1993) Increased frequency of calcium waves in *Xenopus laevis* oocytes that express a calcium-ATPase. *Science* 260:226–229
- Cao P, Donovan G, Falcke M, Sneyd J (2013) A stochastic model of calcium puffs based on single-channel data. *Biophys J* 105(5):1133–1142
- Cuthbertson KSR, Chay TR (1991) Modelling receptor-controlled intracellular calcium oscillators. *Cell Calcium* 12(2):97–109
- De Pitt'a M, Goldberg M, Volman V, Berry H, Ben-Jacob E (2009) Glutamate regulation of calcium and IP₃ oscillating and pulsating dynamics in astrocytes. *J Biol Phys* 35(4):383–411
- DeRemigio H, Groff JR, Smith GD (2008) Calcium release site ultrastructure and the dynamics of puffs and sparks. *Math Med Biol* 25(1):65. ISSN 1477–8599

- DeYoung G, Keizer J (1992) A single-pool inositol 1,4,5-trisphosphate-receptor-based model for agonist-stimulated oscillations in Ca^{2+} concentration. *Proc Nat Acad Sci USA* 89:9895–9899
- Di Capite J, Ng SW, Parekh AB (2009) Decoding of cytoplasmic Ca^{2+} oscillations through the spatial signature drives gene expression. *Current Biol* 19(10):853–858. ISSN 0960-9822
- Dolmetsch RE, Xu K, Lewis RS (1998) Calcium oscillations increase the efficiency and specificity of gene expression. *Nature* 392:933–936
- Dupont G, Combettes L, Bird GS, Putney JW (2011) Calcium oscillations. *Cold Spring Harb Perspect Biol* 3(3)
- Dupont G, Erneux C (1997) Simulations of the effect of inositol 1,4,5-trisphosphate 3-kinase and 5-phosphatase on Ca^{2+} oscillations. *Cell Calcium* 22:321–331
- Falcke M (2003) On the role of stochastic channel behavior in intracellular Ca^{2+} dynamics. *Biophys J* 84(1):42–56
- Falcke M (2004) Reading the patterns in living cells—the Physics of Ca^{2+} signaling. *Adv Phys* 53(3):255–440
- Flegg MB, Chapman SJ, Erban R (2011) The two-regime method for optimizing stochastic reaction-diffusion simulations. *J Royal Soc Interface*, rsif20110574
- Flegg M, Ruediger S, Erban R (2013) Diffusive spatio-temporal noise in a first-passage time model for intracellular calcium release. *J Chem Phys* 138:154103
- Fox RF (1997) Stochastic versions of the Hodgkin-Huxley equations. *Biophysical J* 72:2068–2074
- Fox RF, Lu Y (1994) Emergent collective behavior in large numbers of globally coupled independently stochastic ion channels. *Phys Rev E* 49(4):3421–3431
- Gaspers LD, Bartlett PJ, Politi A, Burnett P, Metzger W, Johnston J, Joseph SK, Hofer T, Thomas AP (2014) Hormone-induced calcium oscillations depend on cross-coupling with inositol 1, 4, 5-trisphosphate oscillations. *Cell Rep* 9(4):1209–1218
- Gillespie DT (1976) A general method for numerically simulating the stochastic time evolution of coupled chemical reactions. *J Comput Phys* 22:403–434
- Gillespie DT (1977) Exact stochastic simulation of coupled chemical reactions. *J Phys Chem* 81:2340–2361
- Gibson MA, Bruck J (2000) Efficient exact stochastic simulation of chemical systems with many species and many channels. *J Phys Chem A* 104(9):1876–1889
- Hodgkin AL, Huxley AF (1952) A quantitative description of membrane current and its application to conduction and excitation in nerve. *J Phys* 117(4):500
- Huang YD, Rüdiger S, Shuai JW (2011) Modified Langevin approach for a stochastic calcium puff model. *Eur Phys J B* 83:401–407
- Huang YD, Ruediger S, Shuai JW (2013) Channel-based Langevin approach for the stochastic Hodgkin-Huxley neuron. *Phys Rev E* 87:012716
- Johenning FW, Theis A-K, Pannasch U, Rückl M, Rüdiger S, Schmitz D (2015) Ryanodine receptor activation induces long-term plasticity of spine calcium dynamics. *PLoS Biol* 13(6):e1002181
- Lechleiter JD, Girard S, Peralta E, Clapham D (1991) Spiral calcium wave propagation and annihilation in *Xenopus laevis* oocytes. *Science* 252:123–126
- Li Y, Rinzel J (1994) Equations for inosp3 receptor-mediated $[\text{Ca}^{2+}]$ oscillations derived from a detailed kinetic model: a hodgkin-huxley like formalism. *J Theoret Biol* 166:461–473
- Lytton J, Westlin M, Burk SE, Shull GE, MacLennan DH (1992) Functional comparisons between isoforms of the sarcoplasmic or endoplasmic reticulum family of calcium pumps. *J Biol Chem* 267(20):14483–14489
- Neher E (1998) Vesicle pools and Ca^{2+} microdomains: New tools for understanding their roles in neurotransmitter release. *Neuron* 20:389–399
- Nov'ak B, Tyson JJ (2008) Design principles of biochemical oscillators. *Nat Rev Mo Cell Biol* 9(12):981–991
- Marchant JS, Parker I (2001) Role of elementary Ca^{2+} puffs in generating repetitive Ca^{2+} oscillations. *EMBO J* 20:65–76
- Meyer T, Stryer L (1988) Molecular model for receptor-stimulated calcium spiking. *Proc Nat Acad Sci* 85(14):5051–5055

- Orio P, Soudry D (2012) Simple, fast and accurate implementation of the diffusion approximation algorithm for stochastic ion channels with multiple states. *PLoS One* 7:e36670
- Parker I, Yao Y (1996) Ca^{2+} transients associated with openings of inositol trisphosphate-gated channels in Xenopus oocytes. *J Physiol (Lond)* 491:663–668
- Parker I, Choi J, Yao Y (1996) Elementary events of InsP_3 -induced Ca^{2+} liberation in Xenopus oocytes: hot spots, puffs and blips. *Cell Calcium* 20(2):105–121
- Qi H, Li LX, Shuai JW (2015) Optimal microdomain crosstalk between endoplasmic reticulum and mitochondria for Ca^{2+} oscillations. *Sci Rep* 5:7984, 1–11
- Roberts WM (1994) Localization of calcium signals by a mobile calcium buffer in frog saccular hair cells. *J Neurosci* 14(5):3246–3262
- Rüdiger S, Shuai JW, Huisenga W, Nagaiah Ch, Warnecke G, Parker I, Falcke M (2007) Hybrid stochastic and deterministic simulations of calcium blips. *Biophys J* 93:1847–1857
- Rüdiger S, Shuai JW, Sokolov IM (2010a) Law of mass action, detailed balance, and the modeling of calcium puffs. *Phys Rev Lett* 105:048103
- Rüdiger S, Nagaiah Ch, Warnecke G, Shuai JW (2010b) Calcium Domains around Single and Clustered IP_3 Receptors and Their Modulation by Buffers. *Biophys J* 99(1):3–12
- Rüdiger S (2014a) Stochastic models of intracellular calcium signals. *Phys Rep* 534(2):39–87
- Rüdiger S (2014b) Excitability in a stochastic differential equation model for calcium puffs. *Phys Rev E* 89(6):062717
- Rüdiger S, Qi H, Huang Y, Shuai J (2014) Frequency and relative prevalence of calcium blips and puffs in a model of small $\text{ip}3\text{r}$ clusters. *Biophysical Journal* 106:2353–2363
- Rückl M, Parker I, Marchant JS, Nagaiah C, Johenning FW, Rüdiger S (2015) Modulation of elementary calcium release mediates a transition from puffs to waves in an $\text{ip}3\text{r}$ cluster model. *PLoS Comput Biol* 11(1):e1003965
- Rusakov DA (2015) Disentangling calcium-driven astrocyte physiology. *Nat Rev Neurosci* 16(4):226–233
- Shuai JW, Jung P (2002) Stochastic properties of Ca^{2+} release of inositol 1, 4, 5-trisphosphate receptor clusters. *Biophys J* 83:87–97
- Shuai JW, Jung P (2003) Langevin modeling of intracellular calcium dynamics. Understanding Calcium, Dynamics, pp 231–252
- Skupin A, Kettenmann H, Falcke M (2010) Calcium signals driven by single channel noise. *PLoS Comput Biol* 6(8):1183–1186. ISSN 1553-734X
- Smith GD (1996) Analytical steady-state solution to the rapid buffering approximation near an open Ca^{2+} channel. *Biophys J* 71:3064–3072
- Smith IF, Parker I (2009) Imaging the quantal substructure of single IP3R channel activity during Ca^{2+} puffs in intact mammalian cells. *Proc Natl Acad Sci USA* 106(15):6404
- Smith IF, Wiltgen SM, Shuai J, Parker I (2009) Ca^{2+} puffs originate from pre-established stable clusters of inositol trisphosphate receptors. *Sci Signaling* 2(98):ra77
- Tanmura A, Morita T, Nezu A, Shitara A, Hashimoto N, Tojo Y (2009) Use of fluorescence resonance energy transfer-based biosensors for the quantitative analysis of inositol 1, 4, 5-trisphosphate dynamics in calcium oscillations. *J Biol Chem* 284(13):8910
- Thurley K, Falcke M (2011) Derivation of Ca^{2+} signals from puff properties reveals that pathway function is robust against cell variability but sensitive for control. *Proc Natl Acad Sci USA* 108(1):427
- Ullah G, Parker I, Mak DOD, Pearson JE (2012) Multi-scale data-driven modeling and observation of calcium puffs. *Cell Calcium* 52:152
- Volterra A, Liaudet N, Savtchouk I (2014) Astrocyte Ca^{2+} signalling: an unexpected complexity. *Nat Rev Neurosci* 15(5):327–335
- Weinberg SH, Smith GD (2014) The influence of Ca^{2+} buffers on free $[\text{Ca}^{2+}]$ fluctuations and the effective volume of Ca^{2+} microdomains. *Biophys J* 106(12):2693–2709
- Wieder N, Fink R, von Wegner F (2015) Exact stochastic simulation of a calcium microdomain reveals the impact of Ca^{2+} fluctuations on $\text{ip}3\text{r}$ gating. *Biophys J* 108(3):557–567

Chapter 5

G Protein-Coupled Receptor-Mediated Calcium Signaling in Astrocytes



Maurizio De Pittà, Eshel Ben-Jacob and Hugues Berry

Abstract Astrocytes express a large variety of G protein-coupled receptors (GPCRs) which mediate the transduction of extracellular signals into intracellular calcium responses. This transduction is provided by a complex network of biochemical reactions which mobilizes a wealth of possible calcium-mobilizing second messenger molecules. Inositol 1,4,5-trisphosphate is probably the best known of these molecules whose enzymes for its production and degradation are nonetheless calcium-dependent. We present a biophysical modeling approach based on the assumption of Michaelis–Menten enzyme kinetics, to effectively describe GPCR-mediated astrocytic calcium signals. Our model is then used to study different mechanisms at play in stimulus encoding by shape and frequency of calcium oscillations in astrocytes.

Keywords Inositol 1, 4, 5-trisphosphate metabolism · Calcium encoding · Signal integration · Calcium-induced calcium release threshold · Protein kinase C · Diacylglycerol

Abbreviations

2-AG	2-Arachidonoylglycerol
CaMKII	Ca ²⁺ /calmodulin-dependent protein kinase II
CICR	Calcium-induced calcium release
cPKC	Conventional protein kinase C

Eshel Ben-Jacob: Deceased June 5, 2015.

M. De Pittà(✉)
BCAM – Basque Center for Applied Mathematics, Bilbao, Spain
e-mail: maurizio.depitta@gmail.com

E. Ben-Jacob
School of Physics and Astronomy, Tel Aviv University, Ramat Aviv, Israel

H. Berry
EPI BEAGLE, INRIA Rhône-Alpes, Villeurbanne, France

DAG	Diacylglycerol
DAGK (DAGL)	DAG kinase (lipase)
ER	Endoplasmic reticulum
GPCR	G protein-coupled receptor
GTP (GDP)	Guanosine-5'-triphosphate (guanosine diphosphate)
IP ₃ (IP ₃ R)	Inositol 1,4,5-trisphosphate (receptor)
IP ₃ 3K	IP ₃ 3-kinase
IP-5P	Inositol polyphosphate 5-phosphatase
PIP ₂	Phosphatidylinositol 4,5-bisphosphate
PLC β (PLC δ)	Phospholipase C β (C δ)

5.1 Introduction

Calcium signaling is the most commonly measured readout of astrocyte activity in response to stimulation, be it by synaptic activity, by neuromodulators diffusing in the extracellular milieu, or by exogenous chemical, mechanical, or optical stimuli. In this perspective, the individual astrocytic Ca^{2+} transient is thought, to some extent, as an integration of the triggering stimulus (Perea and Araque 2005) and it is thus regarded as an encoding or decoding of this stimulus, depending on the point of view (Carmignoto 2000; De Pittà et al. 2013).

Multiple and varied are the spatiotemporal patterns of Ca^{2+} elevations recorded from astrocytes in response to stimulation, each possibly carrying its own encoding (Bindocci et al. 2017). Insofar as different encoding modes could correspond to different downstream signaling, including gliotransmission and thereby regulation of synaptic function, understanding the biophysical mechanisms underlying rich Ca^{2+} dynamics in astrocytes is crucial.

Calcium-induced Ca^{2+} release (CICR) from the endoplasmic reticulum (ER) is arguably the best characterized mechanism of Ca^{2+} signaling in astrocytes (Zorec et al. 2012). It ensues from nonlinear properties of Ca^{2+} channels which are found on the ER membrane and are gated by the combined action of cytosolic Ca^{2+} and the second messenger molecule inositol 1,4,5-trisphosphate (IP₃) (Shinohara et al. 2011; see also Chaps. 2–4). This second messenger molecule can be produced by the astrocyte either spontaneously or, notably, in response to activation by extracellular insults of G protein-coupled receptors (GPCRs) on the cell's plasma membrane (Parri and Crunelli 2003; Panatier et al. 2011; Volterra et al. 2014). Hence, these receptors and their triggering of IP₃ signaling can be regarded as integral components of the interface whereby an astrocyte transduces extracellular insults into Ca^{2+} responses (Marinissen and Gutkind 2001). Characterizing this interface is thus an essential step in our understanding of the emerging complexity of Ca^{2+} signals, and we devote this chapter to this purpose. In the first part of the chapter, we will present a concise framework to model intracellular IP₃ signaling in astrocytes. This framework is general and can easily be extended to include additional biological details, such as the regulation of GPCR binding efficiency by protein kinase C. Some of the models

presented in this chapter are also subjected to revision and comparison with other astrocyte models in Chaps. 16 and 18.

5.2 Modeling Intracellular IP₃ Dynamics

5.2.1 Agonist-Mediated IP₃ Production

G protein-coupled receptors form a large family of receptors which owe their name to their extensively studied interaction with heterotrimeric G proteins (composed of an α -, β -, and γ -subunit) which undergo conformational changes that lead to the exchange of GDP for GTP, bound to the α -subunit, following receptor activation. Consequently, the $\text{G}\alpha_q$ - and $\text{G}\beta\gamma$ -subunits stimulate enzymes thereby activating or inhibiting the production of a variety of second messengers (Marinissen and Gutkind 2001).

Among all GPCRs, those that contain the $\text{G}\alpha_q$ subunit are linked with the cascade of chemical reactions that leads to IP₃ synthesis. There, the $\text{G}\alpha_q$ subunit promotes activation of the enzyme phospholipase C β (PLC β) which hydrolyzes the plasma membrane lipid phosphatidylinositol 4,5-bisphosphate (PIP₂) into diacylglycerol (DAG) and IP₃ (Rebecchi and Pentyala 2000). Examples of such receptors expressed by astrocytes ex vivo and in vivo are the group 1 metabotropic glutamate receptor of type 1 and 5 (mGluR1/5) (Wang et al. 2006; Sun et al. 2013), the purinergic receptor P2Y1 (Jourdain et al. 2007; Di Castro et al. 2011; Sun et al. 2013), the muscarinic receptor mAchR1 α (Takata et al. 2011; Chen et al. 2012; Navarrete et al. 2012), and the adrenergic α_1 receptor (Bekar et al. 2008; Ding et al. 2013). While these receptors bind different agonists, and likely display receptor-specific binding kinetics, they all share the same downstream signaling pathway and therefore may be modeled in a similar fashion.

Several are the available models for $\text{G}\alpha_q$ -containing receptors, and the choice of what model to use rather than another depends on the level of biological detail and the questions one is interested in. Here our focus is on the rate of IP₃ production upon activation of these receptors, so we wish to keep as simple as possible the description of the reactions that regulate the activation of PLC β by α_q -, β -, and γ -subunits. This is possible, assuming that these reactions are much faster than the downstream ones that result in IP₃ production. In this case, a *quasi steady-state approximation* (QSSA) holds, whereby in the series of reactions that leads from receptor agonist binding to activation of PLC β , the intermediate reactions involving the three receptor's subunits are at equilibrium on the timescale of the production of activated PLC β . Accordingly, assuming that on average the receptor at rest (R) requires n molecules of an agonist (A) to promote activation of PLC β (R^*) at rate O_N , we can write



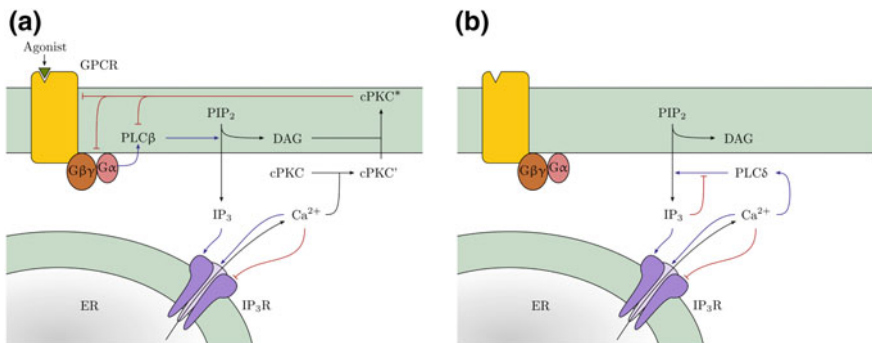


Fig. 5.1 IP₃ production. **a** Hydrolysis of the membrane lipid phosphatidylinositol 4,5-bisphosphate (PIP₂) by PLC β and PLC δ isoenzymes produces IP₃ and diacylglycerol (DAG). The contribution of PLC β to IP₃ production depends on agonist binding to astrocyte G protein-coupled receptors (GPCRs). This production pathway is inhibited via receptor phosphorylation by Ca²⁺-dependent activation of conventional protein kinases C (cPKCs). *Blue:* promoting pathway; *red:* inhibitory pathway

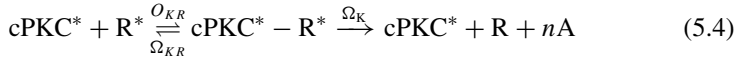
We further make another assumption: that the cascade of reactions that leads to GPCR-mediated IP₃ synthesis has a Michaelis–Menten kinetics (see Appendix 1), so the IP₃ production by PLC β (J_β) can be taken proportional to the fraction of bound receptors, defined as $\Gamma_A = [R^*]/[R]_T$, with $[R]_T = [R] + [R^*]$ being the total receptor concentration at the site of IP₃ production, i.e.,

$$J_\beta = O_\beta \cdot \Gamma_A \quad (5.2)$$

In the above equation, O_β is the maximal rate of IP₃ production by PLC β and lumps information on receptor surface density as well as on the size of the PIP₂ reservoir. Importantly, these two quantities may not be fixed, insofar as receptors are subjected to desensitization, internalization, and recycling, and the reservoir of PIP₂ could also be modulated by cytosolic Ca²⁺ and IP₃ (Rhee and Bae 1997). The reader interested in modeling these aspects may refer to Lemon et al. (2003). In the following, we will assume O_β constant for simplicity.

To seek an expression for J_β , termination of PLC β signaling has to be considered. With this regard, as illustrated in Fig. 5.1a, there are two possible pathways whereby IP₃ production by PLC β ends (Rebecchi and Pentala 2000). One is by reconstitution of the inactive G protein heterotrimer and coincides with unbinding of the agonist from the receptor, due to the intrinsic GTPase activity of the activated G α_q subunit. The other is by phosphorylation of the receptor, the G α_q subunit, PLC β or some combination thereof by conventional protein kinases C (cPKC) (Ryu et al. 1990; Codazzi et al. 2001). This phosphorylation modulates either receptor affinity for agonist binding, or coupling of the bound receptor with the G protein, or coupling of the activated G protein with PLC β , ultimately resulting in receptor desensitization (Fisher 1995).

Denoting by $cPKC^*$ the active, receptor-phosphorylating kinase C, termination of $PLC\beta$ -mediated IP_3 production can then be modeled by the following pair of chemical reactions:



From Eq. 5.3–5.4 we have:

$$\frac{dR^*}{dt} = O_N[A]^n[R] - \Omega_N[R^*] - O_{KR}[cPKC^*][R^*] + \Omega_{KR}[cPKC^* - R^*] \quad (5.5)$$

$$\frac{d[cPKC^* - R^*]}{dt} = O_{KR}[cPKC^*][R^*] - (\Omega_{KR} + \Omega_K)[cPKC^* - R^*] \quad (5.6)$$

Assuming that production of the intermediate kinase receptor complex is at quasi-steady state in reaction 5.4, i.e., $d[cPKC^* - R^*]/dt \approx 0$, it follows that

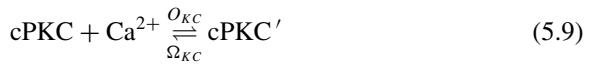
$$[cPKC^* - R^*] = \frac{O_{KR}}{\Omega_{KR} + \Omega_K} [cPKC^*][R^*] \quad (5.7)$$

Then, substituting this latter equation in Eq. 5.5 gives

$$\begin{aligned} \frac{dR^*}{dt} &= O_N[A]^n[R] - \Omega_N[R^*] - O_{KR} \left(1 - \frac{\Omega_{KR}}{\Omega_{KR} + \Omega_K} \right) [cPKC^*][R^*] \\ &= O_N[A]^n[R] - \Omega_N[R^*] - O_K[cPKC^*][R^*] \end{aligned} \quad (5.8)$$

where we defined $O_K = O_{KR}(1 - \Omega_{KR}/(\Omega_{KR} + \Omega_K))$.

To retrieve an equation for $[cPKC^*]$, we consider the fact that activation of cPKC requires binding of free cytosolic Ca^{2+} (C) and DAG to the kinase, but only if Ca^{2+} binds first, cPKC can get sensibly activated by DAG (Oancea and Meyer 1998). Accordingly, the following sequential binding reaction scheme for cPKC activation may be assumed:



where cPKC is the inactive kinase, and $cPKC'$ denotes the Ca^{2+} -bound kinase complex. By QSSA in reaction 5.4, it follows that the available activated kinase approximately equals to $[cPKC^*]_T = [cPKC^*] + [cPKC^* - R^*] \approx [cPKC^*]$. Moreover, it can be assumed that only a small fraction of $cPKC'$ is bound by DAG so

that $[cPKC^*] \ll [cPKC']$. In this fashion, the available cPKC, denoted by $[cPKC]_T$, can be approximated by $[PKC]_T \approx [PKC] + [PKC']$. Accordingly, solving reactions 5.9 and 5.10 for $[PKC^*]$ provides

$$\begin{aligned}[cPKC^*] &= ([cPKC^*] + [cPKC']) \cdot \mathcal{H}_1([DAG], K_{KD}) \\ &\approx [cPKC'] \cdot \mathcal{H}_1([DAG], K_{KD}) \\ &= [cPKC]_T \cdot \mathcal{H}_1(C, K_{KC}) \cdot \mathcal{H}_1([DAG], K_{KD})\end{aligned}\quad (5.11)$$

where $K_{KD} = \Omega_{KD}/O_{KD}$ and $K_{KC} = \Omega_{KC}/O_{KC}$, and $\mathcal{H}_1(x, K)$ denotes the Hill function (Appendix 1). In practice, the activation of the kinase consists of two sequential translocations to the plasma membrane of its C2 and C1₂ domains (Oancea and Meyer 1998). The translocation of C2 is regulated by Ca²⁺ whereas that of C1₂ is by DAG. In this process however, experiments showed that the initial translocation of C2 is the rate-limiting step for kinase activation (Shinomura et al. 1991), inasmuch as C1₂ translocation rapidly follows that of C2 (Codazzi et al. 2001). This agrees with the notion that the cPKC affinity for DAG is regarded to be much higher than the affinity of the kinase for Ca²⁺, i.e., $K_{KD} \ll K_{KC}$ (Nishizuka 1995). Since the product of two Hill functions with widely separated constants can be approximated by the Hill function with the largest constant (De Pittà et al. 2009), Eq. 5.11 can be rewritten as

$$[cPKC^*] \approx [cPKC]_T \cdot \mathcal{H}_1(C, K_{KC}) \quad (5.12)$$

which, once replaced in Eq. 5.8, gives:

$$\frac{d[R^*]}{dt} = O_N[A]^n[R] - \Omega_N \left(1 + \frac{O_K[cPKC]_T}{\Omega_N} \mathcal{H}_1(C, K_{KC}) \right) [R^*] \quad (5.13)$$

Finally, dividing both left and right terms in the above equation by $[R]_T$, Eq. 5.13 can be rewritten as

$$\frac{d\Gamma_A}{dt} = O_N[A]^n (1 - \Gamma_A) - \Omega_N (1 + \zeta \cdot \mathcal{H}_1(C, K_{KC})) \Gamma_A \quad (5.14)$$

where $\zeta = O_{KC}[cPKC]_T/\Omega_N$ quantifies the maximal receptor desensitization by cPKC. In the approximation that receptor binding and activation is much faster than the effective PLCβ-mediated IP₃ production, Γ_A can be solved for the steady state. In this fashion, IP₃ production by PLCβ in Eq. 5.2 becomes

$$J_\beta = O_\beta \cdot \mathcal{H}_n \left([A], (K_N (1 + \zeta \mathcal{H}_1(C, K_{KC})))^{\frac{1}{n}} \right) \quad (5.15)$$

where $K_N = \Omega_N/O_N$. The Hill coefficient n denotes cooperativity of the binding reaction of the agonist with the receptor and is both receptor and agonist specific. For example, glutamate binding to group 1 mGluRs, such as those expressed by astrocytes (Gallo and Ghiani 2000), is characterized by negative cooperativity and

found in association with a Hill coefficient of $n = 0.48 - 0.88$ (Suzuki et al. 2004). On the contrary, binding of ATP to P₂Y₁Rs of dorsal spinal cord astrocytes from rats is characterized instead by almost no cooperativity and $n = 0.9 - 1$ (Fam et al. 2000).

5.2.2 IP₃ Production by Receptors with α -Subunits Other Than q-Type

A series of other astrocytic GPCRs, that traditionally associate with non- α_q subunits, have also been reported to mediate IP₃-triggered CICR, both *in situ* and *in vivo*. These include G $\alpha_{i/o}$ -coupled GABA_B receptors (Kang et al. 1998; Serrano et al. 2006; Mariotti et al. 2016), endocannabinoid CB₁ receptors (Navarrete and Araque 2008; Min and Nevian 2012), adenosinergic A₁ receptors (Cristóvão-Ferreira et al. 2013), adrenergic α_2 receptors (Bekar et al. 2008), and dopaminergic D_{2/3} receptors (Jennings et al. 2017); as well as G α_s -coupled receptors like adenosine A_{2A} receptors (Cristóvão-Ferreira et al. 2013), and dopamine D_{1/5} receptors (Jennings et al. 2017). $\alpha_{i/o}$ and α_s subunits are not expected to be linked with IP₃ synthesis (Marinissen and Gutkind 2001), rather they respectively inhibit or stimulate intracellular production of cAMP. Therefore, the mechanism whereby these receptors could also promote mobilization of Ca²⁺ from IP₃-sensitive ER stores remains a matter of investigation.

One obvious possibility is that some of these receptors could be atypical in astrocytes and also be coupled with G α_q , as it seems the case for example of astrocytic CB₁Rs in the hippocampus (Navarrete and Araque 2008) and in the basal ganglia (Martín et al. 2015). Biased agonism could also be another possibility since the spatiotemporal pattern of agonist action on GPCRs could be quite different depending on agonist-binding kinetics of the receptor, especially if agonists differentially engage dynamic signaling and regulatory processes (Overington et al. 2006), such as in the likely scenario of synapse–astrocyte interactions (Heller and Rusakov 2015). However, there is not yet direct structural evidence for distinct receptor conformations linked to specific signals such as distinct G protein classes, and future studies are required to compare crystal structures of astrocytic GPCRs bound to biased and unbiased ligands to establish these relationships (Violin et al. 2014).

Alternatively, other signaling pathways mediated by cAMP that result in CICR could also be envisaged. In particular, Doengi et al. (2009) reported that GABA-evoked astrocytic Ca²⁺ events in the olfactory bulb are fully prevented by blockers of astrocytic GABA transporters (GATs), but only partially by GABA_B antagonists. GAT activation leads to an increase of intracellular Na⁺, since this ion is cotransported with GABA, and such increase indirectly inhibits the Na⁺/Ca²⁺ exchanger on the plasma membrane. In turn, the ensuing Ca²⁺ increase could be sufficient to induce Ca²⁺ release from internal stores by stimulation of endogenous IP₃ production (Losi et al. 2014; see also the following section). This possibility is further

corroborated by the observation that astrocytic GATs could indeed be inhibited or stimulated by A₁Rs or A_{2A}Rs respectively (Cristóvão-Ferreira et al. 2013).

Yet other mechanisms could be at play for different receptors. Dopaminergic receptors, for example, could either increase (D_{1/5} receptors) or decrease (D_{2/3} receptors) intracellular Ca²⁺ levels in astrocytes (Jennings et al. 2017). This could indeed be explained assuming a possible action of these receptors on GATs which, similarly to adenosinergic receptors, could, respectively, increase or reduce GABA/Na⁺ cotransport into the cell, ultimately promoting or inhibiting CICR according to what was suggested for GABA_BRs. However, there is also evidence that nontoxic levels of dopamine could be metabolized by monoamine oxidase in cultured astrocytes, resulting in the production of hydrogen peroxide (Vaarmann et al. 2010). This reactive oxygen species ultimately activates lipid peroxidation in the neighboring membranes which in turn triggers PLC-mediated IP₃ production and CICR. Overall, these different scenarios unravel additional complexity in the possible mechanisms of GPCR-mediated CICR in astrocytes and call for future modeling efforts that are beyond the scope of this chapter.

5.2.3 Endogenous IP₃ Production

Phospholipase C δ (PLC δ) is the enzyme responsible of endogenous IP₃ production in astrocytes, that is, IP₃ production that does not require external (i.e., exogenous) stimulation (Ochocka and Pawelczyk 2003; Suh et al. 2008). The specific catalytic activity of this enzyme in the presence of cytosolic Ca²⁺ is 50- to 100-fold greater than Ca²⁺-stimulated activity of PLC β in the absence of activating G protein subunits (Rebecchi and Pentyala 2000), suggesting that PLC δ is prominently activated by increases of intracellular Ca²⁺ (Rhee and Bae 1997).

Figure 5.1b exemplifies the biochemical network associated with PLC δ activation. Structural and mutational studies of PLC δ complexes with Ca²⁺ and IP₃, revealed complex interactions of Ca²⁺ with several negatively charged residues within the PLC δ catalytic domain (Essen et al. 1996, 1997; Rhee and Bae 1997), hinting cooperative binding of at least two Ca²⁺ ions with this enzyme (Essen et al. 1997). In agreement with these experimental findings, we model PLC δ -mediated IP₃ production (J_{δ}) as (Pawelczyk and Matecki 1997; Höfer et al. 2002):

$$J_{\delta} = \hat{J}_{\delta}(I) \cdot \mathcal{H}_2(C, K_{\delta}) \quad (5.16)$$

where $\mathcal{H}_2(C, K_{\delta})$ denotes the Hill function of C with coefficient 2 and affinity K_{δ} (Appendix 2), and $\hat{J}_{\delta}(I)$ is the maximal rate of IP₃ production by PLC δ which depends on intracellular IP₃ (I). Experiments revealed that high IP₃ concentrations, i.e., >1 μM, inhibit PLC δ activity by competing with PIP₂ to bind with the enzyme (Allen and Barres 2009). Accordingly, the maximal PLC δ -dependent IP₃ production rate can be modeled by

$$\hat{J}_\delta(I) = \frac{O_\delta}{1 + \frac{I}{\kappa_\delta}} = O_\delta(1 - \mathcal{H}_1(I, \kappa_\delta)) \quad (5.17)$$

where O_δ is the maximal rate of IP_3 production by PLC δ and κ_δ is the inhibition constant of PLC δ activity.

5.2.4 IP_3 Degradation

There are two pathways for IP_3 degradation in astrocytes. The first one is by dephosphorylation of IP_3 by inositol polyphosphate 5-phosphatase (IP-5P). The other one occurs through phosphorylation of IP_3 by the IP_3 3-kinase (IP $_3$ K). Both pathways could be Ca^{2+} -dependent but in opposite ways: while the activity of IP $_3$ K is stimulated by cytosolic Ca^{2+} (Communi et al. 1997), IP-5P is inhibited instead (Communi et al. 2001) (Fig. 5.2a). Thus, depending on the Ca^{2+} concentration in the cytoplasm, different mechanisms of IP_3 degradation could exist (Sims and Allbritton 1998). Moreover, IP-5P-mediated IP_3 degradation could also be inhibited by competitive binding of inositol 1,3,4,5-tetrakisphosphate (IP $_4$) produced by IP $_3$ K-mediated IP_3 phosphorylation (Connolly et al. 1987; Erneux et al. 1998), thereby making the two degradation pathways interdependent (Hermosura et al. 2000). However, we will not consider this aspect any further, since modeling of this reaction pathway requires a detailed consideration of the complex metabolic network underpinning degradation of the large family of inositol phosphates (Communi et al. 2001; Irvine and Schell 2001). The reader interested in these aspects may refer to Dupont and Erneux (1997) for a sample modeling approach to the problem.

Both IP-5P-mediated dephosphorylation (J_{5P}) and IP $_3$ K-mediated phosphorylation of IP_3 (J_{3K}) can be described by Michaelis–Menten kinetics (Irvine et al. 1986; Togashi et al. 1997), i.e.,

$$J_{5P} = \hat{J}_{5P} \cdot \mathcal{H}_1(I, K_5) \quad (5.18)$$

$$J_{3K} = \hat{J}_{3K}(C) \cdot \mathcal{H}_1(I, K_3) \quad (5.19)$$

Since $K_{5P} > 10 \mu\text{M}$ (Verjans et al. 1992; Sims and Allbritton 1998) and such high IP_3 concentrations are unlikely to be physiological (Lemon et al. 2003; Kang and Othmer 2009), the activity of IP-5P can be assumed far from saturation. Accordingly, the IP_3 degradation rate by IP-5P can be linearly approximated by (Stryer 1999):

$$J_{5P} \approx \Omega_{5P} \cdot I \quad (5.20)$$

where $\Omega_{5P} = \hat{J}_{5P}/K_5$ is the maximal rate of IP-5P-mediated IP_3 degradation in the linear approximation.

IP_3 phosphorylation by IP $_3$ K is regulated in a complex fashion (Fig. 5.2a). For resting conditions, when intracellular IP_3 and Ca^{2+} concentrations are below $0.1 \mu\text{M}$

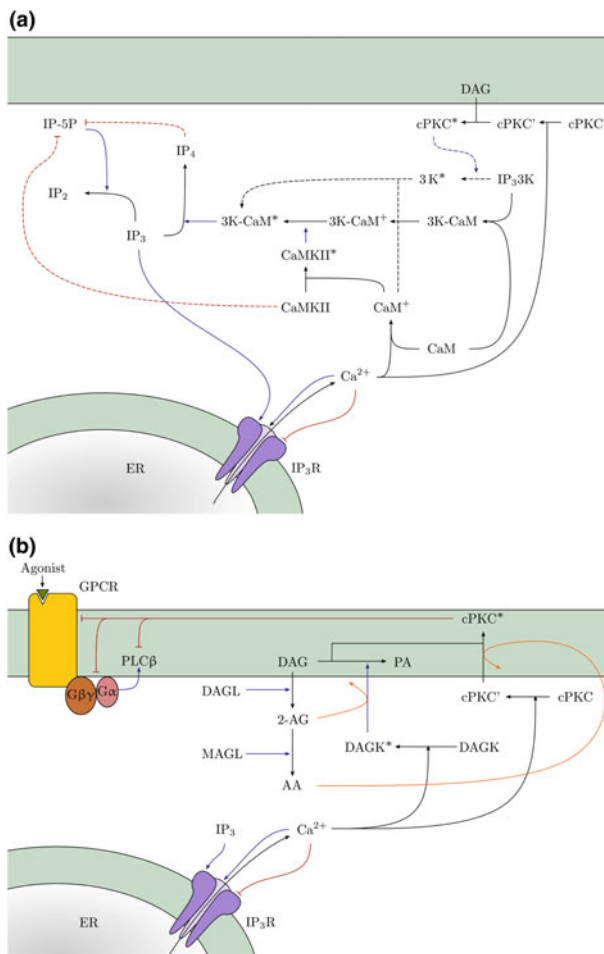
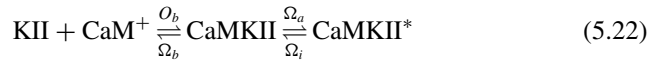


Fig. 5.2 IP₃ and DAG degradation. **a** Degradation of IP₃ occurs by phosphorylation into inositol 1,3,4,5-tetrakisphosphate (IP₄) by IP₃K and dephosphorylation into lower inositol phosphates by IP₅P. Both pathways are regulated by Ca²⁺: IP₃K activity is stimulated by phosphorylation by Ca²⁺/calmodulin-dependent protein kinase II (CaMKII), whereas IP₅P is inhibited thereby. Moreover IP₃K-mediated degradation could also be promoted by Ca²⁺-and DAG-dependent cPKC-mediated phosphorylation, while IP₅P could also be inhibited by IP₄. For the sake of simplicity, IP₅P dependence on Ca²⁺-and IP₄ along with IP₃K dependence on cPKC are not taken into consideration in this study (*dashed pathways*). **b** DAG is mainly degraded into phosphatidic acid (PA) by DAG kinases (DAGK) in a Ca²⁺-dependent fashion, and to a minor extent, into 2-arachidonoylglycerol (2-AG) by DAG lipases (DAGL). In turn 2-AG is hydrolyzed by monoacylglycerol lipase (MAGL) into arachidonic acid (AA). 2-AG and AA may promote activity of DAGK and cPKC* (*orange pathways*) although this scenario is not taken into consideration here. Colors of other pathways as in Fig. 5.1

(Parpura and Haydon 2000; Mishra and Bhalla 2002; Kang and Othmer 2009), it is very slow. On the other hand, as Ca^{2+} increases, IP_3K activity is substantially stimulated by phosphorylation by CaMKII in a Ca^{2+} /calmodulin (CaM)-dependent fashion (Communi et al. 1997). A further possibility could eventually be that IP_3K is also inhibited by Ca^{2+} -dependent PKC phosphorylation (Sim et al. 1990); however, since evidence for the existence of such inhibitory pathway is contradictory (Communi et al. 1995), this possibility will not be taken into further consideration in this study.

Phosphorylation of IP_3K by active CaMKII (i.e., CaMKII*) only occurs at a single threonine residue (Communi et al. 1997, 1999), so that it can be assumed that the rate of IP_3K phosphorylation is $J_{3K}^*(C) \propto [\text{CaMKII}^*]$. On the other hand, activation of CaMKII is $\text{Ca}^{2+}/\text{CaM}$ -dependent and occurs in a complex fashion because of the unique structure of this kinase, which is composed of ~ 12 subunits, with three to four phosphorylation sites each (Kolodziej et al. 2000). Briefly, Ca^{2+} increases lead to the formation of a $\text{Ca}^{2+} - \text{CaM}$ complex (CaM^+) that may induce phosphorylation of some of the sites of each CaMKII subunit. However, only when two of these sites at neighboring subunits are phosphorylated, CaMKII quickly and fully activates (Hanson et al. 1994). Despite the multiple CaM^+ binding reactions in the inactive kinase, experiments showed that KII activation by CaM^+ can be approximated by a Hill equation with unitary coefficient (De Konick and Schulman 1998). Hence, the following kinetic reaction scheme for CaMKII phosphorylation can be assumed:



Consider then first the binding reaction in 5.22. Assuming that the second step is very rapid with respect to the first one (Thiel et al. 1988; De Konick and Schulman 1998), the generation of CaMKII* is in equilibrium with CaMKII consumption, i.e.,

$$[\text{CaMKII}^*] \approx \frac{\Omega_a}{\Omega_i} [\text{CaMKII}] \quad (5.23)$$

Then, under the hypothesis of quasi steady state for CaMKII, it follows that:

$$\frac{d[\text{CaMKII}]}{dt} = O_b [\text{KII}][\text{CaM}^+] - (\Omega_a + \Omega_b) [\text{CaMKII}] + \Omega_i [\text{CaMKII}^*] \approx 0 \quad (5.24)$$

Replacing $[\text{CaMKII}^*]$ from Eq. 5.23 in the latter equation provides

$$[\text{CaMKII}^*] = K_a K_b [\text{KII}][\text{CaM}^+] \quad (5.25)$$

where $K_a = \Omega_a / \Omega_i$ and $K_b = O_b / \Omega_b$. Defining the total kinase II concentration as $[KII]_T = [KII] + [\text{CaMKII}] + [\text{CaMKII}^*]$ and assuming it constant, Eq. 5.25 can be rewritten as

$$[\text{CaMKII}^*] = \frac{K_a [KII]_T}{1 + K_a} \cdot \mathcal{H}_1 ([\text{CaM}^+], K_m) \quad (5.26)$$

with $K_m = (K_b (1 + K_a))^{-1}$.

The substrate concentration for the enzyme-catalyzed reaction 5.22 is provided by reaction 5.21 and reads (by QSSA)

$$[\text{CaM}^+] = [\text{CaM}] \cdot \mathcal{H}_4 (C, K_0) \quad (5.27)$$

with $K_0 = O_0 / \Omega_0$. Therefore, replacing the latter expression for $[\text{CaM}^+]$ in Eq. 5.26, finally provides

$$[\text{CaMKII}^*] = \frac{K_a [KII]_T}{1 + K_a} \left(1 + \frac{K_m}{[\text{CaM}]} \right)^{-1} \cdot \mathcal{H}_4 \left(C, \frac{K_0 K_m}{K_m + [\text{CaM}]} \right) \quad (5.28)$$

Defining the Ca^{2+} affinity constant of IP₃K as $K_D = K_0 K_m / (K_m + [\text{CaM}])$, the above calculations show that, despite its complexity, the reaction cascade underlying the activation of CaMKII can be concisely described by a Hill function of the Ca^{2+} concentration (C) so that $[\text{CaMKII}^*] \propto \mathcal{H}_4 (C, K_D)$. Accordingly, it is also $\hat{J}_{3K}(C) \propto \mathcal{H}_4 (C, K_D)$, and Eq. 5.19 for IP₃K-mediated IP₃ degradation can be rewritten as

$$J_{3K} = O_{3K} \cdot \mathcal{H}_4 (C, K_D) \mathcal{H}_1 (I, K_3) \quad (5.29)$$

where O_{3K} is the maximal rate of IP₃ degradation by IP₃K.

5.3 Encoding of Stimulation by Combined IP₃ and Ca²⁺ dynamics

5.3.1 The G-ChI Model for IP₃/Ca²⁺ Signaling

A corollary of the biological and modeling arguments exposed in the previous section is that Ca²⁺ and IP₃ signals are, generally speaking, dynamically coupled in astrocytes. This implies that a complete model that mimics astrocytic IP₃ signaling must also include a description of CICR. An example of such models is the so-called ChI model originally introduced by De Pittà et al. (2009), which is constituted by three ODEs, respectively, for intracellular Ca²⁺ (C), the IP₃R gating variable h , and the mass balance equation for intracellular IP₃ lumping terms, (5.16), (5.20), and (5.29), i.e.,

$$\frac{dC}{dt} = J_r(C, h, I) + J_l(C) - J_p(C) \quad (5.30)$$

$$\frac{dh}{dt} = \Omega_h(C, I) (h_\infty(C, I) - h) \quad (5.31)$$

$$\frac{dI}{dt} = O_\delta \mathcal{H}_2(C, K_\delta) (1 - \mathcal{H}_1(I, \kappa_\delta)) - O_{3K} \mathcal{H}_4(C, K_D) \mathcal{H}_1(I, K_3) - \Omega_{5P} I \quad (5.32)$$

The above model can also be extended to include GPCR dynamics by the *G-ChI* model. To this aim, we add to the right-hand side of Eq. 5.32 the contribution of GPCR-mediated IP₃ synthesis given by Eq. 5.15. However, if one is interested in how GPCR kinetics evolves with IP₃ and Ca²⁺ dynamics, then the formula for J_β given by Eq. 5.2 must be used instead of Eq. 5.15. Accordingly, the above system of equations must be completed by Eq. 5.14 for astrocytic receptor activation, i.e.,

$$\frac{d\Gamma_A}{dt} = \dots \quad (14)$$

$$\frac{dC}{dt} = \dots \quad (30)$$

$$\frac{dh}{dt} = \dots \quad (31)$$

$$\frac{dI}{dt} = O_\beta \Gamma_A + O_\delta \mathcal{H}_2(C, K_\delta) (1 - \mathcal{H}_1(I, \kappa_\delta)) - O_{3K} \mathcal{H}_4(C, K_D) \mathcal{H}_1(I, K_3) - \Omega_{5P} I \quad (5.33)$$

Regarding the differential equations for the variables C and h above, the original formulation of the *G-ChI* model considered the Li-Rinzel description for CICR previously introduced in Chap. 3 (Li and Rinzel 1994). In the following, we will refer to this formulation. In practice however, it must be noted that any suitable model of Ca²⁺ and IP₃R dynamics discussed in Chaps. 2, 3, and 16 can be adopted in lieu of the Li-Rinzel description, and accordingly different models of *G-ChI* type may be developed, each possibly customized to study specific aspects of coupled IP₃ and Ca²⁺ signaling in astrocytes.

Figure 5.3 illustrates some characteristics of IP₃ and Ca²⁺ dynamics reproduced by the *G-ChI* model. In the left panel of this figure, IP₃R kinetic parameters are chosen to fit, as closely as possible, experimental data points for the steady-state open probabilities of type-2 IP₃Rs at fixed Ca²⁺ (*solid line*) and IP₃ concentrations (*dashed line*). In the right panel, the remainder of the parameters of the model are then set to reproduce a sample Ca²⁺ trace imaged by confocal microscopy on cultured astrocytes (*solid black line* vs. *gray data points*). It may be observed how the associated IP₃ and h oscillations predicted by the model are almost in phase opposition with respect to the Ca²⁺ ones. For h , this is due to IP₃R kinetics, whereby an increase of cytosolic Ca²⁺ promotes receptor inactivation. For IP₃ instead, this dynamics is a direct consequence of the Ca²⁺-dependent rate of degradation of this molecule by the IP₃K enzyme.

This is a crucial aspect of intracellular IP₃ regulation in astrocytes which is addressed more in detail below.

5.3.2 Different Regimes of IP₃ Signaling

To develop the *G-ChI* model in Sect. 5.2, we stressed on the molecular details of the Ca²⁺ dependence of the different enzymes involved in IP₃ signaling, yet how this dependence shapes Ca²⁺ and IP₃ oscillations remains to be elucidated. With this purpose, we consider in Fig. 5.4 the simple scenario of Ca²⁺ oscillations triggered by repetitive stimulation of an astrocyte by puffs of extracellular glutamate (*top three panels*) and look at the different contributions to IP₃ production and degradation underpinning the ensuing Ca²⁺ and IP₃ dynamics (*lower panels*). With this regard, it may be noted how the total rate of IP₃ production (*dashed line* in the *fourth panel* from top) almost resembles the dynamics of activation of astrocyte receptors (Γ_A , *second panel* from top) except for little bumps in correspondence of Ca²⁺ pulse-like elevations (*solid trace*, *third panel* from top). Consideration of the different contributions to IP₃ by PLC β (*orange trace*) and PLC δ (*blue trace*) reveals that,

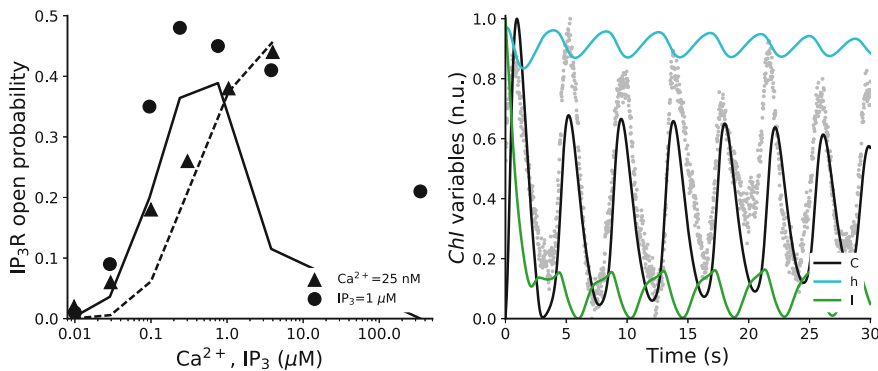


Fig. 5.3 *G-ChI* model. (*left panel*) Fit of IP₃Rs kinetic parameters on experimental data of steady-state open probabilities of type-2 IP₃Rs by Ramos-Franco et al. (2000). In this example, and through all this chapter, we consider the Li-Rinzel description for CICR. This choice allows a reasonable fit (*solid and dashed lines*) of the receptors' open probability as function of either intracellular IP₃ (\blacktriangle) or intracellular Ca²⁺ (\bullet). The only exception is for Ca²⁺ concentrations $>1 \mu\text{M}$ for which the open probability predicted by the Li-Rinzel model (*solid line*) vanishes much more quickly than experimental values. (*right panel*) Sample Ca²⁺ (C), IP₃ (I) and h traces ensuing from a simulation of the *G-ChI* model to reproduce experimental Ca²⁺ oscillations in cultured astrocytes (*gray data points*) triggered by application of $>5 \mu\text{M}$ glutamate. Experimental data courtesy of Nitzan Herzog (University of Nottingham). A saturating glutamate concentration (i.e., $\Gamma_A = 1$) was assumed with initial conditions $C(0) = 0.098 \mu\text{M}$, $h(0) = 0.972$ and $I(0) = 0.190 \mu\text{M}$. Simulated Ca²⁺ and IP₃ traces are reported in normalized units with respect to minimum values of $C_0 = 0.1 \mu\text{M}$ and $I_0 = 0.16 \mu\text{M}$ and peak values of $\hat{C} = 1.42 \mu\text{M}$ and $\hat{I} = 0.19 \mu\text{M}$. Model parameters as in Table 5.1 except for $O_\beta = 0.141 \mu\text{Ms}^{-1}$ and $O_{3K} = 0.163 \mu\text{Ms}^{-1}$

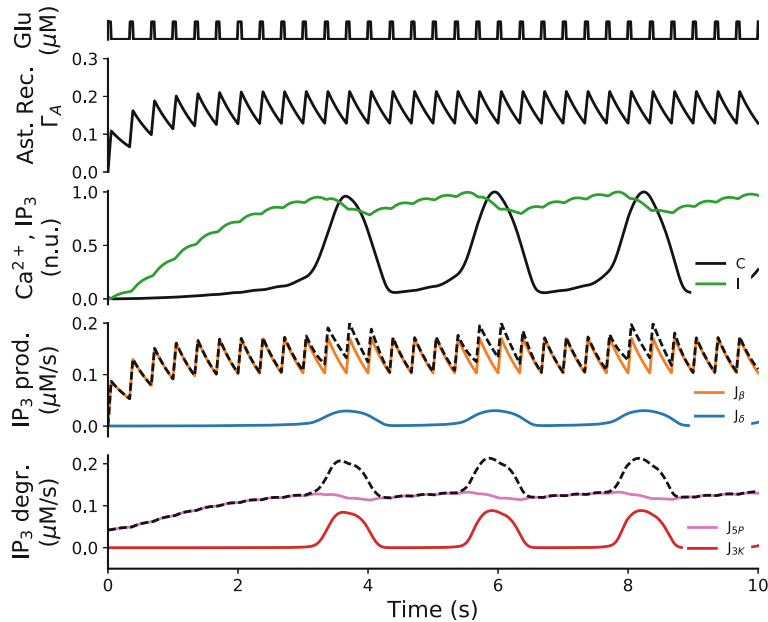


Fig. 5.4 Coexistence of different regimes of IP_3 signaling. From top to bottom: (*first panel*) Repetitive stimulation of an astrocyte by puffs of glutamate ($8 \mu\text{M}$, rectangular pulses at rate 0.33Hz and 15% duty cycle); (*second panel*) fraction of activated astrocytic receptors; (*third panel*) ensuing Ca^{2+} (C) and IP_3 (I) traces (normalized with respect to their maximum excursion: $C_0 = 40\text{nM}$, $I_0 = 50\text{nM}$, $\hat{C} = 0.73 \mu\text{M}$, $\hat{I} = 0.15 \mu\text{M}$); (*fourth panel*) total rate of IP_3 production (dashed line) and contributions to it by $\text{PLC}\beta$ (J_β) and $\text{PLC}\delta$ (J_δ); (*bottom panel*) total rate of IP_3 degradation (dashed line) resulting from the combination of degradation by IP-5P (J_{5P}) and $\text{IP}_3\text{3K}$ (J_{3K}). Besides Ca^{2+} pulsed-oscillations, IP_3 is mainly regulated by $\text{PLC}\beta$ (orange trace) and IP-5P (violet trace), and its concentration tends to increase in an integrative fashion with the number of glutamate puffs. During Ca^{2+} elevations instead, activity of $\text{PLC}\delta$ (blue trace) and $\text{IP}_3\text{3K}$ (red trace) become significant, with this latter responsible for a sharp drop of intracellular IP_3 . Model parameters as in Table 5.1 except for $C_T = 10 \mu\text{M}$, $O_P = 10 \mu\text{Ms}^{-1}$ and $O_\delta = 0.05 \mu\text{Ms}^{-1}$

while most of IP_3 production is driven by mGluR-mediated $\text{PLC}\beta$ activation, those bumps are instead caused by $\text{PLC}\delta$, whose activation is substantially boosted during intracellular Ca^{2+} elevations.

Similar arguments also hold for IP_3 degradation (*bottom panel*). In this case, the total rate of IP_3 degradation (dashed line) closely mimics IP_3 dynamics in between Ca^{2+} elevations (green trace, *third panel* from top) and is mostly contributed by Ca^{2+} -independent IP-5P -mediated degradation (violet trace). This scenario, however, changes during Ca^{2+} elevations, when $\text{IP}_3\text{3K}$ activation becomes significant and promotes faster rates of IP_3 degradation, as mirrored by the dashed line which peaks in correspondence of Ca^{2+} oscillations.

Overall, these observations suggest that Ca^{2+} -independent activity of $\text{PLC}\beta$ and IP-5P vs. Ca^{2+} -dependent activation of $\text{PLC}\delta$ and $\text{IP}_3\text{3K}$ accounts for different

Table 5.1 Model parameters used in the simulations, unless differently specified in figure captions

Symbol	Description	Value	Units
<i>Astrocyte receptors</i>			
Ω_N	Rate of receptor deactivation	1.8	s^{-1}
O_N	Rate of agonist-mediated receptor activation	0.3	$\mu M^{-1}s^{-1}$
n	Agonist-binding cooperativity	1	-
<i>IP₃R kinetics</i>			
d_1	IP ₃ binding affinity	0.1	μM
O_2	Inactivating Ca ²⁺ binding rate	0.325	$\mu M^{-1}s^{-1}$
d_2	Inactivating Ca ²⁺ binding affinity	4.5	μM
d_3	IP ₃ binding affinity (with Ca ²⁺ inactivation)	0.1	μM
d_5	Activating Ca ²⁺ binding affinity	0.05	μM
<i>Ca²⁺ fluxes</i>			
C_T	Total ER Ca ²⁺ content	5	μM
ρ_A	ER-to-cytoplasm volume ratio	0.5	-
Ω_C	Maximal Ca ²⁺ release rate by IP ₃ Rs	7.759	s^{-1}
Ω_L	Ca ²⁺ leak rate	0.1	s^{-1}
O_P	Maximal Ca ²⁺ uptake rate	5.499	μMs^{-1}
K_P	Ca ²⁺ affinity of SERCA pumps	0.1	μM
<i>IP₃ production</i>			
O_β	Maximal rate of IP ₃ production by PLC β	0.8	μMs^{-1}
O_δ	Maximal rate of IP ₃ production by PLC δ	0.025	μMs^{-1}
K_δ	Ca ²⁺ affinity of PLC δ	0.5	μM
κ_δ	Inhibiting IP ₃ affinity of PLC δ	1.0	μM
<i>IP₃ degradation</i>			
Ω_{5P}	Rate of IP ₃ degradation by IP-5P	0.86	s^{-1}
O_{3K}	Maximal rate of IP ₃ degradation by IP ₃ 3K	0.86	μMs^{-1}
K_D	Ca ²⁺ affinity of IP ₃ 3K	0.5	μM
K_{3K}	IP ₃ affinity of IP ₃ 3K	1.0	μM
<i>DAG dynamics</i>			
Ω_D	Unspecific rate of degradation	0.26	s^{-1}
O_D	Rate of degradation by DAGK	0.45	μMs^{-1}
K_{DC}	DAGK affinity for Ca ²⁺	0.3	μM
K_{DD}	DAGK affinity for DAG	0.1	μM
<i>cPKC signaling</i>			
O_{KD}	Rate of cPKC* production	0.28	μMs^{-1}
Ω_{KD}	Rate of cPKC* deactivation	0.33	s^{-1}
K_{KC}	Ca ²⁺ affinity of PKC	0.5	μM
O_K	Rate of receptor phosphorylation	1.0	$\mu M^{-1}s^{-1}$

regimes of IP_3 signaling. One regime corresponds to low intracellular Ca^{2+} close to resting concentrations, whereby IP_3 is mainly produced by receptor-mediated activation of $\text{PLC}\beta$ against degradation by $\text{IP}-5\text{P}$. The other regime significantly adds to the former for sufficiently high Ca^{2+} elevations, where IP_3 production is boosted by $\text{PLC}\delta$, but also IP_3 degradation is faster by IP_3K activation.

The contribution to IP_3 production and degradation by each enzyme clearly depends on their intracellular expression as reflected by the values of the rate constants O_β , O_δ , O_{3K} , and Ω_{5P} in Eq. 14. Nonetheless, it should be noted that the existence of different regimes of IP_3 production and degradation is regardless of these rate values, insofar as it is set by the values of the Michaelis–Menten constants of the underpinning reactions, mostly K_δ and K_D . Remarkably, estimates of these two constants are in the range of $0.1\text{--}1.0 \mu\text{M}$ that is well within the range of Ca^{2+} elevations expected for an astrocyte, whose average resting Ca^{2+} concentration is reported to be $<0.15 \mu\text{M}$ (Zheng et al. 2015). This assures that activation of $\text{PLC}\delta$ and IP_3K is effective only when intracellular Ca^{2+} approaches to or increases beyond K_δ and K_D , as expected by the occurrence of CICR.

5.3.3 Signal Integration

The existence of different regimes of IP_3 signaling shapes the time evolution of IP_3 with respect to stimulation in a peculiar fashion. From Fig. 5.4 (*third panel*), it may indeed be noted that, starting from resting values, IP_3 increases for each glutamate puff almost stepwise, till it reaches a peak (or threshold) concentration (normalized to ~ 1) that triggers CICR, thereby triggering a Ca^{2+} pulse-like elevation. This Ca^{2+} elevation promotes IP_3 degradation to some concentration between its peak and baseline values, in a sort of reset mechanism, leaving IP_3 to increase back again to the CICR threshold until the next elevation. In between each Ca^{2+} elevation, counting from the first one ending at $t \approx 4\text{s}$, we may appreciate how IP_3 increases almost proportionally to the number of glutamate puffs, akin to an integrator of the stimulus.

This may readily be proved by analytical arguments approximating, for simplicity, each glutamate puff occurring at t_k by a Dirac's delta $\delta(t - t_k)$, so that the external stimulus impinging on the astrocyte is modeled by $Y(t) = G \cdot \Delta \sum_k \delta(t - t_k)$, where $G \cdot \Delta$ represents the glutamate concentration delivered in the time unit per puff (i.e., its dimensions are $\mu\text{M} \cdot \text{s}$). Then, assuming that in between oscillations, intracellular Ca^{2+} concentration is close to basal levels, i.e., $C \approx C_0$, with $C_0 < (\ll) K_{KC}, K_\delta, K_3$ and $h \approx h_\infty$, it is possible to reduce Eqs. 5.14 and 14 to

$$\frac{d\Gamma_A}{dt} \approx -(O_N Y(t) + \Omega_N) \Gamma_A + O_N Y(t) \quad (5.34)$$

$$\frac{dI}{dt} \approx -J_{5P} + J_\beta = -\Omega_{5P} I + O_\beta \Gamma_A \quad (5.35)$$

Using the fact that for puffs delivered at rate ν the identity $\int_{t'}^t \sum_k \delta(t - t_k) dt = \nu(t'' - t')$ holds, we can solve Eq. 5.34 for Γ_A obtaining

$$\begin{aligned}\Gamma_A(t) &= \int_{-\infty}^t O_N Y(t') e^{-\int_{t'}^t (\Omega_N + O_N Y(t'')) dt''} dt' \\ &= \int_{-\infty}^t O_N Y(t') e^{-\Omega_N(t-t')} e^{-O_N \int_{t'}^t Y(t'') dt''} dt' \\ &= \int_{-\infty}^t O_N Y(t') e^{-(\Omega_N + O_N G \Delta \nu)(t-t')} dt' \\ &= O_N Y(t') * Z_{\Gamma_A}(t)\end{aligned}\quad (5.36)$$

where “*” denotes the convolution operator. It is thus apparent that the fraction of activated receptors $\Gamma_A(t)$ is an integral transform of the stimulus $Y(t)$ by convolution with the kernel $Z_{\Gamma_A}(t)$. Specifically, $Z_{\Gamma_A}(t)$ may be regarded as the fraction of astrocyte receptors stimulated by one extracellular glutamate puff—or equivalently, by synaptic release triggered by an action potential—and characterizes the encoding of the stimulus by the astrocyte via its activated receptors.

The IP_3 signal resulting from the activated receptors then evolves according to

$$\begin{aligned}I(t) &= \int_{-\infty}^t O_\beta \Gamma_A(t') e^{-\int_{t'}^t \Omega_{5P} dt''} dt' = \int_{-\infty}^t O_\beta \Gamma_A(t') e^{-\Omega_{5P}(t-t')} dt' \\ &= O_\beta \Gamma_A(t) * Z_I(t)\end{aligned}\quad (5.37)$$

That is the IP_3 signal is also an integral transform of the input stimuli through the fraction of activated receptors $\Gamma_A(t)$, by convolution with the kernel $Z_I(t) = e^{-\Omega_{5P}t}$. In particular, experimental evidence hints that the rate constant Ω_{5P} is often small compared to the rate of incoming stimulation (Appendix 2), so that $Z_I(t) \approx 1$. In this case then, Eq. 5.37 predicts that $I(t) \approx \int_{-\infty}^t O_\beta \Gamma_A(t') dt'$, namely that the IP_3 signal effectively corresponds to the integral of the fraction of activated astrocytic receptors.

It is also worth understanding the nature of the threshold concentration that IP_3 must reach in order to trigger CICR. In the *G-ChI* model, based on the Li-Rinzel description of CICR, this threshold may be not well defined and generally varies with the parameter choice as well as with the shape and amplitude of the delivered stimulation (De Pittà et al. 2009). Consider for example Fig. 5.5a, where the Ca^{2+} response of an astrocyte (*bottom panel*) is simulated for different *color-coded* step increases of extracellular glutamate (*top panel*). It may be noted that CICR, reflected by one or multiple Ca^{2+} pulse-like increases, is triggered by glutamate concentrations greater or equal to the *orange trace*. However, the IP_3 threshold for CICR (*central panel*) appears to grow with the extracellular glutamate concentration. This is reflected by the first “knee” of the IP_3 curves which reaches progressively higher values of IP_3 concentration as extracellular glutamate increases from *orange* to *lime* levels. At the same time, as shown by the *black-dashed curve* in the *top panel* of

Fig. 5.5b, the latency for emergence of CICR since stimulus onset (black marks at $t = 0$) decreases. This can be explained by Eqs. 5.34 and 5.35, noting that, while larger glutamate concentrations promote larger receptor-mediated IP_3 production, this increased production is also counteracted by faster degradation by $IP-5P$, since this latter linearly increases with IP_3 . Thus while larger IP_3 production assures shorter delays in the onset of CICR, a larger IP_3 level must be reached to compensate for its faster degradation.

The top panel of Fig. 5.5b further illustrates how the latency period for CICR onset depends on the activity of the different enzymes regulating IP_3 production and degradation. Here the different colored curves were obtained repeating the simulations of Fig. 5.5a for a 50% increase of the activity, respectively, of $PLC\beta$ (orange trace), $PLC\delta$ (blue trace), IP_33K (red trace), and $IP-5P$ (violet trace). In agreement with our previous analysis, $PLC\beta$ and $IP-5P$ have the largest impact on, respectively, reducing or increasing the latency period, given that they are the main enzymes at play in IP_3 signaling before CICR onset. The effect of an increase of IP_3 production by $PLC\delta$ is instead mainly significant for low glutamate concentrations, such that they could promote an activation of this enzyme that is comparable to that of $PLC\beta$. Conversely, IP_33K does not have any role in the control of CICR latency since its activation effectively requires CICR to onset first.

The variability of IP_3 concentrations attained to trigger CICR by different glutamate concentrations, and its correlation with the latency for CICR onset, suggests

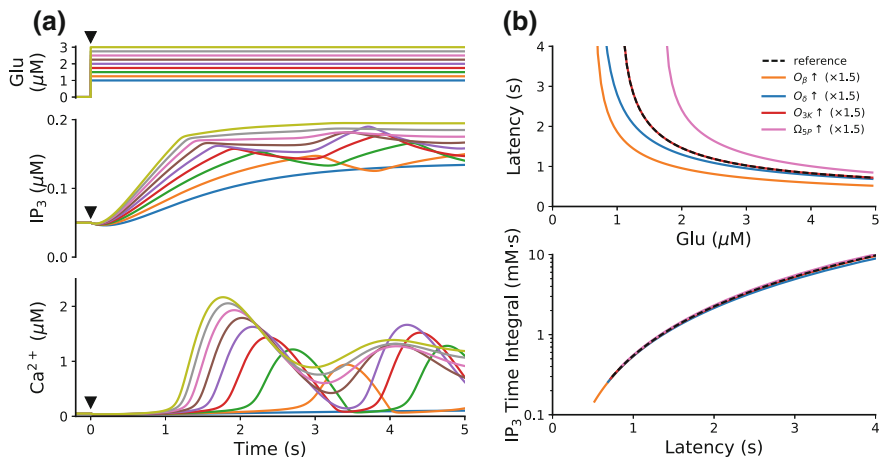


Fig. 5.5 Threshold for CICR. **a** (top panel) Step increases of extracellular glutamate (color coded) and resulting IP_3 (central panel) and Ca^{2+} dynamics (bottom panel) in a *G-ChI* astrocyte model. Black marks at $t = 0$ denote stimulus onset. **b** (top panel) Latency for the onset of CICR as a function of the applied glutamate concentration for the Ca^{2+} traces in **a** (black-dashed curve), as well as for 50% increases in the rate of $PLC\beta$ (O_β), $PLC\delta$ (O_δ), IP_33K (O_{3K}) and $IP-5P$ (Ω_{5P}), respectively. Emergence of CICR was detected for $\frac{dC}{dt} \geq 0.5 \mu M/s$. (bottom panel) Integral of IP_3 concentration as a function of the latency values computed in the top panel. This integral is a better estimator of CICR threshold than the sole IP_3 concentration. Model parameters as in Fig. 5.4

that the mere IP_3 concentration is not an effective indicator of the CICR threshold, rather we should consider instead the total IP_3 amount produced in the astrocyte cytosol during the latency period that precedes CICR onset, that is, the integral in time of IP_3 concentration during such period. This is exemplified in the *bottom panel* of Fig. 5.5b where such integral is plotted as a function of the different latency values computed in the *top panel*. It may be appreciated how this integral is essentially similar for different enzyme expressions (*colored curves*) yet associated with the same latency value.

Taken together, these results put emphasis on the crucial role exerted by IP_3 signaling in the genesis of agonist-mediated Ca^{2+} elevations. In particular, they suggest that the expression of different enzymes responsible of IP_3 production and degradation, which is likely heterogeneous across an astrocyte, could locally set different requirements for integration and encoding of external stimuli by the same cell.

5.3.4 Role of cPKCs and Beyond

Different mechanisms of production and degradation of IP_3 are only one example of the possible many signaling pathways that could shape the nature of Ca^{2+} signaling in astrocytes. There is also compelling evidence *in vitro* that shape and duration of Ca^{2+} oscillations could be controlled by astrocyte receptor phosphorylation by cPKCs (Codazzi et al. 2001). To better understand this aspect of astrocyte Ca^{2+} signaling, we relax the quasi-steady-state approximation on cPKC phosphorylation and thus rewrite Eq. 5.8 as

$$\frac{d\Gamma_A}{dt} = O_N[A]^n (1 - \Gamma_A) - (\Omega_N + O_K P) \Gamma_A \quad (5.38)$$

where P denotes the cPKC* concentration at the receptors' site. This in turn requires to also consider a description of cPKC* dynamics, whereby at least two additional equations in the *G-ChI* model must be included: one that takes into account P dynamics, but also a further one that describes DAG dynamics (D), which is responsible for cPKC activation by Ca^{2+} -dependent translocation of the inactive kinase to the plasma membrane (Oancea and Meyer 1998).

By QSSA, the quantity of cPKC* is conserved during receptor phosphorylation in reaction 5.4. In this fashion, cPKC* production and degradation are only controlled by the pair of reactions 5.9 and 5.10. On the other hand, taking into account from Sect. 5.2.1 that production of cPKC* depends on the availability of the Ca^{2+} -bound kinase complex cPKC', we may assume at first approximation that reaction 5.9 for Ca^{2+} binding to the kinase is at equilibrium, i.e., $[c\text{PKC}'] = [c\text{PKC}]_T \mathcal{H}_1 (C, K_{\text{KC}})$. Accordingly, we can consider cPKC* dynamics to be driven simply by reaction 5.10, i.e.,

$$\begin{aligned}
\frac{dP}{dt} &= J_{KP} - J_{KD} \\
&= O_{KD}[cPKC'] \cdot D - \Omega_{KD} P \\
&= O_{KD}[cPKC]_T \mathcal{H}_1(C, K_{KC}) \cdot D - \Omega_{KD} P \\
&\equiv O_{KD} \mathcal{H}_1(C, K_{KC}) \cdot D - \Omega_{KD} P
\end{aligned} \tag{5.39}$$

where we redefined $O_{KD} \leftarrow O_{KD}[cPKC]_T$ as the maximal rate of cPKC* production (in $\mu\text{M s}^{-1}$).

To model DAG dynamics, we start instead from the consideration that PLC iso-enzymes hydrolyze PIP_2 into one molecule of IP_3 and one of DAG, so that DAG production coincides with that of IP_3 (Berridge and Irvine 1989) and see also Fig. 5.2b). Yet, only part of this produced DAG is used to activate cPKC, while the rest is mainly degraded by diacylglycerol kinases (DAGKs) into phosphatidic acid (Carrasco and Mérida 2007) and, to a minor extent, by diacylglycerol lipases (DAGLs) into 2-arachidonoylglycerol (2-AG), although this latter pathway has only been linked to some types of metabotropic receptors in astrocytes (Bruner and Murphy 1990; Giaume et al. 1991; Walter et al. 2004). Other pathways of use of DAG are also possible in principle, inasmuch as DAG is a key molecule in the cell's lipid metabolism and a basic component of membranes. Nonetheless, there is evidence that DAG levels are strictly regulated within different subcellular compartments, and DAG generated by GPCR stimulation is not usually consumed for metabolic purposes (van der Bend et al 1994; Carrasco and Mérida 2007).

DAGK activation reflects the sequence of Ca^{2+} -mediated translocation, DAG binding and activation that is also required for cPKCs, so the two reactions may be thought to be characterized by similar kinetics, yet with an important difference. Sequence analysis of DAGK α , γ —the two isoforms of DAGKs most likely involved in astrocytic GPCR signaling (Dominguez et al. 2013)—reveals in fact the existence of two EF-hand motifs characteristics of Ca^{2+} binding and two C1 domains for DAG binding (Mérida et al. 2008). In this fashion, a Hill exponent of 2 instead of 1 as in Eq. 5.39 must be considered for the DAGK-activating reaction, so that DAGK-mediated DAG degradation can be modeled by

$$J_D = O_D \mathcal{H}_2(C, K_{DC}) \mathcal{H}_2(D, K_{DD}) \tag{5.40}$$

Finally, to take into account other mechanisms of DAG degradation (J_A), including but not limited to DAGLs, we assume a linear degradation rate, i.e., $J_A = \Omega_D D$. This is a crude approximation insofar as DAGL could also be activated in a Ca^{2+} -dependent fashion (Rosenberger et al. 2007). Nonetheless, the complexity of the molecular reactions likely involved in these other pathways of DAG degradation would require to consider additional equations in our model which are beyond the scope of this chapter. The reader who is interested in these further aspects may refer to Cui et al. (2016) for a possible modeling approach. For the purposes of our analysis instead, we will consider the following equation for DAG dynamics:

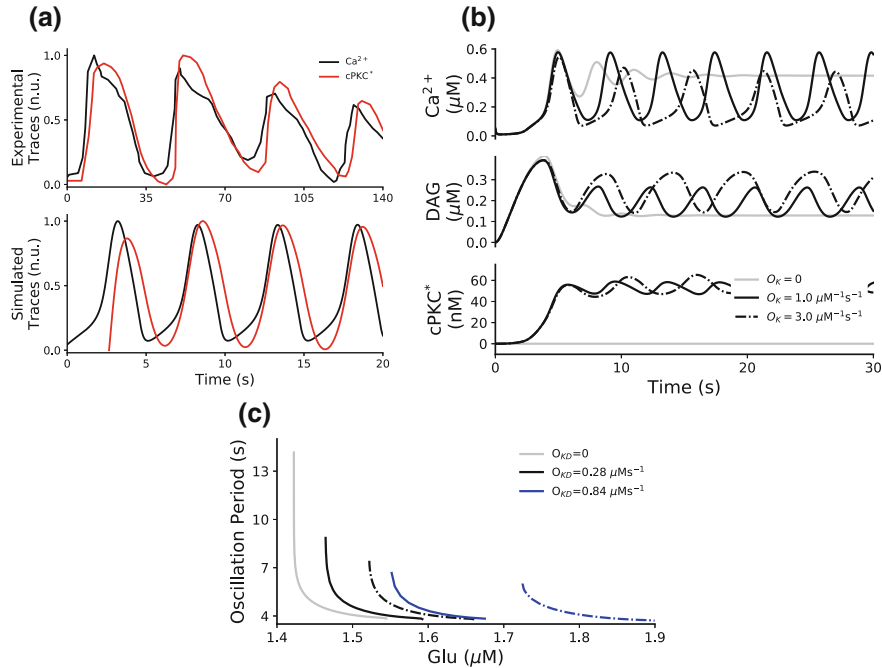


Fig. 5.6 Regulation of Ca^{2+} oscillations by cPKC. **a** (top panel) Comparison between experimental traces for Ca^{2+} (black) and cPKC^* (red) originally recorded in cultured astrocytes by Codazzi et al. (2001) and simulations (bottom panel). Despite quantitative differences in the shape and period of oscillations, the model can reproduce the essential correlation and phase shift between Ca^{2+} and cPKC^* dynamics observed in experiments. Ca^{2+} and cPKC^* oscillations were triggered assuming an extracellular glutamate concentration of $1.48 \mu\text{M}$, and were normalized according to their maximum excursion: $C_0 = 0.04 \mu\text{M}$, $P_0 = 48 \text{nM}$, $\hat{C} = 0.49 \mu\text{M}$ and $\hat{P} = 65 \text{nM}$. **b** DAG and cPKC^* dynamics associated with two different rates of receptor phosphorylation by cPKC (O_K , black traces) in response to a step increase of extracellular glutamate ($1.55 \mu\text{M}$ at $t = 0$). In the absence of receptor phosphorylation (gray traces), Ca^{2+} oscillations would vanish due to saturating intracellular IP_3 levels ensued from large receptor activation. **c** Period of Ca^{2+} oscillations as a function of extracellular glutamate concentration. Receptor phosphorylation by cPKC critically controls the oscillatory range (black and blue curves) with respect to the scenario without cPKC activation (gray curve). Higher glutamate concentrations are required to trigger oscillations for larger rates of DAG-dependent cPKC activation (O_{KD}). Parameters as in Table 5.1 except for $\Omega_C = 6.207 \text{s}^{-1}$, $\Omega_L = 0.01 \text{s}^{-1}$, $O_\beta = 1 \mu\text{M s}^{-1}$

$$\begin{aligned} \frac{dD}{dt} &= J_\beta + J_\delta - J_{KP} - J_D - J_A \\ &= O_\beta \Gamma_A + O_\delta \mathcal{H}_2(C, K_\delta) (1 - \mathcal{H}_1(I, \kappa_\delta)) + \\ &\quad - O_{KD} \mathcal{H}_1(C, K_{KC}) \cdot D - O_D \mathcal{H}_2(C, K_{DC}) \mathcal{H}_2(D, K_{DD}) - \Omega_D D \quad (5.41) \end{aligned}$$

Figure 5.6a shows a comparison of experimental Ca^{2+} and cPKC^* traces with those reproduced by the *G-ChI* model including Eqs. 5.39 and 5.41. For inherent

limitations of the Li-Rinzel description of the gating kinetics of IP₃Rs, which fails to describe these receptors' open probability for large Ca²⁺ concentration (Fig. 5.3) and predicts fast rates of receptor de-inactivation (O_2/d_2 , Table 5.1), the *G-ChI* model cannot generate Ca²⁺ peaks as large as those experimentally observed and shown here. Nonetheless, we would like to emphasize how our model qualitatively matches experimental Ca²⁺-dependent cPKC* dynamics, accurately reproducing the phase shift between Ca²⁺ and cPKC* oscillations. This phase shift is critically controlled by the constant K_{KC} for Ca²⁺ binding to the kinase, along with the rates of cPKC* production versus degradation, i.e., O_{KD} versus Ω_{KD} (Eq. 5.39), and the rate of receptor phosphorylation O_K (Eq. 5.38).

Figure 5.6b further reveals the role of these rate constants in the control of Ca²⁺ oscillations. In this figure, we simulated the astrocyte response for a step increase of $\sim 1.5 \mu\text{M}$ extracellular glutamate, starting from resting conditions, both in the absence of kinase-mediated receptor phosphorylation (*gray trace*) and in the presence of it, for two different O_K rate values (*black traces*). It may be noted how receptor phosphorylation by cPKC can rescue Ca²⁺ oscillations that otherwise would vanish by saturating intracellular IP₃ concentrations ensuing from large receptor activation. This activation indeed is decreased by cPKC* according to Eq. 5.38, thereby regulating intracellular IP₃ within the range of Ca²⁺ oscillations. Nonetheless, as the rate of receptor phosphorylation increases (*dash-dotted trace*), the period of oscillations appears to slow down and oscillations even fail to emerge, if the supply of cPKC* results in a phosphorylation rate of astrocyte receptors that exceeds their agonist-mediated activation (results not shown).

These considerations can be explained considering the period of Ca²⁺ oscillations as a function of the extracellular glutamate concentration. As shown in Fig. 5.6c, cPKC-mediated receptor phosphorylation shifts (*black curves*) the range of glutamate concentrations that trigger Ca²⁺ oscillations to higher values than those otherwise expected in the absence of it (*gray curve*). In particular, and in agreement with experimental findings (Codazzi et al. 2001), the exact value of the rate O_K for receptor phosphorylation sets the entity of this shift, accounting either for Ca²⁺ oscillations of period longer than without receptor phosphorylation, or for the requirement of larger glutamate concentrations to observe such oscillations. This is respectively reflected by the portions of the *black curves* that are within the range of extracellular glutamate concentrations of the *gray curve*, and those that are not instead. On the other hand, longer-period oscillations in the presence of receptor phosphorylation are likely to be observed as long as the rate of cPKC* activation by DAG (O_{KD}) is below some critical value. A threefold increase of this rate indeed requires glutamate concentrations beyond those needed in the absence of receptor phosphorylation to trigger oscillations, regardless of the O_K value at play (*blue curves*). In this scenario in fact, the large supply of cPKC*, resulting from the high O_{KD} value, favors phosphorylation of receptors while hindering intracellular buildup of IP₃ to trigger CICR. This in turn requires a larger recruitment of astrocyte receptors by larger agonist concentrations to evoke Ca²⁺ oscillations.

5.4 Conclusions

The modeling arguments introduced in this chapter overall suggest a great richness in the possible modes, whereby astrocytes could translate extracellular stimuli into intracellular Ca^{2+} dynamics. These modes are brought forth by a complex network of biochemical reactions that is exquisitely nonlinearly coupled with Ca^{2+} dynamics through different second messengers, among which IP_3 and possibly DAG could play a paramount signaling role. In particular, the regulation of different regimes of IP_3 production and degradation by Ca^{2+} in parallel with the differential regulation by this latter and DAG of the activities of cPKCs and DAGKs opens to the scenario of the existence of different regimes of signal transduction that a single astrocyte could multiplex toward different intracellular targets depending on different local conditions of neuronal activity.

An interesting implication emerging from our analysis of the regulation of the period of Ca^{2+} oscillations by cPKCs and DAG-related lipid signals is the possibility that these pathways, which could be crucially linked with inflammatory responses underpinning reactive astrocytosis (Brambilla et al. 1999; Griner and Kazanietz 2007), could be found at different operational states, akin to what suggested for proinflammatory cytokines like $\text{TNF}\alpha$ (Santello and Volterra 2012). In our analysis, for example, intermediate activation of cPKC activity could promote Ca^{2+} oscillations at physiological rates, while an increase of it could exacerbate fast, potentially inflammatory Ca^{2+} responses (Sofroniew and Vinters 2010).

Similar arguments also hold for IP_3 signaling. Calcium-dependent IP_3 production by PLC δ and PLC β (via cPKC) could modulate the rate of integration of synaptic stimuli and thus dictate the threshold synaptic activity triggering CICR. On the other hand, the existence of different regimes of IP_3 degradation could be responsible for different cutoff frequencies of synaptic release, beyond which integration of external stimuli by the cells could cease. In particular, this cutoff frequency could be mainly set by IP-5P during low synaptic activity, possibly associated with low intracellular Ca^{2+} levels, while be dependent on IP $_3$ K in regimes of strong astrocyte Ca^{2+} activation and thus ultimately depend on the history of activation of the astrocyte. The following chapter looks closely at some of these aspects, focusing, in particular, on the role of different IP_3 degradation regimes in the genesis and shaping of Ca^{2+} oscillations.

Acknowledgements MDP was supported by an FP7 Marie Skłodowska-Curie International Outgoing Fellowship by the European Commission (Project 331486 “Neuron-Astro-Nets”), and he currently is a Junior Leader Postdoctoral Fellow sponsored by “la Caixa” Banking Foundation (LCF/BQ/LI18/11630006). MDP also acknowledge the support by the Basque Government through the BERC 2018–2021 program and by the Spanish Ministry of Science, Innovation and Universities: BCAM Severo Ochoa accreditation SEV-2017-0718.

Appendix 1 Arguments of Chemical Kinetics

Appendix 1.1 The Hill Equation

In biochemistry, the binding reaction of n molecules of a ligand L to a receptor macromolecule R , i.e.,



can be mathematically described by the differential equation

$$\frac{d[RL_n]}{dt} = k_f[R][L]^n - k_b[RL_n] \quad (5.43)$$

where k_f, k_b denote the forward (binding) and backward (unbinding) reaction rates, respectively. At equilibrium,

$$0 = k_f[R][L]^n - k_b[RL_n] \Rightarrow [RL_n] = \frac{[R][L]^n}{K_d} \quad (5.44)$$

where $K_d = k_b/k_f$ is the *dissociation constant* of the binding reaction 5.42. Then, the fraction of bound receptor macromolecules with respect to the total receptor macromolecules can be expressed by the Hill equation (Stryer 1999)

$$\frac{\text{Bound}}{\text{Total}} = \frac{[RL_n]}{[R] + [RL_n]} = \frac{\frac{[L]^n}{K_d}}{\frac{[L]^n}{K_d} + 1} = \frac{[L]^n}{[L]^n + K_d} = \frac{[L]^n}{[L]^n + K_{0.5}^n} = \mathcal{H}_n([L], K_{0.5}) \quad (5.45)$$

where the function $\mathcal{H}_n([L], K_{0.5})$ denotes the sigmoid (Hill) function $[L]^n/([L]^n+K_{0.5}^n)$, and $K_{0.5} = \sqrt[n]{K_d}$ is the receptor *affinity* for the ligand L and corresponds to the ligand concentration for which half of the receptor macromolecules are bound (i.e., the midpoint of the $\mathcal{H}_n([L], K_{0.5})$ curve). The sigmoid shape of $\mathcal{H}_n([L], K_{0.5})$ denotes *saturation kinetics* in the binding reaction 5.42, that is, for $[L] \gg K_{0.5}$ almost all the receptor molecules are bound to the ligand, so that the fraction of bound receptor molecules does not essentially change for an increase of $[L]$.

The coefficient n , also known as *Hill coefficient*, quantifies the cooperativity among multiple ligand-binding sites. A Hill coefficient $n > 1$ denotes *positively cooperative binding*, whereby once one ligand molecule is bound to the receptor macromolecule, the affinity of the latter for other ligand molecules increases. Conversely, a value of $n < 1$ denotes *negatively cooperative binding*, namely when binding of one ligand molecule to the receptor decreases the affinity of the latter to bind further ligand molecules. Finally, a coefficient $n = 1$ denotes completely *independent binding* when the affinity of the receptor to ligand molecules is not affected by its state of occupation by the latter.

For unimolecular reactions, $n = 1$ coincides with the number of binding sites of the receptor. For multimolecular reactions involving $\eta > 1$ ligand molecules instead, the Hill coefficient, in general, only loosely estimates the number of binding sites, being $n \leq \eta$ (Weiss 1997). This follows from the hypothesis of total allostery that is implicit in the reaction 5.42, whereby the Hill function is a very simplistic way to model cooperativity. It describes in fact the limit case where affinity is 0 if no ligand is bound and infinite as soon as one receptor binds. That is, only two states are possible: free receptor and receptor with all ligand bound. More realistic descriptions are available in literature, such as the Monod–Wyman–Changeux (MWC) model, but they yield much more complex equations and more parameters (Changeux and Edelstein 2005).

Appendix 1.2 The Michaelis–Menten Model of Enzyme Kinetics

The Michaelis–Menten model of enzyme kinetics is one of the simplest and best-known models to describe the kinetics of enzyme-catalyzed chemical reactions. In general enzyme-catalyzed reactions involve an initial binding reaction of an enzyme E to a substrate S to form a complex ES. The latter is then converted into a product P and the free enzyme by a further reaction that is mediated by the enzyme itself and can be quite complex and involve several intermediate reactions. However, there is typically one rate-determining enzymatic step that allows this reaction to be modeled as a single catalytic step with an apparent rate constant k_{cat} . The resulting kinetic scheme thus reads



By law of mass action, the above kinetic scheme gives rise to four differential equations (Stryer 1999):

$$\frac{d[S]}{dt} = -k_f[E][S] + k_b[ES] \quad (5.47a)$$

$$\frac{d[E]}{dt} = -k_f[E][S] + k_b[ES] + k_{\text{cat}}[ES] \quad (5.47b)$$

$$\frac{d[ES]}{dt} = k_f[E][S] - k_b[ES] - k_{\text{cat}}[ES] \quad (5.47c)$$

$$\frac{d[P]}{dt} = k_{\text{cat}}[ES] \quad (5.47d)$$

In the Michaelis–Menten model, the enzyme is a catalyst, namely it only facilitates the reaction whereby S is transformed into P, hence its total concentration $[E]_T = [E] + [ES]$ must be preserved. This is indeed apparent by the sum of the second and the third equations above, since: $\frac{d([E]+[ES])}{dt} = \frac{d[E]_T}{dt} = 0 \Rightarrow [E]_T = \text{const.}$

The system of Eq. 5.47 can be solved for the products P as a function of the concentration of the substrate [S]. A first solution assumes instantaneous chemical equilibrium between the substrate S and the complex ES, i.e., $\frac{d[S]}{dt} = 0$, whereby the initial binding reaction can be equivalently described by a Hill equation (Keener and Sneyd 2008), i.e.,

$$\frac{[ES]}{[E]_T} = \frac{[S]}{[S] + K_d} \Rightarrow [ES] = \frac{[E]_T[S]}{[S] + K_d} \quad (5.48)$$

Alternatively, the *quasi steady-state assumption* (QSSA) that [ES] does not change on the timescale of product formation can be made, so that $\frac{d}{dt}[ES] = 0 \Rightarrow k_f[E][S] = k_b[ES] + k_{cat}[ES]$ (Keener and Sneyd 2008), and

$$\begin{aligned} k_f[E][S] &= k_b[ES] + k_{cat}[ES] \Rightarrow k_f([E]_T - [ES])[S] = k_b[ES] + k_{cat}[ES] \\ &\Rightarrow k_f[E]_T[S] = (k_f[ES][S] + k_b[ES] + k_{cat}[ES]) \\ &\Rightarrow [ES] = [E]_T \frac{[S]}{[S] + K_M} \end{aligned} \quad (5.49)$$

where $K_M = (k_b + k_{cat}) / k_f$ is the *Michaelis–Menten constant* of the reaction which quantifies the affinity of the enzyme to bind to the substrate.

Regardless of the hypothesis made to find an expression for [ES], the rate v_P of production of P can always be written as

$$v_P = \frac{d[P]}{dt} = k_{cat}[ES] = k_{cat}[E]_T \frac{[S]}{[S] + K_{0.5}} = v_{max} \frac{[S]}{[S] + K_{0.5}} \quad (5.50)$$

where $v_{max} = k_{cat}[E]_T$ is the maximal rate of production of P in the presence of enzyme saturation, when all the available enzyme takes part in the reaction; and the affinity constant $K_{0.5}$ equals the dissociation constant K_d of the initial binding reaction in the chemical equilibrium approximation (Eq. 5.48), or the Michaelis–Menten constant in the QSSA (Eq. 5.49).

An important corollary of the Michaelis–Menten model of enzyme kinetics is that the fraction of the total enzyme that forms the intermediate complex ES can be expressed by a Hill equation of the type

$$\frac{[ES]}{[E]_T} = \frac{[S]}{[S] + K_{0.5}} = \mathcal{H}_1([S], K_{0.5}) \quad (5.51)$$

and $K_{0.5}$ can be regarded as the half-saturating substrate concentration of the reaction. Similarly, the effective reaction rate v_P (Eq. 5.51) is proportional to the maximal reaction rate by a Hill-like term $\mathcal{H}_1([S], K_{0.5})$.

Appendix 2 Parameter Estimation

Appendix 2.1 Metabotropic Receptors

Rate constants O_N , Ω_N (Eq. 5.14) lump information on astrocytic metabotropic receptors' activation and inactivation, namely how long it takes for these receptors, once bound by the agonist, to trigger PLC β -mediated IP₃ production and how long this latter lasts. Since IP₃ production mediated by agonist binding with the receptors controls the initial intracellular Ca²⁺ surge, these two rate constants may be estimated by rise times of agonist-triggered Ca²⁺ signals. With this regard, experiments reported that application of 50 μM DHPG—a potent agonist of mGluR5 which are the main type of metabotropic glutamate receptors expressed by astrocytes (Aronica et al. 2003)—triggers submembrane Ca²⁺ signals characterized by a rise time $\tau_r = 0.272 \pm 0.095$ s. Because mGluR5 affinity ($K_{0.5}$) for DHPG is $\sim 2 \mu\text{M}$ (Brabet et al. 1995), that is much smaller than the applied agonist concentration, receptor saturation may be assumed in those experiments whereby the receptor activation rate by DHPG (O_{DHPG}) can be expressed as a function of τ_r (Barbour 2001), i.e., $O_{\text{DHPG}} \approx \tau_r / (50 \mu\text{M}) = 0.055\text{--}0.113 \mu\text{M}^{-1}\text{s}^{-1}$, so that $\Omega_{\text{DHPG}} = O_{\text{DHPG}} K_{0.5} \approx 0.11\text{--}0.22 \text{ s}^{-1}$. Corresponding rate constants for glutamate may then be estimated assuming similar kinetics, yet with $K_{0.5} = K_N = \Omega_N / O_N \approx 3\text{--}10 \mu\text{M}$ (Daggett et al. 1995), that is 1.5–5-fold larger than $K_{0.5}$ for DHPG. Moreover, since rise times of Ca²⁺ signals triggered by nonsaturating physiological stimulation are faster than in the case of DHPG (Panatier et al. 2011), it may be assumed that $O_N > O_{\text{DHPG}}$. With this regard, for a choice of $O_N \approx 3 \times O_{\text{DHPG}} = 0.3 \mu\text{M}^{-1}\text{s}^{-1}$, with $K_N = 6 \mu\text{M}$ such that $\Omega_N = (0.3 \mu\text{M}^{-1}\text{s}^{-1})(6 \mu\text{M}) = 1.8 \text{ s}^{-1}$, a peak of extracellular glutamate concentration of 250 μM , delivered at $t = 0$ and exponentially decaying at rate $\Omega_c = 40 \text{ s}^{-1}$ (Clements et al. 1992), is consistent with a peak fraction of bound receptors of ~ 0.75 within ~ 70 ms from stimulation (Eq. 5.14), which is in good agreement with experimental rise times.

Appendix 2.2 IP₃R Kinetics

We consider a steady-state receptor open probability in the form of $p_{\text{open}}(C, I) = \mathcal{H}_1^3(I, d_1) \cdot \mathcal{H}_1^3(C, d_5)(1 - \mathcal{H}_1(C, Q_2))^3$ with $Q_2 = d_2(I + d_1)/(I + d_3)$ (see Chap. 3) and choose parameters to fit corresponding experimental data by Ramos-Franco et al. (2000) for (i) different Ca²⁺ concentrations \hat{C} at a fixed IP₃ level of $\bar{I} = 1 \mu\text{M}$, i.e., $\hat{p}(\hat{C})$; and (ii) for different IP₃ concentrations (\hat{I}) at an intracellular Ca²⁺ concentration of $\bar{C} = 25 \text{ nM}$, i.e., $\hat{p}(\hat{I})$. To reduce the problem dimensionality while retaining essential dynamical features of IP₃ gating kinetics, we set $d_1 = d_3$ (Li and Rinzel 1994). Accordingly, defining the vector parameter $\mathbf{x}_p = (d_1, d_2, d_5, O_2)$, we minimize the cost function $c_p(\mathbf{x}_p) = (p_{\text{open}}(\hat{C}, \bar{I}) - \hat{p}(\hat{C}))^2 + (p_{\text{open}}(\bar{C}, \hat{I}) -$

$\hat{p}(\hat{I})^2$ by the Artificial Bee Colony (ABC) algorithm (Karaboga and Basturk 2007) considering 2000 evolutions of a colony of 100 individuals.

Ultrastructural analysis of astrocytes *in situ* revealed that the probability of ER localization in the cytoplasmic space at the soma is between ~ 40 and 70% (Pivneva et al 2008). This suggests that the corresponding ratio between ER and cytoplasmic volumes (ρ_A) is comprised between ~ 0.4 and 0.7.

To estimate the cell's total free Ca^{2+} content C_T we make the consideration that the resting Ca^{2+} concentration in the cytosol is $< 0.15 \mu\text{M}$ (Zheng et al. 2015) and can be neglected with respect to the amount of Ca^{2+} stored in the ER (C_{ER}) (Berridge et al. 2003). Hence, with $C_{ER} \geq 10 \mu\text{M}$ (Golovina and Blaustein 1997) and a choice of $\rho_A \geq 0.4$, it follows that $C_T \approx \rho_A C_{ER} \geq 4 \mu\text{M}$. In conditions close to store depletion during oscillations (Camello et al. 2002), this latter value would also coincide with the peak Ca^{2+} reached in the cytoplasm, which is reported between 5 μM and $\sim 20 \mu\text{M}$ (Csordàs et al. 1999; Parpura and Haydon 2000; Kang and Othmer 2009; Shigetomi et al. 2010).

In our simulations, we set $\rho_A = 0.5$ while leaving arbitrary the choice of C_T as far as the resulting Ca^{2+} oscillations qualitatively resemble the shape of those observed in experiments. The remaining parameters for CICR, i.e., $\mathbf{z}_c = (\Omega_C, O_P)$, were chosen to approximate the number and period of Ca^{2+} oscillations observed *on average* in experiments on cultured astrocytes that were stimulated by glutamate perfusion. By “on average,” we mean that we considered the average trace resulting from $n = 5$ different Ca^{2+} signals generated within the same period of time and by the same stimulus in identical experimental conditions.

Appendix 2.3 IP₃ signaling

Once set the CICR parameters, individual Ca^{2+} traces used to obtained the above-mentioned “average trace” were used to search for $\mathbf{z}_p = (O_\beta, O_\delta, O_{3K}, \Omega_{5P})$, assuming random initial conditions. The ensuing parameter values were also used in Figs. 5.4, 5.5, and 5.6 although O_β , O_δ , and O_{3K} were increased, from case to case, by a factor comprised between 1.2 and 2 either to expand the oscillatory range or to promote CICR emergence (by increasing O_β , O_δ) or termination thereof (by larger O_{3K} values).

Appendix 2.4 cPKC and DAG Signaling

Calcium-dependent cPKC-mediated phosphorylation has been documented for astrocytic mGluRs and P₂Y₁Rs (Codazzi et al. 2001; Hardy et al. 2005) and results in a reduction of receptor binding affinity by a factor $\zeta \approx 2\text{--}10$ (Hardy et al. 2005), or possibly higher depending on the cell's expression of cPKCs (Nakahara et al. 1997; Shinohara et al. 2011). Since experiments showed that cPKC is robustly acti-

vated only when Ca^{2+} increases beyond half of the peak concentration reached during oscillations (Codazzi et al. 2001) then, considering peak Ca^{2+} values of $\sim 1\text{--}3 \mu\text{M}$ (Shigetomi et al. 2010) allows estimating Ca^{2+} affinity of cPKC in the range of $K_{KC} \leq 0.5 - 1.5 \mu\text{M}$ which indeed comprises the value of $\sim 700 \text{ nM}$ predicted experimentally (Mosior and Epand 1994). Of the same order of magnitude also is the Ca^{2+} affinity reported for DAGK, i.e., $K_{DC} \approx 0.3\text{--}0.4 \mu\text{M}$ (Sakane et al. 1991; Yamada et al. 1997).

Reported values of DAG affinities for cPKC and DAGK may considerably differ. Micellar assays of cPKCs activity suggests values of K_{KD} as low as $4.6\text{--}13.3 \text{ nM}$ (Ananthanarayanan et al. 2003), whereas studies on purified DAGK suggest a substrate affinity for this kinase of $K_{DD} \approx 60 \mu\text{M}$ (Kanoh et al. 1983). The differences in experimental setups and the possibility that the activity of these kinases could be widely regulated by different DAG pools make these estimate of scarce utility for our model, where the DAG concentration is of the same order of magnitude of IP_3 one. With this regard, we choose to set these affinities to $0.1 \mu\text{M}$ which corresponded in our simulations to the average intracellular DAG concentration during Ca^{2+} oscillations.

The remaining parameters, namely $\mathbf{z}_k = (O_{KD}, O_K, \Omega_D, O_D, \Omega_D)$, were arbitrarily chosen considering two constraints: (i) DAG concentration for damped Ca^{2+} oscillations must stabilize to a constant value; and (ii) the down phase of cPKC* oscillations must follow that of Ca^{2+} ones as suggested by experimental observations by Codazzi et al. (2001).

Appendix 3 Software

The Python file `figures.py` used to generate the figures of this chapter can be downloaded from the online book repository at <https://github.com/mdepitta/comp-glia-book/tree/master/Ch5.DePitta>. The software for this chapter is organized in two folders. The `data` folder contains data to fit the *G-ChI* model. WebPlotDigitizer 4.0 (<https://automeris.io/WebPlotDigitizer>) was used to extract experimental data by Ramos-Franco et al. (2000, Figs. 6 and 7) and Codazzi et al. (2001, Fig. 5). The Jupyter notebook file `data_loader.ipynb` found in this folder contains the code to load and clean experimental data used in the simulations.

The `code` folder contains instead all the routines (including `figures.py`) used for the simulations of this chapter. The two files `astrocyte_models.h` and `astrocyte_models.cpp` contains the core *G-ChI* model implementation in C/C++11, while the class `Astrocyte` in `astrocyte_models.py` provides the Python interface to simulate the *G-ChI* model. The model was integrated by a variable-coefficient linear multistep Adams method in Nordsieck form which proved robust to correctly solve stiff problems rising from different parameter choices (Skeel 1986). Model fitting is provided by `gchi_fit.py` and relies on the PyGMO 2.6 optimization package (<https://github.com/esa/pagmo2.git>).

The library `gchi_bifurcation.py` provides routines to estimate the period and range of Ca^{2+} oscillation as in Fig. 5.6. These routines use numerical continuation of the extended *G-ChI* model by the Python module PyDSTool 0.92 (Clewley 2012) <https://github.com/robklewley/pydstool>.

References

- Allen NJ, Barres BA (2009) Glia—more than just brain glue. *Nature* 457:675–677
- Ananthanarayanan B, Stahelin RV, Digman MA, Cho W (2003) Activation mechanisms of conventional protein kinase C isoforms are determined by the ligand affinity and conformational flexibility of their C1 domains. *J Biol Chem* 278(47):46886–46894
- Aronica E, Gorter JA, Ijlst-Keizers H, Rozenmuller AJ, Yankaya B, Leenstra S, Troost D (2003) Expression and functional role of mGluR3 and mGluR5 in human astrocytes and glioma cells: opposite regulation of glutamate transporter proteins. *Eur J Neurosci* 17:2106–2118
- Barbour B (2001) An evaluation of synapse independence. *J Neurosci* 21(20):7969–7984
- Bekar LK, He W, Nedergaard M (2008) Locus coeruleus α -adrenergic-mediated activation of cortical astrocytes in vivo. *Cereb Cortex* 18(12):2789–2795
- Berridge MJ, Bootman MD, Roderick HL (2003) Calcium signalling: dynamics, homeostasis and remodelling. *Nat Rev Mol Cell Biol* 4:517–529
- Berridge MJ, Irvine RF (1989) Inositol phosphates and cell signalling. *Nature* 341(6239):197–205
- Bindocci E, Savtchouk I, Liaudet N, Becker D, Carriero G, Volterra A (2017) Three-dimensional Ca^{2+} imaging advances understanding of astrocyte biology. *Science* 356:6339
- Brabet I, Mary S, Bockaert J, Pin J (1995) Phenylglycine derivatives discriminate between mGluR1- and mGluR5-mediated responses. *Neuropharmacology* 34(8):895–903
- Brambilla R, Burnstock G, Bonazzi A, Ceruti S, Cattabeni F, Abbracchio MP (1999) Cyclooxygenase-2 mediates P2Y receptor-induced reactive astrogliosis. *Br J Pharmacol* 126(3):563–567
- Bruner G, Murphy S (1990) ATP-evoked arachidonic acid mobilization in astrocytes is via a P2Y-purinergic receptor. *J Neurochem* 55(5):1569–1575
- Camello C, Lomax R, Petersen OH, Tepikin AV (2002) Calcium leak from intracellular stores - the enigma of calcium signalling. *Cell Calcium* 32(5–6):355–361
- Carmignoto G (2000) Reciprocal communication systems between astrocytes and neurones. *Prog Neurobiol* 62:561–581
- Carrasco S, Mérida I (2007) Diacylglycerol, when simplicity becomes complex. *Trends Biochem Sci* 32(1):27–36
- Changeux J, Edelstein SJ (2005) Allosteric mechanisms of signal transduction. *Science* 308(5727):1424–1428
- Chen N, Sugihara H, Sharma J, Perea G, Petracic J, Le C, Sur M (2012) Nucleus basalis enabled stimulus specific plasticity in the visual cortex is mediated by astrocytes. *Proc Natl Acad Sci USA* 109(41):E2832–E2841
- Clements JD, Lester RAJ, Tong G, Jahr CE, Westbrook GL (1992) The time course of glutamate in the synaptic cleft. *Science* 258:1498–1501
- Clewley R (2012) Hybrid models and biological model reduction with PyDSTool. *PLoS Comput Biol* 8(8):e1002628
- Codazzi F, Teruel MN, Meyer T (2001) Control of astrocyte Ca^{2+} oscillations and waves by oscillating translocation and activation of protein kinase C. *Curr Biol* 11(14):1089–1097
- Communi D, Dewaste V, Erneux C (1999) Calcium-calmodulin-dependent protein kinase II and protein kinase C-mediated phosphorylation and activation of D-myo-inositol 1,4,5-trisphosphate 3-kinase B in astrocytes. *J Biol Chem* 274:14734–14742

- Communi D, Gevaert K, Demol H, Vandekerckhove J, Erneux C (2001) A novel receptor-mediated regulation mechanism of type I inositol polyphosphate 5-phosphatase by calcium/calmodulin-dependent protein kinase II phosphorylation. *J Biol Chem* 276(42):38738–38747
- Communi D, Vanweyenberg V, Erneux C (1995) Molecular study and regulation of D-myo-inositol 1,4,5-trisphosphate 3-kinase. *Cell Signal* 7(7):643–650
- Communi D, Vanweyenberg V, Erneux C (1997) D-myo-inositol 1,4,5-trisphosphate 3-kinase A is activated by receptor activation through a calcium:calmodulin-dependent protein kinase II phosphorylation mechanism. *EMBO J* 16(8):1943–1952
- Connolly T, Bansal V, Bross T, Irvine R, Majerus P (1987) The metabolism of tris-and tetraphosphates of inositol by 5-phosphomonoesterase and 3-kinase enzymes. *J Biol Chem* 262(5):2146–2149
- Cristóvão-Ferreira S, Navarro G, Brugarolas M, Pérez-Capote K, Vaz SH, Fattorini G, Conti F, Lluis C, Ribeiro JA, McCormick PJ, Casadó V, Franco R, Sebastião AM (2013) A₁R-A_{2A}R heteromers coupled to G_s and G_{i/o} proteins modulate GABA transport into astrocytes. *Purinergic Signalling* 9(3):433–449
- Csordás G, Thomas AP, Hajnóczky G (1999) Quasi-synaptic calcium signal transmission between endoplasmic reticulum and mitochondria. *EMBO J* 18(1):96–108
- Cui Y, Prokin I, Xu H, Delord B, Genet S, Venance L, Berry H (2016) Endocannabinoid dynamics gate spike-timing dependent depression and potentiation. *elife* 5:e13185
- Daggett L, Sacaan A, Akong M, Rao S, Hess S, Liaw C, Urrutia A, Jachec C, Ellis S, Dreessen J (1995) Molecular and functional characterization of recombinant human metabotropic glutamate receptor subtype 5. *Neuropharmacology* 34(8):871–886
- De Konick P, Schulman H (1998) Sensitivity of CaM kinase II to the frequency of Ca²⁺ oscillations. *Science* 279:227–230
- De Pittà M, Goldberg M, Volman V, Berry H, Ben-Jacob E (2009) Glutamate-dependent intracellular calcium and IP₃ oscillating and pulsating dynamics in astrocytes. *J Biol Phys* 35:383–411
- De Pittà M, Volman V, Berry H, Parpura V, Liaudet N, Volterra A, Ben-Jacob E (2013) Computational quest for understanding the role of astrocyte signaling in synaptic transmission and plasticity. *Front Comp Neurosci* 6:98
- Di Castro M, Chuquet J, Liaudet N, Bhaukaurally K, Santello M, Bouvier D, Tiret P, Volterra A (2011) Local Ca²⁺ detection and modulation of synaptic release by astrocytes. *Nat Neurosci* 14:1276–1284
- Ding F, O'Donnell J, Thrane AS, Zeppenfeld D, Kang H, Xie L, Wang F, Nedergaard M (2013) α₁-Adrenergic receptors mediate coordinated Ca²⁺ signaling of cortical astrocytes in awake, behaving mice. *Cell Calcium* 54(6):387–394
- Doengi M, Hirnet D, Coulon P, Pape H-C, Deitmer JW, Lohr C (2009) GABA uptake-dependent Ca²⁺ signaling in developing olfactory bulb astrocytes. *Proc National Acad Sci* 106(41):17570–17575
- Dominguez CL, Floyd DH, Xiao A, Mullins GR, Kefas BA, Xin W, Yacur MN, Abounader R, Lee JK, Wilson GM, Harris TE, Purow BW (2013) Diacylglycerol kinase α is a critical signaling node and novel therapeutic target in glioblastoma and other cancers. *Cancer Discov* 3(7):782–797
- Dupont G, Erneux C (1997) Simulations of the effects of inositol 1,4,5-trisphosphate 3-kinase and 5-phosphatase activities on Ca²⁺ oscillations. *Cell Calcium* 22(5):321–331
- Erneux C, Govaerts C, Communi D, Pesesse X (1998) The diversity and possible functions of the inositol polyphosphate 5-phosphatases. *Biochim Biophys Acta* 1436(1–2):185–189
- Essen L, Perisic O, Cheung R, Katan M, Williams RL (1996) Crystal structure of a mammalian phosphoinositide-specific phospholipase C. *Nature* 380:595–602
- Essen L, Perisic O, Lunch DE, Katan M, Williams RL (1997) A ternary metal binding site in the C2 domain of phosphoinositide-specific phospholipase C-δ1. *Biochemistry (Mosc)* 37(10):4568–4680
- Fam S, Gallagher C, Salter M (2000) P2Y₁ purinoceptor-mediated Ca²⁺ signaling and Ca²⁺ wave propagation in dorsal spinal cord astrocytes. *J Neurosci* 20(8):2800–2808

- Fisher SK (1995) Homologous and heterologous regulation of receptor-stimulated phosphoinositide hydrolysis. *Eur J Pharmacol* 288:231–250
- Gallo V, Ghiani A (2000) Glutamate receptors in glia: new cells, new inputs and new functions. *Trends Pharm Sci* 21:252–258
- Giaume C, Marin P, Cordier J, Glowinski J, Premont J (1991) Adrenergic regulation of intercellular communications between cultured striatal astrocytes from the mouse. *Proc Nat Acad Sci* 88(13):5577–5581
- Golovina VA, Blaustein MP (1997) Spatially and functionally distinct Ca^{2+} stores in sarcoplasmic and endoplasmic reticulum. *Science* 275:1643–1648
- Griner EM, Kazanietz MG (2007) Protein kinase C and other diacylglycerol effectors in cancer. *Nat Rev Cancer* 7(4)
- Hanson PI, Meyer T, Stryer L, Schulman H (1994) Dual role of calmodulin in autophosphorylation of multifunctional CaM kinase may underlie decoding of calcium signals. *Neuron* 12:943–956
- Hardy A, Conley P, Luo J, Benovic J, Poole A, Mundell S (2005) P2Y1 and P2Y12 receptors for ADP desensitize by distinct kinase-dependent mechanisms. *Blood* 105(9):3552–3560
- Heller JP, Rusakov DA (2015) Morphological plasticity of astroglia: understanding synaptic microenvironment. *Glia* 63(12):2133–2151
- Hermosura M, Takeuchi H, Fleig A, Riley A, Potter B, Hirata M, Penner R (2000) InsP4 facilitates store-operated calcium influx by inhibition of InsP3 5-phosphatase. *Nature* 408(6813):735–740
- Höfer T, Venance L, Giaume C (2002) Control and plasticity of intercellular calcium waves in astrocytes: a modeling approach. *J Neurosci* 22(12):4850–4859
- Irvine RF, Letcher AJ, Heslop JP, Berridge MJ (1986) The inositol tris/tetrakisphosphate pathway—demonstration of Ins(1,4,5)P₃ 3-kinase activity in animal tissues. *Nature* 320:631–634
- Irvine RF, Schell MJ (2001) Back in the water: the return of the inositol phosphates. *Nat Rev Mol Cell Biol* 2(5):327–338
- Jennings A, Tyurikova O, Bard L, Zheng K, Semyanov A, Henneberger C, Rusakov DA (2017) Dopamine elevates and lowers astrogial Ca^{2+} through distinct pathways depending on local synaptic circuitry. *Glia* 65(3):447–459
- Jourdain P, Bergersen LH, Bhaukaurally K, Bezzi P, Santello M, Domercq M, Matute C, Tonello F, Gundersen V, Volterra A (2007) Glutamate exocytosis from astrocytes controls synaptic strength. *Nat Neurosci* 10(3):331–339
- Kang J, Jiang L, Goldman SA, Nedergaard M (1998) Astrocyte-mediated potentiation of inhibitory synaptic transmission. *Nat Neurosci* 1(8):683–692
- Kang M, Othmer H (2009) Spatiotemporal characteristics of calcium dynamics in astrocytes. *Chaos* 19(3):037116
- Kanoh H, Kondoh H, Ono T (1983) Diacylglycerol kinase from pig brain. Purification and phospholipid dependencies. *J Biol Chem* 258(3):1767–1774
- Karaboga D, Basturk B (2007) A powerful and efficient algorithm for numerical function optimization: artificial bee colony (ABC) algorithm. *J Global Optim* 39(3):459–471
- Keener J, Sneyd J (2008) Mathematical physiology: I: Cellular physiology vol 1. 2nd edn. Springer
- Kolodziej SJ, Hudmon A, Waxham MN, Stoops JK (2000) Three-dimensional reconstructions of calcium/calmodulin-dependent (CaM) kinase II α and truncated CaM kinase II α reveal a unique organization for its structural core and functional domains. *J Biol Chem* 275(19):14354–14359
- Lemon G, Gibson WG, Bennett MR (2003) Metabotropic receptor activation, desensitization and sequestration - I: modelling calcium and inositol 1,4,5-trisphosphate dynamics following receptor activation. *J Theor Biol* 223(1):93–111
- Li Y, Rinzel J (1994) Equations for InsP₃ receptor-mediated $[\text{Ca}^{2+}]_i$ oscillations derived from a detailed kinetic model: A Hodgkin-Huxley like formalism. *J Theor Biol* 166:461–473
- Losi G, Mariotti L, Carmignoto G (2014) GABAergic interneuron to astrocyte signalling: a neglected form of cell communication in the brain. *Phil Trans Royal Soc B: Biol Sci* 369(1654):20130609
- Marinissen MJ, Gutkind JS (2001) G-protein-coupled receptors and signaling networks: emerging paradigms. *Trends Pharmacol Sci* 22(7):368–376

- Mariotti L, Losi G, Sessolo M, Marcon I, Carmignoto G (2016) The inhibitory neurotransmitter GABA evokes long-lasting Ca^{2+} oscillations in cortical astrocytes. *Glia* 64(3):363–373
- Martín R, Bajo-Grañeras R, Moratalla R, Perea G, Araque A (2015) Circuit-specific signaling in astrocyte-neuron networks in basal ganglia pathways. *Science* 349(6249):730–734
- Mérida I, Ávila-Flores A, Merino E (2008) Diacylglycerol kinases: at the hub of cell signalling. *Biochem J* 409(1):1–18
- Min R, Nevian T (2012) Astrocyte signaling controls spike timing-dependent depression at neocortical synapses. *Nat Neurosci* 15(5):746–753
- Mishra J, Bhalla US (2002) Simulations of inositol phosphate metabolism and its interaction with Ins P₃-mediated calcium release. *Biophys J* 83:1298–1316
- Mosior M, Epand RM (1994) Characterization of the calcium-binding site that regulates association of protein kinase C with phospholipid bilayers. *J Biol Chem* 269(19):13798–13805
- Nakahara K, Okada M, Nakanishi S (1997) The metabotropic glutamate receptor mGluR5 induces calcium oscillations in cultured astrocytes via protein kinase C phosphorylation. *J Neurochem* 69(4):1467–1475
- Navarrete M, Araque A (2008) Endocannabinoids mediate neuron-astrocyte communication. *Neuron* 57(6):883–893
- Navarrete M, Perea G, de Sevilla D, Gómez-Gonzalo M, Núñez A, Martín E, Araque A (2012) Astrocytes mediate in vivo cholinergic-induced synaptic plasticity. *PLoS Biol* 10(2):e1001259
- Nishizuka Y (1995) Protein kinase C and lipid signaling for sustained cellular responses. *FASEB J* 9:484–496
- Oancea E, Meyer T (1998) Protein kinase C as a molecular machine for decoding calcium and diacylglycerol signals. *Cell* 95:307–318
- Ochocka A-M, Pawelczyk T (2003) Isozymes delta of phosphoinositide-specific phospholipase C and their role in signal transduction in the cell. *Acta Biochim Pol* 50(4):1097–1110
- Overington JP, Al-Lazikani B, Hopkins AL (2006) How many drug targets are there? *Nat Rev Drug Discov* 5(12):993–996
- Panatier A, Vallée J, Haber M, Murai K, Lacaille J, Robitaille R (2011) Astrocytes are endogenous regulators of basal transmission at central synapses. *Cell* 146:785–798
- Parpura V, Haydon PG (2000) Physiological astrocytic calcium levels stimulate glutamate release to modulate adjacent neurons. *Proc Natl Acad Sci USA* 97(15):8629–8634
- Parri HR, Crunelli V (2003) The role of Ca^{2+} in the generation of spontaneous astrocytic Ca^{2+} oscillations. *Neuroscience* 120(4):979–992
- Pawelczyk T, Matecki A (1997) Structural requirements of phospholipase C δ1 for regulation by spermine, sphingosine and sphingomyelin. *Eur J Biochem* 248:459–465
- Perea G, Araque A (2005a) Synaptic regulation of the astrocyte calcium signal. *J Neur Transm* 112:127–135
- Pivneva T, Haas B, Reyes-Haro D, Laube G, Veh R, Nolte C, Skibo G, Kettenmann H (2008) Store-operated Ca^{2+} entry in astrocytes: different spatial arrangement of endoplasmic reticulum explains functional diversity in vitro and in situ. *Cell Calcium* 43(6):591–601
- Ramos-Franco J, Bare D, Caenepeel S, Nani A, Fill M, Mignery G (2000) Single-channel function of recombinant type 2 inositol 1,4,5-trisphosphate receptor. *Biophys J* 79(3):1388–1399
- Rebecchi MJ, Pentyala SN (2000) Structure, function, and control of phosphoinositide-specific phospholipase C. *Physiol Rev* 80(4):1291–1335
- Rhee SG, Bae YS (1997) Regulation of phosphoinositide-specific phospholipase C isozymes. *J Biol Chem* 272:15045–15048
- Rosenberger TA, Farooqui AA, Horrocks LA (2007) Bovine brain diacylglycerol lipase: substrate specificity and activation by cyclicAMP-dependent protein kinase. *Lipids* 42(3):187–195
- Ryu SH, Kim U, Wahl MI, Brown AB, Carpenter G, Huang K, Rhee SG (1990) Feedback regulation of phospholipase C-β by protein kinase C. *J Biol Chem* 265(29):17941–17945
- Sakane F, Yamada K, Imai S-I, Kanoh H (1991) Porcine 80-kDa diacylglycerol kinase is a calcium-binding and calcium/phospholipid-dependent enzyme and undergoes calcium-dependent translocation. *J Biol Chem* 266(11):7096–7100

- Santello M, Volterra A (2012) TNF α in synaptic function: switching gears. *Trends Neurosci* 35(10):638–647
- Serrano A, Haddjeri N, Lacaille J, Robitaille R (2006) GABAergic network activation of glial cells underlies heterosynaptic depression. *J Neurosci* 26(20):5370–5382
- Shigetomi E, Kracun S, Sovroniew MS, Khakh BS (2010) A genetically targeted optical sensor to monitor calcium signals in astrocyte processes. *Nat Neurosci* 13(6):759–766
- Shinohara T, Michikawa T, Enomoto M, Goto J, Iwai M, Matsu-ura T, Yamazaki H, Miyamoto A, Suzuki A, Mikoshiba K (2011) Mechanistic basis of bell-shaped dependence of inositol 1,4,5-trisphosphate receptor gating on cytosolic calcium. *Proc Natl Acad Sci USA* 108(37):15486–15491
- Shinomura T, Asaoka Y, Oka M, Yoshida K, Nishizuka Y (1991) Synergistic action of diacylglycerol and unsaturated fatty acid for protein kinase C activation: its possible implications. *Proc Natl Acad Sci USA* 88:5149–5153
- Sim SS, Kim JW, Rhee SG (1990) Regulation of D-myo-inositol 1,4,5-trisphosphate 3-kinase by cAMP-dependent protein kinase and protein kinase C. *J Biol Chem* 265:10367–10372
- Sims CE, Allbritton NL (1998) Metabolism of inositol 1,4,5-trisphosphate and inositol 1,3,4,5-tetrakisphosphate by the oocytes of *Xenopus laevis*. *J Biol Chem* 273(7):4052–4058
- Skeel RD (1986) Construction of variable-stepsize multistep formulas. *Mathem Comput* 47(176):503–510
- Sofroniew MV, Vinters HV (2010) Astrocytes: biology and pathology. *Acta Neuropathol* 119(1):7–35
- Stryer L (1999) Biochemistry, 4th edn. W. H. Freeman and Company, New York
- Suh P-G, Park J-I, Manzoli L, Cocco L, Peak JC, Katan M, Fukami K, Kataoka T, Yun S, Ryu SH (2008) Multiple roles of phosphoinositide-specific phospholipase C isozymes. *BMB Rep* 41(6):415–34
- Sun W, McConnell E, Pare J-F, Xu Q, Chen M, Peng W, Lovatt D, Han X, Smith Y, Nedergaard M (2013) Glutamate-dependent neuroglial calcium signaling differs between young and adult brain. *Science* 339(6116):197–200
- Suzuki Y, Moriyoshi E, Tsuchiya D, Jingami H (2004) Negative cooperativity of glutamate binding in the dimeric metabotropic glutamate receptor subtype I. *J Biol Chem* 279(34):35526–35534
- Takata N, Mishima T, Hisatsune C, Nagai T, Ebisui E, Mikoshiba K, Hirase H (2011) Astrocyte calcium signaling transforms cholinergic modulation to cortical plasticity in vivo. *J Neurosci* 31(49):18155–18165
- Thiel G, Czernik AJ, Gorelick F, Nairn AC, Greengard P (1988) Ca $^{2+}$ /calmodulin-dependent protein kinase II: Identification of threonine-286 as the autophosphorylation site in the α subunit associated with the generation of Ca $^{2+}$ -independent activity. *Proc Natl Acad Sci USA* 85:6337–6341
- Togashi S, Takazawa K, Endo T, Erneux C, Onaya T (1997) Structural identification of the myo-inositol 1,4,5-trisphosphate-binding domain in rat brain inositol 1,4,5-trisphosphate 3-kinase. *Biochem J* 326:221–225
- Vaarmann A, Gandhi S, Abramov AY (2010) Dopamine induces Ca $^{2+}$ signaling in astrocytes through reactive oxygen species generated by monoamine oxidase. *J Biol Chem* 285(32):25018–25023
- van der Bend RL, de Widt J, Hilkmann H, Van Blitterswijk WJ (1994) Diacylglycerol kinase in receptor-stimulated cells converts its substrate in a topologically restricted manner. *J Biol Chem* 269(6):4098–4102
- Verjans B, Lecocq R, Moreau C, Erneux C (1992) Purification of bovine brain inositol-1,4,5-trisphosphate 5-phosphatase. *Eur J Biochem* 204:1083–1087
- Violin JD, Crombie AL, Soergel DG, Lark MW (2014) Biased ligands at G-protein-coupled receptors: promise and progress. *Trends Pharmacol Sci* 35(7):308–316
- Volterra A, Liaudet N, Savtchouk I (2014) Astrocyte Ca $^{2+}$ signalling: an unexpected complexity. *Nat Rev Neurosci* 15:327–334

- Walter L, Dinh T, Stella N (2004) ATP induces a rapid and pronounced increase in 2-arachidonoylglycerol production by astrocytes, a response limited by monoacylglycerol lipase. *J Neurosci* 24(37):8068–8074
- Wang X, Lou N, Xu Q, Tian G-F, Peng WG, Han X, Kang J, Takano T, Nedergaard M (2006) Astrocytic Ca^{2+} signaling evoked by sensory stimulation *in vivo*. *Nat Neurosci* 9(6):816–823
- Weiss JN (1997) The Hill equation revisited: uses and misuses. *FASEB J* 11:835–841
- Yamada K, Sakane F, Matsushima N, Kanoh H (1997) EF-hand motifs of α , β and γ isoforms of diacylglycerol kinase bind calcium with different affinities and conformational changes. *Biochem J* 321(1):59–64
- Zheng K, Bard L, Reynolds JP, King C, Jensen TP, Gourine AV, Rusakov DA (2015) Time-resolved imaging reveals heterogeneous landscapes of nanomolar Ca^{2+} in neurons and astroglia. *Neuron* 88(2):277–288
- Zorec R, Araque A, Carmignoto G, Haydon P, Verkhratsky A, Parpura V (2012) Astroglial excitability and gliotransmission: an appraisal of Ca^{2+} as a signaling route. *ASN Neuro* 4(2):e00080

Chapter 6

Emergence of Regular and Complex Calcium Oscillations by Inositol 1,4,5-Trisphosphate Signaling in Astrocytes



Valeri Matrosov, Susan Gordleeva, Natalia Boldyрева, Eshel Ben-Jacob,
Victor Kazantsev and Maurizio De Pittà

Abstract We use tools of bifurcation theory to characterize dynamics of astrocytic IP₃ and Ca²⁺ for different IP₃ regimes. We do so starting from a compact, well-stirred astrocyte model to first identify characteristic IP₃ pathways whereby Ca²⁺ and IP₃ dynamics “bifurcate,” namely their dynamics changes from stable (constant) concentration levels, to oscillating ones. Then, we extend our analysis to the elemental case of two astrocytes, coupled by IP₃ diffusion mediated by gap junction channels, leveraging on the mechanisms of emergence of chaotic oscillations. Finally, we discuss spatiotemporal Ca²⁺ dynamics in a spatially extended astrocyte model, gaining insights on the possible physical mechanisms whereby random Ca²⁺ generation could be orchestrated into robust, spatially confined intracellular Ca²⁺ oscillations.

Keywords Chaotic calcium dynamics · Compartmental astrocyte modeling
Calcium spatial patterns

Eshel Ben-Jacob: Deceased June 5, 2015.

V. Matrosov · S. Gordleeva (✉) · N. Boldyрева · V. Kazantsev
N.I. Lobachevsky State University of Nizhni Novgorod, 603950 Nizhny Novgorod, Russia
e-mail: gordleeva@neuro.nnov.ru

E. Ben-Jacob
School of Physics and Astronomy, Tel Aviv University, 69978 Ramat Aviv, Israel

M. De Pittà
Department of Neurobiology, The University of Chicago, Chicago, IL 60637, USA

M. De Pittà
EPI BEAGLE, INRIA Rhône-Alpes, 60097 Villeurbanne, France

M. De Pittà
Group of Mathematical, Computational and Experimental Neuroscience, Basque Center for Applied Mathematics, Bilbao 48009, Biscay, Spain

Abbreviations

BT	Bogdanov-Takens bifurcation point
CICR	Calcium-induced calcium release
CP	Cusp bifurcation point
ER	Endoplasmic reticulum
F	Fold bifurcation point
FF	Fold-flip bifurcation point
GH	Generalized Andronov-Hopf bifurcation point
H	Andronov-Hopf bifurcation point
HHS	Homoclinic-to-hyperbolic saddle bifurcation point
IP ₃ (IP ₃ R)	Inositol 1,4,5-trisphosphate (receptor)
IP ₃ 3K	IP ₃ 3-kinase
IP-5P	Inositol polyphosphate 5-phosphatase
LPC	Fold bifurcation point of limit cycles
PLC β (PLC δ)	Phospholipase C β (C δ)
PMCA	Plasmalemma membrane Ca ²⁺ -ATPase pump
SERCA	(sarco)-endoplasmic reticulum Ca ²⁺ -ATPase pump
ZH	Double Andronov-Hopf bifurcation point

6.1 Introduction

Although Ca²⁺ ions have been identified as a key component of astrocyte signaling in response to stimuli and could mediate the astrocyte's modulatory effects on the surrounding neuropile (Volterra and Meldolesi 2005; Araque et al. 2014), their functional role remains intensely debated. Arguably, one of the principal reasons for such debate is that astrocytic Ca²⁺ shows highly complex spatiotemporal behavior (Bindocci et al. 2017). In response to agonists, like hormones or neurotransmitters, and spontaneously as well, the majority of astrocytes exhibit oscillations of intracellular Ca²⁺ (Verkhratsky et al. 2012a; Zorec et al. 2012). These oscillations can be grouped into two major types: those that are dependent on periodic fluctuations of the cell membrane potential and are associated with periodic entry of Ca²⁺ through voltage-gated Ca²⁺ channels, and those that occur in the presence of a voltage clamp. Our focus here is on the latter type and, in particular, on the so-called process of Ca²⁺-induced Ca²⁺ release (CICR) from the astrocyte's endoplasmic reticulum stores, which depends on cytosolic concentration of the second messenger inositol 1,4,5-trisphosphate (Verkhratsky et al. 2012b).

Two main types of IP₃-mediated CICR are observed in astrocytes (Volterra et al. 2014; Rusakov 2015): (i) transient Ca²⁺ oscillations that are confined to their (primary) processes and (ii) Ca²⁺ elevations propagating along these processes as regenerative Ca²⁺ waves, often reaching the cell soma and triggering whole-cell Ca²⁺ signaling (Pasti et al. 1997; Sul et al. 2004). Remarkably, this latter kind of response

can even propagate to neighboring astrocytes, through gap junction channels, and give rise to intercellular Ca^{2+} waves (Kuga et al. 2011). Although it is likely that different mechanisms could be in place depending on regional, developmental, and physiological conditions, all these mechanisms likely depend, to some extent, on two key factors: the precise, molecular machinery underpinning IP_3 signaling (Scemes 2001), and the underlying spatiotemporal dynamics of synaptic stimulation of the astrocyte network (Volterra and Meldolesi 2005).

As reviewed in Chap. 5, both production and degradation of IP_3 depend on enzymes that are regulated by cytosolic Ca^{2+} (Berridge et al. 2003). These include Ca^{2+} -dependent phospholipase C δ - (PLC δ -) mediated IP_3 synthesis and Ca^{2+} -dependent IP_3 degradation by IP_3 3-kinase ($\text{IP}_3\text{3K}$) and by inositol polyphosphate 5-phosphatase ($\text{IP}-5\text{P}$) (Zhang et al. 1993; Sims and Allbritton 1998; Rebecchi and Pentyala 2000). Production by PLC δ occurs in a regenerative fashion providing necessary IP_3 amounts to promote CICR against enzymatic degradation of IP_3 or rapid IP_3 dilution by intracellular diffusion (Hofer et al. 2002; Ullah et al. 2006). On the other hand, while the activity of the 3-kinase is stimulated by Ca^{2+} , the 5-phosphatase is inhibited instead (Communi et al. 2001), so that different mechanisms of degradation exist depending on Ca^{2+} concentration. In turn, these different routes for IP_3 degradation have the potential to interact with PLC-mediated production in a diverse fashion, possibly ensuing in variegated IP_3 and Ca^{2+} dynamics (Houart et al. 1999; Goldberg et al. 2010; Matrosov and Kazantsev 2011).

Synaptic activation also constitutes a further mechanism to trigger or modulate IP_3 signaling of the astrocyte, insofar as astrocytic receptors, targeted by synaptically released neurotransmitters, are often part of the family of G_q -coupled receptors which, upon activation, promote IP_3 production by PLC β (Zur Nieden and Deitmer 2006). Clustering of these receptors at points of contact of synapses with astrocytic processes (Di Castro et al. 2011; Panatier et al. 2011; Arizono et al. 2012) provides spatially confined sites of IP_3 production, whose differential activation could result in rich spatiotemporal IP_3 and Ca^{2+} dynamics (Volterra et al. 2014). Nevertheless, it remains a matter of investigation, how the stochastic arrival of synaptic inputs within the anatomical domain of an astrocyte could be concerted to generate temporally precise Ca^{2+} signals.

Intense modeling efforts have been devoted in recent years to understand the richness of possible biophysical mechanisms underlying IP_3 -triggered CICR-mediated spatiotemporal dynamics in astrocytes (see Dupont (2014) for a recent review). One such mechanism—intracellular IP_3 diffusion—coupled with PLC-mediated IP_3 production, has been suggested to crucially account for the whole spectrum of Ca^{2+} signaling, ranging from regular Ca^{2+} oscillations, to asynchronous, sparse, and chaotic spatiotemporal Ca^{2+} dynamics (Houart et al. 1999; Ullah et al. 2006; Kang and Othmer 2009; Matrosov and Kazantsev 2011). From a modeling perspective, the functional role of these IP_3 pathways are studied within the more general framework of bifurcation analysis of the dynamics of nonlinear systems, since IP_3 and Ca^{2+} signaling represent a famed example of such systems being modeled by nonlinear differential equations (Fall et al. 2002). In this perspective, here we use tools of bifurcation theory to characterize dynamics of astrocytic IP_3 and Ca^{2+} for differ-

ent IP_3 regimes from a mathematical point of view. We do so following a bottom-up approach, starting from a compact, well-stirred astrocyte model to first identify characteristic IP_3 pathways whereby Ca^{2+} (and IP_3) dynamics “bifurcate,” namely change from stable (constant) concentration levels, to oscillatory dynamics. Then, we extend our analysis to the elemental case of two astrocytes, coupled by IP_3 diffusion mediated by gap junction channels, putting emphasis on the mechanisms of emergence of chaotic oscillations. Finally, we complete our analysis discussing spatiotemporal Ca^{2+} dynamics in a spatially extended astrocyte model, gaining insights into the possible physical mechanisms whereby random Ca^{2+} generation could be orchestrated into robust, spatially confined intracellular Ca^{2+} oscillations.

6.2 Birth and Death of Calcium Oscillations in a Compact Astrocyte Model

6.2.1 Compact Astrocyte Modeling

Compact astrocyte models are useful to study cell-averaged signals such as whole-cell or somatic Ca^{2+} signals recorded in the majority of experiments (Schuster et al. 2002; Falcke 2004). These models assume the astrocyte to be “well-stirred,” so that the concentration of each species is homogeneous throughout. Thus, for example, we write C for the concentration of free Ca^{2+} ions in the cytoplasm and note that it is $C = C(t)$, that is, C has no spatial dependence. In the following, in particular, we consider emergence (or death) of Ca^{2+} oscillations in a popular compact astrocyte model originally developed by De Pittà et al. (2009a). The model describes astrocytic Ca^{2+} signaling by Ca^{2+} -induced Ca^{2+} release (CICR) from the endoplasmic reticulum (ER) stores to the cytoplasm in combination with intracellular IP_3 dynamics. The model consists of three ordinary differential equations: one for intracellular (cytosolic) IP_3 (I), one for cytosolic Ca^{2+} (C), and a further one for Ca^{2+} -mediated deactivation (h) of IP_3 receptor/ Ca^{2+} channels, whereby these channels turn available to trigger CICR again after its occurrence (see Chap. 5). In particular, cytosolic Ca^{2+} and the IP_3 R deactivation are described by a set of Hodgkin–Huxley-like equations, according to the description originally introduced by Li and Rinzel (1994), and evolve according to (Hofer et al. 2002)

$$\frac{dC}{dt} = J_r(C, h, I) + J_l(C) - J_p(C) + J_m(C, I) \quad (6.1)$$

$$\frac{dh}{dt} = \Omega_h(C, I) (h_\infty(C, I) - h) \quad (6.2)$$

where J_r , J_l , J_p , J_m , respectively, denote the IP_3 R-mediated Ca^{2+} -induced Ca^{2+} -release from the ER (J_r), the Ca^{2+} leak from the ER (J_l), the Ca^{2+} uptake from the cytosol back to the ER by serca-ER Ca^{2+} /ATPase pumps (J_p) (De Pittà et al.

2009a) and the Ca^{2+} flux across the plasmalemma membrane by other Ca^{2+} /ATPase (PMCA) pumps and leak mechanisms (J_m) (Ullah et al. 2006). These terms, together with the IP_3R deactivation rate (Ω_h) and the steady-state deactivation probability (h_∞), are given by (Dupont and Goldbeter 1993; Li and Rinzel 1994; see also Chap. 3)

$$J_r(C, h, I) = \Omega_C m_\infty^3 h^3 (C_T - (1 + \rho_A)C) \quad (6.3)$$

$$J_l(C) = \Omega_L (C_T - (1 + \rho_A)C) \quad (6.4)$$

$$J_p(C) = O_P \mathcal{H}_2(C, K_P) \quad (6.5)$$

$$J_m C, I = O_l + O_s \mathcal{H}_2(I, K_s) - \Omega_s C \quad (6.6)$$

$$\Omega_h(C, I) = \frac{\Omega_2(I + d_1) + O_2(I + d_3)C}{I + d_3} \quad (6.7)$$

$$m_\infty(C, I) = \mathcal{H}_1(C, d_5) \mathcal{H}_1(I, d_1) \quad (6.8)$$

$$h_\infty(C, I) = d_2 \frac{I + d_1}{d_2(I + d_1) + (I + d_3)C} \quad (6.9)$$

where $\mathcal{H}_n(x, K)$ denotes the sigmoid (Hill) function $x^n/(x^n + K^n)$. In the absence of external stimulation, cytosolic IP_3 concentration is regulated by the complex Ca^{2+} -modulated interplay of PLC δ -mediated endogenous production and degradation by IP_3 3K and IP-5P (Zhang et al. 1993; Sims and Albritton 1998; Rebecchi and Pentyala 2000), and evolves according to the mass balance equation (De Pittà et al. 2009a; see also Chap. 5)

$$\frac{dI}{dt} = J_\delta(C, I) - J_{3K}(C, I) - J_{5P}(I) \quad (6.10)$$

where

$$J_\delta(C, I) = O_\delta \frac{\kappa_\delta}{\kappa_\delta + I} \mathcal{H}_2(C, K_\delta) \quad (6.11)$$

$$J_{3K}(C) = O_{3K} \mathcal{H}_4(C, K_D) \mathcal{H}_1(I, K_3) \quad (6.12)$$

$$J_{5P}(I) = \Omega_{5P} I \quad (6.13)$$

A detailed description of the parameters in the above equations along with their estimation is provided in Chap. 5. Table 6.1 in the appendix further summarizes the parameter values hereafter adopted.

Table 6.1 All simulations discussed in this chapter use values of model parameters specified in the following Table. Simulation-specific values of model parameters as well as “free” parameters whose values are not reported in the table are detailed in figure captions instead. For simplicity, we assumed $J_m = 0$ in Eq. 6.1 as well as in the single-cell bifurcation analysis. Moreover, in the compartmental model and simulations in Figs. 6.4 and 6.5 we set the lower (resting) IP_3 equilibrium at $I_0 = 0.16 \mu\text{M}$. This was achieved replacing the variable I by $I - I_0$ in Eqs. 6.19 and 6.23

Parameter	Description	Value	Unit
<i>Compact single astrocyte model</i>			
C_T	Total cell-free Ca^{2+} concentration	2	μM
ρ_A	Ratio between ER and cytosol volumes	0.185	—
Ω_C	Maximal rate of Ca^{2+} release by IP_3Rs	6	s^{-1}
Ω_L	Maximal rate of Ca^{2+} leak from the ER	0.11	s^{-1}
O_P	Maximal rate of Ca^{2+} uptake by SERCA pumps	2.2	μMs^{-1}
K_P	Ca^{2+} affinity of SERCA pumps	0.1	μM
d_1	IP_3 dissociation constant	0.13	μM
d_2	Ca^{2+} inactivation dissociation constant	1.049	μM
d_3	IP_3 dissociation constant	0.9434	μM
d_5	Ca^{2+} activation dissociation constant	0.082	μM
O_2	IP_3R binding rate for Ca^{2+} inhibition	0.1335	$\mu\text{M}^{-1}\text{s}^{-1}$
Ω_2	IP_3R unbinding rate for Ca^{2+} inhibition	0.14	s^{-1}
O_δ	Maximal rate of IP_3 production by $\text{PLC}\delta$	0.15	μMs^{-1}
K_δ	Ca^{2+} affinity of $\text{PLC}\delta$	0.5	μM
κ_δ	Inhibition constant of $\text{PLC}\delta$ by IP_3	1.0	μM
O_{3K}	Maximal rate of IP_3 degradation by $\text{IP}_3\text{-3K}$	Free	μMs^{-1}
K_D	Ca^{2+} affinity of $\text{IP}_3\text{-3K}$	0.5	μM
K_3	IP_3 affinity of $\text{IP}_3\text{-3K}$	1.0	μM
Ω_{5P}	Maximal rate of IP_3 degradation by IP_5P	Free	s^{-1}
<i>Astrocytic compartment model</i>			
O_l	Constant Ca^{2+} influx by plasmalemma membrane	0.025	μMs^{-1}
O_s	Maximal Ca^{2+} -dependent rate of Ca^{2+} influx by PMCA	0.2	μMs^{-1}
K_s	Ca^{2+} affinity of PMCA	1.0	μM
Ω_s	Maximal rate of Ca^{2+} extrusion by PMCA	0.5	s^{-1}
α	Strength of Ca^{2+} dependence of $\text{PLC}\delta$	0.8	—
Ω_I	Maximal rate of IP_3 degradation	0.1349	s^{-1}
D	IP_3 diffusion rate	Free	s^{-1}

6.2.2 Bifurcations of Ca^{2+} and IP_3 Equilibria

We start our analysis of intracellular Ca^{2+} dynamics by considering the bifurcations of C , h , I equilibria, namely of those situations where Ca^{2+} , IP_3 , and IP_3R deinac-

No random activity should happen.

tivation are constant in the astrocyte. In doing so, we set the rate of IP_3 production by $PLC\delta$ sufficiently small so as not to have spontaneous oscillations for typical Ca^{2+} and IP_3 resting concentrations, i.e., $<200 \mu M$ (Kang and Othmer 2009), and we map how many equilibria there are and how their stability changes for different regimes of IP_3 degradation, mimicked by different values of the two IP_3 degradation rates O_{3K} and Ω_{5P} in Eqs. 6.10–6.13.

Figure 6.1a summarizes the results of our bifurcation analysis in the parameter plane $O_{3K} - \Omega_{5P}$. In this plane, four bifurcation curves exist: two *black curves* of fold (or saddle-node) bifurcation points which originate at $O_{3K} \approx 8 \mu M$ by cusp bifurcation (CP) and develop, for decreasing O_{3K} values, into two branches \mathcal{E}' , \mathcal{E}'' ; and two *red curves* of Andronov–Hopf bifurcation points \mathcal{H}' , \mathcal{H}'' , which are born through a pair of consecutive Bogdanov–Takens bifurcations (BT_{1,2}) that are consistent with the existence of two zero eigenvalues for the system of Eqs. 6.1–6.10. Remarkably, the first Lyapunov coefficient along the Andronov–Hopf curves changes from negative to positive in coincidence of the two generalized Hopf points (GH₁, GH₂) for increasing O_{3K} values, marking a transition from subcritical (*dash-dotted red curves*) to supercritical Andronov–Hopf bifurcations (*dashed red curves*).

Fold and Andronov–Hopf curves also intersect in double Hopf points for low Ω_{5P} values – \mathcal{E}' with \mathcal{H}' in ZH₁, and \mathcal{E}'' with \mathcal{H}'' in ZH₂—and ultimately partition the parameter plane into different regions which fall in two categories depending on the number of equilibria: (i) one stable equilibrium, like the four *gray-shaded* regions $R'_1 - R'^v_1$ and (ii) two stable equilibria, as the *yellow-shaded* regions R'_3, R''_3 . Notably, in the case of monostability, the equilibrium is globally stable, that is Ca^{2+} and IP_3 always converge to their equilibrium values from any initial state. In the presence of bistability instead, as schematically illustrated in Fig. 6.1b, the two equilibria N_1, N_2 are separated by a saddle point S whose unstable manifold (*yellow plane*) separates between the basins of attraction of the two equilibria.

Vertical and horizontal sections of the parameter plane in Fig. 6.1a, respectively, provide codim-1 bifurcation diagrams in terms of the rate parameters Ω_{5P} (Fig. 6.1c) and O_{3K} (Fig. 6.1d) and illustrate different possible scenarios for transitions from monostability to bistability and vice versa. In particular, it may be noted that, for increasing rates of IP_3 3K-mediated IP_3 degradation (Fig. 6.1c), the range of Ω_{5P} values for which bistability occurs, is mainly controlled by two fold bifurcations (F_{1,2}), unless BT₁ < Ω_{5P} < ZH₁ (Fig. 6.1c, *cyan diagram*) (or GH₂ < Ω_{5P} < ZH₂, not shown), in which case the high stable equilibrium (N_2) disappears via Andronov–Hopf bifurcation (H₁) as Ω_{5P} increases. Similar considerations also hold for the dual case where IP-5P-mediated IP_3 is kept constant and O_{3K} changes (Fig. 6.1d). In this latter scenario, however, as far as ZH₁ < Ω_{5P} < GH₂, the high Ca^{2+} state can exist for both low and high O_{3K} values (Fig. 6.1d, *green diagram*). In this case, low and high O_{3K} values are separated by an unstable equilibrium comprised of two supercritical Andronov–Hopf points (H_{1,2}, *dashed red line*) for which Ca^{2+} oscillations emerge.

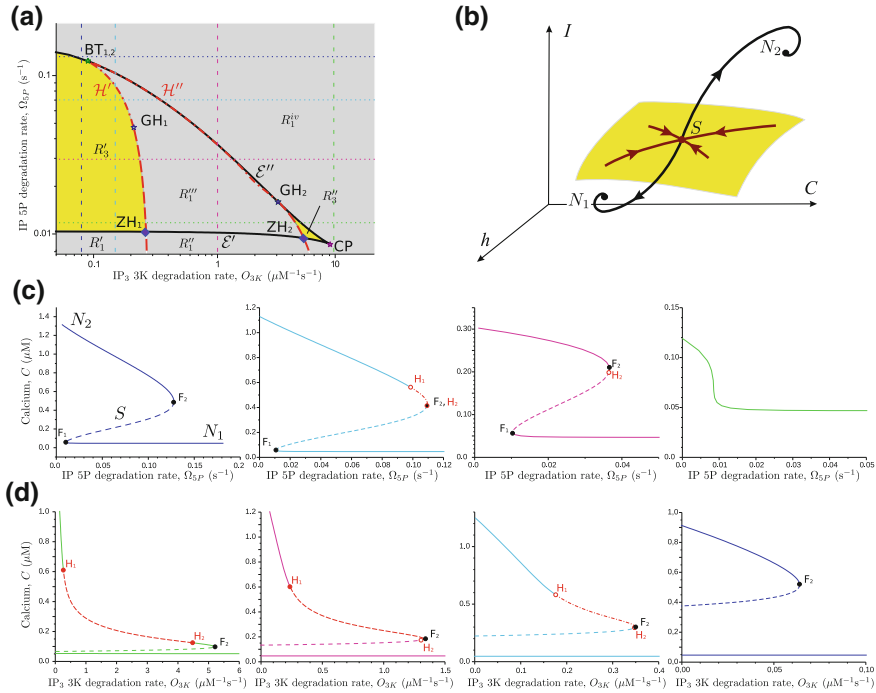


Fig. 6.1 Ca^{2+} equilibria. **a** Regions of existence for one (gray areas, $R'_1 - R'^v_1$) or two stable Ca^{2+} concentrations in an astrocyte (yellow areas, R'_3, R''_3) for different rates of IP₃ degradation by IP₃K (O_{3K}) and IP₅P (Ω_{5P}). The regions result from tiling of the parameter plane by fold (or saddle-node) (E', E'') and Andronov–Hopf bifurcation curves (H', H'' ; subcritical: dashed-dotted curves; supercritical: dashed curves) as detailed in the text. **b** In the presence of bistability, a low (N_1) and a high stable intracellular Ca^{2+} concentration (N_2) may be measured in the same cell, but the probability of observation of each can differ as it is set by the folding of the stable manifold (yellow surface) of the saddle point (S) that separates the domains of attraction of the two stable concentrations. **c, d** Bifurcation diagrams of Ca^{2+} equilibria associated with vertical (dashed) and horizontal (dotted) sections of the bifurcation plane in panel **a** (stable equilibria: solid lines; saddle points: dashed lines). It may be noted that, for some regimes of degradation, the upper branch of the diagram departing from the fold bifurcation F_2 that associates with the stable high Ca^{2+} concentration (N_2) is split into two parts by two Andronov–Hopf bifurcation points ($H_{1,2}$). In between these points (red portions in the diagrams), the high Ca^{2+} state is no longer constant but rather oscillates. Model parameters as in Table 6.1. **c** Vertical sections for: $O_{3K} = 0.08 \mu\text{Ms}^{-1}$ (blue); $O_{3K} = 0.13 \mu\text{Ms}^{-1}$ (cyan); $O_{3K} = 1.0 \mu\text{Ms}^{-1}$ (magenta); $O_{3K} = 9.5 \mu\text{Ms}^{-1}$ (green). **d** Horizontal sections for: $\Omega_{5P} = 0.011 \text{ s}^{-1}$ (green); $\Omega_{5P} = 0.03 \text{ s}^{-1}$ (magenta); $\Omega_{5P} = 0.07 \text{ s}^{-1}$ (cyan); $\Omega_{5P} = 0.135 \text{ s}^{-1}$ (blue)

6.2.3 Emergence of Ca^{2+} and IP_3 Oscillations and Related Limit Cycle Bifurcations

We now turn our analysis to the possible mechanisms underpinning generation and death of Ca^{2+} and IP_3 oscillations. From a dynamical system perspective, Ca^{2+} and IP_3 oscillations are consistent with the existence of limit cycle attractors in the $O_{3K} - \Omega_{5P}$ plane, so that their birth (or death) is by bifurcations of limit cycles. These bifurcations are shown in Fig. 6.2a together with the bifurcation curves of equilibria previously discussed (Fig. 6.1a). In this figure, five different bifurcation curves, \mathcal{F} , \mathcal{D} , \mathcal{S} , \mathcal{M} , and \mathcal{H}'' , delimit a gray-shaded region Z of the parameter plane where stable oscillations of Ca^{2+} and IP_3 exist. In particular, proceeding from left to right, one may note that curve \mathcal{F} , which traces fold-of-cycles bifurcations, is born with curve \mathcal{D} , which represents instead period-doubling bifurcations, through a fold-flip bifurcation (FF). Curve \mathcal{D} then turns into a curve of single-loop homoclinic-to-hyperbolic saddle bifurcations \mathcal{S} at point B_1 . More precisely, this point corresponds to the single-loop separatrix of a saddle-focus bifurcation for which the saddle value of the associated homoclinic-to-hyperbolic saddle orbit is zero (Kuznetsov 1998). An analogous point is also B_2 , at higher O_{3K} values, where the single-loop homoclinic orbit associated with \mathcal{S} becomes multi-loop. This results in the existence of an infinite number of bifurcation lines in the $O_{3K} - \Omega_{5P}$ plane (not shown) which are bounded by curve \mathcal{M} that marks the death of oscillations for increasing Ω_{5P} values. Curve \mathcal{M} ultimately merges with the fold-of-cycle bifurcation curve \mathcal{L}_2 in proximity of the generalized Hopf point GH_2 , whereby the *dashed* supercritical Andronov–Hopf curve \mathcal{H}'' is born and closes the oscillation region Z for high O_{3K} values.

Existence of such diverse bifurcations for different O_{3K} and Ω_{5P} values suggests different scenarios for birth and dynamics of Ca^{2+} and IP_3 oscillations that depend on the regime of IP_3 degradation. A first scenario of interest is the one found in correspondence with small O_{3K} values, in an interval that includes the three curves \mathcal{F} , \mathcal{H}' , and \mathcal{L}_1 (*black segment “1”* in Fig. 6.2a). An inspection of the associated bifurcation diagram (Fig. 6.2b, *top panel*) reveals that, starting from equilibrium Ca^{2+} and IP_3 concentrations in region R'_1 (see Fig. 6.1a), Ca^{2+} and IP_3 oscillations of arbitrarily small amplitude (Λ_1) are born via a supercritical Andronov–Hopf bifurcation H_1 (which lies on \mathcal{H}') for increasing O_{3K} values. The limit cycle Λ_1 associated with these oscillations grows in amplitude with O_{3K} in a small interval, till it disappears by the fold bifurcation LPC_1 (lying on \mathcal{L}_1). Nevertheless, oscillations may still be observed, yet of much larger amplitude, due to the presence of a large limit cycle Λ_2 which emerges via another fold bifurcation for O_{3K} values in R'_1 (LPC_2 , lying on \mathcal{F}). Thus, two scenarios of multistability exist: one for $LPC_2 \leq O_{3K} < H_1$ and $O_{3K} > LPC_1$, whereby constant (resting) Ca^{2+} and IP_3 concentrations coexist with large oscillations of Ca^{2+} and IP_3 oscillations; and another for $H_1 \leq O_{3K} < LPC_1$, where these large oscillations also coexist with smaller ones but there is no possible resting equilibrium for Ca^{2+} and IP_3 . The ensuing astrocytic Ca^{2+} dynamics, namely whether it is constant or oscillatory and, in this latter case, whether oscillations are small or large, ultimately depends on the location of the initial conditions (and thus

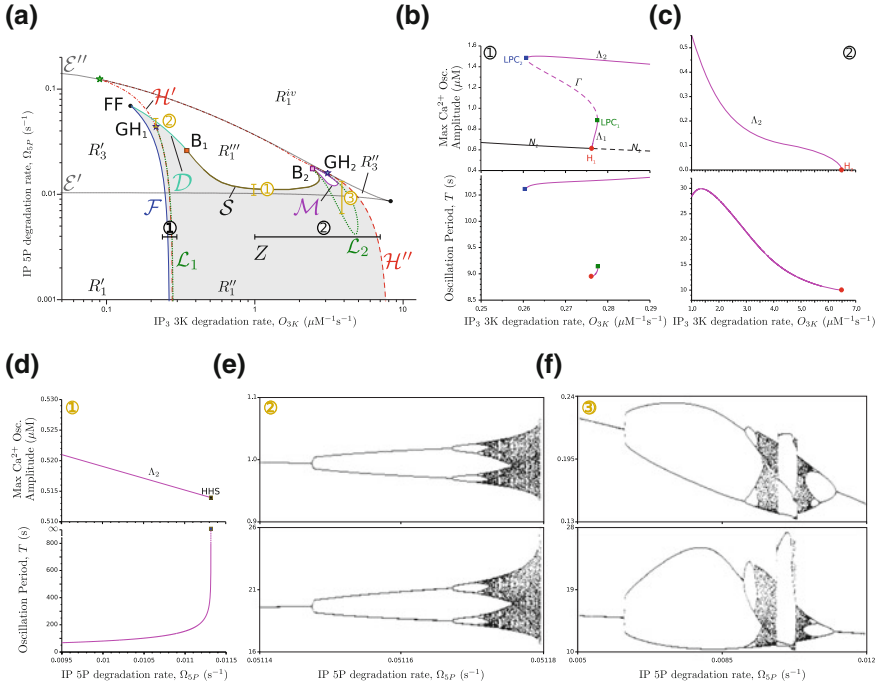


Fig. 6.2 Mechanisms of Ca²⁺ oscillations. **a** The diagram in Fig. 6.1a is reproduced here with the addition of a gray-shaded area Z , where rich oscillatory Ca²⁺ dynamics exists for different regimes of IP₃ degradation. This region is bounded by a fold-of-cycles curve (\mathcal{F}) and a period-doubling curve (\mathcal{D}) which originate by a fold-flip point (FF) for low rates of IP₃ degradation by 3-kinase (O_{3K}). For increasing O_{3K} values instead, curve \mathcal{D} turns into a single-loop homoclinic-to-hyperbolic saddle curve (\mathcal{S}) at point B₁, which later becomes a multi-loop homoclinic-to-hyperbolic saddle curve (\mathcal{M}) via the bifurcation point B₂. Ca²⁺ oscillations ultimately vanish for sufficiently high O_{3K} values by a supercritical Andronov–Hopf bifurcation (dashed part of the \mathcal{H}'' curve). **b, c** Bifurcation diagrams for fixed rate of IP₃3K degradation by IP-5P ($\Omega_{5P} = 0.03 \text{ s}^{-1}$) and increasing rates of 3K-mediated IP₃ degradation. Arbitrarily small Ca²⁺ oscillations (Λ_2) can coexist with large-amplitude ones (Λ_1), independently of 5P-mediated degradation, for low O_{3K} values (**b** and black segment “1” in **a**) although their respective mechanisms of emergence/death are different (see text). **f–e** Bifurcation diagrams for fixed rates of IP₃ degradation by IP₃3K and increasing rates of IP₃ degradation by IP-5P. It may be noted that, as Ω_{5P} approaches either the \mathcal{D} or \mathcal{M} curve, complex multirhythmic and/or chaotic oscillatory dynamics emerges (**d**, **e** and, respectively, yellow segments “2” and “3” in **a**). For sample dynamics within the orange-shaded rectangle, see Fig. 6.3. **d** $O_{3K} = 1.0 \mu\text{Ms}^{-1}$; **e** $O_{3K} = 0.21 \mu\text{Ms}^{-1}$; **f** $O_{3K} = 4.0 \mu\text{Ms}^{-1}$. Other model parameters as in Table 6.1

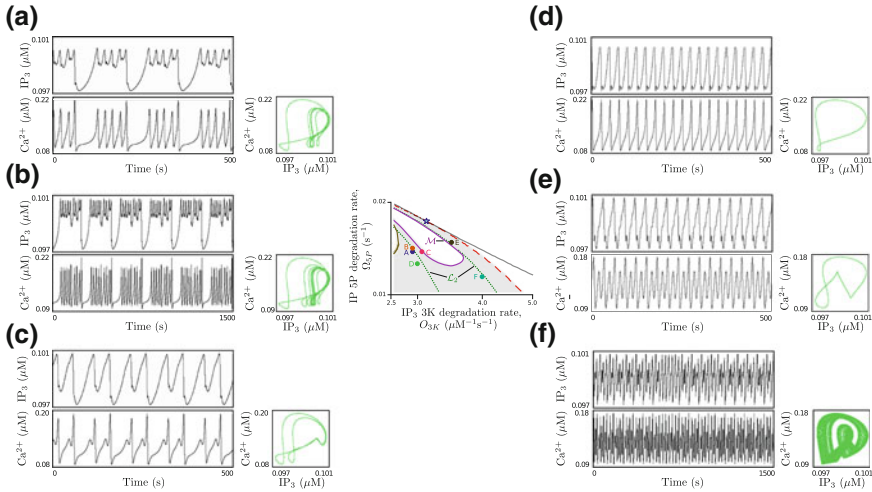


Fig. 6.3 Pathway to chaotic oscillations. **a–f** Ca^{2+} and IP_3 oscillations for different regimes of IP_3 degradation: each figure ensues from degradation rates marked by the corresponding labeled point in the plane O_{3K} vs. Ω_{5P} in the *central panel* (zoom in on the *orange-shaded rectangle* in Figure 6.2a). Complex oscillations, including bursting, may be observed for IP_3 degradation regimes in the region delimited by the two curves \mathcal{M} and \mathcal{L}_2 (**a–c, e**). These oscillations associate with Lissajous-like figures (in green) that present a large, asymmetric “eight”-shaped curve, which maps the slow bursting component, and smaller concentric alike curves (occurring for higher Ca^{2+} and IP_3 concentrations), that represent intraburst oscillations. On the contrary, for degradation rates outside this region, and sufficiently far from \mathcal{L}_2 , simple oscillations exist which result in a single eight-shaped Lissajous curve (**d**). These oscillations can however rapidly turn complex (**e**) and/or chaotic (**f**) for degradation regimes approaching \mathcal{L}_2 . **a** $O_{3K} = 2.939 \mu\text{Ms}^{-1}$, $\Omega_{5P} = 0.0135 \text{s}^{-1}$; **b** $O_{3K} = 2.939 \mu\text{Ms}^{-1}$, $\Omega_{5P} = 0.013513 \text{s}^{-1}$; **c** $O_{3K} = 3.26 \mu\text{Ms}^{-1}$, $\Omega_{5P} = 0.0135 \text{s}^{-1}$; **d** $O_{3K} = 3.0 \mu\text{Ms}^{-1}$, $\Omega_{5P} = 0.012 \text{s}^{-1}$; **e** $O_{3K} = 3.37 \mu\text{Ms}^{-1}$, $\Omega_{5P} = 0.014 \text{s}^{-1}$; **f** $O_{3K} = 4.0 \mu\text{Ms}^{-1}$, $\Omega_{5P} = 0.01055 \text{s}^{-1}$. Other model parameters as in Table 6.1

on the astrocyte’s history of activation) with respect to manifolds of the limit cycle Γ , which separate between the basins of attraction of the equilibrium (N_1) and the two limit cycles (Λ_1 , Λ_2). It is also possible that both oscillations occur together resulting in bursting (not shown, but see Fig. 6.3 for an example). In this case, as evidenced by the period of oscillations (Fig. 6.2b, bottom panel), the small amplitude oscillations (Λ_1) are slower than larger ones, and thus set the interburst period, whereas intraburst oscillations, which must be faster, are those of large amplitude associated with the limit cycle Λ_2 .

The limit cycle Λ_2 , on the other hand, exists across the whole Z region, but its amplitude and period may considerably change depending on the IP_3 degradation regime under consideration. This is illustrated in Fig. 6.2c, where the maximal amplitude of Ca^{2+} oscillations lying on Λ_2 are shown in correspondence with the same rate of 5P-mediated IP_3 degradation as in Fig. 6.2b, but faster rates of 3K-mediated IP_3 degradation (black segment “2” in Fig. 6.2a). In this scenario, it may be noted that the cycle is maximally large for $O_{3K} \approx 1 \mu\text{Ms}^{-1}$ but its amplitude is almost

half of that observed in Fig. 6.2b, while the period is about threefold longer. In the transition from Fig. 6.2b, c, as O_{3K} increases beyond LPC_1 , the nonlinear amplification by the Ca^{2+} -dependent Hill term in $\text{IP}_3\text{3K}$ -mediated IP_3 degradation (Eq. 6.12) grows stronger reducing intracellular IP_3 , thereby limiting availability of open IP_3Rs (Eq. 6.8). This results in a weaker CICR from the ER stores which is reflected by smaller Ca^{2+} oscillations. At the same time, it also takes longer for IP_3 to reach the CICR threshold from baseline concentration values, which accounts for larger oscillation periods. Clearly, the effect is stronger with larger O_{3K} values, and Δ_2 ultimately shrinks to arbitrarily small amplitude oscillations and disappears by supercritical Andronov–Hopf bifurcation in H_1 at $O_{3K} \approx 6.5 \mu\text{Ms}^{-1}$.

Consider now the possible emergence of oscillations by any of the three curves \mathcal{D} , \mathcal{S} , and \mathcal{M} . Among these three curves, \mathcal{S} is remarkable because allows rise or death of regular (i.e., single-loop) oscillations (Δ_2 , Fig. 6.2d) with arbitrarily large period through homoclinic-to-hyperbolic saddle bifurcation (HHS). Here, the saddle originates by a fold (or saddle-node) bifurcation F_1 lying on \mathcal{E}' and occurring at lower Ω_{5P} (*yellow segment “1”* in Fig. 6.2a), so that the limit cycle coexist with the low equilibrium (N_1 in the *third panel* of Fig. 6.1c) for any value of Ω_{5P} comprised between \mathcal{E}' and \mathcal{S} .

Crossing of \mathcal{D} and \mathcal{M} may lead instead to rich oscillatory dynamics. In the case of \mathcal{D} , for example, (*yellow segment “2”* in Fig. 6.2a, d), for increasing rates of degradation by either IP-5P or $\text{IP}_3\text{3K}$ or both, regular Ca^{2+} and IP_3 oscillations become irregular and eventually chaotic through a typical period-doubling cascade sequence (Shilnikov et al. 2001). A similar pathway to chaos may also be observed for Ω_{5P} approaching \mathcal{M} (*yellow segment “3”* in Fig. 6.2a). In particular as Ω_{5P} increases, first chaotic oscillations abruptly vanish via intermittency (type 1) to later re-emerge through period doubling cascade sequence, and finally they become regular by period halving cascade sequence. These complex dynamics ensues from the infinity of bifurcation curves that is found in proximity of \mathcal{M} and which are omitted from the bifurcation portrait of Fig. 6.2a for obvious graphical reasons.

It suffices for the remainder of our analysis, to note that such complex dynamics can be observed in proximity of \mathcal{M} and, in particular, for degradation regimes in the region bounded by this latter curve and the fold-of-cycles bifurcation curve \mathcal{L}_2 , as approximately marked by the *orange-shaded rectangle* in Fig. 6.2a. A zoom in on this region is considered in Fig. 6.3 (*central panel*), where sample Ca^{2+} and IP_3 oscillations are shown for each labeled point therein. Considering, for example, the regimes marked by points A–C, it may be noted how small variations of the degradation rates are sufficient to dramatically alter shape and frequency of oscillations. In all cases, Ca^{2+} and IP_3 oscillate in a bursting fashion with a constant $45^\circ - 175^\circ$ phase shift, as reflected by the Lissajous-like curves in *green*, but both shape and frequency of their intra- and interburst oscillations dramatically differ. Starting, for example, from Fig. 6.3a, a small increase of Ω_{5P} , such as in the scenario of Fig. 6.3b, is sufficient to almost double duration and number of intraburst oscillations while slowing down overall occurrence of bursts (i.e., slower interburst oscillations). The opposite instead occurs for a small increase of O_{3K} , whereby the frequency of bursts increases, but intraburst Ca^{2+} oscillations almost tend to dis-

appear in favor of more complex oscillations (Fig. 6.3c, e). While Ca^{2+} bursting requires coexistence of at least two limit cycles as earlier noted (e.g., Fig. 6.2b) and thus cannot be observed for IP_3 degradation regimes outside curve \mathcal{L}_2 (Fig. 6.3d), it also happens that, for regimes in proximity of this latter curve, the oscillations can become chaotic and highly irregular in shape and frequency (Fig. 6.3f).

To conclude, the possibility for existence of different Ca^{2+} and IP_3 oscillatory dynamics depending on the regime of IP_3 degradation is remarkable as it suggests different modes of encoding of stimuli by the astrocyte. In this fashion, periodic oscillations such as those in Fig. 6.3d, e could represent a mechanism of frequency encoding as far as their frequency, but not their shape nor their amplitude, changes with the stimulus. Conversely, Ca^{2+} bursting or chaotic oscillations (Fig. 6.3a–c, f) could perform more complex encoding, carrying stimulus information both in their frequency and amplitude, ultimately triggering different downstream effects (De Pittà et al. 2008, 2009a).

Noteworthy is that, in our description, chaotic oscillations are more likely to appear for large rates of IP_3 degradation by IP 5-phosphatase. In particular, experimental evidence suggests that this enzyme could mainly localize in proximity of the plasma membrane, differently from IP_3 3-kinase which seems preferentially deeply anchored in the cytoplasm (Rebecchi and Pentyala 2000; Irvine et al. 2006). Because on the other hand, the cytoplasm-to-ER ratio increases across an astrocyte, from soma to processes (Pivneva et al. 2008), we could hypothesize that so does the relative expression of IP_3K versus IP-5P. In this fashion, different regimes of IP_3 degradation could be present within different regions of an astrocyte: more IP_3K -driven ones in the processes at the cell's periphery, and others, where IP-5P contribution is stronger instead, in the soma or in primary processes branching from this latter. In turn, different regions of the astrocyte could differently encode stimuli, and their reciprocal disposition within the astrocyte anatomical domain, and with respect to the surrounding neuropile, could ultimately be correlated, in support of the possibility of subcellular organization of Ca^{2+} and IP_3 signaling within the same cell (Volterra et al. 2014).

6.3 IP_3 Diffusion and Regulation of Ca^{2+} and IP_3 Oscillations in Connected Astrocytic Compartments

6.3.1 Modeling of Astrocytic Ensembles

Either Ca^{2+} and IP_3 signaling could extend to the whole astrocyte or just be confined within a subcellular region of this latter, our hitherto analysis has not taken into account the fact that IP_3 is highly diffusible in the cytoplasm. This could alter IP_3 balance at the CICR site (Eq. 6.10), either by subtracting or by adding IP_3 , with the potential to affect Ca^{2+} signaling (Sneyd et al. 1995). Remarkably, this scenario could hold either for subcellular propagation of Ca^{2+} waves mediated by intracel-

lular IP₃ diffusion between neighboring subcellular regions within the same cell, or for intercellular propagation of whole-cell Ca²⁺ signals in networks of astrocytes connected by IP₃-permeable gap junction channels (Scemes 2001). Because Ca²⁺ waves are an important mechanism, whereby astrocytes could coordinate their behavior with that of neighboring cells, and such waves often travel in an oscillatory manner (Di Castro et al. 2011; Kuga et al. 2011) forming periodic waves, it is the period and the shape of these waves that are thought to control and coordinate a variety of cellular processes (Verkhratsky et al. 2012b).

The mechanisms controlling period and shape of Ca²⁺ waves, both intra- and intercellularly, are not well understood however (Bazargani and Attwell 2016). Thus, we devote this section to study how these wave features could be regulated by IP₃ signaling, and in particular by IP₃ diffusion. For this purpose, we consider a simple description of oscillatory Ca²⁺ waves consisting of two astrocytic compartments coupled by linear IP₃ diffusion, whereby “compartments” we mean either two different astrocytes or two neighboring astrocytic regions. Accordingly, we assume that IP₃ diffusion is respectively inter- or intracellular.

Each astrocytic compartment in our model is described by the same three variables C , h , I used in the previous section. In particular, we keep Eqs. 6.1 and 6.2 for C and h dynamics while we consider a somewhat simplified description of intracellular IP₃ with respect to Eq. 6.10, so as to ease our analysis of the different contributions of IP₃ production, degradation, and diffusion in the emergence of Ca²⁺ waves (Kazantsev 2009; Matrosov and Kazantsev 2011). In particular, we neglect IP₃ competitive inhibition on PLC δ , as this mechanism is known to only marginally affect IP₃ signaling for $I \gg \kappa_\delta$ (De Pittà et al. 2009a), and assume no cooperativity for the binding reaction of Ca²⁺ with this enzyme. Moreover, we linearly scale the dependence of PLC δ activation by Ca²⁺ according to (De Young and Keizer 1992; Kazantsev 2009)

$$J_\delta = O_\delta (\mathcal{H}_1(C, K_\delta) + (1 - \alpha)\mathcal{H}_1(K_\delta, C)) \quad (6.14)$$

where α controls Ca²⁺-dependent PLC δ activation such that for $0 \leq \alpha \leq 1$ it is $O_\delta \mathcal{H}_1(C, K_\delta) \leq J_\delta \leq O_\delta$. We also neglect Ca²⁺ dependence of IP₃ degradation and assume that IP₃ levels in our description are low, at most close to IP₃3K binding affinity for IP₃, i.e., $I \leq K_{3K}$, so that $J_{3K} \approx O_{3K} I / K_{3K}$ (Eq. 6.10). In this fashion, we are able to lump IP₃ degradation into a single term J_{deg} that linearly depends on IP₃, i.e.,

$$J_{deg} = J_{3K} + J_{5P} \approx \frac{O_{3K}}{K_{3K}} I + \Omega_{5P} I = \Omega_I I \quad (6.15)$$

where we defined $\Omega_I = \Omega_{5P} + O_{3K} / K_{3K}$ as the rate of IP₃ degradation. Finally, we consider Fick’s first law of diffusion to describe IP₃ diffusion, so that (Crank 1980)

$$J_{diff} = -D \Delta I \quad (6.16)$$



where D is the IP_3 diffusion rate and ΔI reflects the gradient of IP_3 concentration across the boundary of the astrocytic compartment, moving from inside to outside this latter. In this fashion, coupling two astrocytic compartments together by linear IP_3 diffusion results in the following system of six differential equations (Matrosov and Kazantsev 2011):

$$\frac{dC_i}{dt} = J_r(C_i, h_i, I_i) + J_l(C_i) - J_p(C_i) + J_m(C_i, I_i) \quad (6.17)$$

$$\frac{dh_i}{dt} = \Omega_h(C_i, I_i) (h_\infty(C_i, I_i) - h_i) \quad i = 1, 2 \quad (6.18)$$

$$\frac{dI_i}{dt} = J_\delta(C_i) + J_{deg}(I_i) + J_{diff}(\Delta I_i) \quad (6.19)$$

where $\Delta I_1 = I_1 - I_2 = -\Delta I_2$.

6.3.2 Bifurcation Analysis of Two Linearly Coupled Astrocytic Compartments

Figure 6.4a reveals existence of two bifurcations curves for our system of two-coupled identical astrocytic compartments as a function of the IP_3 diffusion rate (D) and the IP_3 production rate by PLC δ (O_δ): a *red curve* of Andronov–Hopf bifurcation points (\mathcal{H}) and a *blue curve* of fold bifurcation points of limit cycles (\mathcal{L}). These two curves intersect in two generalized Hopf bifurcation points GH_1 and GH_2 , in between of which Andronov–Hopf bifurcations are subcritical, while being supercritical elsewhere. The parameter plane is thereby subdivided into three regions: (i) a *white region* R_1 where only constant (equilibrium) Ca^{2+} and IP_3 concentrations are observed; (ii) a *gray-shaded region* ($P = P' \cup P''$) where regular Ca^{2+} and IP_3 oscillations emerge; and finally (iii) a *yellow region* W where complex and/or chaotic oscillatory dynamics occurs. Remarkably, oscillations either in P or in W can only emerge for sufficiently large rates of PLC δ -mediated IP_3 production, independently of the rate of IP_3 diffusion, with a minimum value of O_δ for oscillations that depends on the rate of IP_3 degradation (results not shown).

Based on the existence of the two curves \mathcal{H} and \mathcal{L} , two main mechanisms for birth (death) of regular Ca^{2+} and IP_3 oscillations may be expected: one for $D < \text{GH}_1$ and $D > \text{GH}_2$, where oscillations of arbitrarily small amplitude appear via supercritical Andronov–Hopf bifurcation (Fig. 6.4b, *panels 1–6*), and the other, for $\text{GH}_1 < D < \text{GH}_2$, whereby oscillations of arbitrarily small frequency emerge via subcritical Andronov–Hopf bifurcation with amplitude set by the limit cycle previously born through \mathcal{L} (results not shown). Analysis of Lissajous-like curves associated with the earlier scenario of oscillations (Fig. 6.4b, *square panels*) show the characteristic “8” shape of antiphase oscillations. This can be explained noting that CICR in one compartment triggers a surge of IP_3 production by PLC δ and an increase in diffusion of IP_3 from that compartment to the neighboring one, promoting

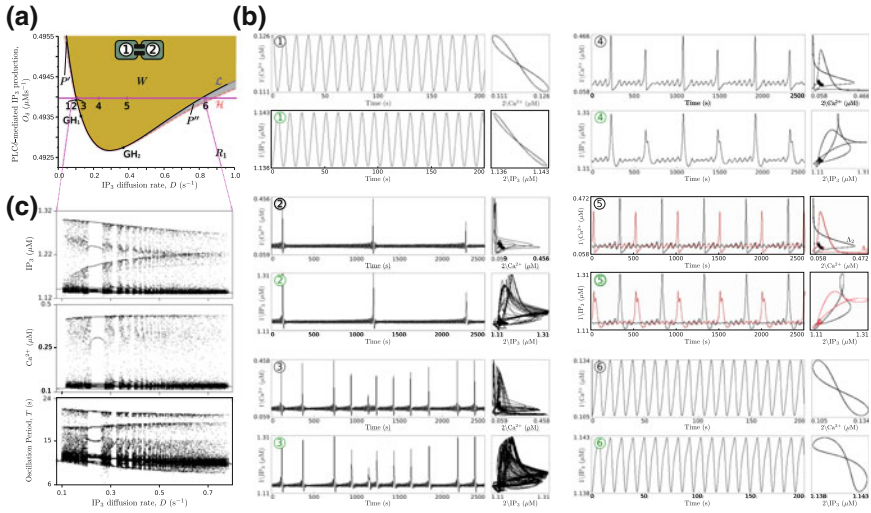


Fig. 6.4 Mechanisms of emergence of oscillations in two astrocytic compartments coupled by linear IP₃ diffusion. **a** For different rates of IP₃ production (O_δ) and diffusion (D), Andronov–Hopf bifurcations (\mathcal{H} , red curve) and fold of limit cycle bifurcations (\mathcal{L} , blue curve) separate between regular (gray-shaded regions P' , P'') and chaotic Ca²⁺ and IP₃ oscillations (yellow-shaded region W). Fixing the rate of IP₃ production by PLC δ at $O_\delta = 0.4939 \mu\text{Ms}^{-1}$, different oscillations ensuing from different rates of IP₃ diffusion between the two compartments (points 1–6 on the magenta line in **a**) are shown in **b**, along with the full bifurcation diagrams in function of IP₃ diffusion in **c**. It may be noted from these diagrams, that both small and large-amplitude oscillations could coexist for D values within the W region in **a** (e.g., panel **b.5**). Intermittent, quasi-periodic chaotic oscillations with decreasing frequency emerge for diffusion rates approaching the supercritical Andronov–Hopf bifurcations for $D < GH_1$ or $D > GH_2$ (dashed segments of the red curve \mathcal{H} in **a**), as shown in panels **b.2** and **b.3** (corresponding to points 2 and 3 on the magenta line in **a**). Regardless of the value of the IP₃ diffusion rate, however, Lissajous curves ensuing from the time evolution of Ca²⁺ and IP₃ dynamics in the two compartments (square panels in **b**) reveal that oscillations in the two compartments tend to be in phase opposition. **b.1:** $D = 0.10562 \text{ s}^{-1}$; **b.2:** $D = 0.106 \text{ s}^{-1}$; **b.3:** $D = 0.12 \text{ s}^{-1}$; **b.4:** $D = 0.25 \text{ s}^{-1}$; **b.5:** $D = 0.3842 \text{ s}^{-1}$; **b.6:** $D = 0.788 \text{ s}^{-1}$. Other parameters as in Table 6.1. In all simulations, IP₃ degradation rate was fixed at $\Omega_I = 0.1349 \text{ s}^{-1}$. Because of symmetry, bifurcation diagrams in **c** for quantities in either compartments are identical

CICR therein. Yet, by the time this occurs, Ca²⁺-mediated inactivation of IP₃R_s in the first compartment has already grown sufficiently to hinder CICR and make Ca²⁺ decrease, till IP₃ diffusion from the other compartment promotes Ca²⁺ increase again in a cyclic fashion, thereby resulting in oscillations in the two compartments that are opposite in phase (or almost so) (Bindschadler and Sneyd 2001; Ullah et al. 2006).

The remarkable proximity between \mathcal{H} and \mathcal{L} curves, which respectively result in birth (or death) of local vs. global attractors in the parameter plane (i.e., equilibria vs. limit cycles) (Kuznetsov 1998), underpins further scenarios of emergence of oscillations that could not be observed in our previous bifurcation analysis of a single astrocytic compartment (Sect. 6.2.3). In particular, for small D values increasing across the left branch of \mathcal{L} (i.e., for $D < GH_1$), Ca²⁺ trajectories along the limit

cycle emerging by \mathcal{H} may transiently enter the basin of attraction of the limit cycle attractor emerging by \mathcal{L} or vice versa, ensuing in intermittent appearance of chaotic, pulse-like Ca^{2+} and IP_3 oscillations (Figs. 6.4b.2, 3) separated by low-amplitude, quasi-periodic oscillations of variable duration.

Sampling of the bifurcation diagram in Fig. 6.4a for varying D with constant O_δ (*magenta segment*) indeed reveals existence of multiple chaotic bands for D values beyond \mathcal{L} , separated by intervals of almost regular oscillations whose amplitude decreases as D increases away from the \mathcal{L} bifurcation boundary (Fig. 6.4c). These bands also reveal existence of two chaotic attractors, one for low and the other for high $\text{Ca}^{2+}/\text{IP}_3$ values, as reflected by the two longitudinal bands in Fig. 6.4c. Notably, these two bands eventually merge for sufficiently large D values (and chaos disappears), ensuing in complex periodic oscillations which bear features of either or both attractors, that is either low- or large-amplitude oscillations (Fig. 6.4b.4) or both (Λ_1 and Λ_2 in Fig. 6.4b.5).

6.4 Oscillatory Ca^{2+} Dynamics in the Presence of Stochastic IP_3 Fluctuations

6.4.1 Spatially Extended Astrocytic Networks

The case of two coupled astrocytic compartments considered in the previous section is arguably the simplest example of a “spatially extended” astrocytic model, where space is defined by two points whose neighboring environment is approximated by a well-stirred compartment governed by Eqs. 6.17–6.19. As previously mentioned, depending on the choice of model parameters, these two “points” (or compartments) can either represent two astrocytes connected by gap junctions, or two contiguous subcellular regions of the same cell. In either scenario, we assume that the (Euclidean) distance between the two compartments is negligible with respect to their spatial extension, so that Ca^{2+} and IP_3 dynamics in between the two compartments is merely a function of the concentrations of these species within the compartments. Remarkably, this can be extended to any number of compartments—as far as properly well-stirred compartments are identified (see Chap. 7)—so that the compartmental approach can be adopted to model both astrocytic networks (Kazantsev 2009; Goldberg et al. 2010; Lallouette et al. 2014; Wallach et al. 2014) and individual astrocytes with spatially extended, coarse-grained yet realistic geometry (De Pittà 2013; Wu et al. 2014).

What distinguishes whether our compartments represent individual cells or sub-cellular regions is a combination of any of the following factors: (i) the choice of model parameters of each compartment, insofar as whole-cell (somatic) Ca^{2+} signals are different in shape, duration and frequency with respect to Ca^{2+} signals that are confined within astrocytic processes (Bindocci et al. 2017); (ii) how the compartments are connected, and (iii) the nature of these connections, since different are the

mechanisms regulating the IP_3 flow between compartments, depending on whether these latter represent cells or subcellular portions, for which nonlinear vs. linear coupling choices can be made accordingly (Goldberg et al. 2010; Lallouette et al. 2014). On the other hand, there is emerging evidence suggesting that Ca^{2+} signaling, both within a single astrocyte or in an astrocytic network, bears some degree of “functional organization” to the extent that, either different cellular regions (Di Castro et al. 2011; Bindocci et al. 2017), or portions of the network display unique spatiotemporal Ca^{2+} dynamics (Kuga et al. 2011; Sasaki et al. 2011). This would mean that once we built a compartmental model of an astrocyte, or of an astrocytic network, we could *a priori* predict that either individual compartments in our model, or specific ensembles of connected compartments, underpin generation of unique, stereotypical Ca^{2+} patterns, namely that Ca^{2+} signaling, ensuing from our simulations, presents some degree of *functional* compartmentalization.

To understand what, in our hypothetical model, could be responsible for the emergence of such functional Ca^{2+} compartmentalization, we could imagine to start considering identical compartments connected in some non-random fashion and argue, somewhat trivially, that the very non-random topology of connections, along with the nature of those connections, are responsible, at least to some extent, to the emergence of unique spatiotemporal Ca^{2+} patterns (Lallouette et al. 2014). There is nonetheless the complimentary possibility that spatiotemporal Ca^{2+} organization could also emerge by intrinsic properties of the very biochemistry beyond IP_3 -mediated CICR (Volterra et al. 2014)—a hypothesis which we are going to investigate for the remainder of this chapter. With this aim, we consider a N -by- N lattice of identical astrocytic compartments, each compartment being linearly coupled to neighboring compartments, so that either 2 or 4 connections per compartment can be counted, depending on whether the compartment is at the borders of the lattice or far from it (Fig. 6.5a). For sufficiently large N , the symmetry of this setup allows linking emergence of spatiotemporal Ca^{2+} patterns that we are presumably going to observe in our simulations, exclusively with the nature of biochemical reactions underpinning astrocytic $\text{IP}_3/\text{Ca}^{2+}$ signaling. Furthermore, to rule out that pattern formation in our simulations could be caused by the nature of the initial perturbation or the choice of initial conditions used to ignite $\text{IP}_3/\text{Ca}^{2+}$ signaling, we set $\alpha = 0$ in Eq. 6.14, thus neglecting the nonlinear Ca^{2+} dependency of $\text{PLC}\delta$ for the sake of simplicity, while adding a further term for stochastic IP_3 production either by spontaneous $\text{PLC}\delta$ activation (Lavrentovich and Hemkin 2008) or by activation of $\text{PLC}\beta$ by stochastic synaptic inputs (Aguado et al. 2002). Accordingly, IP_3 production by PLC isoenzymes is described by (Wu et al. 2014):

$$J_{prod}(t) = O_\beta \mathcal{U}_\beta(0, 1|t_k) \sum_k \delta(t - t_k) + O_\delta \mathcal{U}_\delta(0, 1|\vartheta_n) \sum_n \delta(t - \vartheta_n) \quad (6.20)$$

where $\mathcal{U}_x(0, 1|t)$ (with $x = \beta, \delta$) denotes the generation of a random number at time t withdrawn from the standard uniform distribution and accounts for random modulations of the maximal rate of IP_3 production; t_k and ϑ_n , respectively stand instead for the instants of synaptically evoked and spontaneous nucleation of $\text{IP}_3/\text{Ca}^{2+}$ spikes,

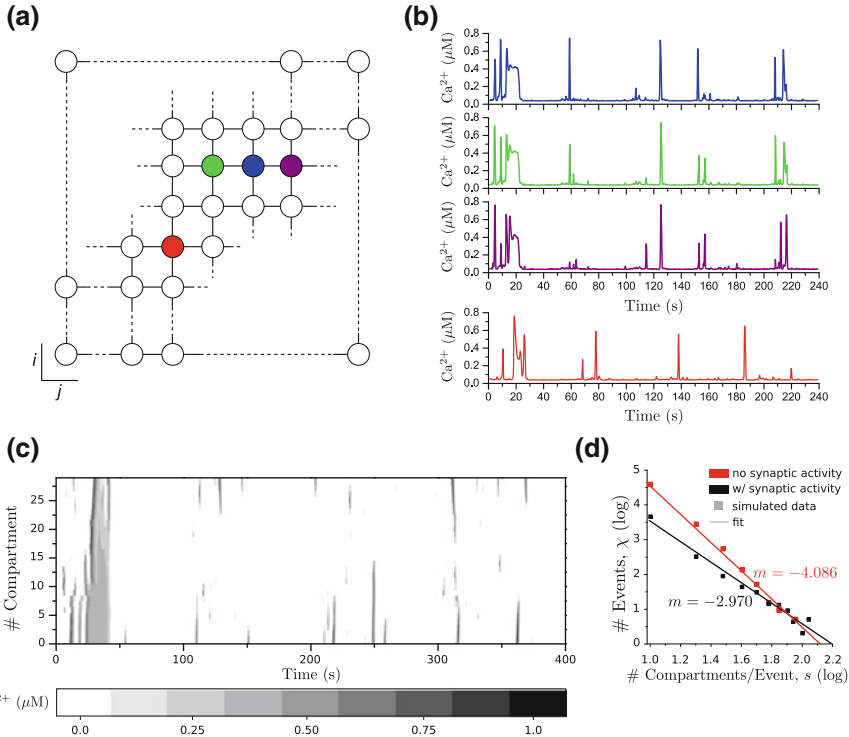


Fig. 6.5 Spatiotemporal Ca^{2+} dynamics emerging by stochastic $\text{IP}_3/\text{Ca}^{2+}$ nucleation. **a** Illustration of the square lattice considered in the simulations for 30×30 astrocytic compartments (circles) connected with their nearest neighbors only. The colored compartments associate with same colors Ca^{2+} traces in **b** which were obtained for spontaneous IP_3 production mediated by $\text{PLC}\delta$. **c** Raster plot of Ca^{2+} concentration dynamics for compartments in the first row of the lattice (**a**, $i = 0$) reveals emergence of different spatiotemporal Ca^{2+} patterns, ranging from frequent, spatially confined Ca^{2+} puffs encompassing $\sim 1\text{--}5$ compartments, to sporadic larger Ca^{2+} events comprising > 5 compartments or even the whole ensemble of compartments (e.g., large gray area for $t < 50$). **d** Log-log plot of the distribution of the number of Ca^{2+} events over their size (in terms of number of active compartments per event) suggests a power-law statistics hallmarking emergence of self-organized Ca^{2+} patterns (*solid line fits*). Remarkably, small Ca^{2+} puffs observed for spontaneous $\text{IP}_3/\text{Ca}^{2+}$ nucleation by $\text{PLC}\delta$ (red data points) tend to disappear in the presence of synaptic activity (black data points) in favor of the emergence of larger Ca^{2+} events. Model parameters as in Table 6.1 except for **b**, **c**: $O_\beta = 0$, $O_\delta = 12 \mu\text{M}$, $v_\delta = 10 \text{ mHz}$; **d**, red points: $O_\beta = 0$, $O_\delta = 12 \mu\text{M}$, $v_\delta = 10 \text{ mHz}$; black points: $O_\beta = 5.5 \mu\text{M}$, $v_\beta = 0.1 \text{ Hz}$; $O_\delta = 0$. In all simulations: $\alpha = 0$, $\Omega_I = 1 \text{ s}^{-1}$ and $D = 10 \text{ s}^{-1}$

which may be assumed to be Poisson distributed at first approximation, in agreement with experimental observations (Softky and Koch 1993; Shadlen and Newsome 1998; Skupin et al. 2008). Each astrocytic compartment in the lattice is thus described by (Kazantsev 2009):

$$\frac{dC_{ij}}{dt} = J_r(C_{ij}, h_{ij}, I_{ij}) + J_l(C_{ij}) - J_p(C_{ij}) + J_m(C_{ij}, I_{ij}) \quad (6.21)$$

$$\frac{dh_{ij}}{dt} = \Omega_h(C_{ij}, I_{ij}) (h_\infty(C_{ij}, I_{ij}) - h_{ij}) \quad (6.22)$$

$$\frac{dI_{ij}}{dt} = J_{prod}(t) + J_{deg}(I_{ij}) + J_{diff}(\Delta_{ij} I) \quad (6.23)$$

where Δ_{ij} is the discrete Laplace operator whereby

$$\Delta_{ij} I = I_{i+1,j} + I_{i-1,j} + I_{i,j+1} + I_{i,j-1} - 4I_{ij} \quad (6.24)$$

with the indices $i, j = 1, \dots, N$ denoting the discrete spatial coordinates in the $N \times N$ lattice.

6.4.2 *Ca²⁺ Wave Propagation and Functional Organization*

We first consider the scenario of spontaneous nucleation of Ca²⁺ waves (i.e., $O_\beta = 0$) at some average rate v_δ in each compartment. Typical values for v_δ are in the range of 1–50 mHz (Skupin et al. 2008; Bindocci et al. 2017); accordingly, we chose an intermediate sample value of $v_\delta = 10$ mHz. Figure 6.5b shows Ca²⁺ traces sampled from different *colored* compartments in the lattice in Fig. 6.5a. It may be appreciated how Ca²⁺ pulse-like fluctuations occur randomly and with variegated amplitudes in close analogy with experimental observations (Nett et al. 2002; Wu et al. 2014). These fluctuations generally present some degree of correlation in contiguous compartments as a result of linear IP₃ diffusion in between compartments (compare *blue*, *green*, and *purple* traces associated with same-color compartments in Fig. 6.5a), but tend to be essentially uncorrelated for compartments far apart (see, e.g., *purple* and *red* traces).

Looking at the raster plot of Ca²⁺ activities in Fig. 6.5c, built by stacking on the y-axis Ca²⁺ traces of all $N = 30$ compartments of the first row of the lattice ($i = 0$ in Fig. 6.5a), it may be seen how, despite spontaneous (random) IP₃/Ca²⁺ pulse nucleation in each compartment, the ensemble of compartments under consideration displays somewhat non-random patterns of Ca²⁺ activity. For example, a large Ca²⁺ wave originates in compartments 15–17 and propagates for $20 < t < 50$ s to neighboring compartments, ultimately engulfing the whole row and other portions of the lattice that are not shown. For $t > 50$ s instead, a series of spatially confined Ca²⁺ puffs spanning few (<5) compartments alternate with larger Ca²⁺ events encompassing several (>5–10) compartments.

To characterize emergence of spatiotemporal Ca²⁺ patterns in our lattice, it is convenient to consider the distribution of the number of Ca²⁺ events (χ) over their size (s), quantified in terms of active compartments per event. Data points from our simulations are shown as *red squares* in Fig. 6.5d, where the choice of logarithmic scales on both axes reveals a linear regression fit for these data points characterized

by a negative slope $m = -4.086$ (*red line*) which is the hallmark of power-law statistic, i.e., $\chi \propto s^{-|m|}$ (Newman 2005). Such statistics suggests that in our setup, spontaneous IP_3/Ca^{2+} nucleation promotes formation of clusters of simultaneously active compartments of different sizes, with decreasing probability as the cluster size increases. These scale-free clusters of active compartments—“scale-free” insofar as there is no specific size (i.e., scale) for the observed clusters, but many sizes are possible—confirm our original hypothesis that CICR molecular machinery itself promotes functional organization of Ca^{2+} dynamics in astrocytic cells and networks. The formation of clusters of active astrocytic compartments may indeed be regarded as a fingerprint of emergence of highly functionally connected cellular or subcellular regions, whose different local Ca^{2+} dynamics are strongly correlated.

It is instructive in this context to also predict how such spontaneous functional organization of astrocytic compartments could change in the presence of synaptically evoked IP_3 production. With this aim, we repeat our simulations assuming that random IP_3 production in Eq. 6.20 is by PLC β rather than by PLC δ (i.e., $O_\delta = 0$). Accordingly, we consider the scenario of synaptic stimuli ensuing from spontaneous neural firing in the range of ~ 0.1 – 5 Hz (Softky and Koch 1993; Haider et al. 2013), with an average synaptic release probability between ~ 0.09 (Schikorski and Stevens 1997) and ~ 0.6 (Stevens and Wang 1995), which sets effective rates v_β of synaptically evoked IP_3 production in the range of ~ 0.01 – 3 Hz (Destexhe et al. 2001). Then, choosing an intermediate value of $v_\beta = 0.1$ Hz, we also consider a low maximal rate of IP_3 production to account for the observation that astrocytic Ca^{2+} puffs by spontaneous synaptic activity are at most similar in size and intensity to spontaneous ones (Di Castro et al. 2011). The resulting distribution of Ca^{2+} events over their size (*black points* in Fig. 6.5d) is still consistent with power-law statistics, but the power-law exponent in this case is smaller ($m = -2.970$) with respect to the case of spontaneous PLC δ mediated IP_3/Ca^{2+} nucleation.

To seek some insights on the possible implications of this result, recall that the exponent m of the power law can be regarded as a measure of the weight of the tail of the distribution that corresponds in our case to the emergence of larger functional Ca^{2+} islands. Hence, the smaller m is, the larger is the proportion of observed large Ca^{2+} events. This is arguably what we expect by synaptic stimulation of astrocytes: namely that small random Ca^{2+} puffs tend to disappear as synaptic activity increases, leaving the place to Ca^{2+} events that progressively encompass larger astrocytic areas in a concerted fashion (Bindocci et al. 2017)—a phenomenon reminiscent of percolation in the context of reactive-diffusive media (Vanag and Epstein 2001). Remarkably, it may be noted that independently of the scenario under consideration, the tails of the two distributions in Fig. 6.5d tend to overlap, suggesting that large Ca^{2+} events emerge with low probability fixed by the inherent properties of the molecular CICR machinery, regardless of the rate of random IP_3/Ca^{2+} nucleation (Wu et al. 2014).

6.5 Conclusions

We have shown how, depending on differences in the underpinning regimes of IP₃ degradation, astrocytic Ca²⁺ signaling could unfold into an incredible, dynamically-rich repertoire of oscillations—from simple periodic oscillations, to complex chaotic bursts and variegated chirps in transitions from different steady states. While this does not answer the question of the functional need for such rich dynamical repertoire by astrocytes, it nevertheless suggests that these cells are capable of implementing complex manipulations of stimuli by encoding these latter by multiple features of different Ca²⁺ oscillations (e.g., Ca²⁺ peaks, frequency, shape, ...) (De Pittà et al. 2008, 2009b).

Two important predictions follow from the models and simulations hitherto discussed. First is the observation that, it is often sufficient to slightly perturb IP₃ degradation rates by IP 5P or IP₃-3K to produce dramatic changes in the ensuing Ca²⁺ dynamics. This could result on one hand in the emergence of periodic, self-sustained stable oscillations (De Pittà et al. 2009a), reminiscent of biological clocks observed, for example, in other cell types such as hepatocytes (Hofer 1999), cardiac myocytes (Maltsev et al. 2011) and other biological systems (Goldbeter 1997). On the other hand, it suggests that Ca²⁺ dynamics could ensue from fine-tuning of cellular properties of the astrocyte, possibly meant to deploy specific physiological needs (Volterra et al. 2014). Second is the consideration, that the molecular CICR machinery beyond the majority of observed astrocytic Ca²⁺ signals, and endows both the single astrocyte and networks of astrocytes by functional organization. Namely, an astrocyte (or a network thereof) could dynamically deploy Ca²⁺ signals of different spatial extension, each with its unique potential functional meaning. It is then plausible to think that heterogeneous expressions of enzymes for IP₃ production and degradation (Irvine et al. 2006), which has not been taken into account in our compartmental approach, could further contribute to the emergence of such functional parcelization of astrocytic anatomical domains—a prediction that is left for proof by future experimental and theoretical investigations.

Acknowledgements This work was supported by the Russian Foundation for Basic Research (Grants No. 17-02-01103 and No. 16-32-60145) and by the Council of the President of the Russian Federation for State Support of Young Scientists and Leading Scientific Schools (Grant No. MK-2909.2017.4). MDP is a Junior Leader Postdoctoral Fellow sponsored by “la Caixa” Banking Foundation (LCF/BQ/LI18/11630006), and he was also previously supported by a FP7 Marie Skłodowska-Curie International Outgoing Fellowship by the European Commission (Project 331486 “Neuron-Astro-Nets”). MDP also wishes to acknowledge the support of the Basque Government by the BERC 2018–2021 program, as well as the support by the Spanish Ministry of Science, Innovation and Universities through the BCAM Severo Ochoa accreditation SEV-2017-0718.

Appendix 1 Numerical Methods

Numerical integration of models in Eqs. 6.1–6.10, 6.17–6.19, 6.21–6.23 was pursued by a fourth-order Runge–Kutta integration scheme with adaptive step-size control and maximum step of 5 ms (Press et al. 1992). To construct bifurcation diagrams, we deployed custom code in Fortran and C++ for standard methods of numerical codim-1 and codim-2 continuations (Guckenheimer and Holmes 1986; Kuznetsov 1998). For each value of the bifurcation parameter considered in a continuation up to 150 peak values of Ca^{2+} and IP_3 oscillations were stored, allowing to reliably detect multistability or chaotic oscillations. Regular vs. chaotic regimes were distinguished by numerical evaluation of Lyapunov eigenvalue spectrum of trajectories on the identified attractor (Shilnikov et al. 2001). Accordingly, the attractor was dubbed chaotic if the Lyapunov spectrum included at least one positive eigenvalue. The complexity of the attractor was instead estimated by numerical evaluation of its power spectrum (Shilnikov et al. 2001).

Stability of equilibria was pursued by numerical computation of the eigenvalue spectrum in the linearized model. Stability of limit cycles was assessed instead by numerical estimation of Floquet multipliers of the corresponding fixed point in Poincaré sections according to classical methods of nonlinear dynamics theory (Guckenheimer and Holmes 1986).

In the study of Ca^{2+} propagation in astrocyte networks in Fig. 6.5d, an astrocyte compartment was dubbed active if its intracellular Ca^{2+} increased beyond a threshold value of $0.4 \mu\text{M}$. Accordingly, an event was counted every time one or more connected compartments were simultaneously active in a time window of 0.1 s. Power-law fit of event number (χ) vs. size (s) was pursued by linear fit of data points on log–log plots by Origin 8.0 software package (OriginLab Corp., Northampton MA).

References

- Aguado F, Espinosa-Parrilla JF, Carmona MA, Soriano E (2002) Neuronal activity regulates correlated network properties of spontaneous calcium transients in astrocytes *in situ*. *J Neurosci* 22(21):9430–9444
- Araque A, Carmignoto G, Haydon PG, Oliet SHR, Robitaille R, Volterra A (2014) Gliotransmitters travel in time and space. *Neuron* 81(4):728–739
- Arizono M, Bannai H, Nakamura K, Niwa F, Enomoto M, Matsu-ura T, Miyamoto A, Sherwood MW, Nakamura T, Mikoshiba K (2012) Receptor-selective diffusion barrier enhances sensitivity of astrocytic processes to metabotropic glutamate receptor stimulation. *Sci Signal* 5(218):ra27
- Bazargani N, Attwell D (2016) Astrocyte calcium signaling: the third wave. *Nat Neurosci* 19(2):182–189
- Berridge MJ, Bootman MD, Roderick HL (2003) Calcium signalling: dynamics, homeostasis and remodelling. *Nat Rev Mol Cell Biol* 4:517–529
- Bindocci E, Savtchouk I, Liaudet N, Becker D, Carrier G, Volterra A (2017) Three-dimensional Ca^{2+} imaging advances understanding of astrocyte biology. *Science* 356:6339
- Bindschadler M, Sneyd J (2001) A bifurcation analysis of two coupled calcium oscillators. *Chaos: an Interdisciplinary J Nonlinear Sci* 11(1):237–246

- Communi D, Gevaert K, Demol H, Vandekerckhove J, Erneux C (2001) A novel receptor-mediated regulation mechanism of type I inositol polyphosphate 5-phosphatase by calcium/calmodulin-dependent protein kinase II phosphorylation. *J Biol Chem* 276(42):38738–38747
- Crank J (1980) The mathematics of diffusion 2nd edn. Oxford University Press, USA
- De Pittà M (2013) Information Processing and Memory in Astrocyte-regulated Synapses. PhD thesis, Tel Aviv University**
- De Pittà M, Goldberg M, Volman V, Berry H, Ben-Jacob E (2009a) Glutamate-dependent intracellular calcium and IP₃ oscillating and pulsating dynamics in astrocytes. *J Biol Phys* 35:383–411
- De Pittà M, Volman V, Levine H, Ben-Jacob E (2009b) Multimodal encoding in a simplified model of intracellular calcium signaling. *Cogn Proc* 10(S1):55–70
- De Pittà M, Volman V, Levine H, Pioggia G, De Rossi D, Ben-Jacob E (2008) Coexistence of amplitude and frequency modulations in intracellular calcium dynamics. *Phys Rev E* 77(3):030903(R)
- De Young GW, Keizer J (1992) A single-pool inositol 1,4,5-trisphosphate-receptor-based model for agonist-stimulated oscillations in Ca²⁺ concentration. *Proc Natl Acad Sci USA* 89:9895–9899
- Destexhe A, Rudolph M, Fellous J, Sejnowski T (2001) Fluctuating synaptic conductances recreate in vivo-like activity in neocortical neurons. *Neuroscience* 107(1):13–24
- Di Castro M, Chauquet J, Liaudet N, Bhaktaally K, Santello M, Bouvier D, Tiret P, Volterra A (2011) Local Ca²⁺ detection and modulation of synaptic release by astrocytes. *Nat Neurosci* 14:1276–1284
- Dupont G (2014) Modeling the intracellular organization of calcium signaling. *Wiley Interdisciplinary Rev: Syst Biol Med* 6(3):227–237
- Dupont G, Goldbeter A (1993) One-pool model for Ca²⁺ oscillations involving Ca²⁺ and inositol 1,4,5-trisphosphate as co-agonists for Ca²⁺ release. *Cell Calcium* 14:311–322
- Falcke M (2004) Reading the patterns in living cells: the physics of Ca²⁺ signaling. *Adv Phys* 53(3):255–440
- Fall CP, Marland ES, M WJ, J TJ (2002) Computational Cell Biology. Springer-Verlag, New York Incorporated
- Goldberg M, De Pittà M, Volman V, Berry H, Ben-Jacob E (2010) Nonlinear gap junctions enable long-distance propagation of pulsating calcium waves in astrocyte networks. *PLoS Comput Biol* 6(8):e1000909
- Goldbeter A (1997) Biochemical oscillations and cellular rhythms. Cambridge University Press, Cambridge, UK
- Guckenheimer G, Holmes P (1986) Nonlinear oscillations, dynamical systems, and bifurcations of vector fields, 2nd edn. Springer-Verlag, New York, U S A
- Haider B, Häusser M, Carandini M (2013) Inhibition dominates sensory responses in the awake cortex. *Nature* 493(7430):97–100
- Höfer T (1999) Model of intercellular calcium oscillations in hepatocytes: synchronization of heterogeneous cells. *Biophys J* 77(3):1244–1256
- Höfer T, Venance L, Giaume C (2002) Control and plasticity of intercellular calcium waves in astrocytes: a modeling approach. *J Neurosci* 22(12):4850–4859
- Houart G, Dupont G, Goldbeter A (1999) Bursting, chaos and birhythmicity originating from self/modulation of the inositol 1,4,5-trisphosphate signal in a model for intracellular Ca²⁺ oscillations. *Bull Math Biol* 61:307–330
- Irvine RF, Lloyd-Burton SM, Yu JCH, Letcher AJ, Schell MJ (2006) The regulation and function of inositol 1,4,5-trisphosphate 3-kinase. *Advan Enzyme Regul* 46:314–323
- Kang M, Othmer H (2009) Spatiotemporal characteristics of calcium dynamics in astrocytes. *Chaos* 19(3):037116
- Kazantsev VB (2009) Spontaneous calcium signals induced by gap junctions in a network model of astrocytes. *Phys Rev E* 79(1):010901
- Kuga N, Sasaki T, Takahara Y, Matsuki N, Ikegaya Y (2011) Large-scale calcium waves traveling through astrocytic networks in vivo. *J Neurosci* 31(7):2607–2614
- Kuznetsov Y (1998) Elements of applied bifurcation theory, 2nd edn. Springer, New York, U S A

- Lallouette J, De Pitta M, Ben-Jacob E, Berry H (2014) Sparse short-distance connections enhance calcium wave propagation in a 3D model of astrocyte networks. *Front Comput Neurosci* 8:45
- Lavrentovich M, Hemkin S (2008) A mathematical model of spontaneous calcium(II) oscillations in astrocytes. *J Theor Biol* 251(4):553–560
- Li Y, Rinzel J (1994) Equations for InsP₃ receptor-mediated [Ca²⁺]_i oscillations derived from a detailed kinetic model: A Hodgkin-Huxley like formalism. *J Theor Biol* 166:461–473
- Maltsev AV, Maltsev VA, Mikheev M, Maltseva LA, Sirenko SG, Lakatta EG, Stern MD (2011) Synchronization of stochastic Ca²⁺ release units creates a rhythmic Ca²⁺ clock in cardiac pacemaker cells. *Biophys J* 100(2):271–283
- Matrosov VV, Kazantsev VB (2011) Bifurcation mechanisms of regular and chaotic network signaling in brain astrocytes. *Chaos* 21:023103
- Nett WJ, Oloff SH, McCarthy KD (2002) Hippocampal astrocytes *in situ* exhibit calcium oscillations that occur independent of neuronal activity. *J Neurophysiol* 87:528–537
- Newman MEJ (2005) Power laws, Pareto distributions and Zipf's law. *Contemporary Phys* 46(5):323–351
- Panatier A, Vallée J, Haber M, Murai K, Lacaille J, Robitaille R (2011) Astrocytes are endogenous regulators of basal transmission at central synapses. *Cell* 146:785–798
- Pasti L, Volterra A, Pozzan T, Carmignoto G (1997) Intracellular calcium oscillations in astrocytes: a highly plastic, bidirectional form of communication between neurons and astrocytes *in situ*. *J Neurosci* 17(20):7817–7830
- Pivneva T, Haas B, Reyes-Haro D, Laube G, Veh R, Nolte C, Skibo G, Kettenmann H (2008) Store-operated Ca²⁺ entry in astrocytes: different spatial arrangement of endoplasmic reticulum explains functional diversity *in vitro* and *in situ*. *Cell Calcium* 43(6):591–601
- Press WH, Teukolsky SA, Vetterling WT, Flannery BP (1992) Numerical Recipes in C, 2nd ed. Cambridge University Press, New York, NY
- Rebecchi MJ, Pentyala SN (2000) Structure, function, and control of phosphoinositide-specific phospholipase C. *Physiol Rev* 80(4):1291–1335
- Rusakov DA (2015) Disentangling calcium-driven astrocyte physiology. *Nat Rev Neurosci* 16:226–233
- Sasaki T, Kuga T, Namiki S, Matsuki N, Ikegaya Y (2011) Locally synchronized astrocytes. *Cortex*, page, *Cereb In press*
- Scemes E (2001) Components of astrocytic intercellular calcium signaling. *Mol Neurobiol* 22(1–3):167–179
- Schikorski T, Stevens CF (1997) Quantitative ultrastructural analysis of hippocampal excitatory synapses. *J Neurosci* 17(15):5858–5867
- Schuster S, Marhl M, Höfer T (2002) Modelling of simple and complex calcium oscillations from single-cell responses to intercellular signalling. *Eur J Biochem* 269:1333–1355
- Shadlen MN, Newsome WT (1998) The variable discharge of cortical neurons: implications for connectivity, computation, and information coding. *J Neurosci* 18(10):3870–3896
- Shilnikov LP, Shilnikov AL, Turaev DV, Chua LO (2001) Methods of Qualitative Theory in Non-linear Dynamics Part II. World Scientific Publishing Company, Singapore
- Sims CE, Allbritton NL (1998) Metabolism of inositol 1,4,5-trisphosphate and inositol 1,3,4,5-tetrakisphosphate by the oocytes of *Xenopus laevis*. *J Biol Chem* 273(7):4052–4058
- Skupin A, Kettenmann H, Winkler U, Wartenberg M, Sauer H, Tovey SC, Taylor CW, Falcke M (2008) How does intracellular Ca²⁺ oscillate: by chance or by clock? *Biophys J* 94:2404–2411
- Sneyd J, Keizer J, Sanderson MJ (1995) Mechanisms of calcium oscillations and waves: a quantitative analysis. *FASEB J* 9(14):1463–1472
- Softky W, Koch C (1993) The highly irregular firing pattern of cortical cells is inconsistent with temporal integration of random EPSPs. *J Neurosci* 13:334–350
- Stevens CF, Wang Y (1995) Facilitation and depression at single central synapses. *Neuron* 14:795–802
- Sul J-Y, Orosz G, Givens RS, Haydon PG (2004) Astrocytic connectivity in the hippocampus. *Neuron Glia Biol* 1:3–11

- Ullah G, Jung P, Cornell-Bell AH (2006) Anti-phase calcium oscillations in astrocytes via inositol (1,4,5)-trisphosphate regeneration. *Cell Calcium* 39(3):197–208
- Vanag VK, Epstein IR (2001) Pattern formation in a tunable medium: the Belousov-Zhabotinsky reaction in an aerosol OT microemulsion. *Phys Rev Lett* 87(22):228301
- Verkhratsky A, Rodriguez JJ, Parpura V (2012a) Neurotransmitters and integration in neuronal-astroglial networks. *Neurochem Re*
- Verkhratsky A, Rodriguez RR, Parpura V (2012b) Calcium signalling in astroglia. *Mol Cell Endocrinol* 353(1–2):45–56
- Volterra A, Liaudet N, Savtchouk I (2014) Astrocyte Ca^{2+} signalling: an unexpected complexity. *Nat Rev Neurosci* 15:327–334
- Volterra A, Meldolesi J (2005) Astrocytes, from brain glue to communication elements: the revolution continues. *Nat Rev Neurosci* 6(8):626–640
- Wallach G, Lallouette J, Herzog N, De Pitta M, Ben-Jacob E, Berry H, Hanein Y (2014) Glutamate-mediated astrocytic filter of neuronal activity. *PLoS Comput Biol* 10(12):e1003964
- Wu Y-W, Tang X, Arizono M, Bannai H, Shih P-Y, Dembitskaya Y, Kazantsev V, Tanaka M, Itohara S, Mikoshiba K, Semenov A (2014) Spatiotemporal calcium dynamics in single astrocytes and its modulation by neuronal activity. *Cell Calcium* 55(2):119–129
- Zhang B-X, Zhao H, Muallem S (1993) Calcium dependent kinase and phosphatase control inositol-1,4,5-trisphosphate-mediated calcium release: modification by agonist stimulation. *J Biol Chem* 268(5):10997–11001
- Zorec R, Araque A, Carmignoto G, Haydon P, Verkhratsky A, Parpura V (2012) Astroglial excitability and gliotransmission: an appraisal of Ca^{2+} as a signaling route. *ASN Neuro* 4(2):e00080
- Zur Nieden R, Deitmer JW (2006) The role of metabotropic glutamate receptors for the generation of calcium oscillations in rat hippocampal astrocytes *in situ*. *Cereb Cortex* 16:676–687

Chapter 7

Astrocyte Networks and Intercellular Calcium Propagation



Jules Lallouette, Maurizio De Pittà and Hugues Berry

Abstract Astrocytes organize in complex networks through connections by gap junction channels that are regulated by extra- and intracellular signals. Calcium signals generated in individual cells can propagate across these networks in the form of intercellular calcium waves, mediated by diffusion of second messengers molecules such as inositol 1,4,5-trisphosphate. The mechanisms underpinning the large variety of spatiotemporal patterns of propagation of astrocytic calcium waves, however, remains a matter of investigation. In the last decade, awareness has grown on the morphological diversity of astrocytes as well as their connections in networks, which seem dependent on the brain area, developmental stage, and the ultrastructure of the associated neuropile. It is speculated that this diversity underpins an equal functional variety, but the current experimental techniques are limited in supporting this hypothesis because they do not allow to resolve the exact connectivity of astrocyte networks in the brain. With this aim, we present a general framework to model intercellular calcium wave propagation in astrocyte networks and use it to specifically investigate how different network topologies could influence shape, frequency, and propagation of these waves.

Keywords Three-dimensional astrocyte networks · Intercellular calcium waves · Spatiotemporal IP₃ dynamics · Shell analysis

Abbreviations

- ATP : Adenosine triphosphate
- CICR : Calcium-induced calcium release
- Cx30 (Cx43) : Connexin type 30 (type 43)
- GJC : Gap junction channel
- ICW : Intercellular calcium wave
- IP₃ (IP₃R) : Inositol 1,4,5-trisphosphate (receptor)

J. Lallouette · M. De Pittà (✉) · H. Berry
EPI BEAGLE, INRIA Rhône-Alpes, Villeurbanne, France
e-mail: mauriziodepitta@gmail.com

M. De Pittà
Basque Center for Applied Mathematics, Bilbao, Spain

IP₃3K : IP₃ 3-kinase
 IP-5P : Inositol polyphosphate 5-phosphatase
 PLC β (PLC δ) : Phospholipase C β (C δ)
 Pn : Postnatal day n

7.1 Introduction

An aspect of astrocytic Ca²⁺ signals is their ability to propagate as regenerative Ca²⁺ waves both intracellularly, i.e., within the same cell, and intercellularly, i.e., through different cells (Scemes and Giaume 2006). In this fashion, processing of synaptic activity by Ca²⁺ in one region of an astrocyte can extend not only to other regions of the same cells but also to neighboring cells, potentially adding nonlocal interactions to the repertoire of neuron-glia interactions (De Pittà et al. 2012; Bazargani and Attwell 2016).

Intercellular calcium waves (ICWs) have originally been reported in astrocyte cultures (Cornell-Bell et al. 1990; Blomstrand et al. 1999; Scemes et al. 2000) and then confirmed to also propagate in astrocytes in brain slices, (Sul et al. 2004; Schipke et al. 2002; Weissman et al. 2004) as well as in live rodents both in physiological (Kurth-Nelson et al. 2009; Kuga et al. 2011) and pathological conditions (Kuchibhotla et al. 2009). They can occur spontaneously (Nimmerjahn et al. 2004) or be evoked by exogenous stimuli (Ding et al. 2013; Sun et al. 2013) and either be restricted to few astrocytes (i.e., <10–30) (Sul et al. 2004; Tian et al. 2006; Sasaki et al. 2011) or engulf hundreds of cells, while propagating in a regenerative fashion (Kuga et al. 2011). The reasons for this variety of modes of propagation remain, however, unknown. Besides differences in the experimental setups that include different brain regions, stimulus protocols, or cellular Ca²⁺ responses, growing evidence suggests a further, previously unknown factor: the organization of astrocytes in variegated networks (Scemes and Giaume 2006; Giaume et al. 2010).

Since the 1970s, our understanding of intercellular communication between astrocytes has fundamentally changed from the notion that they are organized as a syncytium—a multinucleate mass of cytoplasm resulting from the fusion of cells—to the recognition that they are organized into networks with specific topology (Giaume et al. 2010). Neighboring astrocytes in different brain regions are indeed connected at their periphery by gap junctions (GJCs)—channels that allow the intercellular passage of ions and small molecules—and their anatomical domains only minimally overlap, as if they were tiling the brain space (Giaume and McCarthy 1996; Bushong et al. 2002).

The mechanisms establishing whether two astrocytes are connected via GJCs are, however, nontrivial and far from being understood (Giaume 2010). For example, the expression of connexins, in particular of Cx30 and Cx43—the main proteins forming astrocytic GJCs (Giaume et al. 1991; Rouach et al. 2002; Koulakoff et al. 2008)—is known to change across different brain regions (Blomstrand et al. 1999) and in the case of Cx30 during development (Aberg et al. 1999; Montoro and Yuste

2004). Even within the same brain region, GJC expression can considerably change across different structures. Indeed, astrocytes within glomeruli of the olfactory bulb appear to be more connected than outside of these structures (Roux et al. 2011), and similar observations have been made in the somatosensory (barrel) cortex (Houades et al. 2008). While it is believed that this peculiar organization could define precise cellular and anatomical domains, neither the functional relevance of this specialized connectivity is known nor how it could ultimately affect astrocytic Ca^{2+} signaling (Pannasch and Rouach 2013).

Current experimental techniques do not allow to resolve the exact connectivity (topology) of astrocyte networks in the brain and thus are not helpful to address these aspects. In this perspective, computational approaches can provide a valuable tool to investigate general topological principles underpinning ICW propagation (or lack thereof) in astrocyte networks. Here, we review some of these approaches in the context of two-dimensional and three-dimensional astrocyte networks, leveraging our modeling arguments on observations from dedicated experiments in mixed neuron-glia cultures.

7.2 Astrocyte Network Modeling

7.2.1 General Framework

Modeling of astrocyte networks may be pursued in different ways depending on what extent we want to take into account astrocyte anatomy. Astrocytes have indeed complex anatomy, with multiple primary processes irradiating from their somata and branching into secondary and tertiary processes that end in a myriad of tiny lamellipodia and filopodia (Theodosis et al. 2008). Accordingly, ICWs can be described as continuous waves that gradually propagate through this complex medium ensuing from the intricate network of astrocytic processes. While the mathematical theory of these waves is well developed (Falcke 2004), this approach is currently limited, however, by the lack of tools to resolve the fine structure of astrocytic secondary and tertiary processes, except for simplified setups of cell cultures (Kang and Othmer 2009).

Alternatively, we may consider only somatic activation and describe ICWs as propagating waves that hop from one astrocyte to neighboring ones in a coarse-grained fashion, that is counting the number of cells that are activated by a wave rather than the spatial extent to which the wave propagates through the intricate ensemble of astrocytic processes. In this fashion, astrocyte somata are the nodes of the network, whose activation can be described in principle by the (time) evolution of two state vectors: $\mathbf{a} = (C, \dots)$ which lumps the astrocyte's intracellular Ca^{2+} concentration, (C), along with possible other variables that control it, like gating variables of intracellular channels that regulate Ca^{2+} release from the endoplasmic reticulum, or Ca^{2+} buffers that prevent Ca^{2+} accumulation in the cytosol (Falcke

2004, p. 291); and \mathbf{s} which accounts for Ca^{2+} -mobilizing signals that are responsible for regenerative propagation of ICWs. Denoting by \mathcal{N}_i the set of astrocytes that are neighbors of cell i in the network, the equations of these state vectors associated with cell i generally read

$$\frac{d\mathbf{a}_i}{dt} = \mathbf{F}_i(\mathbf{a}_i, \mathbf{s}_i) + \mathcal{D}^{\mathbf{a}}_i(\mathbf{a}_i, \mathbf{a}_j, \mathbf{s}|j \in \mathcal{N}_i) \quad (7.1)$$

$$\frac{d\mathbf{s}_i}{dt} = \mathbf{G}_i(\mathbf{a}_i, \mathbf{s}_i) + \mathcal{D}^{\mathbf{s}}_i(\mathbf{s}_i, \mathbf{s}_j, \mathbf{a}|j \in \mathcal{N}_i) \quad (7.2)$$

where the vector functions \mathbf{F}_i and \mathbf{G}_i are typically nonlinear, and the terms $\mathcal{D}^{\mathbf{a}}_i$ and $\mathcal{D}^{\mathbf{s}}_i$ account for exchange of chemical species (lumped in \mathbf{a}_i and \mathbf{s}_i) between the i th astrocyte and its neighbors.

While Eqs. 7.1 and 7.2 do not account for the totality of models of ICWs, they can nevertheless describe a large class of whole cell models often used in the study of astrocytic ICWs, some example of which we consider in this chapter. In particular, depending on the choice of the astrocyte model, besides cytosolic Ca^{2+} , the components of the state vector \mathbf{a} and the vector function \mathbf{F} can include the Ca^{2+} concentration in the endoplasmic reticulum (Dupont and Goldbeter 1993), the state variables of the Ca^{2+} release channels and their dynamics (De Young and Keizer 1992; Li and Rinzel 1994; Tang and Othmer 1994; Sneyd et al. 1998; Höfer et al. 2002; Stamatakis and Mantzaris 2006). Similarly, in addition to the proper Ca^{2+} mobilizing second messenger molecules, the state vector \mathbf{s} and the vector function \mathbf{G} may also include the state variables for the kinetics of the receptors that control the generation of those second messengers (Kummer et al. 2000; Höfer et al. 2002; Stamatakis and Mantzaris 2006; Ullah et al. 2006a) as well as for other molecular signals involved in the intracellular regulation of such messengers (Chay et al. 1995; Bennett et al. 2005). In many situations, dynamics of the components of \mathbf{a} and \mathbf{s} are interdependent as mirrored by the fact that \mathbf{F} and \mathbf{G} in the above equations are functions of both state vectors. This is obvious for second messengers that control intracellular Ca^{2+} dynamics, but it is also often the case that Ca^{2+} itself can regulate multiple aspects of the dynamics of those second messengers (Chay et al. 1995; Höfer et al. 2002; Ullah et al. 2006a). This may also be the case for the two exchange terms $\mathcal{D}^{\mathbf{a}}$ and $\mathcal{D}^{\mathbf{s}}$, which generally account for intra- and intercellular diffusion of Ca^{2+} along with Ca^{2+} -mobilizing second messenger molecules (Höfer et al. 2002; Stamatakis and Mantzaris 2006; Edwards and Gibson 2010), insofar as the rate of such diffusion may depend on these latter, for example, through Ca^{2+} -dependent buffers (Kupferman et al. 1997; Sherman et al. 2001) or secondary reactions involving second messenger molecules (Dupont and Erneux 1997; Stamatakis and Mantzaris 2006).

In general, two are the routes for chemical exchange between astrocytes that are involved in ICWs: One is by intracellular diffusion of Ca^{2+} and the second messenger molecule inositol 1,4,5-trisphosphate (IP_3) through GJC; the other one is by Ca^{2+} -dependent ATP release from astrocytes into the extracellular space (Scemes and Giaume 2006). Both routes, although brought forth by different biochemical reactions, promote IP_3 -triggered Ca^{2+} -induced Ca^{2+} release (CICR) from the endo-

plasmic reticulum, which is the main mechanism of Ca^{2+} signaling in ICWs (Nedergaard et al. 2003). This is obvious in the intracellular route whereby IP_3 is supplied to resting cells via GJCs. In the extracellular route instead, this is mediated by the activation of metabotropic purinergic receptors which, akin to glutamatergic receptors (Chap. 5), trigger IP_3 production (and CICR) by G_q protein-mediated hydrolysis of phosphoinositol 4, 5-bisphosphate (Scemes and Giaume 2006).

From a modeling perspective, the fact that CICR is the main mechanism of Ca^{2+} signaling in ICWs allows replacing Eq. 7.1 by any model of CICR (Chap. 2). Moreover, it is also possible to neglect intracellular Ca^{2+} diffusion because free Ca^{2+} is rapidly buffered in the astrocyte cytosol, thereby minimally leaking through GJCs (Allbritton et al. 1992; Sneyd et al. 1998; Höfer et al. 2002). This allows to simplify Eq. 7.1 by setting $\mathcal{D}^a_i = 0$ and only leaves to specify s_i and Eq. 7.2. With this regard, both intracellular IP_3 and extracellular ATP can contribute together to ICW, with their relative involvement likely depending on regional, developmental, and experimental conditions (Scemes and Giaume 2006). Nonetheless, because hereafter we aim to characterize how different connections between astrocytes could affect ICW propagation, we limit our analysis to the consideration of GJC-mediated IP_3 diffusion only. The reader who is interested in modeling purinergically mediated ICWs may refer to Bennett et al. (2005) and MacDonald et al. (2008) for astrocyte network models that consider ATP signaling only, or alternatively to Iacobas et al. (2006), Stamatakis and Mantzaris (2006), Kang and Othmer (2009), and Edwards and Gibson (2010) for models that include extracellular ATP signaling in combination with intracellular IP_3 diffusion.

7.2.2 Gap Junction-Mediated IP_3 Diffusion

In its most general form, the flux of IP_3 (I) mediated by diffusion from one astrocyte i to a neighboring one j (J_{ij}) can be thought as some function ϕ of the IP_3 gradient between the two cells, i.e., $\Delta_{ij}I = I_i - I_j$ (Crank 1980), so that

$$J_{ij} = \phi(\Delta_{ij}I) \quad (7.3)$$

In the simplest scenario of short distance and/or fast diffusion, the intracellular environment along the pathway from cell i to j may be assumed homogeneous so that ϕ is linear (Sneyd et al. 1994; Falcke 2004), and J_{ij} is accordingly described by Fick's first diffusion law, i.e.,

$$J_{ij} = -F_{ij} \cdot \Delta_{ij}I \quad (7.4)$$

where F_{ij} is the diffusion coefficient. In practice, however, IP_3 diffusion between astrocyte somata could be more complicated. This is because connections between astrocytes through GJCs are mostly at the cell distal processes (Giaume et al. 2010) whose complex morphology and narrow intracellular space (Witcher et al. 2007; Pivneva et al. 2008) could considerably hinder IP_3 diffusion from/to somata. More-

over, GJC s cluster at discrete sites of these processes (Nagy and Rash 2000), thereby constraining the diffusion pathway of IP₃ from one cell to another. Finally, IP₃ production and degradation in the processes could either promote IP₃ transfer between cells or hamper it. In this fashion, the ensemble of astrocytic processes and GJC s interposed between cell somata could equivalently be regarded as a diffusion barrier for IP₃ exchange between cells, and accordingly, IP₃ diffusion between cells could be inherently nonlinear. This scenario is further substantiated by growing experimental evidence suggesting that GJC permeability could be actively modulated by various factors, including different second messengers (Harris 2001). With this regard, the permeability of Cx43, a predominant connexin in astrocytic GJC s (Nagy and Rash 2000), could be modulated, for example, by phosphorylation by protein kinase C (Bao et al. 2004; Sirnes et al. 2009; Huang et al. 2013). Because the same kinase also takes part in IP₃ degradation as well as in Ca²⁺ signaling (Codazzi et al. 2001; Irvine and Schell 2001), this possibility ultimately hints that GJC permeability could also depend on IP₃ signaling, whose dynamics is notoriously nonlinear (Chap. 5).

The above arguments support the choice of a nonlinear ϕ in Eq. 7.3. With this regard then, we may assume that IP₃ diffusion between two astrocytes, i and j , is a threshold function of the IP₃ gradient between somata of those cells, whose strength is bounded by the maximal GJC permeability. In this way, a possible expression for J_{ij} is (Goldberg et al. 2010):

$$J_{ij} = -\frac{F_{ij}}{2} \left(1 + \tanh \left(\frac{|\Delta_{ij} I| - I_\theta}{\omega_I} \right) \right) \frac{\Delta_{ij} I}{|\Delta_{ij} I|} \quad (7.5)$$

where I_θ represents the threshold gradient for which effective IP₃ diffusion occurs, whereas ω_I scales how fast J_{ij} increases (decreases) with $\Delta_{ij} I$ (see Fig. 7.1c). The parameter F_{ij} , which in the linear approximation sets the slope of J_{ij} (Eq. 7.4), here fixes instead the magnitude of the maximum diffusion flux.

7.2.3 Network Topology

We have introduced so far a general framework to model individual astrocytes (as nodes) of the network (Eqs. 7.1 and 7.2) and their connections by GJC-mediated exchange of IP₃ (Eq. 7.5). In order to complete our description of the astrocyte network, we must then specify the connections of each cell with others in the network.

Generally speaking, astrocytes networks can develop in one, two, or three dimensions. The simplest scenario of 1D networks, that is astrocyte chains, is useful to investigate how cellular properties could affect ICWs. With this regard, for example, cellular mechanisms controlling CICR rate (Höfer et al. 2001; Ullah et al. 2006b), the type of encoding by Ca²⁺ oscillations (Goldberg et al. 2010), or GJC permeability (Matrosov and Kazantsev 2011), have been shown to critically control the number of astrocytes recruited by ICWs. These results have also been confirmed by

2D astrocyte network models that are a valuable tool to investigate the rich variety of patterns of propagation of astrocytic ICWs observed in cell cultures (Sneyd et al. 1994, 1995a,b; Sneyd and Sherratt 1997; Sneyd et al. 1998; Höfer et al. 2002; Shuai and Jung 2003; Dokukina et al. 2008). The vast majority of these models, however, assumes a simplified arrangement of astrocytes on a regular lattice focusing on the CICR nonlinearity to exploit complex modes of ICW propagation. Only few studies have explored instead the potential role of network topology on ICW nucleation and propagation. Dokukina et al. (2008) considered, for example, small ensembles of three or four interconnected astrocytes, showing that only some connection schemes, among all possible ones, can favor ICW generation, while variations in GJC permeability can hamper ICW propagation regardless. More recently, Wallach et al. (2014) and Lallouette et al. (2014) attempted to extend this analysis to large 2D and 3D networks with the aim to derive principles of astrocyte ICW propagation driven by network topological features. The main results of these two studies are reproduced in the next section to illustrate our modeling approach.

7.3 Biophysical Modeling of Intercellular Ca^{2+} Waves

7.3.1 Ca^{2+} Signaling in Mixed Neuronal and Astrocytic Cultures

As a first example of the application of our modeling approach introduced in the previous section, let us consider the task of modeling Ca^{2+} signaling in cultured mixed neuronal and astrocytic networks. With this regard, we consider the experiments by Wallach et al. (2014) where this common experimental setup was used in combination with electrical stimulation of neural activity, at rates from 0.2 to 70 Hz, to trigger astrocytic Ca^{2+} signaling. In those experiments, bath perfusion with antagonists of astrocytic glutamate receptors was shown to block evoked Ca^{2+} activity in astrocytes, and so it was concluded that this signaling ensued from synaptically released glutamate, which likely activated astrocytic group I metabotropic glutamate receptors. Based on these considerations, we replace \mathbf{a} , \mathbf{s} , \mathbf{F} , and \mathbf{G} in Eqs. 7.1 and 7.2 by the biophysical model of glutamate-mediated astrocytic Ca^{2+} signaling discussed in Chap. 5 (see also De Pittà et al. 2009), so that the generic i th astrocyte in the cultured network is described by (Fig. 7.1b):

$$\frac{dC_i}{dt} = J_r(C_i, h_i, I_i) + J_l(C_i) - J_p(C_i) \quad (7.6)$$

$$\frac{dh_i}{dt} = \Omega_h(C_i, I_i) (h_\infty(C_i, I_i) - h_i) \quad (7.7)$$

$$\frac{dI_i}{dt} = J_\beta(C_i, G_i) + J_\delta(C_i, I_i) - J_{3K}(C_i, I_i) - J_{5P}(I_i) + \mathcal{D}_i^I (I_j, I_j | j \in \mathcal{N}_i) \quad (7.8)$$

where intercellular exchange of IP_3 in the last equation is taken equal to the sum of individual diffusion fluxes (Eq. 7.5) between astrocyte i and its connected neighbors, i.e.,

$$\mathcal{D}_i^I (I_i, I_j | j \in \mathcal{N}_i) = \sum_{j \in \mathcal{N}_i} J_{ij} \quad (7.9)$$

To complete the model, we assume that glutamate concentration (G_i) in the medium surrounding astrocytic receptors instantaneously increases for each electrical pulse delivered at time t_k , proportionally to the available synaptic glutamate resources (g), and exponentially decays between pulses at rate Ω_G , mimicking glutamate clearance by diffusion in the extracellular space (Clements et al. 1992), i.e., $G_i(t) \approx \sum_k g(t_k) \exp(-\Omega(t - t_k)) \Theta(t - t_k)$ where $\Theta(\cdot)$ is the Heaviside function (Wallach et al. 2014).

To build realistic astrocytic networks, we then borrow the argument that astrocytes likely tile the space of neuronal networks they are in by their non-overlapping anatomical domains (Bushong et al. 2002). In this fashion, adjacent astrocytes are more likely to be connected by GJC than cells that are far apart (Giaume et al. 2010). Accordingly, we consider immunostaining images of the cultured networks, like the one in Fig. 7.1a where somata of neurons and astrocytes are, respectively, marked by red and green circles, and construct the Voronoi diagram (gray lines) associated

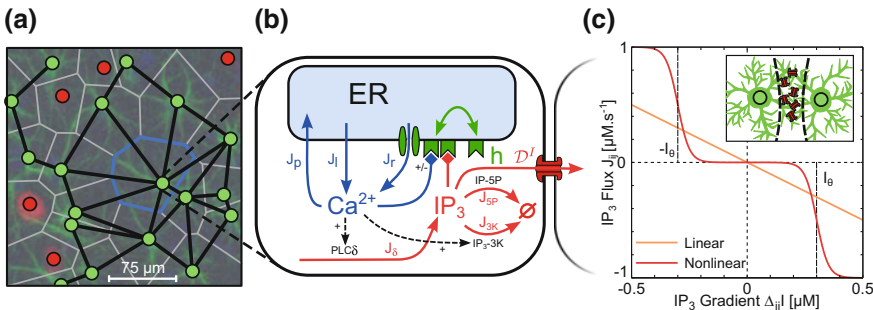


Fig. 7.1 Modeling astrocyte networks. **a** Double immunostaining of a cultured neuron-glia network by the neuronal marker NeuN (red) and the astrocytic marker GFAP (green). Astrocyte anatomical domains (like the one delimited in blue) are reconstructed by Voronoi tessellation (gray lines) of the network, only considering neurons and astrocytes activated by electrical stimulation (see Wallach et al. (2014) for details). Neighboring astrocytes are assumed to be connected by GJC when their Voronoi cells are contiguous. **b** Schematic representation of the biophysical network model. Individual astrocytes are described by the well-known Chl model for astrocytic Ca²⁺-induced Ca²⁺ release from the endoplasmic reticulum (De Pittà et al. 2009), while their coupling with neighboring cells is by intercellular IP₃ diffusion by GJC (D^I). In some simulations, we also consider glutamate-mediated IP₃ production by PLC β to account for synaptically evoked Ca²⁺ signals (not shown). **c** Differently from classic (linear) diffusion (yellow line), IP₃ diffusion between astrocytic somata is modeled by a nonlinear (sigmoid) function of IP₃ gradient between cells. (inset) This choice takes into account that most GJC (in red) are in the processes of astrocytes at the border of their anatomical region

Table 7.1 Parameters of the biophysical model (Eqs. 7.5–7.9)

Symbol	Description	Value		Units
		GChI	ChI	
<i>IP₃R kinetics</i>				
d_1	IP ₃ binding affinity		0.13	μM
O_2	Inactivating Ca ²⁺ binding rate	0.62	0.2	μM ⁻¹ s ⁻¹
d_2	Inactivating Ca ²⁺ binding affinity		1.049	μM
d_3	IP ₃ binding affinity (with Ca ²⁺ inactivation)		0.9434	μM
d_5	Activating Ca ²⁺ binding affinity		0.08234	μM
<i>Calcium fluxes</i>				
C_T	Total ER Ca ²⁺ content		2	μM
ρ_A	ER-to-cytoplasm volume ratio		0.185	—
Ω_C	Maximal Ca ²⁺ release rate by IP ₃ Rs	18.56	6	s ⁻¹
Ω_L	Maximal Ca ²⁺ leak rate	0.3416	0.11	s ⁻¹
O_P	Maximal Ca ²⁺ uptake rate	2.7846	0.9	μMs ⁻¹
K_P	Ca ²⁺ affinity of SERCA pumps		0.05	μM
<i>IP₃ production</i>				
O_δ	Maximal rate of IP ₃ production by PLCδ	0.4641	0.7	μMs ⁻¹
K_δ	Ca ²⁺ affinity of PLCδ		0.1	μM
κ_δ	Inhibiting IP ₃ affinity of PLCδ		1.5	μM
O_β	Maximal rate of IP ₃ production by PLCβ	1.105	—	μMs ⁻¹
K_G	Glutamate affinity of the receptor	1.3	—	μM
K_L	Ca ²⁺ /PKC-dependent inhibition factor	10	—	μM
K_{KC}	Ca ²⁺ affinity of PKC	0.6	—	μM
<i>IP₃ degradation</i>				
Ω_{5P}	Maximal rate of IP ₃ degradation by IP-5P	0.793	0.21	s ⁻¹
O_{3K}	Maximal rate of IP ₃ degradation by IP ₃ -3K	13.923	4.5	μMs ⁻¹
K_D	Ca ²⁺ affinity of IP ₃ -3K		1	μM
K_{3K}	IP ₃ affinity of IP ₃ -3K		0.7	μM
<i>IP₃ diffusion</i>				
F	GJC IP ₃ permeability	3.64	2	μMs ⁻¹
I_θ	Threshold IP ₃ gradient for diffusion	0.15	0.3	μM
ω_I	Scaling factor of diffusion		0.05	μM
<i>Synaptic glutamate release</i>				
Ω_f	Rate of synaptic facilitation	2	—	s ⁻¹
Ω_d	Rate of recovery of released synaptic vesicles	1	—	s ⁻¹
Ω_G	Glutamate clearance rate	60	—	s ⁻¹
U_0	Basal probability of synaptic glutamate release	0.25	—	—
ρ_C	Ratio of synaptic vesicles and mixing volumes	6.5 × 10 ⁻⁴	—	—
G_T	Glutamate content of readily releasable vesicles	200	—	mM
ρ_{so}	Glutamate spill over fraction to the astrocyte	0.075	—	—

with every cell in the network. This diagram partitions the network into as many regions as the cells taken into account, where each region may be regarded as an estimate of the anatomical domain (*blue lines*) of the cell that it contains (Wallach et al. 2014; Galea et al. 2015; Sánchez-Gutiérrez et al. 2016). Thus, considering only the regions associated with activated astrocytes, in our modeling, we assume neighboring astrocytes to be connected by GJCs only if their corresponding Voronoi regions share a border. We repeat this procedure for all cell cultures imaged by Wallach et al. (2014) and consider Ca^{2+} signals evoked by repetitive neural (synaptic) stimulation of our model astrocytes. Since we are interested in the possible influences of different connections between astrocytes on their Ca^{2+} response, we model all astrocytes in each culture identically, varying only their connectivity according to their Voronoi tessellation.

Time–frequency characterization of astrocytic Ca^{2+} responses recorded in experiments by Wallach et al. (2014) is shown in Fig. 7.2a, where two classes of responses may be recognized. *Type I* responses (*top row*) are characterized by astrocyte activation at relatively high frequency of neural activation (*top bars*), while the frequency of Ca^{2+} oscillations does not significantly change as the rate of neural stimulation increases. *Type II* responses instead can be observed for slightly lower frequencies of neural activation (*bottom row*), but are distinguished by Ca^{2+} oscillations whose frequency increases with neural stimulation, reaching values that are generally higher than in type I responses.

Consideration of the distribution of the maximum frequency of Ca^{2+} oscillations of all recorded responses in Fig. 7.2b shows that roughly 80% of recorded astrocytes exhibited responses of type I (*blue bars*), with Ca^{2+} oscillating on average at most at ~ 0.1 Hz (*left peak of the dashed curve*), while the remaining astrocytes displayed type II Ca^{2+} responses (*red bars*), with approximately doubled average maximum frequency, i.e., ~ 0.2 Hz (*right peak of the dashed curve*). In parallel, it may be appreciated from the *inset* how this maximum frequency of Ca^{2+} oscillations inversely correlates with the rate of neural stimulation, with high-frequency/type II-like Ca^{2+} oscillations triggered by lower rates of neural stimulation than low-frequency/type I-like oscillations.

To check consistency of our modeling approach, we reproduce in Fig. 7.2c, d the previous results, yet based on Ca^{2+} responses generated by numerical simulations of our network models built by the procedure above described. It may be appreciated how, despite some inevitable quantitative differences, these figures qualitatively reproduce the essential features of experimental observations on the two types of astrocytic Ca^{2+} responses presented in Fig. 7.2a, b and thereby prove the effectiveness of our approach in modeling Ca^{2+} signaling in cultured neuron–glial networks.

To characterize the effect of astrocytic connectivity on individual Ca^{2+} responses, we next consider the maximum frequency of astrocytic Ca^{2+} oscillations simulated for different rates of neuronal stimulation, distinguishing among responses based on the number of connections (k) of individual astrocytes to unstimulated neighbors—the reason of this specific choice of neighbors will be clarified in the following sections. The results of this analysis are reported in Fig. 7.2e where three observation may be made. First, it may be appreciated how unconnected astrocytes ($k = 0$, *dark*

blue curve) display the highest oscillation frequency for all rates of neural stimulation. On the contrary, as the number of connections to unstimulated neighbors increases, the maximum frequency of oscillations decreases. Second, the threshold rate of neural stimulation to trigger astrocyte Ca^{2+} activation tends to increase with the number of connections, being as low as ~ 2 Hz for unconnected astrocytes (*leftmost blue circle*) while increasing up to ~ 10 Hz for cells with $k = 4$ unstimulated connected neighbors (*leftmost downward red triangle*). Finally, the shape of the curves for different k

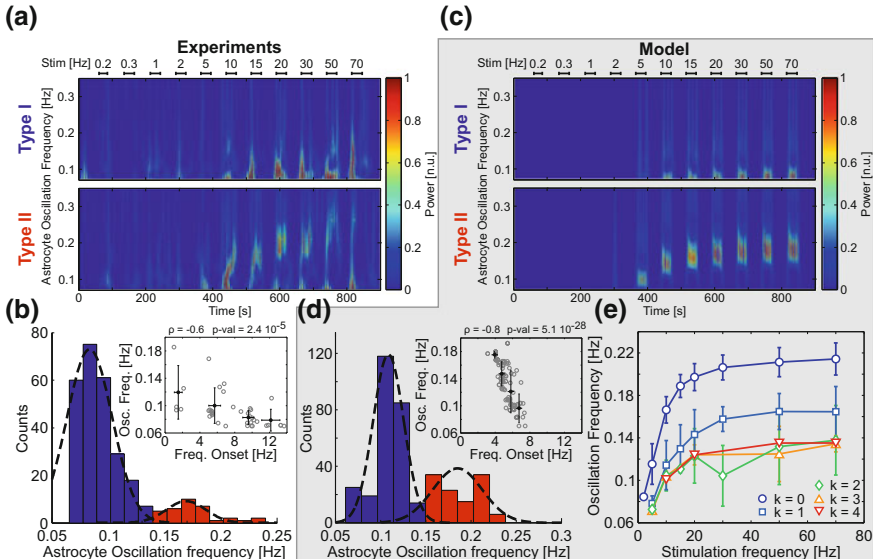


Fig. 7.2 Regulation of Ca^{2+} oscillations in individual astrocytes by GJCs. **a** Time–frequency analysis of Ca^{2+} oscillations evoked in individual astrocytes in cell cultures by repetitive electrical stimulation of neurons at different rates (“Stim.”, top bars). Some astrocytes display low-frequency oscillations (Type I responses, top row), while others show higher oscillation frequencies that increase with the rate of neural stimulation (Type II responses, bottom row). **b** Distribution of maximal frequencies of recorded astrocytic Ca^{2+} oscillations. Type I oscillations (blue bars) and Type II responses (red bars) are neatly separated and fitted by Gaussian distributions with different mean and variance (black dashed curves). (inset) The frequency of Ca^{2+} oscillations is negatively correlated with the threshold rate of neural stimulation (“Onset freq.”) required to trigger them, so that high-frequency/Type II responses are generally observed at lower onset rates of neural activation than low-frequency/Type I responses. Gray circles denote single astrocytic responses; black dots represent means for representative onset rates; error bars denote standard deviation. **c, d** Results from numerical simulations of astrocytic networks reconstructed by immunostaining images (see Fig. 7.1). **e** Maximum frequency of simulated Ca^{2+} oscillations as a function of the rate of neural stimulation for astrocytes with a different number of connections with unstimulated neighbors (k). Increasing the stimulus rate increases the frequency of Ca^{2+} oscillations which plateaus for high rates of stimulation, independently of k . The height of this plateau, however, strongly depends on the number of connections between astrocytes so that unconnected astrocytes ($k = 0$) tend to oscillate much faster than connected ones ($k > 0$). Data points \pm errorbars denote mean values \pm standard deviation for $n = 130$ simulated astrocytes. Adapted from Wallach et al. (2014)

values changes. For those astrocytes characterized by $k \leq 3$, the maximum frequency of Ca^{2+} oscillations nonlinearly increases with the rate of neuronal stimulation, reaching values as high as ~ 0.2 Hz in unconnected ($k = 0$) cells. But this increase is progressively reduced as k grows larger, till it becomes almost negligible as in the case of astrocytes with $k = 4$ (*red curve*), for which the maximum frequency of Ca^{2+} oscillations is ~ 0.1 Hz, independently of the rate of neural activity.

Combining these considerations with the experimental results in Fig. 7.2a, b, it is striking to correlate unconnected astrocytes, or astrocytes with a low number of unstimulated connected neighbors, with low onset rate/high oscillation frequency/type II responses, and vice versa, astrocytes with a high number of unstimulated connected neighbors with high onset rate/low oscillation frequency/type I responses. At the lower extremum of this spectrum of astrocytic connectivity, we find unconnected astrocytes, which represent a minority, up to $\sim 20\%$ of astrocytes in cell cultures (Rouach et al. 2000), to likely account for the 0.2 Hz peak in the distribution of Ca^{2+} oscillations in Fig. 7.2b. Conversely, at the higher extremum of the spectrum, we find those astrocytes with $k = 4$, insofar as they could mainly account, together with some astrocytes with $2 \leq k < 4$, for the 0.1 Hz peak of that distribution.

To summarize, our hitherto analysis hints that the way astrocytes are connected can affect how they respond to neural activity, controlling the threshold neural stimulation required for their activation and the frequency of ensuing Ca^{2+} oscillations (Wallach et al. 2014). These results have been obtained, however, in a somewhat simplified setup which is that of 2D-like cultured astrocyte networks. In practice, astrocytes are organized in three-dimensional networks in the brain; thus, we follow extend our biophysical modeling approach to address how topological differences in 3D networks could ultimately influence astrocytic Ca^{2+} activity.

7.3.2 *Ca^{2+} Wave Propagation in 3D Astrocyte Networks*

To model realistic 3D astrocyte networks we need to specify not only the topology of these networks but also, preliminarily, the arrangement of all cells in the 3D physical space. For 2D-like networks, such as the cultured networks modeled in the previous section, this task is eased by the possibility to exactly map every cell position, for example, by immunostaining and post-fixation optical microscopy of the network. However, this information is currently not accessible experimentally for 3D astrocytic networks, although recent advances of connectomics could soon fill in this gap (Kasthuri et al. 2015). On the other hand, astrocyte arrangement in a number of brain regions has recently been characterized on statistical bases, and we follow base our modeling on these data as originally described by Lallouette et al. (2014).

We consider a pool of $N = 11^3$ astrocytes modeled by Eqs. 7.6–7.8 and position them on a cubic lattice with internode distance a . We then jitter each cell location in the lattice by Gaussian noise with zero mean and variance σ^2 . In doing so, we choose a and σ^2 to minimize the squared error with respect to experimental values of mean

Table 7.2 Spatial and topological parameters of the astrocyte network model (see Appendix 1)

Symbol	Description	Values			Units
		Min.	Step	Max.	
<i>Spatial organization</i>					
a	Internode distance	70			μm
σ^2	Variance of the Gaussian noise	55			μm
<i>Network topology</i>					
k	Degree of regular networks	3	1	15	–
d	Linking distance for link-radius networks	80	5	120	μm
r_c	Spatial parameter for spatial scale-free networks	2	1	4	μm
		5	20	105	μm
m_{sf}	New links for spatial scale-free networks	2	1	5	–
l	Linking distance for shortcut networks	1	1	3	–
p_s	Edge rewiring probability for shortcut networks	0	0.02	0.1	–
		0.2	0.1	0.4	–
p	Linking probability for Erdős-Rényi networks	$\frac{5}{N-1}$	$\frac{1}{N-1}$	$\frac{15}{N-1}$	–

(50 μm), minimum (20 μm), and coefficient of variation of cell distance (~ 0.25) (Sasaki et al. 2011, see Table 7.2 for specific parameter values). After positioning astrocytes in the physical space, we specify their connections, considering different topologies (Fig. 7.3a), ranging from (i) strongly spatially constrained networks such as *link-radius networks*, where an astrocyte connects to all cells located within a given distance from its center, to (ii) completely spatially unconstrained, random networks of *Erdős-Rényi topology*. In between these extrema, we also consider (iii) *regular-degree networks* where each astrocyte connects to its k nearest neighbors, where k is the network *degree* k ; (iv) *shortcut networks* are obtained by rewiring a fraction of the connections (chosen at random) of a regular-degree network, replacing the destination cell of the original connections by a randomly chosen cell of the network (independently of the distance); and (v) *spatial scale-free networks* where astrocyte degree follows a power-law distribution dependent on cell degree and distance.

Let us now consider the propagation of ICWs in the model networks and study how the extent of this propagation, quantified by the number of astrocytes activated at least once by an ICW (N_{act}), depends on network topology. With this aim, we trigger ICW propagation in our model networks stimulating CICR in the cell in the center of the 3D space of the network to minimize boundary effects (see Appendix 1 for details). Two examples of ICWs triggered in this fashion are shown in Fig. 7.3b for two different regular-degree networks. The difference in the number of activated cells, represented by *green circles*, is striking and suggests that simple variations in network topology could account for large variability in ICW propagation. In this example, it suffices indeed to reduce the mean degree of the network from $\langle k \rangle = 6$ to $\langle k \rangle = 3$ to switch from local ICW propagation that recruits <100 astrocytes (*left panel*), to regenerative long-range ICW propagation which activates hundreds of cells (*right panel*).

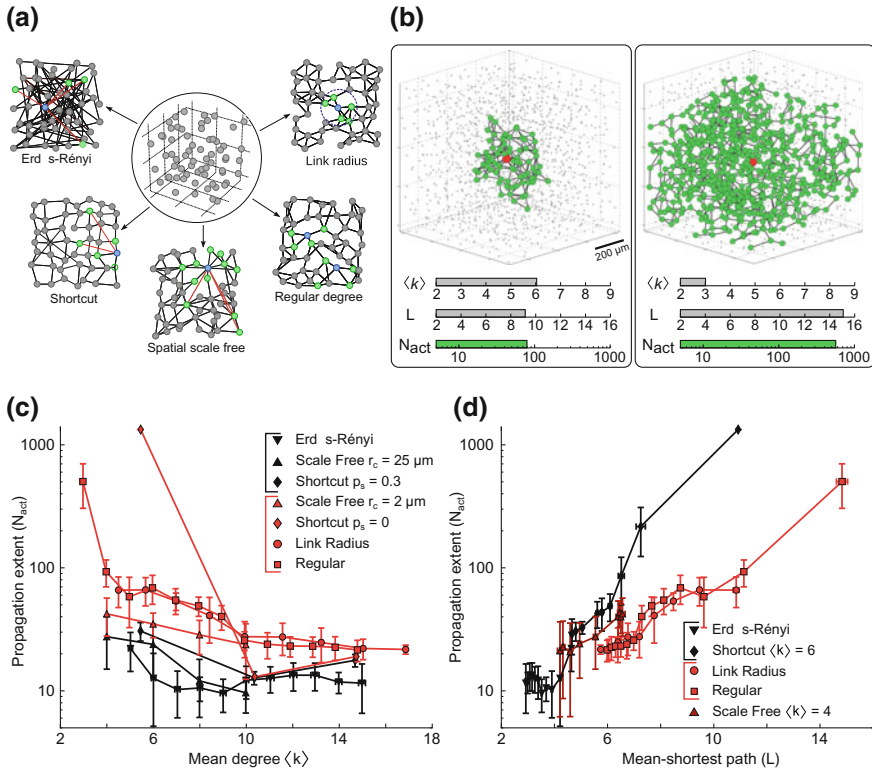


Fig. 7.3 ICW propagation in 3D astrocyte networks. **a** Modeling procedure. (Middle panel) Astrocytes (circles) are first positioned on a cubic lattice, and their positions are randomly jittered to match experimentally derived statistics of intercellular distances. (Other panels) Then, they are connected by GJC (black lines) according to different topologies (shown in 2D for clarity). Red links denote long-distance connections; cells in green are connected neighbors of blue cells. **b** Simulations of ICWs in two regular networks with different mean degree ($\langle k \rangle$) and mean shortest path length (L). Both networks contained the same number of identical cells ($N = 11^3$), and ICW stimulation was delivered to the central red cell in the same fashion (Appendix 1), so that the tenfold difference in the number of cells activated by the two ICWs (N_{act} , green circles) only depended on different connections between the two networks. **c** Extent of ICW propagation as a function of the network's mean degree $\langle k \rangle$ and **d** mean shortest path L . In both cases, spatially constrained topologies (red markers, e.g., link radius, regular degree and shortcut with $p_s = 0$ or $\langle k \rangle = 4$) can support ICW propagation up to several hundreds of astrocytes, whereas spatially unconstrained topologies cannot (black markers, e.g., Erdős-Rényi, shortcut with $p_s > 0$, scale-free). Scale-free networks in **(d)** (dark red upward triangles) can either be spatially constrained or unconstrained, depending on the value of r_c . Data points \pm errorbars correspond to mean values \pm standard deviation over $n = 20$ different realization of the network for fixed statistical parameters. Adapted from Lallouette et al. (2014). Model parameters as in Table 7.1

The dependence of ICW extent of propagation on the network's mean degree ($\langle k \rangle$), namely on the average number of connections per astrocyte, is further investigated in Fig. 7.3c for all network topologies. It may be appreciated how ICW propagation generally decreases with larger $\langle k \rangle$: that is, increasing astrocytic connectivity hinders ICW propagation in our networks, independently of their topology. A closer inspection of the figure, however, allows distinguishing between two classes of networks based on ICW propagation: spatially unconstrained (*black* markers) versus spatially constrained networks (*red* markers). Here, we dub as “spatially unconstrained” those networks that can have long-distance connections, but where ICWs activate only few tens of astrocytes. These include, for example, Erdős-Rényi networks (*black downward triangles*), scale-free networks (*black upward triangles*), or shortcut networks with rewiring probability $p_s = 0.3$ (*black diamonds*). Conversely, “spatially constrained” networks include link-radius (*red circles*) or regular-degree networks (*red squares*), as well as shortcut networks with $p_s = 0$ (*red diamonds*), whose connections between astrocytes are locally confined but ICWs can recruit >100 cells. Based on this classification, one may note that the difference between spatially constrained and spatially unconstrained networks in terms of the number of cells activated by ICWs can range up to ten folds.

A further useful measure to characterize network connectivity is the network's mean shortest path L . Specifically, this measure can be adopted to quantify the degree of spatial constraining of a network, inasmuch as L decreases when short-distance connections are rewired to long-distances ones in networks of the same size (Boccaletti et al. 2006). In this perspective, the differences in ICW propagation shown in Fig. 7.3b can also be correlated with the fact that the network in the right panel has a larger value of L and thus it contains more short-distance connections than the network in the left panel.

These considerations are further elaborated in Fig. 7.3d where the extent of ICW propagation is shown as a function of the network's mean shortest path for different astrocytic connectivities. In contrast with what is observed for the mean degree $\langle k \rangle$ (Fig. 7.3c), the extent of ICW propagation generally increases with L . Nonetheless, our distinction between spatially constrained and spatially unconstrained networks holds true. It may be noted in fact that, as L increases, only link-radius, regular-degree, and shortcut networks allow for ICWs that recruit >100 cells, whereas other network topologies do not. Large L values indeed imply dense local, short-distance connections between cells, which can only exist in networks whose topology is subjected to strong spatial constraints.

Overall, the analysis of ICW propagation in our 3D network models predicts that ICW propagation is hindered in astrocytes networks with a large average number of connections per cells and that contain long-distance connections (Lallouette et al. 2014). These results are somehow at odds with the notion, supported by studies on neuronal networks models, that small values of mean shortest path and long-distance connections could instead promote signal propagation (Zanette 2002; Roxin et al. 2004; Dyhrfjeld-Johnsen et al. 2007). This suggests that the principles at play in ICW propagation in astrocyte networks could be different from those involved in action potential propagation in neuronal networks. We focus on these principles in the next section.

7.3.3 Mechanisms of Ca^{2+} Wave Propagation

At the core of GJC-mediated Ca^{2+} wave propagation is Ca^{2+} -induced Ca^{2+} release from the endoplasmic reticulum in the activated astrocytes. This process requires an initial threshold concentration of intracellular IP_3 to be triggered (Chaps. 2 and 5). Since in unactivated (resting) astrocytes, endogenous production of IP_3 by PLC δ is equilibrated by IP_3 degradation, the only other mechanism that in our model can account for intracellular IP_3 variations is GJC-mediated IP_3 diffusion. Hence, only if the inward flux of IP_3 by diffusion is sufficiently higher than its outward flux, IP_3 can accumulate in the cytosol of an astrocyte up to the threshold to trigger CICR. When this occurs, the astrocyte gets activated and lies on the front of the ICW.

Consider the cartoon of ICW propagation in Fig. 7.4a, where cells **A**, **B**, and **E** lie on the front of an ICW (*green squares*) that is propagating from left to right through the portion of the depicted network. Because IP_3 accumulation in these cells must precede their activation, we can equally think of ICW propagation to be driven by the front of intercellular IP_3 accumulation. In this fashion, what determines if the ICW will propagate to cells **C** or **D** is whether IP_3 will next accumulate in those cells. With this regard, GJC-mediated diffusion of IP_3 is such that IP_3 travels against its gradient. Hence, IP_3 accumulation in **C** or **D** depends on two diffusive fluxes: (i) a large influx from activated cells **A**, **B**, and **E** (*thick red arrows*) driven by the supposedly larger IP_3 concentration found in those cells with respect to unactivated cells **C** and **D** and (ii) an outgoing flux to other unactivated cells in the network (*blue arrows*), which grows as intracellular IP_3 increases in **C** and **D**. In this example, the IP_3 flux incoming to **C** or **D** ensues from IP_3 diffusion from only two activated cells (or “ IP_3 sources”), i.e., **A** and **B** for **C**; and **A** and **E** for **D**. Similarly, because both **C** and **D** are connected only to two unactivated neighbors, these latter, akin to “ IP_3 sinks,” control the strength of the IP_3 flux coming out from **C** and **D**. In general though, it is reasonable to assume that the total inward and outward IP_3 fluxes of an astrocyte in the network depend on its number of connections and are thus correlated with the network’s mean degree $\langle k \rangle$.

To illustrate this, consider the same cells yet in a network where the mean degree is increased to $\langle k \rangle = 6$ (Fig. 7.4b). Astrocytes **A**, **B**, and **E** are now likely weaker sources of IP_3 for cells **C** and **D**, since there exist additional pathways for IP_3 diffusion out of them which compete with those from **A**, **B**, and **E** to **C** and **D** (*red arrows*). In turn, **C** and **D** receive less IP_3 so that they are less likely to reach the IP_3 threshold for CICR activation. This is also exacerbated by the fact that these cells are somehow larger IP_3 sinks, insofar as they experience a larger outward flux of IP_3 for their larger number of unactivated connected neighbors (*blue arrows*).

Similar arguments also hold in the case of a decrease of the network’s mean shortest path L . In the previous section, we saw how this quantity correlates with the existence of long-distance astrocytic connections. Accordingly, we present in Fig. 7.4c the same network of panel 7.4a except for rewiring the connection between **A** and **C** (*gray arrow*) by a long-distance connection between **A** and the astrocyte **F** (*dark red arrow*), which we imagine to be in some part of the network far from the

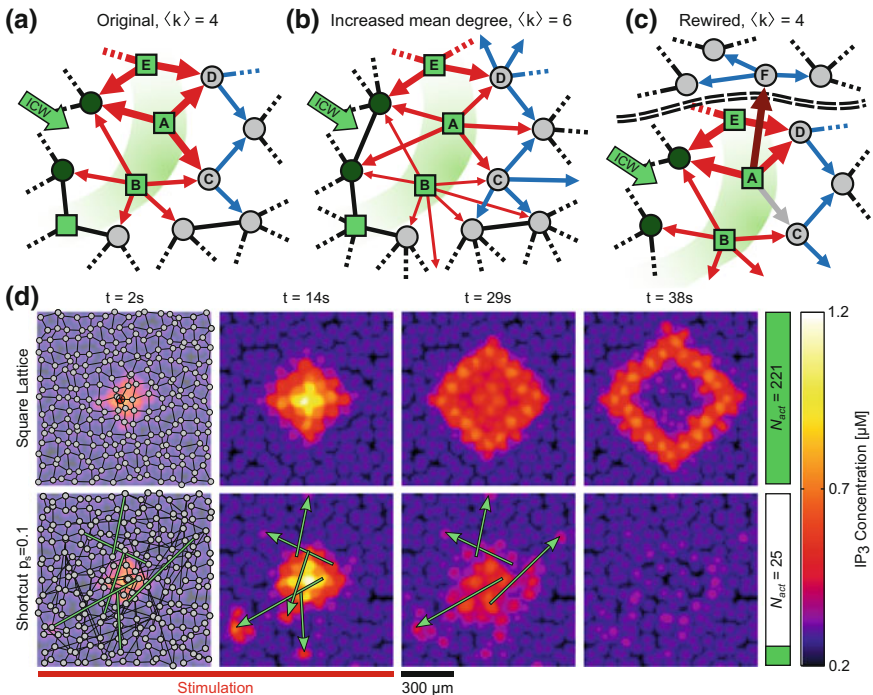


Fig. 7.4 GJC-mediated mechanism of ICW propagation. **a** Propagation of an ICW front (green squares) to an astrocyte depends on IP₃ fluxes mediated by IP₃ diffusion that comes in (red arrows) and out of the cell (blue arrows). Unactivated cells (gray circles) act as “IP₃ sinks,” thereby hindering intracellular IP₃ accumulation. In this fashion, compared with cell A, cell B is less likely to activate other cells for its larger number of connections with unactivated cells. Vice versa, cell D is more likely to get activated than cell C because it has fewer unactivated neighbors than this latter. **b** An increase of the network’s mean degree to $\langle k \rangle = 6$ introduces additional connections that reduce incoming IP₃ fluxes to cells C and D, making these cells less likely to get activated (and thus to get recruited by the ICW). **c** Similarly, replacing the local connection between A and C (gray arrow) by a long-distance connection between A and F (dark red arrow) makes cell C receive less IP₃, “dumping” the missing IP₃ flux to an unactivated region of the network far from the wave front (separated by double dashed lines). **d** Snapshots of intracellular IP₃ dynamics at different time instants in two 2D networks shown in the *leftmost panels*). In the shortcut network with $p_s = 0.1$, the presence of long-distance connections (green edges and arrows) makes IP₃ diffuse away from the wave front (*bottom row*, compare snapshots for $t = 14\text{s}$ and $t = 29\text{s}$). This ultimately results in a considerably lower number of astrocytes activated by an ICW (N_{act} , *rightmost vertical bars*) with respect to the square lattice. ICW propagation was triggered stimulating the astrocyte in red (*leftmost panels*) for $0 \leq t \leq 25\text{s}$ (*bottom red bar*). Adapted from Lallouette et al. (2014)

ICW front of propagation, and marked by the *dashed double line*. In this scenario, cell **C** is clearly less likely to get activated for the reduced IP_3 influx that it receives due to the missing connection with cell **A**. The IP_3 flux from **A** to **F** on the other hand is also likely not as effective in promoting CICR in cell **F** as it would be in **C**, not only because of a missing contribution to IP_3 influx in this cell from **B**, but also because cell **F** is in a remote part of the network and, as such, connected to many more unactivated cells than **C**. In other words, it is as if the introduction of the long-range connection between **A** and **F** prevented IP_3 from accumulating nearby the ICW front, dumping it in a remote, unactivated part of the network.

The interplay between the network's mean degree and mean shortest path in the regulation of IP_3 sources and sinks that control ICW propagation may be promptly elucidated by monitoring intracellular IP_3 dynamics during ICW propagation (Lallouette et al. 2014). Fig. 7.4d shows snapshots of this dynamics at increasing time instants since stimulation onset (at $t = 0$ in the *red cell*) for two different networks: a strongly spatially constrained network such as the square lattice with $\langle k \rangle = 4$ (*top row*), and a less spatially constrained network like a shortcut network (*bottom row*), with the same mean degree, yet with $\sim 10\%$ of connections being between astrocytes far apart (examples marked in *green*). It may be appreciated how the regular architecture of short-distance connections between cells of the square lattice promotes a compact front of IP_3 accumulation (*brighter spots* in the *top heat maps*) as the ICW propagates. Conversely, this front is quickly lost for $t > 14$ s in the shortcut network, due to the redistribution of IP_3 to remote unactivated regions of the network by long-distance connections (*green arrows* in the *bottom heat maps*).

Overall, our modeling of astrocyte networks predicts that the network's mean degree and mean shortest path could be important determinants of ICW variability of propagation inasmuch as they could control the astrocyte's propensity to activate and get recruited by an ICW. This propensity ensues from intracellular IP_3 balance which is regulated by a complex interplay of production, degradation, and diffusion fluxes brought forth by activated and unactivated cells. In particular, the number of unactivated neighbors of a given astrocyte could dramatically control its activation as they set the rate of IP_3 drain from this cell by diffusion. This also accounts for the results discussed in Sect. 7.3.1, where we put emphasis on the number of connections with unconnected neighbors as a critical factor to shape the type of Ca^{2+} response of an astrocyte. We can now explain the reason for this result hypothesizing that a cell connected with few unactivated neighbors is likely to accumulate IP_3 more easily than one with many unactivated neighbors. In this way, that cell not only is likely to get activated faster than the other, but also will display higher frequency of Ca^{2+} oscillations than the cell with many unactivated neighbors, since the frequency of these oscillations grows with intracellular IP_3 concentration in our model (Eqs. 7.6–7.8, but see also De Pittà et al. 2009). Type II versus type I responses are thus mirrored by these two cells characterized by a different degree of unactivated neighbors.

7.3.4 Comparison of Model Predictions with Experiments

An important prediction of our modeling is that the extent of ICW propagation could be highly variable in astrocyte networks with realistic spatially constrained topology, like link-radius or regular connectivities, solely depending on the network's mean degree $\langle k \rangle$. A fivefold decrease of $\langle k \rangle$ from 15 to 3, for example, could result in a 100-fold increase in the number of astrocytes recruited by an ICW, from few tens of cells to about 500 astrocytes (Fig. 7.3). Although no experiments have so far investigated the relationship between ICWs and network topology, there is contingent evidence that astrocytic connectivity could dramatically influence ICW generation and propagation.

Variability of ICW propagation observed in experiments of different astrocyte populations (Charles 1998; Scemes and Giaume 2006; Sasaki et al. 2011; Kuga et al. 2011) has indeed been suggested to depend not only on the experimental setup but also on heterogeneities in the connections between astrocytes (Scemes and Giaume 2006). These heterogeneities have well been characterized for astrocytes in the olfactory bulb which show preferential GJC coupling within rather than outside of glomeruli (Roux et al. 2011). And similar observations have also been made for astrocytes within somatosensory barrels (Houades et al. 2008) and in the stratum pyramidale of the hippocampus (Rouach et al. 2008). In the hippocampus in particular, ICWs could propagate for longer distance in the CA3 region than in the CA1 region (Dani et al. 1992), and it is tempting to speculate that, in light of our modeling, these differences could be due to the fact that CA3 astrocytes are known to be less coupled by GJCs (i.e., their $\langle k \rangle$ is smaller) than their CA1 homologues (D'Ambrosio et al. 1998).

In agreement with the latter hypothesis, is the evidence of reduced ICW propagation in cultures of astrocytoma cells whose coupling was increased by forcing expression of the GJC protein Cx43 (Suadicani et al. 2004). Moreover, the fact that ICWs are observed much more frequently in the developing brain (Parri et al. 2001; Weissman et al. 2004; Fiacco and McCarthy 2006; Scemes and Giaume 2006; Kunze et al. 2009) rather than in the brain of adult animals (Fiacco and McCarthy 2006; Scemes and Giaume 2006) could also be due to developmental differences in GJC expression. Cx30 expression in fact strongly develops between postnatal day 10 (P10) (Aberg et al. 1999) and the third week of life (Rouach et al. 2002). Before this period, neocortical astrocytes are known to be sparsely connected (Aberg et al. 1999) and display ICWs (Iwabuchi et al. 2002). Conversely, during and after this period, the extent of astrocytic ICW propagation seems to drastically reduce. For example, the same stimulation protocol that triggers long-distance ICWs in astrocytes in the CA1 region of the hippocampus before P10 does not after P10, when cell coupling by GJCs is increased (Aberg et al. 1999; Fiacco and McCarthy 2004).

There is also evidence that expression and permeability of GJC proteins, like Cx30 and Cx43, are regulated by neurons (Rouach et al. 2000; Koulakoff et al. 2008; Roux et al. 2011), possibly by extracellular K^+ (Pina-Benabou et al. 2001). Remarkably, increases of GJC coupling mediated by extracellular K^+ were shown to decrease ICW propagation in astrocyte networks (Scemes and Spray 2012), ultimately suggesting

that the (mean) degree of connections of astrocytes in networks is not fixed but rather depends on local conditions, possibly correlated to ongoing neural activity. Inasmuch as the number of connections of an astrocyte could dictate the characteristics of its Ca^{2+} response to neural activity (Sect. 7.3.1), the latter hypothesis opens to the scenario that astrocytes in a network could display different Ca^{2+} responses that depend on activity-dependent modulations of their connectivity. This variegated Ca^{2+} signaling could in turn account for variability of Ca^{2+} activation of individual cells, and ultimately reflect into different modes of recruitment of those cells by ICWs as well as in ICW generation and propagation themselves.

7.4 Simplified Modeling of Intercellular Ca^{2+} Waves

7.4.1 The UAR Astrocyte

The biophysical approach considered so far may be effective to model Ca^{2+} signaling and propagation with realistic qualitative features, but has the drawback of limited mathematical tractability for the strong nonlinearity born by the equations of IP_3 -triggered CICR (Eqs. 7.6–7.8). Moreover, it does not take into account some other aspects of astrocytic Ca^{2+} signaling such as, for example, its complementary spontaneous (stochastic) generation which may remarkably contribute to ICW nucleation (Skupin et al. 2008, but see also Chaps. 3 and 4). To fill in this gap, we present in the remaining part of this chapter, a further model of astrocytic ICW propagation that includes stochastic Ca^{2+} activation and is amenable to analytical tractability, while retaining elementary biophysical realism. The results following discussed were originally introduced by Lallouette et al. (2014) and Lallouette (2014).

We start from the consideration of “realistic” intracellular IP_3 and Ca^{2+} dynamics simulated by our biophysical model of Eqs. 7.6–7.8. Figure 7.5a shows IP_3 and Ca^{2+} traces associated with two ICWs that travel from astrocyte 1 (*top*) to astrocyte 2 (*bottom*) via GJC coupling (Eq. 7.5), respectively, for $20 < t < 40$ s and $110 < t < 120$ s. One can associate each cell, at any time, with one of three possible states: unactivated (U), activated (A), and refractory (R). In the unactivated state, an astrocyte is at rest, meaning that its intracellular IP_3 and Ca^{2+} concentrations are either at a low equilibrium, or subjected to some subthreshold dynamics without CICR. Hence, either astrocytes in our example are unactivated before the arrival of each ICW, i.e., for $t < 20$ s and for sometime $t < 110$ s.

As intracellular IP_3 crosses the threshold to trigger CICR (*dotted lines*), the astrocytes get activated, displaying a large pulse-like increase of their intracellular Ca^{2+} (*green-shaded windows*). For the previously discussed arguments, however, (Sect. 7.3.3), these cells can stay in this active state of CICR generation as long as IP_3 supply, by GJC-mediated diffusion from other cells in the network, is large

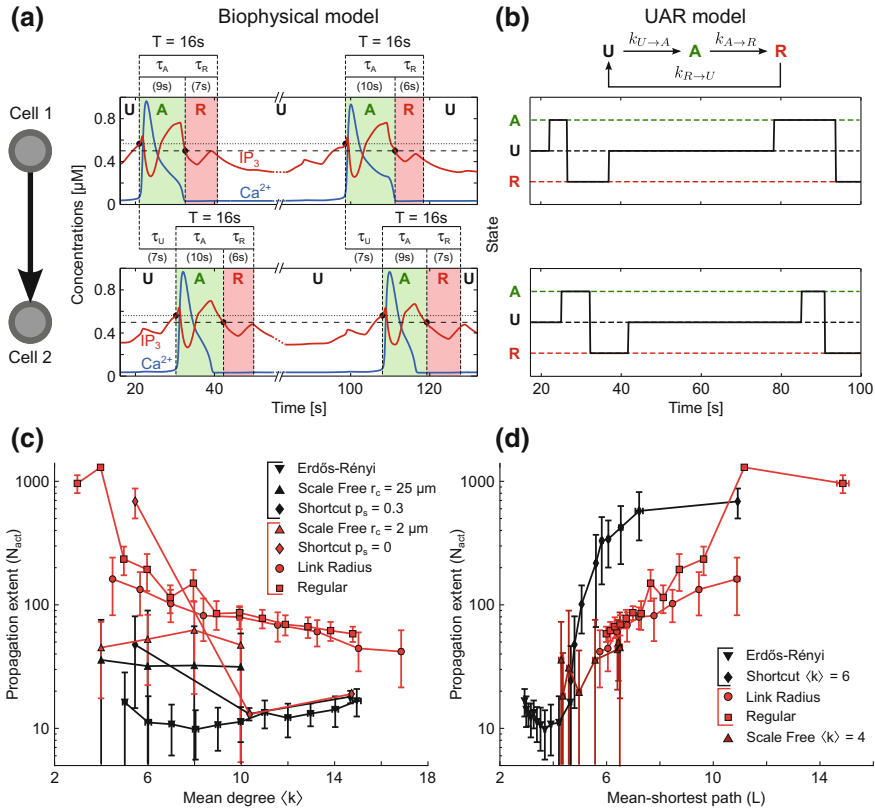


Fig. 7.5 UAR model of ICW propagation. **a, b** Recruitment of an astrocyte by an ICW may be regarded as a three-state process, as exemplified for two connected astrocytes (cell 1, *top row*; cell 2, *bottom row*). Astrocytes are in the unactivated state (U) when at rest. Upon arrival of an ICW, their intracellular IP₃ (red traces) crosses the threshold for CICR initiation (dotted line) and cell 1, followed by cell 2, get activated (A, green-shaded windows), which is marked by a pulse-like increase of intracellular Ca²⁺ in these two cells (blue traces). Following activation, each cell recovers to rest through a refractory period (R, red-shaded windows), when their intracellular IP₃ falls below a supply threshold (dashed line). Time constants of the transitions may be estimated as following: τ_U coincides with the delay between the Ca²⁺ increases in cell 1 and in cell 2; τ_A is estimated by the time interval from the beginning of the Ca²⁺ elevation to the point where IP₃ gets below the diffusion threshold; finally, τ_R is derived from $\tau_A + \tau_R = T$, where $T = 16\text{ s}$ is the minimum period of Ca²⁺ oscillations in the single astrocyte. Transition rates used in the simulations are obtained averaging over all τ values obtained by simulations of the biophysical model in Fig. 7.3. **c, d** ICW propagation for the same networks of Fig. 7.3 (panels C and D), where astrocytes are modeled instead by the UAR description. The extent of ICW propagation (N_{act} : number of activated astrocytes) generally mirrors qualitative characteristics of ICWs simulated in our biophysical network models. Data points \pm errorbars: mean values \pm standard deviation over $n = 20$ networks of similar topology. Parameters of the biophysical model and the UAR model are reported in Table 7.1 and Table 7.3, respectively. Adapted from Lallouette et al. (2014)

enough to guarantee intracellular accumulation of IP_3 up to the CICR threshold. This “threshold for IP_3 supply” is generally lower than the CICR threshold (*dashed lines*), and can roughly be estimated by the sum of the resting intracellular IP_3 concentration ($\sim 0.3 \mu\text{M}$ in our biophysical model) and the gradient $\sim 0.2 \mu\text{M}$ for which nearly no GJC-mediated IP_3 diffusion occurs (see Eq. 7.5 and Fig. 7.1c).

Following activation, when IP_3 drops below the supply threshold, either astrocytes are found in a refractory state (*red-shaded windows*), whereby they do not transmit IP_3 to other astrocytes but cannot get activated again yet. Finally, as IP_3 (and Ca^{2+}) levels approach their resting values, the cells recover to their unactivated state.

The cycling of an astrocyte through unactivated, activated, refractory and back to unactivated states can be formalized by a simple Markov model, dubbed “UAR model” after the initial of its three states, which is schematized on top of Fig. 7.5b. There, we assume constant rates $k_{A \rightarrow R}$ and $k_{R \rightarrow U}$, for the transition of the cell, respectively, from activated to refractory, and from refractory to unactivated, since these transitions are mainly dictated by the cell’s biophysical properties (Chap. 5). Accordingly, we set $k_{A \rightarrow R} = 1/\bar{\tau}_A$ and $k_{R \rightarrow U} = 1/\bar{\tau}_R$, where $\bar{\tau}_A$ is the average time of astrocytic activation during ICW propagation, and $\bar{\tau}_R = T - \bar{\tau}_A$ is the average refractory period, estimated from the minimum period (T) of Ca^{2+} oscillations in a single astrocyte.

In contrast, the transition from the unactivated state to the activated one depends on the cell’s intracellular IP_3 balance which is predominantly altered in resting conditions by IP_3 diffusion from other cells taking part in ICW propagation. Thus, we model the rate of this transition, i.e., $k_{U \rightarrow A}$, as a function of the states of the cell’s neighboring cells. With this aim, we define the efficacy of the i th astrocyte to supply IP_3 by

$$\beta_i(t) = \begin{cases} 1/N_i^U(t) & \text{if } i \text{ is in the A state at time } t \\ 0 & \text{otherwise} \end{cases} \quad (7.10)$$

where $N_i^U(t)$ represents the number of unactivated neighbors of i at time t . The conditional definition of $\beta_i(t)$ is motivated by our previous analysis where we noted that only activated cells could effectively supply IP_3 to unactivated cells that are found next on the pathway of a propagating ICW. The exact functional form $\beta_i(t)$ is inspired instead by the observation that the magnitude of IP_3 supply from an activated astrocyte is inversely proportional to the number of unactivated neighbors, in the assumption of identical neighbors and GJC connections of these latter with cell i (see Sect. 7.3.3).

Building on our previous analysis, we assume that a given cell i gets activated only if the cumulative IP_3 supply from its GJC-connected neighbors (\mathcal{N}_i in total) exceeds some threshold for activation ϑ_i . Accordingly, we define its rate of transition from resting to activated as

$$k_{U \rightarrow A}(t) = \begin{cases} 1/\bar{\tau}_U & \text{if } \sum_{j \in \mathcal{N}_i} \beta_j(t) \geq \vartheta_i \\ 0 & \text{otherwise} \end{cases} \quad (7.11)$$

Table 7.3 UAR model parameters

Symbol	Description	Values	Units
$\bar{\tau}_U$	Average time needed to activate an astrocyte	7	s
$\bar{\tau}_A$	Average activation time of an astrocyte	9	s
$\bar{\tau}_R$	Average refractory time of an astrocyte	6.5	s
m	Slope of the relationship between k_i and ϑ_i	0.02	—
q	Intercept of the relationship between k_i and ϑ_i	0.205	—

where $\bar{\tau}_U$ is estimated from simulations of the biophysical model as the average time needed to activate an astrocyte during ICW propagation, starting from resting intracellular IP₃ (and Ca²⁺) levels. The threshold ϑ_i can instead be estimated by the minimum number of activated versus unactivated astrocytes that are connected to a given cell and are required for its activation. In particular, it may be shown that this threshold is almost linearly dependent on the cell's number of connections k_i , so that we approximate it here by

$$\vartheta_i = m \cdot k_i + q \quad (7.12)$$

where the parameters m and q are numerically estimated and depend on the nature of GJC connections (Lallouette et al. 2014).

The UAR model built in the above fashion is reminiscent of SIR models of disease spread (Newman 2003), and SER models of activity propagation in excitable media (Müller-Linow et al. 2008), yet with an important difference. While in SIR and SER network models, activation of one node of the network generally depends on that node's immediate neighbor characterized by one degree of separation from the node, in our description, activation of an astrocyte also depends on cells with two degrees of separation from it. For the definition of β_i (Eq. 7.10), these cells control in fact the extent at which the connected neighbors of that astrocyte can supply it by enough IP₃ to trigger its activation.

To verify that the UAR model can reproduce essential predictions provided by our previous biophysical model, we use it to simulate ICW propagation in 3D networks with the same topological features as those considered in Fig. 7.3. The results of these simulations are reported in panels c and d of Fig. 7.5, where it may be seen that the functional dependence of the extent of ICW propagation on the network's mean degree ($\langle k \rangle$) and mean shortest path (L) qualitatively resembles the behavior previously observed for our biophysical model, both in spatially constrained and spatially unconstrained networks (cp. panels c and d in Fig. 7.3). The only exception, possibly due to simplifying modeling assumptions on the choice of β , is represented by scale-free networks with short-distance connections ($r_c = 2 \mu\text{m}$, upward red triangles in Fig. 7.5b) which allow ICW propagation for >100 cells for low $\langle k \rangle$ values, whereas in the biophysical model did not.

7.4.2 Shell Propagation Model

A close inspection of Figs. 7.3c and 7.5c reveals a peculiar phenomenon: two network types with very similar spatially constrained topologies, like cubic lattices obtained from shortcut networks with $p_s = 0$ (and $l = 1$, see Appendix 1), and regular-degree networks with $\langle k \rangle = 6$, exhibit, however, a very different behavior, with the former supporting ICWs that could activate tenfold more cells than in the latter (Fig. 7.6a, *pink* versus *dark green bars*). It may be hypothesized that this is due to the fact that cubic lattices with $\langle k \rangle = 6$ have a mean shortest path $L \approx 11$, while regular-degree networks with same $\langle k \rangle$ values associate with $L \approx 8.8$. Nonetheless, as shown by the *light green bar* of the histogram in Fig. 7.6a, reducing $\langle k \rangle$ to 4 in these latter networks, so as to obtain L values comparable to those in cubic lattices, only marginally increases the extent of ICW propagation in regular-degree networks. This ultimately suggests that the topological differences in terms of different $\langle k \rangle$ and L values cannot fully explain variability of ICW propagation, and thus, other aspects of the network's architecture must be at play.

Both cubic lattices and regular-degree networks were constructed in a similar way: in the former, astrocytes first were linked to their nearest neighbors and their positions were then jittered; in the latter, the order of these operations was reversed. Thus, differences in their architectures are subtle and likely relate to the details of local connections of individual cells with their neighbors. To describe these differences, we introduce the notion of propagation shell. Specifically, we define the r th shell with respect to a reference astrocyte, as the ensemble of cells whose topological distance from that astrocyte is r .

Figure 7.6b shows the first four shells of a reference *umber* astrocyte (labeled by '0') in a square lattice. The first shell (*brown* cells with '1' label) is made of the astrocytes that are directly connected with astrocyte '0'. The second shell (*orange* cells with label '2') is composed instead by all the cells with two degrees of separation from the reference astrocyte, that is the shortest path to go from them to astrocyte '0' is 2; the third shell (*light orange*) is made of all astrocytes with three degrees of separation from cell '0' and so on.

When stimulating astrocyte '0', the ICW that generates from this cell and propagates to its periphery may be thought as the result of the progressive activation of shells 1, 2, and so on. Figure 7.6c illustrates this concept, showing in *green* the fraction of astrocytes per shell that get activated by the ICW. It may be noted from Fig. 7.6d that the cells in the first two shells are nearly all activated but, as the wave propagates to outer shells (i.e., $r > 2$), the ratio of activated cells per shell (ρ_r) quickly drops, ultimately halting ICW propagation beyond the fourth shell.

By the same arguments previously exposed in Sect. 7.3.3, what determines the extent of activation of a shell, and whether an ICW propagates to the next one, is respectively, the IP_3 supply to and from that shell. This supply can be estimated by means of the UAR model, resolving for the network's shell structure, including the number of cells per shell (N_r), and the fraction of activated astrocytes per shell (ρ_r) against the number of unactivated cells therein (\hat{N}_r). Denoting by Ψ_{r+1}^{tot} the average

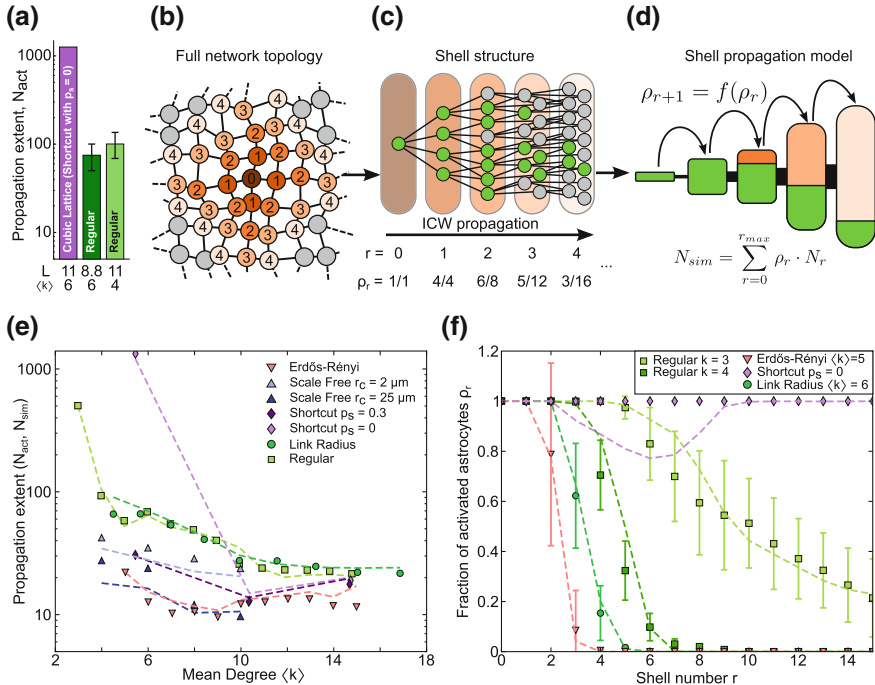


Fig. 7.6 Shell model of ICW propagation. **a** Quantification of ICW propagation by the number of activated cells (N_{act}) in cubic lattices (pink bar) versus regular networks (green bars). The tenfold larger number of activated astrocytes in cubic lattices than in regular networks cannot simply be ascribed to differences in the mean degree ($\langle k \rangle$) and shortest path length (L , bottom values). Cubic lattices were constructed by shortcut networks with $p_s = 0$ and $l = 1$ (see Appendix 1). **b–d** Shell model of propagation. **b** Sample decomposition of a network neighbor around cell ‘0’ (umber circle) by four concentric shells (colors/labels from brown/‘1’ to pale orange/‘4’). **c** Nodes are grouped by their shell distance r from the reference cell ‘0’. In this fashion, ICW propagation is by activation of astrocytes (green circles) from inner to outer shells (i.e., from cell ‘0’ to shell ‘4’ and beyond). **d** At early stages of propagation, the fraction (ρ_r) of activated astrocytes per shell is close, if not equal to unity (i.e., all cells are activated – N^r cells in total per shell), but it decreases as the wave propagates through outer shells. For a given shell $r + 1$, this fraction can be recursively expressed as function of the fraction of activated cells in the inner shell r (top equation). The total number of activated cells by shell propagation of an ICW is quantified by N_{sim} (bottom formula). **e** The number of activated cells (N_{sim}) and **f** the fraction of activated cells (ρ_r) estimated by the shell model (dashed lines) are superimposed on values from simulations of biophysical networks (data points from Fig. 7.3c). The shell model of propagation well predicts ICW extent simulated by biophysical modeling. Model parameters as in Table 7.3

total IP₃ supply to an astrocyte in shell $r + 1$ from shell r , this quantity may be regarded as the sum of two terms in general: (i) an endogenous IP₃ supply by IP₃ production and diffusion from shell r , Ψ_r^{out} ; and (ii) an exogenous IP₃ supply to shell $r + 1$ directly due to the stimulation protocol, i.e., Ψ_{r+1}^{stim} – clearly, the farther the shell is from the stimulated cell, the lesser is the IP₃ directly supplied to it by the applied stimulus. That is

$$\Psi_{r+1}^{tot} = \Psi_r^{out} + \Psi_{r+1}^{stim} \quad (7.13)$$

Then, the IP₃ supplied by the r th shell can be thought to be proportional to the ratio between the number of activated astrocytes (or IP₃ sources) in that shell and the number of unactivated cells (or IP₃ sinks) in the proximal shell $r + 1$, i.e.,

$$\Psi_r^{out} = \rho_r \frac{N_r}{N_{r+1}} \cdot g(r, \rho_r) \quad (7.14)$$

where the multiplicative factor $g(r, \rho_r)$ accounts for the size of shells $r - 1$ and $r + 1$ and the connections of cells therein, with themselves and with cells in other shells. Finally, based on the previous equations, the fraction of activated cells in shell $r + 1$ is given by

$$\rho_{r+1} = \frac{1}{2} \left(1 + \tanh \left(\frac{\Psi_{r+1}^{tot} - \psi_\theta(\langle k \rangle)}{\delta} \right) \right) \quad (7.15)$$

where $\psi_\theta(\langle k \rangle)$ is homologous of the activation threshold ϑ in Eq. 7.11 for the r th shell. The fraction of activated astrocytes per shell is thus a sigmoid function of IP₃ supplied to that shell by inner shells. It approaches 1 when this IP₃ exceeds the threshold $\psi_\theta(\langle k \rangle)$, which corresponds to the ideal scenario of all cells in the shell being activated, and to an ICW that propagates to shell $r + 1$ in a perfectly regenerating fashion. Conversely, it tends to 0 when $\Psi_{r+1}^{tot} < \psi_\theta(\langle k \rangle)$, ensuing in partial ICW propagation to shell $r + 1$, which possibly preludes to wave death in the following shells. The slope of the transition between partial (vanishing) ICW propagation (i.e., $\rho_{r+1} \rightarrow 0$) and fully regenerative ICW propagation ($\rho_{r+1} \rightarrow 1$) is controlled by the parameter δ . The detailed derivation of Eqs. 7.13–7.15 may be found in the online Supplementary Text (Appendix 2).

Table 7.4 Shell model parameters

Symbol	Description	Values	Units
$\frac{\Omega_I}{F}$	Effective degradation rate	2.9883	–
S	IP ₃ supplied to the stimulated cell	2169.32	–
η	Power-law exponent	2.62	–
A	Slope of $\psi_\theta(\langle k \rangle)$	2.622×10^{-15}	–
B	Intercept of $\psi_\theta(\langle k \rangle)$	0.35061	–
δ	Slope of the shell activation function	0.05388	–

Using Eq. 7.15, we can recursively compute the activation ratio of concentric shells of ICW propagation, ultimately estimating the extent of ICW propagation without the need to simulate whole networks. Figure 7.6e reports the results of this estimation, where the extent of ICW propagation is quantified by the number of astrocytes expected to get activated by an ICW, i.e., $N_{sim} = \sum_r N_r \rho_r$. Comparison of N_{sim} values obtained by our shell description of ICW propagation (*dashed lines*) with those for the number of activated astrocytes from simulations of the biophysical model (*data points* from Fig. 7.6c) reveals a close correspondence of our analytical estimation with simulations. Further analysis (Fig. 7.6f) also shows that the estimated fraction of activated astrocytes per shell is in good agreement with the majority of data from ICW propagation simulated in biophysical network models.

Overall, the analysis presented in this section puts emphasis on the importance of regional features of cell connectivity mirrored by the shell structure of astrocyte networks, as a crucial factor in shaping ICW propagation. This propagation appears to depend on the shell-to-shell GJC-mediated diffusion IP_3 by Eq. 7.15 in a strongly nonlinear fashion, with inner shells driving activation of outer shells during ICW radial propagation toward the network periphery of a stimulated cell. In this fashion, as far as the activation of inner shells is guaranteed, an ICW could regenerate and propagate across large portions of the network, if not the whole network. On the other hand, a simple change of the stimulus protocol, resulting in an alteration of IP_3 supply that can no longer robustly activate astrocyte shells that are proximal to the stimulus site, would cause ICWs to propagate only for short distances. This could ultimately explain why the same astrocyte networks sometimes display local Ca^{2+} activity, spatially confined to ensembles of few activated cells, (Sasaki et al. 2011) and some other times long-distance ICWs, engulfing hundreds of cells (Kuga et al. 2011).

7.5 Conclusions

The computational arguments presented in this chapter pinpoint to topological determinants of signal propagation in astrocyte networks that substantially differ from those at play in neural networks. While neurons communicate by electrical signals using distinct pools of neurotransmitters, found at each of their synapses, astrocytes propagate Ca^{2+} signals by a complex exchange of IP_3 fluxes, controlled by the exact spatial arrangement of IP_3 sources and sinks ensuing from activated versus unactivated cells. In a typical neural network model, increasing the number of connected neighbors would yield to the addition of new synapses, thus increased cell excitability. In an astrocyte network instead, this could reduce IP_3 supply to individual cells, thus hindering cell activation and ICW propagation.

In agreement with this view, increasing the average number of connections per cell (i.e., the network's mean degree) in models of networks of excitatory neurons was suggested to promote neural synchronization, that is the coherent activation of neuronal ensembles (Wang et al. 1995; Golomb and Hansel 2000; Olmi et al. 2010;

Luccioli et al. 2012; Tattini et al. 2012). In contrast, we showed how cell hubs (that is, cells with a large number of connections), and long-distance connections between astrocytes could dramatically break ICW fronts, substantially reducing the extent of their propagation. These differences in terms of topology versus dynamics in neural versus astrocyte networks brought forth in this chapter contribute to shed new light on functional and organizational principles beyond astrocyte networks whose topological features are notoriously very different from those on neural networks (Bushong et al. 2002).

Acknowledgements MDP acknowledges the support of Pôle emploi Rhône-Alpes, the “Alain Bensoussan” Postdoctoral Fellowship Program by the European Research Council in Informatics and Mathematics (ERCIM), and the Junior Leader Postdoctoral Fellowship Program by “la Caixa” Banking Foundation (LCF/BQ/LI18/11630006). MDP’s research at BCAM is also made possible thanks to the support of the Basque Government by the BERC 2018–2021 program, as well as by the Spanish Ministry of Science, Innovation and Universities through the BCAM Severo Ochoa accreditation SEV-2017-0718.

Appendix 1 Simulations of 3D Astrocytic Networks

Construction of Networks with Different Topology

The five different topologies for 3D astrocytic networks considered in this chapter were constructed as following detailed (see also Lallouette et al. 2014).

- *Link-radius networks* were constructed connecting each astrocyte i to all cells contained in a sphere of radius d centered on i . The degree distribution of these networks displays some variability around the mean degree $\langle k \rangle$, due to preliminary jitter of astrocyte locations in the absence of highly connected cells.
- *Regular-degree networks* were developed connecting each astrocyte to its k nearest neighbors while forbidding links longer than $d_{max} = 150\text{ }\mu\text{m}$. In doing so, connections were established in k_{reg} iterations to avoid directional biases. Namely, all nodes were randomly taken once per iteration m and linked to the nearest node i with degree $k_i < m \leq k_{reg}$ and located within d_{max} from the selected node.
- *Shortcut networks* were constructed in a way similar to small-world networks (Watts 1999). We started by positioning astrocytes on a cubic lattice with internode distance a , linking each cell to its nearest neighbors at distances that were multiples of a up to l times. We then rewired each connection with probability p_s , thereby randomly assigning one of its endpoint. Finally, we jittered the nodes positions as explained in the main text.
- *Spatial scale-free networks* were incrementally built by spatially constrained preferential attachment (Barthélemy 2010). Briefly, astrocytes were progressively included in the network, one by one, and connected with m_{sf} cells. Each connection between a new astrocyte i and a target cell j was established with probability $p_{i \rightarrow j} \propto k_j \exp(-d_{ij}/r_c)$, where k_j is the degree of the target cell j , d_{ij} represents the Euclidean distance between astrocytes i and j , and r_c sets the range of interac-

tion between cells in the space. Small values of r_c result in connections between astrocytes that are limited to their neighbors, while large r_c values allow establishing long-distance connections. Spatially constrained preferential attachment may also produce some highly connected astrocytes or “hubs.”

- *Erdős-Rényi networks* were built by linking each astrocyte pair with probability p , independently of their distance and existing degree. These networks are the only ones in our analysis that do not bear any spatial constraint.

Depending on whether r_c (respectively p_s) is large or not, spatial scale-free networks (respectively shortcut networks) can be regarded either as spatially constrained networks or as spatially unconstrained networks. Due to random wiring, some of the above procedures could result in disconnected networks. To minimize this scenario, we iterated the wiring procedure to ensure that, in our networks, disconnected node pairs accounted for <2% of all possible node pairs. Parameters used to build the different networks in the simulations discussed in Sect. 7.3.2 are detailed in Table 7.2.

Numerical Procedures

Each network model consisted of $3N = 3993$ ODEs which we numerically solved by fourth-order Runge–Kutta integration with a time step of 0.01 s. The extent of ICW propagation (N_{act}) was quantified by the number of astrocytes that were activated at least once, where an astrocyte was considered to be activated whenever its Ca^{2+} concentration exceeded $0.7 \mu\text{M}$. Each network model was produced into $n = 20$ different realizations, and mean degree ($\langle k \rangle$) and mean shortest path length (L) of each network model were averaged over realizations.

To generate ICWs, we stimulated the cell whose location was the closest to, if not coincident with the center of the 3D cubic lattice containing the network. Stimulation was delivered for $0 \leq t \leq 200$ s connecting an IP_3 reservoir of $2 \mu\text{M}$ to the central cell and allowing IP_3 diffusion into that cell according to Eq. 7.5.

In networks with UAR astrocytes, we considered step increases of time by $\Delta t = 0.1$ s, simulating a transition from a state x to a state y (with rate $k_{x \rightarrow y}$ and $x, y = \text{U}, \text{A}, \text{R}$), every time that a random number r drawn from a uniform distribution in $[0, 1]$ at each Δt was such that $r \leq k_{x \rightarrow y} \cdot \Delta t$. In those networks, stimulation of the central cell was deployed forcing activation of its connected neighbors, since this was observed to be case in the majority of networks with biophysically modeled astrocytes.

Appendix 2 Supplementary Online Material and Software

Detailed derivation of the shell model (Sect. 7.4.2) can be downloaded from <https://github.com/mdepitta/comp-glia-book/tree/master/Ch7.Lallouette>. The file `Shell.derivation.pdf` is provided along with the original L^AT_EX files within the

doc folder associated with this chapter. In the same folder, the WxMaxima file `ODEsystem.wxm` is also provided. This file was used to analytically solve the ODE system at the core of the derivation of the shell model (Eqs. 1–3 in the supplementary online text).

Within the same repository, the code used for simulations of astrocyte networks presented in this chapter is also provided. The core source code is implemented in C++ and is located in `src` folder. This code must preliminarily be compiled by `make` from this directory. The Python script, `RunSimulations.py` relies on the compiled source code to generate all data sets to plot the figures of this chapter. Depending on the hardware configuration, it might take up to a day to complete all the simulations involved. By default, the software will attempt using all available cores on the local machine. Individual figures can be generated by `Figure_3.py` for Fig. 7.3c, d; `Figure_5.py` for Fig. 7.5c, d; and `Figure_6.py` for Fig. 7.6e, f (Table 7.4).

References

- Aberg ND, Rönnbäck L, Eriksson PS (1999) Connexin43 mRNA and protein expression during postnatal development of defined brain regions. *Dev Brain Res* 115(1):97–101
- Allbritton NL, Meyer T, Stryer L (1992) Range of messenger action of calcium ion and inositol 1,4,5-trisphosphate. *Science* 260:107–260
- Bao X, Altenberg GA, Reuss L (2004) Mechanism of regulation of the gap junction protein connexin 43 by protein kinase C-mediated phosphorylation. *Am J Physiol Cell Physiol* 286(3):C647–C654
- Barthélemy M (2010) Spatial networks. *Phys Rep* 499:1–101
- Bazargani N, Attwell D (2016) Astrocyte calcium signaling: the third wave. *Nat Neurosci* 19(2):182–189
- Bennett M, Farnell L, Gibson W (2005) A quantitative model of purinergic junctional transmission of calcium waves in astrocyte networks. *Biophys. J* 89(4):2235–2250
- Blomstrand F, Aberg ND, Eriksson PS, Hansson E, Rönnbäck L (1999) Extent of intercellular calcium wave propagation is related to gap junction permeability and level of connexin-43 expression in astrocytes in primary cultures from four brain regions. *Neuroscience* 92(1):255–265
- Boccaletti S, Latora V, Moreno Y, Chavez M, Hwang D-U (2006) Complex networks: structure and dynamics. *Phys Rep* 424(4–5):175–308
- Bushong EA, Martone ME, Jones YZ, Ellisman MH (2002) Protoplasmic astrocytes in CA1 stratum radiatum occupy separate anatomical domains. *J Neurosci* 22(1):183–192
- Charles A (1998) Intercellular calcium waves in glia. *Glia* 24(1):39–49
- Chay T, Fan YS, Lee SY (1995) Bursting, spiking, chaos, fractals and universality in biological rhythms. *Int J Bifurcat Chaos* 5:595–635
- Clements JD, Lester RAJ, Tong G, Jahr CE, Westbrook GL (1992) The time course of glutamate in the synaptic cleft. *Science* 258:1498–1501
- Codazzi F, Teruel MN, Meyer T (2001) Control of astrocyte Ca^{2+} oscillations and waves by oscillating translocation and activation of protein kinase C. *Curr Biol* 11(14):1089–1097
- Cornell-Bell AH, Finkbeiner SM, Cooper MS, Smith SJ (1990) Glutamate induces calcium waves in cultured astrocytes: long-range glial signaling. *Science* 247(4941):470–473
- Crank J (1980) The mathematics of diffusion, 2nd edn. Oxford University Press, USA
- D'Ambrosio R, Wenzel J, Schwartzkroin PA, McKhann GM, Janigro D (1998) Functional specialization and topographic segregation of hippocampal astrocytes. *J Neurosci* 18(12):4425–4438

- Dani JW, Chernjavsky A, Smith SJ (1992) Neuronal activity triggers calcium waves in hippocampal astrocyte networks. *Neuron* 8(3):429–440
- De Pittà M, Goldberg M, Volman V, Berry H, Ben-Jacob E (2009) Glutamate regulation of calcium and IP_3 oscillating and pulsating dynamics in astrocytes. *J Biol Phys* 35(4):383–411
- De Pittà M, Volman V, Berry H, Parpura V, Liaudet N, Volterra A, Ben-Jacob E (2012) Computational quest for understanding the role of astrocyte signaling in synaptic transmission and plasticity. *Front Comp Neurosci* 6:98
- De Young GW, Keizer J (1992) A single-pool inositol 1,4,5-trisphosphate-receptor-based model for agonist-stimulated oscillations in Ca^{2+} concentration. *Proc Natl Acad Sci* 89(20):9895–9899
- Ding F, O'Donnell J, Thrane AS, Zeppenfeld D, Kang H, Xie L, Wang F, Nedergaard M (2013) α 1-Adrenergic receptors mediate coordinated Ca^{2+} signaling of cortical astrocytes in awake, behaving mice. *Cell Calcium* 54(6):387–394
- Dokukina I, Gracheva M, Grachev E, Gunton J (2008) Role of network connectivity in intercellular calcium signaling. *Physica D* 237(6):745–754
- Dupont G, Erneux C (1997) Simulations of the effects of inositol 1,4,5-trisphosphate 3-kinase and 5-phosphatase activities on Ca^{2+} oscillations. *Cell Calcium* 22(5):321–331
- Dupont G, Goldbeter A (1993) One-pool model for Ca^{2+} oscillations involving Ca^{2+} and inositol 1,4,5-trisphosphate as co-agonists for Ca^{2+} release. *Cell Calcium* 14:311–322
- Dyhrfjeld-Johnsen J, Santhakumar V, Morgan RJ, Huerta R, Tsirring L, Soltesz I (2007) Topological determinants of epileptogenesis in large-scale structural and functional models of the dentate gyrus derived from experimental data. *J Neurophysiol* 97(2):1566–1587
- Edwards JR, Gibson WG (2010) A model for Ca^{2+} waves in networks of glial cells incorporating both intercellular and extracellular communication pathways. *J Theor Biol* 263(1):45–58
- Falcke M (2004) Reading the patterns in living cells: the physics of Ca^{2+} signaling. *Adv Phys* 53(3):255–440
- Fiacco TA, McCarthy KD (2004) Intracellular astrocyte calcium waves in situ increase the frequency of spontaneous AMPA receptor currents in CA1 pyramidal neurons. *J Neurosci* 24(3):722–732
- Fiacco TA, McCarthy KD (2006) Astrocyte calcium elevations: properties, propagation, and effects on brain signaling. *Glia* 54(7):676–690
- Galea E, Morrison W, Hudry E, Arbel-Ornath M, Bacskai BJ, Gómez-Isla T, Stanley HE, Hyman BT (2015) Topological analyses in APP/PS1 mice reveal that astrocytes do not migrate to amyloid- β plaques. *Proc Natl Acad Sci* 112(51):15556–15561
- Giaume C (2010) Astroglial wiring is adding complexity to neuroglial networking. *Front Neuroenergetics* 2:129
- Giaume C, Fromaget C, el Aoumari A, Cordier J, Glowinski J, Gros D (1991) Gap junctions in cultured astrocytes: single-channel currents and characterization of channel-forming protein. *Neuron* 6(1):133–143
- Giaume C, Koulakoff A, Roux L, Holcman D, Rouach N (2010) Astroglial networks: a step further in neuroglial and gliovascular interactions. *Nat Rev Neurosci* 11(2):87–99
- Giaume C, McCarthy KD (1996) Control of gap-junctional communication in astrocytic networks. *Trends Neurosci* 19(8):319–325
- Goldberg M, De Pittà M, Volman V, Berry H, Ben-Jacob E (2010) Nonlinear gap junctions enable long-distance propagation of pulsating calcium waves in astrocyte networks. *PLoS Comput Biol* 6(8):e1000909
- Golomb D, Hansel D (2000) The number of synaptic inputs and the synchrony of large, sparse neuronal networks. *Neural Comput* 12(5):1095–1139
- Harris AL (2001) Emerging issues in connexin channels: biophysics fills the gap. *Q Rev Biophys* 34:325–472
- Höfer T, Politi A, Heinrich R (2001) Intercellular Ca^{2+} wave propagation through gap-junctional Ca^{2+} diffusion: a theoretical study. *Biophys J* 80(1):75–87
- Höfer T, Venance L, Giaume C (2002) Control and plasticity of intercellular calcium waves in astrocytes: a modeling approach. *J Neurosci* 22(12):4850–4859

- Houades V, Koulakoff A, Ezan P, Seif I, Giaume C (2008) Gap junction-mediated astrocytic networks in the mouse barrel cortex. *J Neurosci* 28(20):5207–5217
- Huang Y-F, Liao C-K, Lin J-C, Jow G-M, Wang H-S, Wu J-C (2013) Antofine-induced connexin43 gap junction disassembly in rat astrocytes involves protein kinase C β . *Neurotoxicology* 35:169–179
- Iacobas DA, Suadicani SO, Spray DC, Scemes E (2006) A stochastic two-dimensional model of intercellular Ca $^{2+}$ wave spread in glia. *Biophys J* 90(1):24–41
- Irvine RF, Schell MJ (2001) Back in the water: the return of the inositol phosphates. *Nat Rev Mol Cell Biol* 2(5):327–338
- Iwabuchi S, Kawahara K, Makisaka K, Sato H (2002) Photolytic flash-induced intercellular calcium waves using caged calcium ionophore in cultured astrocytes from newborn rats. *Exp Brain Res* 146(1):103–116
- Kang M, Othmer HG (2009) Spatiotemporal characteristics of calcium dynamics in astrocytes. *Chaos* 19(3):037116
- Kasthuri N, Hayworth K, Berger DR, Schalek RL, Conchello JA, Knowles-Barley S, Lee D, Vázquez-Reina A, Kaynig V, Jones TR, Roberts M, Lyskowski JM, Tapia JC, Seung HS, Roncal WG, Vogelstein JT, Burns R, Sussman DL, Priebe CE, Pfister H, Lichtman JW (2015) Saturated reconstruction of a volume of neocortex. *Cell* 162(3):648–661
- Koulakoff A, Ezan P, Giaume C (2008) Neurons control the expression of connexin 30 and connexin 43 in mouse cortical astrocytes. *Glia* 56(12):1299–1311
- Kuchibhotla KV, Lattarulo CR, Hyman BT, Bacskai BJ (2009) Synchronous hyperactivity and intercellular calcium waves in astrocytes in Alzheimer mice. *Science* 323(5918):1211–1215
- Kuga N, Sasaki T, Takahara Y, Matsuki N, Ikegaya Y (2011) Large-scale calcium waves traveling through astrocytic networks in vivo. *J Neurosci* 31(7):2607–2614
- Kummer U, Olsen LF, Green AK, Bomberg-Bauer E, Baier G (2000) Switching from simple to complex oscillations in calcium signaling. *Biophys J* 79:1188–1199
- Kunze A, Congreso MR, Hartmann C, Wallraff-Beck A, Hüttmann K, Bedner P, Requardt R, Seifert G, Redecker C, Willecke K, Hofmann A, Pfeifer A, Theis M, Steinhäuser C (2009) Connexin expression by radial glia-like cells is required for neurogenesis in the adult dentate gyrus. *Proc Natl Acad Sci USA* 106(27):11336–11341
- Kupferman R, Mitra PP, Hohenberg PC, Wang SS (1997) Analytical calculation of intracellular calcium wave characteristics. *Biophys J* 72(6):2430–2444
- Kurth-Nelson ZL, Mishra A, Newman EA (2009) Spontaneous glial calcium waves in the retina develop over early adulthood. *J Neurosci* 29(36):11339–11346
- Lallouette J (2014) Modeling calcium responses in astrocyte networks: relationships between topology and dynamics. Ph.D. thesis, INSA de Lyon
- Lallouette J, De Pittà M, Ben-Jacob E, Berry H (2014) Sparse short-distance connections enhance calcium wave propagation in a 3D model of astrocyte networks. *Front Comput Neurosci* 8:45
- Li Y, Rinzel J (1994) Equations for InsP₃ receptor-mediated [Ca $^{2+}$]_i oscillations derived from a detailed kinetic model: a Hodgkin–Huxley like formalism. *J Theor Biol* 166(4):461–473
- Luccioli S, Olmi S, Politi A, Torcini A (2012) Collective dynamics in sparse networks. *Phys Rev Lett* 109(13):138103
- MacDonald CL, Yu D, Buibas M, Silva GA (2008) Diffusion modeling of atp signaling suggests a partially regenerative mechanism underlies astrocyte intercellular calcium waves. *Front. Neuroeng* 1:1
- Matrosov VV, Kazantsev VB (2011) Bifurcation mechanisms of regular and chaotic network signaling in brain astrocytes. *Chaos* 21(2):023103
- Montoro RJ, Yuste R (2004) Gap junctions in developing neocortex: a review. *Brain Res. Rev.* 47(1–3):216–226
- Müller-Linow M, Hilgetag CC, Hütt M-T (2008) Organization of excitable dynamics in hierarchical biological networks. *PLoS Comput Biol* 4(9):e1000190
- Nagy JI, Rash JE (2000) Connexins and gap junctions of astrocytes and oligodendrocytes in the CNS. *Brain Res Rev* 32(1):29–44

- Nedergaard M, Ransom B, Goldman SA (2003) New roles for astrocytes: Redefining the functional architecture of the brain. *Trends Neurosci* 26(10):523–530
- Newman MEJ (2003) The structure and function of complex networks. *SIAM Rev.* 45(2):167–256
- Nimmerjahn A, Kirchhoff F, Kerr JND, Helmchen F (2004) Sulforhodamine 101 as a specific marker of astroglia in the neocortex *in vivo*. *Nat Methods* 1(1):31–37
- Olmi S, Livi R, Politi A, Torcini A (2010) Collective oscillations in disordered neural networks. *Phys Rev E* 81(4):046119
- Pannasch U, Rouach N (2013) Emerging role for astroglial networks in information processing: from synapse to behavior. *Trends Neurosci* 36(7):405–417
- Parri HR, Gould TM, Crunelli V (2001) Spontaneous astrocytic Ca^{2+} oscillations in situ drive NMDAR-mediated neuronal excitation. *Nat Neurosci* 4(8):803–812
- Pina-Benabou MHD, Srinivas M, Spray DC, Scemes E (2001) Calmodulin kinase pathway mediates the K^+ -induced increase in gap junctional communication between mouse spinal cord astrocytes. *J Neurosci* 21(17):6635–6643
- Pivneva T, Haas B, Reyes-Haro D, Laube G, Veh R, Nolte C, Skibo G, Kettenmann H (2008) Store-operated Ca^{2+} entry in astrocytes: different spatial arrangement of endoplasmic reticulum explains functional diversity *in vitro* and *in situ*. *Cell Calcium* 43(6):591–601
- Rouach N, Avignone E, Même W, Koulakoff A, Venance L, Blomstrand F, Giaume C (2002) Gap junctions and connexin expression in the normal and pathological central nervous system. *Biol Cell* 94(7–8):457–475
- Rouach N, Glowinski J, Giaume C (2000) Activity-dependent neuronal control of gap-junctional communication in astrocytes. *J Cell Biol* 149(7):1513–1526
- Rouach N, Koulakoff A, Abudara V, Willecke K, Giaume C (2008) Astroglial metabolic networks sustain hippocampal synaptic transmission. *Science* 322(5907):1551–1555
- Roux L, Benchenane K, Rothstein JD, Bonvento G, Giaume C (2011) Plasticity of astroglial networks in olfactory glomeruli. *Proc Natl Acad Sci U S A*
- Roxin A, Riecke H, Solla SA (2004) Self-sustained activity in a small-world network of excitable neurons. *Phys Rev Lett* 92(19):198101
- Sánchez-Gutiérrez D, Tozluoglu M, Barry JD, Pascual A, Mao Y, Escudero LM (2016) Fundamental physical cellular constraints drive self-organization of tissues. *EMBO J* 35(1):77–88
- Sasaki T, Kuga N, Namiki S, Matsuki N, Ikegaya Y (2011) Locally synchronized astrocytes. *Cereb Cortex* 21:1889–1900
- Scemes E, Giaume C (2006) Astrocyte calcium waves: What they are and what they do. *Glia* 54(7):716–725
- Scemes E, Spray DC (2012) Extracellular K^+ and astrocyte signaling via connexin and pannexin channels. *Neurochem Res* 37(11):2310–2316
- Scemes E, Suadicani SO, Spray DC (2000) Intercellular communication in spinal cord astrocytes: fine tuning between gap junctions and P2 nucleotide receptors in calcium wave propagation. *J Neurosci* 20(4):1435–1445
- Schipke CG, Boucsein C, Ohlemeyer C, Kirchhoff F, Kettenmann H (2002) Astrocyte Ca^{2+} waves trigger responses in microglial cells in brain slices. *FASEB J* 16(2):255–257
- Sherman A, Smith GD, Dai L, Miura RM (2001) Asymptotic analysis of buffered calcium diffusion near a point source. *SIAM J Appl Math* 61(5):1816–1838
- Shuai JW, Jung P (2003) Selection of intracellular calcium patterns in a model with clustered Ca^{2+} release channels. *Phys Rev E* 67(3):031905
- Sirnes S, Kjenseth A, Leithe E, Rivedal E (2009) Interplay between PKC and the MAP kinase pathway in connexin43 phosphorylation and inhibition of gap junction intercellular communication. *Biochem Biophys Res Commun* 382(1):41–45
- Skupin A, Kettenmann H, Winkler U, Wartenberg M, Sauer H, Tovey SC, Taylor CW, Falcke M (2008) How does intracellular Ca^{2+} oscillate: by chance or by clock? *Biophys J* 94:2404–2411
- Sneyd J, Charles AC, Sanderson MJ (1994) A model for the propagation of intracellular calcium waves. *Am J Physiol* 266(35):C293–C302

- Sneyd J, Keizer J, Sanderson MJ (1995a) Mechanisms of calcium oscillations and waves: a quantitative analysis. *FASEB J* 9(14):1463–1472
- Sneyd J, Sherratt J (1997) On the propagation of calcium waves in an inhomogeneous medium. *SIAM J Appl Math* 57(1):73–94
- Sneyd J, Wetton BTR, Charles AC, Sanderson MJ (1995b) Intercellular calcium waves mediated by diffusion of inositol trisphosphate: a two-dimensional model. *Am J Physiol* 268(37):C1537–C1545
- Sneyd J, Wilkins M, Strahinja A, Sanderson MJ (1998) Calcium waves and oscillations driven by an intercellular gradient of inositol (1,4,5)-trisphosphate. *Biophys Chem* 72(1):101–109
- Stamatakis M, Mantzaris NV (2006) Modeling of ATP-mediated signal transduction and wave propagation in astrocytic cellular networks. *J Theor Biol* 241:649–668
- Suadicani SO, Flores CE, Urban-Maldonado M, Beelitz M, Scemes E (2004) Gap junction channels coordinate the propagation of intercellular Ca^{2+} signals generated by P2Y receptor activation. *Glia* 48(3):217–229
- Sul J-Y, Orosz G, Givens RS, Haydon PG (2004) Astrocytic connectivity in the hippocampus. *Neuron Glia Biol* 1(1):3–11
- Sun W, McConnell E, Pare J-F, Xu Q, Chen M, Peng W, Lovatt D, Han X, Smith Y, Nedergaard M (2013) Glutamate-dependent neuroglial calcium signaling differs between young and adult brain. *Science* 339(6116):197–200
- Tang Y, Othmer H (1994) A model of calcium dynamics in cardiac myocytes based on the kinetics of ryanodine-sensitive calcium channels. *Biophys J* 67:2223–2235
- Tattini L, Olmi S, Torcini A (2012) Coherent periodic activity in excitatory Erdős–Renyi neural networks: The role of network connectivity. *Chaos* 22(2):023133
- Theodosis DT, Poulain DA, Oliet SHR (2008) Activity-dependent structural and functional plasticity of astrocyte-neuron interactions. *Physiol Rev* 88(3):983–1008
- Tian GF, Takano T, Lin JH-C, Wang X, Bekar L, Nedergaard M (2006) Imaging of cortical astrocytes using 2-photon laser scanning microscopy in the intact mouse brain. *Adv Drug Deliv Rev* 58(7):773–787
- Ullah G, Jung P, Cornell-Bell AH (2006a) Anti-phase calcium oscillations in astrocytes via inositol (1,4,5)-trisphosphate regeneration. *Cell Calcium* 39(3):197–208
- Ullah G, Jung P, Cornell-Bell AH (2006b) Anti-phase calcium oscillations in astrocytes via inositol(1,4,5)-trisphosphate regeneration. *Cell Calcium* 39(3):197–208
- Wallach G, Lallouette J, Herzog N, De Pittà M, Ben Jacob E, Berry H, Hanein Y (2014) Glutamate mediated astrocytic filtering of neuronal activity. *PLoS Comput Biol* 10(12):e1003964
- Wang X, Golomb D, Rinzel J (1995) Emergent spindle oscillations and intermittent burst firing in a thalamic model: specific neuronal mechanisms. *Proc Natl Acad Sci U S A* 92(12):5577–5581
- Watts DJ (1999) Small worlds: the dynamics of networks between order and randomness, chapter 2. Princeton University Press, Princeton, pp 33–36
- Weissman TA, Riquelme PA, Ivic L, Flint AC, Kriegstein AR (2004) Calcium waves propagate through radial glial cells and modulate proliferation in the developing neocortex. *Neuron* 43(5):647–661
- Witcher M, Kirov S, Harris K (2007) Plasticity of perisynaptic astroglia during synaptogenesis in the mature rat hippocampus. *Glia* 55(1):13–23
- Zanette DH (2002) Dynamics of rumor propagation on small-world networks. *Phys Rev E* 65(4):041908

Part III

Tripartite Synapse and Regulation

of Network Activity

Chapter 8

Gliotransmission at Tripartite Synapses



Candela González-Arias and Gertrudis Perea

Abstract Signal exchange between astrocytes and neurons at tripartite synapses has emerged as a crucial element of neural circuits in the brain. The position of astrocyte processes facing synapses provides the proper structural and functional conditions for neuron-astrocyte communication giving rise to the concept of “tripartite synapse”. These synapses envisage an active role for astrocytes in their function whereby: (i) astrocytes sense neurotransmission by neurotransmitter transporter and receptors; (ii) synaptic activity stimulates astrocytic intracellular Ca^{2+} levels; (iii) astrocytes release neuroactive substances, gliotransmitters, that in turn regulate neuronal excitability and synaptic transmission. The ability of astrocytes to release different gliotransmitters and modulate synaptic activity deepens our knowledge of the brain physiology. In addition to the traditional homeostatic roles in the extracellular ion balance, neurotransmitter uptake from the extracellular space, and metabolic energy supply to neurons, astrocytes play active roles in synaptic transmission and plasticity, being involved in the coding information and cognitive processes by brain networks.

Keywords Astrocytes · Gliotransmission · Tripartite synapse · Synaptic plasticity · Information coding

8.1 Introduction

The concept of tripartite synapse was originally proposed by Philip Haydon’s group in 1999 (Araque et al. 1999) to describe the close structural and functional association between astrocytes and synaptic partners. Therefore, a tripartite synapse encompasses the impact of astrocytes on the extracellular space surrounding synapses, modulating synapse formation and remodeling during development (Allen 2013), as well as synaptic function via uptake of neurotransmitters and delivery of active

C. González-Arias · G. Perea (✉)

Functional and Systems Neurobiology, Cajal Institute (CSIC), Av. Doctor Arce 37,
28002 Madrid, Spain

e-mail: gperea@cajal.csic.es

signaling molecules (Araque et al. 2014). Since the first demonstration of astrocytes responding to glutamate by cytosolic Ca^{2+} elevations (Cornell-Bell et al. 1990), a great effort has been done to characterize the mechanisms and properties that govern astrocyte Ca^{2+} signaling, as discussed in detail in Chaps. 1 and 5. Likewise, during the last twenty years numerous neuroscientists have focused their interest on the glial side of tripartite synapses, investigating the influence of astrocytes in synaptic transmission and plasticity. The result of this intense scientific effort has caused a groundbreaking change in recent neuroscience and in our current knowledge of brain physiology (Araque et al. 2014; Perea et al. 2009). Here, the main findings supporting the active role of astrocytes on synaptic physiology and neural circuit function and behavior are reviewed.

8.2 Gliotransmission

Astrocytes express membrane receptors for a vast majority of different neurotransmitters and neuromodulators, including glutamate, GABA, adenosine, norepinephrine, acetylcholine, and endocannabinoids (for reviews, see Perea et al. 2009; Zorec et al. 2012). Most of these neurotransmitters and neuromodulators signal through G_q protein-coupled receptors, which lead to Ca^{2+} release from intracellular stores via activation of IP_3 type 2 receptors. Ca^{2+} is a pivotal substrate of astrocytic cellular excitability as discussed in Chap. 2. Indeed, intracellular Ca^{2+} elevations either induced by spontaneous astrocytic activity or evoked by neuronal firing can trigger the release of different active substances from astrocytes, the so-called gliotransmitters (reviewed in Volterra and Bezzi 2002). These gliotransmitters include glutamate, GABA, D-serine, ATP, adenosine, tumor necrosis factor alpha ($\text{TNF}\alpha$), L-lactate, or prostaglandins among others (Santello et al. 2012; Yoon and Lee 2014) and can modulate and control neuronal activity. The ability of astrocytes to release gliotransmitters has been reported in several brain areas, including the hippocampus, the cerebellum, the thalamus, and the cortex (for a review see Zorec et al. 2012).

The molecular mechanisms responsible for the release of gliotransmitters are diverse and involve vesicular exocytosis (Santello et al. 2012; Zorec et al. 2015), diffusion through the membrane channels (Lee et al. 2010), and translocation via plasma membrane transporters (Hamilton and Attwell 2010). Regulated exocytosis mediates one of the most characterized pathways of gliotransmission (Bezzi et al. 1998; Mothet et al. 2005; Navarrete and Araque 2008; Pascual et al. 2005; Jourdain et al. 2007; Perea and Araque 2007; Santello et al. 2011). Astrocytes express the protein machinery involved in the SNARE complex formation, such as synaptobrevin 2 and its homologue cellubrevin, SNAP-23, and others membrane-trafficking proteins (Santello et al. 2011, 2012; Mothet et al. 2005; Bezzi et al. 2004; Zhang et al. 2004). Accordingly, molecular manipulations of the SNARE complex in astrocytes have shown the requirement of Ca^{2+} -regulated vesicular release mechanisms for gliotransmission. Incubation with Bafilomycin A, which prevents the re-acidification of synaptic vesicles once they have undergone exocytosis, abolishes the release of glu-

tamate and ATP from astrocytes (Araque et al. 2000; Domercq et al. 2006; Bowser 2007). In addition, the intracellular loading of astrocytes with the light chain of tetanus toxin (TeNT-LC) that cleavages synaptobrevin 2 prevents vesicular glutamate (Perea and Araque 2007) and ATP release (Pankratov and Lalo 2015). More recently, *in vivo* studies using transgenic mice have revealed the impact of gliotransmission in brain activity and behavior, specifically disrupting vesicular exocytosis in astrocytes by selective expression of tetanus neurotoxin (TeNT) (Lee et al. 2014) and the dominant-negative domain of vesicular SNARE protein vesicle-associated membrane protein 2 (VAMP2)/synaptobrevin 2 (dnSNARE) (Pascual et al. 2005; Halassa et al. 2009). However, a recent study has shown the widespread expression of the dnSNARE transgene in neurons (Fujita et al. 2014), demonstrating that GFAP promoter drives inducible expression of dnSNARE not only in astrocytes, but also in cortical neuronal of adult mice (Fujita et al. 2014). This study draws our attention to the pitfalls of mouse genetic manipulations and opens a debate about vesicular-dependent release in astrocytes (Araque et al. 2014; Bazargani and Attwell 2016; Sloan and Barres 2014).

Considering that not all astrocyte cytosolic Ca^{2+} increases cause gliotransmission (Fiacco et al. 2007; Agulhon et al. 2010), and release mechanisms can also be Ca^{2+} -independent (for a review, see Hamilton and Attwell 2010; Volterra et al. 2014), future studies are required to elucidate the particular circumstances that activate astrocyte Ca^{2+} -dependent and/or Ca^{2+} -independent mechanisms in physiological and pathological conditions and their consequences on synaptic activity.

8.3 Impact of Tripartite Synapses *In Situ*: Astrocyte Modulation of Synaptic Transmission

One of the key properties of the mammalian brain is the ability to modify neural circuit functions by experience and thereby modify subsequent behavior, that is, plasticity. Via modifications of the strength or efficacy of synaptic transmission at preexisting synapses, transient experiences can be incorporated into the neural circuits as persistent memory traces, during both brain development and adult life. Then, synaptic plasticity is a fundamental mechanism underlying brain function (Citri and Malenka 2008). Gliotransmitters released by astrocytes can contribute to synaptic plasticity both through activation of pre- and postsynaptic receptors. Indeed, astrocytes are involved in the short- and long-term types of synaptic plasticity in the brain (Perea et al. 2014). Transient astrocyte activation can induce short-term plasticity (lasting several minutes) and long-term plasticity (lasting hours) by controlling the release of neurotransmitter from presynaptic terminals. These effects are mediated by glutamate acting on presynaptic group I metabotropic glutamate receptors (mGluRs) (Perea and Araque 2007; Navarrete and Araque 2010; Gomez-Gonzalo et al. 2014) and presynaptic NMDARs (Jourdain et al. 2007; Min and Nevian 2012). Glutamate released by astrocytes also stimulates postsynaptic NMDARs inducing slow inward

currents (SICs) that depolarize neighboring neurons (Navarrete and Araque 2008; Araque et al. 1998; Angulo et al. 2004; Fellin et al. 2004; Perea and Araque 2005; Shigetomi et al. 2008; Sasaki et al. 2011; Mariotti et al. 2016).

In addition to glutamate, D-serine also contributes to NMDA signaling and the subsequent plasticity mediated through these receptors (Mothet et al. 2005; Min and Nevian 2012; Henneberger et al. 2010; Panatier et al. 2006). Therefore, the release of both gliotransmitters ensures the activation of NMDARs at the synapse. One intriguing aspect of NMDAR activation is the subunit selectivity and the pre- or postsynaptic localization. Since the most common forms of synaptic plasticity, which are long-term potentiation (LTP) and long-term depression (LTD), are driven by activation of NMDARs (Liu et al. 2004), the selective supply of glutamate and D-serine by astrocytes could support them. With this regard, experiments have revealed that while glutamate released by astrocytes induces SICs by activation of postsynaptic NR2B-containing extrasynaptic NMDARs (Fellin et al. 2004; Shigetomi et al. 2008; D'Ascenzo et al. 2007) and triggers LTD at cortical synapses by presynaptic activation of NMDARs (Min and Nevian 2012), D-serine activates postsynaptic (NR2A-containing) NMDARs, contributing to the long-term plasticity mediated by these receptors. In particular, astrocytic D-serine contributes to LTP at CA3-CA1 hippocampal synapses (Henneberger et al. 2010; Papouin et al. 2012; Le Bail et al. 2015; Shigetomi et al. 2013), but also to LTD based on its action on synaptic and extrasynaptic NMDARs (Papouin et al. 2012), contributing to the differential role of these receptors in hippocampal operational tasks (for review see Mothet et al. 2015) (Fig. 8.1).

In addition to the regulation of synaptic plasticity, astrocytes play an important role in setting the resting tone of synaptic transmission. In fact, they regulate the threshold of synaptic activity through the release of glutamate and ATP/adenosine which activates presynaptic group I mGluR (Bonansco et al. 2011), adenosine A1 (Pascual et al. 2005; Halassa et al. 2009; Serrano et al. 2006), and A2_A receptors (Panatier et al. 2011). While adenosine through activation of presynaptic A1 receptors decreases neurotransmitter release probability and weakens neuronal signaling (Pascual et al. 2005; Serrano et al. 2006), by activation of presynaptic A2_A receptors, adenosine increases neurotransmitter release probability enhancing synaptic efficacy (Panatier et al. 2011). Therefore, the release of a single gliotransmitter may have diverse effects determined by the receptor subtype. Considering that in the hippocampus (Bushong et al. 2002) and the cortex (Halassa et al. 2007) a single astrocyte has a non-overlapping domain enwrapping ~100,000 synapses (Bushong et al. 2002), 4–8 neurons, and 300–600 dendrites, the regulation of synaptic transmission would be a selective process controlled by the specific gliotransmitter released and the particular nature of local synapses.

To address the precise control and features of astrocyte–neuron signaling at single synapse level, several studies focused on hippocampal glutamatergic tripartite synapses in juvenile mice (Perea and Araque 2007; Panatier et al. 2011; Di Castro et al. 2011) showing how astrocytes detect unitary glutamatergic synaptic transmission by increases of intracellular Ca²⁺ levels at local microdomains (Panatier et al. 2011). Small and fast Ca²⁺ signals were observed in restricted astrocytic com-

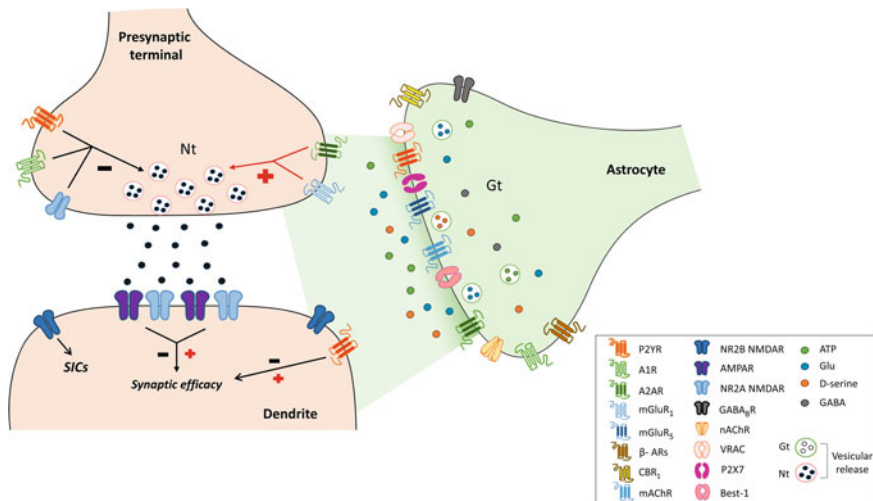


Fig. 8.1 Scheme of a glutamatergic tripartite synapse representing the different actions of gliotransmission. Astrocytes express a wide range of neurotransmitters (Nt) receptors. In turn, astrocytes release gliotransmitters (Gt) (ATP, glutamate, D-serine, and GABA, among others), that modulate neuronal excitability and synaptic transmission acting on presynaptic and postsynaptic receptors. For more details, see text. A1R, A1 receptor; A2AR, A2A receptor; AMPAR, AMPA receptor; Best-1, bestrophin-1; β -AR, beta-adrenergic receptor; CBR1, cannabinoid receptor 1; GABAR, GABAB receptor; Glu, glutamate; mAChR, muscarinic acetylcholine receptor; mGluR1, metabotropic glutamatergic receptor 1; mGluR5, metabotropic glutamatergic receptor 5; nAChR, nicotinic acetylcholine receptor; NR2A NMDAR, NR2A subunit of NMDA receptor; NR2B NMDAR, NR2B subunit of NMDA receptor; P2X7, purinergic receptor 7; P2YR, metabotropic purinergic receptor Y; Slow inward currents (SICs); VRAC, volume-regulated anion channel

parts adjacent to the dendritic spines and induced by activation of glutamatergic mGluR5 (Panatier et al. 2011) and purinergic P2Y1Rs (Di Castro et al. 2011). Release of gliotransmitter ATP/adenosine ensuing from those signals, in association with spontaneous or single-synapse stimulation of astrocytes, triggered a tonic release of purines that regulated basal synaptic transmission (Panatier et al. 2011). Alternatively, transient astrocyte stimulation involving a robust cell Ca²⁺ signaling induced by endogenous signals as endocannabinoids released by neurons (Navarrete and Araque 2010; Gomez-Gonzalo et al. 2014), or intracellular loading with Ca²⁺-caged compounds (Perea and Araque 2007; Navarrete et al. 2012), stimulates the release of glutamate that leads either to short-term or to long-term potentiation of synaptic transmission at single synapses through activation of presynaptic mGluR group I. Thus, tripartite synapses might be tuned by different gliotransmitters, but whether different astrocytic Ca²⁺ levels or dynamics regulate the release of glutamate or ATP/adenosine at single synapses remains to be determined.

The intricate relationships between astrocytes and synapses become even higher when, in addition to their functional diversity, anatomical interactions are considered. Astrocyte processes are extremely dynamic structures that extend and retract away

from synapses in the range of few minutes (Haber et al. 2006; Perez-Alvarez et al. 2014). The dynamics of synapse coverage by astrocytes control the level of neurotransmitter uptake and gliotransmitter actions at the synapse, temporally regulating synaptic transmission and plasticity (Perez-Alvarez et al. 2014; Bernardinelli et al. 2014).

8.4 Gliotransmission Role in Brain Information Processing: Impact on the Animal Behavior

Great effort has been made to elucidate the role of astrocytes not only at local synapses and circuits but also in more complex brain activities that govern animal behavior. With this aim, the combination of cutting-edge technologies and cell-type designed transgenic mice provides a powerful strategy to specifically monitor and manipulate astrocyte signaling *in vivo* while neuronal signaling remains intact. In this scenario, to achieve proper genetic targeting of astrocytes—e.g., transgenes using the promoter of the human glial fibrillary acidic protein (GFAP) or homologous recombination into the glutamate–aspartate transporter (GLAST) locus—the genetic strategies most used are the tamoxifen-inducible Cre/loxP gene recombination and the doxycycline-dependent modulation of gene expression (reviewed in Jahn et al. 2015). Genetic manipulation of astrocyte activity can pursue the selective deletion of glial genes, or alternatively, the insertion of particular genes to monitor, boost, or restore astrocytic function. Both strategies have successfully demonstrated the impact of astrocytes in animal behavior, based both on astrocyte-specific transgenic mouse lines and on viral transfection approaches which target specific genes in astrocytes from particular regions without affecting the whole brain. Viral transfection might show some advantages to target glial cell activity compared with transgenic mouse lines, since they can deliver the gene of interest in a wide range of experimental subjects (for technical details, see Zhang et al. 2010; Kim and Eberwine 2010).

Based on these studies, we know that astrocytes *in vivo* respond with Ca^{2+} increases when specific sensory or motor pathways are activated, either in anesthetized animals (Navarrete et al. 2012; Gee et al. 2014; Chen et al. 2012; Wang et al. 2006; Takata et al. 2011) or in awake-behaving mice (Dombeck et al. 2007; Nimmerjahn et al. 2009; Paukert et al. 2014; Ding et al. 2013). Recent studies have shown that astrocytes are involved in cholinergic processing and plasticity *in vivo*. Stimulation of sensory inputs that activates cholinergic nuclei induces muscarinic receptor-mediated Ca^{2+} signaling in astrocytes. This signaling in turn promotes release of glutamate and D-serine which regulate cholinergic-mediated synaptic plasticity in visual cortex (Chen et al. 2012), hippocampus (Navarrete et al. 2012), and barrel cortex (Takata et al. 2011). In this fashion, astrocytes take part in cholinergic-mediated processing of visual inputs, whisker sensing, and hippocampal oscillatory activity (Navarrete et al. 2012; Chen et al. 2012; Takata et al. 2011). Considering the importance of cholinergic transmission in memory processes, attention, and higher cognitive func-

tions (Perry et al. 1999), it is appealing to speculate a role of astrocytes in these critical brain functions.

D-serine, together with other gliotransmitters such as ATP and adenosine, has also been implicated in slow brain oscillations during sleep. Transgenic dnSNARE mice with downregulated gliotransmission showed a decrease of both slow cortical oscillations and accumulation of sleep pressure (Halassa et al. 2009; Fellen et al. 2009), which caused prolonged wakefulness periods with impaired cognitive functions (Yoo et al. 2007). Overall, these data suggest a role for astrocytic purinergic (and D-serinergic) signaling in cognitive deficits associated with sleep loss (Halassa et al. 2009). However, observations from dnSNARE mice need further experimental validation due to leaky neuronal transgene expression (Fujita et al. 2014) which might account for a neuronal component in addition to the astrocytic one in the observed effects.

Reduced gliotransmission can also be achieved by expression of inducible tetanus neurotoxin (TeNT) specifically in astrocytes. The ensuing transgenic mouse line shows a marked decrease of high-frequency gamma oscillations in awake-behaving mice (Lee et al. 2014). The weakening of cortical gamma oscillations correlates with behavioral impairments, like deficient performance in novel object recognition tasks, suggesting that astrocytes contribute to gamma oscillation cortical activity in memory recognition tasks (Lee et al. 2014).

On the other hand, mice expressing a selective AMPA subunit receptor deletion in Bergmann glia in the cerebellum show impairments in cerebellum-related behavioral tasks, including locomotion, conditioning on the Erasmus Ladder, and Pavlovian eye-blink conditioning motor performance (Saab et al. 2012). Hence, glutamatergic gliotransmission appears to be crucial for the functional integrity of cerebellar networks and plays important role in the ‘fine-tuning’ of neuronal processing responsible of complex motor behaviors (Saab et al. 2012; Sasaki et al. 2012). These results highlight the importance of a right balance of astrocyte–neuron signaling for a proper brain function.

8.5 Emerging Roles of Gliotransmission in Neuropathology

Recent evidences suggest that astrocytic Ca^{2+} signaling is enhanced in the context of certain neurological diseases (Mariotti et al. 2016; Ding et al. 2007), such as Alzheimer’s disease (AD), where astrocytes exhibit higher resting levels of Ca^{2+} and generate synchronous Ca^{2+} oscillations (Mariotti et al. 2016). These higher Ca^{2+} levels enhance glutamate release that promotes astrocyte-mediated SICs and thereby contribute to higher hippocampal excitability by activation of NMDARs (Talantova et al. 2013; Pirttimaki et al. 2013). In the AD model, astrocytes also abnormally release the inhibitory gliotransmitter GABA that likely contributes to reduced synaptic plasticity and memory impairment accounted in AD (Jo et al. 2014).

Astrocyte-mediated NMDAR signaling has also been found to be altered in multiple sclerosis (MS) mouse models (Habbas et al. 2015), where increased $\text{TNF}\alpha$ levels

are related to cognitive alterations. There, high extracellular TNF α promotes glutamate release from astrocytes by over-activation of astrocytic TNF receptor 1. The released glutamate in turn activates presynaptic NMDARs altering local excitatory synaptic transmission which correlates with contextual memory deficits observed in MS mice (Habbas et al. 2015).

Selective deletion of A2A receptors in postnatal astrocytes triggered reduced working memory through mechanisms involving glutamate homeostasis (Matos et al. 2015), and a reduced capability for ATP/adenosine release by astrocytes in prefrontal cortex has been related with depression-like behaviors (Cao et al. 2013; Lima et al. 2014), pinpointing to a crucial role of astrocytic purinergic signaling in cognitive performance and mood disorders.

8.6 Insights from Optogenetic and Chemogenetic Activation of Astrocyte Signaling

Glial cell studies have taken advantage of both optogenetics, using the light-sensitive cation channels channelrhodopsin 2 (ChR2) or archaerhodopsin (ArchT) (Sasaki et al. 2012; Tang et al. 2014; Perea et al. 2014; Beppu et al. 2014; Gourine et al. 2010; Masamoto et al. 2015), and chemogenetics, by the selective astrocyte expression of Designer Receptors Exclusively Activated by Designer Drugs (DREADDs) (Xie et al. 2015; Agulhon et al. 2013; Scofield et al. 2015). These state-of-the-art technologies allow a selective switch of astrocyte function, stimulating or silencing it at precise timing and spatial locations, and have been instrumental in probing the impact of astrocyte signaling and gliotransmission *in vivo* in the regulation of local synaptic activity (Sasaki et al. 2012; Tang et al. 2014; Perea et al. 2014; Beppu et al. 2014; Gourine et al. 2010; Agulhon et al. 2013; Scofield et al. 2015; Gradinaru et al. 2009), information coding by neuronal networks (Perea et al. 2014), and control of blood flow (Masamoto et al. 2015) and animal behavior (Sasaki et al. 2012; Tang et al. 2014; Gourine et al. 2010; Masamoto et al. 2015; Agulhon et al. 2013; Scofield et al. 2015).

A pioneering study using optogenetics in astrocytes demonstrated the influence of astrocyte signaling in fundamental physiological processes like breathing (Gourine et al. 2010). Selective ChR2-astrocyte stimulation was used to evoke ATP release that triggered robust activation of respiratory chemoreceptors in the brainstem (Gourine et al. 2010). In addition, ChR2-astrocyte activation has also been adopted to stimulate glutamate release from astrocytes showing how this pathway of gliotransmission could modulate visual features of inhibitory and excitatory cortical neurons thereby contributing to the processing of visual information by cortical networks (Perea et al. 2014). Likewise, optical activation of Bergmann glial cells induces glutamate release and depression of parallel fiber–Purkinje cell synapses, which arises in eye movement alterations (optokinetic reflex) and pupil dilation, indicating the contribution

of Bergmann glial cells in cerebellar modulation of motor behaviors (Sasaki et al. 2012).

DREADDs are engineered G protein-coupled receptors (GPCRs) activated by inert drug-like small molecules (Clozapine N-oxide (CNO)) that allow non-invasive control of cellular signaling. A recent study used engineered Gq protein-coupled receptor (Gq-GPCR) known as hM3Dq to transfect astrocytes in the Nucleus Accumbens core (NAcore). Then, selective stimulation of these receptors induced astrocyte glutamate release that inhibited cue-induced reinstatement of cocaine seeking (Scofield et al. 2015), suggesting a role for astrocytes in relapse vulnerability to cocaine addiction. Interestingly, after the administration of the CNO to the transgenic GFAP-hM3Dq mice that expresses hM3Dq selectively in astrocytes (Agulhon et al. 2013), mice show a wide range of physiological responses related with the Autonomous Nervous System activation, such as modulation of heart rate, blood pressure, salivation, and body temperature control (Agulhon et al. 2013). Those robust and uncontrolled effects require further attention preceding cognitive and behavioral studies using these mice.

In spite of the advantages of using new genetic techniques, there still are some unresolved issues that need further attention. For example, the underlying mechanisms of astrocyte Ca^{2+} signaling by optogenetic activation are debated (Perea et al. 2014; Figueiredo et al. 2014; Yang et al. 2015), as well the potential consequences of opsins activation on intracellular pH (Beppu et al. 2014), and the accurate control of the expression levels of transgenes and engineered GPCRs driven by exogenous promoter systems (Jahn et al. 2015). The upcoming genetic manipulation techniques will expand toward the *bona fide* recapitulation of the endogenous receptor activation. Future studies along within the refinement of molecular and genetic tools will contribute to reveal the complex and diverse astrocytic signaling and its impact on brain physiology.

8.7 Concluding Remarks

It is now well established that astrocytes and synapses form an entity of dynamic interactions that open to the existence of new pathways of communication between neural elements. Thus, in addition to the well-known signaling route between neurons through pre- and postsynaptic elements, other non-canonical, astrocyte-mediated information channels could exist in the brain. Moreover, through the exchange of signals across interconnected astrocytes, the bidirectional communication between astrocytes and neurons could extend to complex neuron–astrocyte networks. Mounting experimental evidence has shown that astrocytes, by releasing gliotransmitters, can cause diverse effects at local synapses that impact brain activity and, ultimately, animal behavior. Given the variety of gliotransmitters, the underlying release mechanisms, the molecular features of neuronal receptors and their precise location at the synapse, the effects of the astrocyte signaling on synaptic transmission are likely extremely complex and occurring on large scales. Hence, even though important

progress in astrocyte physiology has been achieved in the last twenty years, further experiments are needed for a comprehensive knowledge of the molecular mechanisms along with the physiological properties that govern gliotransmission. The combination of refined molecular and genetic approaches will reveal the actual roles of astrocytes in physiology and pathology, ruling out whether tripartite synapses are integral players in the brain's information coding, processing of behavior and cognitive tasks.

Acknowledgements The authors would like to thank Dr. Washington Buño for his helpful comments on the manuscript. This work was supported by grants from Ministerio de Economía y Competitividad, Spain, MINECO: Consolider, CSD2010-00045; Ramón y Cajal Program, RYC-2012-12014; and BFU2013-47265R.

References

- Agulhon C, Fiacco TA, McCarthy KD (2010) Hippocampal short- and long-term plasticity are not modulated by astrocyte Ca^{2+} signaling. *Science* 327(5970):1250–1254
- Agulhon C, Boyt KM, Xie AX, Friocourt F, Roth BL, McCarthy KD (2013) Modulation of the autonomic nervous system and behaviour by acute glial cell Gq protein-coupled receptor activation *in vivo*. *J Physiol* 591(22):5599–5609
- Allen NJ (2013) Role of glia in developmental synapse formation. *Curr Opin Neurobiol* 23(6):1027–1033
- Angulo MC, Kozlov AS, Charpak S, Audinat E (2004) Glutamate released from glial cells synchronizes neuronal activity in the hippocampus. *J Neurosci: Official J Soc Neurosci* 24(31):6920–6927
- Araque A, Sanzgiri RP, Parpura V, Haydon PG (1998) Calcium elevation in astrocytes causes an NMDA receptor-dependent increase in the frequency of miniature synaptic currents in cultured hippocampal neurons. *J Neurosci: Official J Soc Neurosci* 18(17):6822–6829
- Araque A, Parpura V, Sanzgiri RP, Haydon PG (1999) Tripartite synapses: glia, the unacknowledged partner. *Trends Neurosci* 22(5):208–215
- Araque A, Li N, Doyle RT, Haydon PG (2000) SNARE protein-dependent glutamate release from astrocytes. *J Neurosci: Official J Soc Neurosci* 20(2):666–673
- Araque A, Carmignoto G, Haydon PG, Oliet SH, Robitaille R, Volterra A (2014) Gliotransmitters travel in time and space. *Neuron* 81(4):728–739
- Bazargani N, Attwell D (2016) Astrocyte calcium signaling: the third wave. *Nat Neurosci* 19(2):182–189
- Beppu K, Sasaki T, Tanaka KF, Yamanaka A, Fukazawa Y, Shigemoto R et al (2014) Optogenetic countering of glial acidosis suppresses glial glutamate release and ischemic brain damage. *Neuron* 81(2):314–320
- Bernardinelli Y, Randall J, Janett E, Nikonenko I, Konig S, Jones EV et al (2014) Activity-dependent structural plasticity of perisynaptic astrocytic domains promotes excitatory synapse stability. *Current Biol: CB* 24(15):1679–1688
- Bezzi P, Carmignoto G, Pasti L, Vesce S, Rossi D, Rizzini BL et al (1998) Prostaglandins stimulate calcium-dependent glutamate release in astrocytes. *Nature* 391(6664):281–285
- Bezzi P, Gundersen V, Galbete JL, Seifert G, Steinhauser C, Pilati E et al (2004) Astrocytes contain a vesicular compartment that is competent for regulated exocytosis of glutamate. *Nat Neurosci* 7(6):613–620
- Bonansco C, Couve A, Perea G, Ferradas CA, Roncagliolo M, Fuenzalida M (2011) Glutamate released spontaneously from astrocytes sets the threshold for synaptic plasticity. *Eur J Neurosci* 33(8):1483–1492

- Bowser DN (2007) Khakh BS (2007) Vesicular ATP is the predominant cause of intercellular calcium waves in astrocytes. *J Gener Physiol* 129(6):485–491
- Bushong EA, Martone ME, Jones YZ, Ellisman MH (2002) Protoplasmic astrocytes in CA1 stratum radiatum occupy separate anatomical domains. *J Neurosci: Official J Soc Neurosci* 22(1):183–192
- Cao X, Li LP, Wang Q, Wu Q, Hu HH, Zhang M et al (2013) Astrocyte-derived ATP modulates depressive-like behaviors. *Nat Med* 19(6):773–777
- Chen N, Sugihara H, Sharma J, Perea G, Petracic J, Le C et al (2012) Nucleus basalis-enabled stimulus-specific plasticity in the visual cortex is mediated by astrocytes. *Proc Natl Acad Sci U S A* 109(41):E2832–E2841
- Citri A, Malenka RC (2008) Synaptic plasticity: multiple forms, functions, and mechanisms. *Neuropharmacol Official Publ Am Coll Neuropsychopharmacol* 33(1):18–41
- Cornell-Bell AH, Finkbeiner SM, Cooper MS, Smith SJ (1990) Glutamate induces calcium waves in cultured astrocytes: long-range glial signaling. *Science* 247(4941):470–473
- D'Ascenzo M, Fellin T, Terunuma M, Revilla-Sanchez R, Meaney DF, Auberson YP et al (2007) mGluR5 stimulates gliotransmission in the nucleus accumbens. *Proc Natl Acad U S A* 104(6):1995–2000
- Di Castro MA, Chuquet J, Liaudet N, Bhaukaurally K, Santello M, Bouvier D et al (2011) Local Ca²⁺ detection and modulation of synaptic release by astrocytes. *Nature Neurosci* 14(10):1276–1284
- Ding S, Fellin T, Zhu Y, Lee SY, Auberson YP, Meaney DF et al (2007) Enhanced astrocytic Ca²⁺ signals contribute to neuronal excitotoxicity after status epilepticus. *J Neurosci: Official J Soc Neurosci* 27(40):10674–10684
- Ding F, O'Donnell J, Thrane AS, Zeppenfeld D, Kang H, Xie L et al (2013) alpha1-Adrenergic receptors mediate coordinated Ca²⁺ signaling of cortical astrocytes in awake, behaving mice. *Cell Calcium* 54(6):387–394
- Dombeck DA, Khabbaz AN, Collman F, Adelman TL, Tank DW (2007) Imaging large-scale neural activity with cellular resolution in awake, mobile mice. *Neuron* 56(1):43–57
- Domercq M, Brambilli L, Pilati E, Marchaland J, Volterra A, Bezzi P (2006) P2Y1 receptor-evoked glutamate exocytosis from astrocytes: control by tumor necrosis factor-alpha and prostaglandins. *J Biol Chem* 281(41):30684–30696
- Fellin T, Pascual O, Gobbo S, Pozzan T, Haydon PG, Carmignoto G (2004) Neuronal synchrony mediated by astrocytic glutamate through activation of extrasynaptic NMDA receptors. *Neuron* 43(5):729–743
- Fellin T, Halassa MM, Terunuma M, Succol F, Takano H, Frank M et al (2009) Endogenous nonneuronal modulators of synaptic transmission control cortical slow oscillations in vivo. *Proc Natl Acad Sci U S A* 106(35):15037–15042
- Fiacco TA, Agulhon C, Taves SR, Petracic J, Casper KB, Dong X et al (2007) Selective stimulation of astrocyte calcium in situ does not affect neuronal excitatory synaptic activity. *Neuron* 54(4):611–626
- Figueiredo M, Lane S, Stout RF Jr, Liu B, Parpura V, Teschemacher AG et al (2014) Comparative analysis of optogenetic actuators in cultured astrocytes. *Cell Calcium* 56(3):208–214
- Fujita T, Chen MJ, Li B, Smith NA, Peng W, Sun W et al (2014) Neuronal transgene expression in dominant-negative SNARE mice. *J Neurosci: Official J Soc Neurosci* 34(50):16594–16604
- Gee JM, Smith NA, Fernandez FR, Economo MN, Brunert D, Rothermel M et al (2014) Imaging activity in neurons and glia with a Polr2a-based and cre-dependent GCaMP5G-IRES-tdTomato reporter mouse. *Neuron* 83(5):1058–1072
- Gomez-Gonzalo M, Navarrete M, Perea G, Covelo A, Martin-Fernandez M, Shigemoto R et al (2014) Endocannabinoids induce lateral long-term potentiation of transmitter release by stimulation of gliotransmission. *Cereb Cortex*
- Gourine AV, Kasymov V, Marina N, Tang F, Figueiredo MF, Lane S et al (2010) Astrocytes control breathing through pH-dependent release of ATP. *Science* 329(5991):571–575
- Gradinaru V, Mogri M, Thompson KR, Henderson JM, Deisseroth K (2009) Optical deconstruction of parkinsonian neural circuitry. *Science* 324(5925):354–359

- Habbas S, Santello M, Becker D, Stubbe H, Zappia G, Liaudet N et al (2015) Neuroinflammatory TNF alpha impairs memory via astrocyte signaling. *Cell* 163(7):1730–1741
- Haber M, Zhou L, Murai KK (2006) Cooperative astrocyte and dendritic spine dynamics at hippocampal excitatory synapses. *J Neurosci: Official J Soc Neurosci* 26(35):8881–8891
- Halassa MM, Fellin T, Takano H, Dong JH, Haydon PG (2007) Synaptic islands defined by the territory of a single astrocyte. *J Neurosci: Official J Soc Neurosci* 27(24):6473–6477
- Halassa MM, Florian C, Fellin T, Munoz JR, Lee SY, Abel T et al (2009) Astrocytic modulation of sleep homeostasis and cognitive consequences of sleep loss. *Neuron* 61(2):213–219
- Hamilton NB, Attwell D (2010) Do astrocytes really exocytose neurotransmitters? *Nat Rev Neurosci* 11(4):227–238
- Henneberger C, Papouin T, Oliet SH, Rusakov DA (2010) Long-term potentiation depends on release of D-serine from astrocytes. *Nature* 463(7278):232–236
- Jahn HM, Scheller A, Kirchhoff F (2015) Genetic control of astrocyte function in neural circuits. *Front Cell Neurosci* 9:310
- Jo S, Yarishkin O, Hwang YJ, Chun YE, Park M, Woo DH et al (2014) GABA from reactive astrocytes impairs memory in mouse models of Alzheimer's disease. *Nat Med* 20(8):886–896
- Jourdain P, Bergersen LH, Bhaukaurally K, Bezzini P, Santello M, Domercq M et al (2007) Glutamate exocytosis from astrocytes controls synaptic strength. *Nat Neurosci* 10(3):331–339
- Kim TK, Eberwine JH (2010) Mammalian cell transfection: the present and the future. *Anal Bioanal Chem* 397(8):3173–3178
- Le Bail M, Martineau M, Sacchi S, Yatsenko N, Radzishevsky I, Conrod S et al (2015) Identity of the NMDA receptor coagonist is synapse specific and developmentally regulated in the hippocampus. *Proc Natl Acad Sci U S A* 112(2):E204–E213
- Lee S, Yoon BE, Berglund K, Oh SJ, Park H, Shin HS et al (2010) Channel-mediated tonic GABA release from glia. *Science* 330(6005):790–806
- Lee HS, Ghetti A, Pinto-Duarte A, Wang X, Dziewczapolski G, Galimi F et al (2014) Astrocytes contribute to gamma oscillations and recognition memory. *Proc Natl Acad Sci U S A* 111(32):E3343–E3352
- Lima A, Sardinha VM, Oliveira AF, Reis M, Mota C, Silva MA et al (2014) Astrocyte pathology in the prefrontal cortex impairs the cognitive function of rats. *Mol Psychiatry* 19(7):834–841
- Liu L, Wong TP, Pozza MF, Lingenhoehl K, Wang Y, Sheng M et al (2004) Role of NMDA receptor subtypes in governing the direction of hippocampal synaptic plasticity. *Science* 304(5673):1021–1024
- Mariotti L, Losi G, Sessolo M, Marcon I, Carmignoto G (2016) The inhibitory neurotransmitter GABA evokes long-lasting Ca^{2+} oscillations in cortical astrocytes. *Glia* 64(3):363–373
- Masamoto K, Unekawa M, Watanabe T, Toriumi H, Takuwa H, Kawaguchi H et al (2015) Unveiling astrocytic control of cerebral blood flow with optogenetics. *Sci Rep* 5:11455
- Matos M, Shen HY, Augusto E, Wang Y, Wei CJ, Wang YT et al (2015) Deletion of adenosine A2A receptors from astrocytes disrupts glutamate homeostasis leading to psychomotor and cognitive impairment: relevance to schizophrenia. *Biol Psychiat* 78(11):763–774
- Min R, Nevian T (2012) Astrocyte signaling controls spike timing-dependent depression at neocortical synapses. *Nat Neurosci* 15(5):746–753
- Mothet JP, Pollegioni L, Ouanounou G, Martineau M, Fossier P, Baux G (2005) Glutamate receptor activation triggers a calcium-dependent and SNARE protein-dependent release of the gliotransmitter D-serine. *Proc Natl Acad Sci U S A* 102(15):5606–5611
- Mothet JP, Le Bail M, Billard JM (2015) Time and space profiling of NMDA receptor co-agonist functions. *J Neurochem* 135(2):210–225
- Navarrete M, Araque A (2008) Endocannabinoids mediate neuron-astrocyte communication. *Neuron* 57(6):883–893
- Navarrete M, Araque A (2010) Endocannabinoids potentiate synaptic transmission through stimulation of astrocytes. *Neuron* 68(1):113–126
- Navarrete M, Perea G, Fernandez de Sevilla D, Gomez-Gonzalo M, Nunez A, Martin ED et al (2012) Astrocytes mediate in vivo cholinergic-induced synaptic plasticity. *PLoS Biol* 10(2):e1001259

- Nimmerjahn A, Mukamel EA, Schnitzer MJ (2009) Motor behavior activates Bergmann glial networks. *Neuron* 62(3):400–412
- Panatier A, Theodosis DT, Mothet JP, Touquet B, Pollegioni L, Poulain DA et al (2006) Glia-derived D-serine controls NMDA receptor activity and synaptic memory. *Cell* 125(4):775–784
- Panatier A, Vallee J, Haber M, Murai KK, Lacaille JC, Robitaille R (2011) Astrocytes are endogenous regulators of basal transmission at central synapses. *Cell* 146(5):785–798
- Pankratov Y, Lalo U (2015) Role for astroglial alpha1-adrenoreceptors in gliotransmission and control of synaptic plasticity in the neocortex. *Front Cell Neurosci* 9:230
- Papouin T, Ladepeche L, Ruel J, Sacchi S, Labasque M, Hanini M et al (2012) Synaptic and extrasynaptic NMDA receptors are gated by different endogenous coagonists. *Cell* 150(3):633–646
- Pascual O, Casper KB, Kubera C, Zhang J, Revilla-Sanchez R, Sul JY et al (2005) Astrocytic purinergic signaling coordinates synaptic networks. *Science* 310(5745):113–116
- Paukert M, Agarwal A, Cha J, Doze VA, Kang JU, Bergles DE (2014) Norepinephrine controls astroglial responsiveness to local circuit activity. *Neuron* 82(6):1263–70
- Perea G, Araque A (2005) Properties of synaptically evoked astrocyte calcium signal reveal synaptic information processing by astrocytes. *J Neurosci* 25(9):2192–2203
- Perea G, Araque A (2007) Astrocytes potentiate transmitter release at single hippocampal synapses. *Science* 317(5841):1083–1086
- Perea G, Navarrete M, Araque A (2009) Tripartite synapses: astrocytes process and control synaptic information. *Trends in Neurosci* 32(8):421–431
- Perea G, Sur M, Araque A (2014a) Neuron-glia networks: integral gear of brain function. *Front Cell Neurosci* 8:378
- Perea G, Yang A, Boyden ES, Sur M (2014b) Optogenetic astrocyte activation modulates response selectivity of visual cortex neurons in vivo. *Nat Commun* 5:3262
- Perez-Alvarez A, Navarrete M, Covelo A, Martin ED, Araque A (2014) Structural and functional plasticity of astrocyte processes and dendritic spine interactions. *J Neurosci: Official J Soc Neurosci* 34(38):12738–12744
- Perry E, Walker M, Grace J, Perry R (1999) Acetylcholine in mind: a neurotransmitter correlate of consciousness? *Trends Neurosci* 22(6):273–280
- Pirttimaki TM, Codadu NK, Awini A, Pratik P, Nagel DA, Hill EJ et al (2013) alpha7 Nicotinic receptor-mediated astrocytic gliotransmitter release: Abeta effects in a preclinical Alzheimer's mouse model. *PloS One* 8(11):e81828
- Saab AS, Neumeyer A, Jahn HM, Cupido A, Simek AA, Boele HJ et al (2012) Bergmann glial AMPA receptors are required for fine motor coordination. *Science* 337(6095):749–753
- Santello M, Bezzi P, Volterra A (2011) TNF alpha controls glutamatergic gliotransmission in the hippocampal dentate gyrus. *Neuron* 69(5):988–1001
- Santello M, Cali C, Bezzi P (2012) Gliotransmission and the tripartite synapse. *Adv Exp Med Biol* 970:307–331
- Sasaki T, Kuga N, Namiki S, Matsuki N, Ikegaya Y (2011) Locally synchronized astrocytes. *Cerebral cortex*. 21(8):1889–1900
- Sasaki T, Beppu K, Tanaka KF, Fukazawa Y, Shigemoto R, Matsui K (2012) Application of an optogenetic byway for perturbing neuronal activity via glial photostimulation. *Proc Natl Acad Sci U S A* 109(50):20720–20725
- Scofield MD, Boger HA, Smith RJ, Li H, Haydon PG, Kalivas PW (2015) Gq-DREADD selectively initiates glial glutamate release and inhibits Cue-induced cocaine seeking. *Biol Psychiatry* 78(7):441–451
- Serrano A, Haddjeri N, Lacaille JC, Robitaille R (2006) GABAergic network activation of glial cells underlies hippocampal heterosynaptic depression. *J Neurosci* 26(20):5370–5382
- Shigetomi E, Bowser DN, Sofroniew MV, Khakh BS (2008) Two forms of astrocyte calcium excitability have distinct effects on NMDA receptor-mediated slow inward currents in pyramidal neurons. *J Neurosci* 28(26):6659–6663

- Shigetomi E, Jackson-Weaver O, Huckstepp RT, O'Dell TJ, Khakh BS (2013) TRPA1 channels are regulators of astrocyte basal calcium levels and long-term potentiation via constitutive D-serine release. *J Neurosci: Official J Soc Neurosci* 33(24):10143–10153
- Sloan SA, Barres BA (2014) Looks can be deceiving: reconsidering the evidence for gliotransmission. *Neuron* 84(6):1112–1115
- Takata N, Mishima T, Hisatsune C, Nagai T, Ebisui E, Mikoshiba K et al (2011) Astrocyte calcium signaling transforms cholinergic modulation to cortical plasticity in vivo. *J Neurosci: Official J Soc Neurosci* 31(49):18155–18165
- Talantova M, Sanz-Blasco S, Zhang X, Xia P, Akhtar MW, Okamoto S et al (2013) Abeta induces astrocytic glutamate release, extrasynaptic NMDA receptor activation, and synaptic loss. *Proc Natl Acad Sci U S A* 110(27):E2518–E2527
- Tang F, Lane S, Korsak A, Paton JF, Gourine AV, Kasparov S et al (2014) Lactate-mediated glia-neuronal signalling in the mammalian brain. *Nat Commun* 5:3284
- Volterra A, Bezzì P (2002) Release of transmitters from glial cells. In: Volterra A, Magistretti PJ, Haydon PG (eds) *The tripartite synapse: glia in synaptic transmission*. Oxford University Press, pp 164–184
- Volterra A, Liaudet N, Savtchouk I (2014) Astrocyte Ca^{2+} signalling: an unexpected complexity. *Nat Rev Neurosci* 15(5):327–335
- Wang X, Lou N, Xu Q, Tian GF, Peng WG, Han X et al (2006) Astrocytic Ca^{2+} signaling evoked by sensory stimulation in vivo. *Nat Neurosci* 9(6):816–823
- Xie AX, Petracic J, McCarthy KD (2015) Molecular approaches for manipulating astrocytic signaling in vivo. *Front Cell Neurosci* 9:144
- Yang J, Yu H, Zhou D, Zhu K, Lou H, Duan S et al (2015) $\text{Na}^+–\text{Ca}^{2+}$ exchanger mediates ChR2-induced $[\text{Ca}^{2+}]_{\text{i}}$ elevation in astrocytes. *Cell Calcium* 58(3):307–316
- Yoo SS, Hu PT, Gujar N, Jolesz FA, Walker MP (2007) A deficit in the ability to form new human memories without sleep. *Nat Neurosci* 10(3):385–392
- Yoon BE, Lee CJ (2014) GABA as a rising gliotransmitter. *Front Neural Circ* 8:141
- Zhang Q, Fukuda M, Van Bockstaele E, Pascual O, Haydon PG (2004) Synaptotagmin IV regulates glial glutamate release. *Proc Natl Acad Sci U S A* 101(25):9441–9446
- Zhang F, Gradinaru V, Adamantidis AR, Durand R, Airan RD, de Lecea L et al (2010) Optogenetic interrogation of neural circuits: technology for probing mammalian brain structures. *Nat Protoc* 5(3):439–456
- Zorec R, Araque A, Carmignoto G, Haydon PG, Verkhratsky A, Parpura V (2012) Astroglial excitability and gliotransmission: an appraisal of Ca^{2+} as a signalling route. *ASN Neuro* 4(2)
- Zorec R, Verkhratsky A, Rodriguez JJ, Parpura V (2015) Astrocytic vesicles and gliotransmitters: slowness of vesicular release and synaptobrevin2-laden vesicle nanoarchitecture. *Neuroscience*

Chapter 9

Purinergic Signaling at Tripartite Synapses



Anup Pillai and Suhita Nadkarni

Abstract Astrocytes modulate synaptic transmission and plasticity via the release of gliotransmitters. ATP release by astrocytes and its chief metabolite, adenosine mediate astrocyte–neuron crosstalk through a plethora of ionotropic and metabotropic purinergic receptors and provide a unique framework that enables bidirectional modulation of neuronal excitability over a range of spatial and temporal scales. More recently dysregulation in purinergic signaling has also been associated with several disorders. The complexity of purinergic signaling and overlapping signaling pathways used by astrocytes and neurons makes it difficult to quantify the precise contribution of astrocytic release to function and yet provide a fertile ground for computational and modeling approaches. Here we review seminal experimental evidence on feedback and feedforward regulation of neuronal activity by astrocytes by means of purinergic signaling and pinpoint the essential requirements for a modeling framework to study this signaling at tripartite synapses. The ultimate goal would be to quantify the diverse functions of purinergic transmission stemming from a large variety of receptor type and spatiotemporal landscape.

Keywords ATP · Purinergic receptors · Gliotransmitter release · Adenosine · Calcium signaling

9.1 Introduction

Astrocytes are acknowledged partners in the majority of cortical synapses where they modulate synaptic transmission and plasticity via the release of gliotransmitters. One of the signaling molecules that is primarily released by astrocytes and mediate astrocyte–neuron crosstalk is adenosine triphosphate (ATP) and its chief metabolite,

A. Pillai (✉) · S. Nadkarni (✉)

Indian Institute of Science Education and Research, Dr. Homi Bhabha Road, Pune 41108, India
e-mail: anupgpillai@gmail.com

S. Nadkarni
e-mail: suhita@iiserpune.ac.in

adenosine. In conjunction with gliotransmitter release the activation of purinergic receptors on both neurons and astrocytes results in complex signaling cascades that bidirectionally modulate neuronal excitability, synaptic transmission, and plasticity on a broad range of spatial and temporal scales.

Apart from its well-known role as the “biological currency” for energy, ATP was first identified as an extracellular signaling molecule in heart muscle cells by Alan Drury and Albert Szent-Györgyi in 1929 (Drury and Szent-Györgyi 1929). Roughly three decades later, Pamela Holton reported on the release of ATP from sensory terminals (Holton 1959). These along with other findings that followed led to the formulation of the “purinergic hypothesis” by Geoffrey Burnstock in 1972, where the role of purines as a signaling molecule in the brain was first proposed (Burnstock 2007). However, the hypothesis did not receive wide support from the scientific community until decades later when several major discoveries were made about purinergic receptors as well as about the role purines played as signaling molecules. First, the identification of ionotropic P2X receptors established that ATP, like glutamate and GABA, could mediate fast synaptic transmission at cortical synapses (Evans et al. 1992). Second, ATP and adenosine were found to activate several types of G-protein coupled receptors and result in Ca^{2+} excitability and activation of various downstream signaling pathways on a slower timescale (Salter and Hicks 1995). Third, experiments have associated the diffusive properties of ATP and adenosine with the regulation of hippocampal synaptic transmission at multiple temporal scales (Zhang et al. 2003; Pascual et al. 2005; Gordon et al. 2009).

Recent research on local and global Ca^{2+} elevations in astrocytes further enriched the dual role of ATP whereby it seamlessly alternates from being intracellular molecule for energy to a signaling molecule outside the cell (Coco et al. 2003; Zhang et al. 2007). It has also been recognized that purinergic gliotransmission promotes the long-range propagation of intracellular Ca^{2+} waves in astrocytic networks (Guthrie et al. 1999; Bowser and Khakh 2007a) and modulates synaptic transmission in similar ways to those reported for glutamatergic gliotransmission (Edwards et al. 1992).

Despite this wealth of knowledge about the actions of ATP and purines the exploration of purinergic transmission and its coupling with signaling pathways at microdomain regions around tripartite synapses continues to challenge experimentalists (Volterra et al. 2014). Computational models provide a unique niche in the exploration of the finer scales of spatiotemporal signaling by purines, particularly at the processes. Considerable progress made on our understanding of astrocytic whole-cell Ca^{2+} signaling via computational studies clearly exemplifies their critical role in unraveling astrocytic mechanisms (Höfer et al. 2002; Bellinger 2005; Bennett et al. 2005; Macdonald et al. 2008; Li et al. 2012). The aim of this chapter is to review the essential functional details of the key steps involved in designing a comprehensive modeling framework of purinergic signaling at tripartite synapses.

A formal description of astrocytic purinergic signaling includes at least four fundamental parts. These are: (i) knowledge about Ca^{2+} signaling at astrocytic processes or microdomains that triggers gliotransmitter release; (ii) the mechanism of gliotransmitter release; (iii) the time course of ATP degradation and production of its

metabolites in extracellular space; and finally (iv) the downstream pathways and the loci at which purinergic modulation of synaptic transmission at tripartite synapses take place. While some of these components physiologically resemble neurotransmitter release and calcium signaling in neurons, astrocytic processes occupy a unique niche in terms of the origin, timing, and dynamics of calcium as well as the organization of vesicles and the release machinery. We will elucidate each of these concepts and discuss ways to model them in the following sections.

9.2 Modeling Calcium Signaling via Purinergic Receptors

ATP released from astrocytes binds to ionotropic P2X receptors and metabotropic P2Y receptors that are expressed on both astrocytic processes and pre- and postsynaptic membranes.

9.2.1 *P2X Receptors*

P2X channels function as nonselective cation channels that allow rapid influx of Na^+ , K^+ , and Ca^{2+} ions to mediate fast synaptic transmission. To date, seven major isoforms of P2X receptors have been identified in the mammalian brain (P2X_{1-7}) (Khakh 2001; Egan et al. 2006). A major feature of these channels is the relatively high permeability of Ca^{2+} , which roughly is half the Ca^{2+} influx through NMDA receptors (Egan and Khakh 2004). However, in contrast to NMDARs they have low binding affinity for the ligand and fast activation kinetics. Taking these characteristics into account as well as the high diffusivity and reuptake of released ATP, P2X receptors make ideal candidates for fast synaptic transmission in confined spaces.

While most P2X channels display similar permeability for monovalent ions like Na^+ and K^+ and show current reversal close to zero millivolts, with little or no rectification, there also exists considerable diversity in the mode of action among P2XR subtypes (North 2002). Notably, the P2X_2 and P2X_4 channels have the highest affinity for ATP and higher conductances than other receptors in the family. P2X_4 channels, for instance, have a distinct ATP-evoked current that develops slowly, but reach very high amplitude (Soto et al. 1996). These peaks are also the largest among individual P2XRs and are sensitive to previous ATP exposures. In general, P2XRs exhibit low desensitization, an exception from this rule is the P2X_5 channel whose peak current reduces by half upon prolonged (>10 s) ATP application (Surprenant and North 2009). Another unique feature of this particular channel is its ability to conduct Cl^- ions (Bo 2003). Apart from the P2X_6 channel, which is functional only in the heteromeric assembly, other members of the P2X family exhibit both homomeric and heteromeric subunit configurations (Lê et al. 1998). It has been observed in several of the P2XR subtypes that the channel pore flickers between open and closed states even while the ligand is bound. The P2X_2 receptor with its

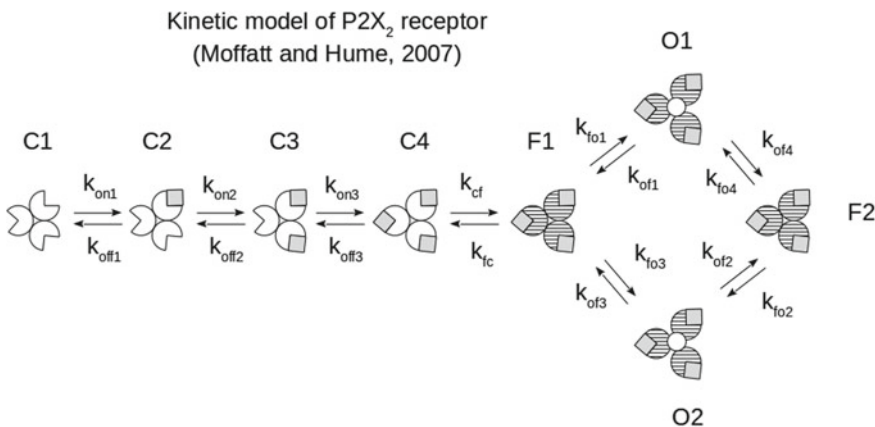


Fig. 9.1 A detailed kinetic scheme for the P2X₂ receptor (from Moffatt and Hume 2007). The model has four closed states (C1–C4), two flip states (F1 and F2), and two conducting states (O1 and O2). P2X₂ channel currents typically reverse around 0 mV and are highly calcium permeable (Table 9.1)

fast channel kinetics and wide distribution in several brain regions is a good candidate to include in theoretical studies of ATP-mediated rapid Ca²⁺ signaling. Accordingly, several simple yet detailed kinetic models for this receptor have been proposed based on maximum likelihood analysis of single-channel patch clamp electrophysiological data (Ding and Sachs 1999; Whitlock et al. 2001; Moffatt and Hume 2007). While the P2X₂ receptor was initially hypothesized to have four closed and two open states, recent studies suggest additional channel configurations that ensue from the inclusion of flip states (Fig. 9.1). P2X₇ channels due to their large pore diameter and high expression levels are also thought provide an additional pathway for rapid efflux of molecules such as glutamate and ATP (Duan et al. 2003; Kukley et al. 2001). A summary of some of the key findings from studies that have used single-channel or whole-cell patch clamp techniques to investigate the properties of various P2X receptor subtypes is presented in Table 9.1.

9.2.2 P2Y Receptors

The P2Y receptor family encompasses a large group of metabotropic ATP receptors that are coupled to G-proteins of G_q, G_s and G_i types (Abbracchio 2006). Like the P2X family, P2YRs are highly expressed in both neurons and astrocytic membranes as homo- and heteromeric assemblies (Abbracchio and Ceruti 2006). Broadly, P2Y receptors activate either or both phospholipase C (PLC) and adenylyl cyclase (AC) to regulate the levels of two of the most critical intracellular second messengers, IP₃ and cAMP, respectively.

Table 9.1 Summary of P2X receptor characteristics

Channel property	Units	P2X ₁	P2X ₂	P2X ₃	P2X ₄	P2X ₅	P2X ₇	P2X _{4/6}	Brain slices (P2X ₂ , P2X ₄ , and P2X ₄)
Conductance	pS		30–34				9–13		29–56
Open probability		0.6				0.26–0.3		0.01–0.58	
Relative permeability for calcium (P _{Ca/Na})		3.9–5	2.2–2.7		4.2	1.5			
Relative permeability for chloride (P _{Cl/Na})			0.02			0.5			
Reversal potential	mV	0	0	0	0	–15 to 0	–2 to 0	0	
Mean open time	ms		2.5				5–20		0.63–2.6
EC ₅₀	μM		11.2–16.3	20	1–10		100–300	6.3	
Hill coefficient		2.3	1.2	1.3–1.9					
Dissociation constant (K _d)	μM	35				139			
Number of open states		2				1			
Number of closed states		5				3			
Rise time constant	ms		0.52						
Decay time constant	ms	61							

At least eight P2Y subtypes have been reported in the mammalian CNS. A majority of them (P2Y₁, P2Y₂, P2Y₄, P2Y₆, and P2Y₁₁) are linked to G_q proteins and activate PLC to promote IP₃ production, while others (P2Y₁₂, P2Y₁₃, and P2Y₁₄) are linked to G_i proteins that inhibit AC and reduce intracellular cAMP levels. This bidirectional modulation of IP₃ and cAMP concentration by P2YR activation produces excitatory and inhibitory effects, respectively, on target cells. Thus, depending on the type of P2YR expressed, ATP-mediated effects can exhibit considerable diversity in direction and magnitude of downstream signaling (Köles et al. 2011).

9.2.3 Adenosine Receptors

Apart from the direct action of ATP on P2X and P2Y receptors, extracellular accumulation of adenosine produced by ectonucleotidase activity acts on four types of G-protein coupled receptors: A₁, A_{2A}, A_{2B}, and A₄. A₁ receptors inhibit presynaptic release of neurotransmitters and cause postsynaptic hyperpolarization (Scanziani et al. 1992). A₁ receptors primarily inhibit cAMP production via adenylate cyclase. However, the exact mechanism behind the suppression of presynaptic release via A₁ receptors is not clear. One of the candidate mechanisms implicated is A₁R-mediated reduction of the conductance of P/Q-type Ca²⁺ channels (Ambrósio et al. 1997).

In opposition to this inhibitory action, adenosine acting on A_{2A} receptors facilitates synaptic release and transmission via protein kinase C-dependent mechanisms (Lopes et al. 2002). Notably, studies also imply that the balance between the activation of A₁ and A_{2A} receptors is critical to the direction of these adenosine-mediated effects on synaptic transmission (Rebola et al. 2005).

Unlike the A₁ and A_{2A} receptors the mechanisms behind A_{2B} and A₄ receptors remain poorly understood, especially with regard to their role in the CNS. However, it is generally agreed that these receptors primarily act via adenylate cyclase, G-proteins (G_q/G₁₁) linked to PLC and through the G_{iα1} and G_{iα3} pathways (Cunha 2001; Fredholm et al. 2005).

9.2.4 Distribution and Location of Purinergic Receptors

P2X₄ and P2X₆ are among the highly expressed P2X channels in the brain, however, the latter is not present in most glial cell including astrocytes. A study by Kukley and collaborators identified that P2X₄ and P2X₆ receptors are equally distributed both in the soma and the processes, whereas P2X₃ is specifically targeted at the perisynaptic processes around synaptic contacts (Kukley et al. 2001). It is worth noting that studies on the distribution of receptors are not always consistent with functional assays. This could be due to specificity issues of antibodies or due to the fact that the presence of mRNA/proteins cannot guarantee the presence of a functional receptor. An example is the recent study about functional evidence for

Table 9.2 Summary of purinergic receptor distribution

Location	P2X receptors/subunits	P2Y receptors	Adenosine receptors
Presynaptic bouton	P2X ₂ , P2X ₃ , P2X ₄ , P2X ₇	P2Y ₁ , P2Y ₁₃ , P2Y ₁₂	A ₁ , A _{2A}
Postsynaptic membrane	P2X ₂ , P2X ₄ , P2X ₆		
Astrocyte	P2X ₁ , P2X ₂ , P2X ₃ , P2X ₄ , P2X ₇	P2Y ₁ , P2Y ₁₂ , P2Y ₁₄	A ₁ , A ₂ , A _{2A}

P2X₇ receptors in cortical nerve terminals despite the reported absence of its mRNA and protein in the brain (Alloisio et al. 2008).

Similar to P2X receptors, P2YRs are also abundantly found in both neurons and astrocytes. In particular, both A₁ and A_{2A} receptors have been reported in hippocampal nerve terminals. Interestingly, several studies have also observed the inhibitory and excitatory actions of adenosine on synaptic transmission upon A₁ or A_{2A} receptor activation, respectively. We refer the reader to a number of excellent reviews on this topic by some of the leading experts in the field (Fields and Burnstock 2006; Burnstock 2007). Table 9.2 presents data compiled from the literature on the distribution of purinergic receptors in neurons and astrocytes.

9.2.5 Intracellular Ca²⁺ Wave Propagation

Since the first observation of intracellular Ca²⁺ waves (ICW) in astrocytic cultures several studies have revealed the mechanisms behind wave initiation and propagation (Cornell-Bell et al. 1990; Dani et al. 1992). These studies established ATP release, its action on P2YRs, and the resultant release of ER Ca²⁺ as critical mediators of astrocytic Ca²⁺ waves (Guthrie et al. 1999; Newman 2001). In parallel, experimental and computational modeling have also highlighted the key role played by the intracellular second messenger IP₃ that diffuses through gap junctions between astrocytes (Boitano et al. 1992; Venance et al. 1997) (see also Chap. 7). While computational models were instrumental in predicting the role played by purinergic signaling in Ca²⁺ waves, they lacked a detailed description of P2YR signaling and gliotransmitter release (Iacobas et al. 2006; Stamatakis and Mantzaris 2006; Kang and Othmer 2009; Edwards and Gibson 2010). Biophysically realistic models are particularly helpful in teasing apart how the mutually opposing ATP mediated effects on Ca²⁺ signaling influence both feedback and feedforward flow of information between neurons and astrocytes (Fellin 2006; Nadkarni et al. 2008; Amiri et al. 2013).

9.3 Modeling Calcium-Dependent ATP Release from Astrocytes

There is increasing evidence on astrocytic release of ATP via Ca^{2+} -dependent exocytosis as well as through nonvesicular pathways such as volume-activated channels (connexin, pannexin, and P2X₇) (Hamilton and Attwell 2010; Sahlender et al. 2014). However, a majority of ATP releases through nonvesicular modes are associated with pathological states (Evanko et al. 2004; Giaume et al. 2013). Conversely, in the healthy brain ATP release is primarily found to be Ca^{2+} -mediated (Araque et al. 2000, 2014). We therefore limit our discussion to vesicular ATP release in this chapter.

Many experimental observations confirm that astrocytes express most, if not all, of the molecular components needed for vesicular exocytosis of ATP (Parpura et al. 1995; Maienschein et al. 1999; Pangršić et al. 2007; Verderio et al. 2012; Singh et al. 2014). Indeed, ATP-filled lysosomes and secretory granules in astrocytes have been found to express vesicular nucleotide transporters (VNUTs), which are necessary for filling the intracellular organelles with ATP (Sawada et al. 2008; Oya et al. 2013). Furthermore, astrocytic terminals contain an analog of the Ca^{2+} sensor, Synaptotagmin-4 (SyT4), which is responsible for triggering vesicular fusion in the presynaptic terminal (Zhang et al. 2004a). However, it remains to be fully elucidated whether SyT4 is the only mediator of astrocytic ATP release. Incidentally, SyT4 is one of the least characterized sensors of the more than 15 known SyTs, of which SyT1, 2, 7 and 9 have been implicated in synaptic neurotransmitter exocytosis (Sudhof and Rothman 2009; Pang and Südhof 2010; Jahn and Fasshauer 2012; Bacaj et al. 2013). Although the astrocytic Ca^{2+} -sensor (SyT4) shares structural similarity with SyT1, its mode of action is marginally different due to the absence one critical Ca^{2+} binding site (Fig. 9.2). Nonetheless, some studies have provided information on the binding affinity and Ca^{2+} cooperativity of astrocytic calcium sensors (Parpura and Haydon 2000; Kref et al. 2004).

An intriguing question that often comes up when modeling ATP release is the fusion mode of ATP release. Astrocytes, akin to neurons, exhibit both kiss-and-run and full-fusion modes of exocytosis the probabilities of which are very much dependent on stimulus identity, concentration, and duration (Bowser and Khakh 2007b;

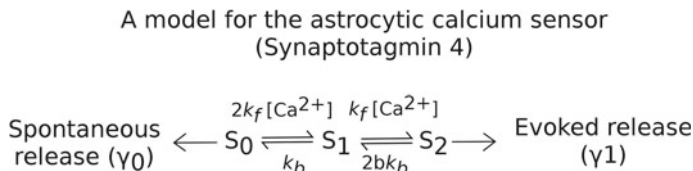


Fig. 9.2 A model for one of the calcium sensors present in astrocytes. A simplified model for the C2B domain of synaptotagmin 4 that can sequentially bind to two calcium ions. S_0 , S_1 , and S_2 : sensors bound to zero, one and two Ca^{2+} ions, respectively; K_f and k_f : forward and backward rates; b: cooperativity factor; γ_0 : spontaneous (Ca^{2+} -independent) release rate; γ_1 : Ca^{2+} -dependent release rate

Malarkey and Parpura 2011). It is conceivable that astrocytes might favor kiss-and-run more as its recycling time is much shorter than full fusion exocytosis (Chen 2006). Consistent with this hypothesis, it has been reported that astrocytic processes harbor far fewer vesicles when compared to presynaptic terminals (Jourdain et al. 2007). A recent study examining the release at microdomains suggests distinct vesicular pools that might mediate kiss-and-run and full-fusion exocytosis (Marchaland et al. 2008). Supporting this argument, it has been reported that astrocytes have both highly mobile and immobile vesicles that may act as the different vesicle pools responsible for the two release modes (Crippa et al. 2006; Kreft et al. 2009). Another possibility is that astrocytes may have two separate sensors that distinctly trigger kiss-and-run versus full-fusion modes. Lastly, the various interacting and intermediary molecules such as Munc 13–18 and Rab3 that are needed to promote vesicular docking have also been identified in astrocytes (Maienschein et al. 1999; Zhang et al. 2004b).

The lack of proper understanding of the release machinery and vesicular arrangement in astrocytic processes continues to be a challenge in the design of a realistic model to reproduce the kinetics of ATP-mediated gliotransmitter release. Ca^{2+} -mediated release in neurons has been modeled using a hybrid sensor that combines both SyT1 and SyT7 into a single mechanism with multiple Ca^{2+} binding and release sites that favor spontaneous, synchronous, and asynchronous types of release (Sun et al. 2007; Bacaj et al. 2013). Such a model reliably predicts release rates at multiple Ca^{2+} concentrations as well as action potential frequencies. Can a similar model for astrocytic ATP release be considered? The answer to this question is contingent on several assumptions on the binding affinity of SyT4; for example, the forward and backward rates of the sensor and the number of Ca^{2+} binding sites. In addition, the source, amplitude, and dynamics of the Ca^{2+} profile itself need to be taken into account.

Note that Ca^{2+} dynamics is generally fast in neurons and influx is the result of VGCCs opening up, the activation of which is triggered by the time course of the fast action potential (Bollmann 2000; Schneggenburger and Neher 2000). Contrary to this, most of the Ca^{2+} increase in astrocytes is the result of release from internal stores via IP₃ receptors (IP₃Rs) that are thought to operate on timescales that are orders of magnitude slower (Cali et al. 2008; Marchaland et al. 2008). Moreover, it has been suggested that the affinity of SyT4 is similar to the fast neuronal Ca^{2+} sensor (SyT1) (Parpura and Haydon 2000; Robinson et al. 2002).

9.3.1 Vesicular ATP Concentration in Astrocytes

It is possible to record fast ATP-mediated currents arising from single quantal events using the sniffer cell approach where isolated astrocytes are placed near HEK cells that express fast ionotropic P2X ATP receptors (Lalo et al. 2014). Amplitude distribution of quantal responses and measurements on single-channel conductance of P2XRs together helps to estimate the concentration of ATP containing vesicles. Accordingly, it has been suggested that a single vesicle may have roughly 1000 ATP

molecules. Several attempts have been made at quantifying astrocytic vesicle volumes. These studies report that astrocytes have organelles whose diameters range from 30 to 700 nm, going all the way from the synaptic-like microvesicles found in the presynaptic terminal to large secretory lysosomes (Bezzi et al. 2004; Chen 2005). Since, unlike neurons, astrocytes can release multiple transmitter molecules from the same processes it seems possible that the different vesicle populations reflect small glutamate-containing vesicles to larger ATP-containing lysosomes.

9.3.2 Spatiotemporal Aspects of Astrocytic ATP Release

Several experimental studies have described the fast-release profile of astrocytic processes (or microdomains) upon stimulation of agonists for metabotropic ATP/glutamate receptors (Domercq et al. 2006; Calì et al. 2008; Marchaland et al. 2008). This might seem surprising given that astrocytic Ca^{2+} increase is not mediated by the fast opening of VGCCs. It turns out that local Ca^{2+} profiles within the tiny domains of a single process are reasonably fast due to the close proximity of ER tubules and the unique spatial organization that further serves to confine Ca^{2+} diffusion and/or buffering (Hua et al. 2004; Marchaland et al. 2008). Indeed, local Ca^{2+} events within these domains can be as fast as tens of milliseconds and are probably mediated by the stochastic opening of IP_3Rs .

9.4 ATP and Adenosine Time Course in Extracellular Space

Unlike glutamate, which is mostly removed from extracellular space via reuptake mechanisms (see Chaps. 12 and 13), ATP is subjected to enzymatic degradation. These enzymes, collectively known as ectonucleotidases, are enriched in sites surrounding synapses. Four major families of ectonucleotidases have been recognized: (i) ecto-5'-nucleotidase, (ii) alkaline phosphatases, (iii) ectonucleoside triphosphate diphosphohydrolases (E-NTPDases), and (iv) ectonucleotide phosphodiesterases (ENPPs) (Cass et al. 1998).

Together, these ectoenzymes dephosphorylate ATP to lower adenine nucleotides via hydrolysis to cause a rise in extracellular adenosine levels that can last tens of seconds. In this fashion ATP released from astrocytes is rapidly degraded by ectoenzymes, causing an appreciable increase in extracellular adenosine levels within hundreds of milliseconds (~ 200 ms) (Dunwiddie et al. 1997). It takes several seconds (~ 5 s), however, to reach the peak of extracellular adenosine, and many more seconds (~ 20 s) before it is fully degraded by the action of extracellular adenosine deaminase.

Apart from this primary route, adenosine can also be directly released by neurons and astrocytes through the reverse action of nucleotide transporters. This mechanism

has been suggested to be involved in the slow equilibration of adenosine levels whose concentration inside the cells is kept very low (a few nanomolars) by the combined action of transporters and the intracellular enzyme called adenosine kinase (Dunwiddie and Masino 2001; Fredholm et al. 2005).

9.5 Modeling Astrocytic Regulation of Neuronal Activity via Purinergic Gliotransmission

9.5.1 Feedback Mechanisms

ATP-mediated astrocytic feedback regulation of neural activity via fast ionotropic (P2X) and slow metabotropic (P2Y) receptors is well characterized. Among P2XRs, P2X₂, P2X₃, P2X₄ and P2X₆ are known to facilitate presynaptic release (Khakh 2009). This effect is thought to arise as a result of direct Ca²⁺ entry via P2X channels located on the presynaptic membrane (Deuchars et al. 2001). Separately, the presence of P2X₇Rs through their relatively large open pores may lead to additional ATP leak (Duan et al. 2003; Alloisio et al. 2008). The abundant expression of P2YRs on cortical axon terminals provides another slower route for the modulation of neuronal release probabilities. Unlike P2XRs, ATP is known to excite or inhibit neurotransmitter release depending on the P2Y subtype expressed. Accordingly, P2Y₁ activation in primary cultures of rat sympathetic neurons enhances release via PLC-mediated inhibition of K⁺ channels (Chandaka et al. 2008). In contrast, other studies carried out on hippocampal cultures demonstrate release suppression and heterosynaptic depression (Proctor and Dunwiddie 1987; Hulme et al. 2014).

Similar to the bidirectional effects of P2YRs, adenosine can also suppress or enhance release via presynaptic A₁ and A_{2A} receptors, respectively (Lopes et al. 2002; Cunha 2008). Indeed, in several synapses both A₁ and A_{2A} are coexpressed, suggesting that tight control of the densities of these receptors is essential for the fine excitation/inhibition balance under normal scenarios (Rebola et al. 2005).

9.5.2 Feedforward Mechanisms

In addition to modulation of presynaptic neurotransmitter release, purinergic gliotransmission is known to affect transmission of information across synapses via several postsynaptic mechanisms that also exhibit considerable region specificity (Rubio and Soto 2001).

In the paraventricular nucleus (PVN) of the hypothalamus, ATP released by noreadrenergic stimulation of astrocytes causes AMPAR insertion in the synapses formed by PVN magnocellular neurons (Gordon et al. 2005). This phenomenon, which also requires activation of phosphatidylinositol 3-kinase, causes heterosynaptic effects on

surrounding synapses too. A similar effect has also been reported on the same cells when stimulated by glutamate, but requires postsynaptic P2X₇ receptor activation (Gordon et al. 2009).

In contrast to the above finding, postsynaptic P2X₂R activation in hippocampal CA1 pyramidal neurons has been associated with dynamin-dependent internalization of AMPA receptors (Pougnet et al. 2014). Whereas expression of GABA_A receptors in the neocortex is downregulated via a P2X₄-mediated mechanism resulting in the reduction of both tonic and phasic inhibition (Lalo et al. 2014).

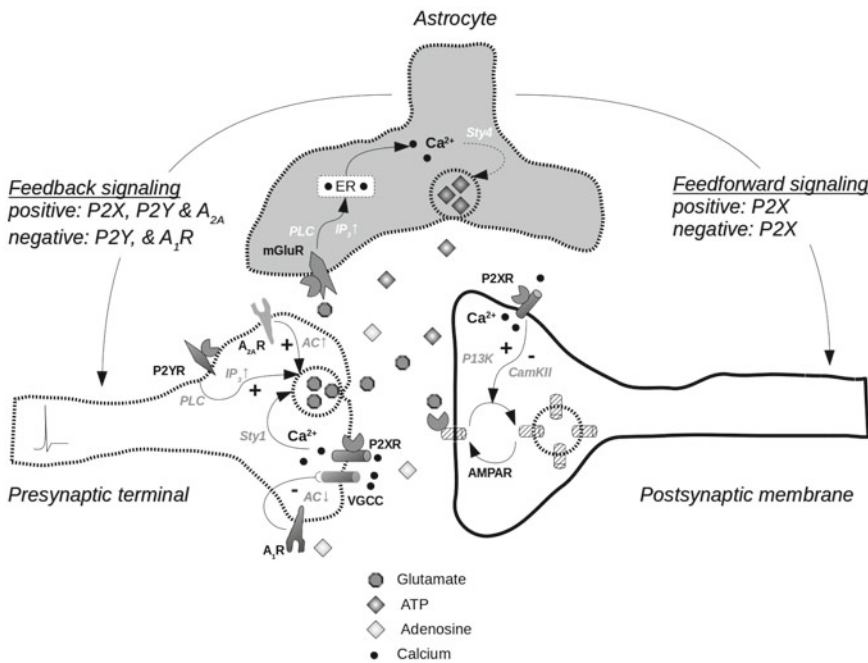


Fig. 9.3 Illustration of the feedback and feedforward signaling routes of gliotransmission. Astrocytic ATP (along with glutamate) can signal both pre- and postsynaptic targets via metabotropic and ionotropic receptors. Activation of these receptors is linked to alterations in intracellular Ca²⁺ levels and in the case of metabotropic receptors may involve second messengers like IP₃ and cAMP. The ensuing effects may include either modulations of release probability from presynaptic terminals or AMPA receptor insertions (or removal) from postsynaptic spines. In parallel, ATP and adenosine (as well as glutamate) can also influence the very astrocyte from which they are released via autoreceptors

9.6 Concluding Remarks

Insights from the studies and data presented here bring to light the multiple and rich modes of purinergic signaling that exist at synaptic junctions (Fig. 9.3). It is clear that ATP released from astrocytic processes together with its chief metabolite adenosine initiate a rich array of responses both in neurons and the surrounding astrocytes. Importantly, these effects are also distributed across a spectrum of timescales via combined activation of ionotropic and metabotropic receptors. While ongoing experimental studies continue to enrich the field with knowledge about newer phenomena and mechanisms, the broad spatiotemporal profiles of purinergic signaling remain major challenges. We believe that computational and biophysically detailed modeling approaches provide a powerful tool to gain a holistic understanding on how this complex and intertwined signaling cascade affects basal synaptic transmission and plasticity at single synapses, both in the healthy and diseased brain.

References

- Abbraccchio MP (2006) International Union of Pharmacology LVIII: Update on the P2Y G protein-coupled nucleotide receptors: from molecular mechanisms and pathophysiology to therapy. *Pharmacol Rev* 58:281–341
- Abbraccchio MP, Ceruti S (2006) Roles of P2 receptors in glial cells: focus on astrocytes. *Purinergic Sig* 2:595–604
- Alloisio S, Cervetto C, Passalacqua M, Barbieri R, Maura G, Nobile M, Marcoli M (2008) Functional evidence for presynaptic P2X7 receptors in adult rat cerebrocortical nerve terminals. *FEBS Lett* 582:3948–3953
- Ambrósio AF, Malva JO, Carvalho AP, Carvalho CM (1997) Inhibition of N-, P/Q- and other types of Ca^{2+} channels in rat hippocampal nerve terminals by the adenosine A1 receptor. *Eur J Pharmacol* 340:301–310
- Amiri M, Hosseini Mardi N, Bahrami F, Janahmadi M (2013) Astrocyte–neuron interaction as a mechanism responsible for generation of neural synchrony: a study based on modeling and experiments. *J Comput Neurosci* 34:489–504
- Araque A, Li N, Doyle RT, Haydon PG (2000) SNARE protein-dependent glutamate release from astrocytes. *J Neurosci* 20:666–673
- Araque A, Carmignoto G, Haydon PG, Oliet SHR, Robitaille R, Volterra A (2014) Gliotransmitters travel in time and space. *Neuron* 81:728–739
- Bacaj T, Wu D, Yang X, Morishita W, Zhou P, Xu W, Malenka RC, Südhof TC (2013) Synaptotagmin-1 and synaptotagmin-7 trigger synchronous and asynchronous phases of neurotransmitter release. *Neuron* 80:947–959
- Bellinger S (2005) Modeling calcium wave oscillations in astrocytes. *Neurocomputing* 65(66):843–850
- Bennett MR, Farnell L, Gibson WG (2005) A quantitative model of purinergic junctional transmission of calcium waves in astrocyte networks. *Biophys J* 89:2235–2250

- Bezzi P, Gundersen V, Galbete JL, Seifert G, Steinhäuser C, Pilati E, Volterra A (2004) Astrocytes contain a vesicular compartment that is competent for regulated exocytosis of glutamate. *Nat Neurosci* 7:613–620
- Bo X (2003) Pharmacological and biophysical properties of the human P2X5 receptor. *Mol Pharmacol* 63:1407–1416
- Boitano S, Dirksen ER, Sanderson MJ (1992) Intercellular propagation of calcium waves mediated by inositol trisphosphate. *Science* 258:292–295
- Bollmann JH (2000) Calcium sensitivity of glutamate release in a calyx-type terminal. *Science* 289:953–957
- Bowser DN, Khakh BS (2007a) Vesicular ATP is the predominant cause of intercellular calcium waves in astrocytes. *J Gen Physiol* 129:485–491
- Bowser DN, Khakh BS (2007b) Two forms of single-vesicle astrocyte exocytosis imaged with total internal reflection fluorescence microscopy. *Proc Natl Acad Sci* 104:4212–4217
- Burnstock G (2007) Physiology and pathophysiology of purinergic neurotransmission. *Physiol Rev* 87:659–797
- Cali C, Marchaland J, Regazzi R, Bezzi P (2008) SDF 1-alpha (CXCL12) triggers glutamate exocytosis from astrocytes on a millisecond time scale: imaging analysis at the single-vesicle level with TIRF microscopy. *J Neuroimmunol* 198:82–91
- Cass CE, Young JD, Baldwin SA (1998) Recent advances in the molecular biology of nucleoside transporters of mammalian cells. *Biochem Cell Biol* 76:761–770
- Chandaka GK, Drobny H, Boehm S (2008) Facilitation of transmitter release from rat sympathetic neurons via presynaptic P2Y1 receptors. *BMC Pharmacol* 8:A8
- Chen X (2005) “Kiss-and-run” glutamate secretion in cultured and freshly isolated rat hippocampal astrocytes. *J Neurosci* 25:9236–9243
- Chen X-K (2006) “Kiss-and-run” exocytosis in astrocytes. *Neurosci* 12:375–378
- Coco S, Calegari F, Pravettoni E, Pozzi D, Taverna E, Rosa P, Matteoli M, Verderio C (2003) Storage and release of ATP from astrocytes in culture. *J Biol Chem* 278:1354–1362
- Cornell-Bell AH, Finkbeiner SM, Cooper MS, Smith SJ (1990) Glutamate induces calcium waves in cultured astrocytes: long-range glial signaling. *Science* 247:470–473
- Crippa D, Schenk U, Francolini M, Rosa P, Verderio C, Zonta M, Pozzan T, Matteoli M, Carmignoto G (2006) Synaptobrevin2-expressing vesicles in rat astrocytes: Insights into molecular characterization, dynamics and exocytosis. *J Physiol* 570:567–582
- Cunha RA (2001) Adenosine as a neuromodulator and as a homeostatic regulator in the nervous system: Different roles, different sources and different receptors. *Neurochem Int* 38:107–125
- Cunha RA (2008) Different cellular sources and different roles of adenosine: A1 receptor-mediated inhibition through astrocytic-driven volume transmission and synapse-restricted A2A receptor-mediated facilitation of plasticity. *Neurochem Int* 52:65–72
- Dani JW, Chernavsky A, Smith SJ (1992) Neuronal activity triggers calcium waves in hippocampal astrocytic networks. *Neuron* 8:429–440
- De Pittà M, Volman V, Berry H, Parpura V, Volterra A, Ben-Jacob E (2012) Computational quest for understanding the role of astrocyte signaling in synaptic transmission and plasticity. *Front Comput Neurosci* 6:98
- Deuchars SA, Atkinson L, Brooke RE, Musa H, Milligan CJ, Batten TF, Buckley NJ, Parson SH, Deuchars J (2001) Neuronal P2X7 receptors are targeted to presynaptic terminals in the central and peripheral nervous systems. *J Neurosci* 21:7143–7152
- Ding S, Sachs F (1999) Single channel properties of P2X2 purinoceptors. *J Gen Physiol* 113:695–720
- Domercq M, Brambilla L, Pilati E, Marchaland J, Volterra A, Bezzi P (2006) P2Y1 receptor-evoked glutamate exocytosis from astrocytes: control by tumor necrosis factor- σ and prostaglandins. *J Biol Chem* 281:30684–30696
- Drury AN, Szent-Györgyi A (1929) The physiological activity of adenine compounds with especial reference to their action upon the mammalian heart. *J Physiol* 68:213–237

- Duan S, Anderson CM, Keung EC, Chen Y, Chen Y, Swanson RA (2003) P2X7 receptor-mediated release of excitatory amino acids from astrocytes. *J Neurosci* 23:1320–1328
- Dunwiddie TV, Masino SA (2001) The role and regulation of adenosine in the central nervous system. *Annu Rev Neurosci* 24:31–55
- Dunwiddie TV, Diao L, Proctor WR (1997) Adenine nucleotides undergo rapid, quantitative conversion to adenosine in the extracellular space in rat hippocampus. *J Neurosci* 17:7673–7682
- Edwards JR, Gibson WG (2010) A model for Ca^{2+} waves in networks of glial cells incorporating both intercellular and extracellular communication pathways. *J Theor Biol* 263:45–58
- Edwards FA, Gibb AJ, Colquhoun D (1992) ATP receptor-mediated synaptic currents in the central nervous system. *Nature* 359:144–147
- Egan TM, Khakh BS (2004) Contribution of calcium ions to P2X channel responses. *J Neurosci* 24:3413–3420
- Egan TM, Samways DSK, Li Z (2006) Biophysics of P2X receptors. *Pflugers Arch Eur J Physiol* 452:501–512
- Evanko DS, Zhang Q, Zorec R, Haydon PG (2004) Defining pathways of loss and secretion of chemical messengers from astrocytes. *Glia* 47:233–240
- Evans RJ, Derkach V, Surprenant A (1992) ATP mediates fast synaptic transmission in mammalian neurons. *Nature* 357:503–505
- Fellin T (2006) Astrocytes coordinate synaptic networks: balanced excitation and inhibition. *Physiology* 21:208–215
- Fields RD, Burnstock G (2006) Purinergic signalling in neuron–glia interactions. *Nat Rev Neurosci* 7:423–436
- Fredholm BB, Chen JF, Cunha RA, Svenssonsson P, Vaugeois JM (2005) Adenosine and brain function. *Int Rev Neurobiol* 63:191–270
- Giaume C, Leybaert L, Naus CC, Sáez JC (2013) Connexin and pannexin hemichannels in brain glial cells: Properties, pharmacology, and roles. *Front Pharmacol* 4(JUL):1–17
- Gordon GRJ, Baimoukhamedova DV, Hewitt SA, Rajapaksha WRAKJS, Fisher TE, Bains JS (2005) Norepinephrine triggers release of glial ATP to increase postsynaptic efficacy. *Nat Neurosci* 8:1078–1086
- Gordon GRJ, Iremonger KJ, Kantevari S, Ellis-Davies GCR, MacVicar BA, Bains JS (2009) Astrocyte-mediated distributed plasticity at hypothalamic glutamate synapses. *Neuron* 64:391–403
- Guthrie PB, Knappenberger J, Segal M, Bennett MV, Charles AC, Kater SB (1999) ATP released from astrocytes mediates glial calcium waves. *J Neurosci* 19:520–528
- Hamilton NB, Attwell D (2010) Do astrocytes really exocytose neurotransmitters? *Nat Rev Neurosci* 11:227–238
- Höfer T, Venance L, Giaume C (2002) Control and plasticity of intercellular calcium waves in astrocytes: a modeling approach. *J Neurosci* 22:4850–4859
- Holton P (1959) The liberation of adenosine triphosphate on antidromic stimulation of sensory nerves. *J Physiol* 145:494–504
- Hua X, Malarkey EB, Sunjara V, Rosenwald SE, Li WH, Parpura V (2004) Ca^{2+} -dependent glutamate release involves two classes of endoplasmic reticulum Ca^{2+} stores in astrocytes. *J Neurosci Res* 76:86–97
- Hulme SR, Jones OD, Raymond CR, Sah P, Abraham WC (2014) Mechanisms of heterosynaptic metaplasticity. *Philos Trans R Soc Lond B Biol Sci* 369:20130148
- Iacobas DA, Suadicani SO, Spray DC, Scemes E (2006) A stochastic two-dimensional model of intercellular Ca^{2+} wave spread in glia. *Biophys J* 90:24–41
- Jahn R, Fasshauer D (2012) Molecular machines governing exocytosis of synaptic vesicles. *Nature* 490:201–207
- Jourdain P, Bergersen LH, Bhaukaurally K, Bezzi P, Santello M, Domercq M, Matute C, Tonello F, Gundersen V, Volterra A (2007) Glutamate exocytosis from astrocytes controls synaptic strength. *Nat Neurosci* 10:331–339

- Kang M, Othmer HG (2009) Spatiotemporal characteristics of calcium dynamics in astrocytes. *Chaos* 19
- Khakh BS (2001) Molecular physiology of P2X receptors and ATP signalling at synapses. *Nat Rev Neurosci* 2:165–174
- Khakh BS (2009) ATP-gated P2X receptors on excitatory nerve terminals onto interneurons initiate a form of asynchronous glutamate release. *Neuropharmacology* 56:216–222
- Köles L, Leichsenring A, Rubini P, Illes P (2011) P2 receptor signaling in neurons and glial cells of the central nervous system. *Adv Pharmacol* 61, 441–493
- Kreft M, Stenovec M, Rupnik M, Grilc S, Kržan M, Potokar M, Pangršič T, Haydon PG, Zorec R (2004) Properties of Ca^{2+} -dependent exocytosis in cultured astrocytes. *Glia* 46:437–445
- Kreft M, Potokar M, Stenovec M, Pangršič T, Zorec R (2009) Regulated exocytosis and vesicle trafficking in astrocytes. *Ann N Y Acad Sci* 1152:30–42
- Kukley M, Barden JA, Steinhäuser C, Jabs R (2001) Distribution of P2X receptors on astrocytes in juvenile rat hippocampus. *Glia* 36:11–21
- Lalo UV, Palygin O, Rasooli-Nejad S, Andrew J, Haydon PG, Pankratov Y (2014) Exocytosis of ATP from astrocytes modulates phasic and tonic inhibition in the neocortex. *PLoS Biol* 12
- Lê KT, Babinski K, Séguéla P (1998) Central P2X4 and P2X6 channel subunits coassemble into a novel heteromeric ATP receptor. *J Neurosci* 18:7152–7159
- Li B, Chen S, Zeng S, Luo Q, Li P (2012) Modeling the contributions of Ca^{2+} flows to spontaneous Ca^{2+} oscillations and cortical spreading depression-triggered Ca^{2+} waves in astrocyte networks. *PLoS ONE* 7:1–12
- Lopes LV, Cunha RA, Kull B, Fredholm BB, Ribeiro JA (2002) Adenosine A2A receptor facilitation of hippocampal synaptic transmission is dependent on tonic A1 receptor inhibition. *Neuroscience* 112:319–329
- Macdonald CL, Yu D, Buibas M, Silva GA (2008) Diffusion modeling of ATP signaling suggests a partially regenerative mechanism underlies astrocyte intercellular calcium waves. *Front Neuroeng* 1:1
- Maienschein V, Marxen M, Volknandt W, Zemmermann H (1999) A plethora of presynaptic proteins associated with ATP-storing organelles in cultured astrocytes. *Glia* 26:233–244
- Malarkey EB, Parpura V (2011) Temporal characteristics of vesicular fusion in astrocytes: Examination of synaptobrevin 2-laden vesicles at single vesicle resolution. *J Physiol* 589:4271–4300
- Marchaland J, Cali C, Voglmaier SM, Li H, Regazzi R, Edwards RH, Bezzi P (2008) Fast subplasma membrane Ca^{2+} transients control exo-endocytosis of synaptic-like microvesicles in astrocytes. *J Neurosci* 28:9122–9132
- Moffatt L, Hume RI (2007) Responses of rat P2X2 receptors to ultrashort pulses of ATP provide insights into ATP binding and channel gating. *J Gen Physiol* 130:183–201
- Nadkarni S, Jung P, Levine H (2008) Astrocytes optimize the synaptic transmission of information. *PLoS Comput Biol* 4
- Newman EA (2001) Propagation of intercellular calcium waves in retinal astrocytes and Müller cells. *J Neurosci* 21:2215–2223
- North RA (2002) Molecular physiology of P2X receptors. *Physiol Rev* 82:1013–1067
- Oya M, Kitaguchi T, Yanagihara Y, Numano R, Kakeyama M, Ikematsu K, Tsuboi T (2013) Vesicular nucleotide transporter is involved in ATP storage of secretory lysosomes in astrocytes. *Biochem Biophys Res Commun* 438:145–151
- Pang ZP, Südhof TC (2010) Cell biology of Ca^{2+} -triggered exocytosis. *Curr Opin Cell Biol* 22:496–505
- Pangršič T, Potokar M, Stenovec M, Kreft M, Fabbretti E, Nistri A, Pryazhnikov E, Khiroug L, Giniatullin R, Zorec R (2007) Exocytotic release of ATP from cultured astrocytes. *J Biol Chem* 282:28749–28758
- Parpura V, Haydon PG (2000) Physiological astrocytic calcium levels stimulate glutamate release to modulate adjacent neurons. *Proc Natl Acad Sci U S A* 97:8629–8634
- Parpura V, Fang Y, Basarsky T, Jahn R, Haydon PG (1995) Expression of synaptobrevin II, cellubrevin and syntaxin but not SNAP-25 in cultured astrocytes. *FEBS Lett* 377:489–492

- Pascual O, Casper KB, Kubera C, Zhang J, Revilla-Sanchez R, Sul J-Y, Takano H, Moss SJ, McCarthy K, Haydon PG (2005) Astrocytic purinergic signaling coordinates synaptic networks. *Science* 310:113–116
- Pougnet JT, Toulme E, Martinez A, Choquet D, Hosy E, Boué-Grabot E (2014) ATP P2X receptors downregulate AMPA receptor trafficking and postsynaptic efficacy in hippocampal neurons. *Neuron* 83:417–430
- Proctor WR, Dunwiddie TV (1987) Pre- and postsynaptic actions of adenosine in the in vitro rat hippocampus. *Brain Res* 426:187–190
- Rebola N, Rodrigues RJ, Lopes LV, Richardson PJ, Oliveira CR, Cunha RA (2005) Adenosine A1 and A2A receptors are co-expressed in pyramidal neurons and co-localized in glutamatergic nerve terminals of the rat hippocampus. *Neuroscience* 133:79–83
- Robinson IM, Ranjan R, Schwarz TL (2002) Synaptotagmins I and IV promote transmitter release independently of Ca^{2+} binding in the C2A domain. *Nature* 418:336–340
- Rubio ME, Soto F (2001) Distinct localization of P2X receptors at excitatory postsynaptic specializations. *J Neurosci* 21:641–653
- Sahlender DA, Savtchouk I, Volterra A (2014) What do we know about gliotransmitter release from astrocytes? *Philos Trans R Soc Lond B Biol Sci* 369:20130592
- Salter MW, Hicks JL (1995) ATP causes release of intracellular Ca^{2+} via the phospholipase C beta/IP3 pathway in astrocytes from the dorsal spinal cord. *J Neurosci* 15:2961–2971
- Sawada K, Echigo N, Juge N, Miyaji T, Otsuka M, Omote H, Yamamoto A, Moriyama Y (2008) Identification of a vesicular nucleotide transporter. *Proc Natl Acad Sci USA* 105:5683–5686
- Scanziani M, Capogna M, Gähwiler BH, Thompson SM (1992) Presynaptic inhibition of miniature excitatory synaptic currents by baclofen and adenosine in the hippocampus. *Neuron* 9:919–927
- Schneggenburger R, Neher E (2000) Intracellular calcium dependence of transmitter release rates at a fast central synapse. *Nature* 406:889–893
- Singh P, Jorgačevski J, Kreft M, Grubišić V, Stout RF, Potokar M, Parpura V, Zorec R (2014) Single-vesicle architecture of synaptobrevin2 in astrocytes. *Nat Commun* 5:3780
- Soto F, Garcia-Guzman M, Gomez-Hernandez JM, Hollmann M, Karschin C, Stühmer W (1996) P2X4: An ATP-activated ionotropic receptor cloned from rat brain. *Proc Natl Acad Sci USA* 93:3684–3688
- Stamatakis M, Mantzaris NV (2006) Modeling of ATP-mediated signal transduction and wave propagation in astrocytic cellular networks. *J Theor Biol* 241:649–668
- Sudhof TC, Rothman JE (2009) Membrane fusion: Grappling with SNARE and SM proteins. *Science* 323:474–477
- Sun J, Pang ZP, Qin D, Fahim AT, Adachi R, Sudhof TC (2007) A dual- Ca^{2+} -sensor model for neurotransmitter release in a central synapse. *Nature* 450:676–682
- Surprenant A, North RA (2009) Signaling at purinergic P2X receptors. *Annu Rev Physiol* 71:333–359
- Venance L, Stella N, Glowinski J, Giaume C (1997) Mechanism involved in initiation and propagation of receptor-induced intercellular calcium signaling in cultured rat astrocytes. *J Neurosci* 17:1981–1992
- Verderio C, Cagnoli C, Bergami M, Francolini M, Schenk U, Colombo A, Riganti L, Frassoni C, Zuccaro E, Danglot L, Wilhelm C, Galli T, Canossa M, Matteoli M (2012) TI-VAMP/VAMP7 is the SNARE of secretory lysosomes contributing to ATP secretion from astrocytes. *Biol Cell* 104:213–228
- Volterra A, Liaudet N, Savtchouk I (2014) Astrocyte Ca^{2+} signalling: An unexpected complexity. *Nat Rev Neurosci* 15:327–335
- Whitlock A, Burnstock G, Gibb AJ (2001) The single-channel properties of purinergic P2X ATP receptors in outside-out patches from rat hypothalamic paraventricular parvocells. *Pflugers Arch Eur J Physiol* 443:115–122
- Zhang JM, Wang HK, Ye CQ, Ge W, Chen Y, Jiang ZL, Wu CP, Poo MM, Duan S (2003) ATP released by astrocytes mediates glutamatergic activity-dependent heterosynaptic suppression. *Neuron* 40:971–982

- Zhang Q, Fukuda M, Van Bockstaele E, Pascual O, Haydon PG (2004a) Synaptotagmin IV regulates glial glutamate release. *Proc Natl Acad Sci U S A* 101:9441–9446
- Zhang Q, Pangrsic T, Kreft M, Krzan M, Li N, Sul J-Y, Halassa M, Van Bockstaele E, Zorec R, Haydon PG (2004b) Fusion-related release of glutamate from astrocytes. *J Biol Chem* 279:12724–12733
- Zhang Z, Chen G, Zhou W, Song A, Xu T, Luo Q, Wang W, Gu X, Duan S (2007) Regulated ATP release from astrocytes through lysosome exocytosis. *Nat Cell Biol* 9:945–953

Chapter 10

Gliotransmitter Exocytosis and Its Consequences on Synaptic Transmission



Maurizio De Pittà

Abstract Calcium-dependent exocytosis of glutamate and purines from astrocytes is the mechanism of gliotransmission that has best been characterized up-to-date, but its putative functional consequences remain elusive. Here we review and expand a mathematical modeling framework originally introduced by De Pittà et al. (2011) to study how gliotransmission could affect synaptic coding and mechanisms of short-term plasticity. Consideration of analytical solutions for rate-based, mean field dynamics of gliotransmission-mediated synaptic neurotransmitter release provides a testable rationale to record functional modulations of synaptic transmission by gliotransmitters in experiments. At the same time, we present theoretical arguments that reveal how functional gliotransmission is a complex phenomenon that depends on the nature of structural and functional coupling between astrocytic and synaptic elements.

Keywords Gliotransmitter release · Short-term synaptic plasticity · Synaptic coding · Tripartite synapse · Mean field dynamics

Abbreviations

Ado	adenosine
AMPA (AMPAR)	α -amino-3-hydroxy-5-methyl-4-isoxazolepropionic acid (receptor)
AP	action potential
EAAT	excitatory amino acid transporter
ECS	extracellular space
GRE	gliotransmitter release event
IP ₃	inositol 1,4,5-trisphosphate
NMDA	<i>N</i> -Methyl-D-aspartate
PPD (PPF)	paired-pulse depression (facilitation)
PPP	paired-pulse plasticity
PPR	paired-pulse ratio
RFD	recovery from depression

M. De Pittà (✉)
Basque Center of Applied Mathematics, Bilbao, Spain
e-mail: maurizio.depitta@gmail.com

10.1 Introduction

An important response of astrocytes to their excitation, both by neuronal inputs and by self-generated stimuli, is the release of gliotransmitters—molecules that act on neighboring neurons, glial cells, and blood vessels (Haydon and Carmignoto 2006). Many neurotransmitters can be gliotransmitters, like glutamate, ATP, and GABA, yet many other neuroactive molecules can also be released from astrocytes and act as gliotransmitters, and these include, but are not limited to, D-serine—an endogenous co-agonist with glutamate of postsynaptic NMDA receptors (Papouin et al. 2012)—, cytokines, like tumor necrosis factor alpha (TNF α), or prostaglandins and metabolic molecules like lactate (Chap. 1) (Bains and Oliet 2007; Santello and Volterra 2009; Attwell et al. 2010; Halassa and Haydon 2010; Santello and Volterra 2012; Losi et al. 2014; Tang et al. 2014; see also Chap. 1). Calcium-dependent exocytosis is the best-characterized mechanism of gliotransmitter release up-to-date and the one considered in this chapter. Both glutamate and ATP can be released by exocytosis from astrocytes (Zorec et al. 2012), and preliminary evidence supports the same mechanism of release for astrocytic D-serine too (Mothet et al. 2005; Bergersen et al. 2012). Once exocytosed, glutamate, ATP, and D-serine can diffuse in the extracellular space (ECS) reaching receptors located on pre- and postsynaptic terminals, thereby modulating synaptic transmission (Araque et al. 2014).

From a computational perspective, the pathway of gliotransmission mediated by Ca $^{2+}$ -dependent astrocytic exocytosis could be regarded as a two-step process. First is the transduction of astrocytic, “analog-like” Ca $^{2+}$ signals into “digital-like,” quantal release events of gliotransmitter by exocytosis. Second is the activation of synaptic receptors by gliotransmitters which translates extracellular gliotransmitter signals into modulations of synaptic transmission. The concurrence of these two steps suggests that regulation of synaptic transmission by astrocytes may not simply mirror astrocytic Ca $^{2+}$ dynamics, but rather be more complex, to a point that gliotransmission could perform genuine processing of astrocytic Ca $^{2+}$ signals (De Pittà et al. 2013).

The mechanisms of regulation of synaptic transmission by gliotransmitters are not fully understood. For example, modulation of synaptic neurotransmitter release by gliotransmitter-bound presynaptic receptors could shape the filtering characteristics of a synapse in response to incoming action potentials (APs), with significant repercussions on what features of these APs are transmitted by the synapse (De Pittà et al. 2015; De Pittà and Brunel 2016). On the other hand, it remains to be elucidated how this scenario could be brought forth by different pathways of gliotransmission, both in terms of release of different gliotransmitters from the astrocyte, and in terms of different presynaptic receptors targeted by those gliotransmitters (Savtchouk and Volterra 2018).

Finally, astrocytic Ca $^{2+}$ dynamics triggering gliotransmitter exocytosis could be modulated both by the very synapses that are regulated by the astrocyte, in the so-called *homosynaptic* scenario of gliotransmission, and by synapses that are not, consistently with a *heterosynaptic* scenario of gliotransmission (Araque et al. 2014).

The heterosynaptic scenario is the one considered in this chapter since it is generally easier to be treated mathematically than the homosynaptic case. Furthermore, for the sake of brevity, we limit our study to the mere consideration of presynaptic pathways of gliotransmission, such as those illustrated in Fig. 10.1. The modeling framework presented here was originally introduced by De Pittà et al. (2011), and the following sections provide a critical revision of that study including in-depth mathematical details that were left out of the original publication. On the other hand, although discussed in the context of presynaptic pathways of gliotransmission, the validity of the modeling arguments presented in this chapter is general, and the modeling framework following introduced can be extended to study postsynaptic pathways of gliotransmission too, and the case of homosynaptic gliotransmission (see De Pittà and Brunel 2016, and also Chap. 18).

10.2 Modeling Gliotransmitter-Mediated Regulation of Synaptic Release

In line with the two-step description of gliotransmission introduced above, we consider a compartmental modeling approach to describe gliotransmitter-mediated regulation of synaptic release, envisaging three compartments: (i) a synaptic compartment competent for neurotransmitter release, (ii) an astrocytic compartment for Ca^{2+} -dependent gliotransmitter exocytosis, and (iii) an ECS compartment, comprised between synaptic and perisynaptic astrocytic processes, that acts as an interface for transduction of gliotransmitter-related signals into synaptically related ones.

10.2.1 *Synaptic Release*

To realistically describe synaptic release for the whole frequency spectrum of neuronal firing, we consider the model of an activity-dependent synapse first introduced by Tsodyks and Markram (Tsodyks and Markram 1997). Although other models may be adopted, the Tsodyks and Markram (TM) one is particularly suitable for our following analysis inasmuch as it is amenable to mathematical tractability while realistically capturing the dependence of synaptic release on past activity—that is presynaptic short-term plasticity, which can substantially influence dynamics of synaptic transmission (Zucker and Regehr 2002). As illustrated in Fig. 10.2a, the TM model describes synaptic release (r_S) by the product of two factors (Tsodyks 2005): (i) the probability of neurotransmitter-containing vesicles to be available for release (x_S), and (ii) the probability of such vesicles to be effectively released by an AP (u_S), which correlates with intrasynaptic Ca^{2+} levels and the ensuing state of occupancy (activation) of the Ca^{2+} sensory of synaptic neurotransmitter exocytosis (Südhof 2004).

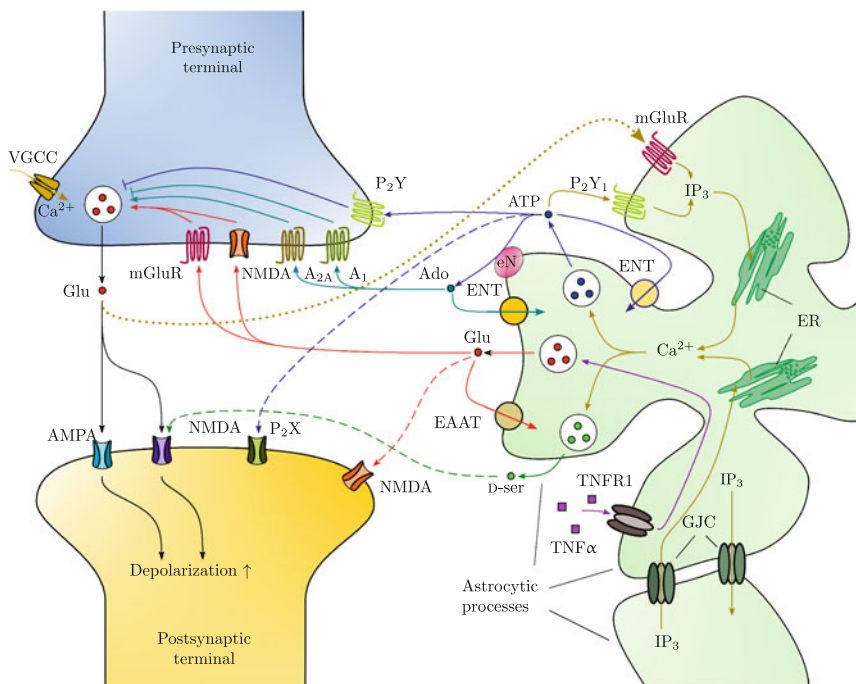
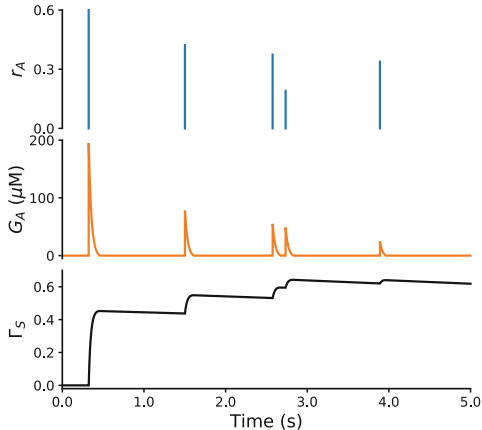
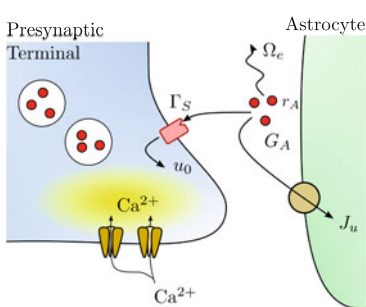
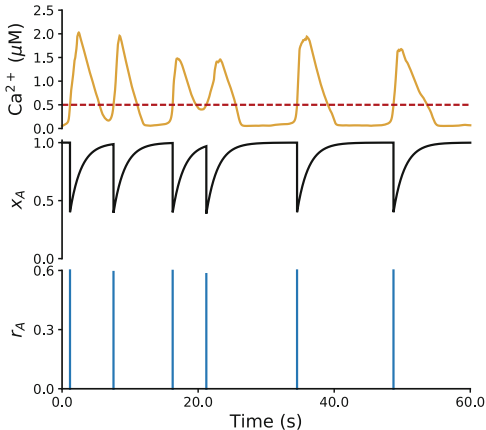
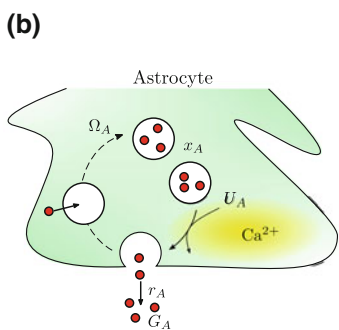
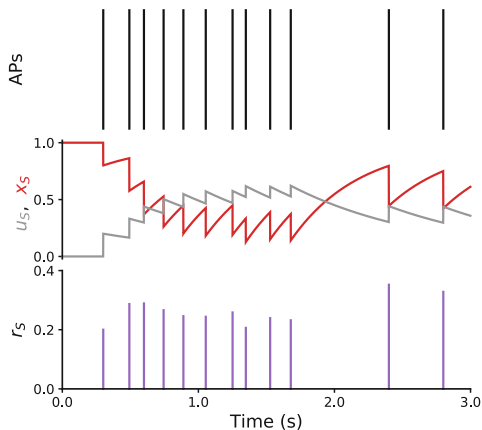
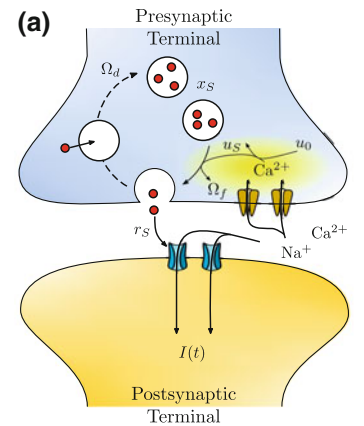


Fig. 10.1 Pathways of gliotransmission by exocytosis. Glutamate (red), ATP (blue) and its derivative adenosine (Ado, turquoise), and probably D-serine as well (D-ser, green) can be released from astrocytes by Ca^{2+} -dependent exocytosis, although different pathways of exocytosis might be at play. For example, ATP seems to be preferentially released by lysosome exocytosis (Zhang et al. 2007), as opposed to glutamate which appears to be released by small synaptic-like vesicles (Marchaland et al. 2008). On the contrary, D-serine is suggested to be contained either in separate secretory organelles or within glutamate-containing vesicles, thereby possibly being co-released with glutamate (Bergersen et al. 2012). In addition, exocytosis of glutamate from astrocytes is controlled by extracellular levels of the cytokine $\text{TNF}\alpha$ through activation of type 1 TNF receptors (TNFR1) (Habbas et al. 2015), but whether this cytokine could control ATP exocytosis too is not known. Ca^{2+} dynamics underpinning gliotransmitter exocytosis can either be stimulated in a homosynaptic fashion by neurotransmitters released from the very synapses modulated by gliotransmitters (*dotted yellow pathway*) or ensue from extracellular diffusion of astrocytic ATP as well as intracellular propagation of inositol 1,4,5-trisphosphate (IP_3). Gliotransmitter concentration in the ECS is regulated by different, gliotransmitter-specific mechanisms of clearance. Glutamate is mainly cleared by diffusion away from the release site and uptake by astrocytic excitatory amino acid transporters (EAAT). ATP is rapidly degraded into lower nucleotides and Ado by ectonucleotidases (eN), and extracellular purines may ultimately reenter cells via equilibrative transport mechanisms (ENT). Finally, glutamate and ATP can target both pre- and postsynaptic receptors (*solid vs. dashed pathways*), whereas D-serine is known to exclusively regulate gating of postsynaptic NMDA receptors (Papouin and Oliet 2014). Presynaptically, glutamate mainly promotes synaptic release while ATP depresses it. On the contrary, adenosine can do both acting through extrasynaptic A_2A and A_1 receptors, respectively. This study considers only those pathways of gliotransmission drawn by *solid lines*. Legend: ER endoplasmic reticulum; A_1 (A_2A): adenosine receptors; GJC: gap junction channel; mGluR: metabotropic glutamate receptor. P_2X (P_2Y): ionotropic (metabotropic) purinergic receptor



◀Fig. 10.2 Model compartments. **a** Synaptic compartment: TM model of synaptic release. (*Left*) Release of synaptic neurotransmitter resources (r_S) ensues from the combination of two variables: x_S and u_S . (*Right*) These two variables evolve with the timing of incoming APs (*top panel*) in a peculiar manner (*middle panel*): x_S (red trace) tends to decrease for consecutive APs at sufficiently sustained rates, mimicking neurotransmitter depletion. Conversely, under the same circumstances, u_S (gray trace) tends to increase, reflecting higher intrasynaptic residual Ca^{2+} levels. As the rate of incoming APs decreases instead (e.g. for $t > 2$ s), x_S and u_S recover toward resting values mirroring reintegration of neurotransmitter resources and return of basal intrasynaptic Ca^{2+} concentration. The interplay between dynamics of u_S and x_S modulates synaptic release by different mechanisms of activity-dependent synaptic plasticity (*bottom panel*) such as short-term facilitation (e.g. $0 < t < 0.5$ s), short-term depression (e.g. $0.5 < t < 2$ s), and recovery from depression (e.g. $2 < t < 2.5$ s). Model parameters: $\Omega_d = 2 \text{ s}^{-1}$, $\Omega_f = 1 \text{ s}^{-1}$, $U_0^* = 0.2$. **b** Ca^{2+} -dependent gliotransmitter exocytosis. (*Left*) Gliotransmitter exocytosis from astrocytes can be described akin to synaptic neurotransmitter exocytosis, yet assuming that a constant fraction (U_A) of available gliotransmitter resources (x_A) is released every time Ca^{2+} increases beyond some threshold. (*Right*) In this fashion, the timing of GREs (*bottom panel*) reflects the timing of crossings of intracellular Ca^{2+} concentration (*top panel*, yellow trace) above the exocytosis threshold (*top panel*, dashed red line). Ca^{2+} dynamics was simulated by the stochastic Li–Rinzel model previously introduced in Chap. 4 (see also Appendix 4). **c** Extracellular compartment. (*Left*) Time course of extracellular gliotransmitter may be regulated by several gliotransmitter-specific factors, including diffusion away from the release site, enzymatic degradation and uptake by transporters. Only a minor part of released gliotransmitters target extrasynaptically located presynaptic receptors, with the potential to affect intrasynaptic basal Ca^{2+} levels. (*Right*) In general, each GRE (*top panel*) results in a sharp transient increase of extracellular gliotransmitter concentration (G_A , *middle panel*), whose magnitude depends on the fraction of released gliotransmitter resources (r_A , *top panel*). In turn, this transient increase of extracellular gliotransmitter produces a sharp increase of activated extrasynaptically located presynaptic receptors (Γ_S , *bottom panel*), which tends to vanish on a much slower timescale. Model parameters as in Table 10.1 except for $\Omega_e = 30 \text{ s}^{-1}$ and $O_G = 0.1 \mu\text{M}^{-1}\text{s}^{-1}$

The variable u_S is zero at rest, when intrasynaptic Ca^{2+} concentration is low and the sensor for neurotransmitter exocytosis is only little bound by Ca^{2+} ions; whereas it increases upon an AP arriving at time t_i , mimicking increased intrasynaptic Ca^{2+} and sensor activation as Ca^{2+} ions flow into the presynaptic terminal via channels gated by the AP. In this interpretation, the model assumes that a fraction u_0 of $1 - u_S$ free binding sites of the sensor is instantaneously occupied by incoming Ca^{2+} ions (Bollmann et al. 2000; Schneggenburger and Neher 2000) and is following recovered at rate Ω_f . Hence, denoting by u_S^+ the value of u_S immediately after a generic AP (i.e. at $t = t_i^+$), it follows that

$$\frac{du_S^+}{dt} = -\Omega_f u_S^+ + u_0 \sum_i (1 - u_S^+) \delta(t - t_i) \quad (10.1)$$

where the Dirac delta function $\delta(t - t_i)$ denotes an action potential arriving at time t_i .

Neurotransmitter resources in the presynaptic terminal are assumed limited and only a fraction $x_S(t)$ of them is available for release at time t . At rest, all resources are available for release, that is $x_S = 1$. Upon arrival of an AP instead, a fraction u_S^+ of the resources is released into the cleft and is following reintegrated at rate Ω_d .

Accordingly, denoting by x_S^- the value of x_S immediately before a generic AP (i.e. at $t = t_i^-$), the equation for x_S^- reads

$$\frac{dx_S^-}{dt} = \Omega_d(1 - x_S^-) - \sum_i u_S^+ x_S^- \delta(t - t_i) \quad (10.2)$$

Accordingly, the fraction of neurotransmitter resources (r_S) that is released by an AP arriving at $t = t_i$ is given by

$$r_S(t_i) = u_S(t_i^+) \cdot x_S(t_i^-) = u_S^+ \cdot x_S^- \quad (10.3)$$

The parameter u_0 in Eq. 10.1 coincides with the value that u_S reaches from resting conditions ($u_S(0) = 0$) immediately after the first AP of a series, i.e. at $t = t_1^+$. Moreover, because it is $x_S(0) = 1$ at rest, it follows that the released fraction of neurotransmitter resources by the first AP of a series is also $r_S = u_0 \cdot 1 = u_0$, and this released fraction is essentially kept identical if the rate of incoming APs (v_S) is low enough to allow recovery of synaptic variables to their resting values. In other words, at very low (basal) frequency of stimulation (i.e. for $v_S \ll \Omega_d, \Omega_f$), when the synapse is allowed recovering to its resting state between APs, u_0 may be regarded as the *basal value* of synaptic release probability, or equally, as the basal value of the fraction of released neurotransmitter resources (Tsodyks et al. 1998). An important observation is that the TM model ignores the stochastic nature of synaptic release, reproducing instead the average synaptic release event that is generated by a train of presynaptic APs with given statistics (Fuhrmann et al. 2002).

10.2.2 Gliotransmitter Exocytosis from the Astrocyte

A large amount of evidence suggests that gliotransmitter exocytosis from astrocytes bears several similarities with its synaptic homologous (Bergersen and Gundersen 2009; Santello and Volterra 2009; Bergersen et al. 2012). Astrocytes indeed possess vesicular compartments that are competent for exocytosis of glutamate (Bezzi et al. 2004; Bergersen and Gundersen 2009) and ATP (Coco et al. 2003; Jaiswal et al. 2007; Zhang et al. 2007). Similarly to synapses, astrocytes also express SNARE proteins necessary for exocytosis (Parpura et al. 1995; Schubert et al. 2011), as well as transporter proteins capable of concentrating glutamate or ATP into vesicles (Bezzi et al. 2004; Montana et al. 2004; Zhang et al. 2004; Sawada et al. 2008). Finally, fusion with plasma membrane, trafficking and recycling of glutamate- and ATP-containing vesicles have also been observed in astrocytes, (Bezzi et al. 2004; Chen et al. 2005; Crippa et al. 2006; Jaiswal et al. 2007; Pangršič et al. 2007; Stenovec et al. 2007), which are indicative of quantal exocytotic release of these gliotransmitters (Pasti et al. 1997; Domercq et al. 2006; Jaiswal et al. 2007; Pangršič et al. 2007; Marchaland et al. 2008; Santello et al. 2011).

Based on the above arguments, we hypothesize to describe gliotransmitter exocytosis from astrocytes in a way that is mathematically similar to the TM description of synaptic neurotransmitter exocytosis (Fig. 10.2b), although the two mechanisms are likely different in their molecular machinery, with the kinetics of astrocytic exocytosis possibly considerably slower than its synaptic homologous (Chen et al. 2005; Bowser and Khakh 2007; Stenovec et al. 2007). Thus, akin to a synapse, we assume existence of a pool of gliotransmitter resources in the astrocyte that is constant in size, and we denote by $x_A(t)$ the fraction of these resources that is available for release at time t . Then, we assume that a fraction U_A of these x_A releasable resources is exocytosed into the ECS every time cytosolic Ca^{2+} in the astrocyte increases beyond some threshold and is following reintegrated at rate Ω_A . The equation for x_A^- thus reads

$$\frac{dx_A^-}{dt} = \Omega_A(1 - x_A^-) - U_A \sum_i x_A^- \delta(t - \tau_i) \quad (10.4)$$

where the Dirac delta function $\delta(t - \tau_i)$ denotes a gliotransmitter release event (GRE) occurring at $t = \tau_i$. Hence, the fraction of gliotransmitter resources released by exocytosis at the instant τ_i is

$$r_A(\tau_i) = U_A \cdot x_A(\tau_i^-) = U_A \cdot x_A^- \quad (10.5)$$

where the parameter U_A in the above equations is the astrocytic analogous of the synapse's basal release probability u_0 (Eq. 10.1).

The instants τ_i of GREs depend on Ca^{2+} dynamics in the astrocyte. Only if intracellular Ca^{2+} exceeds a threshold concentration C_θ , gliotransmitter exocytosis occurs (Marchaland et al. 2008; Pryazhnikov and Khiroug 2008). Moreover, for long-lasting Ca^{2+} transients, gliotransmitter exocytosis is often observed only during the initial rising phase of these transients (Pasti et al. 1997; Marchaland et al. 2008). Therefore, we can assume that a GRE occurs at any instant $t = \tau_i$ of Ca^{2+} dynamics ($C(t)$) such that $C(\tau_i) = C_\theta$ and $dC/dt|_{t=\tau_i} > 0$.

Akin to the TM model of synaptic release, our description of gliotransmitter release ignores the possible stochastic nature of astrocytic exocytosis (Santello et al. 2011) and reproduces the average GRE generated by a single Ca^{2+} elevation beyond the threshold C_θ . In this fashion, the fraction r_A of released gliotransmitter resources in Eq. 10.5 represents the total amount of gliotransmitter released by a single suprathreshold Ca^{2+} elevation. This is regardless of the underlying mechanism of astrocytic exocytosis, which can be either in the form of a “burst” of synchronous vesicle fusion events that peak within the first 50–500 ms of the Ca^{2+} rise (Domercq et al. 2006; Marchaland et al. 2008; Santello et al. 2011), or occur at slower fusion rates, in an asynchronous fashion (Kreft et al. 2004; Malarkey and Parpura 2011). Moreover, our description does not take into account the possibility that the probability of gliotransmitter exocytosis (U_A), and/or its possible kinetics (as mirrored by Ω_A), could be regulated by additional factors such as TNF α in the case of astrocytic glutamate exocytosis (Domercq et al. 2006; Santello et al. 2011). On the other hand,

because at different constitutive TNF α concentrations in the ECS the qualitative features of functional astrocytic glutamate exocytosis seem preserved, our description can generally be adopted in such circumstances, regardless of the exact concentration of TNF α in the ECS, as far as this concentration falls in the range of constitutive, non-pathological levels of this cytokine (Santello and Volterra 2012).

10.2.3 Time Course of Gliotransmitter in the Extrasynaptic Space

The fraction $r_A(\tau_i)$ of gliotransmitter resources released by a Ca $^{2+}$ spike at time τ_i in Eq. 10.5 can readily be converted into gliotransmitter concentration in the perisynaptic ECS. With this regard, it may be assumed that the size of the synaptic pool of releasable gliotransmitter resources (G_T) equals to

$$G_T = n_A G_v \quad (10.6)$$

where n_A is the average number of gliotransmitter-containing vesicles available for release, and G_v is the average vesicular gliotransmitter concentration. Assuming an average vesicular volume Λ_A and a volume Λ_e for the diffusion of gliotransmitter in the ECS, a single GRE occurring at τ_i contributes to the extracellular gliotransmitter concentration by

$$G_{rel}(\tau_i) = \frac{\Lambda_A}{\Lambda_e} G_T \cdot r_A(\tau_i) = \rho_e G_T \cdot r_A(\tau_i) \quad (10.7)$$

where $\rho_e = \Lambda_A / \Lambda_e$.

The time course of gliotransmitter in the ECS (G_A) depends on several mechanisms, including gliotransmitter clearance by diffusion, uptake, and degradation (Clements 1996; Diamond 2005; Abbracchio et al. 2009), although the mechanisms are gliotransmitter-specific (Fig. 10.2c). Glutamate, for example, is rapidly taken up mostly by astrocytic transporters, and the molecules that are not, rapidly diffuse away from the astrocytic release site (Clements 1996; Diamond 2005). The pathway, whereby ATP can bind presynaptic receptors on the other hand, is mainly by diffusion, although it must be noted that this purine is rapidly degraded into ADP, AMP, and mostly adenosine (Ado) by ectoenzymes in the ECS, and together with Ado diffuses to presynaptic targets, or enters surrounding cells by equilibrative transport mechanisms (King et al. 2006; Abbracchio et al. 2009). In the simplest approximation, the contribution of these diverse mechanisms to the time course of gliotransmitter in the ECS can be modeled by a first-order reaction like (Destexhe et al. 1994):



where Ω_e is an unspecific rate of clearance of extracellular gliotransmitter and the three dots ‘...’ represent generic products ensuing from gliotransmitter clearance. The equation for G_A thus reads:

$$\frac{dG_A}{dt} = \sum_i G_{rel}(\tau_i) - \Omega_e G_A \quad (10.9)$$

where the sum is on all GREs.

In the more general scenario, where we aim to consider a more detailed description of gliotransmitter clearance including gliotransmitter uptake by different transporters—excitatory amino acid transporters for glutamate (Danbolt 2001), or equilibrative nucleoside transporters for ATP/Ado (King et al. 2006)—the right-hand side of the above Eq. 10.9 may be complemented by an additional term J_u that accounts for gliotransmitter uptake. Because such uptake can realistically be described by Michaelis–Menten kinetics (Griffiths et al. 1997; Baldwin et al. 2005; Barnes et al. 2006; Tzingounis and Wadiche 2007), J_u then reads

$$J_u = O_u \mathcal{H}_1(G_A, K_u) \quad (10.10)$$

where O_u is the maximal uptake rate, K_u is the transporter affinity for gliotransmitter, and $\mathcal{H}_1(G_A, K_u) = G_A/(G_A + K_u)$. Accordingly, a more detailed equation for the time course of gliotransmitter in the ECS is

$$\frac{dG_A}{dt} = \sum_i G_{rel}(\tau_i) - J_u(G_A) - \Omega_e G_A \quad (10.11)$$

Although of general validity, the description of gliotransmitter dynamics in the ECS put forth by Eqs. 10.4–10.11 relies on the simplifying assumption that the gliotransmitter that is taken up by astrocytic transporters does not directly affect the size of the releasable pool of gliotransmitter resources of the astrocyte. This assumption is motivated by the consideration that vesicular glutamate and purines used in gliotransmission are probably handled by separated molecular pathways with respect to glutamate and purines used for other purposes in the cell, for example, in the case of glutamate, whose uptake seems mostly involved in metabolic coupling with neurons, possibly by the glutamate–glutamine cycle and the astrocyte-to-neuron lactate shuttle (Chap. 1). If this were not the case, the fraction of released gliotransmitter resources would depend on extracellular gliotransmitter concentration (e.g. by some function $G_v(G_A)$), considerably complicating the model beyond the scope of this chapter.

10.2.4 Modulation of Synaptic Release by Gliotransmitters

Depending on the type of gliotransmitter—glutamate, ATP or its derivative Ado—and the type of bound presynaptic receptors, gliotransmission can either increase or decrease synaptic release (De Pittà et al. 2015). The details of the biochemical mechanisms underlying modulation of synaptic release by astrocytic gliotransmitters depend on the receptor type and are not fully understood. The simplest explanation is that all receptors, independently of the type, ultimately regulate intrasynaptic Ca^{2+} levels, thereby modulating release probability of neurotransmitter-containing synaptic vesicles (Cunhaa and Ribeiro 2000; Pinheiro and Mulle 2008). It is important to note though that this kind of modulation does not require synaptic activation by APs and is observed even in basal conditions, that is upon arrival at the synapse at rest of isolated APs (Liu et al. 2004b; Jourdain et al. 2007; Perea and Araque 2007; Panatier et al. 2011). This suggests that gliotransmitter modulation of synaptic release likely reflects changes of occupancy of the Ca^{2+} sensor of synaptic exocytosis, while recycling, trafficking, and pool size of neurotransmitter resources in the presynaptic terminal are not affected.

Based on these arguments, an ansatz can be made whereby gliotransmitter modulation of synaptic release can be reproduced by the TM synapse model, making the variable u_S (Eq. 10.1) depend on gliotransmitter dynamics in the ECS (i.e. G_A in Eq. 10.11). This ansatz was introduced by De Pittà et al. (2011), and the following is a review of the modeling framework originally presented in that study. In particular, it may be assumed that basal synaptic release probability (u_0 in Eq. 10.1) is not constant, but rather it is a function of G_A through the fraction Γ_S of presynaptic receptors that are activated by released gliotransmitter molecules, i.e. $u_0 \equiv u_0(G_A) = u_0(\Gamma_S(G_A))$. In the absence of quantitative physiological data, the function $u_0(\Gamma_S)$ can be taken analytic around zero so that its first-order expansion is considered accordingly, i.e.

$$u_0(\Gamma_S) \simeq u_0(0) + u_0'(0)\Gamma_S + O\Gamma_S^2 \quad (10.12)$$

where $u_0'(0) = \left. \frac{du_0}{d\Gamma_S} \right|_0$. The zeroth-order term $u_0(0) = \text{const} = U_0^*$ corresponds to the value of u_0 in the absence of the astrocyte: that is, in the zeroth-order approximation the model of synaptic release is just the classical TM model (Eqs. 10.1, 10.2). To express $u_0'(0)$ instead, it may be noted that both $u_0(\Gamma_S)$ and Γ_S are defined in the interval $[0, 1]$, so that $u_0(\Gamma_S)$ must either increase or decrease with Γ_S depending on whether gliotransmission stimulates or inhibits synaptic release. In the simplest scenario, the choice of $u_0'(0) = -U_0^* + \alpha$ with $0 \leq \alpha \leq 1$ can be made so that, neglecting the terms of $O\Gamma_S^2$ in Eq. 10.12 ultimately provides

$$u_0(\Gamma_S) = U_0^* + (\alpha - U_0^*)\Gamma_S \quad (10.13)$$

The parameter α in the above equation lumps in a phenomenological way information on the effect of gliotransmission on synaptic release. For $0 \leq \alpha < U_0^*$, u_0 decreases

with Γ_S , consistently with a *release-decreasing* effect of gliotransmission on synaptic release. This could be the case, for example, of astrocytic ATP or Ado, respectively, binding presynaptic purinergic receptors P₂Y₁ or A₁ (Newman 2003; Zhang et al. 2003; Pascual et al. 2005; Serrano et al. 2006; Todd et al. 2010), or of astrocytic glutamate targeting presynaptic kainate receptors or group II/III metabotropic receptors (Araque et al. 1998a; Liu et al. 2004b, a). For $U_0^* < \alpha \leq 1$ instead, u_0 increases with Γ_S , consistently with a *release-increasing* effect of gliotransmission on synaptic release, like in the case of Ado binding to presynaptic A_{2A} receptors (Todd et al. 2010; Panatier et al. 2011), or glutamate in association with presynaptic NMDA receptors of group I metabotropic receptors (Fiacco and McCarthy 2004; Jourdain et al. 2007; Perea and Araque 2007; Navarrete and Araque 2010; Bonansco et al. 2011). Finally, for $\alpha = U_0^*$, it is $u_0 = U_0^*$, independently of Γ_S . This case corresponds to *occlusion*, that is no net effect of gliotransmission on synaptic release due to the simultaneous activation of stimulatory and inhibitory receptors that may be co-expressed at the same synaptic terminal (Shigemoto et al. 1997; Rebola et al. 2005; Covelo and Araque 2018).

To complete our description, we also assume a saturating dynamics for presynaptic receptors, given their limited expression on synaptic terminals. With this regard, the pool of presynaptic receptors targeted by gliotransmitters is composed by a fraction Γ_S of gliotransmitter-bound receptors and a complementary fraction $1 - \Gamma_S$ of available (not bound) receptors, so that Γ_S evolves according to

$$\frac{d\Gamma_S}{dt} = O_G G_A (1 - \Gamma_S) - \Omega_G \Gamma_S \quad (10.14)$$

where O_G and Ω_G denote rate constants that loosely correlate with rise and decay of the modulation of synaptic release by gliotransmitters (De Pittà et al. 2011).

The ensemble of Eqs. 10.4, 10.11, 10.13, and 10.14 provides a model for gliotransmission-mediated regulation of synaptic release probability. Figure 10.3 illustrates how in this model, astrocytic Ca²⁺ oscillations (*top panel*) modulate synaptic basal release probability (*bottom panel*) via activation of presynaptic receptor (Γ_S) that are bound by gliotransmitter released from astrocytes into the ECS (x_A , G_A , *middle panels*). The sawtooth-shaped Γ_S increase is a consequence of the large difference between timescales of rise and decay of the gliotransmitter effect on synaptic release, since $O_G G_A \ll \Omega_G$ (Appendix 2). Moreover, because u_0 is a linear function of Γ_S by the first-order approximation of Eq. 10.13, dynamics of this latter also dictates dynamics of u_0 . Finally, depending on the value of the parameter α , $u_0(\Gamma_S)$ can either decrease for $\alpha < U_0^*$ (*magenta-shaded u₀ range*) and get as low as $u_0(\Gamma_S, \alpha = 0) = (1 - \Gamma_S)U_0^*$ (*magenta trace*), or increase for $\alpha > U_0^*$ (*green-shaded u₀ range*), and reach values as high as $u_0(\Gamma_S, \alpha = 1) = U_0^* + (1 - U_0^*)\Gamma_S$ (*green trace*). In the case of occlusion, for $\alpha = U_0^*$, u_0 is not affected by astrocytic gliotransmission, regardless of the fraction of activated presynaptic receptors (*dashed gray line*).

Table 10.1 Model parameters

Symbol	Description	Range	Value	Units
<i>Synaptic dynamics</i>				
Ω_d	Depression rate constant	0.5–10	†	s^{-1}
Ω_f	Facilitation rate constant	0.5–2	†	s^{-1}
U_0^*	Basal synaptic release probability	<0.09–0.9	†	—
Ω_i	Decay rate of postsynaptic currents	<0.09–0.4	0.05	ms^{-1}
A	Amplitude of postsynaptic currents	15.5–30	30	pA
<i>Gliotransmitter release and time course</i>				
C_θ	Ca ²⁺ threshold for exocytosis	0.15–0.8	0.5	μM
Ω_A	Gt. recycling rate	0.6–300	1	s^{-1}
U_A	Resting gt. release probability	<0.9	0.6	—
G_T	Total vesicular gt. concentration	20–900	150	mM
O_u	Max uptake rate (glutamate)	< 3	0.1	mMs^{-1}
K_u	Transporter affinity (glutamate)	10–30	10	μM
ρ_e	Vesicular versus mixing volume ratio	$2 \cdot 10^{-5}$ – $700 \cdot 10^{-5}$	$65 \cdot 10^{-5}$	—
Ω_e	Gliotransmitter clearance rate	>3	40	s^{-1}
<i>Presynaptic receptors</i>				
O_G	Activation rate	>0.3	0.3	$\mu M^{-1}s^{-1}$
Ω_G	Inactivation rate	<0.005–0.17	0.05	s^{-1}
α	Nature of gliotransmission	0–1	†	—

Simulation-specific parameter values are marked by † and detailed in figure captions when relevant

10.3 Functional Implications of Gliotransmission-Mediated Modulations of Synaptic Release

10.3.1 Synaptic Coding

Let us start our study of the functional implications of gliotransmission considering the setup in Fig. 10.4a where n_S excitatory synapses impinge on a (postsynaptic) neuron P and are stimulated by trains of random, Poisson-distributed APs incoming at average rate v_S . In this setup, we may envisage two complementary scenarios of synaptic transmission. In the first scenario (Fig. 10.4b), the postsynaptic current ($I(t)$, bottom panel) ensuing from consecutive step increases of v_S (top panel) is either proportional to v_S , when v_S is sufficiently small (e.g. $t < 10$ s), or displays large depolarizing transients in coincidence with large step increases of v_S (e.g. at $t = 10$ s and $t = 20$ s). In the complimentary scenario instead (Fig. 10.4c), the postsynaptic current only displays large transients for step increases of sufficiently high presynaptic rates (i.e. at $t = 20$ s), whereas for intermediate or low v_S values, $I(t)$ is either almost constant on average (for $5 < t < 10$ s and $15 < t < 20$ s) or

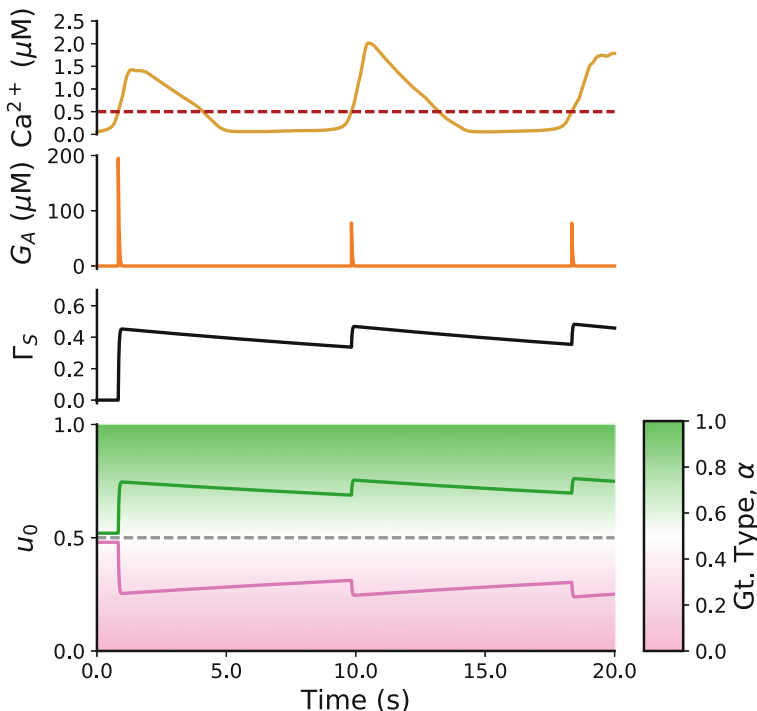


Fig. 10.3 Model of modulation of basal synaptic release probability by gliotransmitter exocytosis. Evolution of presynaptic receptors following GREs, as reflected by the model of the ECS compartment in Fig. 10.2c, modulates synaptic basal release probability (u_0 , bottom panel). We consider the first approximation of this modulation so that u_0 dynamics is a linearly rescaled copy of Γ_S dynamics. In particular, depending on the nature of gliotransmission, lumped in the parameter α , activation of presynaptic receptors can decrease (for $0 \leq \alpha < U_0^*$, magenta-shaded region) or increase u_0 ($U_0^* < \alpha \leq 1$, green-shaded region). For a given sequence of GREs, minimal values of u_0 can be attained for $\alpha = 0$ (magenta trace), whereas maximal ones are for $\alpha = 1$ (green trace). In conditions of occlusion ($\alpha = U_0^*$), the value of basal synaptic release probability equals the one attained by the synapse in the absence of gliotransmission (dashed gray line). Model parameters as in Fig. 10.2c

slowly increases with the duration of presynaptic stimulation (e.g. for $t < 5$ s or $10 < t < 15$ s).

From a coding perspective, a postsynaptic current that is proportional to the presynaptic rate of stimulation may be regarded as a “buffer” of this rate to the postsynaptic neuron. Conversely, transmission of rate step increases by large depolarizing transients of postsynaptic current puts emphasis on the variations of v_S (i.e. its derivative) rather than its magnitude, consistently with “derivative” synaptic coding. Finally, a slowly increasing postsynaptic current, such as that observed in Fig. 10.4c, may be thought, at least to some extent, as an integral of v_S over time. In this fashion, the two scenarios in Fig. 10.4(b, c) may conveniently be summarized saying that in (b)

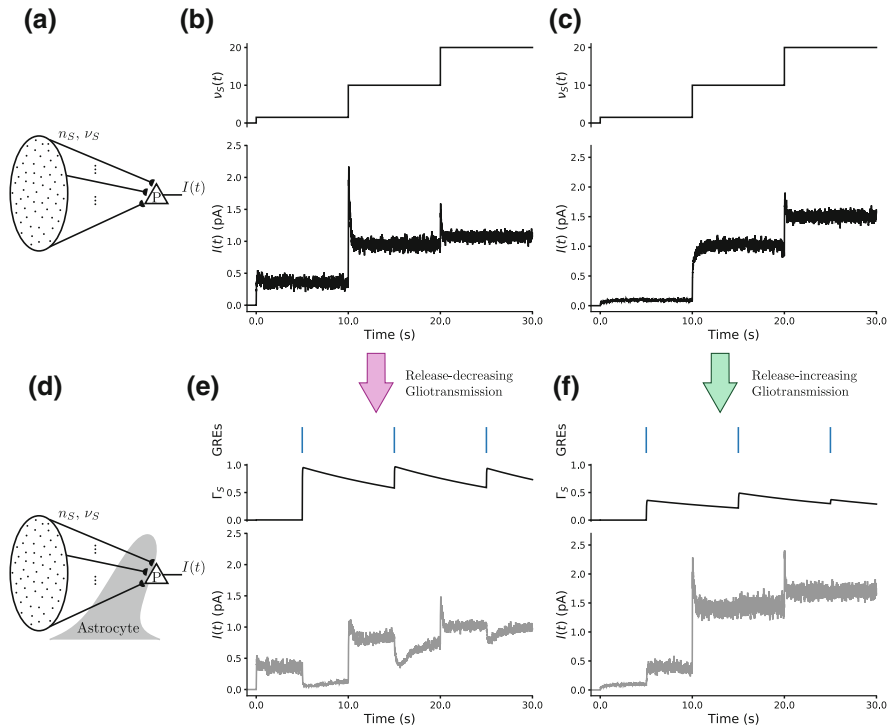


Fig. 10.4 Effects of gliotransmission on synaptic coding. **a** Simulated setup: $n_S = 1000$ independent synapses impinge on the same postsynaptic neuron are stimulated by trains of APs that are Poisson distributed and arrive at rate v_S . **b** Scenario where synaptic parameters are chosen so that the postsynaptic current ($I(t)$, bottom panel) is a buffer of low presynaptic rates (top panel, $t < 10$ s) or it reflects the derivative of v_S for sufficiently high presynaptic rates ($t > 10$ s). **c** Alternative scenario where synapses could also integrate presynaptic rates over time for low to intermediate v_S values (e.g. $0 < t < 5$ s and $10 < t < 15$ s). **d** Simulated setup in the presence of gliotransmission. All n_S synapses in **a** are identically modulated by gliotransmitters released from the same astrocytic domain (gray shaded). **e, f** Average postsynaptic currents (bottom panels) ensuing from the same synapses in **b** and **c**, yet in the presence of activation of presynaptic receptors (Γ_S , middle panels) by three GRES (top panels). Synapses in **e** are considered for the scenario of release-decreasing gliotransmission ($\alpha = 0$), whereas synapses in **f** are modulated by release-increasing gliotransmission ($\alpha = 1$). Postsynaptic currents were obtained by numerical solution of the equation: $\frac{dI}{dt} = -\Omega_d I + A \sum r_S$ (Tsodyks 2005). Model parameters: **b, e**: $\Omega_d = 2 \text{ s}^{-1}$, $\Omega_f = 3.33 \text{ s}^{-1}$, $U_0^* = 0.5$, $O_G = 0.7 \mu\text{M}^{-1}\text{s}^{-1}$; **c, f**: $\Omega_d = 3.33 \text{ s}^{-1}$, $\Omega_f = 1 \text{ s}^{-1}$, $U_0^* = 0.05$, $O_G = 0.1 \mu\text{M}^{-1}\text{s}^{-1}$. Other parameters as in Table 10.1 except for $\Omega_e = 30 \text{ s}^{-1}$.

we consider synapses that either buffer presynaptic rate or transmit its derivative, while in (c) we show the case of synapses that may also perform integration of low presynaptic rates of stimulation.

Consider then the same synapses as in (b) and (c) but with the addition of gliotransmission, whereby all n_S synapses are identically influenced by gliotransmitter released from the same astrocytic domain (Fig. 10.4d). The postsynaptic currents for analogous presynaptic rates as in (b) and (c), yet in the presence of three GRES, are

shown in Fig. 10.4e, f. It may be appreciated how activation of presynaptic receptors that follows GREs (*top* and *middle panels*) dramatically change postsynaptic currents, not only adding transients in coincidence with GRE occurrence, but also modifying the overall nature of transmission of presynaptic rates. In particular, one may notice how in the presence of release-decreasing gliotransmission (Fig. 10.4e), synapses in (b) could display integrative features of postsynaptic current (e.g. for $5 < t < 10$ s or $15 < t < 20$ s), akin to what observed for synapses in (c) in the absence of gliotransmission. Vice versa, in the presence of release-increasing gliotransmission (Fig. 10.4f), synapses in (c) tend to transmit akin to synapses in (b), producing postsynaptic currents that mostly buffer presynaptic rates (for $5 < t < 10$ s) or rather transmit their derivative (e.g. at $t = 10$ s and $t = 20$ s).

Taken together, the above observations reveal at least two important aspects of gliotransmission. First gliotransmission can dramatically change the way presynaptic APs are transmitted to postsynaptic targets by modulating neurotransmitter release dynamics. Second, the whole spectrum of “modes” of synaptic transmission, in terms of what features of the trains of presynaptic APs are transmitted postsynaptically in the absence of gliotransmission, can also be reproduced in the presence of gliotransmission but, in general, for different presynaptic rates. These arguments can readily be derived from the analytical solution of Eqs. 10.1 and 10.2 for a generic time-dependent presynaptic rate $v_S(t)$, under the simplifying assumption of gradual variation of presynaptic rate of stimulation, i.e. $v'_S(t)/v_S(t) \ll v_S(t)$ (Tsodyks 2005). Under this assumption, the first-order expansion of the *average* rate-dependent synaptic variables u_S , x_S , hereafter denoted in uppercase (i.e. U_S , X_S), reads (Appendix 1.1):

$$U_S(t) = \int_{-\infty}^t dt' U_0(t') v_S(t') e^{-\Omega_u(t)(t-t')} \left(1 + U_0(t) v_S'(t) \frac{(t-t')^2}{2} \right) \quad (10.15)$$

$$X_S(t) = \Omega_d \int_{-\infty}^t dt' e^{-\Omega_x(t)(t-t')} \left(1 + U_S(t) v_S'(t) \frac{(t-t')^2}{2} \right) \quad (10.16)$$

where

$$\Omega_u(t) = \Omega_f + U_0(t) v_S(t) \quad (10.17)$$

$$\Omega_x(t) = \Omega_d + U_S(t) v_S(t) \quad (10.18)$$

Assuming the average postsynaptic current to be proportional to the fraction of released neurotransmitter, so that $I(t) \propto U_S X_S v_S$, we may get an idea of the different effects of release-increasing versus release-decreasing gliotransmission, considering $I(t)$ dynamics, respectively, for the two limit scenarios of $U_0 \rightarrow 1$ and $U_0 \ll 1$. For strong release-increasing gliotransmission, such that $U_0 \rightarrow 1$, one may notice that $U_S \rightarrow 1$ as well, so that

$$X_S(t) \approx \Omega_d \int_{-\infty}^t dt' e^{-\Omega_x(t-t')} \left(1 + v_S'(t) \frac{(t-t')^2}{2} \right) = \frac{\Omega_d}{1+v_S(t)} + \frac{\Omega_d}{(1+v_S(t))^3} v_S'(t) \quad (10.19)$$

and thus

$$I(t) \sim X_S(t)v_S(t) = \frac{\Omega_d}{1+v_S(t)} v_S(t) + \frac{\Omega_d}{(1+v_S(t))^3} v_S(t)v_S'(t) \quad (10.20)$$

where it is apparent that the first term dominates unless $v_S'(t)$ is large, such as in coincidence with steep variations of $v_S(t)$. In other words, the closer U_0 is to 1 by means of release-increasing gliotransmission, the more likely the average postsynaptic current $I(t)$ is proportional to the rate of incoming APs (first term in the right-hand side of Eq. 10.20), thus accounting for buffering synaptic transmission. Alternatively, in the presence of large variations of presynaptic rate, like the step increases considered in Fig. 10.4f, the product of the presynaptic rate by its derivative (second term in the right-hand side of Eq. 10.20) dominates, resulting in derivative synaptic transmission.

In the case of release-decreasing gliotransmission instead, where $U_0 \rightarrow 0$ (and thus $U_S \rightarrow 0$ too), it follows that

$$U_S(t) \sim U_0 \int_{-\infty}^t dt' v_S(t') e^{-\Omega_f(t-t')} = U_0 v_S(t) * e^{-\Omega_f t} \quad (10.21)$$

$$X_S(t) \approx 1 - \frac{U_S(t)}{\Omega_d} v_S(t) \quad (10.22)$$

where ‘*’ denotes convolution. Accordingly,

$$I(t) \sim U_0 v_S(t) \cdot (v_S(t) * e^{-\Omega_f t}) \cdot \left(1 - \frac{U_0}{\Omega_d} v_S(t) \right) \quad (10.23)$$

and in particular, in the case of low presynaptic rates, it is

$$I(t) \sim U_0 v_S(t) \cdot (v_S(t) * e^{-\Omega_f t}) \quad (10.24)$$

In other words, in the presence of release-decreasing gliotransmission, the average postsynaptic current evolves as an integral transform of the presynaptic rate (by convolution), such that when $v_S(t) \ll \Omega_f$, the convolution integral in Eq. 10.24 roughly approximates the number of incoming presynaptic APs, and thus increases with stimulus duration (as in Fig. 10.4e). For higher $v_S(t)$ rates instead, this increase tends to be attenuated by the second term in Eq. 10.23 along with higher-order terms not considered in the derivation of this latter equation.

Overall the above analytic solutions for rate-based synaptic dynamics reveal that different modes of synaptic transmission are possible, such as integrative versus derivative coding or simply “buffering” of $v_S(t)$, depending on timing of presynaptic

APs. Because on the other hand, U_0 is modulated by gliotransmission, so are these different modes of synaptic transmission, suggesting that different features of the same stimulus may be transmitted by synapses in the absence vs. in the presence of gliotransmission. To the extent that synaptic coding critically shapes computations performed by the neural circuitry, this possibility could also be reflected at the network level, hinting a scenario where a neuron–glial network could be involved in different computational tasks that are defined, time by time, by activity-dependent gliotransmitter release by astrocytes in the network (De Pittà et al. 2015; De Pittà and Brunel 2016).

10.3.2 Short-Term Plasticity

Short-term plasticity refers to the ability of a synapse to modify its release of neurotransmitter in an activity-dependent fashion, thereby displaying *short-term depression* or *facilitation*, that is, a transient decrease (respectively increase) of neurotransmitter release during consecutive APs, which recovers to basal values (i.e. u_0) upon stimulus cessation. Short-term depression and facilitation can be characterized considering synaptic release due to pairs of APs, computing for each pair the paired-pulse ratio (PPR) of the fraction of neurotransmitter released by the second AP in the pair over the fraction of neurotransmitter released by the first AP, i.e. $\text{PPR} = r_{S_2}/r_{S_1}$. When $\text{PPR} < 1$, the amount of neurotransmitter released by the second AP is less than the amount released by the first AP, that is synaptic release decreases with incoming APs, consistently with the onset of short-term depression (also termed in this case “paired-pulse depression,” i.e. ‘PPD’). Conversely, if $\text{PPR} > 1$, then $r_{S_2} > r_{S_1}$, so that synaptic release increases with incoming APs, in agreement with ongoing short-term facilitation (also dubbed “paired-pulse facilitation,” i.e. ‘PPF’) (Zucker and Regehr 2002).

Unfortunately, recognition of PPD and PPF by PPR is constrained to the consideration of opportunely spaced AP pairs, and thus it does not generally allow monitoring short-term mechanisms of plasticity *dynamically*, that is for continuously incoming random APs as in the likely scenario of physiological synaptic activity (Softky and Koch 1993). It is nevertheless possible to extend the notions of PPD and PPF to generic AP trains, breaking down changes of synaptic release r_S from one AP to the following one in terms of changes of synaptic variables u_S , x_S . Consider in fact the difference in synaptic release between the i th AP and the $(i - 1)$ th one, defined by

$$\begin{aligned}\Delta r_{S_i} &= r_{S_i} - r_{S_{i-1}} = u_{S_i}^+ x_{S_i}^- - u_{S_{i-1}}^+ x_{S_{i-1}}^- \left(u_{S_i}^+ - u_{S_{i-1}}^+ \right) x_{S_i}^- + u_{S_{i-1}}^+ \left(x_{S_i}^- - x_{S_{i-1}}^- \right) \\ &= x_{S_i}^- \Delta u_{S_i}^+ + u_{S_{i-1}}^+ \Delta x_{S_i}^-\end{aligned}\quad (10.25)$$

According to the above equation, whether it is $\Delta r_{S_i} < 0$ (PPD) or $\Delta r_{S_i} > 0$ (PPF) ultimately depends on sign and magnitude of variations of synaptic variables between APs, i.e. $\Delta u_{S_i}^+$ and $\Delta x_{S_i}^-$. In particular, as summarized in Table 10.2, the above equa-

tion predicts that PPF occurs whenever the probability of effective neurotransmitter release increases (i.e. $\Delta u_{S_i}^+ > 0$), unless the interspike variation of probability of available neurotransmitter resources is such that $|\Delta x_{S_i}^-|/x_{S_i}^- > \Delta u_{S_i}^+ / u_{S_{i-1}}^+$, in which case PPD is observed instead (Table 10.2). In all other cases, PPD generally is the predominant form of plasticity, except when $\Delta r_{S_i} > 0$ because of $\Delta x_{S_i}^- > 0$, in spite of the fact that $\Delta u_{S_i}^+ < 0$. This happens for $|\Delta u_{S_i}^+|/u_{S_{i-1}}^+ < \Delta x_{S_i}^-/x_{S_i}^-$ and corresponds to the scenario of *recovery from depression* (RFD). In this case, the increase of synaptic release is due to an increase of releasable neurotransmitter resources that could ensue, for example, when the $(i - 1)$ th AP lags behind the i th one longer than this latter did with respect to the $(i - 2)$ th AP (Debanne et al. 1996).

In Fig. 10.5a, b, we show raster plots of neurotransmitter release in the absence of gliotransmission for 20 sample synapses (out of n_S in total), respectively, from Fig. 10.4b, c, in response to trains of APs of similar statistics arriving at an average rate $v_S = 2.5$ Hz. Each row of these rasters shows when neurotransmitter is released from one synapse, with every release event being colored in *orange/green/black* in accordance with Table 10.2 when PPD/PPF/RFD occurs. The bottom panels of Fig. 10.5a, b show instead the average rate of occurrence of different paired-pulse plasticity (PPP) events for all n_S synapses, thereby providing a snapshot of how different mechanisms of short-term plasticity evolve during stimulation. It may be noted how synapses in (a), that were shown to carry out buffering or derivative coding in Fig. 10.4b, display preponderant PPD and RFD (*bottom panel* in Fig. 10.5a), consistently with the notion that buffering and derivative synaptic coding are usually displayed by depressing synapses (Tsodyks 2005). Conversely, the ability to integrate stimulation by synapses in (b) (as seen in Fig. 10.4c) can be associated with their inherently facilitating nature, as reflected by prominent ongoing PPF with respect to PPD and RFD (*bottom panel* in Fig. 10.5b) (Tsodyks 2005).

Next we consider how depressing and facilitating synapses are respectively affected by release-decreasing and release-increasing gliotransmission. Analysis of the raster plot in Fig. 10.5c that was obtained for the same synapses/AP trains in (a), yet in the presence of release-decreasing gliotransmission, reveals how the originally depressing synapses in a show a robust increase of PPF versus a decrease of PPD and RFD in coincidence with GREs (*blue trace* for $2 < t < 30$ s in the *bottom panel* in

Table 10.2 Paired-pulse plasticity in a generic AP train. Characterization of paired-pulse plasticity during synaptic release due to multiple consecutive APs is based on variations of synaptic variables (Δu_S , Δx_S) across consecutive pairs of APs. PPD: *orange*; PPF: *light blue*; RFD: *gray*

	$\Delta x_S < 0$	$\Delta x_S > 0$
$\Delta u_S < 0$	PPR < 1	PPR < 1 PPR > 1
$\Delta u_S > 0$	PPR < 1 PPR > 1	PPR > 1

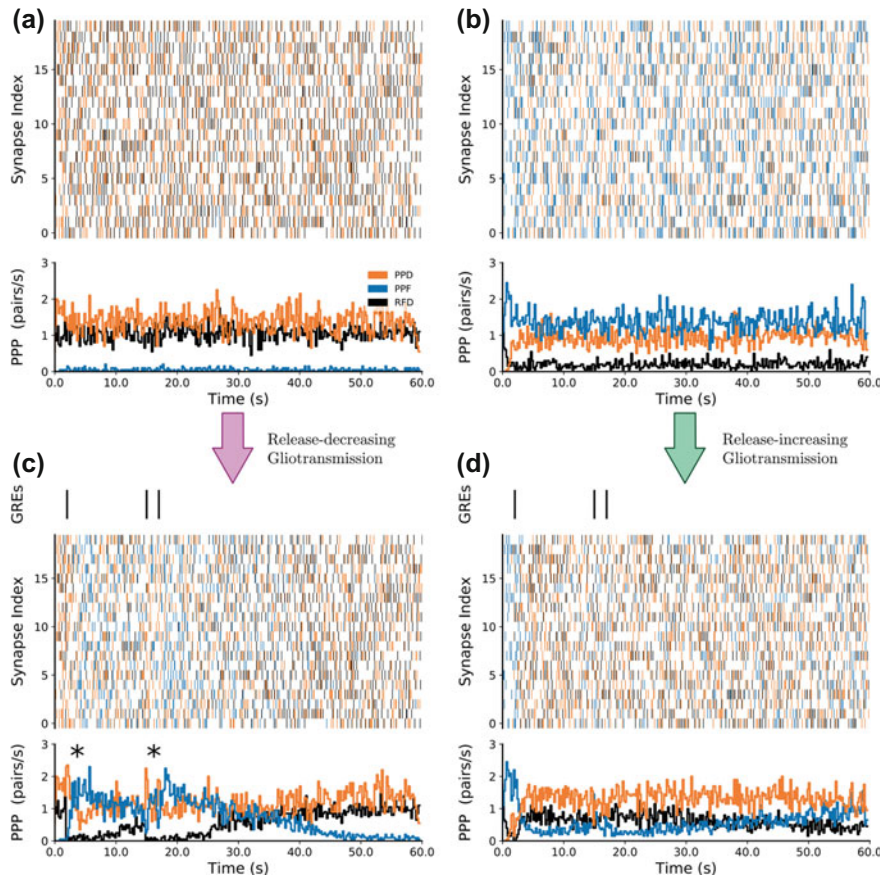


Fig. 10.5 Effects of gliotransmission on short-term plasticity. **a, b** (*Top*) Raster plots of synaptic release events (r_S) of 20 out of $n_S = 1000$ depressing versus facilitating synapses considered in Fig. 10.4b. **c, d** Release events are color coded according to the rationale for paired-pulse plasticity (PPP) summarized in Table 10.2. Synapses were stimulated by independent trains of Poisson-distributed APs incoming at rate $v_S = 2.5$ s. (*Bottom*) Rates of different PPP events during stimulation were computed by the count of PPP events from all n_S synapses in consecutive 200 ms-long time bins. **c, d** Synaptic release in **a** and **b** is reproduced in the presence of release-decreasing gliotransmission (**c**, $\alpha = 0$) and release-increasing gliotransmission respectively (**d**, $\alpha = 1$), considering three GREs at $t = 2, 15, 17$ s (*top panels*). Model parameters as in Fig. 10.4

Fig. 10.5c). Conversely, the facilitating synapses in (b) turns mostly depressing in the presence of release-increasing gliotransmission, as reflected by an increase of PPD and RFD versus a decrease of PPF following the first GRE at $t = 2$ s (*orange* and *black* traces in the *bottom panel* in Fig. 10.5d). These results are in agreement with the experimental observation that synapses whose release probability is increased by astrocytic gliotransmitters, display a reduced PPR (Jourdain et al. 2007; Bonansco

et al. 2011), whereas synapses whose release probability is decreased by gliotransmission are prone to display an increase of PPR (Liu et al. 2004b).

In conclusion, our hitherto analysis hints that gliotransmission can substantially alter synaptic transmission, potentially dictating what features of the neural code (in terms of rate dynamics of incoming APs) are transmitted to postsynaptic neurons, along with how these features are molded by different mechanisms of short-term plasticity. With this regard, a closer inspection of the raster plots in Fig. 10.5 also reveals that the timing and the number (rate) of GREs can dramatically change the effect of gliotransmission on synaptic plasticity. Take the example of depressing synapses in the presence of release-decreasing gliotransmission in the bottom panel of Fig. 10.5c. There, the switch from depression to facilitation observed by the first GRE at $t = 2$ s rapidly decays if it were not for a second GRE and a third one, respectively, at $t = 15$ s and $t = 17$ s (*asterisks*), that keep PPF predominant over PPD up to $t \approx 30$ s. This suggests that the effect of gliotransmission on synaptic transmission is not an ON/OFF phenomenon, but it can be rather variegated, depending on several factors including timing and frequency of GREs. In the next section, we introduce a framework to better characterize these conditions, in an attempt to derive a quantitative description for the requirements of functional gliotransmission, meaning by “functional,” any form of gliotransmission that can produce a measurable change in the synapse’s paired-pulse plasticity.

10.4 Mean Field Description of Gliotransmission-Mediated Modulations of Synaptic Release

10.4.1 Mean Field Derivation

One of the advantages of the simple model of gliotransmitter-regulated synapse introduced in Sect. 10.2 is that the model equations can be manipulated to derive a mean description of synaptic dynamics, and thus of short-term plasticity, in the presence of gliotransmission. This mean description ensues from a two-step averaging process. First we average over different trials of stimulation of the synapse by different realizations of trains of random APs in the presence of randomly occurring GREs, with statistics of APs and GREs fixed. Then, we average in time across AP and GRE time series. The ensuing “mean field” synaptic dynamics can be analytically solved to derive formulas that can be used to guide experiments and predict whether gliotransmission at specific synaptic loci may (or may not) affect synaptic transmission, and if so, to what extent.

The first step in the derivation of a mean field description of synaptic release in the presence of gliotransmission is to recast Eq. 10.1 in terms of $u_S^- = u_S(t_i^-)$ so as to have u_S to change simultaneously with x_S . With this regard, it is (Tsodyks 2005):

$$u_S^- = u_S^+ + u_0(1 - u_S^+) \Rightarrow u_S^+ = \frac{u_S^- - u_0}{1 - u_0} \quad (10.26)$$

Accordingly, substituting u_S^+ in terms of u_S^- in Eq. 10.1 provides

$$\frac{du_S^-}{dt} = \Omega_f(u_0 - u_S^-) + u_0 \sum_i (1 - u_S^-) \delta(t - t_i) \quad (10.27)$$

To simplify notation, we following redefine u_S and x_S by $u_S \leftarrow u_S^-$ and $x_S \leftarrow x_S^-$. Consider then n_S trials of stimulation of a synapse by trains of APs of equal length and same statistics, delivered to the synapse at identical initial conditions. The trial-averaged synaptic dynamics for the mean AP train is described by Eqs. 10.2 and 10.27, in terms of mean quantities $\bar{u}_S = 1/n_S \sum_k^n u_{S_k}$ and $\bar{x}_S = 1/n_S \sum_k^n x_{S_k}$. At the same time, because in our description u_0 dynamically evolves with timing of GREs in each trial, assuming the same statistics for GREs across trials, we also consider the trial-averaged quantity $\bar{u}_0 = 1/n_S \sum_k^n u_{0_k}$. Accordingly,

$$\frac{d\bar{u}_S}{dt} = \Omega_f(\bar{u}_0 - \bar{u}_S) + \frac{\bar{u}_0}{n_S} \sum_k^n \sum_i (1 - u_S) \delta(t_{i_k}) \quad (10.28)$$

$$\frac{d\bar{x}_S}{dt} = \Omega_d(1 - \bar{x}_S) - \frac{1}{n_S} \sum_k^n \sum_i u_S x_S \delta(t_{i_k}) \quad (10.29)$$

In a small time interval Δt , the above equations can be rewritten in terms of finite differences as

$$\bar{u}_S(t + \Delta t) - \bar{u}_S(t) = \Omega_f(\bar{u}_0 - \bar{u}_S(t)) \Delta t + \frac{\bar{u}_0}{n_S} \sum_k^n (1 - u_S(t)) \Delta_k(\Delta t) \quad (10.30)$$

$$\bar{x}_S(t + \Delta t) - \bar{x}_S(t) = \Omega_d(1 - \bar{x}_S(t)) \Delta t - \frac{1}{n_S} \sum_k^n u_S(t) x_S(t) \Delta_k(\Delta t) \quad (10.31)$$

where $\Delta_k(\Delta t)$ is the number of APs in the time interval Δt for the k th trial and is a strongly fluctuating (stochastic) quantity.

Analysis of neurophysiological data revealed that individual neurons in vivo fire irregularly at all rates, reminiscent of a Poisson process (Softky and Koch 1993). Mathematically, the Poisson assumption means that, at each moment, the probability that a neuron fires equals the neuron's instantaneous firing rate and is independent of the timing of previous APs. Then, assuming that the n_S trains of APs under consideration are different realizations of the same Poisson process with average rate $v_S(t)$, Eqs. 10.30 and 10.31 can be averaged in time over a proper Δt (Amit and Tsodyks 1991). In particular, thanks to the Poisson hypothesis, the variables u_S , x_S , $u_S x_S$ and $\Delta_k(\Delta t)$ can be considered independent and thus be averaged independently.

Therefore, taking Δt of the order of several intervals between APs, but shorter than the longest timescale in the system between synaptic dynamics ($1/\Omega_d$ and $1/\Omega_f$) and gliotransmission ($1/\Omega_G$, $1/\Omega_e$ and $1/\Omega_A$) (Amit and Tsodyks 1991), the time average (denoted by “ $\langle \cdot \rangle$ ”) of $\Delta_k(\Delta t)$ can be estimated by $\langle \Delta_k(\Delta t) \rangle = v_S(t)\Delta t$. Accordingly,

$$\langle \bar{u}_S(t + \Delta t) \rangle - \langle \bar{u}_S(t) \rangle = \Omega_f (\langle \bar{u}_0 \rangle - \langle \bar{u}_S(t) \rangle) \Delta t + \frac{\langle \bar{u}_0 \rangle}{n_S} \sum_k^{n_S} (1 - \langle u_S(t) \rangle) v_S(t) \Delta t \quad (10.32)$$

$$\langle \bar{x}_S(t + \Delta t) \rangle - \langle \bar{x}_S(t) \rangle = \Omega_d (1 - \langle \bar{x}_S(t) \rangle) \Delta t - \frac{1}{n_S} \sum_k^{n_S} \langle u_S(t) x_S(t) \rangle v_S(t) \Delta t \quad (10.33)$$

Finally, dividing by Δt yields

$$\frac{d\langle \bar{u}_S \rangle}{dt} = \Omega_f (\langle \bar{u}_0 \rangle - \langle \bar{u}_S \rangle) + \langle \bar{u}_0 \rangle (1 - \langle u_S \rangle) v_S(t) \quad (10.34)$$

$$\frac{d\langle \bar{x}_S \rangle}{dt} = \Omega_d (1 - \langle \bar{x}_S \rangle) - \langle u_S \rangle \langle x_S \rangle v_S(t) \quad (10.35)$$

where the time average of the product $\bar{r}_S = \bar{u}_S \bar{x}_S$ was approximated by the product of the time-averaged variables, i.e. $\langle \bar{r}_S \rangle = \langle \bar{u}_S \rangle \langle \bar{x}_S \rangle$. This approximation is exact only in case \bar{u}_S and \bar{x}_S are statistically independent, which are not in practice. Nevertheless, as elucidated in Appendix 1.2, the error introduced by this approximation is generally $<10\%$ for realistic parameter ranges and thus negligible, so that Eqs. 10.34 and 10.35 can be safely used to seek a realistic rate-based description of synaptic dynamics (Tsodyks 2005).

In order to complete our mean field description of synaptic dynamics, we seek an expression of $\langle \bar{u}_0 \rangle$ in terms of mean field dynamics of Γ_S and x_A (where $x_A \leftarrow x_A^-$). With this aim, we build up on the observation that nucleation of spontaneous Ca^{2+} spikes in an astrocyte may be approximated by a Poisson process with time-dependent frequency $v_A(t)$ that exponentially tends to a constant value v_{A_0} at rate ξ (Skupin and Falcke 2010), i.e.

$$v_A(t) = v_{A_0} (1 - e^{-\xi t}) \quad (10.36)$$

For simplicity, we assume that the majority (if not all) of Ca^{2+} spikes in the astrocyte crosses the threshold of gliotransmitter exocytosis, so that nucleation of GREs can also be approximated by a Poisson process with rate given by Eq. 10.36. In general, the exact expression of the GRE rate is not crucial for the validity of our mean field description, what is crucial instead is the Poisson assumption. By this assumption in fact, the probability of an event of gliotransmitter exocytosis can be taken independent of the timing of the preceding exocytotic event, so that the mean instantaneous rate $v_A(t)$ of GREs can be considered in the averaging of Eq. 10.4 (Amit and Tsodyks 1991). That is,

$$\frac{d\langle \bar{x}_A \rangle}{dt} = \Omega_A (1 - \langle \bar{x}_A \rangle) - \langle \bar{r}_A \rangle v_A(t) \quad (10.37)$$

where $\langle \bar{r}_A \rangle = U_A \langle \bar{x}_A \rangle$. Similarly, Eq. 10.9 can also be averaged to obtain a description of gliotransmitter concentration in the ECS as a function of $v_A(t)$, that is,

$$\frac{d\langle \bar{G}_A \rangle}{dt} = -\Omega_e \langle \bar{G}_A \rangle + \rho_e G_T \cdot \langle \bar{r}_A \rangle v_A(t) \quad (10.38)$$

In particular, experimental data suggest that the timescale of gliotransmitter modulation is much slower than the time course of gliotransmitter in the ECS (Araque et al. 1998a,b; Serrano et al. 2006; Jourdain et al. 2007; Perea and Araque 2007). Accordingly, it may be assumed that $\Omega_G \ll \Omega_A, \Omega_e$, and only the timescale slower than $1/\Omega_e$ can be considered in Eq. 10.38 so that

$$\langle \bar{G}_A \rangle \simeq \frac{\rho_e G_T}{\Omega_e} \cdot \langle \bar{r}_A \rangle v_A(t) \quad (10.39)$$

Substituting the above expression in Eq. 10.14 for Γ_S , and averaging the latter, finally provides:

$$\begin{aligned} \frac{d\langle \bar{\Gamma}_S \rangle}{dt} &= O_G \langle \bar{G}_A \rangle (1 - \langle \bar{\Gamma}_S \rangle) - \Omega_G \langle \bar{\Gamma}_S \rangle = O_G \cdot \frac{\rho_e G_T}{\Omega_e} \langle \bar{r}_A \rangle (1 - \langle \bar{\Gamma}_S \rangle) v_A(t) - \Omega_G \langle \bar{\Gamma}_S \rangle \\ &= J_S \langle \bar{r}_A \rangle (1 - \langle \bar{\Gamma}_S \rangle) v_A(t) - \Omega_G \langle \bar{\Gamma}_S \rangle \end{aligned} \quad (10.40)$$

where

$$J_S = \rho_e \frac{O_G G_T}{\Omega_e} \quad (10.41)$$

represents the maximum fraction of presynaptic receptors that can be activated by astrocytic gliotransmitter. Akin to the derivation of Eqs. 10.34 and 10.35, the above equation was obtained by the approximation of $G_A (1 - \bar{\Gamma}_S) \approx \langle \bar{G}_A \rangle (1 - \langle \bar{\Gamma}_S \rangle)$. As shown in Appendix 1.2, the maximum error introduced by this approximation is generally <10% for values of model parameters in their physiological range, so that Eq. 10.40 can generally be used to reliably estimate the mean field dynamics of u_0 by Eq. 10.12, i.e.

$$\langle \bar{u}_0 \rangle = U_0^* + (\alpha - U_0^*) \langle \bar{\Gamma}_S \rangle \quad (10.42)$$

The ensemble of Eqs. 10.34, 10.35, 10.37, 10.40, and 10.42 provides a mean field description of synaptic transmission in the presence of gliotransmission. This description, as exemplified by the *solid dark-colored traces* in 10.6, well captures the average dynamics (in *lighter colors*) of the corresponding spiking model considered in Figs. 10.4 and 10.5. In general, the error introduced by the mean field description, is negligible for steady-state dynamics but grows larger in coincidence with steep transients of stimulation, such as step increases of the rate of GREs in this figure (e.g.

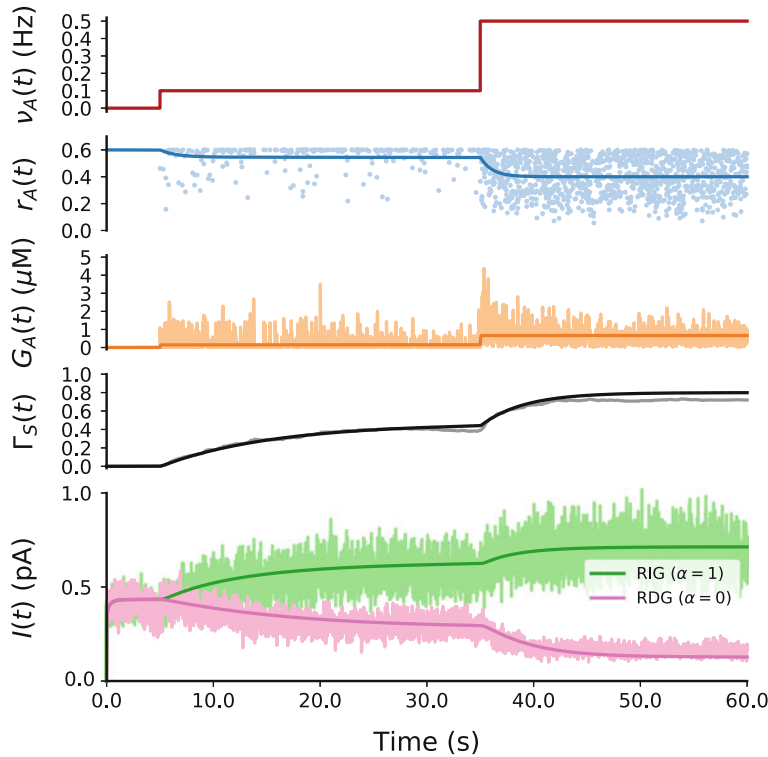


Fig. 10.6 Mean field dynamics. Solutions of the mean field equations for two step increases of the GRE rate ($v_A(t)$, top panel) are shown by solid dark traces against light-colored numerical solutions of the spiking model used in Figs. 10.4 and 10.5. Postsynaptic currents ($I(t)$, bottom panel) are reported for both scenarios of release-decreasing gliotransmission (RDG, magenta, $\alpha = 0$) and release-increasing gliotransmission (RIG, green, $\alpha = 1$). Numerical solutions of the spiking model are reported here as average over 100 different realization of Poisson-distributed GREs considering 10 identical synapses identically modulated by gliotransmission per realization. Synapses were stimulated independent Poisson-distributed AP trains incoming at average rate $v_S = 2$ Hz. Model parameters as in Table 10.1 except for $\Omega_d = 3.33 \text{ s}^{-1}$, $\Omega_f = 2 \text{ s}^{-1}$, $U_0^* = 0.3$, $O_u = 0$

at $t = 35$ s). This error dynamics is a consequence of the inherent assumptions of the averaging process, but it is not detrimental to the analysis of synaptic behavior, which is generally well reproduced qualitatively and quantitatively, by numerical solutions of the mean field equations, in the presence of both of release-decreasing and release-increasing gliotransmission (magenta and green traces, respectively).

10.4.2 Conditions for Functional Gliotransmission

One of the advantages of the mean field description derived in the previous section is the possibility to obtain an analytical expression for the average fraction of neu-

rotransmitter resources released from any synapse in response to presynaptic APs incoming at mean rate v_S , as well as in the presence of GREs occurring at average rate v_A . With this regard, using uppercase letters for mean field variables to simplify notation (e.g. $X_S \equiv \langle \bar{x}_S \rangle$, $U_S \equiv \langle \bar{u}_S \rangle, \dots$), we note that Eqs. 10.34 and 10.35 can be solved for the steady state (denoted by the subscript ‘ ∞ ’), whereby

$$\frac{dU_S}{dt} = 0 \Rightarrow U_{S_\infty} = U_{0_\infty} \frac{\Omega_f + v_{S_\infty}}{\Omega_f + U_{0_\infty} v_{S_\infty}} \quad (10.43)$$

$$\frac{dX_S}{dt} = 0 \Rightarrow X_{S_\infty} = \frac{\Omega_d}{\Omega_d + U_{S_\infty} v_{S_\infty}} \quad (10.44)$$

Accordingly, the mean steady-state fraction of released neurotransmitter resources R_{S_∞} is given by Eq. 10.3 and reads (in the approximation of statistical independence of U_S and X_S)

$$R_{S_\infty} = U_{S_\infty} X_{S_\infty} = \frac{U_{0_\infty} \Omega_d (\Omega_f + v_{S_\infty})}{\Omega_d \Omega_f + U_{0_\infty} (\Omega_d + \Omega_f) v_{S_\infty} + U_{0_\infty} v_{S_\infty}^2} \quad (10.45)$$

In the limit of $v_S \rightarrow 0$, the slope of R_{S_∞} , i.e. R_{S_∞}' , is indicative of the synapse’s nature, namely whether the synapse can be facilitating ($R_{S_\infty}' > 0$) or merely depressing ($R_{S_\infty}' < 0$) (Tsodyks et al. 1998). This slope reads

$$R_{S_\infty}'(v_S \rightarrow 0) = \left. \frac{\partial R_{S_\infty}}{\partial v_S} \right|_{v_S \rightarrow 0} = \frac{\Omega_d - (\Omega_d + \Omega_f) U_{0_\infty}}{(\Omega_d \Omega_f)^2} \quad (10.46)$$

which can be either positive or negative, depending on whether U_{0_∞} is respectively below or above a threshold value U_θ , defined as (Tsodyks 2005):

$$U_\theta = \frac{\Omega_d}{\Omega_d + \Omega_f} \quad (10.47)$$

We will hereafter refer to U_θ as the threshold of basal synaptic release that could make synaptic transmission switch from facilitating to depressing and vice versa.

Because in the presence of gliotransmission U_{0_∞} depends on the steady-state GRE rate (via Eq. 10.42) then, in agreement with the arguments raised in Sect. 10.3.2, it may be predicted that, depending on v_A , U_0 could be made to change across the threshold value U_θ , thereby modulating synaptic plasticity through a continuous spectrum of different magnitudes of short-term facilitation and depression. This is revealed considering the steady-state solutions of X_A , Γ_S , and U_0 , respectively, given by Eqs. 10.37, 10.40, and 10.42, whereby

$$\frac{dX_A}{dt} = 0 \Rightarrow X_{A_\infty} = \frac{\Omega_A}{\Omega_A + U_A v_{A_\infty}} \quad (10.48)$$

$$\frac{d\Gamma_S}{dt} = 0 \Rightarrow \Gamma_{S_\infty} = \frac{J_S \Omega_A U_A v_{A_\infty}}{\Omega_A \Omega_G + (J_S \Omega_A + \Omega_G) U_A v_{A_\infty}} \quad (10.49)$$

$$U_{0_\infty}(v_{A_\infty}) = \frac{\Omega_A \Omega_G U_0^* + (\Omega_G U_0^* + \alpha J_S \Omega_A) U_A v_{A_\infty}}{\Omega_A \Omega_G + (J_S \Omega_A + \Omega_G) U_A v_{A_\infty}} \quad (10.50)$$

Figure 10.7 shows the behavior of $U_{0_\infty}(v_{A_\infty})$ as predicted by the above equation for the two scenarios of release-decreasing ($\alpha = 0$, panel A) versus release-increasing gliotransmission ($\alpha = 1$, panel B). In particular, U_{0_∞} decreases with increasing v_{A_∞} under release-decreasing gliotransmission, so that synaptic depression tends to get weaker for progressively higher GRE rates (since depletion of synaptic resources is weaker), while facilitation grows stronger. In this fashion, an originally depressing synapse becomes progressively more facilitating as v_A increases (Fig. 10.7b). The opposite instead occurs in the presence of release-increasing gliotransmission (Fig. 10.7c), so that a facilitating synapse displays more and more depression as U_{0_∞} increases with v_{A_∞} , in line with faster depletion of synaptic resources as basal synaptic release probability increases with the GRE rate.

The curves for U_{0_∞} versus v_{A_∞} in Fig. 10.7 also show that for a particular value of the frequency of gliotransmitter release, denoted hereafter by v_θ (*vertical dashed magenta line*), U_0 crosses the threshold release probability U_θ (*horizontal blue line*). Such frequency v_θ can be regarded as the threshold rate of gliotransmitter exocytosis that makes a synapse switch its mode of transmission and plasticity. That is, a depressing synapse, that is originally characterized by $U_0 > U_\theta$, could turn facilitating for $v_A > v_\theta$ in the presence of release-decreasing gliotransmission whereby $U_0(v_A > v_\theta) < U_\theta$ (Fig. 10.7a, *blue-shaded area*). Vice versa, a synapse that is originally facilitating, namely a synapse for which $U_0 < U_\theta$, could turn depressing by release-increasing gliotransmission, since in this case it is $U_0(v_A > v_\theta) > U_\theta$ (Fig. 10.7b, *blue-shaded area*).

An expression of v_θ can be obtained solving Eq. 10.50 for $U_{0_\infty}(v_{A_\infty} = v_\theta) = U_\theta$, and reads

$$v_\theta = \frac{(U_\theta - U_0^*) \Omega_A \Omega_G}{J_S U_A (\alpha - U_\theta) \Omega_A - U_A (U_\theta - U_0^*) \Omega_G} \quad (10.51)$$

where three aspects of the astrocyte-synapse coupling are apparent in setting v_θ : (i) the nature of gliotransmitter release, reflected by parameters U_A and Ω_A ; (ii) the nature of the gliotransmitter pathway, as mirrored by parameters like J_S and Ω_G ; and significantly, (iii) the nature of the synapse ensheathed by the astrocyte, via parameters like U_0^* and U_θ . The fact that v_θ is not only determined by astrocytic properties, but also depends on the synapse's nature, suggests that, among all possible synapses in the brain represented by the parameter plane U_0 versus Ω_d/Ω_f , only those that associate with $v_\theta > 0$ can, in principle, switch transmission mode by gliotransmission. Or, in other words, the very nature of the synapse dictates whether gliotransmission can have a functional effect on synaptic transmission. In this spirit

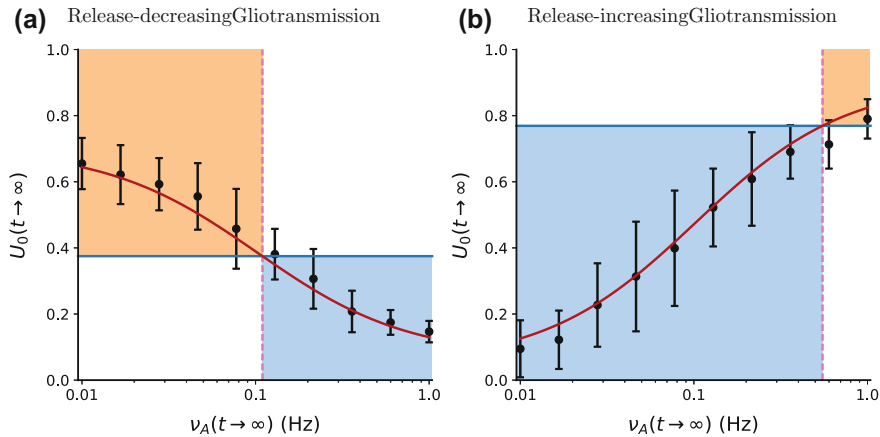


Fig. 10.7 Basal synaptic release probability is controlled by the rate of gliotransmitter release. The rate of GREs (v_A) regulates the strength of the effect of astrocytic gliotransmitters on basal synaptic release probability (U_0). This can be well elucidated considering the dependence of U_0 on v_A at steady state (i.e. for $t \rightarrow \infty$, red curves). **a** In the scenario of release-decreasing gliotransmission ($\alpha = 0$) on a depressing synapse ($U_0(v_A \rightarrow 0) > U_\theta$, orange-shaded region), U_0 decreases with v_A and a threshold rate for GRE (v_θ in Eq. 10.51) can be identified (vertical dashed magenta line) in correspondence with the crossing of U_θ (horizontal blue line) by the curve $U_0(v_A)$. This means, that for proper rates of synaptic stimulation and $v_A(t \rightarrow \infty) > v_\theta$, the originally depressing synapse turns essentially facilitating (blue-shaded region). **b** In the dual scenario of release-increasing gliotransmission ($\alpha = 1$) on a facilitating synapse, v_θ marks instead the threshold rate of gliotransmitter release beyond which the synapse becomes essentially depressing. Data points: mean \pm std of u_0 values in correspondence of 30 GREs in conditions of steady-state gliotransmitter release (i.e. for $v_A \rightarrow v_A(t \rightarrow \infty)$). **a:** $\Omega_d = 2 \text{ s}^{-1}$, $\Omega_f = 3.33 \text{ s}^{-1}$, $U_0^* = 0.7$; **b:** $\Omega_d = 3.33 \text{ s}^{-1}$, $\Omega_f = 1 \text{ s}^{-1}$, $U_0^* = 0.05$. Other model parameters as in Table 10.1

then, it is instructive to see how the population of synapses that could be modulated by gliotransmission changes with synaptic and astrocytic parameters. With this regard, it may be noted that Eq. 10.51 describes a hyperbola in terms of U_0^* with a vertical asymptote at

$$\hat{U}_0^* = U_\theta + J_S \frac{\Omega_A}{\Omega_G} (U_\theta - \alpha) \quad (10.52)$$

which can be either positive or negative depending on the sign of the difference $U_\theta - \alpha$. The asymptote \hat{U}_0^* (Eq. 10.52) sets a boundary for the values of basal synaptic release probability (U_0^*) for which v_θ exists, thus limiting the possible synapses that can be modulated by gliotransmission. In particular, v_θ exists only for depressing synapses characterized by $U_\theta < U_0^* < \min(\hat{U}_0^*, 1)$, and only for facilitating synapses for which $\max(0, \hat{U}_0^*) < U_0^* < U_\theta$ (Table 10.3). This implies that if \hat{U}_0^* is outside of $[0, 1]$, v_θ always exists for all values of $U_0^* \in [0, 1]$. In this case then, the domain of existence of v_θ is the whole parameter plane U_0 versus Ω_d / Ω_f , and for all synapses

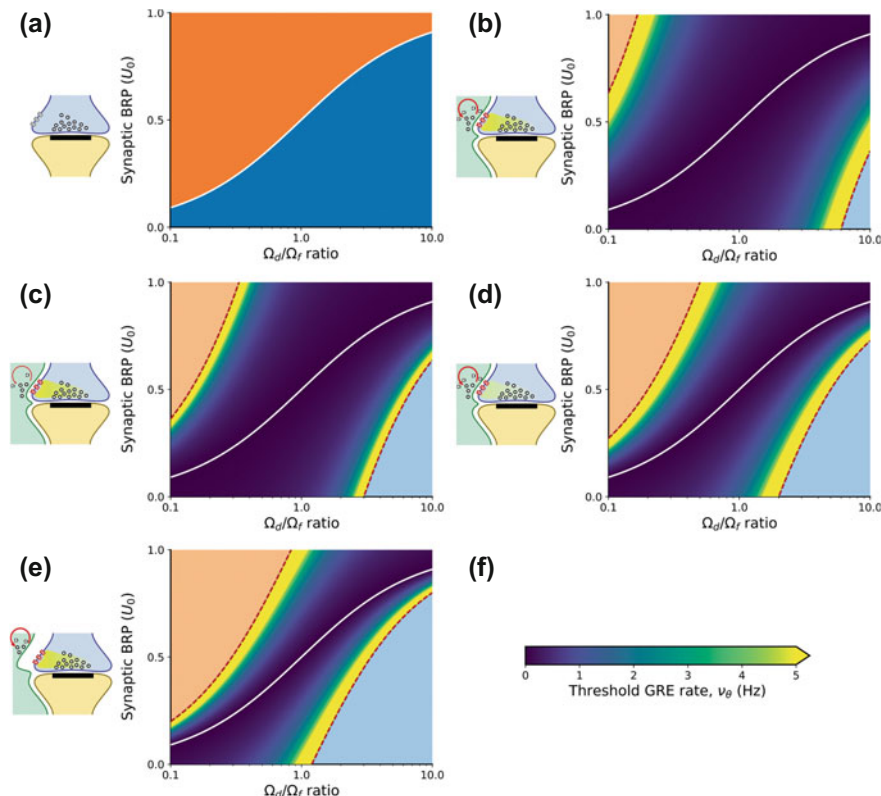


Fig. 10.8 Conditions for the observation of switches of short-term plasticity by gliotransmission. **a** The space of synaptic parameters can be partitioned in terms of depressing (orange region) versus facilitating synapses (blue region), depending on the value of synaptic rates Ω_d and Ω_f (Eqs. 10.1 and 10.2) and whether the average synaptic basal release probability (BRP, U_0), is above or below a threshold value U_θ (white curve, Eq. 10.47). **b** Not all synapses can switch their plasticity mode by gliotransmission, but rather only a subset of them (colored regions between dashed magenta lines) may, depending on whether a threshold GRE rate for plasticity switch exists and, if so, how large it is (colorbar in **f**). The subset of synapses that, in the presence of gliotransmission, can turn depressing from facilitating and vice versa, shrinks in any of the following scenarios or combination thereof: **c** when reintegration of released gliotransmitter is slow; **d** when the effect of modulation of synaptic release by activated presynaptic receptors quickly vanishes; and **e** when morphology of astrocyte-synapse coupling does not allow efficient activation of presynaptic receptors (e.g. when the astrocytic process is not close enough to the presynaptic terminal of the synapse). Model parameters in **(b)** as in Table 10.1 except for $\Omega_G = 2 \text{ min}^{-1}$ and $J_S = 0.2$. Panels **c–e** consider the same parameters as in **(b)** except for: **c** a twofold decrease of Ω_A ; **d** a threefold reduction of Ω_G ; and **e** a fivefold decrease of J_S . Model parameters as in Table 10.1 except for $\Omega_e = 40 \text{ s}^{-1}$ and $\Omega_G = 0.033 \text{ s}^{-1}$. All panels except **e** consider a value of $J_S = 0.2$ (Eq. 10.41)

in this plane, there can always exist, at least in principle, a rate of GREs that can account for plasticity switches (Fig. 10.8a).

Table 10.3 Conditions for gliotransmission-mediated transitions between short-term depression and facilitation. The conditions for the existence of v_θ are summarized for different scenarios of gliotransmission in terms of synapse type. Empty table entries (denoted by ‘–’) represent scenarios for which v_θ is not defined

Synapse type	Gliotransmitter effect	
	Release-decreasing $\alpha < U_\theta$	Release-increasing $\alpha > U_\theta$
Depressing $U_0^* > U_\theta$	$U_\theta < U_0^* < \min(\hat{U}_0^*, 1)$	–
Facilitating $U_0^* < U_\theta$	–	$\max(0, \hat{U}_0^*) < U_0^* < U_\theta$

If instead $\hat{U}_0^* \in [0, 1]$, only a subset of synapses can effectively be modulated by gliotransmission. This is exemplified in Fig. 10.8b, where the color-coded region of possible v_θ in the parameter plane U_0 versus Ω_d/Ω_f is comprised between the *magenta dashed lines* which mark the asymptotic value \hat{U}_0^* and delimit the subset of synapses, among all possible ones, that can effectively be modulated by gliotransmission, thereby alternating between short-term depression and facilitation. In practice, this subset of synapses is likely narrower since $v_\theta \rightarrow \infty$ as $U_0^* \rightarrow \hat{U}_0^*$, and thus realistic v_θ values can only be found for U_0^* values sufficiently far from the asymptotic value \hat{U}_0^* . On the other hand, switches between short-term depression and facilitation could hardly be detected in synapses whose basal release probability is close to U_θ , since PPF or PPD (or lack thereof) that could be displayed by these synapses are likely too weak to be measured in experiments. Accordingly, this raises a warning flag for those experiments that aim to study functional effects of gliotransmission on synaptic transmission, but inadvertently target synapses whose basal release probability is close to the theoretical threshold U_θ , insofar as detection (or not) of a change of synaptic plasticity/mode of transmission at those synapses, cannot generally be taken as conclusive evidence of existence of functional gliotransmission nor as a lack thereof.

A further, previously mentioned aspect is the dependence of v_θ on the nature of gliotransmission, including gliotransmitter release kinetics (in terms of Ω_A), kinetics of presynaptic receptors targeted by gliotransmitter molecules (as reflected by Ω_G), and geometry of the ECS which mediates how effectively gliotransmitter released from astrocytic processes can diffuse to and bind presynaptic receptors (parameter J_S in our model). Figure 10.8c–e show synaptic subsets for which v_θ is defined for three different scenarios where these parameters were changed with respect to Fig. 10.8a, b, resulting in somehow weaker gliotransmission. In panel (c), for example, we consider the case of a twofold slower recovery rate of gliotransmitter resources, that would thus hinder gliotransmitter release by faster depletion of gliotransmitter resources. Panel (d) showcases instead the scenario where the effect of presynaptic receptors activated by gliotransmitter decays faster, as a result of a threefold increase of Ω_G , thereby making modulations of short-term plasticity vanish more quickly. Finally, in panel (e) the scenario of a reduced morphological coupling between astrocytic and synaptic processes is considered in terms of a fivefold decrease of J_S that could for

example ensue from activity-dependent retractions of perisynaptic astrocytic processes (Perez-Alvarez et al. 2014). It may be observed how in all these scenarios, the subset of synapses that could be modulated by gliotransmission substantially shrinks while the color gradient of v_θ values (Fig. 10.8f) generally increases, suggesting that modulations of short-term plasticity may not be detected in these conditions, despite ongoing gliotransmitter release from astrocytes (De Pittà et al. 2015).

10.5 Conclusions

The theoretical arguments exposed in this chapter delineate a scenario where synaptic transmission could be profoundly influenced by gliotransmission from astrocytes, with important repercussions on the neural code and the information it carries while propagating through synaptic networks ensheathed by glia. On the other hand, and in line with ongoing debate in the community (Fiacco and McCarthy 2018; Savtchouk and Volterra 2018), measuring a functional effect of gliotransmission on synaptic dynamics—for example, a change in paired-pulse plasticity—is not trivial and must likely meet several conditions. While these conditions do not rule out at all the possibility that gliotransmission could effectively occur on physiological basis, they put strong emphasis on the specificity of astrocyte–synapse signaling interaction and morphological coupling. In turn, this specificity depends on both synaptic and astrocytic/gliotransmission properties and includes: (i) the nature of the synapse under consideration, namely how much the synapse is depressing or facilitating as quantified by $|U_0^* - U_\theta|$ in Fig. 10.8; (ii) the capacity of the astrocyte to efficiently produce gliotransmitter exocytosis, as reflected by the rate of reintegration of releasable gliotransmitter resources (Ω_A); and (iii) the nature of the pathway for gliotransmission characterized by parameters such as Ω_G and J_S (Eq. 10.41), where this latter lumps information on the amount of gliotransmitter available (G_T), the functional and morphological ultrastructure of the extracellular space between the astrocyte and the synapse that mediates gliotransmission (ρ_e , Ω_e), and the density of presynaptic receptors as well as their activation kinetics (O_G). In strong agreement with experiments, this reasoning ultimately supports the notion that gliotransmission could be a focal, spatially precise mechanism of communication between astrocytes and synapses, possibly mediated by specialized sites of interaction formed by astrocytes with synaptic elements, akin to those mediated by synapses themselves between neurons (Anderson and Swanson, 2000; Jourdain et al. 2007; Santello and Volterra 2009; Bergersen et al. 2012).

Acknowledgements Research work presented here is supported by the Junior Leader Postdoctoral Fellowship Program from “la Caixa” Banking Foundation (grant LCF/BQ/LI18/11630006) and was also previously sponsored by the European Commission through an International Outgoing Marie Skłodowska-Curie Fellowship (Project 331486 “Neuron-Astro-Nets”). MDP also wishes to acknowledge the support of the Basque Government by the BERC 2018–2021 program, as well as the support by the Spanish Ministry of Science, Innovation and Universities through the BCAM Severo Ochoa accreditation SEV-2017-0718.

Appendix 1 Derivation of Analytical Results

Appendix 1.1 Time-Dependent Solution of Mean Field Synaptic Dynamics

Equations 10.34 and 10.35 can conveniently be rewritten in the form

$$\frac{dU_S(t)}{dt} = (\Omega_f + v_S(t)) U_0(t) - (\Omega_f + U_0(t)v_S(t)) U_S(t) = (\Omega_f + v_S(t)) U_0(t) - \Omega_u(t) U_S(t) \quad (10.53)$$

$$\frac{dX_S(t)}{dt} = \Omega_d - (\Omega_d + U_S(t)v_S(t)) X_S(t) = \Omega_d - \Omega_x(t) X_S(t) \quad (10.54)$$

where $\Omega_u(t)$, $\Omega_x(t)$ are, respectively, defined by Eqs. 10.17 and 10.18. The equations for U_S , X_S are thus in the general form

$$\frac{dx}{dt} = -a(t) \cdot x + b(t) \quad (10.55)$$

so that their solutions are of the type

$$x(t) = h(t) e^{-\int_0^t a(t') dt'} \quad (10.56)$$

In particular, an expression for $h(t)$ in the above equation can be obtained replacing the generic solution $x(t)$ in Eq. 10.55 and reads:

$$\begin{aligned} \frac{dh(t)}{dt} e^{-\int_0^t a(t') dt'} - a(t)x(t) &= b(t) - a(t)x(t) \\ \Rightarrow h(t) &= \int_{-\infty}^t b(t') e^{\int_{t'}^t a(t'') dt''} dt' \end{aligned} \quad (10.57)$$

Accordingly,

$$\begin{aligned} U_S(t) &= \int_{-\infty}^t U_0(t') (\Omega_f + v_S(t')) e^{-\int_{t'}^t \Omega_u(t'') dt''} dt' \\ &= \int_{-\infty}^t U_0(t') (\Omega_f + v_S(t')) e^{-\int_{t'}^t (\Omega_f + U_0(t'') v_S(t'')) dt''} dt' \end{aligned} \quad (10.58)$$

$$X_S(t) = \Omega_d \int_{-\infty}^t e^{-\int_{t'}^t \Omega_x(t'') dt''} dt' = \Omega_d \int_{-\infty}^t e^{-\int_{t'}^t (\Omega_d + v_S(t'')) dt''} dt' \quad (10.59)$$

Under the assumptions that $v_S(t)$ is continuous and differentiable, its value at t'' can conveniently be expressed by the mean value theorem as $v_S(t'') = v_S(t) - v_S'(t)(t - t')$. Substituting this latter in the above equations, we obtain

$$\begin{aligned}
U_S(t) &\approx \int_{-\infty}^t U_0(t') (\Omega_f + v_S(t')) e^{-\Omega_f(t-t') - U_0(t)v_S(t)(t-t') + U_0(t)v_S'(t)\frac{(t-t')^2}{2}} dt' \\
&= \int_{-\infty}^t U_0(t') (\Omega_f + v_S(t')) e^{-\Omega_u(t)(t-t')} \cdot e^{U_0(t)v_S'(t)\frac{(t-t')^2}{2}} dt' \\
&= \int_{-\infty}^t U_0(t') (\Omega_f + v_S(t')) e^{-\Omega_u(t)(t-t')} \left(1 + U_0(t)v_S'(t)\frac{(t-t')^2}{2}\right) dt' \\
X_S(t) &\approx \Omega_d \int_{-\infty}^t e^{-\Omega_d(t-t') - U_S(t)v_S(t)(t-t') + U_S(t)v_S'(t)\frac{(t-t')^2}{2}} dt' \\
&= \Omega_d \int_{-\infty}^t e^{-\Omega_x(t)(t-t')} \cdot e^{U_S(t)v_S'(t)\frac{(t-t')^2}{2}} dt' \\
&= \Omega_d \int_{-\infty}^t e^{-\Omega_x(t)(t-t')} \left(1 + U_S(t)v_S'(t)\frac{(t-t')^2}{2}\right) dt'
\end{aligned}$$

where the rightmost terms in parentheses follow by first-order Taylor series expansion of the last exponential by the assumption of gradual rate changes such that $v_S'/v_S \ll v_S$. The expressions for $U_S(t)$ and $X_S(t)$ obtained in this fashion coincide with those reported in Eqs. 10.15 and 10.16 and may then be used to study mean field synaptic transmission for different ranges of $U_0(t)$ values. In particular, in the likely scenario of slowly decaying gliotransmitter modulation of synaptic release (Appendix 2), $U_0(t)$ can be assumed almost constant during variations of $v_S(t)$, i.e. $U_0(t) \approx U_0 = \text{const}$, so that

$$U_S(t) \approx U_0 \int_{-\infty}^t (\Omega_f + v_S(t')) e^{-\Omega_u(t)(t-t')} \left(1 + U_0 v_S'(t) \frac{(t-t')^2}{2}\right) dt' \quad (10.60)$$

which, in the release-decreasing regime of gliotransmission such that $0 < U_0 \ll 1$, provides

$$\begin{aligned}
U_S(t) &\approx U_0 \int_{-\infty}^t (\Omega_f + v_S(t')) e^{-\Omega_f(t-t')} dt' = U_0 + U_0 \int_{-\infty}^t v_S(t') e^{-\Omega_f(t-t')} dt' \\
&= U_0 + U_0 v_S(t) * e^{-\Omega_f t}
\end{aligned} \quad (10.61)$$

in line with Eq. 10.21. In the case of $X_S(t)$ instead, one may notice that the integral can be solved regardless of the functional form of $v_S(t)$ and $U_S(t)$, since the variable of integration is t' and not t , so that

$$X_S(t) = \frac{\Omega_d}{\Omega_x(t)} + \frac{\Omega_d U_S(t) v_S(t)}{\Omega_x^3(t)} \quad (10.62)$$

which accounts for Eq. 10.19 in the main text.

Appendix 1.2 Validity of the Mean Field Description

The error introduced by the approximation of statistical independence between u_S and x_S in the derivation of Eqs. 10.34 and 10.35 may be estimated by the Cauchy–Schwarz inequality of probability theory whereby (Tsodyks et al. 1998):

$$\frac{|\langle \bar{u}_S \bar{x}_S \rangle - \langle \bar{u}_S \rangle \langle \bar{x}_S \rangle|}{\langle \bar{u}_S \rangle \langle \bar{x}_S \rangle} \leq \chi_{u_S} \cdot \chi_{x_S} \quad (10.63)$$

where χ_{u_S} and χ_{x_S} stand for the coefficients of variation of the random variables u_S, x_S and, in the approximation of slow $U_0(t)$ dynamics (i.e. $\Omega_G \ll \Omega_d, \Omega_f$), they are equal to (Tsodyks et al. 1998; De Pittà et al. 2011):

$$\chi_{u_S}^2 = \frac{\Omega_f (1 - U_0)^2 v_S}{(\Omega_f + v_S) (2\Omega_f + U_0(2 - U_0)v_S)} \quad (10.64)$$

$$\chi_{x_S}^2 = \frac{U_S^2 v_S}{2\Omega_d + (2 - U_S)U_S v_S} \quad (10.65)$$

Only if $\chi_{u_S} \chi_{x_S} < 0.1$, and Eqs. 10.34 and 10.35 provide a realistic mean field description of synaptic dynamics (Tsodyks et al. 1998; Tsodyks 2005). In the simulations presented here, as well as for the majority of values of synaptic parameters within their estimated physiological range (Appendix 2), this constraint on the error is generally satisfied, resulting in an error that overall is less than 8%, thereby validating our mean field description of synaptic dynamics.

Analogous considerations can also be made for the derivation of Eq. 10.40. In that equation, the error introduced by the approximation of statistical independence between x_A (via G_A) and Γ_S is upper bounded by the Cauchy–Schwarz inequality

$$\frac{|\langle x_A \Gamma_S \rangle - \langle x_A \rangle \langle \Gamma_S \rangle|}{\langle x_A \rangle \langle \Gamma_S \rangle} \leq \chi_{x_A} \cdot \chi_{\Gamma_S} \quad (10.66)$$

where $\chi_{x_A}, \chi_{\Gamma_S}$ denote the coefficients of variation of x_A and Γ_S for stochastic gliotransmitter release. Derivation of χ_{x_A} directly follows from the above formula for $\chi_{x_S}^2$ replacing u_S, Ω_d , and v_S by U_A, Ω_A , and v_A , thus providing

$$\chi_{x_A}^2 = \frac{U_A^2 v_A}{2\Omega_A + (2 - U_A)U_A v_A} \quad (10.67)$$

More involved is instead the estimation of χ_{Γ_S} . For this latter, we start from a recursive expression of the peak value of activated presynaptic receptors (Γ_{S_n}) as a function of the timing of gliotransmitter release (τ_n). With this regard, the rate of GReEs (v_A) can be assumed much lower than the recovery rate of released gliotransmitter resources, i.e. $v_A \ll \Omega_A$ (Montana et al. 2006; Bowser and Khakh 2007), so that, at every release event it is $r_{A_n} = U_A x_{A_n} \approx U_A$. In this fashion, each release event increases

gliotransmitter concentration in the ECS by (Eq. 10.7):

$$G_{rel_n} = \rho_e G_T r_{A_n} \approx \rho_e G_T U_A = \hat{G}_A \quad (10.68)$$

Hence, following the n th release event occurring at $t = \tau_n$, the time course of gliotransmitter in the ECS is (Eq. 10.9):

$$G_A(t \geq \tau_n) = \hat{G}_A e^{-\Omega_e t} \quad (10.69)$$

Experimental evidence hints that onset of modulation of synaptic release by gliotransmitters and gliotransmitter clearance from the ECS is generally much faster than recovery of synaptic dynamics from gliotransmitter-mediated modulation, that is $\Omega_G \ll \Omega_e$, $O_G G_A$ (Appendix 2). Therefore, it may be assumed that, between the onset of modulation of synaptic release by gliotransmitters (at $t = \tau_n$) and the peak of this modulation (at $t = \hat{t}_n$), the effect of modulation on synaptic release evolves according to Eq. 10.14 as:

$$\frac{d\Gamma_S}{dt} \simeq O_G G_A (1 - \Gamma_S) \quad \text{for } \tau_n \leq t < \hat{t}_n \quad (10.70)$$

where G_A is given by Eq. 10.69. Accordingly, the general solution of Eq. 10.70 reads:

$$\Gamma_S(t) = 1 + (\Gamma_S(\tau_n) - 1) \beta^{1-e^{-\Omega_e t}} \quad \text{for } \tau_n \leq t < \hat{t}_n \quad (10.71)$$

with $\beta = \exp(-J_S U_A)$, and asymptotically reaches a maximum value of $\hat{\Gamma}_{S_n} = \Gamma_S(t \rightarrow \infty) = 1 + (\Gamma_S(\tau_n) - 1) \beta$.

Following fast gliotransmitter clearance from the extracellular space instead, the effect of modulation of synaptic release essentially decays from its peak value (at $t = \hat{t}_n$) at rate Ω_G till the next event of gliotransmitter release from the astrocyte (at $t = \tau_n + \Delta t = \tau_{n+1}$). That is:

$$\frac{d\Gamma_S}{dt} \simeq -\Omega_G \Gamma_S \quad \text{for } \hat{t}_n \leq t < \tau_n + \Delta t \quad (10.72)$$

so that

$$\Gamma_S(t) = \Gamma_S(\hat{t}_n) e^{-\Omega_G t} \quad \text{for } \hat{t}_n \leq t < \tau_n + \Delta t \quad (10.73)$$

Then, assuming that $\Omega_e \gtrsim O_G G_A$, we can make the approximation that $\Gamma_S(\hat{t}_n) \approx \hat{\Gamma}_{S_n}$. Furthermore, since $v_A \ll \Omega_A \ll \Omega_e$, $O_G G_A$ (Appendix 2), we may assume that the quasi-totality of gliotransmitter released by the n th GRE is cleared from the ECS before the following release event, so that upon any GRE, $\Gamma_S(\tau_n)$ in Eq. 10.71 is given by solution 10.73 for $t \rightarrow \tau_n$. In this fashion, posing $\Gamma_{S_n} \equiv \Gamma_S(\tau_n)$, we obtain the recursive expression

$$\Gamma_{S_{n+1}} \approx \hat{\Gamma}_{S_n} e^{-\Omega_G \Delta t} \approx (1 - \beta(1 - \Gamma_{S_n})) e^{-\Omega_G t} \quad (10.74)$$

In this fashion, in the hypothesis of steady-state gliotransmitter release (i.e. $\Gamma_{S_{n+1}} = \Gamma_{S_n}$), Eq. 10.74 can be used to estimate $\langle \Gamma_S \rangle$ and $\langle \Gamma_S^2 \rangle$ to eventually obtain an analytical expression for χ_{Γ_S} . With this purpose, it may be noted that the average value of the exponential decay factor in Eq. 10.74 is the integral over all positive Δt values of $e^{-\Omega_G \Delta t}$ multiplied by the probability density of GREs in the time interval Δt . Under the assumption that such GREs are Poisson distributed (Skupin and Falcke 2010) and occur at an average frequency v_A (Eq. 10.36), the probability of an inter-event interval of duration Δt is then $f(\Delta t) = v_A(\Delta t) e^{-v_A(\Delta t)\Delta t}$; that is, Δt is exponentially distributed. Accordingly, denoting by $(\mathcal{L}f)(s)$ the Laplace transform of $f(\Delta t)$, the average exponential decay reads

$$\langle e^{-\Omega_G \Delta t} \rangle = \int_0^\infty e^{-\Omega_G \Delta t} f(\Delta t) = (\mathcal{L}f)(\Omega_G) \underset{\lim \xi \rightarrow 0}{\underset{\sim}{\longrightarrow}} \frac{v_A}{\Omega_G + v_A} \quad (10.75)$$

where, for simplicity of notation, we redefined $v_A \leftarrow v_{A,0}$ (Eq. 10.36) in the last equality. Thus, at steady state and in the limit of $\xi \rightarrow 0$ (i.e. homogeneous Poisson process at constant rate v_A), it follows that (Eq. 10.74):

$$\begin{aligned} \langle \Gamma_S \rangle &= \langle \Gamma_{S_{n+1}} \rangle = \langle \Gamma_{S_n} \rangle \\ &= (1 - \beta(1 - \langle \Gamma_S \rangle)) \langle e^{-\Omega_G \Delta t} \rangle \\ \Rightarrow \langle \Gamma_S \rangle &= \frac{(1 - \beta)v_A}{\Omega_G + (1 - \beta)v_A} \end{aligned} \quad (10.76)$$

In a similar fashion, averaging over the square of Γ_{S_n} given by Eq. 10.74 provides $\langle \Gamma_S^2 \rangle$, which reads

$$\begin{aligned} \langle \Gamma_S^2 \rangle &= \langle \Gamma_{S_{n+1}}^2 \rangle = \langle \Gamma_{S_n}^2 \rangle \\ &= ((1 - \beta)^2 + \beta^2 \Gamma_S^2 + 2\beta(1 - \beta)\langle \Gamma_S \rangle) \langle e^{-2\Omega_G t} \rangle \\ \Rightarrow \langle \Gamma_S^2 \rangle &= \frac{(1 - \beta)^2 (\Omega_G + (1 + \beta)v_A) v_A}{(\Omega_G + (1 - \beta)v_A) (2\Omega_G + (1 - \beta^2)v_A)} \end{aligned} \quad (10.77)$$

Accordingly, the coefficient of variation of Γ_S (χ_{Γ_S}) satisfies the equation:

$$\chi_{\Gamma_S}^2 = \frac{\langle \Gamma_S^2 \rangle - \langle \Gamma_S \rangle^2}{\langle \Gamma_S \rangle^2} = \frac{\Omega_G^2}{(\Omega_G + (1 - \beta)v_A) (\Omega_G + (1 + \beta)v_A)} \quad (10.78)$$

Comparison of Eq. 10.76 with Eq. 10.49 shows that the error introduced by the above rationale in the computation of χ_{Γ_S} roughly reaches $\sim 10\%$ within the frequency range of Ca^{2+} oscillations $v_A = 0.01 - 1 \text{ Hz}$ considered in this chapter (Fig. 10.9). Therefore, Eq. 10.78 can be taken as an acceptable estimation of the χ_{Γ_S} and be used in the evaluation of the upper boundary of the error introduced by the mean field description

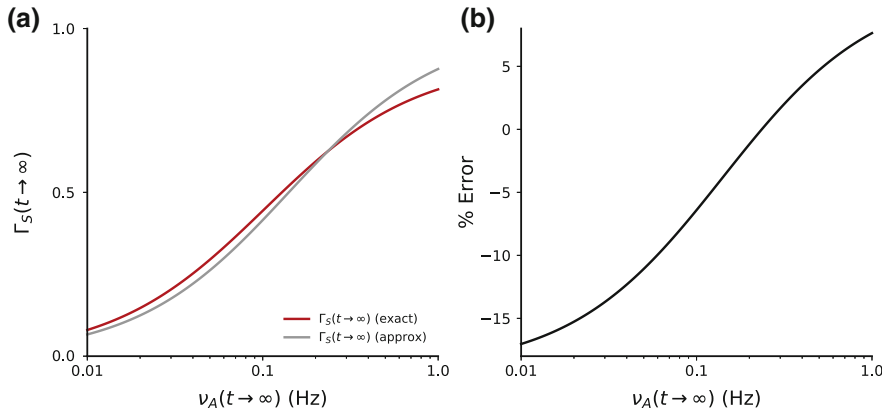


Fig. 10.9 **a** Approximation of $\langle \Gamma_S \rangle$. Comparison between exact steady state, mean field solution of $\langle \Gamma_S \rangle$ (Eq. 10.40, red curve), and the approximated solution in Eq. 10.76 (gray curve). **b** Percentage error of the approximating solution with respect to the exact mean field solution. Model parameters as in Table 10.1

(Eq. 10.66). Computation of this boundary for different values of gliotransmission parameters across their estimated physiological range reveals that this boundary is generally $<7\%$, implying that our description of mean field gliotransmission is generally realistic and introduces a negligible error.

Appendix 2 Parameter Estimation

An in-depth estimation of parameters of gliotransmitter-regulated synapses was produced by De Pittà and Brunel (2016), and the reader is referred to that study for details on the derivation of most of the parameter ranges reported in Table 10.1. In addition, we consider new estimations on rise (τ_r) and decay time constants (τ_d) of gliotransmitter modulation of synaptic release, that can be obtained by manual fitting of experimental data by difference of exponentials

$$y(t) = C \left(e^{-\frac{t}{\tau_d}} - e^{-\frac{t}{\tau_r}} \right) \quad (10.79)$$

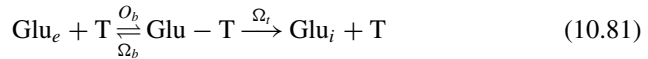
where C is a normalization factor equal to

$$C = \left(\left(\frac{\tau_r}{\tau_d} \right)^{\frac{\tau_x}{\tau_d}} - \left(\frac{\tau_r}{\tau_d} \right)^{\frac{\tau_x}{\tau_r}} \right)^{-1} \quad (10.80)$$

with $\tau_x = \tau_r \tau_d / (\tau_d - \tau_r)$. Limiting our analysis, for simplicity, to release-increasing effects of glutamatergic gliotransmission, both of short- (Covelo and Araque 2018)

and long-term nature (Perea and Araque 2007), and short-term release-decreasing effect mediated by purinergic gliotransmission (Covelo and Araque 2018), we obtain: for glutamatergic gliotransmission $\tau_r > 0.05 - 0.2$ s, $\tau_d = 5.9 - 6.7$ s ($n = 2$, short-term); $\tau_r = 6.2 - 28.3$ s, $\tau_d = 18.7 - 95.7$ s ($n = 3$, long-term); and for purinergic gliotransmission ($n = 2$): $\tau_r = 1.6 - 8.2$ s, $\tau_d = 8.2 - 12.0$ s. These values may be translated into equivalent ranges for O_G and Ω_G considering $O_G G_A \approx 1/\tau_r$ and $\Omega_G \approx 1/\tau_d$, whereby for an average gliotransmitter concentration in the ECS of $100 - 300 \mu\text{M}$, we get $O_G = 1.2 \times 10^{-4} - 0.2 \mu\text{M}^{-1}\text{s}^{-1}$ and $\Omega_G = 0.01 - 0.17 \text{ s}^{-1}$.

Concerning gliotransmitter uptake, because the inclusion of J_u (Eq. 10.10) in the time course of gliotransmitter in the ECS was only marginally considered in this study, mostly for the sake of completeness, we provide here only estimates for glutamate uptake by astrocytic EAATs, leaving more detailed investigations on the effect of gliotransmitter uptake on functional gliotransmission to future studies. In this spirit, the kinetic of glutamate (Glu) uptake by astrocytic transporters (T) may be approximated by the Michaelis–Menten reaction



where $O_b = 10^4 \text{ M}^{-1}\text{ms}^{-1}$, $\Omega_b = 0.2 \text{ ms}^{-1}$, and $\Omega_t = 0.1 \text{ ms}^{-1}$ (Rusakov 2001). In this fashion $K_u = (\Omega_b + \Omega_t)/O_b = 30 \mu\text{M}$ which is in agreement with independent estimates of EAAT binding affinity in the range of $\sim 10 - 20 \mu\text{M}$ (Tzingounis and Wadiche 2007). More problematic is instead the estimation of the maximal rate of glutamate uptake O_u which depends on the expression of available transporters. With this regard, reported values of transporter concentration in the perisynaptic volume occupied by astrocytic transporters are comprised in a wide range of values, i.e. $[T]_0 = 30 - 1300 \mu\text{M}$, depending on how this volume is defined (Lehre and Danbolt 1998). These values were, however, estimated assuming uniform transporter distribution, which is likely not the case at perisynaptic astrocytic processes, where transporters are known to cluster in proximity of synaptic interface, and be instead poorly expressed away from it (Danbolt et al. 2002). Consequently, because gliotransmitter release sites are located away from synaptic interfaces as they rather face extrasynaptic targets (Jourdain et al. 2007), it is plausible to consider smaller values for $[T]_0$. In this fashion, it follows that $O_u = \Omega_t \cdot [T]_0 < 3 \text{ mM s}^{-1}$.

Appendix 3 Software

The Python file `figures.py` used to generate the figures of this chapter can be downloaded from the online book repository at <https://github.com/mdepitta/comp-glia-book/tree/master/Ch10.DePitta>. The software for this chapter is organized in two folders. The `data` folder contains experimental data from Perea and Araque (2007) and Covelo and Araque (2018) used for parameter estimations in Appendix

2. Experimental data from those studies were extracted by WebPlotDigitizer 4.0 (<https://automeris.io/WebPlotDigitizer>). The same folder also contains the Jupyter notebook `gliotransmission_kinetics.ipynb` used to fit those data by Eq. 10.79.

The `code` folder contains instead all the routines (including `figures.py`) used for the simulations of this chapter. The files `gliotransmission_models.*` contain the classes that implement spiking and mean field models for gliotransmitter-regulated synapses introduced here. The core model is implemented in C/C++11 (`.h` and `.cpp` files), whereas the `.py` file provides a user-friendly Python interface for simulations.

Numerical solutions of the spiking model were computed by a hybrid integration scheme that combined an event-based strategy to compute exact solutions of synaptic variables (u_S , x_S , r_S , and I) and releasable gliotransmitter resources (x_A), with a backward Gaussian second-order Runge–Kutta integration scheme for G_A and Γ_S . Integration of the stochastic Li–Rinzel model in Figs. 10.2b and 10.3 was performed by a Milstein integration scheme for Stratonovich formulation of multiplicative noise (Milstein 1975). On the contrary, numerical solutions of mean field model in Fig. 10.6 were computed by an implicit Bulirsch–Stoer method suitable for stiff problems like ours, for the existence of largely separated timescales between synaptic dynamics and gliotransmitter-mediated modulations.

Appendix 4 Model Parameters Used in Simulations

Parameter of the stochastic Li–Rinzel model used to simulate astrocytic calcium dynamics in Figs. 10.2 and 10.3 is as following (see also Chap. 4): $d_1 = 0.1 \mu\text{M}$, $O_2 = 0.4 \mu\text{M}^{-1}\text{s}^{-1}$, $d_2 = 2.1 \mu\text{M}$, $d_3 = 0.9967 \mu\text{M}$, $d_5 = 0.2 \mu\text{M}$, $C_T = 4 \mu\text{M}$, $\rho_A = 0.4$, $\Omega_C = 7 \text{s}^{-1}$, $\Omega_L = 0.05 \text{s}^{-1}$, $O_P = 0.1 \mu\text{Ms}^{-1}$, $K_P = 0.1 \mu\text{M}$. To induce oscillations, we set intracellular IP₃ at $0.4 \mu\text{M}$ starting from initial conditions $C(0) = 0.05 \mu\text{M}$ and $h(0) = 0.9$.

References

- Abbracchio MP, Burnstock G, Verkhratsky A, Zimmermann H (2009) Purinergic signalling in the nervous system: an overview. *Trends Neurosci.* 32:19–29
- Amit DJ, Tsodyks MV (1991) Quantitative study of attractor neural network retrieving at low spike rates: I. Substrate-spikes, rates and neuronal gain. *Network* 2:259–273
- Anderson MC, Swanson RA (2000) Astrocyte glutamate transport: review of properties, regulation, and physiological functions. *Glia* 32:1–14
- Araque A, Parpura V, Sanzgiri RP, Haydon PG (1998a) Glutamate-dependent astrocyte modulation of synaptic transmission between cultured hippocampal neurons. *Eur. J. Neurosci.* 10:2129–2142
- Araque A, Sanzgiri RP, Parpura V, Haydon PG (1998b) Calcium elevation in astrocytes causes an NMDA receptor-dependent increase in the frequency of miniature synaptic currents in cultured hippocampal neurons. *J. Neurosci.* 18(17):6822–6829
- Araque A, Carmignoto G, Haydon PG, Oliet SHR, Robitaille R, Volterra A (2014) Gliotransmitters travel in time and space. *Neuron* 81(4):728–739

- Attwell D, Buchan AM, Charpak S, Lauritzen M, MacVicar BA, Newman EA (2010) Glial and neuronal control of brain blood flow. *Nature* 468(7321):232–243
- Bains JS, Oliet SHR (2007) Glia: they make your memories stick!. *Trends Neurosci.* 30(8):417–424
- Baldwin SA, Yao SYM, Hyde RJ, Ng AML, Foppolo S, Barnes K, Ritzel MWL, Cass CE, Young JD (2005) Functional characterization of novel human and mouse equilibrative nucleoside transporters (hENT3 and mENT3) located in intracellular membranes. *J Biol Chem* 280(16):15880–15887
- Barnes K, Dobrzynski H, Foppolo S, Beal PR, Ismat F, Scullion ER, Sun L, Tellez J, Ritzel MWL, Claycomb WC, Cass CE, Yound JD, Billeter-Clark R, Boyett MR, Baldwin SA (2006) Distribution and functional characterization of equilibrative nucleoside transporter-4, a novel cardiac adenosine transporter activated at acidic pH. *Circ Res* 99(5):510–519
- Bergersen LH, Gundersen V (2009) Morphological evidence for vesicular glutamate release from astrocytes. *Neuroscience* 158:260–265
- Bergersen L, Morland C, Ormel L, Rinholm JE, Larsson M, Wold JFH, Røe AT, Stranna A, Santello M, Bouvier D, Ottersen OP, Volterra A, Gundersen V (2012) Immunogold detection of L-glutamate and D-serine in small synaptic-like microvesicles in adult hippocampal astrocytes. *Cereb Cortex* 22(7):1690–1697
- Bezzi P, Gundersen V, Galbete JL, Seifert G, Steinhäuser C, Pilati E, Volterra A (2004) Astrocytes contain a vesicular compartment that is competent for regulated exocytosis of glutamate. *Nat Neurosci* 7(6):613–620
- Bollmann JH, Sakmann B, Gerard J, Borst G (2000) Calcium sensitivity of glutamate release in a calyx-type terminal. *Science* 289:953–957
- Bonansco C, Couve A, Perea G, Ferradas CA, Roncagliolo M, Fuenzalida M (2011) Glutamate released spontaneously from astrocytes sets the threshold for synaptic plasticity. *Eur J Neurosci* 33:1483–1492
- Bowser DN, Khakh BS (2007) Two forms of single-vesicle astrocyte exocytosis imaged with total internal reflection fluorescence microscopy. *Proc Natl Acad Sci U S A* 104(10):4212–4217
- Chen X, Wang L, Zhou Y, Zheng L-H, Zhou Z (2005) “Kiss-and-run” glutamate secretion in cultured and freshly isolated rat hippocampal astrocytes. *J Neurosci* 25(40):9236–9243
- Clements JD (1996) Transmitter timecourse in the synaptic cleft: its role in central synaptic function. *Trends Neurosci* 19(5):163–171
- Coco S, Calegari F, Pravettoni E, Pozzi D, Taverna E, Rosa P, Matteoli M, Verderio C (2003) Storage and release of ATP from astrocytes in culture. *J Biol Chem* 278(2):1354–1362
- Covelo A, Araque A (2018) Neuronal activity determines distinct gliotransmitter release from a single astrocyte. *eLife* 7:e32237
- Crippa D, Schenk U, Francolini M, Rosa P, Verderio C, Zonta M, Pozzan T, Matteoli M, Carmignoto G (2006) Synaptobrevin2-expressing vesicles in rat astrocytes: insights into molecular characterization, dynamics and exocytosis. *J Physiol* 570(3):567–582
- Cunhaa R, Ribeiro J (2000) ATP as a presynaptic modulator. *Life Sci* 68:119–137
- Danbolt NC (2001) Glutamate uptake. *Prog Neurobiol* 65:1–105
- Danbolt NC, Lehre KP, Dehnes Y, Ullensvang K (2002) Transporters for synaptic transmitter on the glial cell plasma membrane. In: Volterra A, Magistretti PJ, Haydon PG (eds) *The tripartite synapse: Glia in synaptic transmission*, Chapter 1. Oxford University Press, New York, pp 47–61
- De Pittà M, Brunel N (2016) Modulation of synaptic plasticity by glutamatergic gliotransmission: a modeling study. *Neural Plast* 7607924
- De Pittà M, Volman V, Berry H, Ben-Jacob E (2011) A tale of two stories: astrocyte regulation of synaptic depression and facilitation. *PLoS Comput Biol* 7(12):e1002293
- De Pittà M, Volman V, Berry H, Parpura V, Liaudet N, Volterra A, Ben-Jacob E (2013) Computational quest for understanding the role of astrocyte signaling in synaptic transmission and plasticity. *Front Comput Neurosci* 6:98
- De Pittà M, Brunel N, Volterra A (2015) Astrocytes: orchestrating synaptic plasticity? *Neuroscience*

- Debanne D, Guerineau NC, Gähwiler BH, Thompson SM (1996) Paired-pulse facilitation and depression at unitary synapses in rat hippocampus: quantal fluctuation affects subsequent release. *J Physiol* 491(1):163–176
- Destexhe A, Mainen ZF, Sejnowski TJ (1994) Synthesis of models for excitable membranes, synaptic transmission and neuromodulation using a common kinetic formalism. *J Comput Neurosci* 1:195–230
- Diamond JS (2005) Deriving the glutamate clearance time course from transporter currents in CA1 hippocampal astrocytes: transmitter uptake gets faster during development. *J Neurosci* 25(11):2906–2916
- Domercq M, Brambilla L, Pilati E, Marchaland J, Volterra A, Bezzi P (2006) P2Y1 receptor-evoked glutamate exocytosis from astrocytes: control by tumor necrosis factor- α and prostaglandins. *J Biol Chem* 281:30684–30696
- Fiacco TA, McCarthy KD (2004) Intracellular astrocyte calcium waves in situ increase the frequency of spontaneous AMPA receptor currents in CA1 pyramidal neurons. *J Neurosci* 24(3):722–732
- Fiacco TA, McCarthy KD (2018) Multiple lines of evidence indicate that gliotransmission does not occur under physiological conditions. *J Neurosci* 38(1):3–13
- Fuhrmann G, Segev I, Markram H, Tsodyks M (2002) Coding of temporal information by activity-dependent synapses. *J Neurophysiol* 87:140–148
- Griffiths M, Yao YMS, Abidi F, Phillips EVS, Cass EC, Young DJ, Baldwin AS (1997) Molecular cloning and characterization of a nitrobenzylthioinosine-insensitive (*ei*) equilibrative nucleoside transporter from human placenta. *Biochem J* 328(3):739–743
- Habbas S, Santello M, Becker D, Stubbe H, Zappia G, Liaudet N, Klaus FR, Kollias G, Fontana A, Pryce CR, Suter T, Volterra A (2015) Neuroinflammatory TNF α impairs memory via astrocyte signaling. *Cell* 163(7):1730–1741
- Halassa M, Haydon P (2010) Integrated brain circuits: astrocytic networks modulate neuronal activity and behavior. *Annu Rev Physiol* 72:335–355
- Haydon PG, Carmignoto G (2006) Astrocyte control of synaptic transmission and neurovascular coupling. *Physiol Rev* 86:1009–1031
- Jaiswal J, Fix M, Takano T, Nedergaard M, Simon S (2007) Resolving vesicle fusion from lysis to monitor calcium-triggered lysosomal exocytosis in astrocytes. *Proc Natl Acad Sci U S A* 104(35):14151–14156
- Jourdain P, Bergersen LH, Bhaukaurally K, Bezzi P, Santello M, Domercq M, Matute C, Tonello F, Gundersen V, Volterra A (2007) Glutamate exocytosis from astrocytes controls synaptic strength. *Nat Neurosci* 10(3):331–339
- King AE, Ackley MA, Cass CE, Young JD, Baldwin SA (2006) Nucleoside transporters: from scavengers to novel therapeutic targets. *Trends Pharmacol Sci* 27(8):416–425
- Kreft M, Stenovec M, Rupnik M, Grilc S, Kržan M, Potokar M, Pangršič T, Haydon PG, Zorec R (2004) Properties of Ca $^{2+}$ -dependent exocytosis in cultured astrocytes. *Glia* 46(4):437–445
- Lehre KP, Danbolt NC (1998) The number of glutamate transporter subtype molecules at glutamatergic synapses: chemical and stereological quantification in young adult rat brain. *J Neurosci* 18(21):8751–8757
- Liu Q, Xu Q, Arcuino G, Kang J, Nedergaard M (2004a) Astrocyte-mediated activation of neuronal kainate receptors. *Proc Natl Acad Sci U S A* 101(9):3172–3177
- Liu Q-S, Xu Q, Kang J, Nedergaard M (2004b) Astrocyte activation of presynaptic metabotropic glutamate receptors modulates hippocampal inhibitory synaptic transmission. *Neuron Glia Biol* 1:307–316
- Losi G, Mariotti L, Carmignoto G (2014) GABAergic interneuron to astrocyte signalling: a neglected form of cell communication in the brain. *Philos Trans R Soc B Biol Sci* 369(1654):20130609
- Malarkey E, Parpura V (2011) Temporal characteristics of vesicular fusion in astrocytes: examination of synaptobrevin 2-laden vesicles at single vesicle resolution. *J Physiol* 589(17):4271–4300
- Marchaland J, Cali C, Voglmaier SM, Li H, Regazzi R, Edwards RH, Bezzi P (2008) Fast subplasma membrane Ca $^{2+}$ transients control exo-endocytosis of synaptic-like microvesicles in astrocytes. *J Neurosci* 28(37):9122–9132

- Milshtejn G (1975) Approximate integration of stochastic differential equations. *Theory Probab Appl* 19(3):557–562
- Montana V, Ni Y, Sunjara V, Hua X, Parpura V (2004) Vesicular glutamate transporter-dependent glutamate release from astrocytes. *J Neurosci* 24(11):2633–2642
- Montana V, Malarkey EB, Verderio C, Matteoli M, Parpura V (2006) Vesicular transmitter release from astrocytes. *Glia* 54:700–715
- Mothet J-P, Pollegioni L, Ouanounou G, Martineau M, Fossier P, Baux G (2005) Glutamate receptor activation triggers a calcium-dependent and SNARE protein-dependent release of the gliotransmitter D-serine. *Proc Natl Acad Sci U S A* 102(15):5606–5611
- Navarrete M, Araque A (2010) Endocannabinoids potentiate synaptic transmission through stimulation of astrocytes. *Neuron* 68(1):113–126
- Newman EA (2003) Glial cell inhibition of neurons by release of ATP. *J Neurosci* 23(5):1659–1666
- Panatier A, Vallée J, Haber M, Murai K, Lacaille J, Robitaille R (2011) Astrocytes are endogenous regulators of basal transmission at central synapses. *Cell* 146:785–798
- Pangršič T, Potokar M, Stenovec M, Kreft M, Fabbretti E, Nistri A, Pryazhnikov E, Khiroug L, Giniatullin R, Zorec R (2007) Exocytotic release of ATP from cultured astrocytes. *J Biol Chem* 282(39):28749–28758
- Papouin T, Oliet SHR (2014) Organization, control and function of extrasynaptic NMDA receptors. *Philos Trans R Soc B Biol Sci* 369(1654):20130601
- Papouin T, Ladépêche L, Ruel J, Sacchi S, Labasque M, Hanini M, Groc L, Pollegioni L, Mothet J, Oliet S (2012) Synaptic and extrasynaptic NMDA receptors are gated by different endogenous coagonists. *Cell* 150(3):633–646
- Parpura V, Fang Y, Basarsky T, Jahn R, Haydon PG (1995) Expression of synaptobrevin II, cellubrevin and syntaxin but not SNAP-25 in cultured astrocytes. *FEBS Lett* 377:489–492
- Pascual O, Casper KB, Kubera C, Zhang J, Revilla-Sánchez R, Sul JY, Takano H, Moss SJ, McCarthy K, Haydon PG (2005) Astrocytic purinergic signaling coordinates synaptic networks. *Science* 310:113–116
- Pasti L, Volterra A, Pozzan T, Carmignoto G (1997) Intracellular calcium oscillations in astrocytes: a highly plastic, bidirectional form of communication between neurons and astrocytes in situ. *J Neurosci* 17(20):7817–7830
- Perea G, Araque A (2007) Astrocytes potentiate transmitter release at single hippocampal synapses. *Science* 317:1083–1086
- Perez-Alvarez A, Navarrete M, Covelo A, Martin ED, Araque A (2014) Structural and functional plasticity of astrocyte processes and dendritic spine interactions. *J Neurosci* 34(38):12738–12744
- Pinheiro PS, Mulle C (2008) Presynaptic glutamate receptors: physiological functions and mechanisms of action. *Nat Rev Neurosci* 9:423–436
- Pryazhnikov E, Khiroug L (2008) Sub-micromolar increase in $[Ca^{2+}]_i$ triggers delayed exocytosis of ATP in cultured astrocytes. *Glia* 56(1):38–49
- Rebola N, Rodrigues R, Lopes L, Richardson P, Oliveira C, Cunha R (2005) Adenosine A₁ and A_{2A} receptors are co-expressed in pyramidal neurons and co-localized in glutamatergic nerve terminals of the rat hippocampus. *Neuroscience* 133(1):79–83
- Rusakov DA (2001) The role of perisynaptic glial sheaths in glutamate spillover and extracellular Ca²⁺ depletion. *Biophys J* 81(4):1947–1959
- Santello M, Volterra A (2009) Synaptic modulation by astrocytes via Ca²⁺-dependent glutamate release. *Neuroscience* 158(1):253–259
- Santello M, Volterra A (2012) TNFα in synaptic function: switching gears. *Trends Neurosci* 35(10):638–647
- Santello M, Bezzi P, Volterra A (2011) TNFα controls glutamatergic gliotransmission in the hippocampal dentate gyrus. *Neuron* 69:988–1001
- Savtchouk I, Volterra A (2018) Gliotransmission: beyond black-and-white. *J Neurosci* 38(1):14–25
- Sawada K, Echigo N, Juge N, Miyaji T, Otsuka M, Omote H, Yamamoto A, Moriyama Y (2008) Identification of a vesicular nucleotide transporter. *Proc Natl Acad Sci U S A* 105(15):5683–5686

- Schneggenburger R, Neher E (2000) Intracellular calcium dependence of transmitter release rates at a fast central synapse. *Nature* 406:889–893
- Schubert V, Bouvier D, Volterra A (2011) SNARE protein expression in synaptic terminals and astrocytes in the adult hippocampus: A comparative analysis. *Glia* 59(10):1472–1488
- Serrano A, Haddjeri N, Lacaille J, Robitaille R (2006) GABAergic network activation of glial cells underlies heterosynaptic depression. *J Neurosci* 26(20):5370–5382
- Shigemoto R, Kinoshita A, Wada E, Nomura S, Ohishi H, Takada M, Flor P, Neki A, Abe T, Nakanishi S, Mizuno N (1997) Differential presynaptic localization of metabotropic glutamate receptor subtypes in the rat hippocampus. *J Neurosci* 17(19):7503–7522
- Skupin A, Falcke M (2010) Statistical analysis of calcium oscillations. *Eur Phys J Spec Top* 187:231–240
- Softky W, Koch C (1993) The highly irregular firing pattern of cortical cells is inconsistent with temporal integration of random EPSPs. *J Neurosci* 13:334–350
- Stenovec M, Kreft M, Grilc S, Pokotar M, Kreft ME, Pangršič T, Zorec R (2007) Ca^{2+} -dependent mobility of vesicles capturing anti-VGLUT1 antibodies. *Exp Cell Res* 313:3809–3818
- Südhof TC (2004) The synaptic vesicle cycle. *Annu Rev Neurosci* 27:509–547
- Tang F, Lane S, Korsak A, Paton JFR, Gourine AV, Kasparov S, Teschemacher AG (2014) Lactate-mediated glia-neuronal signalling in the mammalian brain. *Nat Commun* 5:3284
- Todd KJ, Darabid H, Robitaille R (2010) Perisynaptic glia discriminate patterns of motor nerve activity and influence plasticity at the neuromuscular junction. *J Neurosci* 30(35):11870–11882
- Tsodyks M (2005) Activity-dependent transmission in neocortical synapses. In: Chow C, Gutkin B, Hansel D, Meunier C, Dalibard, J (eds) *Methods and models in neurophysics* (Chap. 7). Elsevier, pp 245–265
- Tsodyks MV, Markram H (1997) The neural code between neocortical pyramidal neurons depends on neurotransmitter release probability. *Proc Natl Acad Sci U S A* 94:719–723
- Tsodyks M, Pawelzik K, Markram H (1998) Neural networks with dynamic synapses. *Neural Comput* 10:821–835
- Tzingounis AV, Wadiche JI (2007) Glutamate transporters: confining runaway excitation by shaping synaptic transmission. *Nat Rev Neurosci* 8:935–947
- Zhang J-M, Wang H-K, Ye C-Q, Ge W, Chen Y, Jiang Z-L, Wu C-P, Poo M-M, Duan S (2003) ATP released by astrocytes mediates glutamatergic activity-dependent heterosynaptic suppression. *Neuron* 40:971–982
- Zhang Q, Fukuda M, Van Bockstaele E, Pascual O, Haydon PG (2004) Synaptotagmin IV regulates glial glutamate release. *Proc Natl Acad Sci U S A* 101(25):9441–9446
- Zhang Z, Chen G, Zhou W, Song A, Xu T, Luo Q, Wang W, Gu X, Duan S (2007) Regulated ATP release from astrocytes through lysosome exocytosis. *Nat Cell Biol* 9(8):945–953
- Zorec R, Araque A, Carmignoto G, Haydon P, Verkhratsky A, Parpura V (2012) Astroglial excitability and gliotransmission: An appraisal of Ca^{2+} as a signaling route. *ASN Neuro* 4(2):e00080
- Zucker RS, Regehr WG (2002) Short-term synaptic plasticity. *Annu Rev Physiol* 64:355–405

Chapter 11

Computational Models of Pathophysiological Glial Activation in CNS Disorders



Vladislav Volman and Maxim Bazhenov

Abstract Glial cells, in general, and astrocytes, in particular, are indispensable for homeostatic regulation of neural function, which positions these non-neuronal cells in the limelight of CNS pathologies. The renewed interest in glial physiology and the advent of new experimental methods motivated the development of computational models of glial cells. In this contribution, we review the development and challenges of computational models of pathophysiological glial activation in CNS disorders.

Keywords Brain injury · Homeostatic plasticity · Computational neurology · Quantitative systems pharmacology · Neuroinflammation

11.1 Introduction

Astrocytes have become one of the important foci of brain research since the discovery of glutamate-mediated astrocyte-neuron signaling in 1994 (Papura et al. 1994). A significant body of experimental data on astrocytes physiology and biochemistry has accumulated thanks to the development of increasingly sophisticated techniques. New methodology enabled to scrutinize, refine, and revisit previous findings and hypotheses. For example, it is now clear that the extent of astrocytic involvement in neuronal function and synaptic transmission depends on the context (e.g., Ca^{2+} signaling characteristics are likely to be different in normal vs. reactive astrocytes) (Agulhon et al. 2012). Further, the relatively slow response timescale of these glial cells (tens of seconds for astrocytic Ca^{2+} events vs. milliseconds for synaptic transmission) implies that astrocytes are not likely to release gliotransmitter for acute modulation of neuronal activity in healthy brains. Rather, and because of their slow response timescale and a variety of factors that can be released in a

V. Volman (✉)

Progenity Inc., 4330 La Jolla Village Dr., San Diego, CA 92122, USA

e-mail: vlad.volman@gmail.com

M. Bazhenov

Department of Medicine, University of California, La Jolla, San Diego, CA 92093, USA

© Springer Nature Switzerland AG 2019

289

M. De Pittà and H. Berry (eds.), *Computational Glioscience*, Springer Series in Computational Neuroscience, https://doi.org/10.1007/978-3-030-00817-8_11

controlled manner, astrocytes are likely to take part in slowly developing processes involved in homeostatic regulation. Deficiencies and abnormalities of homeostatic regulation are closely related to brain disorders; thus, astrocytes are expected to play an important role in development (and, by the same token, in prevention) of brain pathologies. Computational models can help testing the current hypotheses; this is especially important given the methodological and ethical concerns associated with the experimental studies on humans. In this chapter, we attempt to review the existing evidence for astrocytic involvement in brain disorders related to the dynamics of neuronal networks, with particular emphasis on computational and mathematical modeling aspects of underlying biophysical processes.

11.2 Biophysical Mechanisms of Astrocytic Involvement in Brain Disorders

11.2.1 *Detection of Normal and Aberrant Neuronal Activity*

The shape of a neuronal action potential is governed by ionic gradients across the membrane, implying that the action potential itself causes changes in local ion concentrations. Normally, these spike-induced changes in ionic environment are quickly dissipated by the action of various mechanisms, such as pumps and transporters. Yet, in pathological conditions (e.g., prolonged high-frequency activity or metabolic deficit) pumps and transporters may fail to adequately restore ionic gradients, leading to persistent accumulation of ions in extracellular or intracellular space. The abnormal accumulation of ions in the extracellular space provides the means for nearby astrocytes to “estimate” the level of neuronal activity in their proximity.

The principal outcome of intense spiking activity is accumulation of potassium ions (K^+) in extracellular space, known as the “Frankenhaeuser–Hodgkin effect” (Frankenhaeuser and Hodgkin 1956). Significant experimental evidence indicates that astrocytes play crucial role in clearing excess extracellular K^+ (Walz 2000). Astrocytes maintain K^+ homeostasis by employing inward rectifying K^+ channels (Kir4.1 channels) to take up excess K^+ and possibly redistribute it across spatial compartments. The redistribution process has been termed “potassium siphoning” and is considered as a candidate process for mediating fast neurovascular coupling (Paulson and Newman 1987, but see Metea et al. (2007) for a possible revision of this mechanism). Experimental evidence also suggests that astrocytic response to excess K^+ is accompanied by astrocytic uptake of water molecules and swelling and subsequent reduction of extracellular volume (Simard and Nedergaard 2004). Water transport across astrocytic membranes likely involves aquaporin 4 (AQP4) channels that are widely expressed in astrocytic end-feet (Nagelhus et al. 2004). Experiments performed on primary astrocyte cultures from mice indicate that in astrocyte cultures from AQP4 deficient mice osmotic water permeability is reduced sevenfold, suggesting that AQP4 provides the principal route for water transport in astrocytes

(Solenov et al. 2004). Yet, other evidence suggests that under physiological conditions AQP4 may not be the only (and maybe not the principal) route of water transport. Under physiological conditions of relatively mild extracellular K⁺ elevations, swelling of astrocytes in the stratum radiatum of the hippocampus CA1 region was observed to be mediated by bicarbonate (HCO₃⁻) ions and sodium bicarbonate cotransporters (NBC) (Florence et al. 2012).

Several computational models, capturing various levels of biological complexity, have been developed for studying the mechanisms underlying astrocytic swelling and regulation of extracellular K⁺. The basic dynamics of extracellular K⁺ concentration ([K⁺]_o) can be captured by the following general equation:

$$\frac{d[K^+]_o}{dt} = \sum I_K + D_K \nabla^2 [K^+]_o - G([K^+]_o) \quad (11.1)$$

in which ΣI_K represents the sum over all neuronal K⁺ currents (from K⁺ channels and/or pumps in nearby volume), $D_K \nabla^2 [K^+]_o$ captures the diffusion of K⁺ in extracellular space, and the functional form G captures the regulation of extracellular K⁺ by astrocytes. In the simplest phenomenological form the latter term can be modeled as “glial buffer” that binds free K⁺ ions (Bazhenov et al. 2004):

$$G([K]_o) = -\frac{d[B]}{dt} = k_{ON}[K^+]_o[B] - k_{OFF}([B]_T - [B]) \quad (11.2)$$

with

$$k_{ON} = \frac{k_{OFF}}{1 + \exp\left(\frac{[K^+]_{TH} - [K^+]_o}{\alpha_{KG}}\right)} \quad (11.3)$$

where k_{ON} and k_{OFF} are forward (binding) and backward (unbinding) rates, respectively, $[B]_T$ is the total buffer concentration, and $[K^+]_{TH}$ is the threshold concentration of extracellular K⁺ above which glial buffer is activated (usually set to ~10 mM) (Bazhenov et al. 2004; Somjen et al. 2009).

More recently, detailed computational models have started to probe the astrocytic dynamics of water transport and swelling in the context of K⁺ regulation. As mentioned above, although osmotic water redistribution through astrocytic AQP4 channels appears to be the principal candidate mechanism to explain astrocytic swelling induced by high extracellular K⁺, there is evidence that other mechanisms (e.g., bicarbonate ions) are important as well. Thus, detailed models of interstitial space and astrocytic mechanisms have been constructed to elucidate the contribution of different swelling mechanisms. Typically, in addition to including the mechanisms of K⁺ redistribution, these models also include a variety of mechanisms for redistribution of other ionic species like Na⁺, Cl⁻, and HBO₃⁻, by sodium–potassium pumps (NKP), NBC, and Cl⁻ transport mechanisms such as Na⁺/K⁺/2Cl⁻ cotransporter (NKKC1) and K⁺/Cl⁻ cotransporter (KCC2) (Østby et al. 2009; Øyehaug et al. 2011).

The relation between extracellular K⁺, glial function, metabolic deficit, and abnormal activity (in the form of seizures and spreading depression) has been recently elucidated by Wei et al. (2014a, b), who designed and analyzed a very detailed model of neuronal activity. Although the model by Wei et al. focused on neuronal dynamics, the components of ions redistribution are likely to be the same in astrocytes; thus, the methodological conclusions are likely to be similar as well. The model results suggested that seizures and spreading depression (believed to be responsible for migraine) can be unified through aberrant extracellular K⁺ regulation. The importance of astrocytes in clearance of extracellular K⁺ and the proposed putative unifying role of extracellular K⁺ suggest a glial-centered dynamic mechanism of epilepsy and spreading depression.

11.2.2 Modulation of Synaptic Transmission

Synaptic plasticity can critically mold the functional strength of synaptic coupling; thus, it is possible that specific characteristics of synaptic transmitter release (dynamic regulation of synaptic strength) could suppress or promote aberrant patterns of network dynamics.

Astrocytes are ideally positioned to modulate both presynaptic and postsynaptic components of synaptic transmission. Early in vitro experiments (reviewed by Araque et al. (1999)) clearly demonstrated that in neural cultures astrocytic processes are often opposed to synaptic junctions, giving rise to the concept of “tripartite synapse” consisting of the presynaptic bouton, the astrocyte, and the postsynaptic density. It was subsequently suggested that these glial processes can “eavesdrop” on synaptic activity (reviewed by Haydon (2001)).

The observations of astrocytic involvement in synaptic transmission in vitro led to the realization that astrocytes can potentially modulate the properties of short-term synaptic plasticity (both short-term depression and short-term facilitation). On semi-phenomenological level, short-term synaptic plasticity is conveniently described by using Tsodyks–Markram type models of use-dependent synaptic plasticity (Tsodyks and Markram 1997). These models are focused on presynaptic release and assume that at any given time, “synaptic resources” per synaptic bouton (proportional to the number of neurotransmitter vesicles available for release) are constrained and are present only in finite amount.

The first model investigating the putative effect of astrocytes on presynaptic transmission has been proposed by Volman et al. (2007). To avoid conflating the possible effects of astrocytic modulation with effects of dynamical feedbacks due to network connectivity, the authors had considered the simplest possible circuit—a neuron with an autapse (self-synapse). The model by Volman et al. (2007) considered only the inhibitory effects of astrocytic modulation of synaptic transmission (and thus relating to the in vitro observations of Zhang et al. (2003) of purinergic astrocyte–neuron interaction). However, evidence suggests that, at least at hippocampal CA3-CA1 synapses, transmitter molecules released from astrocytes can potentiate the release

of neurotransmitter from synaptic terminals (Perea and Araque 2007). How these different mechanisms can be mediated by astrocyte-neuron interaction has been investigated by De Pittà and co-workers (2011, 2012). In this model (De Pittà et al. 2011, 2012), synaptic transmission has been described by using a Tsodyks–Markram type model:

$$\frac{dx}{dt} = \Omega_d(1 - x) - \sum_i ux\delta(t - t_i) \quad (11.4)$$

$$\frac{du}{dt} = -\Omega_f u + U_0(\Gamma) \sum_i (1 - u)\delta(t - t_i) \quad (11.5)$$

where x represents the amount of synaptic neurotransmitter available for release. The parameters Ω_d and Ω_f represent the rates of recovery from short-term depression and astrocytic “effects,” respectively. The parameter u is the fraction of available resource released per synaptic action potential. Most critical to the model, the functional $U_0(\Gamma)$ (the “gating function”) determines how the resource utilization is affected by the astrocytic signaling (see also Chap. 10). The exact form of the gating function depends on the specifics of synapse under consideration (different ultra-structural organization parameters as well as different transmitters released by the astrocyte and different receptors expressed on the presynaptic membrane will result in different functional forms of this gating function). Depending on these factors, the action of $U_0(\Gamma)$ can be either facilitating (resulting in synaptic facilitation) or depressing (resulting in synaptic depression). Thus, this general model by De Pittà et al. (2011, 2012) can explain dichotomous modulation of presynaptic plasticity by astrocytes and can be used for modeling the *in vitro* results. These studies, aiming to describe the dichotomous astrocytic regulation of synaptic transmission, are complemented by detailed modeling of presynaptic boutons showing how the “nature” of a synapse (depressing or facilitating) is determined by its ultra-structural organization (Nadkarni et al. 2010, 2012).

11.2.3 Modulation of Neuronal Excitability

In response to the stimulation of their G-protein coupled receptors, astrocytes can release a variety of factors, the most documented ones being adenosine triphosphate (ATP) (Zhang et al. 2003), glutamate (Araque et al. 1998), and D-serine (Mothet et al. 2005). Depending on the localization of glial release site, released molecules can bind to their dedicated receptors on presynaptic membranes (and thus modulate the properties of presynaptic neurotransmitter release) or activate receptors on post-synaptic membranes (thus modulating neural excitability). In *in vitro* models, the former modulatory pathway has been shown to be mediated by ATP and glutamate (also see section of modulation of synaptic transmission) while the latter (modulation of neuronal excitability) has been shown to be accomplished by glutamate binding

to N-methyl-D-aspartate (NMDA) receptors on the postsynaptic membrane (Parpura and Haydon 2000). D-serine, that is released by astrocytes, modulates the properties of post-synaptic NMDA receptors (Oliet and Mothet 2009) and thus should be considered in the context of NMDA signaling. In principle, this glial-generated NMDA current can be modeled as:

$$I_{\text{ASTRO}}^{\text{NMDA}}(t) = \frac{g_F(t) - g_S(t)}{1 + 0.33[\text{Mg}^{2+}]_O \exp(-0.06V_m)} (V_m - E_{\text{NMDA}}) \quad (11.6)$$

with

$$\frac{dg_\alpha}{dt} = -\frac{g_\alpha}{\tau_\alpha} + G_{\text{ASTRO}}^{\text{GLU}}(t) \quad (\alpha = F, S) \quad (11.7)$$

where V_m is the neuronal membrane voltage at the NMDA conductance channel, $[\text{Mg}^{2+}]_O$ is the extracellular magnesium concentration in the proximity of NMDA conductance channel, $G_{\text{ASTRO}}^{\text{GLU}}(t)$ is the astrocytic glutamate signal in the proximity of NMDA conductance channel; τ_F (τ_S) is the fast (slow) NMDA conductance timescales, and E_{NMDA} is the conductance reversal potential (usually set to 0 mV). However, this description, although biophysically correct, remains a challenge for modelers, for several reasons. First, the dependence of $G_{\text{ASTRO}}^{\text{GLU}}(t)$ is not fully available at the moment, and the biophysical characteristics of gliotransmitter release from astrocytes is still an active area of research (Parpura and Zorec 2010). Second, and more critical, is the notion of spatial scale. Owing to a relatively weak expression of fast voltage-gated Na^+ channels in astrocytes, intra-astrocytic signaling is accomplished by slow calcium (Ca^{2+}) waves rather than by fast spikes. This, combined with the notion of ramified astrocytic morphology, implies that relatively temporally independent release sites might be targeting different compartments of neuronal dendritic trees. Given the existence of “dendritic computation” (London and Häusser 2005), a complex spatiotemporal interaction between astrocytic signals and neuronal excitability can be easily envisioned.

Nadkarni and Jung (2003) were the first to propose a simpler, while tractable, computational model of astrocyte-to-neuron signaling for exploring the potential contribution of astrocytes to neuronal excitability. That model assumed that the sole effect of neuronal activity-dependent astrocytic Ca^{2+} elevations was to promote neuronal depolarization. The excitatory current due to the astrocytes was modeled as:

$$I_{\text{ASTRO}} = 2.11\Theta(\log(y)) \log(y) \quad (11.8)$$

$$y = [\text{Ca}^{2+}]_{\text{ASTRO}} - 196.69 \quad (11.9)$$

While definitely being much simpler than the detailed NMDA-based description, this model has generated some testable predictions and remains a model of choice for network models of astrocytic effects on neuronal excitability (where a relatively simple and computationally cheap description is desired for reducing the system complexity).

11.2.4 Homeostatic Regulation

Homeostasis refers to the ability of a system to maintain stable internal conditions by adjusting (regulating) its variables. In the neural context, homeostasis suggests maintenance of physiologically relevant neuronal firing rates. The central dogma of neural theory asserts that neuronal firing rate depends on the strength of its coupling to other neurons; thus, a reduction in firing rate (e.g., as a result of external perturbation such as head injury) can be compensated for by increasing the strengths of afferent synapses, a process known as “homeostatic scaling” (Turrigiano 1999). Evidence suggests that astrocytes are critically involved in the homeostatic scaling of synaptic conductance following prolonged neuronal inactivity, releasing tumor necrosis factor alpha (TNF α) that causes insertion of α -amino-3-hydroxy-5-methyl-4-isoxazolepropionic acid (AMPA) and NMDA receptors and removal of γ -aminobutyric acid (GABA) receptors (Beattie et al. 2002; Stellwagen and Malenka 2006; Steinmetz and Turrigiano 2010). In the most general form, this homeostatic regulation of AMPA/NMDA and GABA conductance by astrocytes can be captured phenomenologically with the following equations:

$$g_{\text{AMPA,NMDA}} = g_{\text{AMPA,NMDA}} + \alpha_{\text{HSP}}^{\text{GLU}} \cdot (f_0 - \langle f \rangle_{T,\text{PY}}) \quad (11.10)$$

$$g_{\text{GABA}} = g_{\text{GABA}} - \alpha_{\text{HSP}}^{\text{GABA}} \cdot (f_0 - \langle f \rangle_{T,\text{PY}}) \quad (11.11)$$

where f_0 is the preset (physiologically feasible) target firing rate of pyramidal (PY) neurons (usually set to ~ 1 Hz, corresponding to the mean firing rate of PY neurons in healthy cortex), $\langle f \rangle_{T,\text{PY}}$ is the averaged (overtime and relevant population of PY neurons) firing rate of PY neurons in “astrocytic domain” (Volman et al. 2011a, b, 2013), and $\alpha_{\text{HSP}}^{\text{GLU}}$ and $\alpha_{\text{HSP}}^{\text{GABA}}$ are the rates of homeostatic synaptic plasticity convergence for specific type of synaptic receptor (AMPA and GABA, respectively).

Homeostatic scaling is a bidirectional process that aims to maintain a target firing rate through the strengthening and weakening of synaptic connections. It was recently demonstrated that the scaffolding protein PSD-95 is necessary for synaptic scaling, and its role in scaling synaptic strength was dependent on age and directionality of the scaling (Sun and Turrigiano 2011). Expression levels of PSD-95 increased as the neurons aged and PSD-95 affected mainly the downregulation of synaptic strength while up-regulation was much less affected. These results suggest the hypothesis that the downregulation of synaptic strength in older animals may be more difficult to regulate (Grand et al. 2013).

Astrocytes appear to be critical for maintaining neuronal homeostasis, but are astrocytes themselves subject to homeostatic regulation of their characteristics? At least one study suggests that this could indeed be the case. In acute mouse hippocampal slices, astrocytic metabotropic glutamate receptor signaling was found to depend on the extent of neuronal activity (Xie et al. 2012). When neuronal activity in CA3 region of hippocampus was persistently upregulated following application of high bath K $^{+}$, the activity of surface mGluRs on astrocytes in stratum radiatum of downstream CA1 region was downregulated. By contrast, prolonged

deprivation of neuronal CA3 activity yielded increased activity of surface mGluR on CA1 astrocytes. Although these results indicate that astrocytes are, too, subjected to homeostatic regulation, the underlying mechanisms, and the relation of this regulation to modulation of neuronal activity, remain elusive.

11.3 Astrocytic Contribution to the Etiology of Brain Disorders

11.3.1 Traumatic Brain Injury

Traumatic brain injury (TBI) has been widely recognized as one of the most important acquired brain disorders. The spectrum of TBI encompasses all CNS impairments induced by mechanical perturbations, arising in different settings such as automobile accidents, violent sports (e.g., rugby or American football), and military environment (McCrory 2011; Theye and Mueller 2004; Rigg and Moonery 2011). Likely owing to this universality, and likely for its high potential frequency of occurrence (most of us are potentially in danger of TBI owing to our daily use of automobiles), TBI has gained wide recognition. The different levels of TBI range from mild TBI (mTBI) (concussive TBI, leading to relatively mild functional consequences) to penetrative TBI (resulting in extensive damage and severe functional consequences such as post-traumatic epilepsy). Nevertheless, the injury mechanisms in these TBIs of different gradations are qualitatively the same in that all these mechanisms describe the impact of mechanical perturbations on cellular structures. Because astrocytes pervade the brain and assume an important role in cellular homeostasis, the logical conclusion is that these cells are likely to be affected in TBI.

Responses of astrocytes to mechanical perturbation were studied in an *in vitro* model of stretch injury (Neary et al. 2002; Rzigalinski et al. 1998; Ahmed et al. 2000). The emerging picture is that astrocytes respond to stretch injury by Ca^{2+} elevations (Rzigalinski et al. 1998; Ahmed et al. 2000) and release of ATP (Neary et al. 2002). Both these two factors were shown to be positively correlated with stretch magnitude (strain) and rate (strain rate) (Neary et al. 2002; Rzigalinski et al. 1998; Ahmed et al. 2000).

Astrocytes response to trauma-induced perturbations with a series of processes, collectively termed “reactive gliosis,” including significant relatively rapid morphological remodeling and cell proliferation (Sofroniew 2009). Computational modeling suggested that astrocytic morphological remodeling post-trauma could reduce the incidence of paroxysmal activity by providing better functional segregation of synaptic input from intact vs. injured neurons (Volman et al. 2013). Yet, the biophysical processes underlying this remodeling remain elusive. On the other hand, cell proliferation is mediated by extracellular signal-regulated protein kinase (ERK), and it has been shown that astrocytic ERK activation involves ATP and P2 purinergic receptors (Neary et al. 2002). Along with the observations of stretch injury-induced

astrocytic and neuronal release of ATP (Ahmed et al. 2000), this suggests a mechanism relating stretch injury to cellular proliferation facet of reactive gliosis.

A question of practical importance is whether astrocytes exert protective effects or aggravate the injury sequelae. Experimental evidence and computational models suggest a protective role. Computational modeling suggests that morphological changes in reactive astrocytes may help reduce the incidence of paroxysmal events in deafferentation model of post-traumatic epilepsy (Volman et al. 2013). In an experimental model of repetitive injury, the glial S100 β protein (expressed in astrocytes enwrapping blood vessels) had a protective role (Slemmer and Weber 2005). Computational modeling of stretch injury in white matter axons suggested that glial buffering of extracellular K $^{+}$ at nodes of Ranvier can help prevent or postpone the development of axonal degeneration (Volman and Ng 2014). However, injury-induced release of ATP from astrocytes (Neary et al. 2002) and downregulation of tonic and phasic inhibition by ATP release from cortical astrocytes (Lalo et al. 2014) may indicate astrocytic up-regulation of cortical network activity post-trauma. Activation of this pathway may help partially restore network activity following injury-induced cortical deafferentation.

Although the work reviewed above provides strong neurophysiological evidence regarding the role of astrocytes in TBI, a real extent of astrocytic involvement remains elusive. In vitro models of TBI allow dissecting the basic mechanisms underlying neurological processes of injury; however, mechanical strains that are used in these models are notional at best, and may not reflect physiologically relevant strains *in vivo*. The relevant scenarios (automobile accidents, contact sports games, exposure to explosive devices) may induce lower or higher strains compared with those used in in vitro experiments, owing to dampening or facilitating effects of the skull, supporting tissue, and fluids. Injury models that account for these factors and combine them with neural/glial structures (Ng et al. 2014) may help to more precisely assess the injury-dose dependent extent of astrocytic involvement in TBI.

11.3.2 Epilepsy

Epilepsy is widely considered to be a “network disease,” driven by aberrant synaptic interactions between neurons (McCormick and Contreras 2001). The main common features of epilepsy are the presence of unprovoked seizures and the abnormal local neuronal synchronization (Timofeev et al. 2012). Traumatic brain injury is a major risk factor for epileptogenesis (Feeney and Walker 1979; Temkin et al. 1995; Annegers et al. 1998). Because astrocytes are ideally positioned to modulate the properties of synaptic transmission and neuronal excitability, it is natural to expect that these non-neuronal cells will be involved, to some extent, in the etiology of epilepsy. And in fact, significant body of evidence has accumulated over the years, demonstrating that astrocytes play a critical role in the emergence of different forms of epilepsy.

In principle, astrocytic contribution to the etiology of epilepsy can be roughly categorized into three pathways: (1) dysregulation of synaptic transmission; (2) dysregulation of extracellular ion balance and subsequent dysregulation of neuronal excitability; (3) inflammatory reaction during reactive gliosis. To the best of our knowledge, there have been no reports on astrocytic involvement in the etiology of epilepsy through dysregulation of synaptic transmission (e.g., dysregulation of short-term depression/facilitation). Thus, we can speculate that pathway (1) is “reserved” for slow modulation of presynaptic plasticity and in itself does not directly contribute to the emergence of pathological dynamics (although untimely facilitation of synaptic transmitter release could, in principle, increase the positive feedback effect and thus indirectly contribute to seizure escalation).

Astrocyte-mediated dysregulation of neuronal excitability has been shown to contribute to epileptogenesis. Astrocytic modulation of neuronal excitability through glutamate release linked to physiologically relevant Ca^{2+} elevations in astrocytes has been demonstrated by Parpura and Haydon (2000). Based in part on these findings, Nadkarni and Jung (2003) devised the first computational model of astrocyte-neuron interaction and predicted, based on their modeling results, that astrocytes might take part in epileptogenesis. This hypothesis has been later extensively addressed in a computational modeling study by Silchenko and Tass (2008). Finally, in an *in vitro* model of focal seizures in rat entorhinal cortex, NMDA-mediated astrocytic modulation of postsynaptic neuronal excitability enhanced ictal discharges, and this involvement was mediated by astrocytic Ca^{2+} signaling (Gomez-Gonzalo et al. 2010). Interestingly, selective inhibition of astrocytic Ca^{2+} signaling did not affect the generation of interictal discharges. These data suggest that astrocytes might be engaged in a recurrent excitatory loop that promotes seizure generation and sustains ictal discharges (Gomez-Gonzalo et al. 2010). These *in vitro* experimental studies validated the conclusions of earlier computational models. Recently, the NMDA pathway of astrocytic involvement in the emergence of temporal lobe epilepsy has been demonstrated *in vivo* (Clasadonte et al. 2013). In mice, genetic impairment of transmitter release from astrocytes by the expression of a glial dominant-negative soluble NSF attachment protein receptor (SNARE) domain attenuated seizure frequency, hippocampal damage, and behavioral deficits (Clasadonte et al. 2013). These findings provide strong evidence implicating the involvement of astrocytes in epileptogenesis through NMDA signaling pathway.

As mentioned above, the principal outcome of intense spiking activity is accumulation of K^+ in extracellular space, known as the “Frankenhaeuser–Hodgkin effect” (Frankenhaeuser and Hodgkin 1956). One of the long-standing hypotheses of epileptogenesis is the “high K^+ hypothesis,” according to which activity-dependent accumulation of extracellular K^+ acts as a positive feedback mechanism promoting dynamical instability that culminates in seizure generation (Fisher et al. 1976; Lothman and Somjen 1976; Janigro et al. 1997; Frohlich et al. 2008). Because astrocytes are involved in maintaining extracellular K^+ homeostasis, these cells are likely to contribute to “high K^+ ” epileptogenesis. This contribution has indeed been extensively demonstrated and will not be reviewed here (see Seifert et al. (2006) for a good review). K^+ clearance is mediated by Kir4.1 channels that are often co-localized with

AQP4 channels in astrocytes (Nagelhus et al. 2004), suggesting co-occurrence of K⁺ regulation and swelling. In fact, K⁺ clearance was significantly compromised in AQP4 knockout mice (Binder et al. 2006). Although the threshold for seizure generation was higher in AQP4^{-/-} mice, the seizures were more prolonged compared with controls (Binder et al. 2006; Amiry-Moghaddam et al. 2003). The important role of AQP4 channels in K⁺ clearance was recently confirmed in a data-driven computational model (Jin et al. 2012).

Given the evidence for involvement of astrocytic Kir4.1 channels in the etiology of epilepsy, a broader question that arises is whether these astrocytic channels affect neuronal excitability and activity of non-epileptic neurons. Unfortunately, although Kir4.1 knockout mouse models are available and have been studied, it is difficult to address this question using this model, because Kir4.1^{-/-} mice develop pathologies (e.g., ataxia and seizures) and die prematurely, suggesting that chronic deletion of glial Kir4.1 channels yields lethal effects (Djukic et al. 2007). Thus, this question was recently addressed in a computational model of K⁺-based neuron-glial interaction (Sibille et al. 2015). In the model, astrocytic Kir4.1 channels significantly modulated neuronal activity in the 3–5 Hz band (the theta band) (Sibille et al. 2015), suggesting that this mechanism of K⁺ clearance may affect the characteristics of normal function.

As mentioned above, acquired epilepsy has been associated with moderate and severe forms of TBI. Traumatic brain injury can increase the predisposition to epileptic seizures after a period of latency following the traumatic event (Annegers et al. 1998). A possible immediate outcome of moderate to severe TBI is the massive death of neurons and damage to synaptic connectivity (deafferentation). Both of these injury pathways are likely to result in chronic neuronal inactivity. Evidence from *in vitro* studies suggests that, following chronic inactivity, several characteristics of neuronal circuitry (such as synaptic connectivity, organization of dendritic spines, intrinsic neuronal excitability) are modified to compensate for the reduction of activity incurred by injury. Quite generally, chronic inactivity promotes the upregulation of depolarizing influences and downregulation of hyperpolarizing influences. This suggests that chronic inactivity activates homeostatic regulatory pathways for offsetting the persistent perturbations in electrical activity (Turrigiano 1999). Regional homeostatic adjustments of neuronal excitability and synaptic transmission could contribute to breaching the excitation–inhibition balance (Fritschy 2008), thus promoting seizure generation in traumatized networks (Timofeev et al. 2010). Indeed, it was proposed that homeostatic plasticity, which normally serves to maintain moderate levels of activity in the cortex, may fail to control “normal” excitability in heterogeneous networks, where there are subpopulations of neurons with dramatically different levels of activity—conditions found in traumatized cortex (Topolnik et al. 2003; Houweling et al. 2005). Thus, the etiology of post-traumatic epilepsy can be at least partially explained by the action of homeostatic plasticity.

Because astrocytic signaling occurs on a relatively slow timescale and because astrocytes are involved in maintaining synaptic transmission and neuronal environment, these cells are likely to be at least partially involved in the etiology of post-traumatic epilepsy. This involvement can be expected to be manifested in astrocyte-mediated homeostatic regulation of neuronal excitability and synaptic

transmission. Also, note that relatively severe mechanical impact (as a result of moderate to severe TBI) is likely to be sufficient for mechanistically triggering reactive gliosis; thus, even based only on these mechanistic arguments, astrocytes are likely to be involved in neurological sequelae of moderate to severe TBI.

In vitro studies suggest that astrocytes are critically involved in the homeostatic scaling of synaptic conductance that follows prolonged period of synaptic inactivity (Beattie et al. 2002; Stellwagen and Malenka 2006; Steinmetz and Turrigiano 2010). Following chronic synaptic inactivity, astrocytes release tumor necrosis factor alpha (TNF α), which diffuses in the extracellular space and acts on postsynaptic neurons to scale-up the number of depolarization-promoting AMPA and NMDA receptors and to scale-down the number of hyperpolarization-promoting GABA receptors. Thus, signaling by TNF α could represent a homeostatic regulatory mechanism compensating for a chronic reduction in neural excitability and could contribute to post-traumatic epileptogenesis. Computational models, incorporating mechanisms of homeostatic regulation as described above, explored this hypothesis by assuming a phenomenological variable “glia” (Volman et al. 2011a; b, 2013; Houweling et al. 2005; Frohlich et al. 2008; Savin et al. 2009). Savin et al. (2009), by studying the dynamics in the deafferentation model of trauma and introducing a phenomenological diffusive TNF α variable, concluded that glial release of TNF α could affect post-traumatic paroxysmal activity. Volman et al. (2013) designed a model of deafferentation trauma to study the implications of rapid astrocytic morphological remodeling that is often observed following traumatic events (Oberheim et al. 2008). In vitro, astrocytes that were located relatively close (within 200 μ m) to the boundary between intact and injured cortical regions lost their trademark star-like shape and elongated in the direction perpendicular to the trauma boundary (Oberheim et al. 2008). Computational modeling of deafferentation trauma suggested that such trauma-induced morphological reorganization of astrocytes could reduce the incidence of paroxysmal activity by providing better functional segregation of synaptic input from intact versus injured neurons (Volman et al. 2013). It was further proposed that functional segregation of synaptic input could help localize the release of TNF α to the regions of synaptic inactivity and thus reduce pathological over-excitation of relatively intact areas.

11.3.3 Schizophrenia

Converging evidence from animal models and quantitative electroencephalography (qEEG) recordings suggests that schizophrenia might be associated with alterations in gamma frequency band (25–80 Hz) oscillatory activity. Altered gamma band activity has been linked to dysfunction of parvalbumin-positive (PV+) fast-spiking interneurons, explaining the deficit of these PV+ neurons observed in animal models of schizophrenia and postmortem imaging studies of patients with psychiatric disorders such as schizophrenia (Volman et al. 2011). However, gamma oscillations in vivo are likely to be mediated by pyramidal inhibitory gamma (PING) mechanism (Buzsaki and Wang 2012), necessitating (sensory) activation of pyramidal neurons

that drive and synchronize the PV+ neurons, with PV+ neurons in turn gating and synchronizing the pyramidal cells. Thus, while PV+ neurons are important for tuning the frequency of collective oscillation, pyramidal (PY) neurons are likely to be necessary for maintaining the oscillation per se, by maintaining sufficiently strong activity during episodes of gamma band activity. In light of astrocytic modulation of neuronal excitability, it is plausible to assume that, at least *in vitro*, astrocytes might contribute to collective oscillations in the gamma frequency band.

The contribution of astrocytes to gamma oscillations has been explored by Lee et al. (2014). To determine the involvement of astrocytic signaling in generation and maintenance of gamma oscillations, the authors used the sensitivity of astrocytic Ca²⁺-dependent vesicular release to clostridial toxins (TeNT) and developed a genetic system capable of targeting TeNT expression to astrocytes (Lee et al. 2014). Glutamate release from astrocytes was inhibited in mice with astrocyte-specific TeNT expression, resulting in weaker depolarization of pyramidal neurons (the effect of astrocyte-specific TeNT expression on GABAergic interneurons was not reported by the authors). Interestingly, while the duration of carbachol-induced gamma oscillation was shorter in slices with astrocyte-specific TeNT expression, the EEG spectra were altered by astrocyte-specific TeNT expression in a behavioral state-dependent manner. In addition, behavioral deficits in novel object recognition were observed in mice with astrocyte-specific TeNT expression. *In vitro*, the duration of carbachol-induced gamma oscillation in slices with astrocyte-specific TeNT expression was restored after application of glutamate receptor agonist AMPA. Thus, this study suggests that, *in vivo*, astrocytes might provide the “background excitation” for maintaining gamma-band oscillations. Further, extending the conclusions of (Lee et al. 2014), a speculation can be raised that the etiology of schizophrenia can be ascribed, at least partially, to dysfunctional astrocytic signaling pathways. Interestingly, analysis of postmortem patients with schizophrenia revealed reduced glial fibrillary acidic protein (GFAP) expression in the prefrontal cortex (Cotter et al. 2001), in line with observations by Lee et al. (2014). Additional studies and computational models of astrocyte–neuron communication are likely to elucidate the involvement of astrocytes in psychiatric disorders such as schizophrenia.

11.4 Conclusion

This brief review provides convincing evidence for critical role of astrocytes in the genesis of several neurological disorders, including epilepsy and schizophrenia. It suggests that future studies of the pathologies of astrocytes regulation in brain diseases are important and may likely lead to new clinical treatment strategies.

Acknowledgements MB acknowledges financial support through the research grants from the Office of Naval Research (MURI, N000141310672) and National Institutes of Health (R01 EB009282 and R01 MH099645). The work of VV was sponsored by the US Army Medical Research and Materiel Command under contract W81XWH-11-D-0011. This document is cleared for all

audiences for OPSEC purposes. Cleared for public release 09/25/2015. The opinions or assertions contained herein are private views of the authors and are not to be construed as official or as reflecting views of the Department of the Army or the Department of Defense. PAO reviewed.

References

- Agulhon C, Sun MY, Murphy T, Myers T, Lauderdale K et al (2012) Calcium signaling and gliotransmission in normal vs. reactive astrocytes. *Front Pharmacol* 3:1–16
- Ahmed SM, Rzigalinski BA, Willoughby KA, Sitterding HA, Ellis EF (2000) Stretch-induced injury alters mitochondrial membrane potential and cellular ATP in cultured astrocytes and neurons. *J Neurochem* 74:1951–1960
- Amiry-Moghaddam M, Williamson A, Palomba M, Eid T, de Lanerolle NC et al (2003) Delayed K⁺ clearance associated with aquaporin-4 mislocalization: phenotypic defects in brains of alpha-syntrophin-null mice. *Proc Natl Acad Sci USA* 100:13615–13620
- Annegers JF, Hauser A, Coan SP, Rocca WA (1998) A population-based study of seizures after traumatic brain injury. *N Eng J Med* 338:20–24
- Araque A, Parpura V, Sanzgiri RP, Haydon PG (1998) Glutamate-dependent astrocyte modulation of synaptic transmission between cultured hippocampal neurons. *Eur J Neurosci* 10:2129–2142
- Araque A, Parpura V, Sanzgiri RP, Haydon PG (1999) Tripartite synapses: glia, the unacknowledged partner. *Trends Neurosci* 22:208–215
- Bazhenov M, Timofeev I, Steriade M, Sejnowski TJ (2004) Potassium model for slow (2–3 Hz) in vivo neocortical paroxysmal oscillations. *J Neurophysiol* 92:1116–1132
- Beattie EC, Stellwagen D, Morishita W, Bresnahan JC, Ha BK et al (2002) Control of synaptic strength by glial TNF α . *Science* 295:2282–2285
- Binder DK, Yao X, Sick TJ, Verkman AS, Manley GT (2006) Increased seizure duration and slowed potassium kinetics in mice lacking aquaporin-4 water channels. *GLIA* 53:631–636
- Buzsaki G, Wang XJ (2012) Mechanisms of gamma oscillations. *Ann Rev Neurosci* 35:203–225
- Clasadonte J, Dong J, Hines DJ, Haydon PG (2013) Astrocyte control of synaptic NMDA receptors contributes to the progressive development of temporal lobe epilepsy. *Proc Natl Acad Sci USA* 110:17540–17545
- Cotter DR, Pariante CM, Everall IP (2001) Glial cell abnormalities in major psychiatric disorders: the evidence and implications. *Brain Res Bull* 55:585–595
- De Pittà M, Volman V, Berry H, Ben-Jacob E (2011) A tale of two stories: astrocyte regulation of synaptic depression and facilitation. *PLoS Comput Biol* 7:e1002293
- De Pittà M, Volman V, Berry H, Parpura V, Volterra A et al (2012) Computational quest for understanding the role of astrocyte signaling in synaptic transmission and plasticity. *Front Comput Neurosci* 6:98
- Djukic B, Casper KB, Philpot BD, Chin LS, McCarthy KD (2007) Conditional knock-out of Kir4.1 leads to glial membrane depolarization, inhibition of potassium and glutamate uptake, and enhanced short-term synaptic potentiation. *J Neurosci* 27:11354–11365
- Feeney DM, Walker AE (1979) The prediction of posttraumatic epilepsy. A mathematical approach. *Arch Neurol* 36:8–12
- Fisher RS, Pedley TA, Moody WJ, Prince DA (1976) The role of extracellular potassium in hippocampal epilepsy. *Arch Neurol* 33:76–83
- Florence CM, Baillie LD, Mulligan SJ (2012) Dynamic volume changes in astrocytes are an intrinsic phenomenon mediated by bicarbonate ion flux. *PLoS ONE* 7:e51124
- Frankenhaeuser B, Hodgkin AL (1956) The after-effects of impulses in the giant nerve fibers of *Loilgo*. *J Physiol* 131:341–376
- Fritschy JM (2008) Epilepsy, E/I balance and GABAa receptor plasticity. *Front Mol Neurosci* 1:5

- Frohlich F, Bazhenov M, Iragui-Madoz V, Sejnowski TJ (2008a) Potassium dynamics in the epileptic cortex: new insights on an old topic. *Neuroscientist* 14:422–433
- Frohlich F, Bazhenov M, Sejnowski TJ (2008b) Pathological effects of homeostatic synaptic scaling on network dynamics in diseases of the cortex. *J Neurosci* 28:1709–1720
- Gomez-Gonzalo M, Losi G, Chiavegato A, Zonta M, Cammarota M et al (2010) An excitatory loop with astrocytes contributes to drive neurons to seizure threshold. *PLoS Comput Biol* 8:e1000352
- Grand L, Ftomov S, Timofeev I (2013) Long-term synchronized electrophysiological and behavioral wireless monitoring of freely moving animals. *J Neurosci Meth* 212:237–241
- Haydon PG (2001) GLIA: listening and talking to the synapse. *Nat Rev Neurosci* 2:185–193
- Houweling AR, Bazhenov M, Timofeev I, Steriade M, Sejnowski TJ (2005) Homeostatic synaptic plasticity can explain post-traumatic epileptogenesis in chronically isolated neocortex. *Cereb Cortex* 15:834–845
- Janigro D, Gasparini S, D'Ambrosio R, McKhann G, DiFrancesco D (1997) Reduction of K⁺ uptake in glia prevents long-term depression maintenance and causes epileptiform activity. *J Neurosci* 17:2813–2824
- Jin BJ, Zhang H, Binder DK, Verkman AS (2012) Aquaporin-4-dependent K⁺ and water transport modeled in brain extracellular space following neuroexcitation. *J Gen Physiol* 141:119–132
- Lalo U, Palygin O, Rasooli-Nejad S, Andrew J, Haydon PG et al (2014) Exocytosis of ATP from astrocytes modulates phasic and tonic inhibition in the neocortex. *PLoS Biol* 12:e1001747
- Lee HS, Ghetti A, Pinto-Duarte A, Wang X, Dziewczapski G et al (2014) Astrocytes contribute to gamma oscillations and recognition memory. *Proc Natl Acad Sci USA* 111:E3343–E3352
- London M, Häusser M (2005) Dendritic computation. *Ann Rev Neurosci* 28:503–532
- Lothman EW, Somjen GG (1976) Functions of primary afferents and responses of extracellular K⁺ during spinal epileptiform seizures. *Electroencephalogr Clin Neurophysiol* 41:253–267
- McCormick DA, Contreras D (2001) On the cellular and network bases of epileptic seizures. *Ann Rev Physiol* 63:815–846
- McCrory P (2011) Sports concussion and the risk of chronic neurological impairment. *Clin J Sport Med* 21:6–12
- Metea MR, Kofuji P, Newman EA (2007) Neurovascular coupling is not mediated by potassium siphoning from glial cells. *J Neurosci* 27:2468–2471
- Mothet JP, Pollegioni L, Ouanounou G, Martineau M, Fossier P et al (2005) Glutamate receptor activation triggers a calcium-dependent and SNARE protein-dependent release of the gliotransmitter D-serine. *Proc Natl Acad Sci USA* 102:5606–5611
- Nadkarni S, Jung P (2003) Spontaneous oscillations of dressed neurons: a new mechanism for epilepsy? *Phys Rev Lett* 91:1–4
- Nadkarni S, Bartol TM, Sejnowski TJ, Levine H (2010) Modelling vesicular release at hippocampal synapses. *PLoS Comp Biol* 6:e1000983
- Nadkarni S, Bartol TM, Stevens CF, Sejnowski TJ, Levine H (2012) Short-term plasticity constrains spatial organization of a hippocampal presynaptic terminal. *Proc Natl Acad Sci USA* 109:14657–14662
- Nagelhus EA, Mathiisen TM, Ottersen OP (2004) Aquaporin-4 in the central nervous system: cellular and subcellular distribution and coexpression with KIR4.1. *Neurosci* 129:905–913
- Neary JT, Kang Y, Willoughby KA, Ellis EF (2002) Activation of extracellular signal-regulated kinase by stretch-induced injury in astrocytes involves extracellular ATP and P2 purinergic receptors. *J Neurosci* 23:2348–2356
- Ng LJ, Gibbons M, Phohomsiri P, Volman V, Cui J et al (2014) Investigation of the concussion mechanism: an end-to-end model that translates external measures to internal neurologic injury, Tampa, FL
- Oberheim NA, Tian GF, Han X, Peng W, Takano T et al (2008) Loss of astrocytic domain organization in the epileptic brain. *J Neurosci* 28:3264–3276
- Oliet SHR, Mothet JP (2009) Regulation of N-methyl-D-aspartate receptors by astrocytic D-serine. *Neuroscience* 158:275–283

- Østby I, Øyehaug L, Einevoll GT, Nagelhus EA, Plahte E et al (2009) Astrocytic mechanisms explaining neural-activity-induced shrinkage of extraneuronal space. *PLOS Comp Biol* 5:e1000272
- Øyehaug L, Østby I, Lloyd CM, Omholt SW, Einevoll GT (2011) Dependence of spontaneous neuronal firing and depolarization block on astroglial membrane transport mechanisms. *J Comput Neurosci*
- Parpura V, Haydon PG (2000) Physiological astrocytic calcium levels stimulate glutamate release to modulate adjacent neurons. *Proc Natl Acad Sci USA* 97:8629–8634
- Parpura V, Zorec R (2010) Gliotransmission: exocytotic release from astrocytes. *Brain Res Rev* 63:83–92
- Parpura V, Basarsky TA, Liu F, Jeftinija K, Jeftinija S et al (1994) Glutamate-mediated astrocyte-neuron signaling. *Nature* 369:744–747
- Paulson OB, Newman EA (1987) Does the release of potassium from astrocyte endfeet regulate cerebral blood flow? *Science* 237:896–898
- Perea G, Araque A (2007) Astrocytes potentiate transmitter release at single hippocampal synapses. *Science* 317:1083–1086
- Rigg JL, Moonery SR (2011) Concussions and the military: issues specific to service members. *PM R* 3:S380–S386
- Rzigelinski BA, Weber JT, Willoughby KA, Ellis EF (1998) Intracellular free calcium dynamics in stretch-induced astrocytes. *J Neurochem* 70:2377–2385
- Savin C, Triesch J, Meyer-Hermann M (2009) Seizure induction by glia-mediated synaptic scaling. *J R Soc Interface* 6:655–668
- Seifert G, Schilling K, Steinhauser C (2006) Astrocyte dysfunction in neurological disorders: a molecular perspective. *Nat Rev Neurosci* 7:194–206
- Sibille J, Duc KD, Holcman D, Rouach N (2015) The neuroglial potassium cycle during neurotransmission: role of Kir4.1 channels. *PLoS Comp Biol* 11: e1004137
- Silchenko AN, Tass PA (2008) Computational modeling of paroxysmal depolarization shifts in neurons induced by glutamate release from astrocytes. *Biol Cybern* 98:61–74
- Simard M, Nedergaard M (2004) The neurobiology of glia in the context of water and ion homeostasis. *Neurosci* 129:877–896
- Slemmer JE, Weber JT (2005) The extent of damage following repeated injury to cultured hippocampal cells is dependent on the severity of insult and inter-injury interval. *Neurobiol Dis* 18:421–431
- Sofroniew MV (2009) Molecular dissection of reactive astrogliosis and glial scar formation. *Trends Neurosci* 32:638–847
- Solenov E, Watanabe H, Manley GT, Verkman AS (2004) Sevenfold-reduced osmotic water permeability in primary astrocyte cultures from AQP-4-deficient mice, measured by a fluorescence quenching method. *Am J Physiol Cell Physiol* 286:C426–C432
- Somjen GG, Kager H, Wadman WJ (2009) Computer simulations of neuron-glial interactions mediated by ion flux. *J Comput Neurosci* 25:349–365
- Steinmetz CC, Turrigiano GG (2010) Tumor necrosis factor- α signaling maintains the ability of cortical synapses to express synaptic scaling. *J Neurosci* 30:14685–14690
- Stellwagen D, Malenka RC (2006) Synaptic scaling mediated by glial TNF α . *Nature* 440:1054–1059
- Sun Q, Turrigiano GG (2011) PSD-95 and PSD-93 play critical but distinct roles in synaptic scaling up and down. *J Neurosci* 31:6800–6808
- Temkin NR, Haglund MM, Winn HR (1995) Causes, prevention, and treatment of post-traumatic epilepsy. *New Horiz* 3:518–522
- Theye F, Mueller KA (2004) “Heads up”: concussions in high school sports. *Clin Med Res* 2:165–171
- Timofeev I, Bazhenov M, Avramescu S, Nita DA (2010) Posttraumatic epilepsy: the roles of synaptic plasticity. *Neuroscientist* 16:19–27
- Timofeev I, Bazhenov M, Seigneur J, Sejnowski TJ (2012) Neuronal synchronization and thalamocortical rhythms in sleep, wake, and epilepsy. In: Noebels JLAM, Rogawski MA, Olsen RW,

- Delgado-Escueta AV (eds) Jasper's basic mechanisms of the epilepsies. Oxford University Press, New York, pp 157–175
- Topolnik L, Steriade M, Timofeev I (2003) Partial cortical deafferentation promotes development of paroxysmal activity. *Cereb Cortex* 13:883–893
- Tsodyks MV, Markram H (1997) The neural code between neocortical pyramidal neurons depends on neurotransmitter release probability. *Proc Natl Acad Sci USA* 94:719–723
- Turrigiano GG (1999) Homeostatic plasticity in neuronal networks: the more things change, the more they stay the same. *Trends Neurosci* 22:221–227
- Volman V, Ng LJ (2014) Primary paranode demyelination modulates slowly developing axonal depolarization in a model of axonal injury. *J Comput Neurosci* 37:439–457
- Volman V, Ben-Jacob E, Levine H (2007) The astrocyte as a gatekeeper of synaptic information transfer. *Neural Comput* 19:303–326
- Volman V, Bazhenov M, Sejnowski TJ (2011a) Pattern of trauma determines the threshold for epileptic activity in a model of cortical deafferentation. *Proc Natl Acad Sci USA* 108:15402–15407
- Volman V, Sejnowski TJ, Bazhenov M (2011b) Topological basis of epileptogenesis in a model of severe cortical trauma. *J Neurophysiol* 106:1933–1942
- Volman V, Behrens MM, Sejnowski TJ (2011c) Downregulation of parvalbumin at cortical GABA synapses reduces network gamma oscillatory activity. *J Neurosci* 31:18137–18148
- Volman V, Bazhenov M, Sejnowski TJ (2013) Divide and conquer: functional segregation of synaptic inputs by astrocytic microdomains could alleviate paroxysmal activity following brain trauma. *PLoS Com Biol* 9:e1002856
- Walz W (2000) Role of astrocytes in the clearance of excess extracellular potassium. *Neurochem Intl* 36:291–300
- Wei Y, Ullah G, Ingram J, Schiff SJ (2014a) Oxygen and seizure dynamics: II. Computational modeling. *J Neurophysiol* 112:213–223
- Wei Y, Ullah G, Schiff SJ (2014b) Unification of neuronal spikes, seizures, and spreading depression. *J Neurosci* 34:11733–11743
- Xie AX, Sun MY, Murphy T, Lauderdale K, Tiglao E et al (2012) Bidirectional scaling of astrocytic metabotropic glutamate receptor signaling following long-term changes in neuronal firing rates. *PLoS ONE* 7:e49637
- Zhang JM, Wang HK, Ye CQ, Ge W, Chen Y et al (2003) ATP released by astrocytes mediates glutamatergic activity-dependent heterosynaptic suppression. *Neuron* 40:971–982

Part IV

Homeostasis and Metabolic Coupling

Chapter 12

The Role of Astrocytes in Neurotransmitter Uptake and Brain Metabolism



Annalisa Scimemi

Abstract Termination of synaptic transmission relies on neurotransmitter diffusion and removal from the extracellular space by specific molecules called transporters, abundantly expressed in astrocytes. Here we describe the biophysical mechanisms of neurotransmitter transport across the astrocyte membrane and the biochemical pathways that supply energy to these cells. These findings indicate that astrocytes are crucial regulators of brain activity, due to their ability to shape synaptic transmission and control the energy budget of the entire brain.

Keywords Transporters · Astrocytes · Metabolism

12.1 Introduction

Glial cells are abundant in the brain and are known to lack some of the fundamental properties of cell excitability that are typical of neurons: they do not fire action potentials and do not show any form of spontaneous activity that is reminiscent of spontaneous excitatory and/or inhibitory postsynaptic potentials in neurons (Bergles and Jahr 1997; Parpura and Verkhratsky 2012a). Due to their different functional properties, glial cells have long been thought to exert only structural and metabolic roles in the brain, all taking place over a much longer timescale relative to that of synaptic transmission among neurons (Parpura and Verkhratsky 2012b). There is a definitive truth in this viewpoint, because glial cells form 3D scaffolds that support neuron migration during development (Clarke and Barres 2013; Stogsdill and Eroglu 2017) and have a well-established role in brain energy delivery, production, and storage (Marcaggi and Attwell 2004; Attwell et al. 2010).

Over the years, however, it has become apparent that structural and metabolic support are not the only functions that glial cells exert. There are different types of

A. Scimemi (✉)
Department of Biology, SUNY Albany,
1400 Washington Avenue, Albany, NY 12222-0100, USA
e-mail: scimemiam@gmail.com; ascimemi@albany.edu

glial cells, with very different structural and functional properties. Astrocytes, for example, can rapidly modulate synaptic transmission between neurons, due to their ability to regulate neurotransmitter diffusion and uptake at the millisecond timescale (Bergles and Jahr 1997, 1998; Bergles et al. 2002; Diamond et al. 1998). The unique combination of functional properties exhibited by astrocytes allows these cells to act as a key point of interface between the neuronal, glial, and vasculature components of the brain. Presumably for this reason, astrocytes have earned the attention of numerous research groups around the world and, to these days, they represent one of the most studied types of glial cells. In this chapter, I provide a brief overview of the fundamental functional properties of astrocytes that allow them to regulate synaptic signaling and brain metabolism.

12.2 Neurotransmitter Uptake: Glutamate Transporters

Among all glial cells, astrocytes are the ones with the highest expression of transporters for glutamate, the main excitatory neurotransmitter in the brain (Danbolt 2001). Current estimates of glutamate transporter surface expression, based on protein extracts from the mature rodent hippocampus, indicate that their surface density is $\sim 10,800 \mu\text{m}^{-2}$ (Lehre and Danbolt 1998). Unlike other neurotransmitters, including acetylcholine and the amine neurotransmitters serotonin and dopamine, glutamate released by neurons in the extracellular space is not subject to enzymatic breakdown. Through passive diffusion, the extracellular glutamate concentration decreases progressively following glutamate release from synaptic vesicles (Rusakov and Kullmann 1998a; Barbour 2001; Scimemi and Beato 2009) (Fig. 12.1). If glutamate were to persist in the extracellular space for a sufficiently long time, at sufficiently high concentration, it would remain biologically active. This could lead to prolonged activation of neuronal glutamate receptors and increase the duration of postsynaptic excitatory synaptic potentials, ultimately triggering potentially neurotoxic effects. Under physiological conditions, the brain prevents this from happening through the activity of astrocytic glutamate transporters. In acute slice preparations from the hippocampus or the *nucleus accumbens*, astrocytic glutamate transporters maintain the ambient extracellular glutamate concentration at $\sim 25 \text{ nM}$, well below the steady-state affinity for glutamate binding to ionotropic and metabotropic neuronal glutamate receptors (Herman and Jahr 2007; Chiu and Jahr 2017). This ensures low levels of sustained glutamate receptor activation by ambient glutamate (Herman and Jahr 2007; Chiu and Jahr 2017).

In humans, the two major types of astrocytic glutamate transporters contributing to both effects are the excitatory amino acid transporter 1 and 2 (EAAT1 and EAAT2, respectively). EAAT1 is homolog to the rodent astrocytic glutamate transporter GLAST; EAAT2 is homolog to the rodent astrocytic glutamate transporter GLT-1 (Danbolt 2001). In the brain of developing rodents, the peak expression of GLAST precedes that of GLT-1, but GLT-1 is the most abundant glutamate transporter type in the adult brain (Furuta et al. 1997). Likewise, in the human brain, the

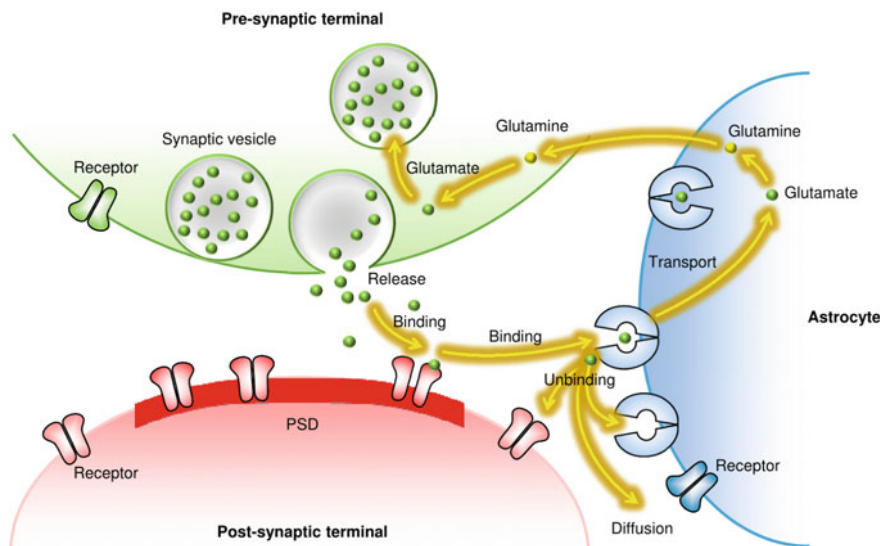


Fig. 12.1 The journey of synaptically released glutamate. Once released from the lumen of a presynaptic vesicle into the synaptic cleft, glutamate can diffuse and bind to/unbind from receptors in the PSD, extrasynaptic and presynaptic terminal. A significant proportion of glutamate molecules diffusing away from the synaptic cleft binds to glutamate transporters, abundantly expressed in the membrane of astrocytes around the synapse. The transport efficiency of glutamate transporters is ~50%. The glutamate molecules that unbind from the transporters are released back in the extracellular space and can either bind to extrasynaptic neuronal receptors, astrocytic receptors/transporters or continue diffusing further in the extracellular space. The glutamate molecules translocated toward the astrocyte cytoplasm are eventually converted into glutamine, which is shuttled back to neurons, converted into glutamate, and stored into synaptic vesicles, ready to be released back in the synaptic cleft during a release event

expression of EAAT2 increases progressively after birth until it becomes the most abundant glutamate transporter type during adulthood (DeSilva et al. 2012; Bar-Peled et al. 1997; Milton et al. 1997). Although the exact kinetic properties of glutamate binding and the rate of glutamate transport across the cell membrane via EAAT1 and EAAT2 are slightly different, their general thermodynamic properties are very similar and reminiscent of those exhibited by the prokaryotic glutamate transporter homolog Glt_{Ph} (Wadiche et al. 1995; Akyuz et al. 2013). For example, both EAAT1 and EAAT2 couple the translocation of glutamate across the membrane with the movement of a fixed number of other cations (Zerangue and Kavanaugh 1996; Levy et al. 1998; Owe et al. 2006). EAAT1 and EAAT2 show similar *capture efficiency*, which is indicative of the proportion of glutamate molecules that, after being initially bound by the transporters, are eventually translocated across the membrane (Wadiche and Kavanaugh 1998; Tzingounis and Wadiche 2007). Last, EAAT1 and EAAT2 exhibit similar *translocation and turnover rates*, which are inversely proportional to the time

it takes for the transporters to move glutamate across the membrane and re-orient themselves in the lipid bilayer, ready to bind other glutamate molecules in the extracellular space (Wadiche and Kavanaugh 1998; Tzingounis and Wadiche 2007). It is interesting to note that the rate at which EAAT1 and EAAT2 bind glutamate (i.e., the *binding rate*) is similar to the rate of glutamate binding to ionotropic AMPA and NMDA receptors (i.e., 10^6 – $10^7 \text{ M}^{-1} \text{ s}^{-1}$) (Wadiche and Kavanaugh 1998). For this reason, one may be tempted to think that astrocytic glutamate transporters and neuronal glutamate receptors compete with each other for binding synaptically released glutamate. This would actually happen if glutamate transporters in astrocytes and glutamate receptors in neurons had similar expression levels at a given distance from an active synapse. However, there are no astrocytic glutamate transporters within the synaptic cleft and a few perisynaptic neuronal glutamate transporters (He et al. 2000; Holmseth et al. 2012). In contrast, there are many more astrocyte glutamate transporters than neuronal glutamate receptors in the extrasynaptic region (Danbolt 2001). This means that glutamate preferentially binds to neuronal receptors as it diffuses within the synaptic cleft and is largely bound by astrocytic transporters as it spills out of the synaptic cleft (Barbour 2001; Scimemi and Beato 2009; Rusakov and Kullmann 1998b) (Fig. 12.1). The rapid glutamate binding rate and high level of expression of astrocyte glutamate transporters put them in an ideal position to rapidly quench the extracellular glutamate concentration and limit extrasynaptic glutamate receptor activation (Zheng et al. 2008). Despite this, the probability of glutamate binding to extrasynaptic receptors is not null (it's just low!). In fact, numerous studies have shown that extrasynaptic glutamate spillover can be detected by specific subtypes of NMDA and metabotropic glutamate receptors and is involved in regulating the magnitude and direction of long-term changes in synaptic strength (Scimemi et al. 2004, 2009; Asztely et al. 1997; Huang et al. 2004).

Not all glutamate molecules that bind to astrocytic glutamate transporters are ultimately moved across the membrane, toward the cell cytoplasm: Many of them are released back in the extracellular space (Bergles et al. 2002) (Fig. 12.1). The proportion of glutamate molecules that are actually moved across the membrane over the ones that are initially bound by the transporters is known as the *capture efficiency*. The capture efficiency of EAAT1 and EAAT2 is only 50% (Bergles et al. 2002; Wadiche and Kavanaugh 1998; Tzingounis and Wadiche 2007). This means that there is a significant proportion of glutamate molecules that are only transiently bound by the transporters and is eventually released back into the extracellular space. This low capture efficiency that allows glutamate transporters to act as *buffers* (i.e., transient traps) for glutamate. As counterintuitive as this may sound, by acting as buffers, glutamate transporters can *prolong* the lifetime of synaptically released glutamate in the extracellular space (Scimemi et al. 2009). That is to say, due to the low capture efficiency of transporters, glutamate persists in the extracellular space for a longer time than it would if the capture efficiency of astrocyte glutamate transporters was 100%. Glutamate unbinding from glutamate transporters is unlikely to activate neuronal receptors. This is because the high density of expression of glutamate transporters in astrocytes makes glutamate more likely to bind to them as opposed to extrasynaptic neuronal glutamate receptors.

The *translocation rate* at which glutamate is moved across the membrane and transported from the extracellular space toward the astrocytic cytoplasm ($\sim 2,000\text{ s}^{-1}$) is slower than the glutamate binding rate to the transporters ($\sim 6 \times 10^6\text{ M}^{-1}\text{ s}^{-1}$). The *turnover rate*, representing the rate at which glutamate transporters re-orient themselves across the membrane, is even slower ($\sim 40\text{ s}^{-1}$). This means that it takes a longer time to get rid of glutamate from the extracellular space than to release it and let it diffuse through the synaptic cleft (less than 1 ms) (Bergles et al. 2002; Wadiche and Kavanaugh 1998; Mennerick et al. 1999; Watzke et al. 2000; Grewer et al. 2000). The ability of glutamate transporters to rapidly influence the time course of excitatory synaptic transmission is heavily influenced by the fact that these molecules have a fast glutamate binding rate, act as buffers, and have high expression levels in astrocytes (Tzingounis and Wadiche 2007).

All these steps, including glutamate binding and unbinding from the transporters, translocation, and re-orientation in the cell membrane are energy demanding. They involve the molecular reorganization of chemical bonds within the glutamate transporter protein and eventually the translocation of glutamate against an unfavorable transmembrane concentration gradient that keeps the steady-state astrocytic glutamate concentration in the cytoplasm at $\sim 100\text{ nM}$ (Attwell et al. 1993) and the extracellular glutamate concentration at $\sim 25\text{ nM}$ (Herman and Jahr 2007). The energy supply for these demanding tasks is not supported by any hydrolytic activity of glutamate transporters. Instead, it relies on the activity of *primary active transporters* including the Na^+/K^+ -ATPase and the H^+ -pump, which establish an electrochemical gradient for Na^+ , H^+ and K^+ ions that are co-transported with glutamate across the cell membrane (Fig. 12.2). The energy accumulated in the form of the electrochemical gradients for these ions is harnessed by glutamate transporters and used to support glutamate binding and translocation, as well as transporter re-orientation in the astrocytic membrane. For this reason, glutamate transporters are called *secondary active transporters*: they do not hydrolyze ATP themselves, but they rely on the energy of the electrochemical gradients established by other primary transporters through the hydrolysis of ATP.

The translocation of one glutamate molecule toward the astrocytic cytoplasm is coupled to the movement of a fixed number of Na^+ , H^+ , and K^+ ions across the membrane, according to the scheme $1\text{Glutamate}^-:3\text{Na}^+:1\text{H}^+:1\text{K}^+$ (i.e., glutamate transport is *stoichiometrically* coupled to the movement of Na^+ , H^+ , K^+ ions) (Fig. 12.2) (Zerangue and Kavanaugh 1996). While glutamate is transported toward the cytoplasm, the other ions move in the direction dictated by their electrochemical gradient: typically, Na^+ and H^+ move toward the astrocytic cytoplasm, whereas K^+ moves toward the extracellular space (Zerangue and Kavanaugh 1996). Although a number of kinetics schemes have been proposed to describe the ionic coupling of glutamate transport (Bergles et al. 2002; Barbour 2001), the exact sequence in which different ions bind to the transporters has not yet been fully established. For example, it is unclear whether one or two Na^+ ions bind before glutamate and whether this precedes or follows H^+ binding to the transporter. Since the lumen of neurotransmitter-containing synaptic vesicles is acidic ($\text{pH} = 5.5$), glutamate release has been suggested to facilitate glutamate binding to transporters. This would happen

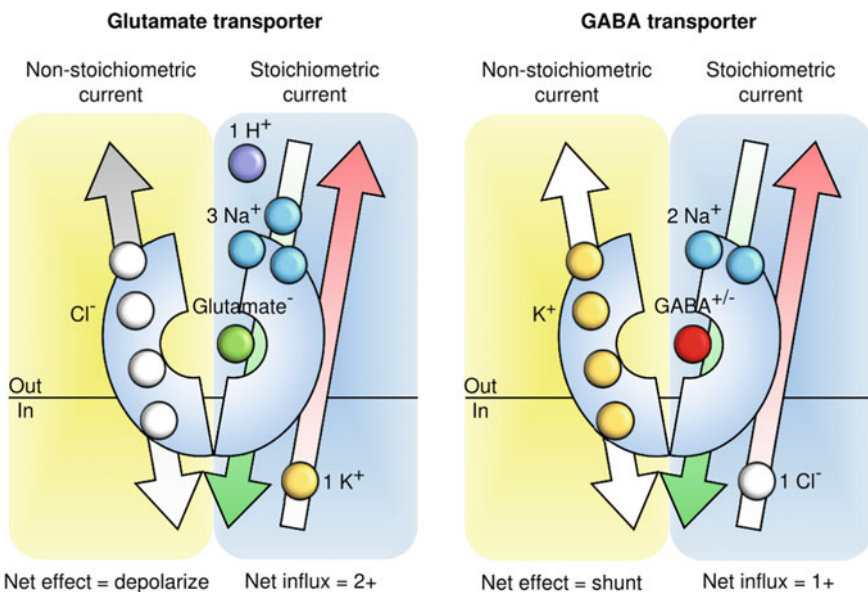


Fig. 12.2 Ionic currents associated with glutamate and GABA transport. Schematic representation of ionic currents stoichiometrically coupled and uncoupled to glutamate and GABA transport. Glutamate uptake is driven by the translocation of three Na^+ ions and one H^+ toward the astrocyte cytoplasm and the countertransport of one K^+ ion. The stoichiometrically uncoupled anionic current is driven by Cl^- . The driving force for this current (DF), determined by the resting membrane potential ($V_r \sim -90 \text{ mV}$) and the reversal potential for Cl^- in the astrocyte ($E_{\text{Cl}} \sim -60 \text{ mV}$) favors the movement of Cl^- toward the extracellular space ($\text{DF} = V_r - E_{\text{Cl}} = -30 \text{ mV}$). Its net effect is to transiently depolarize the membrane potential of the cell. GABA uptake is stoichiometrically coupled to the influx of two Na^+ ions and one Cl^- ion. For GABA transporters, the stoichiometrically uncoupled cationic current is carried by K^+ ions. The astrocytic resting membrane potential ($V_r \sim -90 \text{ mV}$) is similar to the reversal potential for K^+ ($E_K \sim -90 \text{ mV}$). Therefore, the driving force for this current is close to 0 mV ($\text{DF} = V_r - E_K = 0 \text{ mV}$). However, this current can exert an important functional role by transiently reducing the membrane resistance of the astrocyte, acting as a shunt

if protons released in the extracellular space bound to glutamate transporters before glutamate itself (Tzingounis and Wadiche 2007).

Glutamate binding to transporters also triggers the activation of a stoichiometrically uncoupled anionic current. Under physiological conditions, this anionic current is carried by Cl^- ions and has a single-channel conductance of $\sim 1 \text{ pS}$ (Fig. 12.2) (Wadiche et al. 1995; Wadiche and Kavanaugh 1998; Otis and Kavanaugh 2000). The stoichiometrically coupled and uncoupled anion currents are independent of one another within each transporter subunit (Grewer et al. 2005; Koch and Larsson 2005; Koch et al. 2007). In comparison with the stoichiometric current, the rise and decay time of the non-stoichiometric anion current are two times slower (Bergles et al. 2002). Recent studies shed light on the permeation paths for both the stoichiometrically coupled and uncoupled currents. Nonetheless, while the physiological relevance of the stoichiometric current is to shape glutamate clearance, that of the uncoupled

anion current in astrocytes remains elusive (Reyes et al. 2009). One exception is represented by retinal synapses, where the non-stoichiometric anion current mediated by presynaptic neuronal glutamate transporters is suggested to reduce neuronal excitability (Picaud et al. 1995; Palmer et al. 2003; Veruki et al. 2006; Wersinger et al. 2006).

12.3 What Do Glutamate Transporter Currents Tell Us About Glutamate Clearance?

The entire process of glutamate transport is electrogenic, because it is coupled with the movement of different ions across the astrocytic membrane, with a net influx of two positive charges per transport cycle (Fig. 12.2) (Zerangue and Kavanaugh 1996). The electrogenic nature of the stoichiometric component of the glutamate transporter current allows it to be recorded experimentally, by performing whole-cell patch-clamp recordings from astrocytes (Bergles and Jahr 1997, 1998; Diamond et al. 1998; Hanson et al. 2015). The stoichiometric current can be isolated from other currents generated in astrocytes that are not stoichiometrically coupled to glutamate transport. For example, one can patch an astrocyte in the presence of drugs that block neurotransmitter receptors and under conditions that do not allow the anionic current to be detected. Under these conditions, the stoichiometric current is the current sensitive to broad-spectrum glutamate transporter antagonists like TBOA (Bergles and Jahr 1997). Ba²⁺, a divalent cation that acts as an antagonist of inward rectifier K⁺ channels abundantly expressed in astrocytes, can be used to block K⁺ currents in astrocytes. The caveat with this approach is that, once applied extracellularly, Ba²⁺ can also alter the profile of the stoichiometric transporter current (Afzalov et al. 2013) and the properties of synaptic transmission by permeating through voltage-gated Ca²⁺ channels (De Saint Jan and Westbrook 2005; Newman 1993). The good news is that the stoichiometric glutamate transporter current and the leak K⁺ current can also be separated from each other without recurring to drugs, by using a specific analytical approach. This strategy relies on experimental evidence collected at facilitating hippocampal Schaffer collateral synapses, showing that the kinetics of the facilitated portion of the stoichiometric transporter current is similar to that of the stoichiometric component of the transporter current isolated pharmacologically with TBOA (Diamond 2005). The isolation of the stoichiometric current has been instrumental to derive the lifetime of synaptically released glutamate in the extracellular space, commonly referred to as *glutamate clearance*. It has also been used to identify developmental changes in the glutamate uptake capacity of the brain neuropil (Diamond 2005). Last, it has allowed to understand how neuronal glutamate transporters shape synaptic transmission and plasticity at Schaffer collateral, hippocampal synapses (Scimemi et al. 2009).

Because of its importance, in the last part of this section, I describe the analytical method to estimate the time course of glutamate clearance from astrocytic membranes using the stoichiometric component of astrocyte glutamate transporter currents.

Due to their kinetics and high expression, in the rodent hippocampus, astrocytic glutamate transporters are far from being saturated during single and repeated synaptic events. This means that, in the rodent hippocampus, glutamate transporters operate in a *linear regime*, whereby increasing the concentration of glutamate at the astrocytic membrane leads to a progressive increase in the amplitude of the stoichiometric transporter current without altering its kinetics (Diamond 2005). In contrast, increasing the number of glutamate transporters on the astrocytic membrane speeds the time course (i.e., rise and mostly decay time) of the stoichiometric transporter current and the lifetime of glutamate in the extracellular space (Diamond 2005). In mathematical terms, the presence of a linear relationship between the lifetime of extracellular glutamate and the time course of the stoichiometric transporter current can be expressed using an operation called convolution (*), whereby

$$\text{Stoichiometric transporter current} = \frac{\text{Extracellular glutamate lifetime}}{\text{Temporal distortion factor}} * \text{Filter}(t) \quad (12.1)$$

This expression allows us to describe the stoichiometric transporter current as the convolution of the extracellular glutamate lifetime with a temporal distortion factor. If we denote $\text{TC}(t)$ as the time course of the stoichiometric transporter current (which can be experimentally measured as the centroid of the stoichiometric transporter current, $\langle t \rangle$), in the time domain, Eq. 12.1 corresponds to:

$$\text{TC}(t) = \text{Clearance}(t) * \text{Filter}(t) \quad (12.2)$$

and

$$\text{Clearance}(t) * \text{Filter}(t) = \int \text{Clearance}(t') \cdot \text{Filter}(t - t') dt' \quad (12.3)$$

In this formula, $\text{Clearance}(t)$ represents the time course of the glutamate lifetime at the astrocytic membrane and $\text{Filter}(t)$ represents the distortion factors (including but not limited to the passive membrane properties of astrocytes) that convert the brief event of glutamate clearance into the slower $\text{TC}(t)$, which typically lasts a few milliseconds at room temperature (Diamond 2005; Scimemi and Diamond 2013). Therefore, according to Eq. 12.2, the time course of the stoichiometrically coupled transporter current corresponds to the convolution of the time course of glutamate clearance with the time course of the filter. Given that $\text{TC}(t)$ can be experimentally measured, we can use Eq. 12.2 to estimate $\text{Clearance}(t)$, which represents the time course of glutamate clearance from the extracellular space, analogous to the lifetime of glutamate at astrocytic membranes. To do this, we need to deconvolve the time course of $\text{Filter}(t)$ from the time course of $\text{TC}(t)$. This operation is not easily performed in the time domain. On the other hand, in the frequency domain, one may recall that the Fourier transform ($\mathcal{F}[\cdot]$) of the convolution of two functions is the product of the Fourier transforms of these functions. Therefore, in the frequency domain, Eq. 12.2 can be rewritten as:

$$\mathcal{F}[\text{TC}(t)] = \mathcal{F}[\text{Clearance}(t)] \cdot \mathcal{F}[\text{Filter}(t)] \quad (12.4)$$

In this way, the estimate of *Clearance(t)* breaks down to a three-step procedure. *First*, we calculate the Fourier transforms of $\text{TC}(t)$ and $\text{Filter}(t)$, which is easily achieved by available software for scientific computation by fast Fourier transform. *Second*, we calculate their point-wise ratio and estimate *Clearance(t)* according to Eq. 12.3. *Third*, we calculate the inverse (fast) Fourier transform of this ratio to obtain *Clearance(t)* (Scimemi and Diamond 2013). The main limitation to use this approach to calculate *Clearance(t)* is that we do not know the time course of the *Filter(t)*. One way out of this conundrum is to assume that *Filter(t)* does not differ in control conditions and in the presence of low concentrations of TBOA, used to prolong $\text{TC}(t)$ without blocking it. If $\text{Filter}(t) = \text{Filter}(t)_{\text{TBOA}}$, we know have to calculate $\text{Filter}(t)_{\text{TBOA}}$ (Fig. 12.3). When the astrocytic glutamate uptake capacity is low (i.e., in the presence of a low concentration of TBOA), $\text{Clearance}(t)_{\text{TBOA}}$ is slow and dominates the time course of $\text{TC}(t)_{\text{TBOA}}$. For this reason, we can approximate $\text{Clearance}(t)_{\text{TBOA}}$ with an instantaneously rising function (mimicking the instantaneous release of glutamate) that decays with the same decay time of $\text{TC}(t)_{\text{TBOA}}$. Once we have information on $\text{TC}(t)_{\text{TBOA}}$ and $\text{Clearance}(t)_{\text{TBOA}}$, we can easily obtain $\text{Filter}(t)_{\text{TBOA}}$ by deconvolving $\text{Clearance}(t)_{\text{TBOA}}$ from $\text{TC}(t)_{\text{TBOA}}$. Since $\text{Filter}(t) = \text{Filter}(t)_{\text{TBOA}}$, we can derive *Clearance(t)* by deconvolving *Filter(t)* from $\text{TC}(t)$, the stoichiometric transporter current in control conditions (Fig. 12.3) (Diamond 2005; Scimemi and Diamond 2013).

Although this analytical approach allows deriving the waveform that describes the onset and decay of glutamate clearance from astrocytes, it does not give us information on the actual amount of glutamate released by synapses and bound by the transporters. This is because there are inaccuracies when estimating the peak of glutamate clearance, due to space clamp errors and asynchronous release of glutamate across multiple synapses. In contrast, information on the *duration* of glutamate clearance is extremely accurate. The duration of glutamate clearance can be quantified as the centroid ($\langle t \rangle$) of $\text{TC}(t)$, which is computed as the ratio of the first moment of $\text{TC}(t)$ to its area:

$$\langle t \rangle_{\text{TC}} = \frac{\int t \cdot \text{TC}(t) dt}{\int \text{TC}(t) dt} \quad (12.5)$$

One interesting property of centroids is that they sum under convolution. Accordingly, it follows from Eq. 12.2 that:

$$\langle t \rangle_{\text{TC}} = \langle t \rangle_{\text{Clearance}} + \langle t \rangle_{\text{Filter}} \quad (12.6)$$

This expression is particularly useful to validate the accuracy of the deconvolution procedure based on Eq. 12.2. If the deconvolution is accurate, then the sum of the centroid of glutamate clearance and of the filter must match the experimentally measured centroid for the stoichiometric transporter current.

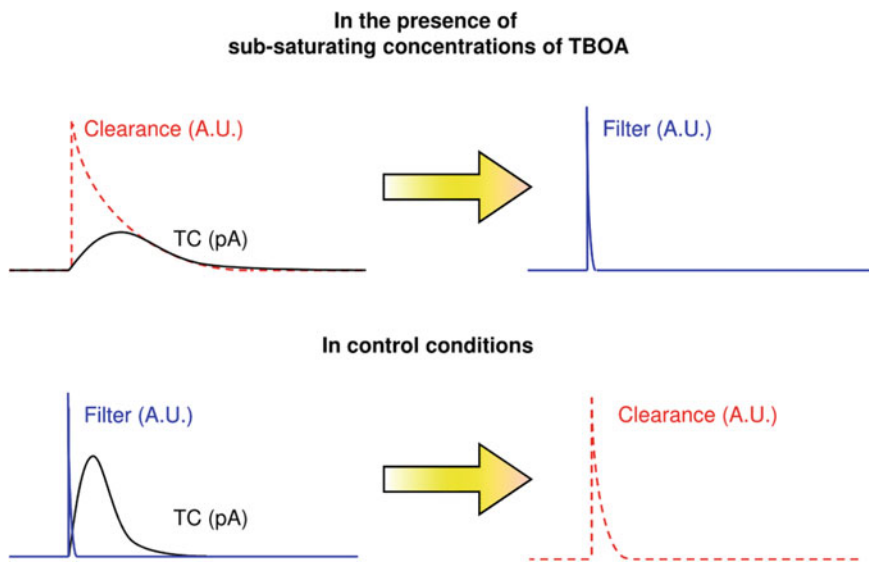


Fig. 12.3 Transporter currents provide information on the time course of glutamate clearance from astrocytes. The scheme represents the analytical steps required to derive the time course of glutamate clearance through deconvolution analysis of transporter currents (TCs) recorded in control conditions (*bottom*) and in the presence of a small, sub-saturating concentration of the broad spectrum, glutamate transporter antagonist TBOA (*top*). Under these sub-saturating conditions, the decay time of glutamate clearance can be approximated as the decay time of the TC. The clearance and TC waveforms in TBOA are deconvolved to derive the filter, which represents the distortion factor that converts a brief event like clearance into a slower waveform like the TC. The analysis works under the assumption that the kinetic properties of the filter do not change between sub-saturating TBOA and control conditions. Therefore, by deconvolving the filter from the TC recorded in control conditions, it is possible to derive the time course of glutamate clearance in control conditions. The derived clearance waveform provides important information on the efficiency with which synaptically released glutamate is cleared from the extracellular space in a variety of experimental conditions, in different brain regions and at different stages of development. For references and applications, see (Scimemi et al. 2009; Diamond 2005; Scimemi and Diamond 2013; Sweeney et al. 2017)

To conclude, the ensemble of Eqs. 12.1–12.6 provide a valuable tool to extract information on the lifetime of glutamate at astrocytic membranes, and therefore on its clearance, in a variety of experimental conditions aimed at reproducing physiological and pathological states (Scimemi et al. 2013).

12.4 Neurotransmitter Uptake: GABA Transporters

The general operational principles of transporter function described above for glutamate transporters are largely shared by transporters for other small neurotransmitter

molecules, including GABA. The GABA transporter type most abundantly expressed in astrocytes is GAT3, but there are still uncertainties on its surface density of expression (Minelli et al. 1996; Ribak et al. 1996). Although GAT3 is exclusively localized in astrocytic processes in mice, it is also expressed in oligodendrocytes in the brain of humans, cats, and monkeys (Melone et al. 2005; Pow et al. 2005). As for glutamate transporters, GABA transport via GAT3 is an active process not directly coupled to the hydrolysis of ATP and requires the presence of an electrochemical gradient for Na^+ , which is typically established by the Na^+/K^+ ATPase. The most accredited stoichiometry of mammalian GABA transporters is a co-transport of 1GABA:2 Na^+ :1 Cl^- (Radian and Kanner 1983; Kavanaugh et al. 1992; Mager et al. 1993; Hilgemann and Lu 1999). Since GABA is a zwitterion, this leads to a net influx of one positive charge per GABA transport cycle (Fig. 12.2). The movement of Cl^- is suggested to occur in a reaction step that is distinct but thermodynamically coupled to the translocation of GABA and Na^+ across the membrane, while the transporters are in a conformational state that allows them to take up GABA and Na^+ (Bicho and Grewer 2005). Therefore, the entire transport cycle consists of three steps: rapid binding and translocation of GABA and Na^+ , slower intracellular dissociation of GABA and Na^+ , and rapid Cl^- exchange (Bicho and Grewer 2005).

There are different estimates for the translocation rate of GABA and co-transported ions across the membrane, and they have all been established for GAT1, the most abundant GABA transporter in the brain, prevalently expressed in neurons. Early estimates at 22 °C suggested turnover rates for GAT1 of 2.5–13 s⁻¹ at -60/-80 mV (Mager et al. 1993; Bicho and Grewer 2005; Radian et al. 1986; Eckstein-Ludwig et al. 1999; Liu et al. 1998). More recent estimates at 37 °C suggest turnover rates of 73–93 s⁻¹ at -50/-90 mV, much higher values than would be predicted by correcting the earlier rates for the Q_{10} temperature coefficient value of 2.8 (Gonzales et al. 2007). This discrepancy may be attributed to methodological differences, as the latter estimates were obtained using correlative freeze-fracture and electrophysiology experiments.

GABA binding to the transporter gates at least two more currents that are stoichiometrically uncoupled from the translocation of GABA, Na^+ , and Cl^- across the membrane. These include an agonist-induced Na^+ inward current (Risso et al. 1996) and an agonist-independent leak cationic current carried by alkali ions (Fig. 12.2) (Cammack and Schwartz 1996). The contribution of the leak current to the total current generated by GABA transporters is modest, and this current is inhibited by intracellular Na^+ concentrations that are typically found in the cytosol of living cells ($K_i = 3 \text{ mM}$).

The ability of GABA transporters to act both as ion channels and translocating molecules is reminiscent of the mechanisms of action of glutamate transporters previously described (Wadiche et al. 1995). The stoichiometric current is inwardly directed for GABA and glutamate transporters (Fig. 12.2). However, the agonist-induced, stoichiometrically uncoupled current is cationic (and often shunting) in GABA transporters and anionic (and often hyperpolarizing) in glutamate transporters. As for the stoichiometrically uncoupled glutamate transporter current, the functional role of the analogous current generated by GABA transporters in astrocytes is not known. The latest insights into the structural properties of GABA transporters are based on the

crystal structure of LeuT_{Aa}, a bacterial homolog from *Aquifex aeolicus* (Yamashita et al. 2005), which holds the promise of providing additional details on the molecular events underlying the process of GABA transport.

12.5 The Energetic Budget of Astrocyte Metabolism: Consumption and Production

Uptake of neurotransmitters, together with maintenance and restoration of ionic gradients dissipated by the uptake process, are major energy-demanding processes for astrocytes, though hardly the only ones (Attwell and Laughlin 2001; Lennie 2003). The ongoing activity of astrocytes also includes regulation of intracellular signaling pathways, generation of Ca²⁺ waves, and clearance of extracellular K⁺. The main source of energy to support all these processes is glucose, which is present in the systemic circulation and can easily cross the blood–brain barrier. Astrocytes and neurons metabolize glucose through (i) glycolytic, (ii) pentose phosphate-mediated, and (iii) oxidative pathways (Fig. 12.4). In the glycolytic pathway, two molecules of ATP are produced as glucose is converted into pyruvate which, under low oxygen tension, is converted into lactate to regenerate NAD⁺ and sustain glycolysis (Magistretti and Allaman 2015). The pentose phosphate pathway uses glucose as a source of NADPH and 5-carbon sugars (Fig. 12.4). The glycolytic and pentose phosphate pathways both take place in the cytosol. In contrast, the oxidative pathway involves oxidation of glucose and of its metabolites, pyruvate and lactate, to produce ATP and takes place in the mitochondria.

Astrocytes, differently from neurons, store energy in the form of glycogen, which they use in the process of glycogenolysis. All the activities carried out by astrocytes at rest account for 30% of the oxidative and 50% of the glycolytic metabolism of the entire brain (Hertz et al. 2007; Mangia et al. 2009). The relevance of these processes for the entire energy demand of the astrocyte, however, varies across distinct subcellular domains. The fine membrane protrusions in contact with synaptic appositions account for 40% of the astrocyte volume and 80% of its surface area, but are too small to accommodate mitochondria. Their energy demand is supported by glycolysis, glycogenolysis, and intracellular diffusion of ATP and phosphocreatine (Hertz et al. 2007; Mangia et al. 2009). During activation, for example in response to neurotransmitter release in the extracellular space, the energy demand of the peripheral astrocytic processes increases with respect to that of the cell body and leads to a disproportionate increase in glucose utilization with respect to oxidative metabolism (Hertz et al. 2007). Therefore, glycolysis is the major energy-forming pathway in astrocytes (Belanger et al. 2015; Hyder et al. 2006; Zhang et al. 2014). One of the reasons for the low oxidative metabolism of astrocytes is that the enzyme pyruvate dehydrogenase (PDH), responsible for the entry of pyruvate in the TCA (Krebs) cycle, is maintained in a highly phosphorylated and less active state, because of the high expression of the enzyme pyruvate dehydrogenase kinase 4 (PDK4) in

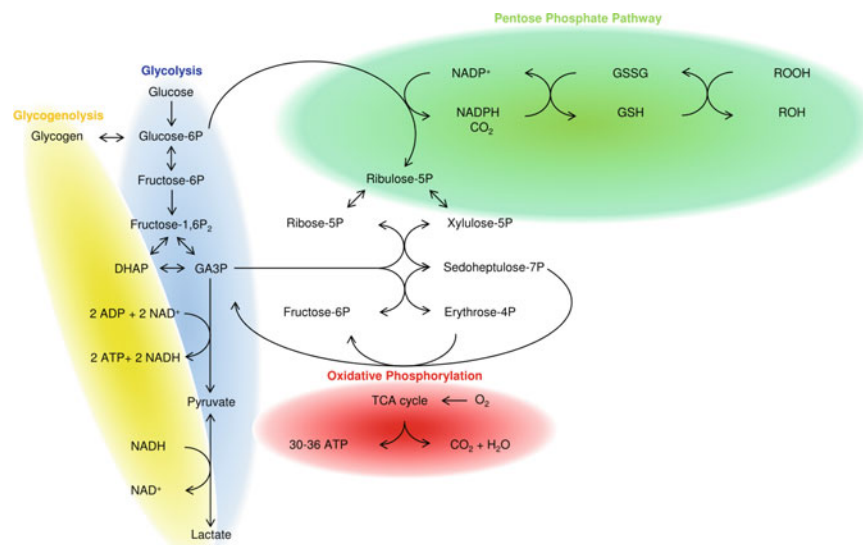


Fig. 12.4 Biochemical pathways of energy production and storage. Glycogen is the main form of energy storage, and glucose is the main ready-to-use form of energy supply for astrocytes. Glucose is transported across the cell membrane by glucose transporters. It is then phosphorylated to produce glucose-6-phosphate, which can be metabolized through glycolysis (blue), generating ATP, NADH and two molecules of pyruvate, which can enter mitochondria to be metabolized through the tricarboxylic acid cycle and oxidative phosphorylation (red). Under hypoxic conditions, pyruvate can be converted into lactate and released in the extracellular space. Glucose-6P can also be processed through the pentose phosphate pathway (green), which leads to the production of NADPH used against oxidative stress through the metabolism of glutathione. In astrocytes, glucose-6P can also be stored as glycogen, which can then be used through the glycogenolysis pathway (yellow)

astrocytes (Zhang et al. 2014; Halim et al. 2010). In agreement with these findings, PDH dephosphorylation results in increased glucose oxidation and decreased lactate production in astrocytes (Itoh et al. 2003). Another enzyme that acts as a key regulator of glycolysis is pyruvate kinase (PK), which is present in two different isoforms in neurons and astrocytes (PKM1 and PKM2, respectively). Interestingly, it is only PKM2 that can up-regulate the glycolytic flux in response to increased energy demands, an aspect that accounts, at least in part, for the ability of astrocytes to metabolize glucose through the glycolytic pathway. Astrocytes also express high levels of glyoxalase 1 and 2, enzymes that are involved in the degradation of methylglyoxal, one of the by-products of glycolysis. This allows astrocytes to support high levels of glycolysis without incurring into methylglyoxal-induced toxicity (Belanger et al. 2011). Aerobic glycolysis in astrocytes can be triggered by the energy costs associated with neuronal glutamate release and astrocytic glutamate uptake, through a chain of events leading to activation of the astrocyte–neuron lactate shuttle (ANLS) (Pellerin and Magistretti 1994). Briefly, the stoichiometric translocation of three Na⁺ ions and one K⁺ ion by astrocytic glutamate transporters partially dissipates the

electrochemical gradient for these ions across the cell membrane. The baseline Na^+ and K^+ concentration is re-established by the Na^+/K^+ -ATPase, a primary active transporter that extrudes three Na^+ ions and imports two K^+ at the cost of one molecule of ATP. Once in the astrocytic cytoplasm, glutamate is converted into glutamine, which is then delivered to neurons through the glutamate–glutamine cycle. The process of converting glutamate to glutamine also occurs at the cost of one molecule of ATP.

The glutamate–glutamine cycle allows a large portion of glutamate released through synaptic transmission to be delivered back to neurons, which use it to replenish neurotransmitter vesicles (Bak et al. 2006; McKenna 2007; Stobart and Anderson 2013) (Fig. 12.1). The remaining glutamate that is taken up by astrocytes but is not been converted into glutamine enters the TCA cycle after being converted into α -ketoglutarate (Bak et al. 2006; McKenna 2007; Stobart and Anderson 2013). The glutamate–glutamine cycle increases the energy demand for astrocytes, while the TCA cycle promotes glucose uptake, which is used for glycolysis and therefore for the production of ATP and lactate (Mangia et al. 2009, 2011). The lactate molecules produced by astrocytes are released in the extracellular space and taken up by neurons through monocarboxylate transporters (MCT1 and MCT4 in astrocytes, MCT2 in neurons) (Belanger et al. 2011). In turn, neurons use lactate to fuel the energetic costs of synaptic transmission, although to a much lesser extent than glucose. Accordingly, once is taken up by neuron, lactate is converted into pyruvate and oxidized it in the mitochondria to produce ATP (Pellerin and Magistretti 1994). The ANLS hypothesis, originally proposed based on experimental evidence by Pellerin and Magistretti (Pellerin and Magistretti 1994), has also been supported by modeling studies of brain energy metabolism (Aubert and Costalat 2005; Aubert et al. 2007; Jolivet et al. 2009). However, the validity of the ANLS hypothesis has been recently questioned by modeling studies proposing the existence of a neuron–astrocyte lactate shuttle (NALS) (Mangia et al. 2011; DiNuzzo et al. 2010; Simpson et al. 2007), sparkling some questions on the directionality of the lactate flow during brain activity (Mangia et al. 2011; Jolivet et al. 2010).

In contrast to glycolysis, glycogenolysis is essential for astrocytes in response to increasing energy demands. Glycogen, the storage form of glucose metabolized by astrocytes, is mobilized during periods of prolonged activity (Obel et al. 2012; Dienel et al. 2002), in response to sensory stimulation (Swanson et al. 1992; Cruz et al. 2005) and also to release of neurotransmitters like noradrenaline (NA) and vasoactive intestinal peptide (VIP) (Magistretti et al. 1981), and neuromodulators like adenosine and ATP (Sorg and Magistretti 1991; Sorg et al. 1995). Increasing extracellular K^+ increases glycogen utilization (Hof et al. 1988) which, in turn, fuels astrocytic K^+ uptake in response to neuronal activity (Xu et al. 2013). The fact that inhibiting glycogenolysis abolishes K^+ uptake in cultured astrocytes and that K^+ uptake cannot be rescued by glucose (Xu et al. 2013; Choi et al. 2012) suggest the existence of fine regulatory mechanisms that make glycogen capable of exerting a specific control of extracellular K^+ sequestration by astrocytes.

12.6 Concluding Remarks

Taken together, the data presented in this chapter indicate that astrocytes play a number of functional roles that are essential to couple synaptic activity with glucose metabolism through the activity of glutamate transporters. This metabolic coupling between neurons and astrocytes seems to be specific for glutamatergic transmission, because GABA uptake in astrocytes does not change the levels of glucose or ATP in the brain (Mangia et al. 2009; Chatton et al. 2003). Based on these findings, astrocytes emerge key regulators of brain activity, not only by virtue of their role as homeostatic regulators of extracellular glutamate/GABA concentrations but also because, via glutamate uptake, they tweak the energetic budget of the entire brain.

References

- Afzalov R, Pryazhnikov E, Shih PY, Kondratskaya E, Zobova S, Leino S et al (2013) Low micromolar Ba(2+) potentiates glutamate transporter current in hippocampal astrocytes. *Front Cell Neurosci* 7:135
- Akyuz N, Altman RB, Blanchard SC, Boudker O (2013) Transport dynamics in a glutamate transporter homologue. *Nature* 502(7469):114–118
- Asztely F, Erdemli G, Kullmann DM (1997) Extrasynaptic glutamate spillover in the hippocampus: dependence on temperature and the role of active glutamate uptake. *Neuron* 18(2):281–293
- Attwell D, Laughlin SB (2001) An energy budget for signaling in the grey matter of the brain. *J Cereb Blood Flow Metab* 21(10):1133–1145
- Attwell D, Barbour B, Szatkowski M (1993) Nonvesicular release of neurotransmitter. *Neuron* 11(3):401–417
- Attwell D, Buchan AM, Charpak S, Lauritzen M, Macvicar BA, Newman EA (2010) Glial and neuronal control of brain blood flow. *Nature* 468(7321):232–243
- Aubert A, Costalat R (2005) Interaction between astrocytes and neurons studied using a mathematical model of compartmentalized energy metabolism. *J Cereb Blood Flow Metab* 25(11):1476–1490
- Aubert A, Pellerin L, Magistretti PJ, Costalat R (2007) A coherent neurobiological framework for functional neuroimaging provided by a model integrating compartmentalized energy metabolism. *Proc Natl Acad Sci USA* 104(10):4188–4193
- Bak LK, Schousboe A, Waagepetersen HS (2006) The glutamate/GABA-glutamine cycle: aspects of transport, neurotransmitter homeostasis and ammonia transfer. *J Neurochem* 98(3):641–653
- Barbour B (2001) An evaluation of synapse independence. *J Neurosci* 21(20):7969–7984
- Bar-Peled O, Ben-Hur H, Biegon A, Groner Y, Dewhurst S, Furuta A et al (1997) Distribution of glutamate transporter subtypes during human brain development. *J Neurochem* 69(6):2571–2580
- Belanger M, Yang J, Petit JM, Laroche T, Magistretti PJ, Allaman I (2011) Role of the glyoxalase system in astrocyte-mediated neuroprotection. *J Neurosci* 31(50):18338–18352
- Belanger M, Allaman I, Magistretti PJ (2015) Brain energy metabolism: focus on astrocyte-neuron metabolic cooperation. *Cell Metab* 14(6):724–738
- Bergles DE, Jahr CE (1997) Synaptic activation of glutamate transporters in hippocampal astrocytes. *Neuron* 19(6):1297–308
- Bergles DE, Jahr CE (1998) Glial contribution to glutamate uptake at Schaffer collateral-commissural synapses in the hippocampus. *J Neurosci* 18(19):7709–7716
- Bergles DE, Tzingounis AV, Jahr CE (2002) Comparison of coupled and uncoupled currents during glutamate uptake by GLT-1 transporters. *J Neurosci* 22(23):10153–10162

- Bicho A, Grewer C (2005) Rapid substrate-induced charge movements of the GABA transporter GAT1. *Biophys J* 89(1):211–231
- Cammack JN, Schwartz EA (1996) Channel behavior in a gamma-aminobutyrate transporter. *Proc Natl Acad Sci USA* 93(2):723–727
- Chatton JY, Pellerin L, Magistretti PJ (2003) GABA uptake into astrocytes is not associated with significant metabolic cost: implications for brain imaging of inhibitory transmission. *Proc Natl Acad Sci USA* 100(21):12456–12461
- Chiu DN, Jahr CE (2017) Extracellular glutamate in the nucleus accumbens is nanomolar in both synaptic and non-synaptic compartments. *Cell Rep* 18(11):2576–2583
- Choi HB, Gordon GR, Zhou N, Tai C, Rungta RL, Martinez J et al (2012) Metabolic communication between astrocytes and neurons via bicarbonate-responsive soluble adenylyl cyclase. *Neuron* 75(6):1094–1104
- Clarke LE, Barres BA (2013) Emerging roles of astrocytes in neural circuit development. *Nat Rev Neurosci* 14(5):311–321
- Cruz NF, Lasater A, Zielke HR, Dienel GA (2005) Activation of astrocytes in brain of conscious rats during acoustic stimulation: acetate utilization in working brain. *J Neurochem* 92(4):934–947
- Danbolt NC (2001) Glutamate uptake. *Prog Neurobiol* 65(1):1–105
- De Saint Jan D, Westbrook GL (2005) Detecting activity in olfactory bulb glomeruli with astrocyte recording. *J Neurosci* 25(11):2917–2924
- DeSilva TM, Borenstein NS, Volpe JJ, Kinney HC, Rosenberg PA (2012) Expression of EAAT2 in neurons and protoplasmic astrocytes during human cortical development. *J Comp Neurol* 520(17):3912–3932
- Diamond JS (2005) Deriving the glutamate clearance time course from transporter currents in CA1 hippocampal astrocytes: transmitter uptake gets faster during development. *J Neurosci* 25(11):2906–2916
- Diamond JS, Bergles DE, Jahr CE (1998) Glutamate release monitored with astrocyte transporter currents during LTP. *Neuron* 21(2):425–433
- Dienel GA, Wang RY, Cruz NF (2002) Generalized sensory stimulation of conscious rats increases labeling of oxidative pathways of glucose metabolism when the brain glucose-oxygen uptake ratio rises. *J Cereb Blood Flow Metab* 22(12):1490–1502
- DiNuzzo M, Mangia S, Maraviglia B, Giove F (2010) Changes in glucose uptake rather than lactate shuttle take center stage in subserving neuroenergetics: evidence from mathematical modeling. *J Cereb Blood Flow Metab* 30(3):586–602
- Eckstein-Ludwig U, Fei J, Schwarz W (1999) Inhibition of uptake, steady-state currents, and transient charge movements generated by the neuronal GABA transporter by various anticonvulsant drugs. *Br J Pharmacol* 128(1):92–102
- Furuta A, Rothstein JD, Martin LJ (1997) Glutamate transporter protein subtypes are expressed differentially during rat CNS development. *J Neurosci* 17(21):8363–8375
- Gonzales AL, Lee W, Spencer SR, Oropeza RA, Chapman JV, Ku JY et al (2007) Turnover rate of the gamma-aminobutyric acid transporter GAT1. *J Membr Biol* 220(1–3):33–51
- Grewer C, Watzke N, Wiessner M, Rauen T (2000) Glutamate translocation of the neuronal glutamate transporter EAAC1 occurs within milliseconds. *Proc Natl Acad Sci USA* 97(17):9706–9711
- Grewer C, Balani P, Weidenfeller C, Bartusel T, Tao Z, Rauen T (2005) Individual subunits of the glutamate transporter EAAC1 homotrimer function independently of each other. *Biochemistry* 44(35):11913–11923
- Halim ND, McFate T, Mohyeldin A, Okagaki P, Korotchkina LG, Patel MS et al (2010) Phosphorylation status of pyruvate dehydrogenase distinguishes metabolic phenotypes of cultured rat brain astrocytes and neurons. *Glia* 58(10):1168–1176
- Hanson E, Armbruster M, Cantu D, Andresen L, Taylor A, Danbolt NC et al (2015) Astrocytic glutamate uptake is slow and does not limit neuronal NMDA receptor activation in the neonatal neocortex. *Glia*

- He Y, Janssen WG, Rothstein JD, Morrison JH (2000) Differential synaptic localization of the glutamate transporter EAAC1 and glutamate receptor subunit GluR2 in the rat hippocampus. *J Comp Neurol* 418(3):255–269
- Herman MA, Jahr CE (2007) Extracellular glutamate concentration in hippocampal slice. *J Neurosci* 27(36):9736–9741
- Hertz L, Peng L, Dienel GA (2007) Energy metabolism in astrocytes: high rate of oxidative metabolism and spatiotemporal dependence on glycolysis/glycogenolysis. *J Cereb Blood Flow Metab* 27(2):219–249
- Hilgemann DW, Lu CC (1999) GAT1 (GABA: Na^+ : Cl^-) cotransport function. Database reconstruction with an alternating access model. *J Gen Physiol* 114(3):459–475
- Hof PR, Pascale E, Magistretti PJ (1988) K^+ at concentrations reached in the extracellular space during neuronal activity promotes a Ca^{2+} -dependent glycogen hydrolysis in mouse cerebral cortex. *J Neurosci* 8(6):1922–1928
- Holmseth S, Dehnes Y, Huang YH, Follin-Arbelet VV, Grutle NJ, Mylonakou MN et al (2012) The density of EAAC1 (EAAT3) glutamate transporters expressed by neurons in the mammalian CNS. *J Neurosci* 32(17):6000–6013
- Huang YH, Sinha SR, Tanaka K, Rothstein JD, Bergles DE (2004) Astrocyte glutamate transporters regulate metabotropic glutamate receptor-mediated excitation of hippocampal interneurons. *J Neurosci* 24(19):4551–4559
- Hyder F, Patel AB, Gjedde A, Rothman DL, Behar KL, Shulman RG (2006) Neuronal-glial glucose oxidation and glutamatergic-GABAergic function. *J Cereb Blood Flow Metab* 26(7):865–877
- Itoh Y, Esaki T, Shimoji K, Cook M, Law MJ, Kaufman E et al (2003) Dichloroacetate effects on glucose and lactate oxidation by neurons and astroglia in vitro and on glucose utilization by brain in vivo. *Proc Natl Acad Sci USA* 100(8):4879–4884
- Jolivet R, Magistretti PJ, Weber B (2009) Deciphering neuron-glia compartmentalization in cortical energy metabolism. *Front Neuroenergetics* 1:4
- Jolivet R, Allaman I, Pellerin L, Magistretti PJ, Weber B (2010) Comment on recent modeling studies of astrocyte-neuron metabolic interactions. *J Cereb Blood Flow Metab* 30(12):1982–1986
- Kavanaugh MP, Arriza JL, North RA, Amara SG (1992) Electrogenic uptake of gamma-aminobutyric acid by a cloned transporter expressed in Xenopus oocytes. *J Biol Chem* 267(31):22007–22009
- Koch HP, Larsson HP (2005) Small-scale molecular motions accomplish glutamate uptake in human glutamate transporters. *J Neurosci* 25(7):1730–1736
- Koch HP, Brown RL, Larsson HP (2007) The glutamate-activated anion conductance in excitatory amino acid transporters is gated independently by the individual subunits. *J Neurosci* 27(11):2943–2947
- Lehre KP, Danbolt NC (1998) The number of glutamate transporter subtype molecules at glutamatergic synapses: chemical and stereological quantification in young adult rat brain. *J Neurosci* 18(21):8751–8757
- Lennie P (2003) The cost of cortical computation. *Curr Biol* 13(6):493–497
- Levy LM, Warr O, Attwell D (1998) Stoichiometry of the glial glutamate transporter GLT-1 expressed inducibly in a Chinese hamster ovary cell line selected for low endogenous Na^+ -dependent glutamate uptake. *J Neurosci* 18(23):9620–9628
- Liu Y, Eckstein-Ludwig U, Fei J, Schwarz W (1998) Effect of mutation of glycosylation sites on the Na^+ dependence of steady-state and transient currents generated by the neuronal GABA transporter. *Biochim Biophys Acta* 1415(1):246–254
- Mager S, Naeve J, Quick M, Labarca C, Davidson N, Lester HA (1993) Steady states, charge movements, and rates for a cloned GABA transporter expressed in Xenopus oocytes. *Neuron* 10(2):177–188
- Magistretti PJ, Allaman I (2015) A cellular perspective on brain energy metabolism and functional imaging. *Neuron* 86(4):883–901

- Magistretti PJ, Morrison JH, Shoemaker WJ, Sapin V, Bloom FE (1981) Vasoactive intestinal polypeptide induces glycogenolysis in mouse cortical slices: a possible regulatory mechanism for the local control of energy metabolism. *Proc Natl Acad Sci USA* 78(10):6535–6539
- Mangia S, Giove F, Tkac I, Logothetis NK, Henry PG, Olman CA et al (2009) Metabolic and hemodynamic events after changes in neuronal activity: current hypotheses, theoretical predictions and *in vivo* NMR experimental findings. *J Cereb Blood Flow Metab* 29(3):441–463
- Mangia S, DiNuzzo M, Giove F, Carruthers A, Simpson IA, Vannucci SJ (2011) Response to ‘comment on recent modeling studies of astrocyte-neuron metabolic interactions’: much ado about nothing. *J Cereb Blood Flow Metab* 31(6):1346–1353
- Marcaggi P, Attwell D (2004) Role of glial amino acid transporters in synaptic transmission and brain energetics. *Glia* 47(3):217–225
- McKenna MC (2007) The glutamate-glutamine cycle is not stoichiometric: fates of glutamate in brain. *J Neurosci Res* 85(15):3347–3358
- Melone M, Barbaresi P, Fattorini G, Conti F (2005) Neuronal localization of the GABA transporter GAT-3 in human cerebral cortex: a procedural artifact? *J Chem Neuroanat* 30(1):45–54
- Mennerick S, Shen W, Xu W, Benz A, Tanaka K, Shimamoto K et al (1999) Substrate turnover by transporters curtails synaptic glutamate transients. *J Neurosci* 19(21):9242–9251
- Milton ID, Banner SJ, Ince PG, Piggott NH, Fray AE, Thatcher N et al (1997) Expression of the glial glutamate transporter EAAT2 in the human CNS: an immunohistochemical study. *Brain Res Mol Brain Res* 52(1):17–31
- Minelli A, DeBiasi S, Brecha NC, Zuccarello LV, Conti F (1996) GAT-3, a high-affinity GABA plasma membrane transporter, is localized to astrocytic processes, and it is not confined to the vicinity of GABAergic synapses in the cerebral cortex. *J Neurosci* 16(19):6255–6264
- Newman EA (1993) Inward-rectifying potassium channels in retinal glial (Muller) cells. *J Neurosci* 13(8):3333–3345
- Obel LF, Muller MS, Walls AB, Sickmann HM, Bak LK, Waagepetersen HS et al (2012) Brain glycogen-new perspectives on its metabolic function and regulation at the subcellular level. *Front Neuroenergetics* 4:3
- Otis TS, Kavanagh MP (2000) Isolation of current components and partial reaction cycles in the glial glutamate transporter EAAT2. *J Neurosci* 20(8):2749–2757
- Owe SG, Marcaggi P, Attwell D (2006) The ionic stoichiometry of the GLAST glutamate transporter in salamander retinal glia. *J Physiol* 577(Pt 2):591–599
- Palmer MJ, Taschenberger H, Hull C, Tremere L, von Gersdorff H (2003) Synaptic activation of presynaptic glutamate transporter currents in nerve terminals. *J Neurosci* 23(12):4831–4841
- Parpura V, Verkhratsky A (2012a) The astrocyte excitability brief: from receptors to gliotransmission. *Neurochem Int* 61(4):610–621
- Parpura V, Verkhratsky A (2012b) Astrocytes revisited: concise historic outlook on glutamate homeostasis and signaling. *Croat Med J* 53(6):518–528
- Pellerin L, Magistretti PJ (1994) Glutamate uptake into astrocytes stimulates aerobic glycolysis: a mechanism coupling neuronal activity to glucose utilization. *Proc Natl Acad Sci USA* 91(22):10625–10629
- Picaud S, Larsson HP, Wellis DP, Lecar H, Werblin F (1995) Cone photoreceptors respond to their own glutamate release in the tiger salamander. *Proc Natl Acad Sci USA* 92(20):9417–9421
- Pow DV, Sullivan RK, Williams SM, Scott HL, Dodd PR, Finkelstein D (2005) Differential expression of the GABA transporters GAT-1 and GAT-3 in brains of rats, cats, monkeys and humans. *Cell Tissue Res* 320(3):379–392
- Radian R, Kanner BI (1983) Stoichiometry of sodium- and chloride-coupled gamma-aminobutyric acid transport by synaptic plasma membrane vesicles isolated from rat brain. *Biochemistry* 22(5):1236–1241
- Radian R, Bendahan A, Kanner BI (1986) Purification and identification of the functional sodium- and chloride-coupled gamma-aminobutyric acid transport glycoprotein from rat brain. *J Biol Chem* 261(33):15437–15441

- Reyes N, Ginter C, Boudker O (2009) Transport mechanism of a bacterial homologue of glutamate transporters. *Nature* 462(7275):880–885
- Ribak CE, Tong WM, Brecha NC (1996) GABA plasma membrane transporters, GAT-1 and GAT-3, display different distributions in the rat hippocampus. *J Comp Neurol* 367(4):595–606
- Risso S, DeFelice LJ, Blakely RD (1996) Sodium-dependent GABA-induced currents in GAT1-transfected HeLa cells. *J Physiol* 490(Pt 3):691–702
- Rusakov DA, Kullmann DM (1998a) Extrasynaptic glutamate diffusion in the hippocampus: ultrastructural constraints, uptake, and receptor activation. *J Neurosci* 18(9):3158–3170
- Rusakov DA, Kullmann DM (1998b) A tortuous and viscous route to understanding diffusion in the brain. *Trends Neurosci* 21(11):469–470
- Scimemi A, Beato M (2009) Determining the neurotransmitter concentration profile at active synapses. *Mol Neurobiol* 40(3):289–306
- Scimemi A, Diamond JS (2013) Deriving the time course of glutamate clearance with a deconvolution analysis of astrocytic transporter currents. *J Vis Exp* (78)
- Scimemi A, Fine A, Kullmann DM, Rusakov DA (2004) NR2B-containing receptors mediate cross talk among hippocampal synapses. *J Neurosci* 24(20):4767–4777
- Scimemi A, Tian H, Diamond JS (2009) Neuronal transporters regulate glutamate clearance, NMDA receptor activation, and synaptic plasticity in the hippocampus. *J Neurosci* 29(46):14581–14595
- Scimemi A, Meabon JS, Woltjer RL, Sullivan JM, Diamond JS, Cook DG (2013) Amyloid-beta1–42 slows clearance of synaptically released glutamate by mislocalizing astrocytic GLT-1. *J Neurosci* 33(12):5312–5318
- Simpson IA, Carruthers A, Vannucci SJ (2007) Supply and demand in cerebral energy metabolism: the role of nutrient transporters. *J Cereb Blood Flow Metab* 27(11):1766–1791
- Sorg O, Magistretti PJ (1991) Characterization of the glycogenolysis elicited by vasoactive intestinal peptide, noradrenaline and adenosine in primary cultures of mouse cerebral cortical astrocytes. *Brain Res* 563(1–2):227–233
- Sorg O, Pellerin L, Stoltz M, Beggah S, Magistretti PJ (1995) Adenosine triphosphate and arachidonic acid stimulate glycogenolysis in primary cultures of mouse cerebral cortical astrocytes. *Neurosci Lett* 188(2):109–112
- Sweeney AM, Fleming KE, McCauley JP, Rodriguez MF, Martin ET, Sousa AA et al (2017) PAR1 activation induces rapid changes in glutamate uptake and astrocyte morphology. *Sci Rep* 7:43606
- Stobart JL, Anderson CM (2013) Multifunctional role of astrocytes as gatekeepers of neuronal energy supply. *Front Cell Neurosci* 7:38
- Stogsdill JA, Eroglu C (2017) The interplay between neurons and glia in synapse development and plasticity. *Curr Opin Neurobiol* 42:1–8
- Swanson RA, Morton MM, Sagar SM, Sharp FR (1992) Sensory stimulation induces local cerebral glycogenolysis: demonstration by autoradiography. *Neuroscience* 51(2):451–461
- Tzingounis AV, Wadiche JI (2007) Glutamate transporters: confining runaway excitation by shaping synaptic transmission. *Nat Rev Neurosci* 8(12):935–947
- Veruki ML, Morkve SH, Hartveit E (2006) Activation of a presynaptic glutamate transporter regulates synaptic transmission through electrical signaling. *Nat Neurosci* 9(11):1388–1396
- Wadiche JI, Kavanaugh MP (1998) Macroscopic and microscopic properties of a cloned glutamate transporter/chloride channel. *J Neurosci* 18(19):7650–7661
- Wadiche JI, Amara SG, Kavanaugh MP (1995) Ion fluxes associated with excitatory amino acid transport. *Neuron* 15(3):721–728
- Watzke N, Rauen T, Bamberg E, Grewer C (2000) On the mechanism of proton transport by the neuronal excitatory amino acid carrier 1. *J Gen Physiol* 116(5):609–622
- Wersinger E, Schwab Y, Sahel JA, Rendon A, Pow DV, Picaud S et al (2006) The glutamate transporter EAAT5 works as a presynaptic receptor in mouse rod bipolar cells. *J Physiol* 577(Pt 1):221–234
- Xu J, Song D, Xue Z, Gu L, Hertz L, Peng L (2013) Requirement of glycogenolysis for uptake of increased extracellular K⁺ in astrocytes: potential implications for K⁺ homeostasis and glycogen usage in brain. *Neurochem Res* 38(3):472–485

- Yamashita A, Singh SK, Kawate T, Jin Y, Gouaux E (2005) Crystal structure of a bacterial homologue of Na⁺/Cl⁻dependent neurotransmitter transporters. *Nature* 437(7056):215–223
- Zerangue N, Kavanaugh MP (1996) Flux coupling in a neuronal glutamate transporter. *Nature* 383(6601):634–637
- Zhang Y, Chen K, Sloan SA, Bennett ML, Scholze AR, O'Keeffe S et al (2014) An RNA-sequencing transcriptome and splicing database of glia, neurons, and vascular cells of the cerebral cortex. *J Neurosci* 34(36):11929–11947
- Zheng K, Scimemi A, Rusakov DA (2008) Receptor actions of synaptically released glutamate: the role of transporters on the scale from nanometers to microns. *Biophys J* 95(10):4584–4596

Chapter 13

Glutamate Uptake by Astrocytic Transporters



Konstantin Mergenthaler, Franziska Oschmann and Klaus Obermeyer

Abstract Astrocytes express glutamate transporters at high density at perisynaptic processes which can tightly control extracellular glutamate levels in proximity of postsynaptic receptors with the potential to modulate functional neuronal activity. Glutamate uptake by these transporters also closely depends on activity-dependent extracellular ion concentrations and may also be regulated by the astrocyte's intracellular calcium. On the other hand, intracellular Ca^{2+} dynamics in the astrocyte too can be modulated by glutamate uptake, with potential for functionally relevant interactions with neural activity. Here, we introduce original modeling arguments to study functional implications of glutamate uptake by astrocytes both on their physiology and on that of neurons. In the first case, we consider the contribution of Na^+ and K^+ homeostasis to astrocytic glutamate uptake, revealing that intracellular anisotropy could account for spatial segregation of transporter- versus receptor-mediated calcium signaling pathways. In the second case, we study how regulation of extracellular glutamate levels by astrocytic transporters could affect tuning responses of primary sensory areas, linking our analysis to experimental observations in the ferret's primary visual cortex by Schummers et al. (2008, *Science* 320:1638). We conclude that glutamate uptake by astrocytes can modulate function of neuronal circuits in multiple ways that may look subtle at individual synaptic contacts, but at network level, lead instead to functionally relevant changes in neuronal tuning and stimulus discrimination.

Keywords Sodium-Calcium-Exchanger (NCX) · Sodium · Network dynamics · Dynamic astrocyte-neuron interactions · Postsynaptic coupling · NMDA-receptors

K. Mergenthaler · F. Oschmann · K. Obermeyer (✉)

Neural Information Processing, Electrical Engineering & Computer Science
and Bernstein Center for Computational Neuroscience, Technische Universität Berlin,
Berlin, Germany

e-mail: klaus.obermayer@tuberlin.de

Abbreviations

AMPA(AMPAR)	α -amino-3-hydroxy-5-methyl-4-isoxazolepropionic acid (receptor)
CICR	Ca^{2+} -induced Ca^{2+} release
EAAT	Excitatory amino acid transporters
EPSC	Excitatory postsynaptic current
GABA	γ -aminobutyric acid
GABAR	GABA _A receptor
GLAST	Glutamate aspartate transporter
GLT1	Type 1 glutamate transporter
HWHM	Half width at half maximum
mGluR	Metabotropic glutamate receptor
IP ₃ R	Inositol 1,4,5-trisphosphate receptor
NCX	$\text{Na}^+/\text{Ca}^{2+}$ exchanger
NKP	Na^+/K^+ ATPase
NMDA (NMDAR)	<i>N</i> -Methyl-D-aspartate (receptor)
TBOA	<i>DL-threo</i> - β -benzyloxyaspartate
V1	Primary visual cortex

13.1 Introduction

Among the five identified excitatory amino acid transporters (EAATs), types 1 and 2 EAATs are the most abundant ones and are predominantly found in astrocytes (Furness et al. 2008; Holmseth et al. 2012; Divito and Underhill 2014). EAAT1 and EAAT2, as well as their murine homologues—respectively, the glutamate aspartate transporter (GLAST) and the type 1 glutamate transporter (GLT1)—, are transporters with high affinity for glutamate whereby they can rapidly bind this neurotransmitter, promptly buffering high extracellular concentrations of it that could otherwise result in excitotoxicity (Danbolt 2001; Tzingounis and Wadiche 2007). This is crucial, since there is no enzymatic mechanism of degradation for extracellular glutamate, and thus uptake of this neurotransmitter by EAATs is the only mean whereby extracellular levels of glutamate can be regulated (Tsacopoulos 2002).

Although EAATs are also expressed in neurons (typically EAAT2–4), glutamate uptake by astrocytic transporters seems to be the main mechanism for clearance of extracellular glutamate at central synapses (Furness et al. 2008; Scimemi et al. 2009; Holmseth et al. 2012; Petr et al. 2015). At present, there is no defined consensus on the relative contribution to glutamate uptake by different astrocytic transporters, although different pharmacological studies pinpoint to a preponderant action of EAAT2 with respect to EAAT1. With this regard, application of the selective EAAT inhibitor *DL-threo*- β -benzyloxyaspartate (TBOA) in the mouse brain *in situ* was shown to substantially increase baseline extracellular glutamate, where selective blockade of GLAST could contribute up to 13-fold higher extracellular glutamate levels, while

GLT1 inhibition may even account for twice as large or larger increases (Rothstein et al. 1996). This is in line with experimental reports that suggest that the contribution to uptake activity appears to be dominated by EAAT2/GLT1 (Haugeto et al. 1996; Tanaka et al. 1997; Huang et al. 2004), with estimates as high as >95% in the hippocampus (Holmseth et al. 2012). This, however, can only be partially attributed to different kinetics of GLT1 vs. GLAST, with the rate of glutamate update by GLAST being ~6-fold slower than that of GLT1 (Grewer et al. 2008). Another factor that must be taken into account is the relative expression of these two transporters, which depends on the brain region. While in fact, GLT1 expression is larger than GLAST one in the murine hippocampus, the opposite holds true in the mouse cerebellum (Danbolt 2001; Holmseth et al. 2012).

A key observation is that astrocytic EAAT expression is anisotropic (Benedikts-son et al. 2012), with most of the transporters clustering at perisynaptic astrocytic processes, reaching densities of the order of $>10^4 \mu\text{m}^{-2}$ (Lehre and Danbolt 1998). This hints a critical role of these transporters in the regulation of the time course of synaptically released glutamate in the extracellular space, and thus in the regulation of excitatory synaptic transmission, insofar as the time course of extracellular glutamate regulates activation of postsynaptic receptors (Clements et al. 1992; Clements 1996). This regulation is nonetheless complex and brought forth by the combination of synapse-specific morphology of neuron-glia interactions with activity-dependent factors (De Pittà et al. 2015; De Pittà and Brunel 2016). Perisynaptic astrocytic processes indeed undergo dynamical reshaping depending on synaptic activity (Reichenbach et al. 2010) and chemical composition of the extracellular milieu (Scimemi et al. 2013; Tanaka et al. 2013), possibly in relation to different behavioral conditions (Oliet et al. 2001; Piet et al. 2004). On the other hand, both extracellular glutamate and intracellular astrocytic calcium activity can control surface diffusion of astrocytic transporters (Underhill et al. 2015), supporting the notion that glutamate uptake by astrocytes is not a constant process, but rather a highly plastic one put in force to meet synapse-specific activity requirements. In the barrel cortex, for example, expression of astrocytic glutamate transporters increases following whisker stimulation, and correlates with a significant increase in the astrocytic envelopment of excitatory synapses on dendritic spines (Genoud et al. 2006), possibly to finely control excitatory synaptic drive ensuing from episodes of sustained sensory stimulation. Similarly, in the hippocampus, astrocytic GLT1 may laterally diffuse in to and out of perisynaptic regions, modulating the efficacy of excitatory synaptic inputs (Murphy-Royal et al. 2015).

Although the above experimental observations strongly support the notion that astrocytic transporters could be more than simple scavengers of extracellular glutamate, their functional role in synaptic transmission and regulation of neuronal excitability remains elusive due to inherent limits of current technology. In particular, in recent years, along with a heated debate on the effective existence of synapse-astrocyte functional interactions (Agulhon et al. 2008; Nedergaard and Verkhratsky 2012; Fiacco and McCarthy 2018; Savtchouk and Volterra 2018), a number of issues have been raised regarding the way astrocytes could contribute to synaptic signaling through feedforward and/or feedback actions by glutamate uptake (Smith and

Häusser 2010). Glutamate uptake could indeed both slow down extracellular glutamate clearance by re-release of this neurotransmitter by transporters (Scimemi et al. 2009) and speed up the time course of extracellular glutamate due to the transporters' rapid binding and uptake kinetics (Barbour et al. 1994; Tong and Jahr 1994; Wadiche et al. 1995; Murphy-Royal et al. 2015). In this context then, computational modeling represents a promising approach to address these issues as it allows analysis of synaptic transmission and neuronal activity in the presence of astrocytic glutamate uptake for various stimuli and conditions that would otherwise be difficult to achieve experimentally, either for the lack of the necessary technology or for difficulties in accessing readouts at the subcellular level (Diamond 2005; Scimemi and Beato 2009, see also Chap. 12).

Different modeling strategies can be deployed in principle, depending on what aspects of regulation of excitatory synaptic transmission by astrocytic glutamate uptake we are interested in. For example, at the subcellular level, the recognition of a tight dynamical coupling between astrocytic processes, transporter expression, and synaptic activity could be explored combining existing models for constrained protein diffusion in cellular membranes (Holcman and Schuss 2014) with those accounting for dynamical reshaping of such membranes by either intracellular (Tsaneva-Atanasova et al. 2009) or extracellular factors (Mironov et al. 2014) or a combination thereof. If instead, we are mainly interested in glutamate time course at astrocyte-modulated synapses, transporter diffusion and dynamics of astrocytic processes' morphology may be neglected at first glance, given that they occur on timescales of the order of minutes (Haber et al. 2006; Murphy-Royal et al. 2015) compared to those in the range of hundreds of milliseconds to few seconds involved in synaptic transmission (Destexhe et al. 1994; Okubo et al. 2010). In this perspective then, either a stochastic or a deterministic modeling approach can be adopted. In the stochastic scenario, Monte Carlo methods can conveniently be used to study interactions of individual glutamate molecules with perisynaptic transporters and postsynaptic receptors, yet with the caveat that their predictive values is inevitably hampered by uncertainties associated with most of the parameters of the model being used. Within cell populations, there can be such a wide range of synapses differing in their structure, size, number and distribution of receptors, release properties, and glial coverage that the derived "average" neurotransmitter profile may occur only at a small fraction of all synaptic contacts (Scimemi and Beato 2009).

Deterministic models on the other hand can produce reliable predictions for limited parameter ranges but generally require a significant computational overhead to extrapolate meaningful statistics on the average glutamate time course. Nonetheless, these models have been proved useful not only to study important aspects related to extracellular glutamate dynamics, such as the optimal size of the synaptic cleft for efficient synaptic transmission (Savtchenko and Rusakov 2007) or the rate of neurotransmitter spillover to neighboring synapses (Barbour 2001), but also to evaluate putative glutamate diffusion profiles at different locations within synapses (Greget et al. 2011; Raynaud et al. 2015) and so their regulation of and by neuronal and astrocytic transporters (Allam et al. 2012). The downside of these models is that they require simplifying assumptions on the geometry of the extracellular space where

glutamate diffusion occurs (Rusakov and Kullmann 1998; Rusakov 2001; Rusakov and Lehre 2002), which may come at odds with the theoretical prediction for the need of a tight ensheathment of synapses by astrocytic processes for effective functional uptake to occur (Freche et al. 2011).

In what follows, we limit our analysis to the time course of “local” extracellular glutamate, without specifying any particular geometry for the extracellular space. In doing so, we assume that the extracellular space can be assimilated to a spatial compartment comprised between a synaptic (neuronal) one and an astrocytic one, where all compartments are well-stirred with respect to concentrations of chemical species found at their interior (Fig. 13.4). We start from a simple phenomenological formula for the average time evolution of glutamate concentration in the synaptic cleft, to qualitatively illustrate how glutamate time course can dramatically regulate postsynaptic currents (Sect. 13.2). Then, we introduce a biophysical model to reproduce this qualitative behavior and assess its potential functional implications on neuronal excitability (Sect. 13.3), ultimately discussing these implications in the context of tuning responses of neurons in the primary visual cortex (Sect. 13.4).

13.2 Glutamate Uptake Shapes Postsynaptic Receptor Activation

A simple experiment to characterize the effect of astrocytic glutamate transporters on postsynaptic AMPA and NMDA receptor-mediated currents can be put forth recording these currents in response to a variable number of equally timed, brief electrical pulses, akin to presynaptic action potentials, in the presence of TFB-TBOA—a variant of TBOA that specifically targets glial transporters—and compare the time course of those currents to the one attained by corresponding EPSCs in the presence of glutamate uptake (control conditions). Considering this setup, Tsukada et al. (2005) showed how EAATs can differently affect AMPA versus NMDA currents. AMPA currents evoked by isolated pulses in fact are essentially not affected by TFB-TBOA. On the other hand, these currents sensibly increase when multiple (<5) consecutive pulses are delivered presynaptically, but decay faster, consistently with a competition between larger recruitment of AMPA receptors with rapid receptor desensitization by increased glutamate levels (Tsukada et al. 2005; Goubard et al. 2011). On the contrary, the peak current mediated by NMDA receptors does not seem to be altered with respect to control conditions, independently of the number of delivered pulses, while instead, the corresponding decay time constant grows with a >5 pulse number (Tsukada et al. 2005).

A set of independent experiments in the dorsal horn, further revealed how application of the transporter blocker dihydrokainate correlates with a delayed decay of EPSCs which, remarkably, *could* also depend on the strength of synaptic connections under consideration, quantified by the synapse’s baseline peak EPSC value in control conditions (Weng et al. 2007). The use of the conditional form is required,

inasmuch as it cannot be ruled out that some of these observations only apply to specific synapses and/or are biased by the experimental protocol (Tzingounis and Wadiche 2007). Modeling arguments can be invoked on this regard, to substantiate the notion that multiple factors could shape EPSC dynamics, even when we limit our scope to the sole interplay between postsynaptic receptors and astrocytic transporters. These factors are: (i) transporter and receptor densities, (ii) receptor versus transporter kinetics, and (iii) constraints on glutamate diffusion in synaptic cleft and by perisynaptic space geometry (Scimemi and Beato 2009). Accordingly, it may be argued that while extracellular glutamate levels are under tight regulation by astrocytic transporters, their effect on AMPA and NMDA currents is strongly dependent on the relative position of postsynaptic receptors with respect to astrocytic transporters. This seems to find experimental substantiation by the observation that perisynaptic astrocytic processes, both in the cerebellum and the hippocampus, colocalize mostly with postsynaptic spines (Rusakov and Kullmann 1998; Rusakov 2001). Diffusion models further corroborate this hypothesis, revealing how uptake could effectively influence extracellular glutamate only locally, that is within <300 nm from the transporter site (Rusakov and Kullmann 1998; Montes et al. 2015). On the other hand, with the exception of special geometries or astrocytic processes invading synaptic clefts (Pannasch et al. 2014), this spatial range is likely shorter than the putative distance of astrocytic transporters from synaptic processes, taking into account that the size of synaptic spines can be as large as >500 nm (Montes et al. 2013), ultimately raising the question of under what circumstances astrocytic transporters could play a role in excitatory synaptic transmission.

To address this question, we need to frame our hitherto reasoning in the context of synaptic activity. Once again, in fact, computational modeling reveals how different scenarios of synaptic activation could be differently affected by astrocytic glutamate uptake. If indeed, the majority of diffusion models generally agree on the functional relevance of astrocytic transporters in shaping glutamate spillover from the synaptic cleft, and NMDA currents thereby, in conditions of sustained synaptic glutamate release (Zheng and Rusakov 2015), the impact of astrocytic transporters on AMPA currents remains marginal with respect to that on NMDA receptors and may only be detected for sufficiently high rates of presynaptic activity (Zheng et al. 2008).

The essence of the latter observations can also be easily illustrated by a “simplified” description of excitatory synaptic transmission based on the receptor kinetic schemes in Fig. 13.1, where the open fraction of glutamate-bound receptors O_x ($x = \text{AMPA, NMDA}$) is estimated considering a simple sum of biexponential profiles for extracellular glutamate dynamics (G), with each profile being associated with a synaptic release event occurring at t_k (Dayan and Abbott 2001), i.e.,

$$G(t) = \frac{1}{\tau_d - \tau_r} \sum_{t_k < t} \left(\exp\left(-\frac{t - t_k}{\tau_d}\right) - \exp\left(-\frac{t - t_k}{\tau_r}\right) \right) \Theta(t - t_k) \quad (13.1)$$

In the above equation, we assume that the peak concentration of glutamate in the extracellular space is 1 mM, and that rise (τ_r) and decay time constants (τ_d) are

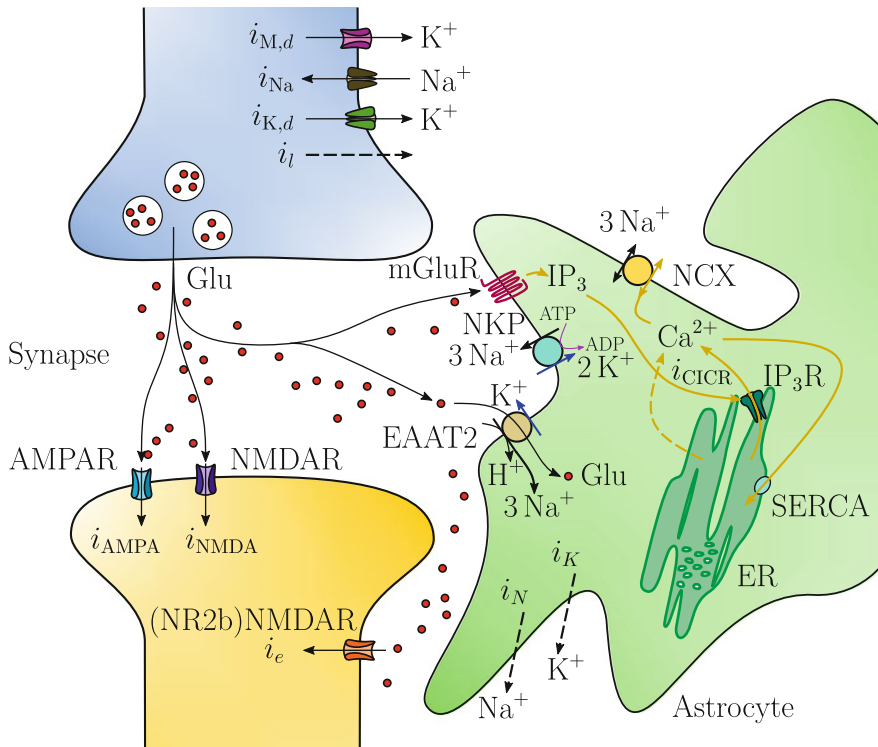


Fig. 13.1 Glutamate uptake by astrocytic transporters. Function of glutamate transporters (EAAT2) expressed on perisynaptic astrocytic processes is coupled with intracellular ion homeostasis and Ca^{2+} signaling. In particular, astrocytic Ca^{2+} signaling can be triggered either by metabotropic glutamate receptors (mGluR, yellow pathways) through the well-known pathway of IP_3 -mediated Ca^{2+} -induced Ca^{2+} release (CICR), or by glutamate transporter-mediated modulations of the Na^+/K^+ -ATPase pumps (NKP) and $\text{Na}^+/\text{Ca}^{2+}$ -exchangers (NCX). Modeling arguments presented in this chapter only consider intracellular dynamics of Na^+ , K^+ and Ca^{2+} . Dashed arrow lines denote leakage currents

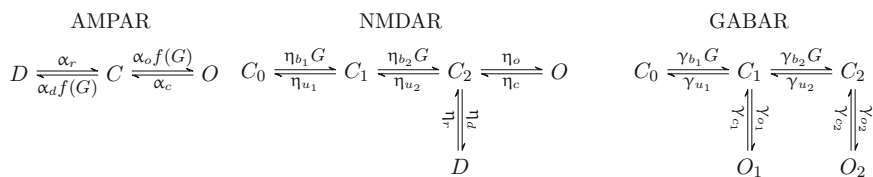


Fig. 13.2 Kinetic schemes for postsynaptic receptors considered in this chapter are borrowed from Saftenku (2005) (AMPA), Lester and Jahr (1992) (NMDA), and Destexhe et al. (1998) (GABA). Each receptor can generally be found in one of three states: closed (C), open (O), desensitized (D). G denotes extracellular glutamate concentration and $f(G) = G^2/(G + \kappa_B)^2$. Rate values are in Table 13.1

Table 13.1 Ligand-gated receptor kinetics

Symbol	Description	Value	Units
<i>AMPA receptors</i> (Saftenku 2005)			
α_o	Opening rate	25.39	s^{-1}
α_c	Closing rate	4	s^{-1}
α_d	Desensitization rate	5.11	s^{-1}
α_r	Resensitization rate	0.065	s^{-1}
κ_B	Dissociation constant	0.44	mM
<i>NMDA receptors</i> (Destexhe et al. 1998)			
η_{b1}	Binding rate	1	$\mu M^{-1} s^{-1}$
η_{u1}	Unbinding rate	12.9	s^{-1}
η_{b2}	Binding rate	1	$\mu M^{-1} s^{-1}$
η_{u2}	Unbinding rate	12.9	s^{-1}
η_o	Opening rate	46.5	s^{-1}
η_c	Closing rate	73.8	s^{-1}
η_d	Desensitization rate	8.4	s^{-1}
η_r	Resensitization rate	6.8	s^{-1}
<i>GABA receptors</i> (Destexhe et al. 1998)			
γ_{b1}	Binding rate	20	$\mu M^{-1} s^{-1}$
γ_{u1}	Unbinding rate	$4.6 \cdot 10^3$	s^{-1}
γ_{b2}	Binding rate	10	$\mu M^{-1} s^{-1}$
γ_{u2}	Unbinding rate	$9.2 \cdot 10^3$	s^{-1}
γ_{o1}	Opening rate	$3.3 \cdot 10^3$	s^{-1}
γ_{c1}	Closing rate	$9.8 \cdot 10^3$	s^{-1}
γ_{o2}	Opening rate	$1.06 \cdot 10^4$	s^{-1}
γ_{c2}	Closing rate	$0.41 \cdot 10^3$	s^{-1}

such that $\tau_r < \tau_d$. The function $\Theta(\cdot)$ denotes the Heaviside function (Table 13.1 and Table 13.2).

Figure 13.2a shows the fraction of open AMPA and NMDA receptors (*middle* and *bottom panels*) in response to a series of presynaptic glutamate release events (*top panel*). To mimick different scenarios of astrocytic glutamate uptake, we consider three different decay time constants of glutamate time course for $0.6 \leq \tau_d < 1\text{ms}$. It may be appreciated how variations of τ_d mostly affect the fraction of open NMDARs while leaving that of open AMPARs essentially unchanged. On the contrary, the decay time of open AMPARs, but not that of open NMDARs, tends to increase with τ_d . Significantly, as further illustrated in Fig. 13.2b, these effects are modulated by the rate of synaptic release. With this regard, it may be observed how the average fraction of AMPA receptors (*top panel, solid lines*) tends to increase larger as synaptic release increase, although for synaptic release rates $>60\text{Hz}$ the standard deviation for the fraction of open AMPA receptors is larger for shorter

Table 13.2 Ligand-gated neuronal currents

Symbol	Description	Value	Units
<i>Neurotransmitter time course (Diamond 2005)</i>			
τ_r^E	Glutamate rise time	0.16	ms
τ_d^E	Glutamate decay time	0.545–1.35	ms
τ_r^I	GABA rise time	0.29 ^a	ms
τ_d^I	GABA decay time	0.291 ^a	ms
<i>Postsynaptic currents (Destexhe et al. 1998)</i>			
$g_{\text{AMPA}}^{\text{EX}}$	Max AMPA conductance of EX connections	549.51 ^b	nS
$g_{\text{AMPA}}^{\text{IX}}$	Max AMPA conductance of IX connections	439.61 ^b	nS
g_{AMPA}^E	Max AMPA conductance in E neurons	1593.57 ^b	nS
g_{AMPA}^I	Max AMPA conductance in I neurons	4249.36 ^b	nS
E_{AMPA}	AMPA receptor reversal potential	0	mV
g_{NMDA}^E	Max NMDA conductance in E neurons	398.37 ^b	nS
g_{NMDA}^I	Max NMDA conductance in I neurons	1062.32 ^b	nS
Mg_e^{2+}	Extracellular magnesium concentration	1	mM
E_{NMDA}	NMDA receptor reversal potential	0	mV
g_{GABA}	Max GABA _A conductance	281.8 ^b	nS
E_{GABA}	GABA _A receptor reversal potential	-70	mV
<i>Extrasynaptic currents (Herman and Jahr 2007; Bentzen et al. 2009)</i>			
g_e	Max. conductance	2.6	nS
E_e	Reversal potential	55	mV
G_0^E	Ambient extracellular glutamate at E neurons	0–2.75	μM
G_0^I	Ambient extracellular glutamate at I neurons	0–2.75	μM

^a Maximum synaptic conductances were estimated per average fraction of open receptors, according to the procedure described by Stiemberg et al. (2009), assuming an AMPA-to-NMDA ratio of 4 : 1 to match correspondent maximum values in that study

^b Time constants for the time course of extracellular GABA were estimated by particle swarm optimization to fit inhibitory postsynaptic currents ensuing from the receptor's kinetic scheme in Fig. 13.1c with time-dependent extracellular concentrations reported in Destexhe et al. (1998)

τ_d values (*yellow shaded area*). This can be explained taking into account that at lower τ_d values the fractions of desensitized and resensitized receptors follow more closely faster rates of synaptic release, thereby increasing variability of the associated fraction of open receptors. Conversely, the increase in open NMDAR fraction (*bottom panel*) is only observed for low-to-intermediate synaptic release rates comprised between ~20–60 Hz and always sees a larger standard deviation for longer τ_d values. Contrarily to AMPARs, this behavior ensues from the slower kinetics of NMDARs whereby an effective modulation of the peak fraction of open receptors can only be achieved when synaptic release rates are sufficiently low to allow receptors to open and close cyclically. As these rates increase, the peak fraction of open NMDARs tends to grow independently of the decay time of extracellular glutamate.

13.3 Glutamate Uptake Modulates Astrocytic Calcium Dynamics

So far, our analysis on the potential functional relevance of astrocytic EAATs has focused on synaptic physiology in terms of dynamics of recruitment of postsynaptic receptors, and thus of ensuing postsynaptic currents. However, the effects of EAATs on astrocytic physiology should also be taken into account. In particular, in a series of landmark experiments in the primary visual cortex (V1) of ferrets, Schummers et al. (2008) showed that blocking of glutamate uptake by TBOA, strongly abates visually evoked Ca^{2+} signals in astrocytes while making neurons to respond stronger to a wider range of visual stimuli. While we address the effect of astrocytic transporters on neuronal responses in the next section, for the remainder of this section we focus instead on the possible biophysical mechanisms underpinning coupling of glutamate uptake with astrocytic Ca^{2+} signals.

Let us start by considering the stoichiometry of EAAT2/GLT1. A key aspect of glutamate uptake mediated by this transporter is that it is electrogenic, namely it occurs with an exchange of ions across the astrocytic plasma membrane. The whole uptake process can in fact be described by a cycle akin to the kinetic scheme in Fig. 13.3 (Bergles et al. 2002). The entry point of this cycle, that is, the effective glutamate uptake step, takes place with the cotransport of glutamate (G) with Na^+ and H^+ ions, to which a conformational change of the transporter follows that results in the counter-transport of K^+ (Wadiche et al. 1995; Bergles et al. 2002). A complete cycle results in the uptake of one glutamate molecule, the cotransport of three Na^+ and one H^+ ions into the astrocytic cytosol, and the release of one K^+ from the cytosol into the extracellular space (Zerangue and Kavanaugh 1996; Levy et al. 1998).

In spite of its complexity, the essence of EAAT2/GLT1 kinetics in Fig. 13.3 can be conveniently approximated by the product of a maximum transporter current ($i_{\text{T}0}$) with Hill terms (Chap. 5) accounting for binding reactions of glutamate, Na^+ and K^+ to the transporter, so that the net transporter current flowing across the astrocytic membrane (i_{T}) reads (Zerangue and Kavanaugh 1996; Oschmann et al. 2017), such that

$$i_{\text{T}} = i_{\text{T}0} \cdot \mathcal{H}_1(K_i, T_K) \cdot \mathcal{H}_3(N_e, T_N) \cdot \mathcal{H}_1(G, T_G) \quad (13.2)$$

where K_i and N_e , respectively, stand for the intracellular K^+ and extracellular Na^+ concentrations. This formulation neglects the dependence of the uptake process on extra- and intracellular pH by the cotransport of H^+ (Rose and Ransom 1996), and thus limits the validity of our following modeling arguments to a scenario where pH changes can be negligible. Notwithstanding, this scenario holds true for all the regimes of stimulation of transporters considered in this chapter.

An important implication of the electrogenic nature of glutamate uptake by astrocytic transporters is that their uptake efficiency can be modulated by the astrocyte's membrane potential (v_a), since this latter depends on ion homeostasis (Drejer et al. 1982; Zerangue and Kavanaugh 1996; Li and Stys 2001; Kelly et al. 2009). In turn, to seek an effective model of astrocytic glutamate transport, equations for the dynamics

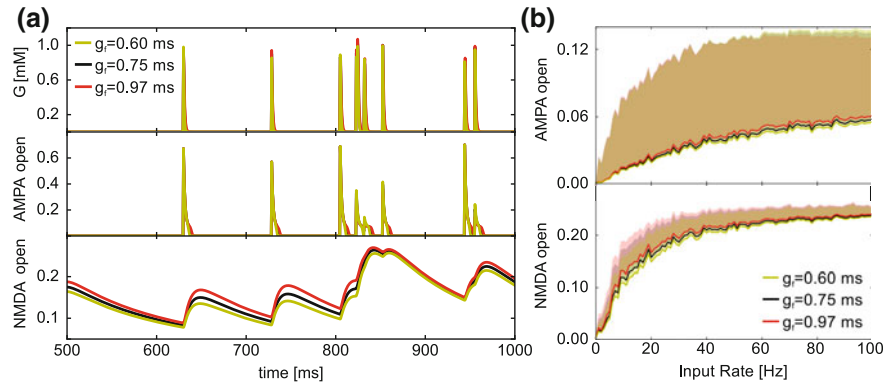


Fig. 13.3 Glutamate time course modulates the fraction of open postsynaptic receptors. **a** Glutamate time course in the synaptic cleft (*top*) and associated open fractions of postsynaptic AMPARs (*middle*) and NMDARs (*bottom*) for three different decay time constants (τ_d) for extracellular glutamate concentration (*color coded*). **b** Average fraction of open AMPARs (*top*) and NMDARs (*bottom*) as functions of synaptic release rate (*solid lines and shaded areas*: mean+std from 2s-long simulations). Synaptic release was simulated by trains of Poisson-distributed Dirac deltas (see Chap. 5) with average constant rate between 0–100Hz. Parameters as in Tables 13.1 and 13.2

of K^+ and Na^+ must also be taken into account to complement (13.2). To this extent, along with currents across the astrocytic membrane mediated by different channels that are permeable to these two ions (Chap. 1), at least two further mechanisms of transport must be considered (Fig. 13.4, Oschmann et al. 2017): (i) an active extrusion of Na^+ from the cytosol with the uptake of K^+ from the extracellular space by the Na^+/K^+ -ATPase pump (NKP) (Rose et al. 2009) and (ii) an exchange of extracellular Na^+ with intracellular Ca^{2+} by the Na^+/Ca^{2+} exchanger (NCX) (Rojas et al. 2007). In this fashion, K^+ and Na^+ homeostasis are interdependent via NKP, with Na^+ dynamics that is also directly linked with the astrocyte's intracellular Ca^{2+} dynamics via NCX (Fig. 13.3).

In general, both α_1 and α_2 isoforms of NKP are found in astrocytes (Geering 2008; Böttger et al. 2012). The two isoforms have similar kinetics although the α_1 isoform displays a lower affinity for Na^+ than α_2 (Zahler et al. 1997), so that this latter is the main NKP isoform involved in efficient extrusion of Na^+ following glutamate uptake (Illarionava et al. 2014). NKP stoichiometry is such that the pump extrudes three Na^+ from the cytosol with the uptake of two K^+ from the extracellular space. The net ion current mediated by NKPs (i_{NKP}) can be approximated by Michaelis–Menten kinetics (Luo and Rudy 1994; Østby et al. 2009), and thus be written in terms of products of Hill terms, akin to the transporter current in (13.2), i.e.,

$$i_{NKP} = i_{NKP0} \cdot \mathcal{H}_{1.5}(N_i, P_N) \cdot \mathcal{H}_1(K_e, P_K) \quad (13.3)$$

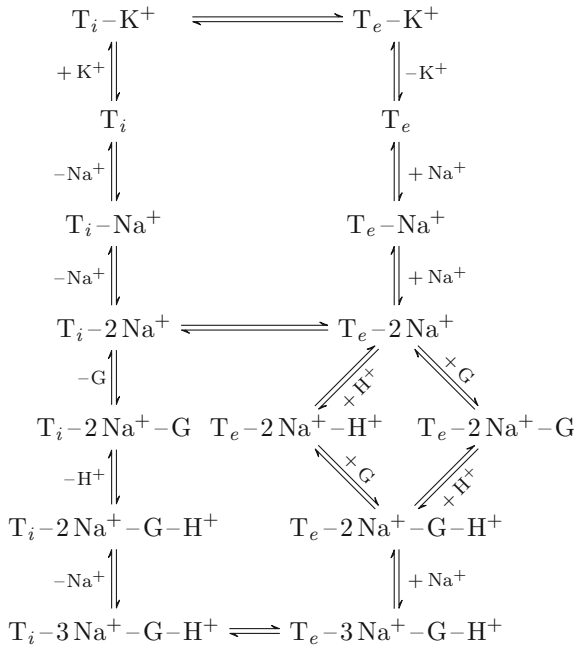


Fig. 13.4 A sample kinetic scheme for glutamate uptake by EAAT2/GLT1 (Bergles et al. 2002). The scheme describes a cycle whose halves are for the transporter's binding site for glutamate being exposed, respectively, to the extracellular (T_e) or the intracellular (T_i) side of the cell's membrane. Three conformational states of the transporter— $T_e - 2 Na^+ - H^+$, $T_e - 3 Na^+ - G - H^+$ and $T_i - K^+$ —also account for a leak of chloride ions (not shown), which is suggested to mitigate variations of membrane potential by cationic currents mediated by the transporter and favor efficient glutamate uptake (Billups et al. 1996; Kanner 2006)

NCX stoichiometry sees the exchange of three Na^+ by one Ca^{2+} (Rojas et al. 2007). However, the direction of the ensuing ion current across the astrocyte's membrane (i_{NCX}) depends on the potential of this latter, according to the general equation (Luo and Rudy 1994):

$$i_{NCX} = i_{NCX0} \cdot \mathcal{H}_3(N_e, X_N) \cdot \mathcal{H}_1(C_e, X_C) \cdot \frac{\frac{N_e^3}{C_e} e^{\eta \frac{v_a}{V_T}} - \frac{C_e}{C_e} e^{(\eta-1) \frac{v_a}{V_T}}}{1 + \bar{k} e^{(\eta-1) \frac{v_a}{V_T}}} \quad (13.4)$$

where C stands for calcium concentration, η denotes an energy barrier ensuing from the NCX molecular structure that modulates the exchanger's efficiency by the cell membrane potential, \bar{k} is a factor that ensures saturation at large negative membrane potentials, and V_T is the thermal voltage which equals to ~ 26 mV at body temperature (i.e., at $37^\circ C$).

Finally, we complete our description of ionic fluxes across the astrocytic membrane considering also Na^+ and K^+ currents mediated by a variety of channels that

are permeable to these ions (Simard and Nedergaard 2004; Rose and Chatton 2016). For the sake of simplicity, we model these currents akin to nonspecific leakage ohmic currents that flow out of the cell's membrane, such that

$$i_x = g_x(v_a - E_x) \quad \text{where } x = K, N \quad (13.5)$$

where g_x , E_x , respectively represent the maximal leakage conductance and the cation's Nernst potential. In this fashion, based on the equations for Na^+ and K^+ currents across the astrocytic plasma membrane introduced so far, we can write the differential equations for the dynamics of intracellular concentrations of these ions by

$$\frac{dN_i}{dt} = \frac{\varsigma_A}{F} (3i_T - 3i_{\text{NKP}} - 3i_{\text{NCX}} - i_N) \quad (13.6)$$

$$\frac{dK_i}{dt} = \frac{\varsigma_A}{F} (-i_T + 2i_{\text{NKP}} - i_K) \quad (13.7)$$

where F stands for the Faraday constant and ς_A is the astrocyte's surface-to-volume ratio which we use to convert currents per unit area into concentration fluxes. The multiplicative coefficients preceding each current term in the above equations represent the ionic charge carried by each current in terms of numbers of Na^+ and K^+ ions (omitted when unitary).

With the ultimate aim to derive an equation for the astrocyte's membrane potential v_a , we also need to take into account the contribution to this potential by intracellular Ca^{2+} signaling. This is motivated by a body of experimental observations suggesting a tight morphological and functional coupling between NCX and IP_3 receptors mediating Ca^{2+} -induced Ca^{2+} release (CICR) from the cell's endoplasmic reticulum (ER) (Goldman et al. 1994; Takuma et al. 1994; Blaustein et al. 1999; Rojas et al. 2007). In this fashion, extracellular glutamate in our model comes to regulate astrocytic Ca^{2+} signaling through two signaling routes: one is by uptake mediated by transporters that is possibly coupled with NCX activity and Na^+/K^+ homeostasis, the other is by activation of astrocytic metabotropic receptors (mGluRs) that trigger the well-known route of IP_3 -(I -)mediated CICR (See Fig. 13.4). With this regard, we consider the *G-ChI* model for CICR originally introduced by De Pittà et al. (2009) and discussed in detail in Chap. 5, to derive an equation for the Ca^{2+} current (i_C) that flows from the ER membrane into the cytosol. This current in fact is proportional to the change of cytosolic Ca^{2+} concentration (C) (i.e., its derivative) ensuing from CICR and can ultimately be obtained from this latter by converting ion fluxes in units of $\mu\text{M}/\text{s}$ to electric currents in units of $\text{pA}/\mu\text{m}^2$ by rescaling Ca^{2+} variations by the Faraday constant F and the ratio between the ER surface and the cytoplasm volume ratio, which can conveniently be expressed in terms of $\varsigma_A\sqrt{\rho}$, with ρ representing

the ER-to-total cell volume ratio¹ (Oschmann et al. 2017), i.e.,

$$i_C = \frac{\varsigma_A \sqrt{\rho}}{F} \frac{dC_i}{dt} \quad (13.8)$$

Then, C_i is controlled by two processes: (i) the Ca^{2+} flux mediated by NCX (13.4), and (ii) CICR due to glutamate-bound metabotropic receptors on the astrocytic plasma membrane, i.e., $\frac{dC_i}{dt}|_{\text{CICR}}$, i.e.,

$$\frac{dC_i}{dt} = \left. \frac{dC_i}{dt} \right|_{\text{CICR}} + \frac{F}{\varsigma_A \sqrt{\rho}} i_{\text{NCX}} \quad (13.9)$$

where CICR-mediated Ca^{2+} flux is provided by the *G-ChI* model (De Pittà et al. 2009) with the addition of an equation for C_{ER} motivated by the fact that in our formulation, due to the consideration of an extracellular Ca^{2+} pool, the total intracellular Ca^{2+} concentration is generally not conserved (Chap. 3), i.e.,

$$\left. \frac{dC_i}{dt} \right|_{\text{CICR}} = J_r(C_i, h, I) + J_l(C_i) - J_p(C_i) \quad (13.10)$$

$$\frac{dC_{\text{ER}}}{dt} = -\frac{1}{\rho_A} \left. \frac{dC_i}{dt} \right|_{\text{CICR}} \quad (13.11)$$

$$\frac{dh}{dt} = \Omega_h(C_i, I) (h_\infty(C_i, I) - h) \quad (13.12)$$

$$\frac{dI}{dt} = J_\beta(C_i, G) + J_\delta(C_i, I) - J_{3K}(C_i, I) - J_{5P}(I) \quad (13.13)$$

where, in first approximation, we assume astrocytic mGluR kinetics to be fast with respect to $\text{IP}_3/\text{Ca}^{2+}$ signaling so that (Eq. 15 in Chap. 5):

$$J_\beta(C_i, G) = O_\beta \cdot \mathcal{H}_{0.7} \left(G, (K_N (1 + \zeta \mathcal{H}_1(C, K_{KC})))^{1.43} \right) \quad (13.14)$$

We are now able to write the equation for the astrocyte's membrane potential v_a . By convention, this potential equals the difference of electric potential between the cytosol and the exterior of the astrocyte. In this fashion, because we are dealing with cationic currents, it follows that any of such currents that flows into the cytosol of the astrocyte must promote an increase of v_a , while the opposite must hold for currents

¹We can simplistically think of an astrocyte as a cylindrical cell of radius r and length l with a concentric ER cylinder of radius r_{ER} . In this fashion, the two cylinders respectively have volumes $\Lambda = \pi r^2 h$ and $\Lambda_{\text{ER}} = \pi r_{\text{ER}}^2 h$. Defining $\rho \equiv \Lambda_{\text{ER}}/\Lambda$, then it must be $r_{\text{ER}} = \sqrt{\rho} r$. In the assumption that all relevant fluxes in our analysis are through the compartment's lateral surface, the area of this latter for the ER cylinder equals the area of the whole cell cylinder rescaled by $\sqrt{\rho}$. In astrocytic processes, ρ can be expressed as a function of ς_A whereby $\rho \approx 0.15 \exp(-0.55 \times 10^6 \varsigma_A^{2.32})$ (Patrushev et al. 2013). Moreover ρ can also be expressed in terms of ER-to-cytosol volume ratio (ρ_A in the *G-ChI* model in Chap. 5), as $\rho = \rho_A/(1 + \rho_A)$.

that flows out of the cytosolic compartment. Accordingly (Oschmann et al. 2017),

$$c_a \frac{dv_a}{dt} = 2i_C - i_N - i_N + 2i_T - i_{\text{NKP}} - i_{\text{NCX}} \quad (13.15)$$

where c_a stands for the astrocytic membrane capacitance, and the premultiplicative factors preceding each current are set based on the *net* charge contributed by each current to the cytosolic compartment.

To close our model, we note that the extracellular variation of an ionic species is linearly related to its intracellular variation, whereby, defining the variation of the generic Y ion concentration from the resting concentration Y_0 by $\Delta Y = Y - Y_0$, it is

$$\Delta N_e = -\Delta N_i \quad (13.16)$$

$$\Delta K_e = -\Delta K_i \quad (13.17)$$

$$\Delta C_e = -\Delta C_i - \Delta C_{\text{ER}} \quad (13.18)$$

In this fashion, Eqs.(13.1), (13.6), (13.7), (13.10)–(13.13) and (13.15) provide a model in terms of extracellular glutamate concentration G , intracellular Na^+ , K^+ , Ca^{2+} concentrations (i.e., N_i , K_i , C_i) and the astrocyte's membrane potential to describe astrocytic glutamate uptake.

Figure 13.5 illustrates results from our model in response to a burst increase of extracellular glutamate (panel (a)) that could resemble a brief episode of intense synaptic release from afferent projections to V1 neurons following the protocol of brief intervals of visual stimulation by oriented gratings adopted by Schummers et al. (2008). Significantly, in agreement with observations by those investigators, the model can reproduce a delayed astrocyte Ca^{2+} response to stimulation (panel (b), *blue trace*) which is otherwise strongly attenuated when glutamate transport is blocked (TBOA, *red trace*). As previously mentioned, this Ca^{2+} response ensues from a non-trivial interplay between intracellular Na^+ (and K^+) dynamics with agonist-mediated IP₃R-triggered Ca^{2+} signaling. With this regard, one may note that blocking of glutamate uptake also abates Na^+ influx (panel (c), *red trace*) which, in turn, affects the NCX function (Blaustein and Santiago 1977). The current mediated by this exchanger in fact promotes Ca^{2+} inflow in control conditions but reverses direction in the presence of TBOA (panel (d)), implying that in such conditions part of the intracellular Ca^{2+} excess is dumped extracellularly via NCX. Crucially, this prevents intracellular Ca^{2+} concentration to increase up to the threshold value required to trigger robust CICR (see Chap. 5) as reflected by the *red trace* in panel (e). Further analysis of the different components of Ca^{2+} signaling also suggests that the modest increase of intracellular Ca^{2+} with blocked transporters is mostly driven by leakage from the ER (panel (f), *red trace*), while the actual fraction of deinactivated IP₃Rs—namely the fraction of IP₃Rs that could in principle be recruited by CICR, if intracellular Ca^{2+} were reaching the CICR threshold—tend to the ideal limit of 1 (panel (g)).

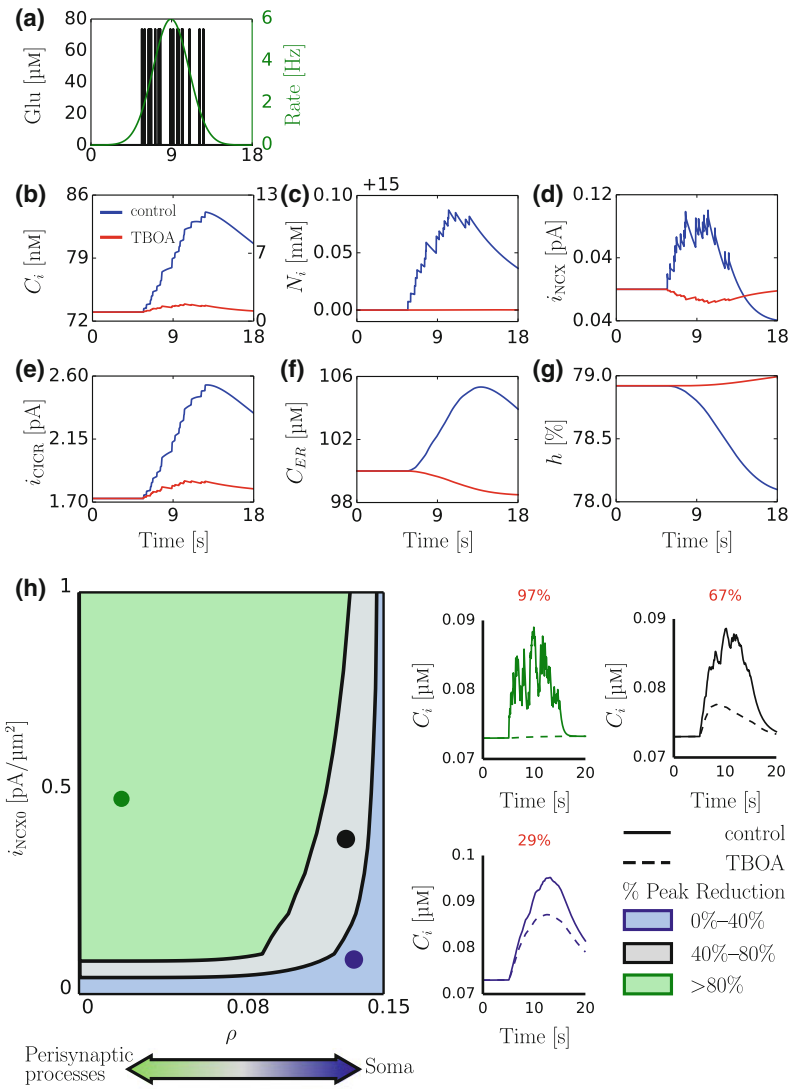


Fig. 13.5 Coupling of glutamate uptake with astrocytic Ca^{2+} signaling. **a** Sample stimulus/release paradigm: a burst of extracellular glutamate increase events (black trace) modeled by an inhomogeneous Poisson process with time-dependent bell-shaped instantaneous rate (green curve). **b–g** Comparison of different model variables in the presence (control, blue traces) vs. in the absence of glutamate uptake by astrocytic transporters (TBOA, red traces). **h** Relative contributions of different glutamate-mediated pathways for Ca^{2+} signaling in an astrocyte: uptake/NCX-mediated Ca^{2+} signaling is predominant in astrocytic processes, or more generally, in those cell regions characterized by a low ER-to-cell volume ratio (ρ). On the contrary, mGluR-mediated CICR is predominant toward soma or primary processes of the astrocyte, where ρ tends to be large. Right panels refer to sample Ca^{2+} traces in response to burst increases of glutamate akin to that in (a) for parameter sets denoted by colored dots in the left panel. Percentage peak reduction associated with individual sample traces is reported in red. Adapted from Oschmann et al. (2017). Parameters as in $\Lambda_i = 8\text{pL}$, $\Lambda_{\text{ER}} = 0.8\text{pL}$, $\Lambda_e = 4\text{pL}$ and $A_a = 1.6 \times 10^{-2} \text{cm}^2$ (astrocytic membrane surface). Tables 13.3, 13.4 and 13.7

Table 13.3 Agonist-mediated Ca^{2+} signaling. The majority of the parameters are based on De Pittà et al. (2009) except for parameter values marked by ‘**’, which were specifically chosen for simulations presented in this chapter

Symbol	Description	Value	Units
<i>Astrocytic mGlu receptors</i>			
K_N	Min. glutamate affinity	1.3	μM
K_{KC}	Ca^{2+} affinity of cPKC	0.6	μM
ζ	Max. receptor desensitization by cPKC	10	–
<i>IP₃R kinetics</i>			
d_1	IP ₃ binding affinity	0.13	μM
O_2	Inactivating Ca^{2+} binding rate	0.2	$\mu\text{M}^{-1} \text{s}^{-1}$
d_2	Inactivating Ca^{2+} binding affinity	1.049	μM
d_3	IP ₃ binding affinity (with Ca^{2+} inactivation)	0.9434	μM
d_5	Activating Ca^{2+} binding affinity	0.08234**	μM
<i>Ca²⁺ fluxes</i>			
C_T	Total ER Ca^{2+} content	5	μM
ρ_A	ER-to-cytoplasm volume ratio	0.15	–
Ω_C	Maximal Ca^{2+} release rate by IP ₃ Rs	6	s^{-1}
Ω_L	Ca^{2+} leak rate	0.55**	s^{-1}
O_P	Maximal Ca^{2+} uptake rate	44**	μMs^{-1}
K_P	Ca^{2+} affinity of SERCA pumps	0.1	μM
<i>IP₃R production</i>			
O_β	Maximal rate of IP ₃ R production by PLC β	0.2	μMs^{-1}
O_δ	Maximal rate of IP ₃ R production by PLC δ	0.02	μMs^{-1}
K_δ	Ca^{2+} affinity of PLC δ	0.1	μM
κ_δ	Inhibiting IP ₃ R affinity of PLC δ	1.5	μM
<i>IP₃R degradation</i>			
Ω_{5P}	Rate of IP ₃ R degradation by IP-5P	0.04	s^{-1}
O_{3K}	Maximal rate of IP ₃ R degradation by IP ₃ -3K	2	μMs^{-1}
K_D	Ca^{2+} affinity of IP ₃ -3K	0.7	μM
K_{3K}	IP ₃ R affinity of IP ₃ -3K	1	μM

A key aspect that regulates the effect of glutamate uptake (or lack thereof) on astrocytic Ca^{2+} signaling is where glutamate uptake takes place in the astrocyte. The astrocyte cytoplasm is indeed highly complex, displaying a highly heterogeneous volume ratio between ER and cytosol (ρ_A). As this ratio enters the equation for v_A (13.15) through ρ in (13.8) for i_C (see Footnote 1), then it may be predicted that variations of ρ across different cell regions, such as in the soma vs. the peripheral processes (Pivneva et al. 2008; Patrushev et al. 2013), could also modulate the transporter-mediated Ca^{2+} response. This is illustrated in Fig. 13.5h where Ca^{2+} responses are mapped onto three regions of the space i_{NCX} versus ρ that are defined

Table 13.4 Astrocytic transport systems and transmembrane currents. ^aParameter values adopted from Oschmann et al. 2017

Symbol	Description	Value	Units
<i>EAAT2/GLT1</i> (Drejer et al. 1990)			
i_{T0}	Max. uptake current	0.68 ^a	pA/ μm^2
T_N	Na ⁺ binding affinity	5 ^a	mM
T_K	K ⁺ binding affinity	15	mM
T_G	Glutamate binding affinity	34	μM
<i>Na⁺/K⁺-ATPase</i> (Luo and Rudy 1994)			
i_{NKP0}	Max. current	1.52 ^a	pA/ μm^2
P_N	Na ⁺ binding affinity	10	mM
P_K	K ⁺ binding affinity	1.5	mM
<i>Na⁺/Ca²⁺-exchanger</i> (Luo and Rudy 1994)			
i_{NCX0}	Max. current	0.1 ^a	pA/ μm^2
X_N	Na ⁺ binding affinity	87.5	mM
X_C	Ca ²⁺ binding affinity	1.38	mM
η	Energy barrier	0.35	–
\bar{k}	Saturation factor	0.1	–
<i>Leakage currents</i>			
g_N	Na ⁺ conductance	6.5 ^a	pS/ μm^2
g_K	K ⁺ conductance	79.1 ^a	pS/ μm^2

by different ranges of percentage reduction of peak Ca²⁺ in response to a burst glutamate stimulus like the one in panel A (*blue*: <40%; *beige*: 40–80%; *green*: >80%), in TBOA vs. control conditions (*dashed* vs. *solid* Ca²⁺ traces associated with *colored dots*). One may appreciate how the reduction of Ca²⁺ response by TBOA tends to decrease independently of the magnitude of i_{NCX} as ρ increases. This may be explained considering that the contribution to Ca²⁺ signaling by NCX and CICR is different in small cytosolic compartments like in astrocytic process, for example, with respect to large cytosolic compartments akin to somatic ones. In this latter case in fact, the majority of Ca²⁺ response is likely mediated by CICR from the ER (which is large), whereas in the former, the opposite occurs, making NCX the main player in the regulation intracellular Ca²⁺ homeostasis at peripheral processes. In line with emerging experimental evidence (Bazargani and Attwell 2016), this ultimately suggests two modalities of Ca²⁺ signaling within the same astrocyte, one at the cell peripheral processes that is predominantly mediated by glutamate uptake by transporters coupled with NCX/NKP functions, and the other, toward primary process and in the soma, where the ER volume is large, that is mainly brought forth by mGluR-mediated CICR (Oschmann et al. 2017).

13.4 Neuronal Tuning Responses Depend on Activity-Dependent Regulation of Astrocytic Glutamate Uptake

Theory and experiments on cortical neuronal networks support the notion that network-wide modulations of synaptic connectivity promote emergence (death) of different states of network activity, which could associate with different task-dependent processes, either in terms of computation, behavior or cognition, or their disruption thereof, thereby resulting in the emergence of pathological network states (Brunel 2000; Danbolt 2001; Uhlhaas and Singer 2006). It may thus be expected that glutamate uptake is a functionally relevant process both in healthy and diseased brain networks, inasmuch as it modulates postsynaptic currents and thus neuronal excitability.

On the pathological side, astrocytic transporters have been identified as chief players in neuronal protection, for their key role in preventing excitotoxicity (Petr et al. 2015). Indeed inhibition of glutamate uptake by EAAT2/GLT1 was shown to increase extracellular glutamate beyond the threshold for excitotoxicity, triggering epileptiform activity (Campbell and Hablitz 2004; Tsukada et al. 2005) and ultimately neuronal death (Rothstein et al. 1996). In addition, GLT1 dysfunction has also been linked with neurodegenerative disorders, including Alzheimer's and Huntington's diseases, although the mechanisms at play remain a matter of active investigation (Danbolt 2001; Hassel et al. 2008; Li et al. 2009; Scott et al. 2011; Estrada-Sánchez and Rebec 2012).

On the physiological side, EAAT2/GLT1 function has been linked with a variety of behavioral and cognition-related network dynamics. For example, mice whose GLT1-mediated glutamate uptake was blocked in the amygdala displayed anxiety and depressive behavior (John et al. 2015). In primary cortical areas, blocking of GLT1 correlates with an increased rate of UP states and larger number of astrocytic Ca^{2+} responses (Poskanzer and Yuste 2011, 2016), hinting a potential link between astrocytic glutamate uptake and the regulation of cognitively relevant synchronous vs. asynchronous network states (Poskanzer and Molofsky 2018). Moreover, emerging evidence also suggest that this regulation could occur on multiple timescales, since, not only it could ensue from fast uptake of extracellular glutamate, but also from the possibility that GLT1 function may control density of postsynaptic AMPA receptors (Jarzylo and Man 2012).

Despite growing recognition that glutamate uptake by astrocytes could be involved in computationally relevant modulations of neuronal network activity, the mechanisms whereby this could be achieved have only been little investigated. With this regard, the landmark study by Schummers et al. (2008) that we mentioned in the previous section revealed that astrocytic glutamate uptake can shape the tuning response of V1 neurons. As these neurons are selective to orientation of visual cues, those investigators showed that such selectivity was significantly reduced when TBOA was infused to the cortex of living ferrets, with neurons showing a sustained firing activity for a broad range of orientations, while Ca^{2+} responses in orientation-associated

astrocyte populations, that would otherwise be observed in association with neuronal firing without TBOA, were practically absent instead.

The large literature on V1 argues that several factors could contribute to the emergence of neuronal orientation selectivity, including, but not limited to, the neuron's location, its neighbors, and the nature of synaptic connections impinging on it. In the remainder of this section, we question whether glutamate uptake by astrocytes could modulate any of these factors, or a combination thereof, or rather it should be considered as an additional independent causative factor in shaping neuronal tuning responses in V1. With this aim, we use the simplified description of glutamate uptake introduced in Sect. 13.2 to study neuronal tuning in a network model of V1 originally introduced by Stimberg et al. (2009) (see Appendix 1 for details). Briefly, the network model consists of both excitatory (E) and inhibitory (I), Hodgkin–Huxley-type neurons in the proportion of 3 : 1 that are recurrently connected and are also stimulated by independent afferents that mimic inputs to the network from other cortical areas (X). Synaptic conductances for E → E, I → E, E → I, and I → I connections are modeled by the (deterministic) kinetic schemes in Fig. 13.1. The network design, as exemplified in Fig. 13.6a, is such that each neuron has a preferred orientation based on its

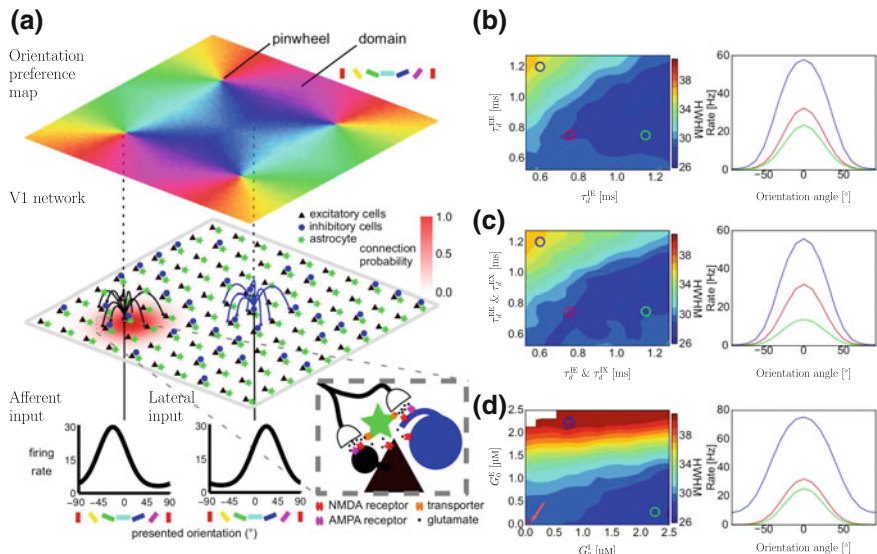


Fig. 13.6 Regulation of V1 neuronal tuning curves by astrocytic glutamate uptake. **a** Illustration of V1 network model [adapted from Stimberg et al. (2009)]. Lateral synaptic inputs account for any synaptic connection of the type $\beta \rightarrow \alpha$ with ($\alpha, \beta = E, I$). Afferent inputs instead stand for $X \rightarrow \alpha$ synaptic connections incoming to the network from other areas of the cortex. **b–d** Heat maps for half width at half maximum (HWHM) of neuronal tuning curves for independent variations of glutamate clearance time at lateral ($\tau_d^{\alpha\beta}$ for $\beta \rightarrow \alpha$ synapses) and/or afferent excitatory synapses ($\tau_d^{\alpha X}$) as well as for changes of extracellular glutamate concentration at excitatory (G_0^E) and inhibitory neurons (G_0^I). Right panels show sample tuning curves in association with same color circles in heat maps. Model description as in Appendix 1. Parameters as in Tables 13.2, 13.5, 13.6 and 13.7

Table 13.5 Neuronal parameters

Symbol	Description	Value	Units
<i>Membrane and leak channel</i> (Schummers et al. 2007)			
c_m	Membrane capacitance	0.35	nF
g_l^E	Leakage current of E cells	15.66	nS
g_l^I	Leakage current of I cells	31.31	nS
E_l	Leakage current reversal potential	-80	mV
<i>Voltage-gated channels</i> (Mariño et al. 2005)			
g_{Na}	Max. Na^+ channel conductance	17.87	μS
E_{Na}	Na^+ channel reversal potential	50	mV
μ_{Na}	Na^+ /Number of activation sites	3	-
v_{Na}	Na^+ /Number of inactivation sites	1	-
$g_{K,d}$	K^+ channel conductance	3.46	μS
$E_{K,d}$	K^+ channel reversal potential	-90	mV
μ_{Na}	K^+ /Number of activation sites	4	-
v_{Na}	K^+ /Number of inactivation sites	0	-
g_M^E	M -channel conductance (E cells)	278.82	nS
g_M^I	M -channel conductance (I cells)	27.88	nS
E_M	M -channel reversal potential	-85	mV
μ_M	M /Number of activation sites	1	-
v_M	M /Number of inactivation sites	0	-
<i>Background activity</i> (Schummers et al. 2007)			
g_{EE}^X	Background $E \rightarrow E$ conductance	8.77	nS
g_{EI}^X	Background $E \rightarrow I$ conductance	17.53	nS
g_{EI}^X	Background $I \rightarrow E$ conductance	28.81	nS
g_{II}^X	Background $I \rightarrow I$ conductance	57.61	nS
σ_E^X	Standard deviation excitatory noise	0.16	nS
σ_I^X	Standard deviation inhibitory noise	0.31	nS
E_E^X	Reversal potential of background excitatory current	-5	mV
E_I^X	Reversal potential of background inhibitory current	-70	mV
τ_E^X	Relaxation time background excitatory current	2.7	ms
τ_I^X	Relaxation time background inhibitory current	10.7	ms

location in a two-dimensional orientation preference map, and it is also driven by orientation-selective afferent synapses.

We consider modulation of neuronal responses for three different scenarios of glutamate uptake by astrocytes, and characterize neuronal tuning curves in terms of their half width at half maximum (HWHM)—namely the extent of the tuning curve given by the difference between the two extreme values of the visual cue’s orientation

Table 13.6 Network parameters (Stimberg et al. 2009)

Symbol	Description	Value	Units
<i>Network geometry</i>			
N_X	Number of afferent inputs	20	cell^{-1}
N_E	Number of excitatory neurons	2500	—
N_I	Number of inhibitory neurons	833	—
N_{EE} (N_{IE})	Number of excitatory recurrent inputs	100	cell^{-1}
N_{EI} (N_{II})	Number of inhibitory recurrent inputs	50	cell^{-1}
σ_E (σ_I)	Standard deviation of lateral connections	4	—
k_E	Shape of Γ_d^E distribution	7	—
θ_E	Scale of Γ_d^E distribution	0.6	—
k_I	Shape of Γ_d^I distribution	2.5	—
θ_I	Scale of Γ_d^I distribution	0.6	—
<i>Stimulation</i>			
\bar{v}	Max. afferent firing rate	30	Hz
a_0	Fraction of stimulus-independent firing rate	0.1	—
w	Afferent input tuning width	27.5	°

Table 13.7 Initial conditions are mainly set according to Østby et al. (2009) marked with ^a; Golovina (1997) marked with ^b; Oschmann et al. (2017) marked with **;

Symbol	Description	Value	Units
N_i	Intracellular Na^+ concentration	15 ^a	mM
N_e	Extracellular Na^+ concentration	145 ^a	mM
K_i	Intracellular K^+ concentration	3 ^a	mM
K_e	Extracellular K^+ concentration	100 ^a	mM
C_i	Intracellular Ca^{2+} concentration	0.073**	μM
C_e	Extracellular Ca^{2+} concentration	1.8	mM
C_{ER}	Ca^{2+} concentration in the ER	19 ^b	μM
h	Fraction of deinactivated IP_3 Rs	0.789**	—
I	Intracellular IP_3 concentration	0.157**	μM
v_a	Astrocytic membrane potential	-85	mV

angle at which the associated neuronal firing rate is equal to half of its maximum value. Figure 13.6b shows a color-coded heat map for HWHMs of neuronal tuning curves associated with multiple values for the time course of glutamate clearance from the synaptic cleft by astrocytic transporters ensuing from independent changes of both at E→E and E→I synapses. Moving along increasing x -values of the heat map is equivalent to selectively prolonging the decay of glutamate clearance at E→I synapses (i.e., τ_d^{IE}) and generally results in a moderate reduction of HWHM, as it may be evinced by the reduction of <30% of the peak rate of neuronal responses

in the *green* versus *red* tuning curves in the *right panel*. Conversely, as we move along *y*-values, the decay time for glutamate concentrations at recurrent excitatory synapses ($E \rightarrow E$) increases, thereby causing a stronger, yet more broadly tuned neuronal response (*right panel, blue curve*).

Similar observations also hold when analogous changes of decay time of glutamate clearance are taken into account for *all* excitatory synapses (Fig. 13.6c), that is, for lateral $E \rightarrow E$ and $E \rightarrow I$ *together with* excitatory afferent connections (associated with glutamate decay time constants τ_d^{EX} and τ_d^{IX} , respectively). Significantly, in this scenario, the effect of delayed clearance of extracellular glutamate at synapses on inhibitory neurons can reduce HWHMs much more than observed in panel B, insofar as the peak neuronal firing frequency can now decrease by a factor $>50\%$ (*right green vs. red tuning curves*). Overall, these results are in general agreement with experimental observations by Schummers et al. (2008) and predict that astrocytic glutamate uptake at excitatory synapses in E versus I neurons has functionally different consequences that tightly associate with the nature of synaptic inputs to these neurons, either in terms of excitatory versus inhibitory inputs or in terms of presynaptic activity or both.

An important additional contribution to postsynaptic neuronal depolarization could also come from extrasynaptically located postsynaptic receptors, most notably, NMDA receptors (Nie and Weng 2009; Nie et al. 2010, see also Fig. 13.4). Several experimental and modeling studies have specifically targeted these receptors (Rusakov and Kullmann 1998; Szapiro and Barbour 2007; Zheng et al. 2008; Scimemi et al. 2009), revealing an important contribution to neuronal depolarization by them, in conditions of increased ambient extracellular glutamate concentration such as those that would be expected in the presence of TBOA or a genetic disruption of astrocytic transporter function (Diamond 2001; Jabaudon et al. 1999; Tsukada et al. 2005; Bentzen et al. 2009). Accordingly, we consider this scenario in our model, characterizing neuronal tuning responses for variations of ambient extracellular glutamate both at excitatory and inhibitory neurons (G_0^E and G_0^I , respectively). Two observations can then be made based on the heat map in Fig. 13.6d. First, the variation of HWHM of tuning responses is strongly skewed—with E neurons being much more affected by changes of ambient glutamate than I neurons. Second, the maximum variation of HWHM attained by “global” variations of ambient glutamate can be considerably larger than those predicted for in panels (b) and (c) for “local” glutamate variations, respectively, at lateral *and* afferent synapses. This is ultimately accounted by the consideration of sample tuning curves in the right panel of Fig. 13.6d that reveals how neuronal tuning substantially broadens as G_0^E increases, with a neuron responding to visual cues of any orientation with a baseline firing rate >0 (*blue curve*).

13.5 Conclusions

The modeling arguments introduced in this chapter delineate a variegated picture for multiple potential modes of regulation of neuronal functional activity by glutamate uptake by astrocytic transporters. These modes span across different scenarios of neuron-astrocyte interactions that could range from individual synapses to synaptic ensembles and local neural networks, both by mere control of postsynaptic currents by the transporter's uptake efficiency (Sect. 13.2) and by complex interplay between synaptic release and astrocytic calcium signaling through regulation of glutamate uptake by modulation of Na^+ and K^+ intracellular homeostasis (Sect. 13.3).

Although further consideration of geometrical constraints—for example, size and morphology of different synapse types (e.g., spiny vs. non-spiny) (Tarczy-Hornoch et al. 1998; Gulyás et al. 1999), local transporter density and expression (Rusakov 2001; Piet et al. 2004; Scimemi and Beato 2009), and dynamic morphological coupling between synapses, and perisynaptic astrocytic processes (Reichenbach et al. 2010)—is expected to contribute to the complexity of this picture, our modeling framework proves valid to provide general predictions to drive future experiments on neuron-glial networks, revealing how even small variations of astrocytic glutamate uptake could dramatically impact neuronal function.

At the network level, the example of V1 neuronal tuning presented in Sect. 13.4 clearly pinpoints to a functional role for astrocytic glutamate uptake in computationally relevant tasks, such as processing of orientation features of visual stimuli by V1 neurons. While these results call for future experimental validation, it is intriguing to speculate that similar considerations could hold true for other brain regions too. The above prediction that equal perturbations of glutamate uptake at synapses onto excitatory versus inhibitory cells could result in different variations of neuronal firing activity, indeed seems in agreement with experimental reports on cerebellar synapses where the effects of prolongation of extracellular glutamate clearance were shown to depend on the nature of postsynaptic neuron (Barbour et al. 1994; Koester and Johnston 2005). On the other hand, robustness of this hypothesis against different experimental conditions reflected by different model parametrization requires further exploration (Allam et al. 2012), especially in relation to the possibility that cortical networks could be tuned to operate on the edge of phase transitions (Bertschinger and Natschläger 2004), such as in excitatory dominated or balanced recurrent regimes (Brunel 2000). It is then speculated that changes in astrocytic transporters' physiology could dramatically affect neuronal firing dynamics, ultimately accounting for functionally relevant transitions between different network regimes (Poskanzer and Molofsky 2018).

Acknowledgements The authors wish to thank Jeremy Petracic and Mriganka Sur for insightful discussions and Maurizio De Pittà for helping to revise and edit this manuscript in its final form. This work was supported by the Bundesministerium für Bildung und Forschung to KM (grant 01GQ-1009) and by the Deutsche Forschungsgemeinschaft to FO (Graduiertenkolleg 1589).

Appendix 1 Network Model

Neurons

Membrane potential of excitatory (E) and inhibitory (I) neurons changes by the sum of several conductance-based currents following a Hodgkin–Huxley formalism. The currents modulating a neuron's membrane potential are: (i) an intrinsic voltage-gated current accounting for firing properties of the cell (i_{AP}); (ii) an ohmic leakage current (i_l); (iii) a postsynaptic current mediated by ionotropic glutamate/GABA receptors at lateral (in-network) connections (i_s); (iv) a depolarizing current mediated by extrasynaptically located (postsynaptic) NMDA receptors (i_e); (v) an external background current accounting for synaptic inputs to the neurons from outside the network (i_X). Equation for the membrane potential of the generic α neuron (i.e., v_α , with $\alpha = E, I$) thus reads

$$c_m^\alpha \frac{dv_\alpha}{dt} = -i_{AP}^\alpha - i_l^\alpha - i_s^\alpha - i_e^\alpha - i_X^\alpha \quad (13.19)$$

where c_m^α denoting the neuron membrane capacitance.

Intrinsic and Leakage Currents

The voltage-gated intrinsic current that is responsible for making the neuron fire ensues from the sum of: (i) a fast Na^+ -mediated current (i_{Na}); (ii) a delayed rectifying K^+ current ($i_{\text{K},d}$); and (iii) a population-specific, slow noninactivating K^+ -mediated M-current (i_M^α), i.e.,

$$i_{AP}^\alpha = i_{\text{Na}} + i_{\text{K},d} + i_M^\alpha \quad (13.20)$$

The generic expression for any of the currents on the right hand side of the previous equation is

$$i_y = g_y^\alpha m_y^{\mu_y} n_y^{v_y} (v_\alpha - E_y) \quad \text{with } y = \text{Na, Kd, M} \quad (13.21)$$

where activating (inactivating) gating variables m_y (n_y) are in the form

$$\frac{d\chi_y}{dt} = \beta_{y,o}^\chi (1 - \chi_y) - \beta_{y,c}^\chi \chi_y \quad \text{with } \chi = m, n \quad (13.22)$$

$$\beta_x = \frac{b_1 b_2 (v_\alpha)}{\exp(b_3(v_\alpha)) + b_4} \quad \text{with } x = o, c \quad (13.23)$$

and current-specific voltage dependence of gating variables is detailed in Table 13.8. The leakage current is modeled by a standard ohmic current, i.e.,

Table 13.8 Voltage dependence of intrinsic gating variables (Destexhe and Paré 1999)

Gating variable	b_1 (mV $^{-1}$)	b_2 (mV)	b_3 (mV)	b_4
$\beta_{\text{Na},o}^m$	0.32	$-(v_\alpha + 45)$	$-\frac{v_\alpha + 45}{4}$	-1
$\beta_{\text{Na},o}^n$	0.128	1	$\frac{v_\alpha + 51}{18}$	0
$\beta_{\text{Kd},o}^m$	0.032	$-(v_\alpha + 40)$	$-\frac{v_\alpha + 40}{5}$	-1
$\beta_{\text{M},o}^m$	2.9529×10^{-4}	$-(v_\alpha + 30)$	$-\frac{v_\alpha + 30}{9}$	-1
$\beta_{\text{Na},c}^m$	0.28	$v_\alpha + 18$	$\frac{v_\alpha + 18}{5}$	-1
$\beta_{\text{Na},c}^n$	4	1	$-\frac{v_\alpha + 28}{5}$	1
$\beta_{\text{Kd},c}^m$	0.5	1	$\frac{v_\alpha + 45}{40}$	0
$\beta_{\text{M},c}^m$	2.9529×10^{-4}	$v_\alpha + 30$	$\frac{v_\alpha + 30}{9}$	-1

$$i_l^\alpha = g_l^\alpha (v_\alpha - E_\alpha) \quad (13.24)$$

Synaptic and Extrasynaptic Currents

Each neuron receives glutamatergic and GABAergic lateral synaptic inputs and is stimulated by glutamatergic afferents. Lateral glutamatergic connections are mediated by both AMPARs and NMDARs, whereas for afferent synapses we only consider AMPAR-mediated currents. Accordingly, the total synaptic drive to a generic α neuron ($\alpha = E, I$) is given by

$$i_s^\alpha = \frac{1}{N_{\alpha X}} \sum_{j \in X} i_{\text{AMPA}}^{\alpha j} + \frac{1}{N_{\alpha E}} \sum_{j \in E} (i_{\text{AMPA}}^{\alpha j} + i_{\text{NMDA}}^{\alpha j}) + \frac{1}{N_{\alpha I}} \sum_{j \in I} i_{\text{GABA}}^{\alpha j} \quad (13.25)$$

where $N_{\alpha\phi}$ ($\phi = E, I, X$), and receptors-specific currents are given by (Destexhe et al. 1998; Saftenku 2005):

$$i_{\text{AMPA}}^{\alpha j} = g_{\text{AMPA}} O_{\text{AMPA}}^{\alpha j} (v_\alpha - E_{\text{AMPA}}) \quad (13.26)$$

$$i_{\text{NMDA}}^{\alpha j} = g_{\text{NMDA}} O_{\text{NMDA}}^{\alpha j} B_\alpha ([\text{Mg}^{2+}]_e) O_{\text{NMDA}}^{\alpha j} (v_\alpha - E_{\text{NMDA}}) \quad (13.27)$$

$$i_{\text{GABA}}^{\alpha j} = g_{\text{GABA}} O_{\text{GABA}}^{\alpha j} (v_\alpha - E_{\text{GABA}}) \quad (13.28)$$

with $B_\alpha ([\text{Mg}^{2+}]_e) = 1 / (1 + \exp(-0.062v_\alpha)[\text{Mg}^{2+}]_e/3.57)$ (Jahr and Stevens 1990), where g_x , E_x ($x = \text{AMPA}, \text{NMDA}, \text{GABA}$), respectively, stand for receptor-specific conductances and reverse potentials, and $[\text{Mg}^{2+}]_e$ is the extracellular magnesium concentration.

Currents mediated by extrasynaptic NMDARs in neuron α are modeled akin to synaptic currents, yet considering an expression for the fraction of open receptors that is a power law function of the extracellular ambient glutamate concentration in the neuron's surroundings (G_0^α) (Bentzen et al. 2009), i.e.,

$$i_e^\alpha = g_e^\alpha B_\alpha ([\text{Mg}^{2+}]_e) O_e^\alpha (G_0^\alpha)(v_\alpha - E_e) \quad (13.29)$$

$$O_e^\alpha (G_0^\alpha) = 0.397 (G_0^\alpha)^{1.5} \quad (13.30)$$

Background Current

All neurons in the network are stimulated by a conductance-based background current that comprises both excitatory and inhibitory contributions, i.e.,

$$i_X^\alpha = g_{\alpha E}^X(t)(v_\alpha - E_E^X) - g_{\alpha I}^X(t)(v_\alpha - E_I^X). \quad (13.31)$$

where conductances $g_{\alpha\beta}^X$ follow an Ornstein-Uhlenbeck process, i.e.,

$$\frac{dg_{\alpha\beta}^X}{dt} = \frac{1}{\tau_\alpha^X} (g_{\alpha\beta}^X(t) - g_{\alpha\beta}^X) + \sigma_\beta^X \Gamma(t) \quad (13.32)$$

with $\Gamma(t)$ denoting white Gaussian noise.

Network Architecture

The V1 network considered in this chapter was constructed following the procedure originally outlined Stimberg et al. (2009), and the reader may refer to that study for implementation details on pinwheel domain-organized, two-dimensional orientation-selective cortical maps, such as that considered in Fig. 13.6. In our model, excitatory neurons are located on regular grid of $N_E \times N_E$ nodes. Inhibitory neurons are instead randomly positioned on 1/3 of all available nodes. All neurons receive $N_{\alpha X}$ afferent inputs in addition to a fixed number of recurrent (lateral) excitatory ($N_{\alpha E}$) and inhibitory inputs ($N_{\alpha I}$). Recurrent connections were randomly drawn from a cell-centered, two-dimensional Gaussian distance distribution with standard deviation σ_α according to Efraimidis and Spirakis (2008), so that nearest-neighbor connections are more likely. Synaptic delays (not shown in the model equations) were drawn from a gamma distribution $\Gamma_d^\alpha(k_\alpha, \theta_\alpha)$. To minimize finite-size artifacts, periodic boundary conditions were adopted accordingly. Stimulation was modeled by Poisson-distributed spike trains delivered by afferent inputs at orientation-dependent rate given by

$$f(\vartheta) = \bar{v} \left(a_0 + (1 - a_0) \exp \left(-\frac{(\vartheta - \theta(x, y))^2}{4w} \right) \right) \quad (13.33)$$

where ϑ is the orientation of the visual stimulus, \bar{v} is the maximum firing rate attained at preferred afferent orientation, a_0 denotes the part of firing rate that is independent

of stimulation, $\theta(x, y)$ is the spatial map of preferred orientations in the network, and w stands of the afferent input tuning width.

Numerical Methods

The network model was implemented in Python-based Brian 2.0 simulating environment (Chap. 18) using a standard Euler integration scheme with 0.01 ms time step. Simulations were run for 2 s of simulated time, discarding the first 0.4 s.

References

- Agulhon C, Petracic J, McMullen AB, Sweger EJ, Minton SK, Taves SR, Casper KB, Fiacco TA, McCarthy KD (2008) What is the role of astrocyte calcium in neurophysiology? *Neuron* 59(6):932–946
- Allam SL, Ghaderi VS, Bouteiller J-MC, Legendre A, Ambert N, Greget R, Bischoff S, Baudry M, Berger TW (2012) A computational model to investigate astrocytic glutamate uptake influence on synaptic transmission and neuronal spiking. *Front Comput Neurosci* 6:70
- Barbour B (2001) An evaluation of synapse independence. *J Neurosci* 21(20):7969–7984
- Barbour B, Keller BU, Llano I, Marty A (1994) Prolonged presence of glutamate during excitatory synaptic transmission to cerebellar Purkinje cells. *Neuron* 12(6):1331–1343
- Bazargani N, Attwell D (2016) Astrocyte calcium signaling: the third wave. *Nat Neurosci* 19(2):182–189
- Benediktsson AM, Marrs GS, Tu JC, Worley PF, Rothstein JD, Bergles DE, Dailey ME (2012) Neuronal activity regulates glutamate transporter dynamics in developing astrocytes. *Glia* 60(2):175–188
- Bentzen NCK, Zhabotinsky AM, Laugesen JL (2009) Modeling of glutamate-induced dynamical patterns. *Int J Neural Syst* 19(6):395–407
- Bergles DE, Tzingounis AV, Jahr CE (2002) Comparison of coupled and uncoupled currents during glutamate uptake by GLT-1 transporters. *J Neurosci* 22(23):10153–10162
- Bertschinger N, Natschläger T (2004) Real-time computation at the edge of chaos in recurrent neural networks. *Neural Comput* 16(7):1413–1436
- Billups B, Rossi D, Attwell D (1996) Anion conductance behavior of the glutamate uptake carrier in salamander retinal glial cells. *J Neurosci* 16(21):6722–6731
- Blaustein MP, Santiago EM (1977) Effects of internal and external cations and of ATP on sodium-calcium and calcium-calcium exchange in squid axons. *Biophys J* 20(1):79–111
- Blaustein MP, Blaustein MP, Lederer WJ, Lederer WJ (1999) Sodium/calcium exchange: its physiological implications. *Physiol Rev* 79(3):763–854
- Böttger P, Doganli C, Lykke-Hartmann K (2012) Migraine- and dystonia-related disease-mutations of Na⁺/K⁺-ATPases: relevance of behavioral studies in mice to disease symptoms and neurological manifestations in humans. *Neurosci Biobehav Rev* 36(2):855–871
- Brunel N (2000) Dynamics of sparsely connected networks of excitatory and inhibitory spiking neurons. *J Comput Neurosci* 8(3):183–208
- Campbell SL, Hablitz JJ (2004) Glutamate transporters regulate excitability in local networks in rat neocortex. *Neuroscience* 127(3):625–635
- Clements JD (1996) Transmitter timewcourse in the synaptic cleft: its role in central synaptic function. *Trends Neurosci* 19(5):163–171

- Clements JD, Lester RA, Tong G, Jahr CE, Westbrook GL (1992) The time course of glutamate in the synaptic cleft. *Science* 258(5087):1498–1501
- Danbolt NC (2001) Glutamate uptake. *Prog Neurobiol* 65(1):1–105
- Dayan P, Abbott LF (2001) Theoretical neuroscience: computational and mathematical modeling of neural systems. The MIT Press, Cambridge, Massachusetts, London, England
- De Pittà M, Brunel N (2016) Modulation of synaptic plasticity by glutamatergic gliotransmission: a modeling study. *Neural Plasticity*, p 7607924
- De Pittà M, Goldberg M, Volman V, Berry H, Ben-Jacob E (2009) Glutamate regulation of calcium and IP₃ oscillating and pulsating dynamics in astrocytes. *J Biol Phys* 35(4):383–411
- De Pittà M, Brunel N, Volterra A (2015) Astrocytes: orchestrating synaptic plasticity? *Neuroscience* 323
- Destexhe A, Paré D (1999) Impact of network activity on the integrative properties of neocortical pyramidal neurons in vivo. *J Neurophysiol* 81(4):1531–1547
- Destexhe A, Mainen ZF, Sejnowski TJ (1994) Synthesis of models for excitable membranes, synaptic transmission and neuromodulation using a common kinetic formalism. *J Comput Neurosci* 1(3):195–230
- Destexhe A, Mainen ZF, Sejnowski TJ (1998) Kinetic models of synaptic transmission. In: Koch C, Segev I (eds) Methods neuronal model, 2nd edn. MIT Press, Cambridge, pp 1–25
- Diamond JS (2001) Neuronal glutamate transporters limit activation of NMDA receptors by neurotransmitter spillover on CA1 pyramidal cells. *J Neurosci* 21(21):8328–8338
- Diamond JS (2005) Deriving the glutamate clearance time course from transporter currents in CA1 hippocampal astrocytes: transmitter uptake gets faster during development. *J Neurosci* 25(11):2906–2916
- Divito CB, Underhill SM (2014) Excitatory amino acid transporters: roles in glutamatergic neurotransmission. *Neurochem Int* 73(1):172–180
- Drejer J, Larsson O, Schousboe A (1982) Characterization of L-glutamate uptake into and release from astrocytes and neurons cultured from different brain regions. *Exp Brain Res* 47(2):259–269
- Drejer J, Larsson OM, Schousboe A (1990) Characterization of glutamate uptake into and release from astrocytes and neurons cultured from different brain regions. *Exp Brain Res* 87, 167–177
- Efraimidis P, Spirakis P (2008) Weighted random sampling. In: Kao M-Y (ed) Encyclopedia of Algorithms. Springer, US, pp 1024–1027
- Estrada-Sánchez AM, Rebec GV (2012) Corticostriatal dysfunction and glutamate transporter 1 (GLT1) in Huntington's disease: interactions between neurons and astrocytes. *Basal Ganglia* 2(2):57–66
- Fiacco TA, McCarthy KD (2018) Multiple lines of evidence indicate that gliotransmission does not occur under physiological conditions. *J Neurosci* 38(1):3–13
- Freche D, Pannasch U, Rouach N, Holcman D (2011) Synapse geometry and receptor dynamics modulate synaptic strength. *PLoS One* 6(10)
- Furness DN, Dehnes Y, Akhtar AQ, Rossi DJ, Hamann M, Grutle NJ, Gundersen V, Holmseth S, Lehre KP, Ullensvang K, Wojewodzic M, Zhou Y, Attwell D, Danbolt NC (2008) A quantitative assessment of glutamate uptake into hippocampal synaptic terminals and astrocytes: new insights into a neuronal role for excitatory amino acid transporter 2 (EAAT2). *Neuroscience* 157(1):80–94
- Geering K (2008) Functional roles of Na⁺ K⁺-ATPase subunits. *Curr Opin Nephrol Hypertens* 17(5):526–532
- Genoud C, Quairiaux C, Steiner P, Hirling H, Welker E, Knott GW (2006) Plasticity of astrocytic coverage and glutamate transporter expression in adult mouse cortex. *PLoS Biol* 4(11):e343
- Goldman WF, Yarowsky PJ, Juhaszova M, Krueger BK, Blaustein MP (1994) Sodium/calcium exchange in rat cortical astrocytes. *J Neurosci* 14(10):5834–5843
- Golovina VA (1997) Spatially and functionally distinct Ca²⁺ stores in sarcoplasmic and endoplasmic reticulum. *Science* (80-.) 275(5306):1643–1648
- Goubard V, Fino E, Venance L (2011) Contribution of astrocytic glutamate and GABA uptake to corticostriatal information processing. *J Physiol* 589(Pt 9):2301–2319

- Greget R, Pernot F, Bouteiller J-MC, Ghaderi VS, Allam SL, Keller AF, Ambert N, Legendre A, Sarmis M, Haeberle O, Faupel M, Bischoff S, Berger TW, Baudry M (2011) Simulation of postsynaptic glutamate receptors reveals critical features of glutamatergic transmission. *PLoS One* 6(12):e28380
- Grewer C, Gameiro A, Zhang Z, Tao Z, Braams S, Rauen T (2008) Glutamate forward and reverse transport: from molecular mechanism to transporter-mediated release after ischemia. *IUBMB Life* 60(9):609–619
- Gulyás AI, Megías M, Emri Z, Freund TF (1999) Total number and ratio of excitatory and inhibitory synapses converging onto single interneurons of different types in the CA1 area of the rat hippocampus. *J Neurosci* 19(22):10082–10097
- Haber M, Zhou L, Murai KK (2006) Cooperative astrocyte and dendritic spine dynamics at hippocampal excitatory synapses. *J Neurosci* 26(35):8881–8891
- Hassel B, Tessler S, Faull RLM, Emson PC (2008) Glutamate uptake is reduced in prefrontal cortex in Huntington's disease. *Neurochem Res* 33(2):232–237
- Haugeto Ø, Ullensvang K, Levy LM, Chaudhry FA, Honoré T, Nielsen M, Lehre KP, Danbolt NC (1996) Brain glutamate transporter proteins form homomultimers. *J Biol Chem* 271(44):27715–27722
- Herman MA, Jahr CE (2007) Extracellular glutamate concentration in hippocampal slice. *J Neurosci* 27(36):9736–9741
- Holcman D, Schuss Z (2014) Time scale of diffusion in molecular and cellular biology. *J Phys A* 47(17):173001
- Holmseth S, Dehnes Y, Huang YH, Follin-Arbelet VV, Grutle NJ, Mylonakou MN, Plachez C, Zhou Y, Furness DN, Bergles DE, Lehre KP, Danbolt NC (2012) The density of EAAC1 (EAAT3) glutamate transporters expressed by neurons in the mammalian CNS. *J Neurosci* 32(17):6000–6013
- Huang YH, Sinha SR, Tanaka K, Rothstein JD, Bergles DE (2004) Astrocyte glutamate transporters regulate metabotropic glutamate receptor-mediated excitation of hippocampal interneurons. *J Neurosci* 24(19):4551–4559
- Illarionava NB, Brismar H, Aperia A, Gunnarsson E (2014) Role of Na₊K₊-ATPase α1 and α2 isoforms in the support of astrocyte glutamate uptake. *PLoS One* 9(6)
- Jabaudon D, Shimamoto K, Yasuda-Kamatani Y, Scanziani M, Gähwiler BH, Gerber U (1999) Inhibition of uptake unmasks rapid extracellular turnover of glutamate of nonvesicular origin. *Proc Natl Acad Sci U S A* 96(15):8733–8738
- Jahr CE, Stevens CF (1990) Voltage dependence of NMDA-activated macroscopic conductances predicted by single-channel kinetics. *J Neurosci* 10(9):3178–3182
- Jarzylo LA, Man H-Y (2012) Parasympaptic NMDA receptor signaling couples neuronal glutamate transporter function to AMPA receptor synaptic distribution and stability. *J Neurosci* 32(7):2552–2563
- John CS, Sypek EI, Carlezon WA, Cohen BM, Öngür D, Bechtholt AJ (2015) Blockade of the GLT-1 transporter in the central nucleus of the Amygdala induces both anxiety and depressive-like symptoms. *Neuropsychopharmacology* 40(7):1700–1708
- Kanner BI (2006) Structure and function of sodium-coupled GABA and glutamate transporters. *J Membr Biol* 213(2):89–100
- Kelly T, Kafitz KW, Roderigo C, Rose CR (2009) Ammonium-evoked alterations in intracellular sodium and pH reduce glial glutamate transport activity. *Glia* 57(9):921–934
- Koester HJ, Johnston D (2005) Target cell-dependent normalization of transmitter release at neocortical synapses. *Science* 308(5723):863–866
- Lehre KP, Danbolt NC (1998) The number of glutamate transporter subtype molecules at glutamatergic synapses: chemical and stereological quantification in young adult rat brain. *J Neurosci* 18(21):8751–8757
- Lester RA, Jahr CE (1992) NMDA channel behavior depends on agonist affinity. *J Neurosci* 12(2):635–643

- Levy LM, Warr O, Attwell D (1998) Stoichiometry of the glial glutamate transporter GLT-1 expressed inducibly in a Chinese hamster ovary cell line selected for low endogenous Na⁺-dependent glutamate uptake. *J Neurosci* 18(23):9620–9628
- Li S, Hong S, Shepardson NE, Walsh DM, Shankar GM, Selkoe D (2009) Soluble oligomers of amyloid β protein facilitate hippocampal long-term depression by disrupting neuronal glutamate uptake. *Neuron* 62(6):788–801
- Luo CH, Rudy Y (1994) A dynamic model of the cardiac ventricular action potential. I. Simulations of ionic currents and concentration changes. *Circ Res* 74(6):1071–1096
- Li S, Stys PK (2001) Na⁺-K⁺-ATPase inhibition and depolarization induce glutamate release via reverse Na⁺-dependent transport in spinal cord white matter. *Neuroscience* 107(4):675–683
- Mariño J, Schummers J, Lyon DC, Schwabe L, Beck O, Wiesing P, Obermayer K, Sur M (2005) Invariant computations in local cortical networks with balanced excitation and inhibition. *Nat Neurosci* 8(2):194–201
- Mironov VI, Romanov AS, Simonov AY, Vedunova MV, Kazantsev VB (2014) Oscillations in a neurite growth model with extracellular feedback. *Neurosci Lett* 570:16–20
- Montes J, Gomez E, Merchán-Pérez A, DeFelipe J, Peña JM (2013) A machine learning method for the prediction of receptor activation in the simulation of synapses. *PloS One* 8(7):e68888
- Montes J, Peña JM, DeFelipe J, Herreras O, Merchan-Perez A (2015) The influence of synaptic size on AMPA receptor activation: a Monte Carlo model. *PLoS One* 10(6):e0130924
- Murphy-Royal C, Dupuis JP, Varela JA, Panatier A, Pinson B, Baufreton J, Groc L, Oliet SHR (2015) Surface diffusion of astrocytic glutamate transporters shapes synaptic transmission. *Nat Neurosci* 18(2)
- Nedergaard M, Verkhratsky A (2012) Artifact versus reality: how astrocytes contribute to synaptic events. *Glia* 60(7):1013–1023
- Nie H, Weng H-R (2009) Glutamate transporters prevent excessive activation of NMDA receptors and extrasynaptic glutamate spillover in the spinal dorsal horn. *J Neurophysiol* 101(4):2041–2051
- Nie H, Zhang H, Weng H-R (2010) Bidirectional neuron-glia interactions triggered by deficiency of glutamate uptake at spinal sensory synapses. *J Neurophysiol* 104(2):713–725
- Østby I, Øyehaug L, Einevoll GT, Nagelhus EA, Plahte E, Zeuthen T, Lloyd CM, Ottersen OP, Omholt SW, (2009) Astrocytic mechanisms explaining neural-activity-induced shrinkage of extraneuronal space. *PLoS Comput Biol* 5(1):e1000272
- Okubo Y, Sekiya H, Namiki S, Sakamoto H, Iinuma S, Yamasaki M, Watanabe M, Hirose K, Iino M (2010) Imaging extrasynaptic glutamate dynamics in the brain. *Proc Nat Acad Sci USA* 107(14):6526–6531
- Oliet SH, Piet R, Poulin DA (2001) Control of glutamate clearance and synaptic efficacy by glial coverage of neurons. *Science* 292(5518):923–926
- Oschmann F, Mergenthaler K, Jungnickel E, Obermayer K (2017) Spatial separation of two different pathways account for the generation of calcium signals in astrocytes. *PLoS Comput Biol* 13(2):e1005377
- Pannasch U, Freche D, Dallérac G, Ghézali G, Escartin C, Ezan P, Cohen-Salmon M, Benchenane K, Abudara V, Dufour A, Lübke JHR, Déglon N, Knott G, Holcman D, Rouach N (2014) Connexin 30 sets synaptic strength by controlling astroglial synapse invasion. *Nat Neurosci* 17(4):549–558
- Patrushev I, Gavrilov N, Turlapov V, Semyanov A (2013) Subcellular location of astrocytic calcium stores favors extrasynaptic neuron-astrocyte communication. *Cell Calcium* 54(5):343–349
- Petr GT, Sun Y, Frederick XNM, Zhou Y, Dhamne SC, Hameed XMQ, Miranda XC, Bedoya EA, Fischer KD, Armsen W, Wang J, Danbolt NC, Rotenberg A, Aoki XCJ, Rosenberg PA (2015) Conditional deletion of the glutamate transporter GLT-1 reveals that astrocytic GLT-1 protects against fatal epilepsy while neuronal GLT-1 contributes significantly to glutamate uptake into synaptosomes. *J Neurosci* 35(13):5187–5201
- Piet R, Vargová L, Syková E, Poulin DA, Oliet SHR (2004) Physiological contribution of the astrocytic environment of neurons to intersynaptic crosstalk. *Proc Natl Acad Sci USA* 101(7):2151–2155

- Pivneva T, Haas B, Reyes-Haro D, Laube G, Veh R, Nolte C, Skibo G, Kettenmann H (2008) Store-operated Ca^{2+} entry in astrocytes: different spatial arrangement of endoplasmic reticulum explains functional diversity in vitro and in situ. *Cell Calcium* 43(6):591–601
- Poskanzer KE, Molofsky AV (2018) Dynamism of an astrocyte in vivo: perspectives on identity and function. *Ann Rev Physiol* 80:143–157
- Poskanzer KE, Yuste R (2011) Astrocytic regulation of cortical UP states. *Proc Natl Acad Sci* 108(45):18453–18458
- Poskanzer KE, Yuste R (2016) Astrocytes regulate cortical state switching in vivo. *Proc Natl Acad Sci* 113(19):E2675–E2684
- Raynaud X, Nordaas M, Lehre KP, Danbolt NC (2015) Well-posedness of a model equation for neurotransmitter diffusion with reactive boundaries. *Math Model Methods Appl Sci* 25(02):195–227
- Reichenbach A, Derouiche A, Kirchhoff F (2010) Morphology and dynamics of perisynaptic glia. *Brain Res Rev* 63(1):11–25
- Rojas H, Colina C, Ramos M, Benaim G, Jaffe EH, Caputo C, DiPolo R (2007) Na^+ entry via glutamate transporter activates the reverse $\text{Na}^+/\text{Ca}^{2+}$ exchange and triggers $\text{Ca}(\text{i})^{2+}$ -induced Ca^{2+} release in rat cerebellar Type-1 astrocytes. *J Neurochem* 100(5):1188–1202
- Rose CR, Chatton J-Y (2016) Astrocyte sodium signaling and neuro-metabolic coupling in the brain. *Neuroscience* 323:121–134
- Rose CR, Ransom BR (1996) Mechanisms of H^+ and Na^+ changes induced by glutamate, kainate, and D-aspartate in rat hippocampal astrocytes. *J Neurosci* 16(17):5393–5404
- Rose EM, Koo JCP, Antflick JE, Ahmed SM, Angers S, Hampson DR (2009) Glutamate transporter coupling to Na^+ , K^+ -ATPase. *J Neurosci* 29(25):8143–8155
- Rothstein JD, Dykes-Hoberg M, Pardo CA, Bristol LA, Jin L, Kuncl RW, Kanai Y, Hediger MA, Wang Y, Schielke JP, Welty DF (1996) Knockout of glutamate transporters reveals a major role for astroglial transport in excitotoxicity and clearance of glutamate. *Neuron* 16(3):675–686
- Rusakov DA (2001) The role of perisynaptic glial sheaths in glutamate spillover and extracellular Ca^{2+} depletion. *Biophys J* 81(4):1947–1959
- Rusakov DA, Kullmann DM (1998) Extrasynaptic glutamate diffusion in the hippocampus: ultrastructural constraints, uptake, and receptor activation. *J Neurosci* 18(9):3158–3170
- Rusakov DA, Lehre KP (2002) Perisynaptic asymmetry of glia: new insights into glutamate signalling. *Trends Neurosci* 25(10):492–494
- Saftenku EE (2005) Modeling of slow glutamate diffusion and AMPA receptor activation in the cerebellar glomerulus. *J Theor Biol* 234(3):363–382
- Savchenko LP, Rusakov DA (2007) The optimal height of the synaptic cleft. *Proc Natl Acad Sci USA* 104(6):1823–1828
- Savchenko I, Volterra A (2018) Gliotransmission: beyond black-and-white. *J Neurosci* 38(1):14–25
- Schummers J, Cronin B, Wimmer K, Stimberg M, Martin R, Obermayer K, Koerding K, Sur M (2007) Dynamics of orientation tuning in cat v1 neurons depend on location within layers and orientation maps. *Front Neurosci* 1(1):145–159
- Schummers J, Yu H, Sur M (2008) Tuned responses of astrocytes and their influence on hemodynamic signals in the visual cortex. *Science* 320(5883):1638–1643
- Scimemi A, Beato M (2009) Determining the neurotransmitter concentration profile at active synapses. *Mol Neurobiol* 40(3):289–306
- Scimemi A, Tian H, Diamond JS (2009) Neuronal transporters regulate glutamate clearance, NMDA receptor activation, and synaptic plasticity in the hippocampus. *J Neurosci* 29(46):14581–14595
- Scimemi A, Meabon JS, Woltjer RL, Sullivan JM, Diamond JS, Cook DG (2013) Amyloid- β 1–42 slows clearance of synaptically released glutamate by mislocalizing astrocytic GLT-1. *J Neurosci* 33(12):5312–5318
- Scott HA, Gebhardt FM, Mitrovic AD, Vandenberg RJ, Dodd PR (2011) Glutamate transporter variants reduce glutamate uptake in Alzheimer's disease. *Neurobiol Aging* 32(3):553–e1
- Simard M, Nedergaard M (2004) The neurobiology of glia in the context of water and ion homeostasis. *Neuroscience* 129(4):877–896

- Smith SL, Häusser M (2010) Parallel processing of visual space by neighboring neurons in mouse visual cortex. *Nat Neurosci* 13(9):1144–1149
- Stimberg M, Wimmer K, Martin R, Schwabe L, Mariño J, Schummers J, Lyon DC, Sur M, Obermayer K (2009) The operating regime of local computations in primary visual cortex. *Cereb Cortex* 19(9):2166–2180
- Szapiro G, Barbour B (2007) Multiple climbing fibers signal to molecular layer interneurons exclusively via glutamate spillover. *Nat Neurosci* 10(6):735–742
- Takuma K, Matsuda T, Hashimoto H, Asano S, Baba A (1994) Cultured rat astrocytes possess Na⁺-Ca²⁺ exchanger. *Glia* 12(4):336–342
- Tanaka K, Watase K, Manabe T, Yamada K, Watanabe M, Takahashi K, Iwama H, Nishikawa T, Ichihara N, Kikuchi T, Okuyama S, Kawashima N, Hori S, Takimoto M, Wada K (1997) Epilepsy and exacerbation of brain injury in mice lacking the glutamate transporter GLT-1. *Science* 276(5319):1699–1702
- Tanaka M, Shih P-Y, Gomi H, Yoshida T, Nakai J, Ando R, Furuichi T, Mikoshiba K, Semyanov A, Itohara S (2013) Astrocytic Ca²⁺ signals are required for the functional integrity of tripartite synapses. *Mol Brain* 6(1):6
- Tarczy-Hornoch K, Martin KAC, Jack JJB, Stratford KJ (1998) Synaptic interactions between smooth and spiny neurones in layer 4 of cat visual cortex *in vitro*. *J Physiol* 508(2):351–363
- Tong G, Jahr CE (1994) Block of glutamate transporters potentiates postsynaptic excitation. *Neuron* 13(5):1195–1203
- Tsacopoulos M (2002) Metabolic signaling between neurons and glial cells: a short review. *J Physiol* 96(3–4):283–288
- Tsaneva-Atanasova K, Burgo A, Galli T, Holcman D (2009) Quantifying neurite growth mediated by interactions among secretory vesicles, microtubules, and actin networks. *Biophys J* 96(3):840–857
- Tsukada S, Iino M, Takayasu Y, Shimamoto K, Ozawa S (2005) Effects of a novel glutamate transporter blocker, (2S, 3S)-3-[3-[4-(trifluoromethyl)benzoylamino]benzyloxy]aspartate (TFB-TBOA), on activities of hippocampal neurons. *Neuropharmacology* 48(4):479–491
- Tzingounis AV, Wadiche JI (2007) Glutamate transporters: confining runaway excitation by shaping synaptic transmission. *Nat Rev Neurosci* 8(12):935–947
- Uhlhaas P, Singer W (2006) Neural synchrony in brain disorders: relevance for cognitive dysfunctions and pathophysiology. *Neuron* 52(1):155–168
- Underhill SM, Wheeler XDS, Amara SG (2015) Differential regulation of two isoforms of the Glial glutamate transporter EAAT2 by DLG1 and CaMKII. *J Neurosci* 35(13):5260–5270
- Wadiche JI, Arriza JL, Amara SG, Kavanaugh MP (1995) Kinetics of a human glutamate transporter. *Neuron* 14(5):1019–1027
- Weng H-R, Chen JH, Pan ZZ, Nie H (2007) Glial glutamate transporter 1 regulates the spatial and temporal coding of glutamatergic synaptic transmission in spinal lamina II neurons. *Neuroscience* 149(4):898–907
- Zahler R, Zhang ZT, Manor M, Boron WF (1997) Sodium kinetics of Na, K-ATPase alpha isoforms in intact transfected HeLa cells. *J Gen Physiol* 110(2):201–213
- Zerangue N, Kavanaugh MP (1996) Flux coupling in a neuronal glutamate transporter. *Nature* 383(6601):634–637
- Zheng K, Rusakov DA (2015) Efficient integration of synaptic events by NMDA receptors in three-dimensional neuropil. *Biophys J* 108(10):2457–2464
- Zheng K, Scimemi A, Rusakov DA (2008) Receptor actions of synaptically released glutamate: the role of transporters on the scale from nanometers to microns. *Biophys J* 95(10):4584–4596

Chapter 14

Astrocytic Ion Dynamics: Implications for Potassium Buffering and Liquid Flow



Geir Halnes, Klas H. Pettersen, Leiv Øyehaug, Marie E. Rognes and Gaute T. Einevoll

Abstract We review modelling of astrocyte ion dynamics with a specific focus on the implications of so-called spatial potassium buffering where excess potassium in the extracellular space (ECS) is transported away to prevent pathological neural spiking. The recently introduced Kirchhoff–Nernst–Planck (KNP) scheme for modelling ion dynamics in astrocytes (and brain tissue in general) is outlined and used to study such spatial buffering. We next describe how the ion dynamics of astrocytes may regulate microscopic liquid flow by osmotic effects and how such microscopic flow can be linked to whole-brain macroscopic flow. We thus describe key elements in a putative multiscale theory with astrocytes linking neural activity on a microscopic scale to macroscopic fluid flow.

Keywords Tissue modelling · Ion concentration dynamics · Electrodiffusion
Neuron–glia interactions · Potassium buffering

G. Halnes (✉) · G. T. Einevoll
Faculty of Science and Technology,
Norwegian University of Life Sciences, Ås, Norway
e-mail: geir.halnes@nmbu.no

K. H. Pettersen
Letten Centre and GliaLab, Centre for Molecular Medicine,
University of Oslo, Oslo, Norway

L. Øyehaug
Faculty of Technology, Art and Design,
OsloMet - Oslo Metropolitan University, Oslo, Norway

M. E. Rognes
Simula Research Laboratory, Fornebu, Norway

M. E. Rognes
Department of Mathematics, University of Oslo, Oslo, Norway

G. T. Einevoll
Department of Physics, University of Oslo, Oslo, Norway

14.1 Introduction

Brain function is fundamentally about movement of ions and molecules. When modelling neuronal dynamics, it is common to neglect the dynamics of individual ion species and rather just simulate the net electrical currents and resulting changes in membrane potentials. The justification is that on the typical timescale of neural integration (milliseconds), the concentrations of the major charge carriers in brain tissue (i.e. Na^+ , K^+ , Cl^- , ...) vary little. For astrocytic dynamics, the situation is different. For one, the typical timescale for astrocytic membrane processes is longer, i.e. seconds rather than milliseconds, so that the fixed ion concentration assumption is a priori more dubious. Further, many key astrocytic functions are related just to their responses to shifts in extracellular ion concentrations (Wang and Bordey 2008).

As discussed in Chaps. 1 and 12, astrocytes have several homeostatic functions in the brain. They provide metabolic support for neurons, synthesize extracellular matrix proteins, adhesion molecules and trophic factors controlling neuronal maturation, are involved in the formation of blood vessels and in maintenance of the blood-brain barrier and maintain the ECS via uptake of K^+ and neurotransmitters (Wang and Bordey 2008). In the present chapter, we describe theoretical frameworks for modelling astrocytic ion concentration dynamics, with particular focus on K^+ clearance mechanisms, and possible consequences for microscopic liquid flow in the brain.

When neurons fire action potentials (APs), they absorb Na^+ and expel K^+ from/to the ECS. At low to moderate firing frequencies, the time interval between two APs is sufficient for neuronal $\text{Na}^+ - \text{K}^+$ pumps to restore the baseline levels of Na^+ and K^+ . Ion concentrations then remain essentially constant over time (Somjen 2004). However, during periods of intense neural signalling, the neuronal ion pumps may fail to keep up, and ECS ion concentrations can change significantly (Frankenhaeuser and Hodgkin 1956; Coldingley and Somjen 1978; Dietzel et al. 1989; Gardner-Medwin 1983; Chen and Nicholson 2000; Haj-Yasein et al. 2014). The most critical effects of this relate to changes in the K^+ -concentration in the ECS, which can increase from a relatively low baseline level of around 3 mM up to levels between 8 and 12 mM during non-pathological conditions (Hertz et al. 2013; Chen and Nicholson 2000; Newman et al. 1993). Increases beyond this can occur under pathological conditions such as hypoxia, anoxia, ischaemia epilepsy and spreading depression (Syková and Nicholson 2008; Enger et al. 2015; Park and Durand 2006; Florence et al. 2009). During spreading depression, K^+ -concentrations in the ECS can become as high as 60 mM (Somjen 2001).

Astrocytes have several membrane mechanisms for local uptake of excess K^+ (Orkand et al. 1966; Lux et al. 1986; Somjen 2004; Gardner-Medwin 1983; Newman et al. 1993; Chen and Nicholson 2000; Wang and Bordey 2008; Øyehaug et al. 2012). They are therefore likely to play a role in pathological conditions related to ion dynamics in the ECS, and evidence suggests that changes in astrocytic function are implicated in spreading depression, epilepsy and ischaemia (De Keyser et al. 2008; Nedergaard and Dirnagl 2005). In Sect. 14.2, we briefly review some modelling

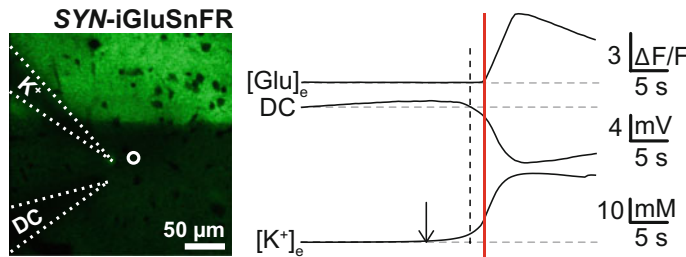


Fig. 14.1 Changes in extracellular K^+ -concentration, extracellular glutamate and extracellular potential (DC) during cortical spreading depression. *Left* The green fluorescent tracer shows the extracellular glutamate wave, which travels with a speed of 50 mm/s. The dashed white lines indicate the positioning of the recording electrodes, while the solid white line shows the region of interest (ROI) for glutamate. *Right* The glutamate signal within the ROI ($[Glu^+]$ _e, upper), extracellular potential (DC, middle) and extracellular K^+ concentration ($[K^+]$ _e, lower), all as functions of time. The figure is modified from Fig. 4 in Enger et al. (2015)

works that have investigated the relationship between astrocytic regulation of ECS K^+ and neuronal firing patterns.

Increases in the ECS K^+ -concentration are often accompanied by a slow negative shift in the ECS potential. These potential shifts can be on the order of a few millivolts (Syková and Nicholson 2008; Kríz et al. 1975; Lothman and Somjen 1975; Dietzel et al. 1989; Coldingley and Somjen 1978). Figure 14.1 shows an extreme example from an experiment on cortical spreading depression, where a K^+ -concentration shift of 20–30 mM was accompanied by a 5–10 mV shift in the ECS potential (Enger et al. 2015). It has been argued that this link between sustained potentials and the ECS K^+ concentration is the signature of glial K^+ buffering currents (Dietzel et al. 1989). In addition to local uptake and storage in astrocytes (Dietzel et al. 1989; Coles and Orkand 1986), clearance of excess K^+ from local high-concentration regions may occur by transport through the ECS (Nicholson et al. 2000) and by a process coined *spatial K^+ buffering*, where astrocytes take up K^+ from high-concentration regions, transport it intracellularly and release it in regions where the ECS concentration is lower (Orkand et al. 1966; Gardner-Medwin 1983; Newman et al. 1993; Chen and Nicholson 2000; Halnes et al. 2013). As astrocytes often are interconnected by gap junctions into a syncytium, intracellular transport can in principle occur over quite large distances and via several cells (Chen and Nicholson 2000). The relative importance of these different clearance mechanisms is under debate (Macaulay and Zeuthen 2012). As these processes involve variations in both ionic concentrations and electrical potentials, ionic transports may be propelled both by voltage and concentration gradients (Kofuji and Newman 2004). In Sect. 14.3, we explore spatial K^+ buffering in detail and present a recently developed biophysical modelling formalism for simulating electrodiffusive processes—the *Kirchhoff–Nernst–Planck (KNP)* scheme.

Changes in ionic concentrations will also induce osmotic pressures, which may lead to water uptake, astrocyte swelling and microscopic liquid flow in the brain (Østby et al. 2009; Øyehaug et al. 2012). A complete modelling framework that combines spatial K^+ buffering processes with processes related to water flows is

currently lacking, but in Sect. 14.4.2 we review the theoretical foundation that such a framework would need to be based on.

14.2 Influence of Glial K⁺ Buffering on Neuronal Activity

The effect of ion concentration shifts on neuronal activity can, to a larger extent, be explained by its impact on the reversal potential e_k of an ion species k :

$$e_k = \frac{\psi}{z_k} \log([k]_E/[k]_I). \quad (14.1)$$

As Eq. 14.1 shows, the reversal potential depends on the ion concentrations on the outside ($[k]_E$) and inside ($[k]_I$) of the membrane (z_k is the valence of ion species k , and $\psi = RT/F$ where R is the gas constant, T the absolute temperature and F Faraday's constant). For example, when K⁺ accumulates in the ECS, the K⁺ reversal potential will increase. As a consequence, neurons will become depolarized and brought closer to their firing threshold, which in turn may lead to enhanced neuronal activity and to further increases in $[K^+]_E$. Computational models that study disorders related to extracellular K⁺ are many (see, e.g., Øyehaug et al. 2012; Ullah and Schiff 2009; Hübel and Dahlem 2014; Kager et al. 2000, 2006; Cressman et al. 2009; Florence et al. 2009; Park and Durand 2006; Somjen et al. 2008; Sibille et al. 2015). Figure 14.2 shows an example from a previous modelling study where we explored the positive feedback loop described above (Øyehaug et al. 2012). The model used in (Øyehaug et al. 2012) combined a Hodgkin–Huxley-type neuron model (Kager et al. 2000) with a detailed model of glial membrane ion and water transport (Østby et al. 2009).

Figure 14.2a, b shows the results of two numerical simulations of the neuron–glia model when the neuron was stimulated by electrical currents of different durations and magnitudes. Elevated levels of $[K^+]_E$ were observed with both the briefest current stimulation (Fig. 14.2a) and a longer and stronger current stimulation (Fig. 14.2b). However, in terms of the resulting spiking patterns, the difference was striking: with the briefest stimulation, the neuron fired several APs after the stimulation had ceased, and then returned to the resting state. By contrast, the larger and longer stimulus drove the neuron into a deactivated state where the neuron lingered at a depolarized level with a nonzero K⁺-efflux. In this case, $[K^+]_E$ reached very high levels (Fig. 14.2b, inset). The behaviour encountered in the former situation is referred to as *spontaneous discharge*, while the latter situation is referred to as *depolarization block*.

Whereas Fig. 14.2a and b illustrate the interplay between neuronal activity and $[K^+]_E$, Fig. 14.2c shows more directly the effect that astrocytes may have on neurodynamics. Here, the neuron received no external input. When the astrocyte had the default parametrization, $[K^+]_E$ was maintained at a low level, and the neuron was at rest (red lines). However, when we modelled astrocytic dysfunction as a reduction in the astrocyte's Na⁺/K⁺-pump rate, $[K^+]_E$ increased and drove the neuron into

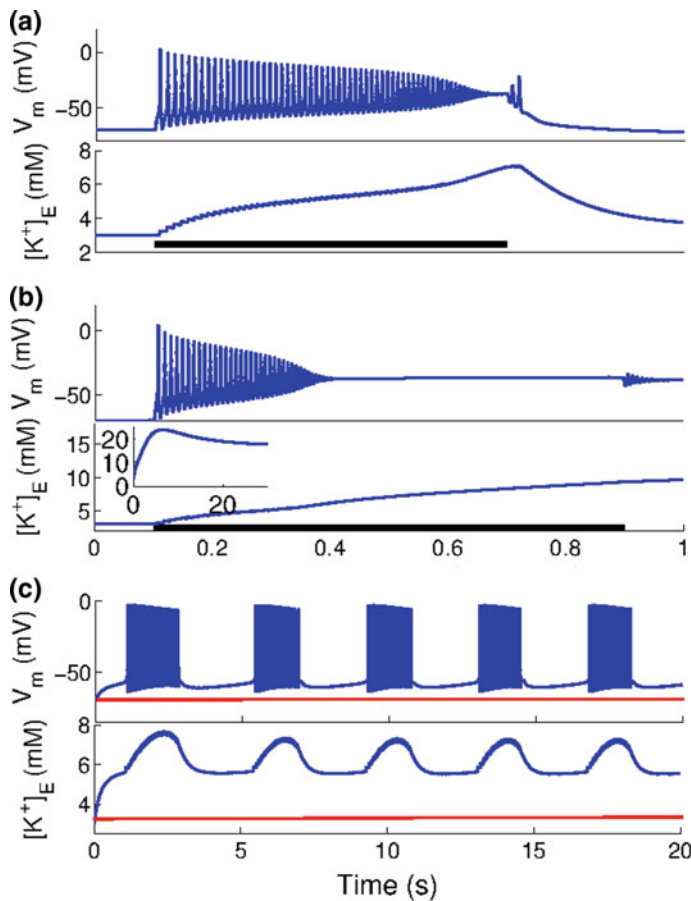


Fig. 14.2 Dynamical repertoire of neuron–glia model. The model (Øyehaug et al. 2012) included voltage-gated sodium and potassium channels and the NaKATPase pump in the neuronal membrane (following Kager et al. (2000)), and sodium, potassium and chloride channels, as well as the NaKATPase pump, the NKCC1 and NBC cotransporters and water channels in the glial membrane (Østby et al. 2009). To ensure charge neutrality of the ECS, the assumption was made that the amounts of sodium and potassium crossing the neuronal membrane were identical so that the cation current was exactly zero. **a, b** Dynamics of neuronal membrane potential V_m (top) and $[K^+]'_E$ (bottom) when the neuron was stimulated (**a**) with a short pulse of relatively small magnitude and (**b**) with a longer pulse of larger magnitude (inset in **b** shows long-time dynamics). **c** Dynamics of neuronal membrane potential V_m (top) and $[K^+]'_E$ (bottom) compared to resting conditions (red lines) in the absence of stimulation with a reduction of the maximum rate of the glial sodium–potassium pump by a factor 0.62, see (Øyehaug et al. 2012) for details

periodic bursting. This bursting behaviour, also encountered in another model of neuron–glia interaction (Cressman et al. 2009), was previously observed in experiments and has been interpreted as relevant to some types of epilepsy (Jensen and Yaari 1997; Ziburkus et al. 2006). Further, in human epilepsy patients it has been

found that the overall activity of NaKATPase is reduced (Grisar et al. 1992), consistent with the results in Fig. 14.2, showing that neurons are more likely to fire spontaneous discharges, go into depolarization block or display bursting behaviour when the glial sodium–potassium pump rate was reduced.

Figure 14.2 just showed a few illustrative examples on how K^+ buffering can be relevant for neurodynamics. For a more thorough analysis of this, we refer to the original publication (Øyehaug et al. 2012), where we presented a bifurcation analysis that systematically mapped out how different neuronal firing states depended on variations in selected model parameters. In the following, we direct our focus towards the main topic of this chapter, i.e. on the glial K^+ buffering process as such.

14.3 An Electrodiffusive Model of Spatial K^+ Buffering by Astrocytes

Unlike neurons, glial cells are not predominantly driven by synaptic input and do not produce fast unitary events such as action potentials. To a large extent, astrocytic membrane dynamics appears rather to be driven by slow variations in ECS ion concentrations and voltage differences between the ECS and the intracellular astrocytic space. Astrocyte resting membrane potentials have been reported to be heterogeneous, in part because of the heterogeneity in K^+ conductance (Verkhratsky and Butt 2013; Zhang and Barres 2010). However, as a tentative approximation, we assume that all astrocytes within a (relatively large) spatial region receive roughly the same input and perform roughly the same processing, and can be collapsed into a single astrocyte domain, representing the mass average astrocytic response (this assumption was motivated previously (Gardner-Medwin 1983; Chen and Nicholson 2000; Halnes et al. 2013). Furthermore, astrocytes are often coupled with gap junctions, allowing intracellular ionic transports over larger distances through a syncytium of many interconnected cells (Chen and Nicholson 2000; Enger et al. 2015). Intracellular transports in the astrocyte domain are therefore conceptually similar to ECS transports and not limited by the spatial extension of a single cell.

A framework for modelling long-term astrocytic processing on an extended spatial scale is summarized in Fig. 14.3. As argued above, transport processes through the ECS and the astrocytic syncytium (panel A) can be described by a simplified two-domain model (panel B), which includes an ECS domain and an astrocyte domain that exchange ions via typical astrocytic membrane mechanisms. In this aspect, the astrocyte modelling framework is simpler than computational neural models, which are often described with a high degree of spatial specificity. However, in the spatial K^+ buffering model, axial fluxes in the ECS or inside the astrocyte must be described by the Nernst–Planck equations for electrodiffusion (see Sect. 14.3.1). Then, not only electrical currents but also ion concentration dynamics are explicitly modelled. In this aspect, the astrocyte modelling framework is more complex than computational neural models.

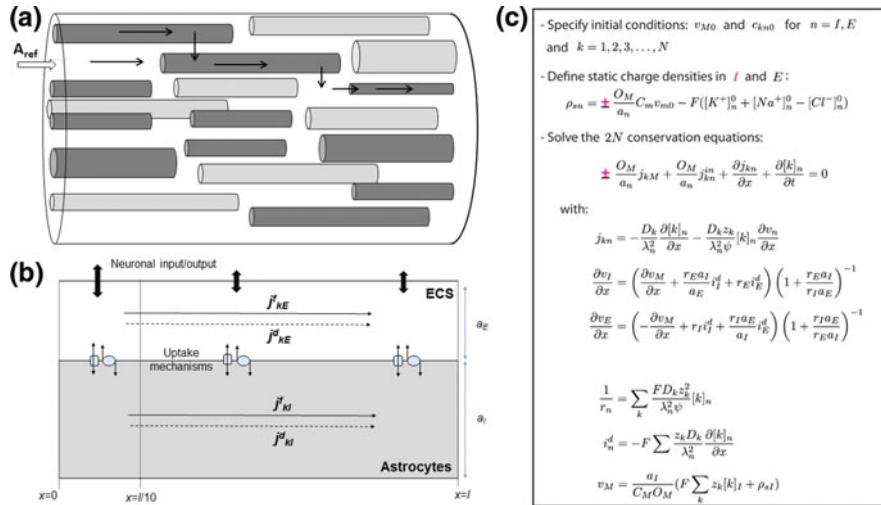


Fig. 14.3 A two-domain model for ion concentration dynamics in astrocytes and extracellular space when macroscopic transport is essentially one-dimensional. **a** A piece of brain tissue with cross-sectional area A_{ref} and an arbitrary extension l in the x -direction. Tissue astrocytes (dark grey) participate in the transport process, and other cells do not (light grey). **b** The interior of all astrocytes represented as a single domain (essentially an equivalent cylindrical cable coated by ECS), where all parts of all astrocytes at a given location x are assumed to undergo the same activity. Here, a_I and a_E are, respectively, the fractions of A_{ref} occupied by astrocytes and the ECS. Due to the presence of other cells (non-participatory), we generally have that $a_I + a_E < 1$. The astrocyte domain exchanges ions with the ECS via astrocytic membrane mechanisms. Axial transport processes in the ECS and inside astrocytes occur due to electrical migration (j^f) and diffusion (j^d). Neuronal activity is represented as an external input to the ECS. Enhanced neuronal input to a specific region of the ECS (e.g. the region $0 < x < l/10$ in the figure) will evoke spatial buffering processes in the system. **c** A set of equations that summarizes the electrodiffusive formalism. In equations containing the symbol “ \pm ”, “+” should be used for intracellular domain ($n = I$) and “-” should be used for the extracellular domain ($n = E$). The formalism is general to the choice of j_{kM} , representing system-specific membrane mechanisms (ion pumps, ion channels, cotransporters, etc.), which will depend on the case at hand. External input to the system must also be specified. The figure was modified from Halnes et al. (2013)

14.3.1 Model Constituents

In computational neuroscience, the main focus has been on modelling the short-term electrical signalling of neurons. Integration of synaptic input and generation of action potentials typically take place on a timescale of less than 100 ms. At this short timescale, ionic concentrations of the main ionic charge carriers (Na^+ , K^+ and Cl^-) vary little. With the possible exception of the signalling molecule Ca^{2+} (see, e.g., Destexhe et al. 1996; Halnes et al. 2011), ion concentrations are typically assumed to be constant during the simulated period or, at least, to vary so little that they do not evoke notable diffusive currents. This is, for example, an underlying

assumption in the cable equation (e.g. Rall 1977; Koch 1999), upon which most multicompartmental neural models are built.

Contrarily, spatial K⁺ buffering by astrocytes typically takes place at the timescale of seconds and must account for ion concentration changes. The dynamics of ion concentrations will depend not only on transmembrane fluxes but also on intra- and extracellular transports due to diffusion along concentration gradients and electrical migration along voltage gradients (Chen and Nicholson 2000; Halnes et al. 2013; Kofuji and Newman 2004). If ion concentration gradients become sufficiently steep, the electrical currents associated with diffusion of charged ions can be of comparable magnitude to the ohmic currents driven by electrical fields and will therefore influence the electrodynamics of the system (Qian and Sejnowski 1989; Halnes et al. 2013). An accurate description of long timescale processing in brain tissue thus calls for an electrodiffusive formalism based on the Nernst–Planck equations.

In earlier, pioneering modelling works on astrocytic K⁺-buffering (Gardner-Medwin 1983; Chen and Nicholson 2000; Odette and Newman 1988; Newman et al. 1993), the transient charge accumulation associated with the capacitive membrane current was neglected. Due to this, the models might be inaccurate in response to transient signals and do not guarantee a strictly consistent relationship between electrical fields and ionic concentrations. Given that K⁺-buffering likely depends on an intricate balance between diffusive and field-driven forces, this shortcoming inspired us to develop a new model (Halnes et al. 2013), which we present below. A key achievement of that work was the derivation of the general mathematical equations for electrodiffusion in a two-domain set-up as that in Fig. 14.3b.

14.3.1.1 Kirchhoff–Nernst–Planck Framework

The challenge in solving the Nernst–Planck equations typically lies in how to compute the local electrical potential v . Generally, v can be computed from Poisson's equations, as it is done in Poisson–Nernst–Planck solvers (Léonetti and Dubois-Violette 1998; Lu et al. 2007; Lopreore et al. 2008; Nanninga et al. 2008; Pods et al. 2013). However, to do this one must explicitly model charge relaxation processes, which demands an extremely fine spatiotemporal resolution (Mori et al. 2009). This makes Poisson–Nernst–Planck solvers computationally expensive and unsuited for predictions at a tissue level. For the K⁺-buffering model (Halnes et al. 2013), we developed an alternative framework, which we may refer to as the Kirchhoff–Nernst–Planck (KNP) framework. The KNP-framework is summarized in Fig. 14.3c and briefly introduced below. Useful entities and parameter definitions are listed in Table 14.1. For a full derivation of this formalism, the reader is referred to the original work (Halnes et al. 2013).

The KNP-framework is a means of solving the continuity equations for the one-dimensional model system in Fig. 14.3b, for the intracellular ($n = I$) and ECS ($n = E$) domains, for all ion species k with valence z_k and concentration $[k]_n$. The longitudinal intra- and extracellular fluxes are described by the Nernst–Planck

Table 14.1 Model parameters

Parameter	Description	Value	Units
k (index)	Ion species: K^+ , Na^+ or Cl^-	–	–
n (index)	Domain: I (ICS) or E (ECS)	–	–
a_I	Astrocyte volume per total tissue volume	0.4	–
a_E	ECS volume per total tissue volume	0.2	–
O_M	Astrocyte membrane area per total tissue volume	–	m^{-1}
l	Length of astrocyte	300	μm
z_k	Valence of ion species k	–	–
$[k]_n$	Ion concentration of species k in domain n	–	$ mM$
v_M	Membrane potential	–	$ mV$
j_{kM}	Membrane flux density of species k	–	$\mu mol/(m^2 s)$
j_{kn}^f	Axial flux density due to electrical migration	–	$\mu mol/(m^2 s)$
j_{kn}^d	Axial flux density due to diffusion	–	$\mu mol/(m^2 s)$
j_{Kir}	Transmembrane K^+ flux density (Kir channel)	–	$\mu mol/(m^2 s)$
j_{Nap}	Passive, transmembrane Na^+ flux density	–	$\mu mol/(m^2 s)$
j_{Clp}	Passive, transmembrane Cl^- flux density	–	$\mu mol/(m^2 s)$
P	Na^+/K^+ exchanger pump rate	–	$\mu mol/(m^2 s)$
r_n	Resistivity	–	Ωm
D_K	K^+ diffusion constant	1.96×10^{-9}	m^2/s
D_{Na}	Na^+ diffusion constant	1.33×10^{-9}	m^2/s
D_{Cl}	Cl^- diffusion constant	2.03×10^{-9}	m^2/s
λ_I	Intracellular tortuosity	3.2	–
λ_E	Extracellular tortuosity	1.6	–
C_M	Specific membrane capacitance	1	$\mu F/cm^2$
$\Delta[k]_n$	Deviance from baseline concentration	–	$ mM$
${}^a[K^+]_E^0$	Baseline ECS K^+ -concentration	3.082	$ mM$
${}^a[K^+]_I^0$	Baseline ICS K^+ -concentration	99.059	$ mM$
${}^a[Na^+]_E^0$	Baseline ECS Na^+ -concentration	144.622	$ mM$
${}^a[Na^+]_I^0$	Baseline ICS Na^+ -concentration	15.189	$ mM$
${}^a[Cl^-]_E^0$	Baseline ECS Cl^- -concentration	133.71	$ mM$
${}^a[Cl^-]_I^0$	Baseline ICS Cl^- -concentration	5.145	$ mM$
${}^a v_{M0}$	Initial membrane potential	-83.6	$ mV$
k_{dec}	Decay factor for $[K^+]_E$	2.9×10^{-8}	$ m/s$
j_{in}	Constant input in input zone	7×10^{-8}	$ mol/(m^2 s)$

^aInitial values correspond to the resting state of the model (static steady state in the case of no external input). For the origin of the table values, see (Halnes et al. 2013)

equation, i.e. j_{kn} in Fig. 14.3c, where first term on the right represents the diffusive flux density (j_{kn}^d) and the last term is the flux density due to ionic migration in the electrical field (j_{kn}^f).

Instead of using Poisson's equation to derive v , the KNP-framework derives the voltage gradients ($\partial v / \partial x$ in Fig. 14.3c) from the constraint that the sum of currents into a compartment should always be zero (i.e. Kirchhoff's current law). This zero-sum includes longitudinal diffusive and field currents, transmembrane ionic currents and transmembrane capacitive currents. The three first of these are ionic currents, whereas the latter reflects the accumulation of charge on the astrocyte membrane. Hence, in the KNP-framework, the total electrical charge in a compartment is always consistent with the membrane charge associated with the membrane potential v_M , whereas the bulk solution is always electroneutral (Halnes et al. 2013). This is typically true for the bulk solution in brain tissue at timescales larger than 1 nanosecond (Grodzinsky 2011).

The KNP-framework has proven to be useful not only for modelling astrocytic buffering processes (Halnes et al. 2013), but also other processes taking place in brain tissue at long timescales (Halnes et al. 2016, 2017). A three dimensional version of the KNP framework was recently developed (Solbrå et al. 2018).

14.3.1.2 Astrocyte Model

The KNP-framework (Fig. 14.3c) is general to the choice of membrane mechanisms (reflected in the transmembrane flux density j_{kM}). In the modelling study in (Halnes et al. 2013), the astrocyte possessed the standard passive transmembrane fluxes of Na^+ (j_{Nap}) and Cl^- (j_{Clp}), a passive K^+ flux (j_{Kir}) through the inward rectifying K^+ channel and the fluxes through the Na^+/K^+ -pump which exchanges 2 K^+ (inwards) for 3 Na^+ ions (outwards). The transmembrane fluxes of K^+ , Na^+ and Cl^- were, respectively

$$j_{kM} = j_{Kir} - 2P \quad (14.2)$$

$$j_{NaM} = j_{Nap} + 3P \quad (14.3)$$

$$j_{ClM} = j_{Clp}. \quad (14.4)$$

The expressions for j_{Kir} , j_{Nap} , j_{Clp} depend on the reversal potentials and conductances of the respective ion species, and the full expressions are given in the original work (Halnes et al. 2013). Also for the Na^+/K^+ -pump rate, P , we refer to the original work for the full expression (Halnes et al. 2013).

14.3.1.3 Simulation Set-up

Below, we will present some simulations that explore how astrocytes transfer K⁺ out from high-concentration regions. To induce such a high-concentration region, a selected region of the ECS (the *input zone* $0 < x < l/10$ as indicated in Fig. 14.3b) was exposed to a constant influx (j_{in}) of K⁺ and a corresponding efflux of Na⁺. In this way, the external input to the system was locally electroneutral, so that no net charge was added to the system (otherwise, the electroneutrality constraint would be violated). We assumed that this input signal reflected the effect of intense local AP firing in the input zone, where neurons take up Na⁺ and expel K⁺ from/to the ECS. Furthermore, we also implicitly included the effect of neuronal uptake mechanisms, i.e. neurons that take up K⁺ and expel Na⁺ via exchanger pumps. Unlike j_{in} , these mechanisms were evenly distributed in the system, so that all points in space $0 < x < l$ experienced a K⁺ concentration-dependent decay towards the baseline ECS K⁺ concentration $[K^+]_E^0$. The input function was given by:

$$j_K^{in} = -j_{Na}^{in} = j_{in} - k_{dec}([K^+]_E - [K^+]_E^0). \quad (14.5)$$

Here, j_{in} is a constant input which was applied only in the input zone ($0 < x < l/10$) and in a selected time window ($100 \text{ s} < t < 400 \text{ s}$). The decay term was applied at all locations at all time. The decay factor (k_{dec}) and input flux density (j_{in}) are defined in Table 14.1.

The model was implemented in MATLAB, and the code is publicly available at ModelDB (<https://senselab.med.yale.edu/ModelDB>ShowModel.cshtml?model=151945>). We only included the dynamics of the main charge carriers (K⁺, Na⁺ and Cl⁻), and the simulations were run with sealed-end boundary conditions (see Halnes et al. 2013 for details).

14.3.2 A Mechanistic Understanding of the K⁺-Buffering Process

Below, we aim to give a mechanistic picture of the K⁺-buffering process by presenting selected simulations from the original study (Halnes et al. 2013). We focus on mapping out the transport routes of K⁺, from entering to leaving the system, and on exploring how this depends on electrical forces, diffusive forces and astrocytic uptake.

14.3.3 Ion Concentration Dynamics and Steady State

In Fig. 14.4, we see how the extracellular ion concentrations (panel A), the intracellular ion concentrations (panel C) and v_M (panel E) changed after the input was turned on (at $t = 100 \text{ s}$). It took the system roughly 30 s to reach steady state, after

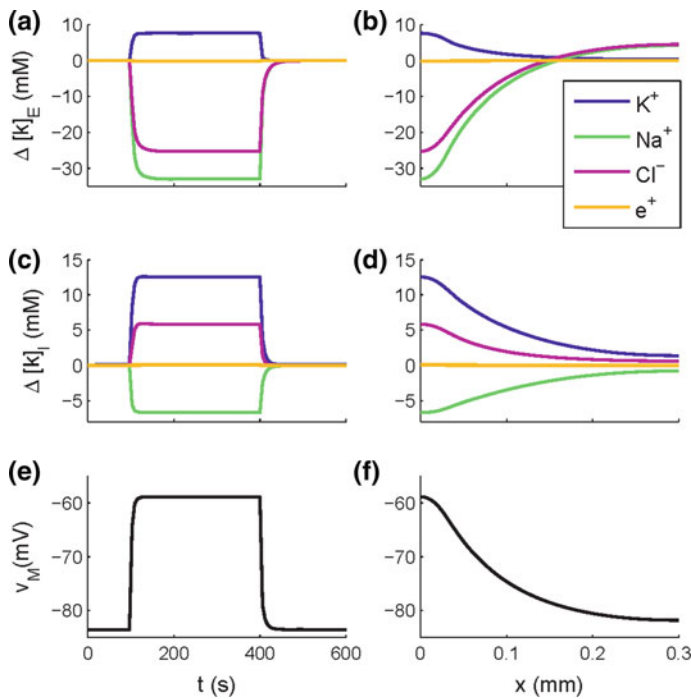


Fig. 14.4 Dynamics and steady-state profiles for the astrocyte/ECS system. **a, c, e** Dynamics of selected variables in a point ($x = 0$) in the input zone. The constant cation-exchange input was applied to the ECS of the input ($0 < x < l/10$, $l = 0.3$ mm) zone from $t = 100$ s to $t = 400$ s. During the input, ion concentrations in the ECS and ICS changed, but reached steady state after about 10–50 s after stimulus onset. $[K^+]_E$ ($x = 0$) had then increased by about 7.7 mM with respect to the baseline value (**a**), while $[K^+]_I$ had increased by about 12.5 mM due to uptake by the astrocyte (**c**). The astrocytic membrane potential had been depolarized to about -59 mV at $x = 0$ (**e**). **b, d, f** Spatial profiles of selected variables at a time $t = 400$ s, when the system was in steady state. Deviations from the baseline ionic concentrations and v_M were smaller outside the input zone and typically decreased with x . Far away from the input zone ($x \sim l = 0.3$ mm), the conditions were close to the baseline conditions (**a–d**). Ionic concentrations were represented in terms of deviations from resting concentrations: $\Delta[k]_n = [k]_n - [k]_n^0$ for $n = I, E$. For direct comparison with ion concentrations, the charge density was represented as an equivalent concentration of unit charges $[e^+] = [K^+] + [Na^+] + [Cl^-]$. The figure was modified from Halnes et al. (2013)

which the state variables remained at fixed values until the input was turned off (at $t = 400$ s). For ion concentrations, deviations from basal concentrations are shown. For example, $\Delta[K^+]_E$ was about 7.7 mM at steady state, corresponding to a concentration $[K^+]_E \simeq 10.8$ mM (as the baseline concentration was ~ 3.1 mM). This value lies on the threshold between functional and pathological conditions (Chen and Nicholson 2000; Newman et al. 1993; Hertz et al. 2013) and is thus likely to represent a scenario where the K^+ buffering process is of paramount importance. Although the input was applied to the ECS of the input zone, $\Delta[K^+]_I \simeq 12.5$ mM

was larger than $\Delta[K^+]_E$, reflecting the astrocyte's propensity for local K^+ -uptake. As has been also seen experimentally (Newman et al. 1987; Dietzel et al. 1989; Chen and Nicholson 2000), the shifts in $[K^+]_E$ coincided with a local depolarization of the astrocytic membrane (panel E).

In the following, we focus on the spatial aspect of the buffering process and limit the exploration to when the system is in steady state (the time $t = 400$ s was selected for the steady-state situation). For all system variables, the deviation from the baseline conditions was biggest in the input zone and generally decayed with increasing x (Fig. 14.4b, d, f). Note that the properties of the system lead to a rearrangement of Cl^- in the system, although Cl^- (unlike K^+ and Na^+) was not added/subtracted to/from the system. The gradients of both the ionic concentrations and electrical potential were quite pronounced, and we may thus expect that both diffusive and electrical forces contribute to transporting ions through the system (from entering to leaving). This is explored further in the following section.

14.3.4 System Throughput During Steady State

Figure 14.5 shows all the ionic flows in the system during steady state. Due to the input configuration (Eq. 14.5), there was a net external influx of K^+ to the ECS in the input zone ($0 < x < l/10$) and a net efflux of K^+ at all points outside this region (Fig. 14.5a). As all external input/output was an electroneutral cation exchange, Na^+ and K^+ had opposite input profiles (compare blue and green curves).

Our main interest was on how the astrocyte influences the route that K^+ follows through the system. Figure 14.5b shows how the transmembrane fluxes vary along the x -axis. The transmembrane flux of K^+ (dark blue) was much larger than for Na^+ (green) and Cl^- (magenta). By definition, the transmembrane flux is negative for inward fluxes. According to Fig. 14.5b, there was thus a pronounced astrocytic uptake of K^+ in the high-concentration region and a release outside this region.

To complete the picture of the spatial buffering process, we must also look at the intra- and extracellular fluxes of all ion species. To assess the relative roles of diffusion and electrical migration, we distinguished between field fluxes, which essentially reflect transports due to the extra- (Fig. 14.5c) and intracellular (Fig. 14.5d) voltage gradients in the system, and diffusive fluxes along the extra- (Fig. 14.5e) and intracellular (Fig. 14.5f) concentration gradients in the system. As expected, since the astrocyte absorbed K^+ in the input zone and released it outside this region (Fig. 14.5b), there was an intracellular longitudinal transport of K^+ in the positive x -direction. This transport was partly due to diffusion (Fig. 14.5f), as we could have predicted from the intracellular concentration gradient that we saw in Fig. 14.4d. However, due to the strong depolarization of the astrocyte in the input zone (Fig. 14.4f), electrical migration gave an even larger contribution to the intracellular transport of K^+ (Fig. 14.5d).

K^+ diffused in the positive x -direction also in the ECS (Fig. 14.5e). However, a depolarization of the astrocyte corresponded to a decrease in the ECS potential ($v_m =$

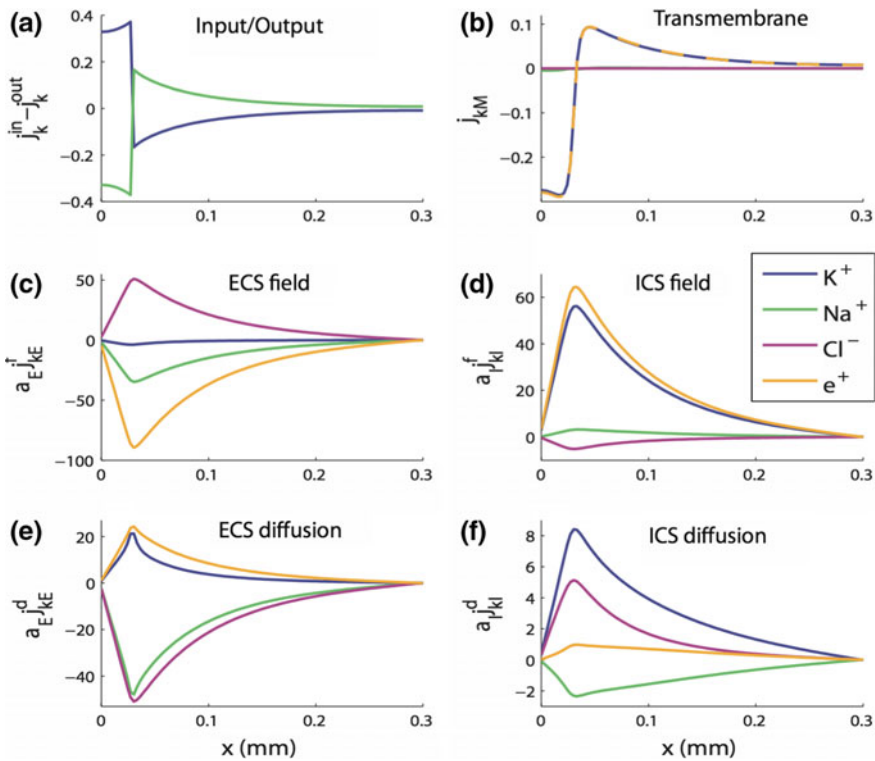


Fig. 14.5 Ion transport in the astrocyte/ECS system at steady state. **a** Total flux densities into system (input–output). **b** Transmembrane flux densities. **c–f** Longitudinal flux densities due to **(c)** electrical migration in the ECS, **d** electrical migration in the ICS, **e** diffusion in the ECS and **f** diffusion in the ICS. **a–d** To aid comparison, flux densities j_{kn} were scaled by the relative area fraction a_n (e.g. if $a_E j_{KE} = a_I j_{kl}$, I and E carry the same net flux of ion species k). For direct comparison with ionic fluxes, the net electrical current was represented as a flux of positive unit charges $j_{e+} = j_{K+} + j_{Na+} - j_{Cl-}$. The input zone was in the region $0 < x < l/10$. Units on the y -axis are $\mu\text{mol}/(\text{m}^2 \text{s})$ in all panels. The figure was modified from Halnes et al. (2013)

$v_I - v_E$). Accordingly, the voltage gradient in the ECS drove K^+ in the negative x -direction (Fig. 14.5c). That is, diffusion and electrical migration had opposite directions in the ECS. This finding predicts that the astrocyte not only provides an additional and more effective domain for longitudinal K^+ -transport but even reduces the net transport of K^+ through the ECS, thus shielding the ECS from K^+ .

Figure 14.6 qualitatively summarizes the ionic flows through the system during steady state. K^+ entered the system in the ECS of the input zone, where a major fraction of it crossed the membrane, was transported intracellularly in the positive x -direction and was released to the ECS at higher x -values, from where it eventually left the system (via neuronal uptake). Whereas the main transport route for K^+ was intracellular, the situation for Na^+ was opposite. Na^+ entered the system outside the

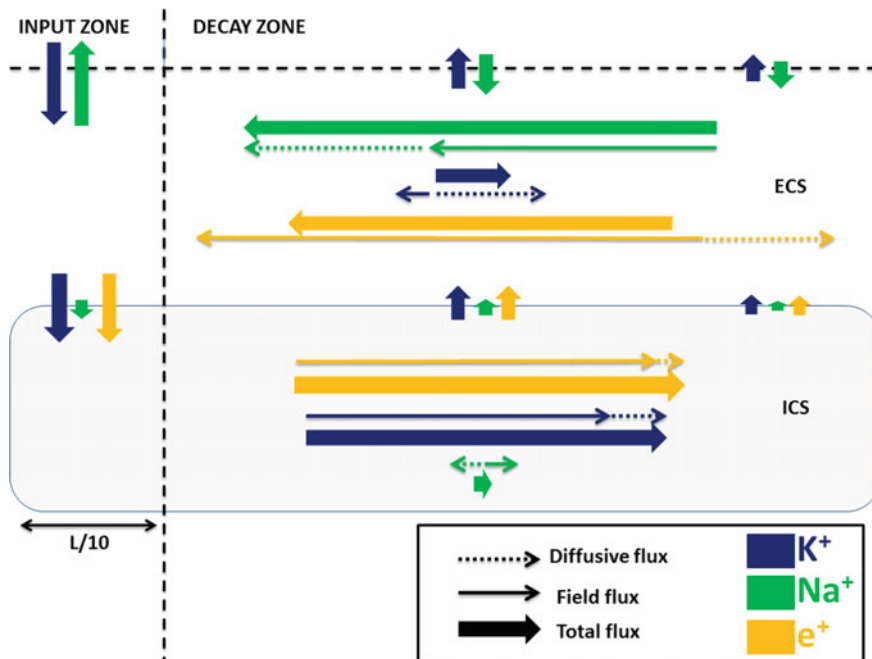


Fig. 14.6 A flow chart of the ion transport in the astrocyte/ECS system at steady state. A flow chart that qualitatively summarizes the essential information in Fig. 14.5, showing the main transport routes of K^+ and Na^+ during steady state (Cl^- -excluded from the overview). K^+ generally entered the system in the input zone and left the system from some point along the astrocyte axis. The transport route of K^+ (from entering to leaving the system) was predominantly intracellular, demonstrating the astrocyte's efficiency as a spatial buffer. Na^+ entered in the decay zone and left from the input zone. Na^+ transport predominantly took place in the ECS. The net electrical current cycled in the system. The illustration is qualitative—longer arrows mean higher flux densities—but the mapping from Fig. 14.5 to the flow chart is not quantitatively exact. The figure was modified from Halnes et al. (2013)

input zone, was predominantly transported in the negative x -direction through the ECS and left the system in the input zone (neuronal AP firing). The net Cl^- -transport was very small (flux densities due to diffusion and electrical migration cancelled each others out) and is not included in Fig. 14.6.

The simulations shown here illustrate that K^+ buffering depends on a fine interplay between electrical and diffusive transport processes and could thus not be reliably simulated without a consistent electrodiffusive modelling scheme, such as the KNP-framework. We conclude that astrocytes seem tailored for shielding the ECS from excess K^+ . In the original work (Halnes et al. 2013), we also showed that K^+ clearance from high concentration was much more efficient when astrocytes were present than in the case of a correspondingly enlarged ECS, a hypothesis that had been posed earlier, but not yet tested (Amedee et al. 1997).

14.4 Microscale Water Flow

A striking difference between astrocytes and neurons is that astrocytes have water-specific channels, aquaporin-4 (AQP4), embedded in the membrane. In the astrocytic end-feet, i.e. the processes that reach out and collectively create a sheath around the blood vessels and towards the pial surface, the AQP4 density has been reported to be as high as $2400/\mu\text{m}^2$ (see Furman et al. 2003, Fig. 6). At the astrocytic membrane facing neuropil, the AQP4 density is about a factor 20 lower (Enger et al. 2012), but this is still dense compared to standard ion channel densities: in neurons the sodium channel densities are estimated to be about $1/\mu\text{m}^2$ in the cell body and about $100\text{--}200/\mu\text{m}^2$ in the densest regions such as the axon hillock (Safronov et al. 1999).

Throughout the body, the lymphatic system removes excess fluid and waste from the tissue, but there is no lymphatic system within neuropil, although lymph vessels were recently discovered within the meningeal compartment (Louveau et al. 2015). This lack of lymph system within the neuropil led Iliff et al. (2012) to suggest a ‘glymphatic pathway’ – the brain’s counterpart to a lymphatic pathway – between the vasculature and the astrocyte end-feet, i.e. a flow of water through the interstitial space directed from the perivascular space to the perivenous space (see Fig. 14.7e) functions as a clearance mechanism for waste products such as amyloid beta. AQP4 deletion has shown to reduce clearance of amyloid beta by 65% (Iliff et al. 2012), and thus AQP4 seems to play an important role in the ‘glymphatic system’.

The role of astrocytic AQP4 in potassium buffering is controversial (Haj-Yasein et al. 2015; Zhang and Verkman 2008; Amiry-Moghaddam et al. 2003). Here, we show how AQP4 can both stabilize the extracellular concentration of solutes and possibly also induce a convective water flow. We also show that there is a possible interplay between osmotic forces and water fluxes through AQP4 interactions, which may be important for both potassium buffering and for the glymphatic system.

14.4.1 Transport Mechanisms

The osmotic pressure over the membrane is strong compared to typical hydrostatic pressures (see Sect. 14.4.2). Upon osmotic changes, water flows through the high density of AQP4 in the astrocyte membrane and reestablishes the osmotic balance between the ECS and the intracellular volume of the astrocytes. Depending on cortical state, this may lead to swelling or shrinkage of the astrocytes. Xie et al. (2013) found that during sleep the extracellular volume increases by about 60% and that this increase in volume leads to a better clearance of amyloid beta due to an increased convective flow through the ECS. Although osmosis may regulate the ECS volume and thereby the convective flow, it is not clear whether osmosis is a driving force for the flow itself. Cerebral arterial pulsation has, however, been demonstrated to be a key driver for this flow (Iliff et al. 2013).

Many aspects of the glymphatic system are not understood, and the concept itself is still debated (Hladky and Barrand 2014; Smith et al. 2015; Thrane et al. 2015; Holter et al. 2017). However, for water to be driven through the interstitial space, from the periarterial to the perivenous space, either hydrostatic or osmotic pressure gradients must act as driving forces. Note, however, that the osmotic pressure and the hydrostatic pressure act very differently: the hydrostatic pressure may cause pressure difference between any two extracellular (or intracellular) sites, whereas the osmotic pressure acts over membranes.

If we assume an elevated hydrostatic pressure in the periarterial space compared to the perivenous space, there will be a net hydrostatic pressure gradient over the end-feet layers and through the interstitial space (see black arrows in Fig. 14.7e). This may cause an extracellular flow, and the convection may serve as a clearance mechanism for amyloid beta and other waste products.

In Fig. 14.7, we have calculated pressure gradients in the astrocyte/ECS model presented in Sect. 14.3, using identical parameters and input conditions as there. The changes in ionic concentrations induced by the input (cf. Eq. 14.5) were most dramatic in the input zone. In Fig. 14.7b, the summed intracellular and ECS concentrations are shown at different time points after the input was turned on. The concentration shifts gave rise to a maximal, activity-induced change in osmolarity of more than 60 mOsm/L; i.e. the induced change in concentrations between the intracellular and extracellular sites was more than 60 mM. The pressure shift was largest in the input zone, where the shift in osmotic pressure across the membrane was about 1000 mmHg (see Fig. 14.7c, and see also Eq. 14.8 for the formula for osmotic pressure). Further, the spatial extension of the cable leads to an osmotic gradient along the membrane.

We did not explicitly include water flow in the modelling framework, but the observations in Fig. 14.7 allow us to make some qualitative predictions from the pressure gradients. Firstly, from the osmotic pressure in the input zone, we would predict a local influx of water, which would lead to astrocyte swelling (Østby et al. 2009). Secondly, depending on the membrane elasticity, a hydrostatic pressure would build up intracellularly and cause an intracellular water flow away from the input zone. Figure 14.7e illustrates two different flow patterns that we would expect if astrocytes were connected either to the arterial site (left) or to the venous site (right). The high intracellular pressure would cause an intracellular water flux out from the input zone (orange arrows), directed both towards the arterial site and towards the venous site, depending on astrocyte density, their connections to the vasculature, their respective AQP4 densities, etc. In Fig. 14.7e, black arrows indicate the expected flow caused by arterial pulsation and pressure differences between the periarterial and perivenous spaces.

As of now, it is still an open question whether K^+ buffering evokes osmotic forces strong enough to produce a convective flow of considerable magnitude. In general, it is not clear whether the net extracellular convective flow is mainly driven by arterial pulsation or by osmotic forces. Experiments show that both AQP4 and arterial pulsation are important for the glymphatic flow: for AQP4 deletion, clearance of amyloid beta was reduced by 65% (Iliff et al. 2012), and Iliff et al. (2013) suggested that cerebral arterial pulsatility is a key driver of paravascular CSF influx into and through

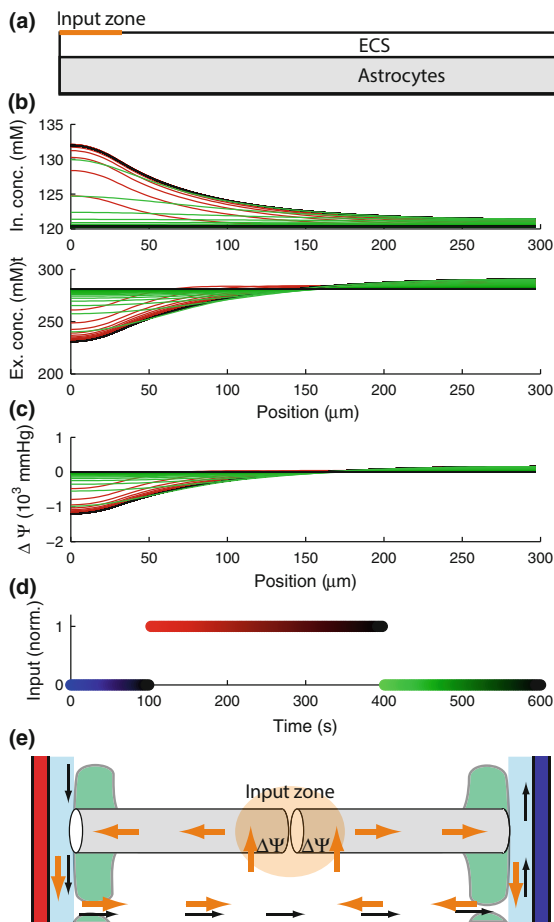


Fig. 14.7 Illustration of how the astrocyte machinery may generate an osmotic gradient following neural activity and induce water flow into the astrocyte. The model shown in Fig. 14.3 is run with default parameters. **a** Illustration of the electrodiffusion model, see Fig. 14.3 for details. At time $t = 100$ s, the model is triggered by neural activity (decreased extracellular Na^+ and increased extracellular K^+) within the input zone. **b** The spatial distribution of net concentration of intracellular (upper) and extracellular ions (lower), leading to change in osmotic pressure seen in **c**. The osmotic pressure is here assumed to be zero in equilibrium. **d** The colour coding of **(b)** and **(c)** depicts time. Input is given in red, bright red at the beginning of the input, darker towards the end, whereas times after the 300 s input stimulus is turned off are shown in green. **e** An assumed system of two types of astrocytes, one type approaching the arterial site, the other type approaching the venous site. Red (left) is the arterial site, and blue (right) is the venous site. The end-feet, shown in green, cover the vasculature and define perivascular spaces filled with water (light blue) along both arterioles and venules. Osmotically induced flow pattern depicted with orange arrows, and the hypothesized hydrostatic flow with black arrows. Note that the hydrostatic flow may go both through the end-feet and through the tiny clefts between end-feet.

the brain parenchyma. It is presently not possible to measure the small hydrostatic pressure differences within the tiny astrocytic compartments. Thus, to understand the role of osmotic forces in potassium buffering a tight interplay between experiments and modelling is needed. This also applies to the glymphatic system and the question of clearance of waste products. Future astrocyte models with spatial extension should emphasize to incorporate not only electrodiffusion but also the convective flow caused both by osmotic pressures and by hydrostatic pressure originating from arterial pulsation or respiration. Such a complete modelling framework is not available yet, but below we assess some of the key ingredients that it will need.

14.4.2 Osmosis and Astrocyte Swelling

Above we showed some qualitative results of possible convective flows, both extracellularly and intracellularly in astrocytes. Here, we will give quantitative estimates of the strength of the osmotic forces, the water flow and the typical timescale for this mechanism.

The lipid bilayer without AQP4 channels has a rather low water permeability compared to the permeability of the astrocyte with a normal AQP4 density (Silberstein 2004). As an additional boosting effect, AQP4 is often arranged in so-called orthogonal arrays. These arrays may increase the collective permeability of AQP4 as much as 10 times compared to the sum of the single-channel permeabilities (Silberstein 2004), and orthogonal arrays are especially prominent within the astrocyte end-feet.

The membrane permeability, which is determined by the density of AQP4, has a direct impact on how fast the ECS volume can be regulated upon osmotic stress. In Tong et al. (2012), the ECS osmolarity was manipulated, and small proteoliposomes of diameter ~ 100 nm with AQP4 inserted into the membrane swelled until they reached a new equilibrium. The swelling was fitted to exponential functions, and the estimated time constants were as small as $\tau = 1/(120.5 \text{ s}^{-1}) \approx 8.3 \text{ ms}$ for cells with high densities of AQP4. In contrast, in (Pangrsic et al. 2006) an astrocyte soma of diameter $10 \mu\text{m}$ was shown to swell with a time constant of tens of seconds. Size seems to matter, and a rapid swelling of astrocytes would serve to regulate the ECS osmolarity, thereby stabilizing the ECS environment and presumably preventing osmotic pressure differences to cause swelling of neurons, as neurons do not have AQP4 water channels and thus have a much longer time constant for water inflow.

Below we describe the basic formalism for osmotically induced swelling of astrocytes. Note that a similar formalism has been integrated with single compartment models of ion dynamics (see, e.g., Østby et al. 2009; Øyehaug et al. 2012), but not yet in spatially extended models.

14.4.2.1 Basic Formalism for Osmotically Induced Volume Changes

Similarly to Ohm's law for electricity, Darcy's law defines the water flow Q as a product of the permeability G_{tot} and the pressure difference $\Delta\Psi$,

$$Q = G_{\text{tot}} \Delta\Psi, \quad (14.6)$$

where Q has units of m^3/s , $\Delta\Psi$ has units of Pa, and G_{tot} has units of $\text{m}^3/\text{Pa/s}$. We use the symbol Ψ for the water potential, since flow across a membrane is caused by both hydrostatic and osmotic pressure differences over the membrane,

$$\Psi = \Psi_p + \Psi_\Pi. \quad (14.7)$$

Here, Ψ_Π is called the solute potential, and the hydrostatic pressure (the pressure potential) is denoted Ψ_p . Differences in the solute potential over the membrane correspond to the osmotic pressure. Both Ψ_Π and Ψ_p have units of Pascal. Water flows from a high water potential to a lower water potential, and the solute water potential is defined to be zero for pure water and is negative for any solute.

If we assume ideal solutions with low concentrations of solutes, we can use the Morse equation to compute the solute potential (Amiji and Sandmann 2002):

$$\Psi_\Pi = iMRT. \quad (14.8)$$

Here, i is the ionization factor (van't Hoff factor), i.e. the ratio between the actual concentration of particles produced when the substance is dissolved, and the concentration of a substance as calculated from its mass, $R \approx 8.3 \text{ J}/(\text{mol K})$ is the gas constant, T , here assumed to be 310 K, is the absolute temperature, and M is the osmotic concentration of solutes measured in moles per cubic meter. Our solutes are here assumed to be ions, thus $i = 1$.

If we combine Eqs. 14.6 and 14.8, assume the hydrostatic pressure Ψ_p to be the same at both sides of the membrane, and notice that Q is the flow rate of the extracellular volume V_e across the membrane and into the intracellular volume, i.e. $Q = dV_e/dt$, the volume dynamics is given by

$$\frac{dV_e}{dt} = -RTGA \left(\frac{N_a}{V - V_e} - \frac{N_e}{V_e} \right). \quad (14.9)$$

Here, N_e and N_a are the number (moles) of extracellular and intracellular (astrocytic) solutes, respectively, and $V = V_e + V_a$ is the sum of the ECS and astrocyte volumes. We have expressed the total membrane permeability G_{tot} from Eq. 14.6 as $G_{\text{tot}} = GA$, where G is the permeability per membrane area and A is total membrane area within the volume V . If we assume the volume V and the number of ions N_e and N_a to be constants, a general solution can be written

$$-tRTGA = \frac{N_a V V_e}{(N_a + N_e)^2} - \frac{V_e^2}{2(N_a + N_e)} + \frac{N_a N_e V^2 \ln([N_a + N_e]V_e - N_e V)}{(N_a + N_e)^3} + C, \quad (14.10)$$

where C is an integration constant. This expression cannot be converted into a simple formula for V as a function of the time t , but for typical parameters (see Sect. 14.4.2.2) we find that the logarithmic term dominates the right-hand side of the equality. Thus, an approximate solution can be written on a simple functional form as

$$\frac{V_e}{V} \approx \tilde{C} e^{-t/\tau} + \tilde{N}_e, \quad (14.11)$$

with the constant $\tilde{C} = V_0/V - \tilde{N}_e$, where V_0 is the initial extracellular volume and $\tilde{N}_e = N_e/(N_e + N_a)$ is the relative extracellular number fraction. The time constant is given by

$$\tau = \frac{N_a N_e V^2}{(N_e + N_a)^3 RTGA} = \frac{\tilde{N}_a \tilde{N}_e}{c RTGA / V}. \quad (14.12)$$

In the last equality, we have used the relative number fractions \tilde{N}_e and $\tilde{N}_a = N_a/(N_e + N_a)$, and c is the net concentration of solutes within V , i.e. $c = (N_e + N_a)/V$. From the expression, we find that the time constant is inversely proportional to the volume density A/V of AQP4.

14.4.2.2 Experimentally Extracted Parameters

Based on experimentally measured quantities, we will in this subsection estimate typical transmembrane water flow and the time constant τ , derived in Eq. 14.12, for astrocytes. The most important parameters are found in Table 14.2.

Estimates of the AQP4 water channel permeability are typically based on osmotic permeability experiments relating the concentration difference ΔM (in units of mol/m³) of impermeable molecules between two sides of a cell membrane, to the molar flux Q_m of water through the membrane,

$$P_{f,cell} = Q_m / \Delta M. \quad (14.13)$$

The molar flux Q_m can be estimated from cell swelling measurements. Further, the single-channel AQP4 permeability or the permeability per unit area can be estimated by additional electron microscopy of the density of AQP4 channels within the membrane (Tong et al. 2012). If we assume the hydrostatic pressure Ψ_p to be the same at both sides of the membrane, the correspondence between reported osmotic permeability per unit area P_f and the permeability per unit area $G = G_{tot}/A$, where A is the membrane area, is found by substituting Eqs. 14.8 and 14.13 into Eq. 14.6. This gives

Table 14.2 Model parameters, Sect. 14.4

Parameter	Description	Value	Units
\tilde{N}_a	Fraction of intracellular ions	0.55	–
\tilde{N}_e	Fraction of extracellular ions	0.45	–
c	Net solute concentration $c = (N_a + N_e)/V$	300	mOsm/L
R	Gas constant	8.314	kPa·L/K/mol
T	Absolute temperature	310	K
P_f	Osmotic permeability per unit area	0.01	cm/s
G	Water permeability per unit area	7.0×10^{-13}	m ³ /Pa/s
ΔM	Concentration difference of solutes	60	mM
M_w	Molarity of water	55.5	M
Q_m	Molar flux	–	mol/s
Q	Transmembrane water flow	–	m ³ /s
A/V	Area to volume fraction	20	μm ² /μm ³

$$G = P_f / (RTM_w), \quad (14.14)$$

with $M_w = Q_m/Q$ denoting the molarity of water.

The permeability per unit area G was used in Eq. 14.10 to relate the volumetric flow rate $Q = dV_e/dr$ through the membrane to the osmotic pressure difference, and it was shown that its value is inversely proportional to the time constant τ ; see Eq. 14.12. Based on data for the relative density of AQP4 in end-feet vs. the membrane facing neuropil (Enger et al. 2012), as well as estimates for both P_f (Silberstein 2004; Jung et al. 1994) and single-channel permeability (Tong et al. 2012; Hashido et al. 2007), we use $P_f = 0.01$ cm/s to arrive at a numerical value for the time constant τ .

The total neuronal membrane area is estimated to be 25,000 m² for human (Bear et al. 2001, p. 97), and the brain volume is about 1350 cm³. This leads to a membrane area to volume density of 18.5/μm. A similar density can be found for mouse. We assume a default value for the volume density of astrocytic membrane area to be similar to the volume density of neuronal membrane area, i.e. $A/V = 20/\mu\text{m}$.

We further assume increased osmotic pressure equivalent to 1000 mmHg within a cube of sides 100 μm. According to our assumptions, this volume will contain $A_m = 2 \cdot 10^7$ μm² of membrane area. The osmotic pressure corresponds to a concentration difference of less than 60 mOsm/L between the inside and the outside of the membrane, cf. Eq. 14.8. The net rate of water influx to the astrocytes within the volume is then

$$Q = GA_m \Delta \Psi = 0.002 \text{ mm}^3/\text{s}. \quad (14.15)$$

This initial influx rate corresponds to twice the total volume V per second, and for a standard extracellular volume fraction of 20% it corresponds to a net influx rate of 10 times the ECS volume per second. However, as water moves from the ECS to the intracellular space, the osmotic pressure will be reduced according to Eq. 14.10. If we assume both the ECS and the astrocytic volume fraction to be 20% of the total volume (Hertz et al. 2006), the astrocytic osmolarity to be 330 mOsm/L and the extracellular osmolarity to be 270 mOsm/L, the system will, according to Eqs. 14.11 and 14.12, reach equilibrium when the extracellular volume fraction is 18% and the intracellular is 22%, and the time constant will be $\tau = 9.2$ ms. This is in good agreement with experimental results from Tong et al. (2012), and is a consequence of the high area to volume density of astrocytic membrane area within the brain.

These simple considerations show that the osmotic response to neural activity is fast and the transmembrane influx rate of water may be substantial within a given volume of tissue, although single astrocyte somas swell substantially slower when located in an extracellular solution with constant extracellular osmolarity (Pangrsic et al. 2006).

14.5 Macroscale Fluid Flow Through Brain Tissue

Fluid flow through the central nervous system is inherently of a multiscale character and thus amenable to a multitude of modelling approaches; for a recent review in the context of biomechanics, see, e.g., (Goriely et al. 2015). At the macroscale, that is, at the whole-brain scale, three distinctive approaches to the continuum modelling of fluid and solute flow through the brain tissue are: (i) single or multiple-network poroelasticity theory, (ii) direct modelling and coupling of the interstitial tissue flow with free flow (Darcy–Stokes flow) (Baber et al. 2012) and (iii) coupling the micro-circulation (vasculature) with the tissue itself via one-dimensional networks (Darcy flow with embedded Navier–Stokes flow) (Cattaneo and Zunino 2013). Of these, the first approach has gained momentum for the biomechanical modelling of fluid flow through brain tissue and also through the spinal cord; see e.g., (Goriely et al. 2015) and references therein.

These single- and multiple-network poroelasticity theories originally originate from geoscience (Biot 1941; Bai et al. 1993), but have been proposed to model the flow and exchange of fluid through biological tissue in general and the brain in particular (Tully and Ventikos 2011). The theory is based on modelling the tissue as a solid matrix permeated by interconnecting multiple pathways or networks where each network is characterized by its porosity. For instance, Vardakis et al. (2013) consider a model incorporating the intracellular space permeated by four networks corresponding to the arteries, the arterioles/capillaries, the veins and the extracellular space, respectively. In the case of a single fluid network (here, the extracellular space) and under the assumptions of linear tissue elasticity, isotropy and incompressibility,

the general multiple-network poroelasticity model reduces to the well-known Biot equations (Biot 1941). In addition, to modelling the flow of interstitial fluid through the tissue itself, computational models typically also need to account for the interplay with the cerebrospinal fluid flow in the subarachnoid spaces and ventricles as illustrated for example by Rutkowska et al. (2012); Støverud et al. (2013) and Vardakis et al. (2013).

The multiple-network poroelasticity equations, in the absence of local body forces, sources or sinks, and inertial terms, and assuming incompressible fluid networks for the sake of simpler presentation, take the form (Tully and Ventikos 2011): find the spatially and temporally varying tissue deformation u and the pressures p_a for each network $a = 1, \dots, A$ such that

$$-\nabla \cdot \sigma(u) + \sum_a \nabla p_a = 0, \quad (14.16)$$

where σ is the stress tensor, for instance given by Hooke's law under the assumptions of linearly deformatting elastic tissue, and for each $a = 1, \dots, A$:

$$\nabla \cdot \dot{u} - \nabla \cdot (G_a \nabla p_a) = \sum_{b \neq a} s_{b \rightarrow a}. \quad (14.17)$$

In Eq. 14.17, $G_a = \kappa_a / \mu_a$ where κ_a is the permeability and μ_a the viscosity of network a . The exchange coefficients $s_{b \rightarrow a}$ govern the rate of transfer from network b to network a and are subject to modelling. The fluid velocity in network a is defined in terms of the network pressure p_a by:

$$v_a = -G_a \phi_a^{-1} \nabla p_a, \quad (14.18)$$

where ϕ_a is the porosity or volume fraction of network a which, note, may or may not be spatially varying.

The multiple-network poroelasticity framework is attractive in that it allows for specific incarnations, at different levels of complexity, and modelling fluid flow in, e.g., the different compartments of the 'glymphatic system'. Variations in the extracellular and astrocytic volume fractions, cf. Sect. 14.4.2, are naturally modelled via the network porosities, while microscale water flow and AQP4 densities, as discussed in Sect. 14.4, govern the dynamics of the exchange coefficients.

14.6 Concluding Remarks

The recent years have seen the launching of several ambitious large-scale projects aiming to link the different scales in the brain, from molecules to systems. Prominent examples are EUs Human Brain Project, the US BRAIN Initiative and Project Mind-Scope at Allen Institute of Brain Sciences (Kandel et al. 2013). Here, computational

neuroscience will play a key role in integrating neurobiological data, storing current knowledge and testing hypotheses by means of a set of interconnected mathematical models together bridging the different scales. The main focus of these projects is to understand the information processing in the brain, and a central goal is to link processing and spiking activity at the single-neuron level to systems level measures of neural activity such as the local field potential (LFP) (Einevoll et al. 2013), electroencephalography (EEG) (Nunez and Srinivasan 2006) or magnetoencephalography (MEG) (Hämäläinen et al. 1993).

In these projects, the astrocytes will be secondary to the neurons as their main role is likely to be of a homeostatic nature, i.e. to provide the neurons with stable environments for their information processing (but see other chapters in the present volume). An example is the presently discussed role of astrocytes in providing spatial K^+ buffering to maintain low concentrations of potassium in the ECS and avoid pathological neuronal firing.

Another multiscale brain project is to try to link neural activity to macroscopic fluid flow. Here, astrocytes will likely be at centre stage as their ion concentration dynamics appear to provide a key connection to fluid flow via osmotic effects. In the present chapter, we have outlined some elements that we believe will be of key importance for this multiscale approach: In Sect. 14.2, we discussed how neuronal and astrocytic dynamics are linked via ions in ECS; in Sect. 14.3, we described the recently introduced Kirchhoff–Nernst–Planck (KNP) scheme for modelling ion dynamics in astrocytes (and brain tissue in general); in Sect. 14.4, we described how astrocytes may regulate microscopic liquid flow by osmotic effects; in Sect. 14.5, we finally discussed how such microscopic flow can be linked to whole-brain macroscopic flow.

A long-term ultimate goal would be to make joint multiscale, multimodal models for brain tissue including both information processing by spikes, liquid flow, hemodynamic activity and metabolic activity (Devor et al. 2012). Such models could not only represent invaluable mathematical ‘microscopes’ for exploring brain function but also, and hopefully, become important tools for understanding brain pathologies and suggest new treatments.

References

- Amedee T, Robert A, Coles J (1997) Potassium homeostasis and glial energy metabolism. *Glia* : 599–630
- Amiji MM, Sandmann BJ (2002) Applied physical pharmacy. McGraw-Hill
- Amiry-Moghaddam M, Williamson A, Palomba M, Eid T, de Lanerolle NC (2003) Delayed K^+ clearance associated with aquaporin-4 mislocalization: phenotypic defects in brains of alpha-syntrophin-null mice. *Proc Nat Acad Sci United States Am* 100:13615–13620
- Baber K, Mosthaf K, Flemisch B, Helmig R, Müthing S (2012) Numerical scheme for coupling two-phase compositional porous-media flow and one-phase compositional free flow. *IMA J Appl Math* 77:887–909

- Bai M, Elsworth D, Roegiers JC (1993) Multiporosity/multipermeability approach to the simulation of naturally fractured reservoirs. *Water Resour Res* 29:1621–1633
- Bear MF, Paradiso MA, Connors BW (2001) Neuroscience: Exploring the brain, 2nd edn. Lippincott Williams and Wilkins, Baltimore
- Biot MA (1941) General theory of three-dimensional consolidation. *J Appl Phys* 12:155–164
- Cattaneo L, Zunino P (2013) Computational models for coupling tissue perfusion and microcirculation. MOX Report 25/2013
- Chen KC, Nicholson C (2000) Spatial buffering of potassium ions in brain extracellular space. *Biophys J* 78:2776–97
- Coles J, Orkand R (1986) Free Concentrations of Na, K, and Cl in the Retina of the Honeybee Drone: Stimulus induced redistribution and Homeostasis. *Ann New York Acad Sci* 481: 303–317
- Cordingley G, Somjen G (1978) The clearing of excess potassium from extracellular space in spinal cord and cerebral cortex. *Brain Res* 151:291–306
- Cressman J, Ullah G, Ziburkus J, Schiff S, Barreto E (2009) The influence of sodium and potassium dynamics on excitability, seizures, and the stability of persistent states: I. single neuron dynamics. *J Comput Neurosci*
- De Keyser J, Mostert JP, Koch MW (2008) Dysfunctional astrocytes as key players in the pathogenesis of central nervous system disorders. *J Neurol Sci* 267:3–16
- Destexhe A, Bal T, McCormick DA, Sejnowski TJ, Sejnowski J et al (1996) Ionic mechanisms underlying synchronized oscillations and propagating waves in a model of ferret thalamic slices. *J Neurophysiol* 76:2049–2070
- Devor A, Boas D, Einevoll G, Buxton R, Dale A (2012) Neuronal basis of non-invasive functional imaging: from bold fmri to microscopic neurovascular dynamics. In: Gruetter R (ed) Choi IY. *Neural Metabolism In Vivo*, Springer, pp 433–500
- Dietzel I, Heinemann U, Lux H (1989) Relations between slow extracellular potential changes, glial potassium buffering, and electrolyte and cellular volume changes during neuronal hyperactivity in cat. *Glia* 2:25–44
- Einevoll G, Kayser C, Logothetis N, Panzeri S (2013) Modelling and analysis of local field potentials for studying the function of cortical circuits. *Nat Rev Neurosci* 14:770–785
- Enger R, Gundersen GA, Haj-Yasein NN, Eilert-Olsen M, Thoren AE (2012) Molecular scaffolds underpinning macroglial polarization: an analysis of retinal Müller cells and brain astrocytes in mouse. *Glia* 60:2018–2026
- Enger R, Tang W, Vindedal GF, Jensen V, Johannes Helm P, et al. (2015) Dynamics of ionic shifts in cortical spreading depression. *Cerebral cortex*. New York 1991, pp 1–8
- Florence G, Dahlem MA, Almeida ACG, Bassani JWM, Kurths J (2009) The role of extracellular potassium dynamics in the different stages of ictal bursting and spreading depression: a computational study. *J Theor Biol* 258:219–228
- Frankenhaeuser B, Hodgkin AL (1956) The after-effects of impulses in the giant nerve fibres of loligo. *J Physiol* 131:341–76
- Furman CS, Gorelick-Feldman DA, Davidson KGV, Yasumura T, Neely JD (2003) Aquaporin-4 square array assembly: opposing actions of M1 and M23 isoforms. *Proc Natl Acad Sci United States Am* 100:13609–13614
- Gardner-Medwin A (1983) Analysis of potassium dynamics in mammalian brain tissue. *J Physiol*: 393–426
- Goriely A, Geers MG, Holzapfel GA, Jayamohan J, Jrusalem A, et al (2015) Mechanics of the brain: perspectives, challenges, and opportunities. *Biomech Model Mechanobiol*: 1–35
- Grisar T, Guillaume D, Delgado-Escueta AV (1992) Contribution of Na⁺, K⁽⁺⁾-ATPase to focal epilepsy: a brief review. *Epilepsy Res* 12:141–149
- Grodzinsky F (2011) Fields, forces, and flows in biological systems. Garland Science, Taylor & Francis Group, London & New York
- Haj-Yasein NN, Bugge CE, Jensen V, Ostby I, Ottersen OP (2014) Deletion of aquaporin-4 increases extracellular K⁽⁺⁾ concentration during synaptic stimulation in mouse hippocampus. *Brain Struct Funct* 220:2469–74

- Haj-Yasein NN, Bugge CE, Jensen V, Østby I, Ottersen OP (2015) Deletion of aquaporin-4 increases extracellular K(+) concentration during synaptic stimulation in mouse hippocampus. *Brain Struct Funct* 220:2469–2474
- Halnes G, Augustinaitė S, Heggelund P, Einevoll GT, Migliore M (2011) A multi-compartment model for interneurons in the dorsal lateral geniculate nucleus. *PLoS Comput Biol* 7:e1002160
- Halnes G, Ostby I, Pettersen KH, Omholt SW, Einevoll GT (2013) Electrodiffusive model for astrocytic and neuronal ion concentration dynamics. *PLoS Computat Biol* 9:e1003386
- Halnes G, Mäki-Marttunen T, Keller D, Pettersen KH, Andreassen OA, Einevoll GT (2016) Effect of ionic diffusion on extracellular potentials in neural tissue. *PLOS Comput Biol* 12(11):e1005193
- Halnes G, Mäki-Marttunen T, Pettersen KH, Andreassen OA, Einevoll GT (2017) Ion diffusion may introduce spurious current sources in current-source density (CSD) analysis. *J Neurophysiol* 118(1):114–120
- Hämäläinen M, Hari R, Ilmoniemi R, Knuutila J, Lounasmaa OV (1993) Magnetoencephalography—theory, instrumentation, and applications to noninvasive studies of the working human brain. *Rev Mod Phys* 65:413–497
- Hashido M, Kidera A, Ikeguchi M (2007) Water transport in aquaporins: osmotic permeability matrix analysis of molecular dynamics simulations. *Biophys J* 93:373–385
- Hertz L, Peng L, Dienel GA (2006) Energy metabolism in astrocytes: high rate of oxidative metabolism and spatiotemporal dependence on glycolysis/glycogenolysis. *J Cereb Blood Flow Metab* (Official J Int Soc Cereb Blood Flow Metab) 27:219–249
- Hertz L, Xu J, Song D, Yan E, Gu L et al (2013) Astrocytic and neuronal accumulation of elevated extracellular K+ with a 2/3 K+/Na+ flux ratioconsequences for energy metabolism, osmolarity and higher brain function. *Front Computat Neurosci* 7:1–22
- Hladky SB, Barrand MA (2014) Mechanisms of fluid movement into, through and out of the brain: evaluation of the evidence. *Fluids Barriers CNS* 11:26
- Holter KE, Kehlet B, Devor A, Sejnowski TJ, Dale AM, Omholt SW, ... Pettersen KH (2017) Interstitial solute transport in 3D reconstructed neuropil occurs by diffusion rather than bulk flow. *Proceedings of the National Academy of Sciences*, 201706942
- Hübel N, Dahlem MA (2014) Dynamics from seconds to hours in Hodgkin-Huxley model with time-dependent ion concentrations and buffer reservoirs. *PLoS Comput Biol* 10:e1003941
- Iliff JJ, Wang M, Liao Y, Plog BA, Peng W et al (2012) A Paravascular pathway facilitates CSF flow through the brain Parenchyma and the clearance of interstitial solutes, including amyloid β . *Sci Transl Med* 4: 147ra111–147ra111
- Iliff JJ, Wang M, Zeppenfeld DM, Venkataraman A, Plog BA (2013) Cerebral arterial pulsation drives paravascular CSF-interstitial fluid exchange in the murine brain. *J Neurosci* 33:18190–18199
- Jensen MS, Yaari Y (1997) Role of intrinsic burst firing, potassium accumulation, and electrical coupling in the elevated potassium model of hippocampal epilepsy. *J Neurophysiol* 77:1224–33
- Jung JS, Bhat RV, Preston GM, Guggino WB, Baraban JM (1994) Molecular characterization of an aquaporin cDNA from brain: candidate osmoreceptor and regulator of water balance. *Proc Nat Acad Sci United States Am* 91:13052–13056
- Kager H, Wadman WJ, Somjen GG (2000) Simulated seizures and spreading depression in a neuron model incorporating interstitial space and ion concentrations. *J Neurophysiol* 84:495–512
- Kager H, Wadman WJ, Somjen GG (2006) Seizure-like afterdischarges simulated in a model neuron. *J Comput Neurosci* 22:105–128
- Kandel ER, Markram H, Matthews PM, Yuste R, Koch C (2013) Neuroscience thinks big (and collaboratively). *Nat Rev Neurosci* 14:659–664
- Koch C (1999) Biophysics of computation: information processing in single neurons, 1st edn. Oxford University Press, New York
- Kofuji P, Newman EA (2004) Potassium buffering in the central nervous system. *Neuroscience* 129:1045–56

- Kríz N, Syková E, Vyklický L (1975) Extracellular potassium changes in the spinal cord of the cat and their relation to slow potentials, active transport and impulse transmission. *J Physiol* 1:167–182
- Léonetti M, Dubois-Violette E (1998) Theory of electrodynamic instabilities in biological cells. *Phys Rev Lett* 81:1977–1980
- Lopreore CL, Bartol TM, Coggan JS, Keller DX, Sosinsky GE (2008) Computational modeling of three-dimensional electrodiffusion in biological systems: application to the node of Ranvier. *Biophys J* 95:2624–35
- Lothman E, Somjen G (1975) Extracellular potassium activity, intracellular and extracellular potential responses in the spinal cord. *J Physiol* 1:115–136
- Louveau A, Smirnov I, Keyes TJ, Eccles JD, Rouhani SJ et al (2015) Structural and functional features of central nervous system lymphatic vessels. *Nature* 523:337–341
- Lu B, Zhou YC, Ga Huber, Bond SD, Holst MJ (2007) Electrodiffusion: a continuum modeling framework for biomolecular systems with realistic spatiotemporal resolution. *J Chem Phys* 127:135102
- Lux HD, Heinemann U, Dietzel I (1986) Ionic changes and alterations in the size of the extracellular space during epileptic activity. *Adv Neurol* 44:619–39
- Macaulay N, Zeuthen T (2012) Glial K clearance and cell swelling: key roles for cotransporters and pumps. *Neurochem Res* 37:2299–309
- Mori Y (2009) From three-dimensional electrophysiology to the cable model: an asymptotic study. [arXiv:0901.3914 \[q-bioNC\]](https://arxiv.org/abs/0901.3914): 1–39
- Nanninga PM (2008) A computational neuron model based on Poisson Nernst Planck theory. *ANZIAM J* 50:46–59
- Nedergaard M, Dirnagl U (2005) Role of glial cells in cerebral ischemia. *Glia* 50:281–6
- Newman EA (1987) Distribution of potassium conductance in mammalian Muller (glial) cells: a comparative study. *J Neurosci* 7:2423–2432
- Newman EA (1993) Inward-rectifying potassium channels in retinal glial (Müller) cells. *J Neurosci (Official J Soc Neurosci)* 13:3333–45
- Nicholson C, Chen K, Hrabětová S, Tao L (2000) Diffusion of molecules in brain extracellular space: theory and experiment. *Progr Brain Res* 125:129–154
- Nunez PL, Srinivasan R (2006) Electric fields of the brain: the Neurophysics of EEG, 2nd edn. Oxford University Press, Inc
- Odette L, Newman EA (1988) Model of potassium dynamics in the central nervous system. *Glia* 210:198–210
- Orkand RK, Nicholls JG, Kuffler SW (1966) Effect of nerve impulses on the membrane potential of glial cells in the central nervous system of amphibia. *J Neurophysiol* 29:788–806
- Østby I, Øyehaug L, Einevoll GT, Nagelhus EA, Plahte E et al (2009) Astrocytic mechanisms explaining neural-activity-induced shrinkage of extraneuronal space. *PLoS Comp Biol* 5:e1000272
- Øyehaug L, Østby I, Lloyd CM, Omholt SW, Einevoll GT (2012) Dependence of spontaneous neuronal firing and depolarisation block on astroglial membrane transport mechanisms. *J Comput Neurosci* 32:147–165
- Pangrcic T, Potokar M, Haydon PG, Zorec R, Kreft M (2006) Astrocyte swelling leads to membrane unfolding, not membrane insertion. *J. Neurochem* 99(2):514–523
- Park EH, Durand DM (2006) Role of potassium lateral diffusion in non-synaptic epilepsy: a computational study. *J Theoret Biol* 238:666–82
- Pods J, Schönenk J, Bastian P (2013) Electrodiffusion models of neurons and extracellular space using the Poisson-Nernst-Planck equations-numerical simulation of the intra- and extracellular potential for an axon model. *Biophys J* 105:242–54
- Qian N, Sejnowski T (1989) An electro-diffusion model for computing membrane potentials and ionic concentrations in branching dendrites, spines and axons. *Biol Cybern* 15:1–15

- Rall W (1977) Core conductor theory and cable properties of neurons. In: Kandel E, Brookhardt J, Mountcastle VM (eds) *Handbook of physiology*, Bethesda: American Physiological Society, chapter 3, pp 39–97
- Rutkowska G, Haughton V, Linge S, Mardal KA (2012) Patient-specific 3d simulation of cyclic csf flow at the craniocervical region. *Am J Neuroradiol* 33:1756–1762
- Safronov BV, Wolff M, Vogel W (1999) Axonal expression of sodium channels in rat spinal neurones during postnatal development. *J Physiol* 514(Pt 3):729–734
- Sibille J, Duc KD, Holcman D, Rouach N (2015) The neuroglial potassium cycle during neurotransmission: role of kir4. 1 channels. *PLoS Comput Biol* 11:e1004137
- Silberstein C (2004) Membrane organization and function of M1 and M23 isoforms of aquaporin-4 in epithelial cells. *AJP. Renal Physiol* 287:F501–F511
- Smith AJ, Jin BJ, Verkman AS (2015) Muddying the water in brain edema? *Trends Neurosci* 38:331–332
- Solbrå A, Bergersen AW, van den Brink J, Malthe-Sørensen A, Einevoll GT, Hahn G (2018) A Kirchhoff-Nernst-Planck framework for modeling large scale extracellular electrodiffusion surrounding morphologically detailed neurons. *BioRxiv*. 261107
- Somjen GG (2004) Ions in the brain: normal function, seizures, and stroke, 1 edn. Oxford University Press, USA
- Somjen GG (2001) Mechanisms of spreading depression and hypoxic spreading depression-like depolarization. *Physiol Rev* 81:1065–1096
- Somjen GG, Kager H, Wadman WJ (2008) Computer simulations of neuron-glia interactions mediated by ion flux. *J Computat Neurosci* 25:349–65
- Støverud K, Langtangen H, Haughton V, Mardal K (2013) Csf pressure and velocity in obstructions of the subarachnoid spaces. *Neuroradiol J* 26:218–226
- Syková E, Nicholson C (2008) Diffusion in brain extracellular space. *Physiol Rev* 88:1277–1340
- Thrane AS, Rangroo Thrane V, Plog BA, Nedergaard M (2015) Filtering the muddled waters of brain edema. *Trends Neurosci* 38:333–335
- Tong J, Briggs MM, McIntosh TJ (2012) Water permeability of aquaporin-4 channel depends on bilayer composition, thickness, and elasticity. *Biophysl J* 103:1899–1908
- Tully BJ, Ventikos Y (2011) Cerebral water transport using multiple-network poroelastic theory: application to normal pressure hydrocephalus. *J Fluid Mech* 667:188–215
- Ullah G, Schiff S (2009) Models of epilepsy. *Scholarpedia* 4:1409
- Vardakas JC, Tully BJ, Ventikos Y (2013) Exploring the efficacy of endoscopic ventriculostomy for hydrocephalus treatment via a multicompartmental poroelastic model of CSF transport: A computational perspective. *PloS ONE* 8:1–16
- Verkhratsky A, Butt AM (2013) Glial physiology and pathophysiology. Wiley
- Wang DD, Bordey A (2008) The astrocyte odyssey. *Progr Neurobiol* 86:342–67
- Xie L, Kang H, Xu Q, Chen MJ, Liao Y (2013) Sleep drives metabolite clearance from the adult brain. *Science* 342:373–377
- Zhang Y, Barres BA (2010) Astrocyte heterogeneity: an underappreciated topic in neurobiology. *Curr Opin Neurobiol* 20:588–594
- Zhang H, Verkman AS (2008) Aquaporin-4 independent Kir4.1 K⁺ channel function in brain glial cells. *Mol Cell Neurosci* 37:1–10
- Ziburkus J, Cressman JR, Barreto E, Schiff SJ (2006) Interneuron and pyramidal cell interplay during in vitro seizure-like events. *J Neurophysiol* 95:3948–54

Chapter 15

Constraint-Based Modeling of Metabolic Interactions in and Between Astrocytes and Neurons



Tunahan Çakır

Abstract Through its metabolic network, a cell distributes the available carbon flux into several pathways. The pathway activity information for a cell is crucial to deduce underlying molecular mechanisms and to monitor the effect of perturbations such as diseases. The constraint-based modeling approach to organism- and tissue-specific metabolic networks has therefore become a popular focus in the computational system's biology field. The approach uses reaction stoichiometries and the reversibility information for the reactions as well as few literature-based flux measurements to calculate flux distributions through all covered pathways in a metabolic network. Therefore, the effect of phenomena such as hypoxia, hyperglycemia, and neurodegenerative diseases on brain metabolism can be computationally documented to enlighten molecular mechanisms and to design new hypotheses. This chapter covers the basics of constraint-based modeling via a toy metabolic network example and gives an overview of the application of the approach to couple neuronal and astrocytic metabolisms. It further utilizes a recently developed genome-scale metabolic network of the brain to calculate fluxes for the resting state and for hypoxia in and between astrocytes and neurons. Finally, the chapter shortly discusses the use of transcriptome data to obtain condition-specific flux distributions.

Keywords Metabolic network · Flux balance analysis
Neuron–astrocyte coupling · Brain metabolism

15.1 Introduction

It is a well-known fact that the major cell types in the brain, glia, and neuron, interact with each other by exchanging biomolecules. Metabolic interactions are an essential subset of such interactions, through which glial cells act as support for neural cells. Such a support guarantees normal functioning of neurons (Hertz and Zielke 2004;

T. Çakır (✉)

Department of Bioengineering, Gebze Technical University, 41400 Kocaeli, Turkey
e-mail: tcakir@gtu.edu.tr

Schousboe et al. 2011). The metabolic cooperation between the two cell types also regulates brain energy metabolism (Bélanger et al. 2011).

With the advent of systems biology, a system-based focus on neuron–astrocyte metabolic interactions resulted in models which simulate the metabolic behavior of brain cells based on the metabolic network structure. The first stoichiometric model to simulate intra- and intercellular metabolic fluxes (Chatzioannou et al. 2003) was based on 16 reactions mainly occurring among glutamate and TCA cycle intermediates. The authors aimed to elucidate the metabolism of neurotransmitter glutamate in rat cerebral cells. The work was followed by larger models covering more than hundred reactions (Çakır et al. 2007; Occhipinti et al. 2007). Biochemical pathways were analyzed in these studies at resting state, at different neural activities, and for the hypoxic state. The genome-associated metabolic models of coupled neurons and astrocytes appeared later (Lewis et al. 2010; Sertbaş et al. 2014). Transcriptome data for neurodegenerative diseases were utilized in these studies to analyze disease-specific effects on brain metabolic pathways. Studies which modeled brain stoichiometrically as a single type of cell without making distinction between astrocyte and neuron metabolisms also appeared (Stempler et al. 2014; Gavai et al. 2015), which are out of the focus of this chapter.

The constraint-based modeling framework of metabolism at genome scale led to a number of different methods (Lewis et al. 2012) as well as software (Rocha et al. 2010; Schellenberger et al. 2011) that enable the use of these methods as built-in functions, especially for researchers with biology backgrounds. In addition to the availability of the softwares, the developments in stable-isotope carbon labeling of brain cells provided estimated values of intracellular metabolic fluxes (Amaral et al. 2011, 2014; Duarte et al. 2015), aiding in the validation of the results of constraint-based simulations.

In this chapter, the constraint-based modeling is first reviewed and illustrated by a metabolic network of two interacting cells mimicking neuron–astrocyte coupling. This simplified setup is used to introduce fundamentals and most common approaches of constraint-based modeling and serves to frame a review of more complex models. Accordingly, a recently reconstructed genome-scale metabolic network of brain (Sertbaş et al. 2014) is then discussed and results of simulations of it are presented to study neuron-astrocytic metabolic coupling at resting (physiological) vs. hypoxic (pathological) conditions. The chapter finally ends with an outlook on methods that allow integration of transcriptome data in constraint-based modeling approaches to simulate specific brain diseases.

15.2 Principles of Constraint-Based Modeling Framework: Formulation and a Sample Toy Network

Flux balance analysis (FBA) is the most popular constraint-based metabolic modeling method. The first example of FBA appeared in 1986 (Fell and Small 1986),

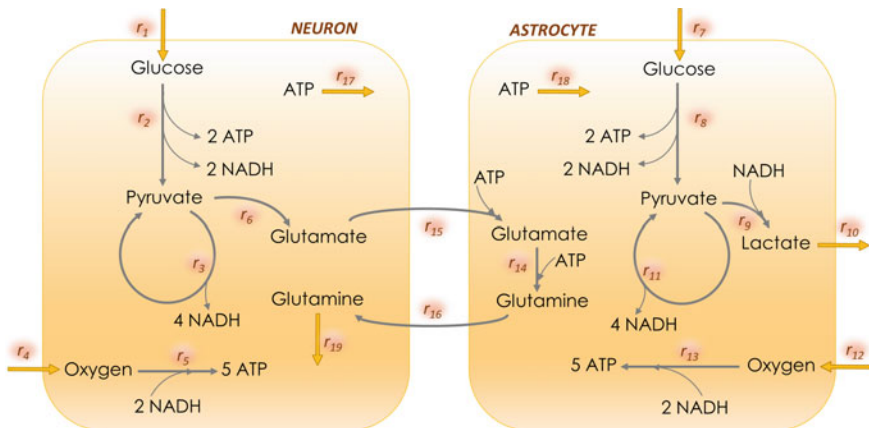


Fig. 15.1 Toy metabolic network of neuron–astrocyte interactions

which examined optimal triacylglycerol synthesis in the adipose tissue by studying a 57-reaction metabolic network of adipocyte metabolism. Following applications of FBA primarily focused on microorganisms in 1990s (Varma and Palsson 1993; van Gulik and Heijnen 1995). Since it only requires the stoichiometries of the reactions involved in the metabolic network together with few measured fluxes as constraints, developing genome-scale modeling frameworks based on FBA was not a daunting challenge, and several models were developed at the beginning of the millennium which consisted of hundreds of reactions occurring in the cell metabolism (Förster et al. 2003; Feist et al. 2007; Mardinoglu et al. 2014). The ease of use of FBA modeling framework, together with its promising outputs from gene deletion phenotype predictions to identification of potential drug targets, increased the widespread use of the approach, along with other constraint-based frameworks. In the year 2017 alone, when this manuscript was submitted for publication, a total of 100 articles were published which included the term “flux balance analysis” in their abstract or keyword list (PubMed search results).

In this section, I will focus on the principles of constraint-based modeling framework via a two-cell toy network mimicking neuron–glia interactions. Specifically, applications of flux balance analysis and flux variability analysis will be demonstrated.

15.2.1 The Toy Metabolic Network

Figure 15.1 presents a simplified toy network of neuron–astrocyte metabolic interactions for the purpose of demonstrating the principles of constraint-based modeling.

The simplified inter- and intracellular metabolic networks of the two cell types include basic characteristics of central carbon metabolism. Glucose uptake (r_1, r_7)

is followed by glycolysis pathway toward pyruvate (r_2, r_8) in both cell types, which enters into Krebs cycle to produce NADH (r_3, r_{11}). The simplified Krebs cycle does not include the replenishment of the pyruvate pool, only covering NADH production. Oxygen uptake (r_4, r_{12}) leads to oxidative phosphorylation (r_5, r_{13}), which converts NADH produced by glycolysis and TCA cycle to energy in the form of ATP. The produced ATP is used for a number of processes in the cell (r_{17}, r_{18}). Besides the central carbon metabolism, the simplified network also covers the glutamate–glutamine cycle between the two cell types. The glutamate–glutamine cycle is one of the key interactions among neurons and astrocytes (Schousboe et al. 1993; Shen et al. 1999; Gruetter et al. 2001). Since neurons cannot convert glutamate to glutamine, glutamate is transferred into astrocytes (r_{15}), where the conversion is handled (r_{14}). Astrocyte-produced glutamine is transferred back to neurons (r_{16}), where it is used to replenish the TCA cycle and for amino acid metabolism (r_{19}). Lactate is a product of glycolysis, and it is known that lactate is primarily produced by astrocytes at resting state, and neurons have only respiratory metabolism (Gjedde et al. 2002). That is why the toy network includes lactate production only by the astrocyte (r_9, r_{10}).

15.2.2 Constraint-Based Framework: Fundamentals

The idea behind constraint-based modeling is to write the mass balance of each intracellular metabolite. For example, the mass balance of pyruvate concentration in neurons (Fig. 15.1) is as follows:

$$\frac{d(C_{\text{Pyruvate}}^N)}{dt} = r_2 - r_6 - r_3 \quad (15.1)$$

Such a balance can be written around six other metabolites of neurons. Moreover, there are eight intracellular metabolites in astrocytes. Therefore, a total of 15 differential mass balances will represent the dynamic behavior of the toy network. One should note that separate balances are written for a metabolite for each different compartment (pool). Therefore, neuronal pyruvate and astrocytic pyruvate are separately balanced.

Mathematical generalized representation of differential mass balances for such a system can be written in vector form as follows:

$$\frac{d\mathbf{C}}{dt} = \mathbf{S} \times \mathbf{v} \quad (15.2)$$

Here, \mathbf{C} is a vector of metabolite concentrations, \mathbf{v} is a vector of reaction rates, called also fluxes, and \mathbf{S} is a stoichiometric matrix based on the stoichiometries of metabolic network reactions. The matrix is formed such that the dimension is $m \times n$, where m is the number of intracellular metabolites, and n is the number of reactions. Similarly, \mathbf{C} is an $m \times 1$ vector, and \mathbf{v} is an $n \times 1$ vector. Therefore, the columns

	r_1	r_2	r_3	r_4	r_5	r_6	r_7	r_8	r_9	r_{10}	r_{11}	r_{12}	r_{13}	r_{14}	r_{15}	r_{16}	r_{17}	r_{18}	r_{19}
Glucose ^N	1	-1	0	0	0	0	0	0	0	0	0	0	0	0	0	0	0	0	0
Pyruvate ^N	0	2	-1	0	0	-1	0	0	0	0	0	0	0	0	0	0	0	0	0
Oxygen ^N	0	0	0	1	-1	0	0	0	0	0	0	0	0	0	0	0	0	0	0
ATP ^N	0	2	0	0	5	0	0	0	0	0	0	0	0	0	0	-1	0	0	0
NADH ^N	0	2	4	0	-2	0	0	0	0	0	0	0	0	0	0	0	0	0	0
Glutamate ^N	0	0	0	0	0	1	0	0	0	0	0	0	0	-1	0	0	0	0	0
Glutamine ^N	0	0	0	0	0	0	0	0	0	0	0	0	0	0	1	0	0	-1	0
Glucose ^A	0	0	0	0	0	0	1	-1	0	0	0	0	0	0	0	0	0	0	0
Pyruvate ^A	0	0	0	0	0	0	2	-1	0	-1	0	0	0	0	0	0	0	0	0
Oxygen ^A	0	0	0	0	0	0	0	0	0	0	1	-1	0	0	0	0	0	0	0
ATP ^A	0	0	0	0	0	0	0	2	0	0	0	0	5	-1	-1	0	0	-1	0
NADH ^A	0	0	0	0	0	0	0	2	-1	0	4	0	-2	0	0	0	0	0	0
Glutamate ^A	0	0	0	0	0	0	0	0	0	0	0	0	0	-1	1	0	0	0	0
Glutamine ^A	0	0	0	0	0	0	0	0	0	0	0	0	0	1	0	-1	0	0	0
Lactate ^A	0	0	0	0	0	0	0	0	1	-1	0	0	0	0	0	0	0	0	0

Fig. 15.2 Stoichiometric matrix, \mathbf{S} , corresponding to the toy metabolic network

of the stoichiometric matrix correspond to reactions and the rows to intracellular metabolites.

For our toy network (Fig. 15.1), the dimensions of the stoichiometric matrix will be 15×19 . In the stoichiometric matrix, the coefficients of reactants are introduced as negative numbers, whereas those of products are positive. Figure 15.2 gives the corresponding stoichiometric matrix. For r_1 , for example, there is no intracellular metabolite as the reactant, and there is a product with a stoichiometry of 1 (glucose). Therefore, the corresponding column in the stoichiometric matrix is all zeros except the neuronal glucose, which has the value of 1.

In the constraint-based modeling framework, Eq. (15.2) is solved at steady-state or pseudo-steady-state conditions. The left side of the equation is zero in such conditions, giving rise to the following simple equation:

$$\mathbf{S} \times \mathbf{v} = 0 \quad (15.3)$$

Equation (15.3) is the key equation for constraint-based modeling approaches, including the famous flux balance analysis (FBA) method. The equation is usually underdetermined since the number of equations (number of intracellular metabolites around which mass balance is written) is lower than the number of unknowns (number of reaction rates). The constraint-based modeling approach aims to search the solution space of an underdetermined problem with the help of proper constraints.

Equation (15.3) is the most essential constraint for the solution space to calculate unknown metabolic reaction rates (fluxes). In addition to the equality constraints, the unknown fluxes are also constrained by the reaction directions. That is, for irreversible reactions, the flux value can change between zero and infinity, whereas the range is from negative to positive infinity for reversible reactions. Similarly, for the fluxes

	r_1	r_2	r_3	r_4	r_5	r_6	r_7	r_8	r_9	r_{10}	r_{11}	r_{12}	r_{13}	r_{14}	r_{15}	r_{16}	r_{17}	r_{18}	r_{19}
Lower-bound (lb)	0.15	0	0	0	0	0	0.15	0	0	0	0	0	0	0	0.14	0	0	0	0
Upper-bound (ub)	0.20	∞	∞	0.80	∞	∞	0.20	∞	∞	∞	∞	0.80	∞	∞	0.28	∞	∞	∞	∞

Fig. 15.3 Lower-bound and upper-bound vectors for the resting state of brain for the toy example

with known experimental measurements, the flux's lower and upper bounds will be constrained by the measured values. Mathematically,

$$\mathbf{lb} \leq \mathbf{v} \leq \mathbf{ub} \quad (15.4)$$

with **lb** and **ub** being $n \times 1$ lower-bound and upper-bound vectors. For our toy example, the constraints are given in Fig. 15.3. It is reported that the human cerebral glucose uptake rate at resting state is around $0.35 \mu\text{mole/g tissue/min}$ (Shen et al. 1999; Dienel and Cruz 2003), which is almost equally shared by astrocytes and neurons (Nehlig et al. 2004; Hertz et al. 2007). Therefore, each of neuronal and astrocytic glucose uptake rates was constrained to be changing between 0.15 and $0.20 \mu\text{mole/g tissue/min}$. The values were not fixed to mimic the relative variability in the uptake rates by the two cell types. The cerebral metabolic rate of oxygen for the resting human brain is reported to be around five times higher than that of glucose (Dienel and Cruz 2003). Therefore, the oxygen uptake rates for each cell were constrained to be lower than $0.80 \mu\text{mole/g tissue/min}$. To capture the behavior of the network towards anaerobicity, the lower bounds for oxygen uptake rates were constrained to be zero. Additionally, it is reported that the glutamine–glutamate cycle flux (r_{15}) is about 40–80% of the total glucose uptake rate (Shen et al. 1999; Gruetter et al. 2001). The related constraints were reflected in the lower- and upper-bound vectors.

15.2.3 Constraint-Based Framework: Flux Balance Analysis

The most popular constraint-based metabolic modeling approach, FBA (Orth et al. 2010), solves for the unknown fluxes by using Eqs. (15.3) and (15.4) as constraints. Since the problem is usually underdetermined as stated above, FBA uses optimization algorithms together with an objective function to solve for the unknown vector. The objective function seeks a particular optimal solution in the solution space. It must be biologically reasonable such as maximal energy (ATP) production (Ramakrishna et al. 2001; Gavai et al. 2015) or minimal NADH production (Savinell and Palsson 1992). For this toy example, we will solve the problem for four different objective functions and compare the resulting flux distributions. The objective functions to be studied are (i) maximization vs. (ii) minimization of ATP production by both cell types, and (iii) maximization vs. (iv) minimization of the lactate production. Mathematically speaking,

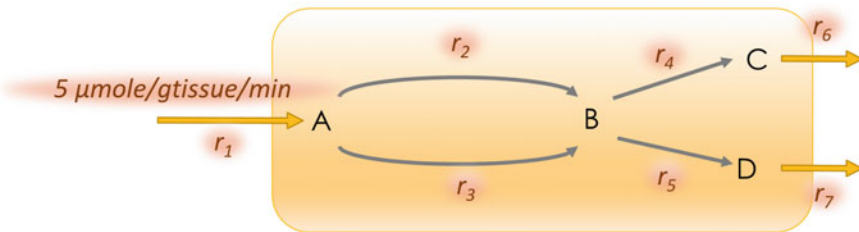


Fig. 15.4 Exemplification of flux variability analysis. In the problem depicted in the figure, the uptake rate of $A(r_1)$ is given as $5 \mu\text{mole/g tissue/min}$. For an objective function of maximization of the production of $C(r_6)$, the value of the corresponding flux would be calculated as 5, with the other competing flux (r_7) attaining the value of zero. However, this problem has alternate optima since there are many solution vectors (with different values of r_2 and r_3) with the same optimum value of the objective function. Flux variability analysis (FVA) first fixes the value of the flux optimized by the objective function to its optimal value and then finds maximal/minimal values of each flux in the system. For this example, the other fluxes do not have any variability. However, both r_2 and r_3 have a range of $[0, 5]$ satisfying the objective function

$$\max/\min(v_{17} + v_{18}) \quad (15.5.a)$$

$$\max/\min(v_{10}) \quad (15.5.b)$$

The coefficients of the objective function can be represented by a vector of $n \times 1$, to be used for the optimization problem. Since the objective function includes linear combination of the unknowns, the problem will be solved by linear programming. Most of the cases, the employed objective function in FBA problems is linear; therefore, the optimization is solved by linear programming. Popular solvers employed in FBA are Gurobi, IBM ILOG CPLEX, GLPK, and GAMS. There are also free softwares which provide built-in functions specific for FBA, facilitating the use of the method by non experts. COBRA (Rocha et al. 2010; Schellenberger et al. 2011) and OptFlux (Rocha et al. 2010; Schellenberger et al. 2011) are among these softwares.

15.2.4 Flux Variability Analysis: A Must-Complement for Flux Balance Analysis

In an optimization problem, there may be alternative flux distributions with the same objective function value, which is known as alternate optima (Lee et al. 2000; Mahadevan and Schilling 2003). The scanning and detection of the availability of alternate optima are crucial in flux balance analysis since the calculated flux values may not be unique. The logic is exemplified in Fig. 15.4.

The variability in flux values due to alternate optima can be minimized if more measurement constraints are introduced, leading to a shrinkage in the solution space. Due to the alternate optima problem, every FBA simulation must be followed by flux

variability analysis (FVA) to identify the variability in fluxes for the fixed value of the optimal flux. It was first introduced in 2003 (Mahadevan and Schilling 2003) and is continuously being used in computational system's biology research for the analysis of genome-scale metabolic networks. The FVA algorithm works as follows: After FBA is performed, the calculated optimal value for the flux representing objective function is set to the optimal value by constraining its lower/upper bounds to the optimal value. Later, each flux in the model is maximized and minimized to get if the flux shows any variability for the optimal flux value. In total, for a network of n reactions, $2n$ optimizations are performed in FVA. FVA can be performed by using built-in functions in constraint-based analysis softwares such as COBRA and OptFlux.

15.2.5 *Simulation Results of the Toy Network*

Equations (15.3) and (15.4) were solved for the inputs of the stoichiometric matrix (given in Fig. 15.2) and the lower- and upper-bound vectors (given in Fig. 15.3). Results obtained for different objective functions based on Eqs. (15.5.a) and (15.5.b) are reported in Table 15.1.

The FBA results show that for the given constraints, lactate production rate (r_{10}) can change between 0 and 0.40 $\mu\text{mole/g tissue/min}$. Since two lactates are formed from one glucose stoichiometrically at maximum, this corresponds to 0–20% of total glucose uptake rate. For the maximal lactate production, the astrocytic oxygen uptake rate (r_{12}) is calculated as zero at its minimum bound. Also, the TCA cycle flux (r_{11}) is inactive since all available pyruvate is used for the lactate production. The anaerobic astrocyte metabolism leads to a maximal lactate production rate. Besides, astrocytic ATP production for the other pathways (r_{18}) is very low due to an inactive oxidative phosphorylation, which cannot contribute to the ATP pool. Astrocytic glucose uptake is at maximum to provide more ATP through glycolysis. For the minimal lactate production, on the other hand, astrocyte has a full respiratory metabolism with a high TCA cycle activity. NADH produced in TCA cycle is converted to ATP in oxidative phosphorylation thanks to a high astrocytic oxygen uptake rate. Oxygen–glucose index is three times higher than the maximal lactate production case. The comparison also shows that the neuronal metabolism is not affected much in between the two objectives.

For the maximal ATP production for other pathways with ($r_{17} + r_{18}$) as the objective, we see high neuronal and astrocytic oxygen uptake rates. Since oxygen uptake is coupled with the TCA cycle through the oxidative phosphorylation, these pathways are upregulated. For the minimization of ATP production rate, the results reveal a higher glutamate–glutamine cycle rate since the cycle consumes overall ATP pool. The TCA cycle activity is very low in both cell types (0.02 $\mu\text{mole/g tissue/min}$) since the surplus NADH will not be converted to ATP via the oxidative phosphorylation route to keep the pool minimal. With this objective, the astrocytic ATP production for other pathways is calculated as zero, meaning all ATP produced in the glycolysis

Table 15.1 Flux distributions calculated with the corresponding objective functions for the toy metabolic networks of neuron and astrocyte

	Minimization of total ATP production	Maximization of total ATP production	Minimization of lactate production	Maximization of lactate production
r_1	0.15	0.2	0.15	0.15
r_2	0.15	0.2	0.15	0.15
r_3	0.02	0.26	0.16	0.16
r_4	0.19	0.72	0.47	0.47
r_5	0.19	0.72	0.47	0.47
r_6	0.28	0.14	0.14	0.14
r_7	0.15	0.20	0.15	0.20
r_8	0.15	0.20	0.15	0.20
r_9	0.28	0.08	0.00	0.40
r_{10}	0.28	0.08	0.00	0.40
r_{11}	0.02	0.32	0.30	0.00
r_{12}	0.05	0.80	0.75	0.00
r_{13}	0.05	0.80	0.75	0.00
r_{14}	0.28	0.14	0.14	0.14
r_{15}	0.28	0.14	0.14	0.14
r_{16}	0.28	0.14	0.14	0.14
r_{17}	1.25	4.00	2.65	2.65
r_{18}	0	4.12	3.77	0.12
r_{19}	0.28	0.14	0.14	0.14
OGI^a	0.81	3.80	4.07	1.34
$Obj. Val.^a$	1.25	8.12	0.00	0.40

^a OGI oxygen–glucose index, $Obj. Val.$ the value of the objective function

cycle at a rate of $0.30 \mu\text{mole/g tissue/min}$ and at the oxidative phosphorylation step at a rate of $0.25 \mu\text{mole/g tissue/min}$ is consumed in glutamate–glutamine cycle (r_{14} , r_{15}), leaving no ATP to be used for other astrocytic pathways.

One should note that the FBA results in Table 15.1 must be checked by flux variability analysis (FVA) for flux variability due to alternate optima. Therefore, the flux values other than the optimal flux must not be trusted. FVA analysis was performed for the maximal value of lactate production for demonstration, and the results are presented in Table 15.2. For this, the lactate flux was fixed to its optimal value of 0.40, and each flux was maximized and minimized subsequently as presented in Sect. 15.2.4.

The results reveal variability in a number of fluxes in the system (Table 15.2). The variability is relatively low for some of the fluxes (e.g., neuronal glucose uptake rate), there is no variability for some of the fluxes (e.g., astrocytic glucose uptake rate), and the variability is huge for some of the fluxes (e.g., neuronal oxygen uptake rate and

Table 15.2 Variability of the fluxes for maximal lactate production calculated by FVA

	r_1	r_2	r_3	r_4	r_5	r_6	r_7	r_8	r_9	r_{10}	r_{11}	r_{12}	r_{13}	r_{14}	r_{15}	r_{16}	r_{17}	r_{18}	r_{19}
min.	0.15	0.15	0.10	0.35	0.35	0.14	0.20	0.20	0.40	0.40	0	0	0	0.14	0.14	0.14	2.05	0	0.14
max.	0.20	0.20	0.26	0.72	0.72	0.20	0.20	0.20	0.40	0.40	0	0	0	0.20	0.20	4.00	0.12	0.20	

neuronal ATP production rate for the other cellular processes). As mentioned above, more precise measurement constraints rather than defining a range will further shrink the solution space, removing the variability observed in the results. Constraints can also be introduced to other fluxes, if available, to minimize available alternate optima. Moreover, a secondary optimization can be employed to eliminate alternate optima problem (see Sect. 15.4.2). On the other hand, the availability of the flux variability can be interpreted as a reflection of biological variability, and FVA can be used to search different metabolic capabilities of the cell.

As exemplified above via the toy network, the characterization of the cell metabolism is possible via the interpretation of flux balance analysis results. As another example, a relevant question can be to document how maximum ATP production (for other cellular processes not covered in the toy network) depends on the lactate production rate. To simulate this via FBA, the lactate production flux can be fixed to a value, and the optimization can be run for the objective function defined in Eq. 15.5.a. Repeating the optimization for the range of lactate production rate (0–0.40), the obtained optimal values are plotted in Fig. 15.5. The figure shows that maximal ATP production slightly increases first up to a value of lactate production rate (0.08), and it starts to decrease afterward; attaining almost the half of the maximum value (4.1) when the lactate production flux is at maximum. The second observed behavior is easy to interpret: Lactate production decreases the available pyruvate to enter TCA cycle, and therefore, less ATP is produced via oxidative phosphorylation due to the limited NADH produced in the cycle. The first behavior, on the other hand, needs a closer inspection. At zero lactate production condition, the glucose uptake rate in astrocytes is $0.16 \mu\text{mole/g tissue/min}$, not at maximum bound while the oxygen uptake is at the maximum boundary (0.80). As the lactate production rate is slightly increased, the glycolytic flux in astrocytes also slightly increases to supply necessary carbon flux so that the rest of the network is not perturbed. This slight increase in the glycolytic flux also increases the amount of glycolytic ATP production, which leads to the slight increase shown in Fig. 15.5. The glucose uptake rate reaches its maximum value of 0.20 when the lactate production rate becomes 0.08. After this point, the increase in lactate production cannot be compensated by further increase in glycolytic rate; therefore, the pyruvate pool available for TCA cycle is reduced, leading to decrease in the available NADH and, hence, ATP.

15.3 FBA-Based Simulation of Neuron–Astrocyte Interactions: Overview of Literature Examples

This section reviews constraint-based modeling studies utilizing neuron–astrocyte coupled metabolic networks. Table 15.3 presents a summary of the studies reviewed below, listing the pathway coverage of the models and the specific FBA approach used in the study.

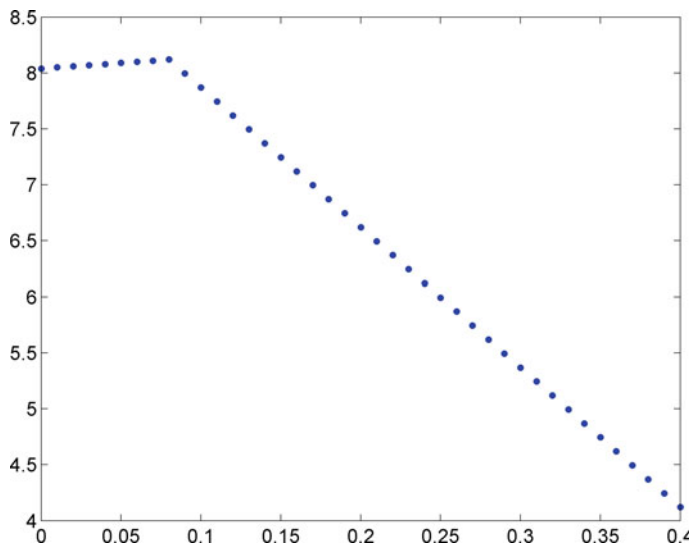


Fig. 15.5 Relationship between lactate production (x axis) and maximal ATP production (y axis) as calculated by FBA for the toy network

The first example of FBA for brain metabolism was reported for rat brain for a condition where glutamate–glutamine cycle was inactive (Chatzioannou et al. 2003). The model included 16 reactions, mostly from Krebs cycle metabolism, and it was used to study the metabolism of neurotransmitter glutamate for non-stimulated and potassium-evoked stimulated conditions. Since the number of measured fluxes they used from literature was higher than the degrees of freedom of the mass balance equations, no optimization was required. Instead, they solved the system of equations based on least squares minimization. Calculated fluxes were in agreement with data reported in the literature.

Later, a comprehensive metabolic network of neuron–astrocyte interactions was reported, covering major amino acid metabolisms, lipid-related pathways as well as neurotransmitter metabolism in addition to central carbon metabolism, summing up to 217 reactions among 216 metabolites (Çakır et al. 2007). The stoichiometric model included 16 intercellular reactions representing metabolite trafficking between astrocytes and neurons. The work used literature-based flux constraints for the uptake rates of glucose, oxygen, ammonia, and essential amino acids with a dual objective function framework to calculate resting-state fluxes, which correctly predicted major flux splits in healthy human brain. The primary objective function employed was the maximization of the sum of glutamate–glutamine–GABA cycle fluxes between the two cell types, which was followed by the minimization of Euclidean norm of fluxes to ensure efficient channeling of fluxes through all pathways with minimal use of enzymes. The study also included FBA-based simulation of the change in metabolic fluxes for cerebral and astrocytic hypoxia.

Table 15.3 Comparison of neuron–astrocyte coupled metabolic networks analyzed by constraint-based modeling

Approach	Genome association	Major pathways covered	References
FBA with least squares	No	Low (~15 reactions) Krebs cycle, glutamate–glutamine cycle	Chatziloannou et al. (2003)
FBA with optimization	No	High (~200 reactions) central carbon metabolism, amino acid metabolism (synthesis and catabolism), lipid metabolism, neurotransmitter metabolism	Çakır et al. (2007)
Stochastic FBA (sampling-based)	No	Moderate (~100 reactions) central carbon metabolism, glutamate–glutamine cycle	Occhipinti et al. (2007, 2009, 2010), Calvetti and Somersalo (2012)
Relaxation FBA (sampling-based)	No	Moderate (~100 reactions) central carbon metabolism, glutamate–glutamine cycle	Massucci et al. (2013)
Hit Run FBA (sampling-based)	Yes (403 genes)	High (~1000 reactions) about 40 pathways (see the related publication for details)	Lewis et al. (2010)
FBA with optimization	Yes (570 genes)	High (~600 reactions) about 40 pathways (see the related publication for details)	Sertbaş et al. (2014)

In a series of articles, a stochastic version of FBA was implemented to study metabolic pathway activities in and between astrocytes and neurons (Occhipinti et al. 2007, 2009, 2010; Calvetti and Somersalo 2012). The constraint-based framework obeys the same equations except that the right-hand side of Eq. (15.3) is replaced by a random vector with zero mean and a small covariance. In this way, a lack of certainty is introduced to FBA on whether the system is really at steady state. The noise vector ensures calculation of solutions that are not strictly at steady state but very close to it. The definition guarantees that such solutions occur with a lower probability. Since the goal of stochastic FBA is not to calculate a single flux state but a high number of flux states populated around steady state, optimization is not

employed in the solution. Instead, solution space is sampled based on Markov chain Monte Carlo sampling method, e.g., for 100,000 times, and the probabilistic behavior of flux profiles is plotted. In their first work (Occhipinti et al. 2007), the authors study the effect of different levels of neural activity on biochemical pathways of astrocytes and neurons. The neural activity is reflected on the model by putting constraints on glutamate–glutamine cycle flux. A low flux means lower neural activity. In the later work (Occhipinti et al. 2009), the stochastic FBA is used to study the validity of well-known astrocyte–neuron lactate shuttle hypothesis (Pellerin et al. 2007) which postulates that neuronal energy metabolism is fueled by the use of astrocyte-derived lactate as carbon substrate, rather than glucose. The simulation results suggest the activity of the shuttle at high neural activity while glucose is the preferred substrate for neurons at low activity. The next study (Occhipinti et al. 2010) focuses on metabolic interactions between astrocytes and GABAergic neurons at different activity levels. In a more recent work (Calvetti and Somersalo 2012), the authors combine three cell types, astrocytes, glutamatergic neurons, and GABAergic neurons, under one model to present a flux-based analysis of metabolic reactions in central carbon metabolism of brain. In all these studies, the metabolic networks cover about 100 reactions occurring in central carbon metabolism, without the consideration of other pathways such as amino acid and lipid metabolism. The authors also developed a free MATLAB package, called METABOLICA, which can be used to perform stochastic FBA (Heino et al. 2010).

In another sampling-based approach, the authors studied the relation between glutamate–glutamine cycle and relative energy demand of neurons and astrocytes by using a similar size network mostly based on central metabolism (Massucci et al. 2013). The authors relaxed Eq. 15.3 in a different way, by changing the equality to inequality such that the left-hand side can be greater than zero. Their motivation is the hypothesis that there will be net production of some metabolites since the considered metabolic network is incomplete and does not cover the consumption and production of some of the model metabolites by other pathways. The sampling of flux solution space is performed by a relaxation method.

In the modeling approaches discussed above, no genome association was considered for the included reactions. The first genome-scale modeling effort for brain included more than 1000 reactions associated with 403 genes (Lewis et al. 2010). The authors reconstructed three independently coupled metabolic networks for astrocyte–glutamatergic neuron, astrocyte–GABAergic neuron, and astrocyte–cholinergic neuron pairs. The networks were derived from the generic human metabolic network reconstruction Recon1, by using databases reporting brain-specific localization of proteins or gene expression (Duarte et al. 2007). They used the models to analyze transcriptome data for Alzheimer’s disease via a constraint-based modeling approach utilizing Monte Carlo sampling of the solution space. They simulated deficiencies of enzymes known to be affected in Alzheimer’s disease with the help of the sampling-based FBA, which led to an *in silico* testing of the neuroprotective effect of GAD for the disease. Their sampling approach is implemented in the free MATLAB package COBRA (Schellenberger et al. 2011), which also has built-in functions for FBA and FVA.

More recently, a new genome-scale reconstruction was introduced, covering 630 reactions controlled by 570 genes functioning in brain (Sertbaş et al. 2014). The reconstruction was developed by introducing several improvements in terms of pathway coverage to a previous model (Çakır et al. 2007). The same dual objective function was used to calculate the healthy state flux distribution, leading to literature-consistent results for major flux splits in central metabolism. The next section covers a detailed presentation of the characteristics of this model as well as its usage for metabolic simulation.

15.4 FBA-Based Simulation of Neuron–Astrocyte Interactions at Genome-Scale

As mentioned above, the metabolic model by Sertbaş et al. (2014), termed iMS570, is the most comprehensive brain metabolic network reconstruction in terms of gene coverage. The naming of the model is based on a naming convention which uses the number of genes and the initials of the person who developed it, with *i* referring to an *in silico* model (Reed et al. 2003). In this section, I use this reconstruction to perform metabolic flux analysis of brain in resting state and in hypoxia. The first subsection gives the main characteristics of the reconstruction, which is followed by its use to characterize flux-based phenotypes of metabolism in resting state and in hypoxia. In the last subsection, the use of transcriptome data to further constrain genome-associated metabolic models is discussed.

15.4.1 Model Properties

The brain metabolic model, iMS570, contains 465 intracellular metabolites and 59 extracellular metabolites. 630 reactions are included in the model, 571 of which are internal reactions describing the conversion between intracellular metabolites. The remaining 59 reactions define exchange of metabolites between extracellular space and astrocytes or neurons. 253 of the reactions occur in neurons, whereas 299 of them are astrocytic. That is, metabolic differences in the two cell types in terms of reaction specificity are considered in the reconstruction. These differences are tabulated in Table 15.4. This specificity is also reflected in the uptakes of metabolites. Uptakes of linoleate, linolenate, cystine, leucine, isoleucine, valine, arginine, ammonia, and glycogen are defined as astrocytic while tyrosine, lysine, phenylalanine, tryptophan, and histidine are neuronal. Additionally, cofactor localization (NADH, NADPH, FADH₂) in cytosol or mitochondria was reflected in the compiled reactions. iMS570 includes 20 reactions which depict the transfer of metabolites between astrocytes and neurons (Table 15.5). These reactions ensure a tight metabolic coupling of the two cell types in the modeling framework. Of 571 internal reactions, 460 have associated

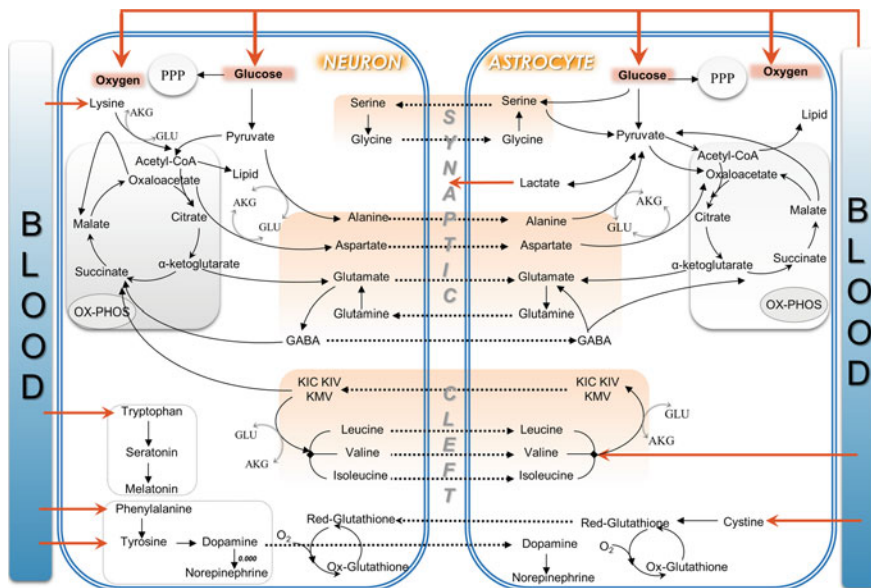


Fig. 15.6 A snapshot of major metabolic interactions in brain based on iMS570. GLU: glutamate, AKG: α -ketoglutarate. Adapted from (Çakır et al. 2007)

gene information, making the percentage of gene-associated reactions in the model 81%. Since many of the reactions have multiple gene associations, the total number of genes included in the metabolic model is 570.

The final reconstructed model includes more than 40 metabolic pathways, covering pathways for central carbon metabolism, all amino acids, reactive oxygen species, creatine, heme, polyamine, neurotransmitter metabolisms, a detailed characterization of lipid pathways including cholesterol, fatty acid, inositol, phosphatidylethanolamine, phosphatidylcholine, cardiolipin, sphingomyelin metabolisms, and pathways for purine and pyrimidine nucleosides. Besides, biochemical entities such as glutamate–glutamine cycle, malate–aspartate shuttle, serine–glycine cycle, branched-chain amino acid cycles, glycerol-3-phosphate shuttle are represented in iMS570. A brief snapshot of the major reactions covered is provided in Fig. 15.6.

15.4.2 Resting-State Fluxes

The resting-state metabolic fluxes of human brain were calculated to validate the reconstructed genome-scale network, iMS570 (Sertbaş et al. 2014). The constraints for the model include uptake rates of glucose, oxygen, essential amino acids, and ammonia (Table 15.6). Ketone body uptake and glycogen uptake were constrained

Table 15.4 Metabolic differences in two cell types reflected in iMS570 for pathway (internal) reactions

Reaction/enzyme/pathway	Coupling/differentiation
Pyruvate carboxylation	Only active in astrocytes
Citrate lyase beta-like protein	Only active in astrocytes
Cytosolic malate dehydrogenation	The one in neurons is in reverse direction of the mitochondrial reaction, thereby mimicking malate-aspartate shuttle active in neurons
Malic enzyme	Cytosolic in astrocytes, mitochondrial in neurons
Cytosolic glycerol 3-phosphate dehydrogenase	Only active in astrocytes
Mitochondrial glycerol 3-phosphate dehydrogenase	The one in astrocytes is in reverse direction of the cytosolic reaction, thereby mimicking glycerol 3-phosphate shuttle active in astrocytes
Glutamine synthetase	Only active in astrocytes
Glutaminase	Only active in neurons
Glutamate decarboxylase	Only active in neurons
Serine biosynthesis	Only active in astrocytes
Serine dehydratase	Only active in astrocytes
Glycine cleavage system	Only active in astrocytes
Branched-chain amino acid catabolism (except branched-chain amino acid aminotransferase)	Only active in astrocytes
2-oxobutanoate dehydrogenase	Only active in astrocytes
Lysine catabolism	Only active in neurons
Histidine catabolism	Only active in neurons
Phenylalanine catabolism	Only active in neurons
Tryptophan catabolism	Only active in neurons
Asparagine synthetase	Only active in neurons
Tyrosine catabolism	Only active in neurons
Acetylcholine metabolism	Only active in neurons
Proline metabolism	Only active in astrocytes
Cholesterol synthesis	Only active in astrocytes
Arachidonate and Decosahexenoate synthesis	Only active in astrocytes
Glycogen degradation	Only active in astrocytes
Cystine reductase	Only active in astrocytes
Cysteinylglycine formation	Only active in astrocytes
Cysteinylglycine degradation	Only active in neurons
Ornithine aminotransferase	Only active in astrocytes
Citrulline synthesis from arginine	Only active in neurons
Arginine synthesis from aspartate	Only active in neurons

(continued)

Table 15.4 (continued)

Reaction/enzyme/pathway	Coupling/differentiation
GABA synthesis from putrescine	Only active in astrocytes
Putrescine production from ornithine and agmatine	Only active in neurons
Interconversion of putrescine, spermine, and spermidine	Only active in neurons

The degree of cell specificity covered by the model is presented. The related references for the presented choice can be found in (Çakır et al. 2007; Sertbaş et al. 2014)

as zero since these mechanisms are known to be inactive in resting state. Cerebral glucose uptake rate, $0.32 \mu\text{mole/g tissue/min}$, was used as the arithmetic average of five different values reported in the literature under resting-state conditions. It was equally shared between the two cell types as discussed in Sect. 15.2.2. Since cerebral oxygen uptake rate is reported to be around 5.5-folds higher than cerebral glucose uptake rate, it was set to $1.76 \mu\text{mole/g tissue/min}$. Oxygen was shared between the two cell types based on the reported thirty percent uptake by astrocytes. In addition, the respiratory quotient ($r_{\text{CO}_2}/r_{\text{O}_2}$) was constrained in the range of 0.91–1.00 for both cell types. The flux through pentose phosphate pathway for astrocytes and neurons was constrained to be lower than 6 and 5% of glucose consumption flux, respectively. Lastly, GABA cycle flux was constrained to be 25% of glutamate–glutamine cycle flux to enable proper coupling of GABA cycle with the overall network. The references for all these constraints including the ones presented in Table 15.6 are available in the previous publications (Çakır et al. 2007; Sertbaş et al. 2014). The genome-scale metabolic model of iMS570 can be downloaded from www.systemsbiology.info.tr in SBML format with all the mentioned constraints defined as lower- and upper-bound constraints, ready for the simulation of the healthy brain state.

The FBA problem was solved by using two consecutive objective functions as discussed in Sect. 15.3. The primary objective function, the maximization of the sum of glutamate–glutamine–GABA cycle fluxes between the two cell types, ensures a tight coupling between the two cell types. It is also in agreement with the fact that these three biomolecules constitute the most important trafficking between astrocytes and neurons. Use of other objective functions such as maximization/minimization of ATP, minimization of redox potential, maximization of malate shuttle in neurons did not result in literature-consistent fluxes (Çakır et al. 2007). After fixing the sum of these three cycle fluxes to the optimum calculated value, the second objective function of minimization of Euclidean norm of fluxes was employed which ensures efficient channeling of fluxes through all pathways. This is in line with the hypothesis that cells aim to fulfill their functions with minimal effort since increasing a flux through any reaction will require an extra investment such as increasing enzyme levels (Bonarius et al. 1996; Holzhütter 2004). Another benefit of the secondary optimization is to eliminate alternate optima discussed in Sect. 15.2.4. Among all possible alternate

Table 15.5 Coupling reactions defining metabolite transfer between the two cell types in iMS570

Crossing metabolite	Direction of transfer
Glutamate	N → A
Glutamine	A → N
GABA	N ↔ A
Aspartate	N ↔ A
Alanine	N ↔ A
Serine	A → N
Glycine	N → A
α-ketoisocaproate (KIC)	A → N
Leucine	N → A
α-keto-isovaleric acid (KIV)	A → N
Valine	N → A
α-keto-methylvalerate (KMV)	A → N
Isoleucine	N → A
Dopamine	N → A
Cholesterol	A → N
Arachidonate	A → N
Decosahexenoate	A → N
Cysteinylglycine	A → N
Arginine	A → N
Putrescine	N → A

The considered direction of the transfer is also shown

flux distributions satisfying the value of the primary objective function, the one with minimal norm is chosen thanks to the secondary optimization.

The major results of FBA simulation of iMS570 subject to the constraints and objective function criteria given above are presented in Table 15.7 in comparison to the literature-reported values. The predictions by FBA are consistent with the experimental major flux splits in central carbon metabolism. The simulations were repeated with a 60–40% split of glucose utilization flux between astrocytes and neurons since there were studies reporting a higher relative use of glucose compared to neurons (Véga et al. 2003). Results show robustness to the relative glucose uptake rates. The table also provides minimum and maximum attainable values of the flux ratios for the verification of the use of employed objective function. With the measurement constraints mentioned above, when the minimum and maximum values of each of these flux ratios are calculated by FBA, a wide range is calculated. This means that it is the power of the employed dual objective function which selects a solution consistent with physiological values among a wide range of solutions satisfying the FBA constraints.

In addition to the comparison provided in Table 15.7, a further inspection of the verification of the calculated flux distribution for central carbon metabolism can be performed. For example, the ratio of neuronal TCA cycle flux to the total TCA cycle flux is an important parameter to show the relative oxidative metabolism of the two

Table 15.6 Metabolite uptake rates, given below, were compiled from the literature and used as measurement constraints in iMS570 to calculate resting-state fluxes of human brain

Metabolite	Uptake rate ($\mu\text{mole/g tissue/min}$)
CMR ^A _{Glucose}	0.160
CMR ^N _{Glucose}	0.160
CMR ^A _{O₂}	0.530
CMR ^N _{O₂}	1.230
Cystine ^A	0.0045
Ammonia ^A	0.0035
Phenylalanine ^N	0.0132
Tryptophan ^N	0.0082
Leucine ^A	0.0145
Isoleucine ^A	0.0040
Tyrosine ^N	0.0041
Valine ^A	0.0018
Lysine ^N	0.0103
Histidine	0.0025
Methionine	0.0017
Threonine	0.0008
Arginine	0.0020
Ornithine	0.0031
3-hydroxybutyrate (BHB)	0
Acetoacetate	0
Glycogen	0

A astrocytes, N neurons, CMR cerebral metabolic rate

cell types. This is calculated as 0.34 based on the resting-state flux distribution by iMS570, in good agreement with the literature-reported value of 30% (Hertz et al. 2007). Astrocytes are reported to make a considerable contribution to the oxidative metabolism of brain under non-stimulated conditions. Another model-calculated flux is a flux of 0.30 $\mu\text{mole/g tissue/min}$ for malate–aspartate shuttle in neurons which transfer NADH from cytosol to mitochondria. This is in agreement with the findings that the shuttle is active in neurons (McKenna et al. 2006). Additionally, the flux through neuronal pyruvate dehydrogenase was 0.29 $\mu\text{mole/g tissue/min}$, in agreement with the report that the magnitude of this flux is similar to the shuttle flux (Gruetter et al. 2001). Besides, the model predicts a flux of 0.06 $\mu\text{mole/g tissue/min}$ for malic enzyme in astrocytes, whereas the flux through the neuronal counterpart is estimated to be zero. This is supported by the finding that malic enzyme is only astrocytic in physiological conditions (Lebon et al. 2002).

Table 15.7 Predicted flux results with iMS570, in comparison to the experimental results in resting (healthy) state

% Flux ratio	Minimum	Maximum	FBA results	Experimental results
% Lactate release flux (r_{11}) with respect to CMR_{glc}	0	21	7.2 (7.7)	3–9
% Glutamate/glutamine cycle flux (r_{95}) with respect to CMR_{glc}	0	73.6	73.1 (61.1)	40–80
% relative oxidative metabolism of astrocytes ($r_{TCA,A}/r_{TCA,\text{total}}, r_{25}/(r_{25} + r_{69})$)	8.9	100	33.9 (34.4)	30
% Total lipid synthesis with respect to CMR_{glc}	0.03	4.6	3.1 (3.1)	2
% Total pentose phosphate pathway flux with respect to CMR_{glc}	0	5.5	5.5 (5.5)	3–6
% pyruvate carboxylase flux (r_{12}) with respect to CMR_{glc}	1.1	>1000	11.1 (9.7)	10

For the references of the literature values, the original article can be referred (Sertbaş et al. 2014). The values in parenthesis in the FBA results column are based on a 60–40% partitioning of glucose utilization between astrocytes and neurons rather than an equal utilization. The minimum and maximum possible values of the ratios are also calculated by introducing only the measurement constraints without an objective function. CMR_{glc} cerebral metabolic rate of glucose

15.4.3 Flux-Based Analysis of Hypoxia

Cerebral hypoxia is the state of oxygen deprivation in brain due to disorders such as epilepsy and asthma. Hypoxia is known to increase the risk of dementia (Desmond et al. 2002). FBA-based analysis of hypoxia in the brain in terms of its effect to major metabolic routes was performed before by using a metabolic network model with about 200 reactions (Çakır et al. 2007). Now, I repeat the analysis by using iMS570.

In simulations of hypoxia, a different constraint-based modeling approach was used that is called minimization of metabolic adjustment (MOMA) (Segre et al. 2002). MOMA uses the flux distribution of the healthy state as a reference and aims to calculate a flux distribution which is as close as possible to the reference state in terms of Euclidean distance. The choice of Euclidean distance minimization as the objective function in MOMA is based on literature findings reporting that deficient cells exhibit a flux profile closest to the non-deficient state (Segre et al. 2002; Holzhütter 2006). Since the objective function includes quadratic terms, quadratic programming is employed in the solution. In MOMA simulations, all of the measurement constraints were removed from the model since these constraints may not be valid during the course of hypoxia. This enables the capturing of hypoxia-dependent increases or decreases in the uptake rates. The constraint on glycogen uptake rate was also removed since it is known that glycogen metabolism is important in hypoxia (Gruetter 2003).

Figure 15.7 presents the change of major metabolic fluxes from the healthy state to the state of anoxia where no oxygen is present. In the MOMA simulations, cerebral oxygen uptake rate was decreased from the resting-state value to a value of zero with small intervals, and for each interval, a MOMA was performed to calculate flux distributions. Results show that major indicators of hypoxic state are captured by the *in silico* analysis. For example, a decrease in the ATP flux produced by the oxidative phosphorylation is observed both in astrocytes and neurons. As the oxygen availability is reduced, ATP production in the oxidative phosphorylation step will also get reduced. This in turn will decrease NADH demand by TCA cycle in both cell types as the simulation results show. Therefore, pyruvate produced in the glycolysis step will divert to lactate production rather than being supplied to the TCA cycle, leading to increased lactate production as hypoxia gets more severe. A different trend in the lactate production of neurons and astrocytes is observed. Since neurons consumed 70% of available oxygen at resting state, the same percent decrease in oxygen consumption makes a lighter effect on neurons in terms of switching to anaerobic metabolism phenotypes such as lactate production. As the anoxic state is approached, a sharp decrease in malate–aspartate shuttle is predicted. The inhibition of the neuron-localized shuttle is known to reduce neuronal oxidative metabolism (Cheeseman and Clark 1988) by reducing the transfer of cytosolic NADH to mitochondria. All these *in silico* results were also obtained by using the model by (Çakır et al. 2007), as reported in the relevant publication. However there were two contradictory simulation results, respectively regarding the dynamics of glutamate flux from neurons to astrocytes and neuronal glucose uptake: iMS570 simulates an increase in the transfer flux while the previous simulations report an impairment. Indeed, lower metabolic trafficking between astrocytes and neurons was reported to be supported by the calculated flux profiles of metabolites other than glutamate: GABA, aspartate, and leucine transfer fluxes all decrease with decreasing cerebral oxygen uptake (Chateil et al. 2001; Benarroch 2005). A sharp increase in neuronal glucose uptake was predicted previously while the current simulations by iMS570 give relatively unchanged neuronal uptake flux. However, increased glyco-

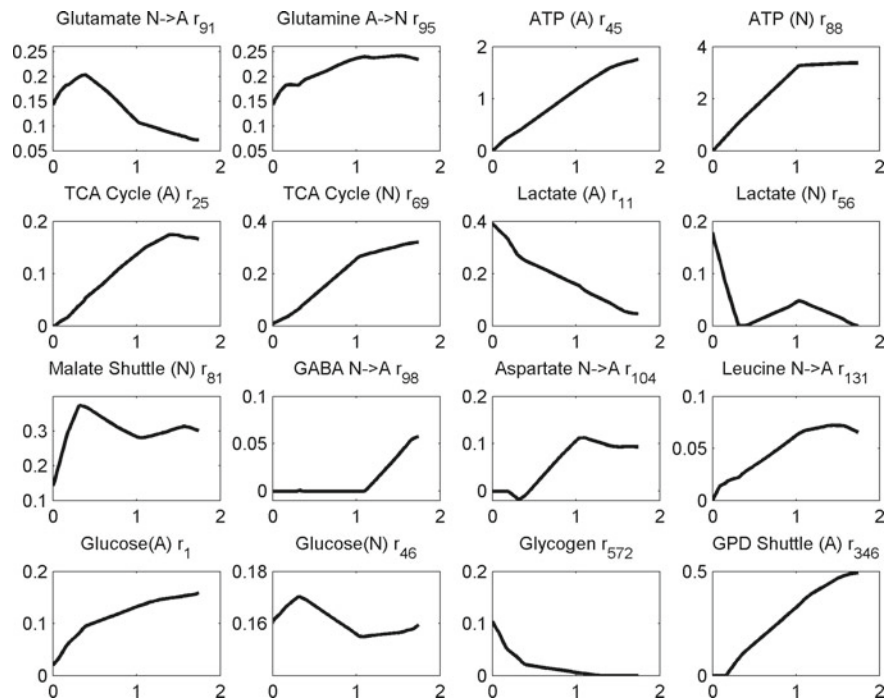


Fig. 15.7 FBA-based analysis of cerebral hypoxia calculated by an FBA-derivative approach: MOMA. The x axis represents CMRO₂ available to brain cells. The change in the fluxes from the basal level ($1.76 \mu\text{mole/g tissue/min}$) to anoxic level with no oxygen uptake is presented

gen breakdown rate towards anoxia is a known phenomenon (Gruetter 2003), which is supported by the simulations (Fig. 15.7).

15.4.4 Transcriptomics Comes into the Picture: Gene Expression as a Constraint for Condition-Specific Metabolic Models

One way to construct condition-specific metabolic models is to use measurement constraints specific to the condition of interest. However, relevant constraints such as uptake rates of metabolites or split ratios in metabolic branch points may not be available in a way that a flux phenotype specific for the condition is calculated. On the other hand, transcriptome, proteome, or metabolome data are increasingly collected for a wide range of neurological disorders and stored in the public databases such as the Gene Expression Omnibus (Edgar et al. 2002). Based on this, new computational methods have emerged which use omics data as an additional constraint to reference-

state metabolic networks to derive an active network for the condition of interest such as diseases or drug treatments.

For the use of transcriptome or proteome data to derive condition-specific metabolic network models, the gene-reaction association information in the genome-scale metabolic networks is utilized. A low gene expression level can imply inactivity of the corresponding reaction. Therefore, the constraint-based modeling can be performed by constraining such reactions to zero. However, due to the post-transcriptional regulation, a perfect agreement between the gene expression and flux states is not expected. Blocking of a reaction based on a low level of the corresponding mRNA may block the paths to the objective function, impairing essential cellular functions implying an upregulation of the corresponding gene. Therefore, the related computational methods employ optimization approaches in such a way that agreement between gene expression data and flux states is not forced to a perfect match but it is maximized. This is a hot topic, and several alternative methods have recently appeared, among which GIMME (Becker and Palsson 2008), iMAT (Shlomi et al. 2008) and MADE (Jensen and Papin 2011) being the most popular ones. A systematic evaluation of seven such methods for the prediction of flux distributions of *S. cerevisiae* and *E. coli* did not reveal a best performer (Machado and Herrgård 2014), indicating that there still is room to improve such approaches. A transcriptomic-constrained genome-scale metabolic model of brain was recently developed based on iMAT approach and used to predict biomarkers and drug targets for Alzheimer's Disease (Stempler et al. 2014). However, the model does not include neuron–astrocyte compartmentation. A recent work integrated the iMS570 metabolic network with glioblastoma transcriptome data by using GIMME and MADE approaches (Özcan and Çakır 2016). The calculated flux distributions using the generated tumor-specific genome-scale metabolic networks could successfully predict flux-level metabolic reprogramming in glioblastoma. Not only transcriptome, but also other omics data such as proteome and metabolome can be used as additional constraints to metabolic networks to identify the active network (Çakır and Khatibipour 2014). The metabolome-based approaches use metabolite concentrations for the calculation of Gibbs energy changes of reactions to predict reaction directions (Hoppe et al. 2007; Soh and Hatzimanikatis 2010; Hamilton et al. 2013). Predicting the condition-specific directions of reversible directions aids in further constraining the solution space to get a flux distribution better representing the studied condition.

The use of omics data as a constraint for brain genome-scale models is just at its infancy. Considering huge amount of such data collected for brain tissues, it is expected that the next decade will witness a sharp increase in the integrated constraint-based analysis of neuron–astrocyte metabolic models with transcriptome, proteome, and metabolome data.

15.5 Final Remarks

Constraint-based modeling of brain metabolism provides significant contribution for the investigation of different physiological conditions such as high or low neural activity or phenomena including hypoxia, hyperglycemia. Considering the crucial role constraint-based modeling plays for the elucidation of molecular mechanisms underlying metabolism (Jerby et al. 2010; Mardinoglu et al. 2014), this chapter aims at elucidating fundaments and advantages of this modeling approach in the context of computational neuroscience, focusing on flux balance analysis in neuron–astrocyte metabolic interactions. With this regard, I analyzed a sample simplified network mimicking neuron–astrocyte coupling, as well as a recently reconstructed genome-scale metabolic model. I further reviewed studies which modeled brain metabolism stoichiometrically through the consideration metabolic interactions in and between astrocytes and neurons. The incorporation of transcriptome data further increases the power of constraint-based approach since this enables the modeling of the effect of several neurological disorders for a number of issues from identifying biomarkers to computing potential drug targets. As more refined high-throughput data are obtained from the neuron–glia metabolic coupling system, the computational processing of this data to extract information will produce more useful hints on the elucidation of molecular mechanisms.

Acknowledgements This work was supported by TUBITAK, The Scientific and Technological Research Council of Turkey, through a career grant (Project Code: 110M464), by Gebze Technical University Research Project (Project Code: BAP 2011-A-27), and by The Turkish Academy of Sciences—Outstanding Young Scientists Award Program (TUBA-GEBIP).

Conflict of Interest The author declares no conflict of interest.

References

- Amaral A, Alves P, Teixeira A (2014) Metabolic flux analysis tools to investigate brain metabolism *in vitro* 90
- Amaral AI, Teixeira AP, Håkonsen BI et al (2011) A comprehensive metabolic profile of cultured astrocytes using isotopic transient metabolic flux analysis and ^{13}C -labeled glucose
- Becker SA, Palsson BO (2008) Context-specific metabolic networks are consistent with experiments. *PLoS Comput Biol* 4:e1000082
- Bélanger M, Allaman I, Magistretti PJ (2011) Brain energy metabolism: focus on astrocyte-neuron metabolic cooperation. *Cell Metab* 14:724–738
- Benarroch EE (2005) Neuron-astrocyte interactions: partnership for normal function and disease in the central nervous system. In: Mayo clinic proceedings. Elsevier, Amsterdam, pp 1326–1338
- Bonarius HP, Hatzimanikatis V, Meesters KP et al (1996) Metabolic flux analysis of hybridoma cells in different culture media using mass balances. *Biotechnol Bioeng* 50:299–318. [https://doi.org/10.1002/\(SICI\)1097-0290\(19960505\)50:3%3c299.AID-BIT9%3e3.0.CO;2-B](https://doi.org/10.1002/(SICI)1097-0290(19960505)50:3%3c299.AID-BIT9%3e3.0.CO;2-B)
- Cakir T, Khatibipour MJ (2014) Metabolic network discovery by top-down and bottom-up approaches and paths for reconciliation. *Front Bioeng Biotechnol* 2:62

- Çakır T, Alsan S, Saybaşılı H et al (2007) Reconstruction and flux analysis of coupling between metabolic pathways of astrocytes and neurons: application to cerebral hypoxia. *Theor Biol Med Model* 4:48
- Calvetti D, Somersalo E (2012) Ménage à trois: the role of neurotransmitters in the energy metabolism of astrocytes, glutamatergic, and GABAergic neurons. *J Cereb Blood Flow Metab* 32:1472–1483
- Chateil J-F, Biran M, Thiaudière E et al (2001) Metabolism of [1-13C] glucose and [2-13C] acetate in the hypoxic rat brain. *Neurochem Int* 38:399–407
- Chatziloannou A, Palaiologos G, Kolisis FN (2003) Metabolic flux analysis as a tool for the elucidation of the metabolism of neurotransmitter glutamate. *Metab Eng* 5:201–210
- Cheeseman AJ, Clark JB (1988) Influence of the malate-aspartate shuttle on oxidative metabolism in synaptosomes. *J Neurochem* 50:1559–1565
- Desmond DW, Moroney JT, Sano M, Stern Y (2002) Incidence of dementia after ischemic stroke results of a longitudinal study. *Stroke* 33:2254–2262
- Dienel GA, Cruz NF (2003) Neighborly interactions of metabolically-activated astrocytes in vivo. *Neurochem Int* 43:339–354
- Duarte JMN, Girault F-M, Gruetter R (2015) Brain energy metabolism measured by (13)C magnetic resonance spectroscopy in vivo upon infusion of [3-(13)C]lactate. *J Neurosci Res* 93:1009–1018. <https://doi.org/10.1002/jnr.23531>
- Duarte NC, Becker SA, Jamshidi N et al (2007) Global reconstruction of the human metabolic network based on genomic and bibliomic data. *Proc Natl Acad Sci* 104:1777–1782
- Edgar R, Domrachev M, Lash AE (2002) Gene Expression Omnibus: NCBI gene expression and hybridization array data repository. *Nucleic Acids Res* 30:207–210. <https://doi.org/10.1093/nar/30.1.207>
- Feist AM, Henry CS, Reed JL et al (2007) A genome-scale metabolic reconstruction for Escherichia coli K-12 MG1655 that accounts for 1260 ORFs and thermodynamic information. *Mol Syst Biol*. <https://doi.org/10.1038/msb4100155>
- Fell DA, Small JR (1986) Fat synthesis in adipose tissue. An examination of stoichiometric constraints. *Biochem J* 238:781–786
- Förster J, Famili I, Fu P et al (2003) Genome-scale reconstruction of the *Saccharomyces cerevisiae* metabolic network. *Genome Res* 13:244–253
- Gavai AK, Supandi F, Hettling H et al (2015) Using bioconductor package BiGGR for metabolic flux estimation based on gene expression changes in brain. *PLoS ONE* 10:e0119016
- Gjedde A, Marrett S, Vafaee M (2002) Oxidative and nonoxidative metabolism of excited neurons and astrocytes. *J Cereb Blood Flow Metab* 22:1–14
- Gruetter R (2003) Glycogen: the forgotten cerebral energy store. *J Neurosci Res* 74:179–183
- Gruetter R, Seaquist ER, Ugurbil K (2001) A mathematical model of compartmentalized neurotransmitter metabolism in the human brain. *Am J Physiol-Endocrinol Metab* 281:100
- Hamilton JJ, Dwivedi V, Reed JL (2013) Quantitative assessment of thermodynamic constraints on the solution space of genome-scale metabolic models. *Biophys J* 105:512–522. <https://doi.org/10.1016/j.bpj.2013.06.011>
- Heino J, Calvetti D, Somersalo E (2010) Metabolica: a statistical research tool for analyzing metabolic networks. *Comput Methods Programs Biomed* 97:151–167
- Hertz L, Peng L, Dienel GA (2007) Energy metabolism in astrocytes: high rate of oxidative metabolism and spatiotemporal dependence on glycolysis/glycogenolysis. *J Cereb Blood Flow Metab: J Int Soc Cereb Blood Flow Metab* 27:219–249. <https://doi.org/10.1038/sj.jcbfm.9600343>
- Hertz L, Zielke HR (2004) Astrocytic control of glutamatergic activity: astrocytes as stars of the show. *Trends Neurosci* 27:735–743. <https://doi.org/10.1016/j.tins.2004.10.008>
- Holzhütter H-G (2004) The principle of flux minimization and its application to estimate stationary fluxes in metabolic networks. *Eur J Biochem/FEBS* 271:2905–2922. <https://doi.org/10.1111/j.1432-1033.2004.04213.x>
- Holzhütter H-G (2006) The generalized flux-minimization method and its application to metabolic networks affected by enzyme deficiencies. *Biosystems* 83:98–107

- Hoppe A, Hoffmann S, Holzhütter H-G (2007) Including metabolite concentrations into flux balance analysis: thermodynamic realizability as a constraint on flux distributions in metabolic networks. *BMC Syst Biol* 1:23. <https://doi.org/10.1186/1752-0509-1-23>
- Jensen PA, Papin JA (2011) Functional integration of a metabolic network model and expression data without arbitrary thresholding. *Bioinformatics* 27:541–547
- Jerby L, Shlomi T, Ruppin E (2010) Computational reconstruction of tissue-specific metabolic models: application to human liver metabolism. *Molecular systems biology* 6:401. <https://doi.org/10.1038/msb.2010.56>
- Lebon V, Petersen KF, Cline GW et al (2002) Astroglial contribution to brain energy metabolism in humans revealed by ¹³C nuclear magnetic resonance spectroscopy: elucidation of the dominant pathway for neurotransmitter glutamate repletion and measurement of astrocytic oxidative metabolism. *J Neurosci* 22:1523–1531
- Lee S, Phalakornkule C, Domach MM, Grossmann IE (2000) Recursive MILP model for finding all the alternate optima in LP models for metabolic networks. *Comput Chem Eng* 24:711–716. [https://doi.org/10.1016/s0098-1354\(00\)00323-9](https://doi.org/10.1016/s0098-1354(00)00323-9)
- Lewis NE, Nagarajan H, Palsson BO (2012) Constraining the metabolic genotype-phenotype relationship using a phylogeny of in silico methods. *Nat Rev Microbiol* 10:291–305. <https://doi.org/10.1038/nrmicro2737>
- Lewis NE, Schramm G, Bordbar A et al (2010) Large-scale in silico modeling of metabolic interactions between cell types in the human brain. *Nat Biotechnol* 28:1279–1285
- Machado D, Herrgård M (2014) Systematic evaluation of methods for integration of transcriptomic data into constraint-based models of metabolism. *PLoS Comput Biol* 10:e1003580. <https://doi.org/10.1371/journal.pcbi.1003580>
- Mahadevan R, Schilling CH (2003) The effects of alternate optimal solutions in constraint-based genome-scale metabolic models. *Metab Eng* 5:264–276
- Mardinoglu A, Agren R, Kampf C et al (2014) Genome-scale metabolic modelling of hepatocytes reveals serine deficiency in patients with non-alcoholic fatty liver disease. *Nat Commun* 5:3083. <https://doi.org/10.1038/ncomms4083>
- Massucci FA, DiNuzzo M, Giove F et al (2013) Energy metabolism and glutamate-glutamine cycle in the brain: a stoichiometric modeling perspective. *BMC Syst Biol* 7:103
- McKenna MC, Waagepetersen HS, Schousboe A, Sonnewald U (2006) Neuronal and astrocytic shuttle mechanisms for cytosolic-mitochondrial transfer of reducing equivalents: current evidence and pharmacological tools. *Biochem Pharmacol* 71:399–407
- Nehlig A, Wittendorp-Rechenmann E, Lam CD (2004) Selective uptake of [14C]2-deoxyglucose by neurons and astrocytes: high-resolution microautoradiographic imaging by cellular 14C-trajectography combined with immunohistochemistry. *J Cereb Blood Flow Metab* 24:1004–1014. <https://doi.org/10.1097/01.WCB.0000128533.84196.D8>
- Occhipinti R, Puchowicz MA, LaManna JC et al (2007) Statistical analysis of metabolic pathways of brain metabolism at steady state. *Ann Biomed Eng* 35:886–902
- Occhipinti R, Somersalo E, Calvetti D (2009) Astrocytes as the glucose shunt for glutamatergic neurons at high activity: an in silico study. *J Neurophysiol* 101:2528–2538
- Occhipinti R, Somersalo E, Calvetti D (2010) Energetics of inhibition: insights with a computational model of the human GABAergic neuron–astrocyte cellular complex. *J Cereb Blood Flow Metab* 30:1834–1846
- Orth JD, Thiele I, Palsson BØ (2010) What is flux balance analysis? *Nat Biotechnol* 28:245–248
- Özcan E, Çakir T (2016) Reconstructed metabolic network models predict flux-level metabolic reprogramming in glioblastoma. *Front Neurosci* 10:156. <https://doi.org/10.3389/fnins.2016.00156>
- Pellerin L, Bouzier-Sore A-K, Aubert A et al (2007) Activity-dependent regulation of energy metabolism by astrocytes: an update. *Glia* 55:1251–1262. <https://doi.org/10.1002/glia.20528>
- Ramakrishna R, Edwards JS, McCulloch A, Palsson BO (2001) Flux-balance analysis of mitochondrial energy metabolism: consequences of systemic stoichiometric constraints. *Am J Physiol Regul Integr Comp Physiol* 280:R695–R704

- Reed JL, Vo TD, Schilling CH, Palsson BO (2003) An expanded genome-scale model of *Escherichia coli* K-12 (iJR904 GSM/GPR). *Genome Biol* 4:54
- Rocha I, Maia P, Evangelista P et al (2010) OptFlux: an open-source software platform for in silico metabolic engineering. *BMC Syst Biol* 4:45
- Savinell JM, Palsson BO (1992) Network analysis of intermediary metabolism using linear optimization. I. Development of mathematical formalism. *J Theor Biol* 154:421–454
- Schellenberger J, Que R, Fleming RM et al (2011) Quantitative prediction of cellular metabolism with constraint-based models: the COBRA Toolbox v2. 0. *Nat Protoc* 6:1290–1307
- Schousboe A, Sickmann HM, Bak LK et al (2011) Neuron–glia interactions in glutamatergic neurotransmission: roles of oxidative and glycolytic adenosine triphosphate as energy source. *J Neurosci Res* 89:1926–1934
- Schousboe A, Westergaard N, Sonnewald U et al (1993) Glutamate and glutamine metabolism and compartmentation in astrocytes. *Dev Neurosci* 15:359–366
- Segre D, Vitkup D, Church GM (2002) Analysis of optimality in natural and perturbed metabolic networks. *Proc Natl Acad Sci* 99:15112–15117
- Sertbaş M, Ulgen K, Cakir T (2014) Systematic analysis of transcription-level effects of neurodegenerative diseases on human brain metabolism by a newly reconstructed brain-specific metabolic network. *FEBS Open Bio* 4:542–553. <https://doi.org/10.1016/j.fob.2014.05.006>
- Shen J, Petersen KF, Behar KL et al (1999) Determination of the rate of the glutamate/glutamine cycle in the human brain by *in vivo* ¹³C NMR. *Proc Natl Acad Sci USA* 96:8235–8240
- Shlomi T, Cabili MN, Herrgård MJ et al (2008) Network-based prediction of human tissue-specific metabolism. *Nat Biotechnol* 26:1003–1010
- Soh KC, Hatzimanikatis V (2010) Network thermodynamics in the post-genomic era. *Curr Opin Microbiol* 13:350–357. <https://doi.org/10.1016/j.mib.2010.03.001>
- Stempler S, Yizhak K, Ruppin E (2014) Integrating transcriptomics with metabolic modeling predicts biomarkers and drug targets for Alzheimer's Disease
- van Gulik WM, Heijnen JJ (1995) A metabolic network stoichiometry analysis of microbial growth and product formation. *Biotechnol Bioeng* 48:681–698. <https://doi.org/10.1002/bit.260480617>
- Varma A, Palsson BO (1993) Metabolic capabilities of *Escherichia coli*: I. Synthesis of biosynthetic precursors and cofactors. *J Theor Biol* 165:477–502
- Véga C, Martiel J, Drouhault D et al (2003) Uptake of locally applied deoxyglucose, glucose and lactate by axons and Schwann cells of rat vagus nerve. *J Physiol* 546:551–564

Part V

**Computational Tools to Analyze and
Model Astrocyte Experiments**

Chapter 16

Computational Models of Astrocytes and Astrocyte–Neuron Interactions: Characterization, Reproducibility, and Future Perspectives



Tiina Manninen, Riikka Havela and Marja-Leena Linne

Abstract Astrocytes have been shown to participate in a variety of brain functions. These include homeostasis, metabolism, neuronal survival in pathological circumstances, and neurovascular coupling. Since astrocytes extend their processes into close proximity to synapses, it has also been proposed that they take active roles in synaptic transmission, learning, and memory. The complexity of dynamic interactions on both molecular and cellular levels of neurons and astrocytes is overwhelming. This underlines the demand for detailed, integrative computational models for advancing our understanding of the functional contribution of astrocytes in the nervous system. This study presents the state of the art in computational models for astrocytes and astrocyte–neuron interactions. First, we characterized the models based on the type of biological entities they described. We then studied several aspects of the models in detail, including reproducibility. We discovered that several publications lack crucial details in how the models were presented, preventing successful reproduction of the results. Graphical illustrations of these models were misleading, mathematical equations incorrect, or selected model components not adequately justified. Moreover, in some cases, it was impossible, after several trials, to reproduce the simulated results presented in the original publications. In order to facilitate reproducible science, we propose some criteria that computational glioscience models should meet. To the best of our knowledge, this study is one of the first to report the detailed categorization and evaluation of astrocyte–neuron models.

Keywords Astrocyte · Astrocyte network · Astrocyte–neuron interaction
Calcium · Computational model · Reproducibility · Simulation

T. Manninen · R. Havela · M.-L. Linne (✉)
Computational Neuroscience Group, Faculty of Biomedical Sciences and Engineering, BioMediTech Institute,
Tampere University of Technology, P.O. Box 553, 33101 Tampere, Finland
e-mail: marja-leena.linne@tut.fi

16.1 Introduction

Extensive biological research over the past 25 years has established that astrocytes actively sense their molecular microenvironment. Astrocytes react to molecules released by neurons and other cells in the brain (Pellerin and Magistretti 1994). They also release neuroactive substances that can potentially modulate the activity of neurons (Parpura et al. 1994). Astrocytes are therefore well positioned to be important homeostatic players in the brain, long known, e.g., for their task of buffering potassium ions (K^+) during intensive firing of neurons. Astrocytes have been shown to take part in a variety of brain functions in addition to homeostasis, e.g., metabolism, neuronal survival in pathological circumstances, and neurovascular coupling. Since astrocytes extend their processes into close proximity to synapses, it has also been proposed that they take a more active role in synaptic transmission—possibly even in learning and memory—than previously thought. Currently, putative roles of astrocytes in higher intrinsic and sensory processing are intensively studied, but the results have been contradictory, at least partly (for further discussion, see, e.g., recent reviews, Agulhon et al. 2012; Min et al. 2012; Linne and Jalonen 2014; Volterra et al. 2014; Magistretti and Allaman 2015; De Pittà et al. 2016).

Although astrocytes do not integrate ionic currents in a way leading to membrane depolarization and hyperpolarization as an action potential waveform, they do use calcium ions (Ca^{2+}) and related signaling pathways to integrate molecular information. Changes in Ca^{2+} concentration have been shown to provide an important intra- and intercellular signaling mechanism for astrocytes. Different types of Ca^{2+} imaging techniques, combined with electrophysiology, have led to the discoveries that astrocytes respond to and modulate synaptic activity *in vitro* (see, e.g., Perea and Araque 2007; Navarrete and Araque 2010; Panatier et al. 2011) and respond to sensory stimulation *in vivo* (see, e.g., Navarrete et al. 2012) by increasing their intracellular Ca^{2+} concentrations. Most recent studies indicate an enormous complexity of astrocytic Ca^{2+} signaling and dynamics as well as compartmentalization of these events (see, e.g., Wang et al. 2006; Shigetomi et al. 2010). This complexity (and compartmentalization) may partly explain the discrepancies observed between *in vitro* and *in vivo* experiments.

The field of computational neuroscience has almost solely been concentrated on modeling the role of neuronal components in a variety of cellular-, network-, and system-level phenomena. The role of astrocytes beyond their role in homeostatic and metabolic control has been much less addressed. Instead of action potential excitability, astrocytes express Ca^{2+} -based excitability which has been shown to be associated in modulation of neuronal signaling. The exclusion of astrocytes cannot therefore be justified, specifically as they possess complex molecular- and cellular-level interactions with neurons. Computational models based on wet-laboratory data provide a systematic way to integrate information and produce a deeper understanding of the studied system. These models can be used to reveal complex interactions and emergent dynamics. Models of dendritic signaling are examples of how this type of work has expanded our understanding of the complexity of neuronal signal processing.

Computational glioscience is a newly emerging subfield of neuroscience in which the structure and function of astrocytes as well as the astrocytic regulation of local and global brain activities are studied by computational means. Despite the short history of computational glioscience, several important theoretical and computational models have already been developed (for a review, see, e.g., Jolivet et al. 2010; Fellin et al. 2012; Volman et al. 2012; Linne and Jalonen 2014; De Pittà et al. 2016; Manninen et al. 2018b). Many of these models reflect the emphasis on experimental work: astrocytic Ca^{2+} signaling is perhaps one of the most described mechanisms in these models. Some of the first computational models that steered the field are the models by Höfer et al. (2002), Nadkarni and Jung (2004), and Volman et al. (2007). A variety of models have been published since these early times. These include models by Silchenko and Tass (2008), De Pittà et al. (2009b), Postnov et al. (2009), and Lallouette et al. (2014). Recently, models that incorporate a variety of metabolic, biochemical, and electrical interactions have been designed (see, e.g., Tewari and Majumdar 2012a, b).

This study presents an overview of computational models for astrocytic functions and astrocyte–neuron signaling. We first analyze the existing models and evaluate them using defined criteria. We then characterize the existing models based on what kind of biological processes has been taken into account. Moreover, we evaluate some of the models in more detail by implementing the equations of the original publications and running the constructed simulation models using MATLAB® (see also Manninen et al. 2017, 2018a). We show how well we are able to reproduce the simulation results of the original publications. Our work is expected to guide future computational glioscience studies and help researchers in selecting suitable models for their research questions. We additionally wish to set some criteria for a successful, reproducible model in the computational neuroscience, including computational glioscience.

16.2 Materials and Methods

Many computational models have been developed to better understand the functions of astrocytes and the specific roles astrocytes may have in neuronal events. In recent years, several publications have provided focused reviews of computational astrocyte and astrocyte–neuron interaction models (see, e.g., Jolivet et al. 2010; De Pittà et al. 2012, 2016; Fellin et al. 2012; Min et al. 2012; Volman et al. 2012; Wade et al. 2013; Linne and Jalonen 2014; Tewari and Parpura 2014; Manninen et al. 2018b). However, a comprehensive review analyzing the characteristics of all the model components, including also neuronal components, is lacking.

16.2.1 Selected Models

In this study, an analysis of 61 astrocyte models published through the year 2014 is presented (see Table 16.1). In addition, a few models have already been published since 2015 (see, e.g., Komin et al. 2015; Naeem et al. 2015; Nazari et al. 2015a, b, c; Soleimani et al. 2015; Yang and Yeo 2015; Amiri et al. 2016; De Pittà and Brunel 2016; Haghiri et al. 2016, 2017; Hayati et al. 2016; Li et al. 2016a, b, c; Liu et al. 2016; Oku et al. 2016; Tang et al. 2016). We limited the present analysis to models of astrocytic signal transduction pathways. Due to the large number of models, we used the following strict criteria to select the models. First, in addition to the astrocyte component, the models could also include pre- and postsynaptic neuron components and other cellular components. Second, models were required to describe biophysically astrocytic Ca^{2+} dynamics with a differential equation that was a function of time and at least one of the other model variables, e.g. inositol trisphosphate (IP_3). Third, astrocytic Ca^{2+} was required to have an effect on signaling variables or intra-

Table 16.1 List of astrocyte and astrocyte–neuron models published each year. Models are ordered alphabetically for each year of publication. Altogether 61 models have been published between the years 1995 and 2014. For chosen criteria, see Sect. 16.2.1

Year	Models	No.
1995	Roth et al. (1995)	1
2002	Höfer et al. (2002)	1
2003	Nadkarni and Jung (2003)	1
2004	Goto et al. (2004), Nadkarni and Jung (2004)	2
2005	Bellinger (2005), Bennett et al. (2005), Nadkarni and Jung (2005)	3
2006	Bennett et al. (2006), Iacobas et al. (2006), Stamatakis and Mantzaris (2006), Ullah et al. (2006)	4
2007	Di Garbo et al. (2007), Nadkarni and Jung (2007), Postnov et al. (2007), Volman et al. (2007)	4
2008	Bennett et al. (2008a, b), Lavrentovich and Hemkin (2008), Nadkarni et al. (2008), Silchenko and Tass (2008)	5
2009	Allegrini et al. (2009), De Pittà et al. (2009a, b), Di Garbo (2009), Kang and Othmer (2009), Kazantsev (2009), Postnov et al. (2009), Zeng et al. (2009)	8
2010	Edwards and Gibson (2010), Goldberg et al. (2010), Skupin et al. (2010)	3
2011	Amiri et al. (2011a, b), DiNuzzo et al. (2011), Dupont et al. (2011), Matrosov and Kazantsev (2011), Riera et al. (2011a, b), Toivari et al. (2011), Valenza et al. (2011), Wade et al. (2011), Wei and Shuai (2011)	11
2012	Amiri et al. (2012a, b, c), Chander and Chakravarthy (2012), Li et al. (2012), Tewari and Majumdar (2012a, b), Wade et al. (2012)	8
2013	Amiri et al. (2013a, b), Diekman et al. (2013), Liu and Li (2013), MacDonald and Silva (2013), Tang et al. (2013), Tewari and Parpura (2013)	7
2014	Lallouette et al. (2014), López-Caamal et al. (2014), Wallach et al. (2014)	3
All		61

cellular signals in astrocytes. Models which were not specified to be explicitly made for astrocytes were left out from this study. As an example, we listed the models that were not detailed enough to meet our criteria or were made for different glial cell type (see, e.g., Jung et al. 1998; Dronne et al. 2006; Aubert et al. 2007; Bennett et al. 2008c; MacDonald et al. 2008; Postnov et al. 2008; Somjen et al. 2008; Occhipinti et al. 2009, 2010; Ullah et al. 2009; De Pittà et al. 2011; Porto-Pazos et al. 2011; Allam et al. 2012; Gordleeva et al. 2012; Øyehaug et al. 2012; Reato et al. 2012; Halnes et al. 2013; Volman et al. 2013; Barrack et al. 2014, 2015; Nazari et al. 2014; Calvetti et al. 2015; Jha and Jha 2015; Jolivet et al. 2015; Kuriu et al. 2015; Piri et al. 2015; Ranjbar and Amiri 2015, 2016). For example, the model by Jolivet et al. (2015) did not meet our criteria because they did not model Ca^{2+} dynamics in the astrocyte.

16.2.2 Characteristics of Models

To assess the applicability of the published models, we analyzed their characteristics (see Sect. 16.3). The number of different types of cells modeled is given for astrocytes and pre- and postsynaptic neurons, as applicable for each model. Authors did not always state clearly how many cells of different types were modeled. If the astrocyte–neuron models excluded pre- or postsynaptic neurons, we marked none under that category. We also categorized the models based on what type of signaling events was modeled by marking either yes (Y), no (N), or simple (S). Pre- and postsynaptic signaling events include neurotransmitter signaling, membrane potential, Ca^{2+} signaling, endoplasmic reticulum (ER), second messenger signaling, and paracrine signaling. Astrocyte signaling events include neurotransmitter signaling, ER, second messenger signaling, paracrine signaling, and gap junction signaling. Note that all astrocyte and astrocyte–neuron models in this study included astrocytic Ca^{2+} signaling. Furthermore, if paracrine signaling was modeled, we marked it for both the releasing and receiving cells.

Neurotransmitter signaling. Neurotransmission occurs between pre- and postsynaptic neuron terminals. The most commonly modeled neurotransmitter is glutamate, but several others are known to exist. We considered that the neurotransmitter signaling was modeled in the studied publications if the amount of neurotransmitter (e.g., glutamate) was described by a differential equation or other type of equation that was a function of time and at least one of the other model variables. If the amount of neurotransmitter was just a constant or a function of time and itself (e.g., the synapse was not modeled, and the neurotransmitter was only used as a stimulus for the astrocyte), we marked it as a simple function (S). We also marked it by ‘S’ if the actual amount of neurotransmitter was not modeled but the phenomenon itself was, e.g., by increasing the astrocytic IP_3 concentration based on neuronal membrane potential.

Neuronal electrophysiology. The electrophysiology of pre- or postsynaptic membrane terminal (i.e., membrane potential) was considered to be modeled in the studied

publications if it was described by a differential equation that was a function of time and at least one of the other model variables.

Intracellular signaling. Various signaling pathways and intracellular second messengers are known to affect intracellular Ca^{2+} signaling. Here, we considered three types of intracellular signaling: Ca^{2+} signaling, ER as a Ca^{2+} source, and second messenger signaling. We considered that Ca^{2+} signaling in the pre- and postsynaptic neurons was modeled if it was described by a differential equation or other type of equation that was a function of time and at least one of the other model variables. Note that Ca^{2+} signaling in the astrocytes was always modeled as a differential equation of the above form in the publications presented in this study. ER was considered to be modeled as a separate entity if pumps and fluxes through the ER membrane were modeled by any equation. Second messenger signaling was considered to be modeled if the amount of second messenger (e.g., IP_3 , excluding Ca^{2+}) was described by a differential equation that was a function of time and at least one of the other model variables. If the amount of second messenger was just a constant or a function of time and itself, we marked it by ‘S’.

Paracrine signaling. Paracrine signaling is a form of molecular signaling, spreading by diffusion, from one cell to nearby cells in the same tissue. In this study, we considered it to be any extracellular signaling between two cells other than the neurotransmitter signaling. Gliotransmission, although controversial, is proposed to occur between the astrocyte and the pre- and/or postsynaptic terminals of a neuron, and we considered it to be one example of paracrine signaling in this study. Proposed gliotransmitters included glutamate and adenosine triphosphate (ATP). Other examples of strategies to model gliotransmission envisaged a neuronal inward current depending on astrocytic Ca^{2+} (I_{astro}), a glion mediator (G_m), or a phenomenological gating variable (f).

Other types of signaling. Gap junction signaling is a special form of intercellular signaling directly from the intracellular space of one cell to the intracellular space of another cell. IP_3 and Ca^{2+} are examples of second messengers that are able to travel via gap junctions.

We also indicated what kind of experimentally obtained physiological event the model was trying to capture (Ca^{2+} dynamics (Ca^{2+}), homeostasis (Home.), vascular (Vasc.), synchronization (Synch.), information transfer (Inf.), plasticity (Plast.), and hyperexcitability (Hyper.)).

16.3 Results

Previous work in experimental and computational cell biology fields has guided the development of computational models for astrocytes and astrocyte-neuron interactions. The computational glioscience field started by introducing relatively simple astrocyte models and expanded to astrocytic regulation of different events and cells in the nervous system. About half of the models are generic, meaning that they are nei-

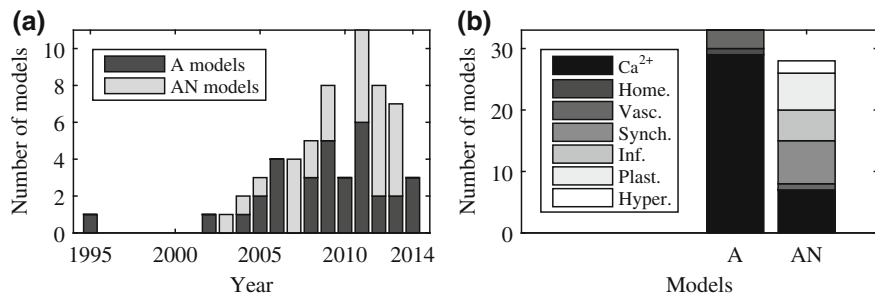


Fig. 16.1 Numbers of published astrocyte (A) and astrocyte–neuron (AN) models. **a** Numbers of published A and AN models per year from 1995 to 2014. **b** Types of A and AN models (see Sects. 16.2, 16.3.1, and 16.3.2 for details)

ther specifically targeted to any brain regions or networks nor verified with specific datasets in mind. Figure 16.1a illustrates the numbers of astrocyte and astrocyte–neuron models published each year, starting from 1995. Figure 16.1b shows what events the models were trying to capture (see also Sect. 16.2.2). Next, we will present the computational models for astrocytes in Sect. 16.3.1 and the computational models that include bidirectional signaling in astrocyte–neuron networks in Sect. 16.3.2.

16.3.1 Computational Astrocyte Models

Extensive research has been done on Ca^{2+} -mediated signals which have been proposed as the main mediator of communication between astrocytes (Nimmerjahn 2009). Two main types of Ca^{2+} responses are observed in astrocytes. Ca^{2+} oscillations are transient Ca^{2+} increases restricted to single cells, and Ca^{2+} waves are Ca^{2+} increases propagating within astrocytes and between neighboring astrocytes. Intracellular Ca^{2+} oscillations mainly depend on IP_3 concentration. Two main routes have been discovered to result in Ca^{2+} waves, the transfer of IP_3 between astrocytes via gap junctions and extracellular diffusion of ATP. The characteristics of the astrocyte models can be found in Table 16.2.

16.3.1.1 Modeled Phenomena and Anatomical Locations

Most of the models studied either Ca^{2+} oscillations in astrocytes (Roth et al. 1995; Lavrentovich and Hemkin 2008; De Pittà et al. 2009a, b; Zeng et al. 2009; Skupin et al. 2010; Dupont et al. 2011; Riera et al. 2011a, b; Toivari et al. 2011; López-Caamal et al. 2014) or Ca^{2+} waves in astrocyte networks (Höfer et al. 2002; Goto et al. 2004; Bellinger 2005; Bennett et al. 2005, 2006; Iacobas et al. 2006; Stamatakis and Mantzaris 2006; Ullah et al. 2006; Kang and Othmer 2009; Kazantsev 2009;

Table 16.2 Characteristics of the astrocyte models. This table shows the following: model, number of astrocytes modeled, astrocytic signaling processes modeled (yes (Y), no (N), simple (S)), and experimentally shown event that the model was finetuned to capture (Ca^{2+} dynamics (Ca^{2+}), homeostasis (Home.), and vascular (Vasc.)). Astrocytic signaling processes include the following: (a) neurotransmitter signaling / (b) ER / (c) second messenger signaling / (d) paracrine signaling / (e) gap junction signaling. Note that all models here included astrocytic Ca^{2+} signaling. In addition to astrocytes, Bennett et al. (2008a,b) and Chander and Chakravarthy (2012) modeled also smooth muscle cells, and Edwards and Gibson (2010) modeled also Müller cells. Chander and Chakravarthy (2012) modeled also neuronal membrane potential and glutamate release. Wallach et al. (2014) used the model by Tsodyks and Markram (1997) as the stimulus. Diekman et al. (2013) modeled also mitochondrial signaling, cell volume, and membrane potential in the astrocyte. Zeng et al. (2009) and Li et al. (2012) modeled VGCCs in astrocytes

Model	Number	Astrocytic (a/b/c/d/e)	Event
Bellinger (2005)	9	N/Y/Y/Y/Y	Ca^{2+}
Bennett et al. (2005)	19–57	N/Y/Y/Y/N	Ca^{2+}
Bennett et al. (2006)	19–95	N/Y/Y/Y/N	Ca^{2+}
Bennett et al. (2008a)	1–7	S/Y/S/Y/N	Vasc.
Bennett et al. (2008b)	1	S/Y/S/Y/N	Vasc.
Chander and Chakravarthy (2012)	1	Y/Y/Y/Y/N	Vasc.
De Pittà et al. (2009a)	1	S/Y/Y/N/N	Ca^{2+}
De Pittà et al. (2009b)	1	N/Y/S/N/N	Ca^{2+}
Diekman et al. (2013)	1	N/Y/S/N/N	Home.
Dupont et al. (2011)	1	S/Y/Y/N/N	Ca^{2+}
Edwards and Gibson (2010)	361	N/Y/Y/Y/Y	Ca^{2+}
Goldberg et al. (2010)	1–100	N/Y/Y/N/Y	Ca^{2+}
Goto et al. (2004)	200	S/Y/Y/N/Y	Ca^{2+}
Höfer et al. (2002)	1–361	N/Y/Y/N/Y	Ca^{2+}
Iacobas et al. (2006)	625	N/Y/S/Y/Y	Ca^{2+}
Kang and Othmer (2009)	11	S/Y/Y/Y/Y	Ca^{2+}
Kazantsev (2009)	30	N/Y/Y/N/Y	Ca^{2+}
Lallouette et al. (2014)	1331	N/Y/Y/N/Y	Ca^{2+}
Lavrentovich and Hemkin (2008)	1	N/Y/Y/N/N	Ca^{2+}
Li et al. (2012)	3–300	N/Y/Y/N/Y	Ca^{2+}
López-Caamal et al. (2014)	1	N/Y/N/N/N	Ca^{2+}
MacDonald and Silva (2013)	1–200	S/Y/Y/Y/N	Ca^{2+}
Matrosov and Kazantsev (2011)	1–10	N/Y/Y/N/Y	Ca^{2+}
Riera et al. (2011a)	1	N/Y/Y/N/N	Ca^{2+}
Riera et al. (2011b)	1	N/Y/Y/N/N	Ca^{2+}
Roth et al. (1995)	1	N/Y/S/N/N	Ca^{2+}
Skupin et al. (2010)	1	N/Y/S/N/N	Ca^{2+}
Stamatakis and Mantzaris (2006)	1–many	N/Y/Y/Y/N	Ca^{2+}

(continued)

Table 16.2 (continued)

Model	Number	Astrocytic (a/b/c/d/e)	Event
Toivari et al. (2011)	1	S/Y/Y/N/N	Ca^{2+}
Ullah et al. (2006)	1–3	S/Y/Y/N/Y	Ca^{2+}
Wallach et al. (2014)	130	Y/Y/Y/N/Y	Ca^{2+}
Wei and Shuai (2011)	169	S/Y/Y/N/Y	Ca^{2+}
Zeng et al. (2009)	1	N/Y/Y/N/N	Ca^{2+}

Edwards and Gibson 2010; Goldberg et al. 2010; Matrosov and Kazantsev 2011; Wei and Shuai 2011; Li et al. 2012; MacDonald and Silva 2013; Lallouette et al. 2014; Wallach et al. 2014). Few models had other topics. Bennett et al. (2008a,b) and Chander and Chakravarthy (2012) studied how activity in glutamatergic synapses at astrocytes affected the blood flow. Diekman et al. (2013) studied homeostasis. Only three models addressed diseases. Riera et al. (2011b) studied Alzheimer’s disease, Diekman et al. (2013) studied how astrocytes can reverse the effect of a stroke, and Toivari et al. (2011) demonstrated how to apply a simplistic stochastic model of an astrocyte to reproduce Ca^{2+} oscillations induced by addition of amyloid beta peptide to cortical primary cell cultures. The characteristics of the astrocyte models can be found in Table 16.2 and Fig. 16.1b.

About half of the models were so-called generic, meaning that they did not describe any specific anatomical location. Others, however, were specified to model astrocytes in different locations of the central nervous system, such as in the cerebrum (Iacobas et al. 2006; Diekman et al. 2013), cortex (De Pittà et al. 2009b; Goldberg et al. 2010; Toivari et al. 2011; Li et al. 2012; Wallach et al. 2014), hippocampus (Goto et al. 2004; Ullah et al. 2006; Riera et al. 2011a,b; Chander and Chakravarthy 2012), retina (Edwards and Gibson 2010), spinal cord (Bennett et al. 2006), striatum (Höfer et al. 2002), as well as visual cortex and somatosensory cortex (Bennett et al. 2008a,b).

16.3.1.2 Neurotransmitters in Astrocyte Models

Most of the astrocyte models did not model synaptic neurotransmitters at all, and with some of these models, spontaneous Ca^{2+} oscillations were studied (see Table 16.2). However, about one-third of the astrocyte models described neurotransmitters just as a stimulus, having either the glutamate as a constant or step function (see Table 16.2). Only two models (Chander and Chakravarthy 2012; Wallach et al. 2014) described the amount of neurotransmitters with differential equations. Chander and Chakravarthy (2012) modeled neuronal membrane potential and glutamate release, and the stimulus to the astrocyte model by Wallach et al. (2014) came from the model by Tsodyks and Markram (1997). We included these models under astrocyte models

because these models excluded gliotransmission; thus, these models did not have bidirectional signaling between astrocytes and neurons.

16.3.1.3 Modeling of Single Astrocytes

Intracellular Ca^{2+} oscillations depend mainly on the IP_3 - and Ca^{2+} -induced Ca^{2+} release (CICR) via IP_3 receptors (IP_3Rs) from the endoplasmic reticulum (ER) to the cytosol in isolated astrocytes (see, e.g., Agulhon et al. 2008). In addition to the CICR, Ca^{2+} influx via voltage-gated Ca^{2+} channels (VGCCs) and from the extracellular space has been shown to be involved in Ca^{2+} oscillations (Aguado et al. 2002).

Most of the single astrocyte models (Bennett et al. 2008b; De Pittà et al. 2009a,b; Skupin et al. 2010; Riera et al. 2011a,b; Chander and Chakravarthy 2012; Diekman et al. 2013) utilized the Ca^{2+} dynamics models by De Young and Keizer (1992) and Li and Rinzel (1994), or a modification of them, to describe Ca^{2+} behavior in the astrocyte even though these two models were not made to describe astrocytic behavior (see Sect. 16.3.3). Thus, these models (De Young and Keizer 1992; Li and Rinzel 1994) were not listed in our tables. Li and Rinzel (1994) actually simplified the model by De Young and Keizer (1992). In the model by Li and Rinzel (1994), the cytosolic Ca^{2+} concentration depends on the CICR, Ca^{2+} pump flux from the cytosol to the ER (SERCA), and leakage flux from the ER to the cytosol. In addition to the cytosolic Ca^{2+} concentration, the model has one more variable, the active fraction of IP_3Rs . In the model by Li and Rinzel (1994), the IP_3 concentration is maintained constant. Li and Rinzel (1994) also presented another model where the total free Ca^{2+} concentration is varying according to a differential equation that depends on Ca^{2+} efflux and influx across the plasma membrane.

On the other hand, few models (Lavrentovich and Hemkin 2008; De Pittà et al. 2009a; Zeng et al. 2009; Riera et al. 2011a,b; Toivari et al. 2011; Diekman et al. 2013) utilized the astrocyte model by Höfer et al. (2002) as a starting point. The model by Höfer et al. (2002) is based on several other models (Atri et al. 1993; Dupont and Goldbeter 1993; Höfer et al. 2001). The model includes CICR and Ca^{2+} leakage from the ER to the cytosol, Ca^{2+} uptake by SERCA pumps, Ca^{2+} extrusion and entry across the plasma membrane (including the leakage flux from the extracellular space to the cytosol), IP_3 degradation, Ca^{2+} and IP_3 transfer via gap junctions and diffusion inside the cytosol, as well as rates for IP_3R inactivation by Ca^{2+} binding and recovery. In addition, the model includes two production terms for IP_3 via phospholipase C (PLC), one corresponding to $\text{PLC}\beta$ and the other to $\text{PLC}\delta$. The model has four variables, the cytosolic Ca^{2+} and IP_3 concentrations, Ca^{2+} concentration in the ER, and active fraction of IP_3Rs .

De Pittà et al. (2009a), Riera et al. (2011a,b), and Diekman et al. (2013) used all these three models (De Young and Keizer 1992; Li and Rinzel 1994; Höfer et al. 2002) as a starting point. It has been shown experimentally that Ca^{2+} signals in response to external stimuli encode information either via frequency modulation (FM) (see e.g., Parpura 2004) or amplitude modulation (AM) (see e.g., Carmignoto 2000). The

models by De Pittà et al. (2009a,b) confirmed that information encoding can occur by AM, FM or by both modulations of Ca^{2+} oscillations.

Riera et al. (2011a,b) combined models by Di Garbo et al. (2007) and Shuai and Jung (2002) that is a stochastic version of the model by Li and Rinzel (1994). Other models based on the model by Di Garbo et al. (2007) are those by Toivari et al. (2011) and Diekman et al. (2013). Toivari et al. (2011) presented actually a stochastic version of the astrocyte model by Di Garbo et al. (2007). Diekman et al. (2013) modeled also mitochondrial signaling, cell volume, and membrane potential in the astrocyte.

In addition to using the details of the model by Li and Rinzel (1994), Bennett et al. (2008b) and Chander and Chakravarthy (2012) also used several other models as a base for their astrocyte model (Fink et al. 1999; Lemon et al. 2003; Bennett et al. 2005, 2006, 2008a). Bennett et al. (2008b) and Chander and Chakravarthy (2012) modeled also smooth muscle cells.

In addition to using the details of the model by Höfer et al. (2002), Lavrentovich and Hemkin (2008) also used the details of the model by Houart et al. (1999) and studied how spontaneous Ca^{2+} oscillations arise in a single astrocyte model. Spontaneous Ca^{2+} oscillations were also studied by Zeng et al. (2009), Skupin et al. (2010), and Riera et al. (2011a,b). Zeng et al. (2009) took into account also details of several other models (Hodgkin and Huxley 1952; Houart et al. 1999; Höfer et al. 2002; Lavrentovich and Hemkin 2008). Especially, Zeng et al. (2009) extended the model by Lavrentovich and Hemkin (2008) by taking into account VGCCs.

Two single astrocyte models were based on other models not named yet. López-Caamal et al. (2014) used the models by Keener and Sneyd (1998, 2009) as the base, and Dupont et al. (2011) used their previous models as the base (see, e.g., Dupont and Croisier 2010). Dupont et al. (2011) studied metabotropic glutamate receptor (mGluR) -induced Ca^{2+} oscillations that have also been observed in astrocytes.

16.3.1.4 Modeling of Astrocyte Networks

Three different routes have been discovered to induce Ca^{2+} waves when astrocytes communicate with each other. The first route depends on the transfer of IP_3 between astrocytes via gap junctions (Giaume and Venance 1998). Transported IP_3 triggers the CICR and Ca^{2+} increase in the coupled astrocyte. Ultimately, the Ca^{2+} waves propagate across nearby astrocytes. The second route depends on the extracellular diffusion of ATP (Newman and Zahs 1997; Guthrie et al. 1999). ATP is released from astrocytes into the extracellular space. This extracellular ATP binds to purinergic receptors on neighboring astrocytes resulting in the activation of G proteins, production of IP_3 , CICR, Ca^{2+} elevation in the cytosol, and ultimately, release of ATP. The third route depends on cortical spreading depression (Peters et al. 2003), which is a pathophysiological phenomenon and does not necessarily depend on Ca^{2+} release from the ER.

The first model developed in the category of IP_3 gap junctions was the model by Höfer et al. (2002) (see Table 16.2). Ullah et al. (2006) and Wei and Shuai (2011)

combined, e.g., the models by Li and Rinzel (1994) and Höfer et al. (2002). In addition, both Kazantsev (2009) and Matrosov and Kazantsev (2011) modified the model by Ullah et al. (2006).

Goldberg et al. (2010) extended the single astrocyte model by De Pittà et al. (2009a,b) to simulate a network of astrocytes linked with gap junctions. On the other hand, Lalloquette et al. (2014) simplified the models by De Pittà et al. (2009a) and Goldberg et al. (2010) to be able to simulate the function of thousands of astrocytes and studied how different topologies in gap junction-coupled astrocytes affected the propagation of intercellular Ca^{2+} waves. Wallach et al. (2014) continued the previous work (De Young and Keizer 1992; Li and Rinzel 1994; Höfer et al. 2002; De Pittà et al. 2009a; Goldberg et al. 2010; Lalloquette et al. 2014) by stimulating the astrocyte model using Tsodyks and Markram (1997) model. The model by Wallach et al. (2014) appears among the astrocyte models because the astrocyte did not have an effect on the neuron.

Li et al. (2012) extended the single astrocyte model by Zeng et al. (2009) for different Ca^{2+} flows between the extracellular space, cytoplasm, and ER and studied spontaneous Ca^{2+} oscillations and cortical spreading depression-triggered Ca^{2+} waves. Li et al. (2012) modeled also VGCCs in the astrocytes. The model was based on several previous models (Höfer et al. 2002; Bennett et al. 2005, 2008a,c; Dronne et al. 2006; Lavrentovich and Hemkin 2008; Zeng et al. 2009; Edwards and Gibson 2010).

In the case of extracellular diffusion of ATP, Bennett et al. (2005, 2006) built the first astrocyte network model in this category where activation of metabotropic purinergic P2Y receptors by ATP triggered the release of ATP and studied Ca^{2+} wave propagation in astrocyte networks based on several earlier models (De Young and Keizer 1992; Li and Rinzel 1994; Fink et al. 1999; Lemon et al. 2003). Bennett et al. (2008a) modified their earlier models (Bennett et al. 2005, 2006) for cellular mechanisms that coupled activity of glutamatergic synapses with changes in blood flow and replaced ATP by glutamate and epoxyeicosatrienoic acid. MacDonald and Silva (2013) modified the models by Bennett et al. (2005, 2006, 2008a). Stamatakis and Mantzaris (2006), on the other hand, used the model by Li and Rinzel (1994) and combined it with the IP_3 model by De Young and Keizer (1992), and extracellular diffusion of ATP. In addition, Bellinger (2005) extended the model by Höfer et al. (2002) by adding extracellular ATP that does not diffuse.

At the end, we also briefly consider the astrocyte network models which combined IP_3 transfer via gap junctions and extracellular diffusion of ATP. These include the models by Iacobas et al. (2006), Kang and Othmer (2009), and Edwards and Gibson (2010). Edwards and Gibson (2010) combined the gap junction model by Höfer et al. (2002) and the ATP diffusion model by Bennett et al. (2005, 2006), and also modeled Müller cells.

16.3.2 Computational Astrocyte–Neuron Models

Bidirectional astrocyte–neuron communication has been the subject of much interest and debate in the field of neuroscience in recent years. It has been shown that astrocytes are capable of releasing substances, called gliotransmitters, which can alter the behavior of neurons (see, e.g., Parpura et al. 1994). There are different views about whether this phenomenon exists in the healthy brain as a part of normal information transfer or is a product of pathological processes possibly related to experimental methods (see, e.g., Agulhon et al. 2012; De Pittà et al. 2016). However, there currently is experimental evidence suggesting the reciprocal signaling of the tripartite synapses is a physiological, not necessarily a pathological phenomenon (see, e.g., Volterra et al. 2014; Magistretti and Allaman 2015). The details of the astrocyte–neuron models can be found in Table 16.3.

16.3.2.1 Modeled Phenomena and Anatomical Locations

Most of the present astrocyte–neuron models focused on astrocytic Ca^{2+} signaling affected by neurotransmitters, such as glutamate, and reciprocal astrocyte–neuron interactions. Many of the models were published without biological or disease-related questions, and concentrated on combining existing studies or adding new components to previous studies (Di Garbo et al. 2007; Nadkarni and Jung 2007; Volman et al. 2007; Nadkarni et al. 2008; Silchenko and Tass 2008; Di Garbo 2009; Postnov et al. 2009; Valenza et al. 2011; Amiri et al. 2013b).

In addition to these more general studies of astrocyte–neuron coupling and behavior, some models focused on specific aspects of neuronal firing affected by astrocytes. There were models analyzing the contribution of astrocytes to epileptic behavior of neuronal networks (Nadkarni and Jung 2003, 2004, 2005; Amiri et al. 2011a,b, 2012a,b,c), astrocytic modulation of neuronal synchrony (Allegrini et al. 2009; Amiri et al. 2013a), effects of astrocytes on neuronal firing patterns (Liu and Li 2013; Tang et al. 2013), contribution of astrocytes to synaptic potentiation or depression (Postnov et al. 2007; Wade et al. 2011, 2012; Tewari and Majumdar 2012a,b), and, on a larger scale, the role of astrocytes in memory retrieval (Tewari and Parpura 2013), and signal formation in magnetic resonance imaging (DiNuzzo et al. 2011). The characteristics of the astrocyte models can be found in Table 16.3 and Fig. 16.1b.

About half of the models were so-called generic models, meaning they did not describe interactions between any specific neuron or astrocyte subtypes in a well-specified anatomical area. Others, however, were specific of astrocyte–neuron interactions in different locations of the brain, such as in the cortex or, more specifically, in the neocortex (Nadkarni and Jung 2003, 2004; Di Garbo et al. 2007; Volman et al. 2007; Allegrini et al. 2009; DiNuzzo et al. 2011; Valenza et al. 2011), in the hippocampus (Nadkarni and Jung 2005, 2007; Nadkarni et al. 2008; Amiri et al. 2012a, 2013a; Tewari and Majumdar 2012a,b; Tewari and Parpura 2013; Tang et al. 2013), or thalamocortical networks (Amiri et al. 2011a, 2012b,c).

Table 16.3 Characteristics of the astrocyte–neuron models. This table shows the following. First, we give the model. Second, we give the number of presynaptic neurons and presynaptic signaling processes modeled (yes (Y), no (N), simple (S)). Third, we give the number of postsynaptic neurons and postsynaptic signaling processes modeled (yes (Y), no (N), simple (S)). Pre- and postsynaptic signaling processes include the following; neurotransmitter signaling/membrane potential/ Ca^{2+} signaling/ER/second messenger signaling/paracrine signaling. Fourth, we give the number of astrocytes and astrocytic signaling processes modeled (yes (Y), no (N), simple (S)). Astrocytic signaling processes include the following: neurotransmitter signaling/ER/second messenger signaling/paracrine signaling/gap junction signaling. Note that all models here included astrocytic Ca^{2+} signaling. Last, we give the experimentally shown event that the model was trying to capture (Ca^{2+} dynamics (Ca^{2+})), vascular (Vasc.), synchronization (Synch.), information transfer (Inf.), plasticity (Plast.), and hyperexcitability (Hyper.). DiNuzzo et al. (2011) modeled also smooth muscle cells. Liu and Li (2013) modeled a triple-neuron feed-forward-loop neuronal network. Thalamocortical neural population model was used by Amiri et al. (2011a, 2012b,c)

Model	Presynaptic	Postsynaptic	Astrocytic	Event
Allegrini et al. (2009)	None	49 S/Y/N/N/N/Y	400 S/Y/S/Y/Y	Synch.
Amiri et al. (2011a)	Many S/N/N/N/N/Y	Many S/N/N/N/N/Y	1 S/Y/Y/Y/N	Synch.
Amiri et al. (2011b)	1 Y/Y/N/N/N/Y	1 Y/Y/N/N/N/Y	1 Y/Y/Y/Y/N	Synch.
Amiri et al. (2012a)	1–5 Y/Y/N/N/N/Y	1–5 Y/Y/N/N/N/Y	1–5 Y/Y/Y/Y/Y	Synch.
Amiri et al. (2012b)	Many S/N/N/N/N/Y	Many S/N/N/N/N/Y	2 S/Y/Y/Y/Y	Hyper.
Amiri et al. (2012c)	Many S/N/N/N/N/Y	Many S/N/N/N/N/Y	2 S/Y/Y/Y/Y	Synch.
Amiri et al. (2013a)	1–50 Y/Y/N/N/N/Y	1–50 Y/Y/N/N/N/Y	1–50 Y/Y/Y/Y/Y	Synch.
Amiri et al. (2013b)	None	1 Y/Y/N/N/N/Y	1 Y/Y/Y/Y/N	Inf.
Di Garbo et al. (2007)	None	0–1 S/Y/N/N/N/Y	1 S/Y/Y/Y/N	Ca^{2+}
Di Garbo (2009)	0–1 S/Y/N/N/N/N	0–1 S/Y/N/N/N/Y	1 S/Y/Y/Y/N	Ca^{2+}
DiNuzzo et al. (2011)	None	1 S/N/N/N/Y	1 S/Y/Y/Y/N	Vasc.
Liu and Li (2013)	2 S/Y/N/N/N/Y	2 S/Y/N/N/N/Y	6 S/Y/Y/Y/Y	Inf.
Nadkarni and Jung (2003)	None	1 S/Y/N/N/N/Y	1 S/Y/Y/Y/N	Ca^{2+}
Nadkarni and Jung (2004)	None	1 S/Y/Y/N/N/Y	1 S/Y/Y/Y/N	Ca^{2+}
Nadkarni and Jung (2005)	1 Y/Y/Y/N/N/Y	1 Y/Y/N/N/N/N	1 Y/Y/Y/Y/N	Hyper.
Nadkarni and Jung (2007)	1 Y/Y/Y/N/N/Y	1 Y/Y/N/N/N/N	1 Y/Y/Y/Y/N	Plast.
Nadkarni et al. (2008)	1 Y/N/Y/N/N/Y	1 Y/N/N/N/N/N	1 Y/Y/Y/Y/N	Inf.
Postnov et al. (2007)	1 S/Y/N/N/N/Y	1 S/Y/N/N/N/Y	1 S/Y/Y/Y/N	Plast.
Postnov et al. (2009)	1–many S/Y/N/N/N/Y	1–many S/Y/N/N/N/Y	1–10 S/Y/Y/Y/Y	Ca^{2+}

(continued)

Table 16.3 (continued)

Model	Presynaptic	Postsynaptic	Astrocytic	Event
Silchenko and Tass (2008)	None	1 Y/Y/Y/N/N/Y	1 Y/Y/Y/Y/N	Ca ²⁺
Tang et al. (2013)	1 Y/Y/N/N/N/N	1 Y/Y/N/N/N/Y	1 Y/Y/Y/Y/N	Inf.
Tewari and Majumdar (2012a)	1 Y/Y/Y/Y/Y/Y	1 Y/Y/Y/N/N/Y	1 Y/Y/Y/Y/N	Plast.
Tewari and Majumdar (2012b)	1 Y/Y/Y/Y/Y/Y	1 Y/Y/N/N/N/N	1 Y/Y/Y/Y/N	Plast.
Tewari and Parpura (2013)	1 Y/Y/Y/Y/Y/N	4 Y/Y/Y/N/N/Y	1 Y/Y/Y/Y/N	Synch.
Valenza et al. (2011)	None	1 S/Y/N/N/N/Y	1 S/Y/Y/Y/N	Ca ²⁺
Volman et al. (2007)	1 Y/Y/N/N/N/Y	None	1 Y/Y/Y/Y/N	Inf.
Wade et al. (2011)	1–2 Y/N/N/N/N/Y	1–2 Y/Y/N/N/N/Y	1 Y/Y/Y/Y/N	Plast.
Wade et al. (2012)	2 S/N/N/N/N/Y	2 S/Y/N/N/N/Y	1 N/Y/Y/Y/N	Plast.

16.3.2.2 Neuron Models and Neurotransmitters

The modeling strategies for neurons varied with the author. Almost half of the studied publications used biophysical neuron models, namely the Hodgkin and Huxley model (Hodgkin and Huxley 1952; Nadkarni and Jung 2003; Tewari and Majumdar 2012a, b; Liu and Li 2013; Tang et al. 2013; Traub et al. 1991), or its compartmental extension by Pinsky and Rinzel (Pinsky and Rinzel 1994; Nadkarni and Jung 2004, 2005, 2007; Silchenko and Tass 2008; Tewari and Parpura 2013), or Olufsen et al. (2003) model (Di Garbo et al. 2007; Di Garbo 2009). However, sometimes the ionic currents or ion channel conductances were not modified by any of the variables in any way during the simulation in which case a more simple model would have been more suitable. Simpler phenomenological models utilized in the studied publications included the FitzHugh-Nagumo model (FitzHugh 1961; Postnov et al. 2007, 2009), the leaky integrate-and-fire model (Gerstner and Kistler 2002; Wade et al. 2011, 2012), the Izhikevich model (Izhikevich 2007; Allegrini et al. 2009; Valenza et al. 2011), the Morris and Lecar model (Morris and Lecar 1981; Volman et al. 2007; Amiri et al. 2011b, 2012a, 2013a, b; Suffczynski et al. 2004) and the model of neuronal populations by Suffczynski et al. (Amiri et al. 2011a, 2012b, c).

In most cases, the neurotransmitter stimulating the astrocyte was glutamate from the excitatory presynaptic neuron, or gamma-aminobutyric acid (GABA) from the inhibitory presynaptic neuron. In the model by Silchenko and Tass (2008), either the astrocyte or the neuron was releasing glutamate. Inhibitory neurons were modeled by Nadkarni and Jung (2005, 2007), Di Garbo (2009), Amiri et al. (2011a, b, 2012a, b, c, 2013a), and Liu and Li (2013). The released neurotransmitter was modeled explicitly by Nadkarni and Jung (2005, 2007), Volman et al. (2007), Nadkarni et al. (2008), Silchenko and Tass (2008), Amiri et al. (2011b, 2012a, 2013a, b), Wade et al. (2011), Tewari and Majumdar (2012a, b), Tang et al. (2013), and Tewari and Parpura (2013). Other models used phenomenological transfer functions to approximate the effect of neurons to astrocytic IP₃ concentration.

16.3.2.3 Modeling of Astrocytes and Gliotransmission

In order for the model to be classified as a tripartite synapse model, it has to include gliotransmitter signaling from astrocytes to neurons. Thus, all the models in Table 16.3 had a mechanism for gliotransmitter release. Most of the studied models considered glutamate as gliotransmitter, except for Di Garbo (2009); Postnov et al. (2009); Amiri et al. (2011b, 2012a, 2013a), that also considered ATP.

Astrocytes react to neurotransmitters with changes in their Ca^{2+} concentrations, and this Ca^{2+} concentration is the trigger initiating gliotransmitter release in astrocyte–neuron models. Almost half of the studied models utilized Li and Rinzel (1994) Ca^{2+} dynamics model, or a modification of it, to describe Ca^{2+} behavior in the astrocyte coupled to a synapse (Nadkarni and Jung 2003, 2004, 2005, 2007; Volman et al. 2007; Nadkarni et al. 2008; Valenza et al. 2011; Wade et al. 2011, 2012; Amiri et al. 2012a, 2013a; Tewari and Majumdar 2012a, b; Liu and Li 2013; Tang et al. 2013; Tewari and Parpura 2013). Other models of Ca^{2+} dynamics, considered the Höfer et al. model (Höfer et al. 2002; Di Garbo et al. 2007; Allegrini et al. 2009; Di Garbo 2009; DiNuzzo et al. 2011; Tewari and Majumdar 2012a, b; Liu and Li 2013; Tewari and Parpura 2013), the models by Keener and Sneyd (Keener and Sneyd 1998, 2009; Postnov et al. 2007, 2009; Amiri et al. 2011a, b, 2012b, c, 2013a, b), the model by Houart et al. (Houart et al. 1999; Silchenko and Tass 2008; DiNuzzo et al. 2011), and the model by Atri et al. (Atri et al. 1993; Allegrini et al. 2009; Liu and Li 2013) (see Sect. 16.3.3). Each model specified a Ca^{2+} concentration related condition which, when satisfied through activation of the IP_3 -mediated Ca^{2+} signaling cascade, activated gliotransmission. See Sect. 16.3.1 for more details on the properties of astrocytic Ca^{2+} models.

As the exact mechanisms of astrocytic signaling are still largely unknown, most of the models had phenomenological descriptions of gliotransmitter release. At present, it is believed that gliotransmitter release is mostly by vesicular exocytosis, but only a few of the studied models took this into account explicitly. These are the models by Silchenko and Tass (2008) and by Tewari and collaborators (2012a; 2012b; 2013). In particular, these models along with that by Wade et al. (2012) explicitly modeled gliotransmitter release. Other models used phenomenological transfer functions to approximate the influence of gliotransmission to the target synaptic terminal.

Modulation of synaptic functioning can be done by regulating the properties of either the pre- or the postsynaptic terminal. Most of the models incorporated modulation of the postsynaptic terminal, usually by injecting an astrocyte-mediated current which could be either hyperpolarizing (Postnov et al. 2009) or depolarizing (Nadkarni and Jung 2003, 2004, 2005; Di Garbo et al. 2007; Postnov et al. 2007, 2009; Silchenko and Tass 2008; Allegrini et al. 2009; Di Garbo 2009; Amiri et al. 2011a, b, 2012a, b, c, 2013a, b; DiNuzzo et al. 2011; Valenza et al. 2011; Wade et al. 2011; Liu and Li 2013; Tang et al. 2013; Tewari and Parpura 2013). Presynaptic modulation was modeled in the studied publications directly by altering the amount of neurotransmitter released from the presynaptic terminal (Nadkarni and Jung 2007; Volman

et al. 2007; Nadkarni et al. 2008; Wade et al. 2011, 2012; Tewari and Majumdar 2012a,b), or indirectly by projecting the presynaptic attenuation to the postsynaptic current induced by the neurotransmitter (Postnov et al. 2007, 2009; Amiri et al. 2011a, 2012a,b,c, 2013a). Moreover, presynaptic modulation could be attenuating (Postnov et al. 2007, 2009; Volman et al. 2007; Amiri et al. 2011a,b, 2012a,b,c, 2013a; Wade et al. 2011, 2012) or facilitating (Nadkarni and Jung 2007; Nadkarni et al. 2008; Tewari and Majumdar 2012a,b; Wade et al. 2012).

16.3.2.4 Modeling of Gap Junctions in Astrocyte–Neuron Models

Some of the studied astrocyte–neuron models also modeled gap junction signaling between astrocytes (see Table 16.3). These were the models by Allegrini et al. (2009), Postnov et al. (2009), Amiri et al. (2012a,b,c, 2013a), and Liu and Li (2013). Gap junction signaling between astrocytes adds another layer of complexity to the dynamics of astrocyte–neuron signaling, as they convey the Ca^{2+} signal initiated by neurotransmission at a specific synapse to other astrocyte–neuron pairs. Allegrini et al. (2009) and Liu and Li (2013) took a partial differential equation approach of modeling the transfer via gap junctions between astrocytes, whereas Postnov et al. (2009) and Amiri et al. (2012a,b,c, 2013a) modeled the transfer via gap junctions with coupling terms.

16.3.3 Model Evolution

It is of interest to understand how computational glioscience models have evolved from each other (see Fig. 16.2). Often, authors have unknowingly used publications as a reference without actually citing them, but we have tried our best to give here as complete picture as possible. Models are connected in Fig. 16.2 if the authors either stated directly that other models were used as a reference or the authors used a subset of the exact same equations appearing in previous publications by the same authors. Models are excluded from Fig. 16.2 if we did not find any proof that the authors had used other models presented in this study when building their model, and that their model was not used by other models presented in this study. Figure 16.2 shows how the models by De Young and Keizer (1992), Li and Rinzel (1994), and Höfer et al. (2002) were the most popular models used as a starting point when developing new models.

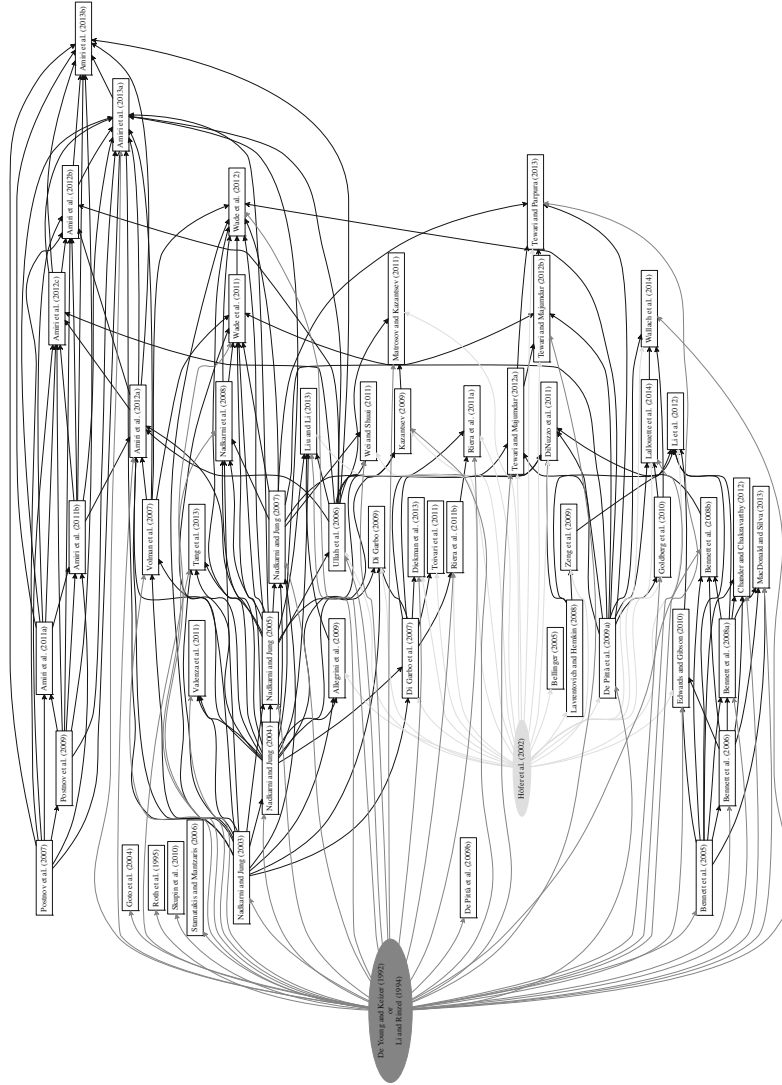


Fig. 16.2 Evolution of astrocyte and astrocyte–neuron models from 1995 to 2014. An arrow starts from the model which was used as a reference for the model pointed by the arrowhead. Dark gray lines represent the models that were based on the models by De Young and Keizer (1992) and Li and Rinzel (1994). Light gray lines represent the models that were based on the model by Höfer et al. (2002)

16.3.4 Reproducibility of Models

In addition to presenting the basic characteristics of the models, it is important to address the reproducibility issue, in other words how well the published simulation results can be reproduced. We have extensive experience in assessing the reproducibility issues in computational neuroscience and in computational cell biology, also in practical terms (see, e.g., Pettinen et al. 2005; Manninen et al. 2010, 2011, 2017, 2018a; Hituri and Linne 2013). Several reviews and commentaries have also addressed the same issue (see, e.g., Cannon et al. 2007; De Schutter 2008; Nordlie et al. 2009; Crook et al. 2013; Topalidou et al. 2015). There are several ways to test if the original results are reproducible (see, e.g., Crook et al. 2013). First, replicability is tested when the original code and tools are used to reproduce the original simulation results. Second, cross-replicability is tested when the original model code is used, but it is simulated with a different software. Sometimes, this means that the model needs to be re-implemented based on the original code. Third, reproducibility means implementing the model based on the information in the original publication and not using available code. In this study, we wanted to test the reproducibility of models; thus, we tested how well we are able to reproduce the original model behavior by implementing the model based on the equations in the original publication (see also Manninen et al. 2017, 2018a).

Before we were able to test the reproducibility of the models, we had to implement the models based on the information in the original publications. While gathering the information of the models to Tables 16.2 and 16.3, we realized that several publications lack crucial details in how the models were presented and only a few models (see e.g., Lavrentovich and Hemkin 2008; Zeng et al. 2009; Edwards and Gibson 2010) were available in model databases or online. Some models were developed or studied with a specific disease aspect in mind, but in reality, none of these models were sophisticated enough to assess the full spectrum of mechanisms possibly leading to diseases because comprehensive experimental data are still lacking. Sometimes, not all equations were explicitly provided by the actual publication, rather referring the reader to previous work, thereby making it difficult to know exactly what the actual model components were (see, e.g., Bennett et al. 2006, 2008b; Tewari and Parpura 2013). On a closer look, we also found errors in the equations or parameter values (see, e.g., Nadkarni and Jung 2003; Riera et al. 2011a,b; Wade et al. 2011, 2012). Too often, graphical illustrations of the models were misleading (see, e.g., Höfer et al. 2002; Bellinger 2005; Silchenko and Tass 2008; DiNuzzo et al. 2011; Valenza et al. 2011) or missing (see, e.g., Nadkarni and Jung 2003; Goto et al. 2004; Bennett et al. 2006; Volman et al. 2007; Kazantsev 2009; Matrosov and Kazantsev 2011; Riera et al. 2011a; Amiri et al. 2013b), making it impossible to easily understand what was modeled and what was left out. Sometimes, the stimuli looked more biological based on the graphical illustrations than were actually used (see, e.g., Höfer et al. 2002; Bellinger 2005; Silchenko and Tass 2008). In addition, we were not sure what mechanisms and phenomena Valenza et al. (2011) aim to model. Their graphical illustration showed both pre- and postsynaptic neurons and an astrocyte.

However, in the text, it was unclear if both the pre- and postsynaptic terminals were modeled, and if both were modeled how they communicated with each other. It is extremely important that graphical illustrations of the models have only those model components that are actually modeled.

Based on Tables 16.2 and 16.3, we selected five relatively simple models (Nadkarni and Jung 2003; Di Garbo et al. 2007; Lavrentovich and Hemkin 2008; Dupont et al. 2011; Wade et al. 2012) to be implemented based on the information in the original publication and tested if we were able to reproduce the original model behavior. It is important to note that our study is one experiment to reproduce the model behavior and may also contain errors. Nevertheless we still consider that our experiment and experience much reflect the situation in the field. In Table 16.4, we reviewed the models based on several details: Was the model available online, were all the equations, parameter values, and initial values given in the original publication, and were we able to reproduce the original results with the information given in the original publication. We implemented the models in MATLAB®. We have also tested the reproducibility and comparability of four single astrocytes models (Lavrentovich and Hemkin 2008; De Pittà et al. 2009a; Dupont et al. 2011; Riera et al. 2011a,b) in a companion study (Manninen et al. 2017) and have provided Python codes for these four models in ModelDB (Accession number, 223648; <http://senselab.med.yale.edu/modeldb/>; Migliore et al. 2003; Hines et al. 2004).

Di Garbo et al. (2007) presented two models, an astrocyte model and astrocyte-neuron model. In this study, we tested just the astrocyte model, so we did not model the neuron at all. The astrocyte model by Di Garbo et al. (2007) was based on the previous model by Höfer et al. (2002), and their model was able to show, in agreement with experimental findings, that the transient Ca^{2+} response to extracellular ATP is mediated by the P2Y receptor and the sustained response by the P2X receptor. Di Garbo et al. (2007) gave all the equations and parameter values in the publication. They did not give the initial values for the variables, but for half of the variables, we were able to obtain those from the results of the original publication. For the cytosolic Ca^{2+} concentration and Ca^{2+} concentration in the ER, we set the initial values to 0.06 and 72 μM , respectively. For the other two variables, the IP_3 concentration and active fraction of IP_3Rs , we set the initial values to steady-state values calculated from their differential equations, about 9.6 nM and 0.92, respectively. Di Garbo et al. (2007) showed three figures for the simulation results of the astrocyte model, Figs. 2, 5, and 8 of the original publication. We were able to reproduce all the original results by our MATLAB® implementation of the model. Of note is that there was a mismatch in the original publication between the time separation for the two ATP applications in Fig. 5 with respect to what specified in the caption of the figure.

Dupont et al. (2011) studied mGluR induced Ca^{2+} oscillations in a single astrocyte model. The model by Dupont et al. (2011) was based on the model by Dupont and Croisier (2010) that originated from the model by Dupont and Goldbeter (1993). Dupont et al. (2011) gave all the equations and parameter values in the original publication. They did not give the initial values for the variables, but for four of the variables, we were able to obtain those from the results of the original publication. The used initial values were 0.1 μM for the Ca^{2+} concentration, 14 nM for the

Table 16.4 Model reproducibility. This table shows how well we were able to reproduce the results of the original publications for five selected models. We reviewed these models by multiple criteria: (i) the code used to implement the model was available online; (ii) all the equations of the model were in the original publication; (iii) values for all parameters and (iv) initial conditions of the model were provided; and (v) all results of the original publication could be reproduced. We used Yes/No labels for online model availability, while for the other criteria, we considered three possibilities: ‘None’, ‘Most’ and ‘All’, where by ‘Most’ we mean that at least two thirds of originally published results could be reproduced. We were able to reproduce all of the original results by Di Garbo et al. (2007). We were not able to reproduce the original results by Dupont et al. (2011). We were able to reproduce all of the original results by Lavrentovich and Hemkin (2008) based on the information in the corrigendum. We were able to reproduce most of the original results by Nadkarni and Jung (2003) after we changed one equation and one parameter value, before these changes we were not able to reproduce the results. We were not able to reproduce the original results by Wade et al. (2012)

Model	Model availability online	Equations given	Parameter values given	Initial conditions given	Reproducibility
Di Garbo et al. (2007)	No	All	All	None	All
Dupont et al. (2011)	No	All	All	None	None
Lavrentovich and Hemkin (2008)	Yes	All	All	All	All
Nadkarni and Jung (2003)	No	All	All	None	None/most
Wade et al. (2012)	No	All	All	Most	None

concentration of non-phosphorylated ligand-bound mGluR dimers, 25 nM for the diacylglycerol (DAG) concentration, and 0.2 for the fraction of active protein kinase C (PKC). For the IP₃ concentration, we finally decided to use 0.2 μM. For fraction of Ca²⁺-inhibited IP₃Rs, we used 0.5. Dupont et al. (2011) showed two figures for the basic simulation results of the astrocyte model, Figs. 2 and 3 of the original publication. With the original parameter values, we were able to reproduce quite the same oscillating behavior as seen in Fig. 2 of the original publication for the non-phosphorylated ligand-bound mGluR dimers, fraction of active PKC, and DAG. However, our values were a bit different compared to the original results. Our Ca²⁺ concentration was very different compared to Fig. 2 of the original publication. Our Ca²⁺ concentration dropped to around 50 nM and did small oscillations around that value. In addition, we were not able to get oscillating Ca²⁺ behavior as in Fig. 3 of the original publication. We checked the references by Dupont et al. (2011) but we were not able to resolve the problem in our implementation even though we tested several initial values for all the variables, parameter values and even changed the equations (see also Manninen et al. 2017 for a modified model).

Lavrentovich and Hemkin (2008) studied spontaneous Ca^{2+} oscillations in a single astrocyte model. Lavrentovich and Hemkin (2008) gave all the equations, parameter values, and initial values in the publication that was based on the models by Houart et al. (1999) and Höfer et al. (2002). Lavrentovich and Hemkin (2008) showed five figures for the basic simulation results of the astrocyte model, Figs. 3, 4, 5, 7, and 9 of the original publication. We were able to reproduce all these figures by our MATLAB® implementation based on the information given in the corrigendum attached to the original publication (see also Manninen et al. 2017). The model in modelDB (Accession Number: 112547) was similar to our implementation.

Nadkarni and Jung (2003) studied Ca^{2+} oscillations with a model consisting of a single astrocyte and single neuron. They gave all the equations and parameters values in the publication that was based on the models by Hodgkin and Huxley (1952) and Li and Rinzel (1994). However, they did not give the initial values for the variables, so we decided to set them all to zero. When implementing the model, we realized that there was one typographical error in the equations related to Hodgkin–Huxley equations ($\alpha_n = (0.1 - 0.01v)/(\exp(1 - 0.1v) - 1)$) and one in the parameter values related to IP_3 equation ($\tau_{\text{IP}_3} = 1/0.000140 \text{ ms}$). Based on these modifications, we were able to reproduce almost all curves of the original Fig. 2. We were able to reproduce almost exactly the curves in Fig. 2A of the original publication; however, our Ca^{2+} curve had a sharper peak. We were not able to reproduce the results in Fig. 2B of the original publication with the given stimulus. However, when we gave the stimulus for 30 s, we were able to reproduce almost similar results as in the original publication. The only difference was that the Ca^{2+} curve started to rise later than in the original results.

Wade et al. (2011) presented a generic, bidirectional signaling model between astrocytes and neurons in the context of spike-timing-dependent plasticity. The simulated results showed that extrasynaptic N-methyl-D-aspartate (NMDA) mediated neuronal currents were able to provide a teaching signal for learning and synchronization of neural activity between neurons. Due to deficiencies in the original model description, we did not attempt to implement the full model. Instead, we evaluated in more detail the model presented by Wade et al. (2012), which gave all the equations, parameter values, and most initial values in the original publication. The model was based on several previous models (Li and Rinzel 1994; Nadkarni and Jung 2003, 2004, 2005, 2007; Volman et al. 2007; Nadkarni et al. 2008; De Pittà et al. 2009a; Wade et al. 2011). However, Wade et al. (2012) gave a few parameter values wrong and did not give initial values for membrane potentials. Thus, we set the initial values for the membrane potentials to zero. We were not able to reproduce similar results compared to the results of the original publication by Wade et al. (2012); e.g., we did not obtain cytosolic Ca^{2+} concentration as high as in Fig. 8 of the original publication. Furthermore, while trying to reproduce the results, we realized that not even the equations given by Wade et al. (2012) matched the simulated results plotted by Wade et al. (2012). As an example, the sum of the curves in Figs. 3A and 3B of the original publication was negative, suggesting based on the Equation (18) that Fig. 3C should be negative, but it was actually shown as a positive curve. Furthermore, the curves on Figs. 5C and 5D of the original publication had exactly the same form before 200 s,

the same applied for Figs. 6A–6E. So there must be something fundamentally wrong in the equations, implementation, and/or results of the original publication.

In summary, it was frustrating to notice that not all necessary information to implement these models was given in the publications. Even though we decided to take five relatively simple models under more detailed study, we were able to reproduce the original results completely from only two of the five models based on the information in the original publications and errata. The core model implementation took very little time in each case, but because four models out of five did not give all the background information needed to implement the model, it took several hours to finalize the implementation and to reproduce the original results. We want to emphasize that when publishing a model, a set of figures describing the function of all model variables needs to be given in addition to the actual model files and relevant information. This will help us in developing even better models and in using the models in teaching younger generations. Reviewers have the responsibility to request all the above-mentioned information in the publications to ensure high reproducibility.

16.4 Discussion

The ultimate goal of computational glioscience is to understand how astrocytic sub-cellular mechanisms and molecular events, as well as the putative mechanisms related to astrocyte–neuron interactions, are linked with cognitive functions and behavior in mammals. A variety of hypotheses are presently accumulating on the roles of astrocytes in neuronal excitability, synaptic transmission, and plasticity. Moreover, hypotheses on the involvement of astrocytes in higher cognitive functions and even in memory consolidation have been presented. Most of these hypotheses stem from *in vitro* experimental studies, but also from the modeling work evaluated in this study.

Research on astrocytes has resulted in a variety of attempts of model the role of these cells in synaptic and neuronal network dynamics. In this study, we evaluated existing computational models developed for astrocytic functions and for astrocyte–neuron interactions. To the best of our knowledge, this study is one of the first to report the detailed categorization and evaluation of astrocyte–neuron models. Models were characterized in detail to help their use in future work. Based on our assessment, we found that the same component models were often used repeatedly in successive publications, with no spelled-out, explicit justification on how suitable the specific component model was for the study in question. Thus, most models describing the subcellular events of astrocytes had limitations and shortcomings. A model typically describes a limited set of molecular mechanisms and provides explanations to a relatively narrow set of astroglial dynamics.

We also evaluated some of the models by implementing the equations according to what was presented in the original publication, with an aim to reproduce the simulation results of the original publication (see also Manninen et al. 2017, 2018a). We discovered that many publications lack crucial details in how the models were presented, preventing the implementation of the models without first contacting the

authors. Moreover, in some cases, it was impossible, after several trials, to reproduce the simulated results of the original publication. This meant often that the equations and simulation results of the original publication did not match. It is important to bear this in mind when assessing the roles of astrocytes in brain functions and when utilizing the previously developed models in future work. We acknowledge that it is not an easy task to master and combine into mathematical form complex biochemical, molecular, and electrophysiological data in order to model the neuron-astroglia interactions. We, however, wish to underline the importance of reproducibility issue in computational neuroscience and glioscience.

Our findings on how glioscience modeling studies are presented in publications stress the importance of proper validation and careful review processes of the developed models against experimental wet-laboratory data. There is a variety of aspects that could be improved when developing new models and, specifically, the way of presenting them in publications. These include the style and comprehensiveness of presenting model details. Specifically, all necessary mathematical equations, as well as parameter values of the equations and the initial values of variables, should be given precisely. We expect that the informatics and large-scale simulation tools presently under development in big neuroscience projects (see, e.g., Markram et al. 2015) worldwide will partially help solve the current challenges in model validation and evaluation—also in the field of computational glioscience.

In order to develop a comprehensive understanding of the relationship between astrocytes and neurons in the future, mathematical modeling across different levels and scales of the brain will undoubtedly be required. This will not only involve developing new models for different levels of physical organization, but also well-grounded theory for how to link the phenomena measured at different levels together. Most importantly, future computational work should also strive to incorporate the state-of-the-art wet-laboratory studies to build models that reflect the biological realism.

In conclusion, it is quite evident based on recent *in vitro* and *in vivo* findings (see, e.g., Volterra et al. 2014; Magistretti and Allaman 2015) that astrocytes are able to exert their effects on a variety of events in the brain functions. It will be of great interest to learn at which developmental phase and in which experimental animals or conditions the functional capabilities of astrocytes are recruited. Due to the complexity of the issue, there is a great demand for detailed, integrative computational models at multiple spatial and temporal scales. We hope that our critical review of computational glioscience literature could promote this demand and give the state of the art in neuron-glia modeling by categorizing and analyzing the existing models, as well as pointing out some challenges for future work. Ultimately, addressing all the above issues is expected to advance our understanding of astrocytic contribution in synaptic information transmission, plasticity, and learning.

Acknowledgements The research leading to these results has received partial funding from the European Union Seventh Framework Programme (FP7) under grant agreement No. 604102 (HBP), European Union's Horizon 2020 research and innovation programme under grant agreement No. 720270, and Academy of Finland (decision Nos. 297893, 315795, and 320072). The authors wish to

thank Tampere University of Technology Graduate School, Emil Aaltonen Foundation, The Finnish Concordia Fund, and Ulla Tuominen Foundation for support for R.H. This work was submitted on October 25th, 2015, and accepted on January 5th, 2016.

References

- Aguado F, Espinosa-Parrilla JF, Carmona MA, Soriano E (2002) Neuronal activity regulates correlated network properties of spontaneous calcium transients in astrocytes *in situ*. *J Neurosci* 22(21):9430–9444
- Agulhon C, Petracic J, McMullen AB, Sweger EJ, Minton SK, Taves SR, Casper KB, Fiacco TA, McCarthy KD (2008) What is the role of astrocyte calcium in neurophysiology? *Neuron* 59(6):932–946
- Agulhon C, Sun M-Y, Murphy T, Myers T, Lauderdale K, Fiacco TA (2012) Calcium signaling and gliotransmission in normal vs. reactive astrocytes. *Front Pharmacol* 3:139
- Allam SL, Ghaderi VS, Bouteiller J-MC, Legendre A, Ambert N, Greget R, Bischoff S, Baudry M, Berger TW (2012) A computational model to investigate astrocytic glutamate uptake influence on synaptic transmission and neuronal spiking. *Front Comput Neurosci* 6:70
- Allegrini P, Fronzoni L, Pirino D (2009) The influence of the astrocyte field on neuronal dynamics and synchronization. *J Biol Phys* 35(4):413–423
- Amiri M, Bahrami F, Janahmadi M (2011a) Functional modeling of astrocytes in epilepsy: a feedback system perspective. *Neural Comput Appl* 20(8):1131–1139
- Amiri M, Montaseri G, Bahrami F (2011b) On the role of astrocytes in synchronization of two coupled neurons: a mathematical perspective. *Biol Cybern* 105(2):153–166
- Amiri M, Bahrami F, Janahmadi M (2012a) Functional contributions of astrocytes in synchronization of a neuronal network model. *J Theor Biol* 292:60–70
- Amiri M, Bahrami F, Janahmadi M (2012b) Modified thalamocortical model: a step towards more understanding of the functional contribution of astrocytes to epilepsy. *J Comput Neurosci* 33(2):285–299
- Amiri M, Bahrami F, Janahmadi M (2012c) On the role of astrocytes in epilepsy: a functional modeling approach. *Neurosci Res* 72(2):172–180
- Amiri M, Hosseini Mardi N, Bahrami F, Janahmadi M (2013a) Astrocyte-neuron interaction as a mechanism responsible for generation of neural synchrony: a study based on modeling and experiments. *J Comput Neurosci* 34(3):489–504
- Amiri M, Montaseri G, Bahrami F (2013b) A phase plane analysis of neuron-astrocyte interactions. *Neural Netw* 44:157–165
- Amiri M, Amiri M, Nazari S, Faez K (2016) A new bio-inspired stimulator to suppress hyper-synchronized neural firing in a cortical network. *J Theor Biol* 410:107–118
- Atri A, Amundson J, Clapham D, Sneyd J (1993) A single-pool model for intracellular calcium oscillations and waves in the *Xenopus laevis* oocyte. *Biophys J* 65(4):1727–1739
- Aubert A, Pellerin L, Magistretti PJ, Costalat R (2007) A coherent neurobiological framework for functional neuroimaging provided by a model integrating compartmentalized energy metabolism. *Proc Natl Acad Sci U S A* 104(10):4188–4193
- Barrack DS, Thul R, Owen MR (2014) Modelling the coupling between intracellular calcium release and the cell cycle during cortical brain development. *J Theor Biol* 347:17–32
- Barrack DS, Thul R, Owen MR (2015) Modelling cell cycle synchronisation in networks of coupled radial glial cells. *J Theor Biol* 377:85–97
- Bellinger S (2005) Modeling calcium wave oscillations in astrocytes. *Neurocomputing* 65–66:843–850
- Bennett MR, Farnell L, Gibson WG (2005) A quantitative model of purinergic junctional transmission of calcium waves in astrocyte networks. *Biophys J* 89(4):2235–2250

- Bennett MR, Buljan V, Farnell L, Gibson WG (2006) Purinergic junctional transmission and propagation of calcium waves in spinal cord astrocyte networks. *Biophys J* 91(9):3560–3571
- Bennett MR, Farnell L, Gibson WG (2008a) Origins of blood volume change due to glutamatergic synaptic activity at astrocytes abutting on arteriolar smooth muscle cells. *J Theor Biol* 250(1):172–185
- Bennett MR, Farnell L, Gibson WG (2008b) Origins of the BOLD changes due to synaptic activity at astrocytes abutting arteriolar smooth muscle. *J Theor Biol* 252(1):123–130
- Bennett MR, Farnell L, Gibson WG (2008c) A quantitative model of cortical spreading depression due to purinergic and gap-junction transmission in astrocyte networks. *Biophys J* 95(12):5648–5660
- Calvetti D, Cheng Y, Somersalo E (2015) A spatially distributed computational model of brain cellular metabolism. *J Theor Biol* 376:48–65
- Cannon RC, Gewaltig M-O, Gleeson P, Bhalla US, Cornelis H, Hines ML, Howell FW, Muller E, Stiles JR, Wils S, De Schutter E (2007) Interoperability of neuroscience modeling software: current status and future directions. *Neuroinformatics* 5(2):127–138
- Carmignoto G (2000) Reciprocal communication systems between astrocytes and neurones. *Prog Neurobiol* 62(6):561–581
- Chander BS, Chakravarthy VS (2012) A computational model of neuro-glio-vascular loop interactions. *PLoS ONE* 7(11):e48802
- Crook SM, Davison AP, Plesser HE (2013) Learning from the past: approaches for reproducibility in computational neuroscience. In: Bower JM (ed) 20 years of computational neuroscience. Springer, New York, pp 73–102
- De Pittà M, Brunel N (2016) Modulation of synaptic plasticity by glutamatergic gliotransmission: a modeling study. *Neural Plast.* 2016:7607924
- De Pittà M, Goldberg M, Volman V, Berry H, Ben-Jacob E (2009a) Glutamate regulation of calcium and IP₃ oscillating and pulsating dynamics in astrocytes. *J Biol Phys* 35(4):383–411, erratum 36:221–222 (2010)
- De Pittà M, Volman V, Levine H, Ben-Jacob E (2009b) Multimodal encoding in a simplified model of intracellular calcium signaling. *Cogn. Process.* 10(Suppl 1):S55–S70
- De Pittà M, Volman V, Berry H, Ben-Jacob E (2011) A tale of two stories: astrocyte regulation of synaptic depression and facilitation. *PLoS Comput. Biol.* 7(12):e1002293
- De Pittà M, Volman V, Berry H, Parpura V, Volterra A, Ben-Jacob E (2012) Computational quest for understanding the role of astrocyte signalling in synaptic transmission and plasticity. *Front. Comput. Neurosci.* 6:98
- De Pittà M, Brunel N, Volterra A (2016) Astrocytes: orchestrating synaptic plasticity? *Neuroscience* 323:43–61
- De Schutter E (2008) Why are computational neuroscience and systems biology so separate. *PLoS Comput. Biol.* 4(5):e1000078
- De Young GW, Keizer J (1992) A single-pool inositol 1,4,5-trisphosphate-receptor-based model for agonist-stimulated oscillations in Ca²⁺ concentration. *Proc Natl Acad Sci U S A* 89(20):9895–9899
- Di Garbo A (2009) Dynamics of a minimal neural model consisting of an astrocyte, a neuron, and an interneuron. *J Biol Phys* 35(4):361–382
- Di Garbo A, Barbi M, Chillemi S, Alloisio S, Nobile M (2007) Calcium signalling in astrocytes and modulation of neural activity. *Biosystems* 89(1–3):74–83
- Diekman CO, Fall CP, Lechleiter JD, Terman D (2013) Modeling the neuroprotective role of enhanced astrocyte mitochondrial metabolism during stroke. *Biophys J* 104(8):1752–1763
- DiNuzzo M, Gili T, Maraviglia B, Giove F (2011) Modeling the contribution of neuron-astrocyte cross talk to slow blood oxygenation level-dependent signal oscillations. *J Neurophysiol* 106(6):3010–3018
- Dronne M-A, Boissel J-P, Grenier E (2006) A mathematical model of ion movements in grey matter during a stroke. *J Theor Biol* 240(4):599–615

- Dupont G, Croisier H (2010) Spatiotemporal organization of Ca^{2+} dynamics: a modeling-based approach. *HFSP J* 4(2):43–51
- Dupont G, Goldbeter A (1993) One-pool model for Ca^{2+} oscillations involving Ca^{2+} and inositol 1, 4, 5-trisphosphate as co-agonists for Ca^{2+} release. *Cell Calcium* 14(4):311–322
- Dupont G, Lokenye EFL, Challiss RAJ (2011) A model for Ca^{2+} oscillations stimulated by the type 5 metabotropic glutamate receptor: an unusual mechanism based on repetitive, reversible phosphorylation of the receptor. *Biochimie* 93(12):2132–2138
- Edwards JR, Gibson WG (2010) A model for Ca^{2+} waves in networks of glial cells incorporating both intercellular and extracellular communication pathways. *J Theor Biol* 263(1):45–58
- Fellin T, Ellenbogen JM, De Pittà M, Ben-Jacob E, Halassa MM (2012) Astrocyte regulation of sleep circuits: experimental and modeling perspectives. *Front Comput Neurosci* 6:65
- Fink CC, Slepchenko B, Loew LM (1999) Determination of time-dependent inositol-1, 4, 5-trisphosphate concentrations during calcium release in a smooth muscle cell. *Biophys J* 77(1):617–628
- FitzHugh R (1961) Impulses and physiological states in theoretical models of nerve membrane. *Biophys J* 1(6):445–466
- Gerstner W, Kistler WM (2002) Spiking neuron models: single neurons, populations, plasticity. Cambridge University Press, Cambridge
- Giaume C, Venance L (1998) Intercellular calcium signaling and gap junctional communication in astrocytes. *Glia* 24(1):50–64
- Goldberg M, De Pittà M, Volman V, Berry H, Ben-Jacob E (2010) Nonlinear gap junctions enable long-distance propagation of pulsating calcium waves in astrocyte networks. *PLoS Comput Biol* 6(8):e1000909
- Gordleeva SY, Stasenko SV, Semyanov AV, Dityatev AE, Kazantsev VB (2012) Bi-directional astrocytic regulation of neuronal activity within a network. *Front Comput Neurosci* 6:92
- Goto I, Kinoshita S, Natsume K (2004) The model of glutamate-induced intracellular Ca^{2+} oscillation and intercellular Ca^{2+} wave in brain astrocytes. *Neurocomputing* 58–60:461–467
- Guthrie PB, Knappenberger J, Segal M, Bennett MVL, Charles AC, Kater SB (1999) ATP released from astrocytes mediates glial calcium waves. *J Neurosci* 19(2):520–528
- Haghiri S, Ahmadi A, Saif M (2016) VLSI implementable neuron-astrocyte control mechanism. *Neurocomputing* 214:280–296
- Haghiri S, Ahmadi A, Saif M (2017) Complete neuron-astrocyte interaction model: digital multiplierless design and networking mechanism. *IEEE Trans Biomed Circuits Syst* 11(1):117–127
- Halnes G, Østby I, Pettersen KH, Omholt SW, Einevoll GT (2013) Electrodiffusive model for astrocytic and neuronal ion concentration dynamics. *PLoS Comput Biol* 9(12):e1003386
- Hayati M, Nouri M, Haghiri S, Abbott D (2016) A digital realization of astrocyte and neural glial interactions. *IEEE Trans Biomed Circuits Syst* 10(2):518–529
- Hines ML, Morse T, Migliore M, Carnevale NT, Shepherd GM (2004) ModelDB: a database to support computational neuroscience. *J Comput Neurosci* 17(1):7–11
- Hituri K, Linne M-L (2013) Comparison of models for IP_3 receptor kinetics using stochastic simulations. *PLoS ONE* 8(4):e59618
- Hodgkin AL, Huxley AF (1952) A quantitative description of membrane current and its application to conduction and excitation in nerve. *J Physiol* 117(4):500–544
- Höfer T, Politi A, Heinrich R (2001) Intercellular Ca^{2+} wave propagation through gap-junctional Ca^{2+} diffusion: a theoretical study. *Biophys J* 80(1):75–87
- Höfer T, Venance L, Giaume C (2002) Control and plasticity of intercellular calcium waves in astrocytes: a modeling approach. *J Neurosci* 22(12):4850–4859
- Houart G, Dupont G, Goldbeter A (1999) Bursting, chaos and birhythmicity originating from self-modulation of the inositol 1, 4, 5-trisphosphate signal in a model for intracellular Ca^{2+} oscillations. *Bull Math Biol* 61(3):507–530
- Iacobas DA, Suadicani SO, Spray DC, Scemes E (2006) A stochastic two-dimensional model of intercellular Ca^{2+} wave spread in glia. *Biophys J* 90(1):24–41
- Izhikevich EM (2007) Dynamical systems in neuroscience. The MIT Press, Cambridge

- Jha BK, Jha A (2015) Two dimensional finite volume model to study the effect of ER on cytosolic calcium distribution in astrocytes. *Procedia Comput Sci* 46:1285–1293
- Jolivet R, Allaman I, Pellerin L, Magistretti PJ, Weber B (2010) Comment on recent modeling studies of astrocyte-neuron metabolic interactions. *J Cereb Blood Flow Metab* 30(12):1982–1986
- Jolivet R, Coggan JS, Allaman I, Magistretti PJ (2015) Multi-timescale modeling of activity-dependent metabolic coupling in the neuron-glia-vasculature ensemble. *PLoS Comput Biol* 11(2):e1004036
- Jung P, Cornell-Bell A, Madden KS, Moss F (1998) Noise-induced spiral waves in astrocyte syncytia show evidence of self-organized criticality. *J Neurophysiol* 79(2):1098–1101
- Kang M, Othmer HG (2009) Spatiotemporal characteristics of calcium dynamics in astrocytes. *Chaos* 19(3):037116
- Kazantsev VB (2009) Spontaneous calcium signals induced by gap junctions in a network model of astrocytes. *Phys Rev E* 79(1):010901
- Keener J, Sneyd J (1998) Mathematical physiology. Springer, Berlin
- Keener J, Sneyd J (2009) Mathematical physiology: I: cellular physiology. Springer, Berlin
- Komin N, Moein M, Ellisman MH, Skupin A (2015) Multiscale modeling indicates that temperature dependent $[Ca^{2+}]_i$ spiking in astrocytes is quantitatively consistent with modulated SERCA activity. *Neural Plast* 2015:683490
- Kuriu T, Kakimoto Y, Araki O (2015) Computational simulation: astrocyte-induced depolarization of neighboring neurons mediates synchronous UP states in a neural network. *J Biol Phys* 41:377–390
- Lallouette J, De Pittà M, Ben-Jacob E, Berry H (2014) Sparse short-distance connections enhance calcium wave propagation in a 3D model of astrocyte networks. *Front Comput Neurosci* 8:45
- Lavrentovich M, Hemkin S (2008) A mathematical model of spontaneous calcium (II) oscillations in astrocytes. *J Theor Biol* 251(4):553–560, corrigendum 260:332 (2009)
- Lemon G, Gibson WG, Bennett MR (2003) Metabotropic receptor activation, desensitization and sequestration-I: modelling calcium and inositol 1, 4, 5-trisphosphate dynamics following receptor activation. *J Theor Biol* 223(1):93–111
- Li Y-X, Rinzel J (1994) Equations for InsP3 receptor-mediated $[Ca^{2+}]_i$ oscillations derived from a detailed kinetic model: a Hodgkin-Huxley like formalism. *J Theor Biol* 166(4):461–473
- Li B, Chen S, Zeng S, Luo Q, Li P (2012) Modeling the contributions of Ca^{2+} flows to spontaneous Ca^{2+} oscillations and cortical spreading depression-triggered Ca^{2+} waves in astrocyte networks. *PLoS ONE* 7(10):e48534
- Li J, Tang J, Ma J, Du M, Wang R, Wu Y (2016a) Dynamic transition of neuronal firing induced by abnormal astrocytic glutamate oscillation. *Sci Rep* 6:32343
- Li J, Wang R, Du M, Tang J, Wu Y (2016b) Dynamic transition on the seizure-like neuronal activity by astrocytic calcium channel block. *Chaos Solitons Fractals* 91:702–708
- Li J-J, Du M-M, Wang R, Lei J-Z, Wu Y (2016c) Astrocytic gliotransmitter: diffusion dynamics and induction of information processing on tripartite synapses. *Int J Bifurcat Chaos* 26(8):1650138
- Linne M-L, Jalonen TO (2014) Astrocyte-neuron interactions: from experimental research-based models to translational medicine. *Prog Mol Biol Transl Sci* 123:191–217
- Liu Y, Li C (2013) Stochastic resonance in feedforward-loop neuronal network motifs in astrocyte field. *J Theor Biol* 335:265–275
- Liu J, Harkin J, Maguire LP, McDaid LJ, Wade JJ, Martin G (2016) Scalable networks-on-chip interconnected architecture for astrocyte-neuron networks. *IEEE Trans Circuits Syst I Reg Papers* 63(12):2290–2303
- López-Caamal F, Oyarzún DA, Middleton RH, García MR (2014) Spatial quantification of cytosolic Ca^{2+} accumulation in nonexcitable cells: an analytical study. *IEEE/ACM Trans Comput Biol Bioinform* 11(3):592–603
- MacDonald CL, Silva GA (2013) A positive feedback cell signaling nucleation model of astrocyte dynamics. *Front Neuroeng* 6:4

- MacDonald CL, Yu D, Buibas M, Silva GA (2008) Diffusion modeling of ATP signaling suggests a partially regenerative mechanism underlies astrocyte intercellular calcium waves. *Front Neuroeng* 1:1
- Magistretti PJ, Allaman I (2015) A cellular perspective on brain energy metabolism and functional imaging. *Neuron* 86(4):883–901
- Manninen T, Hituri K, Hellgren Kotaleski J, Blackwell KT, Linne M-L (2010) Postsynaptic signal transduction models for long-term potentiation and depression. *Front Comput Neurosci* 4:152
- Manninen T, Hituri K, Toivari E, Linne M-L (2011) Modeling signal transduction leading to synaptic plasticity: evaluation and comparison of five models. *EURASIP J Bioinf Syst Biol* 2011:797250
- Manninen T, Havela R, Linne M-L (2017) Reproducibility and comparability of computational models for astrocyte calcium excitability. *Front Neuroinform* 11:11
- Manninen T, Aćimović J, Havela R, Teppola H, Linne M-L (2018a) Challenges in reproducibility, replicability, and comparability of computational models and tools for neuronal and glial networks, cells, and subcellular structures. *Front Neuroinform* 12:20
- Manninen T, Havela R, Linne M-L (2018b) Computational models for calcium-mediated astrocyte functions. *Front Comput Neurosci* 12:14
- Markram H, Muller E, Ramaswamy S, Reimann MW, Abdellah M, Sanchez CA, Ailamaki A, Alonso-Nanclares L, Antille N, Arsever S et al (2015) Reconstruction and simulation of neocortical microcircuitry. *Cell* 163(2):456–492
- Matrosov VV, Kazantsev VB (2011) Bifurcation mechanisms of regular and chaotic network signaling in brain astrocytes. *Chaos* 21(2):023103
- Migliore M, Morse TM, Davison AP, Marenco L, Shepherd GM, Hines ML (2003) ModelDB: making models publicly accessible to support computational neuroscience. *Neuroinformatics* 1(1):135–139
- Min R, Santello M, Nevian T (2012) The computational power of astrocyte mediated synaptic plasticity. *Front Comput Neurosci* 6:93
- Morris C, Lecar H (1981) Voltage oscillations in the barnacle giant muscle fiber. *Biophys J* 35(1):193–213
- Nadkarni S, Jung P (2003) Spontaneous oscillations of dressed neurons: a new mechanism for epilepsy? *Phys Rev Lett* 91(26):268101
- Nadkarni S, Jung P (2004) Dressed neurons: modeling neural-glial interactions. *Phys Biol* 1(1):35
- Nadkarni S, Jung P (2005) Synaptic inhibition and pathologic hyperexcitability through enhanced neuron-astrocyte interaction: a modeling study. *J Integr Neurosci* 4(2):207–226
- Nadkarni S, Jung P (2007) Modeling synaptic transmission of the tripartite synapse. *Phys Biol* 4(1):1–9
- Nadkarni S, Jung P, Levine H (2008) Astrocytes optimize the synaptic transmission of information. *PLoS Comput Biol* 4(5):e1000088
- Naeem M, McDaid LJ, Harkin J, Wade JJ, Marsland J (2015) On the role of astroglial syncytia in self-repairing spiking neural networks. *IEEE Trans Neural Netw Learn Syst* 26(10):2370–2380
- Navarrete M, Araque A (2010) Endocannabinoids potentiate synaptic transmission through stimulation of astrocytes. *Neuron* 68(1):113–126
- Navarrete M, Perea G, de Sevilla DF, Gómez-Gonzalo M, Núñez A, Martín ED, Araque A (2012) Astrocytes mediate in vivo cholinergic-induced synaptic plasticity. *PLoS Biol* 10(2):e1001259
- Nazari S, Faez K, Karami E, Amiri M (2014) A digital neuromorphic circuit for a simplified model of astrocyte dynamics. *Neurosci Lett* 582:21–26
- Nazari S, Amiri M, Faez K, Amiri M (2015a) Multiplier-less digital implementation of neuron-astrocyte signalling on FPGA. *Neurocomputing* 164:281–292
- Nazari S, Faez K, Amiri M, Karami E (2015b) A digital implementation of neuron-astrocyte interaction for neuromorphic applications. *Neural Netw* 66:79–90
- Nazari S, Faez K, Amiri M, Karami E (2015c) A novel digital implementation of neuron-astrocyte interactions. *J Comput Electron* 14(1):227–239
- Newman EA, Zahs KR (1997) Calcium waves in retinal glial cells. *Science* 275(5301):844–847
- Nimmerjahn A (2009) Astrocytes going live: advances and challenges. *J Physiol* 587(8):1639–1647

- Nordlie E, Gewaltig M-O, Plesser HE (2009) Towards reproducible descriptions of neuronal network models. *PLoS Comput Biol* 5(8):e1000456
- Occhipinti R, Somersalo E, Calvetti D (2009) Astrocytes as the glucose shunt for glutamatergic neurons at high activity: an in silico study. *J Neurophysiol* 101(5):2528–2538
- Occhipinti R, Somersalo E, Calvetti D (2010) Energetics of inhibition: insights with a computational model of the human GABAergic neuron-astrocyte cellular complex. *J Cereb Blood Flow Metab* 30(11):1834–1846
- Oku Y, Fresemann J, Miwakeichi F, Hülsmann S (2016) Respiratory calcium fluctuations in low-frequency oscillating astrocytes in the pre-Bötzinger complex. *Respir Physiol Neurobiol* 226:11–17
- Olufsen MS, Whittington MA, Camperi M, Kopell N (2003) New roles for the gamma rhythm: population tuning and preprocessing for the beta rhythm. *J Comput Neurosci* 14(1):33–54
- Øyehaug L, Østby I, Lloyd CM, Omholt SW, Einevoll GT (2012) Dependence of spontaneous neuronal firing and depolarisation block on astroglial membrane transport mechanisms. *J Comput Neurosci* 32(1):147–165
- Panatier A, Vallée J, Haber M, Murai KK, Lacaille J-C, Robitaille R (2011) Astrocytes are endogenous regulators of basal transmission at central synapses. *Cell* 146(5):785–798
- Parpura V (2004) Glutamate-mediated bi-directional signaling between neurons and astrocytes. In: Hatton GI, Parpura V (eds) *Glial ↔ neuronal signaling*. Springer, Berlin, pp 365–395
- Parpura V, Basarsky TA, Liu F, Jeftnija K, Jeftnija S, Haydon PG (1994) Glutamate-mediated astrocyte-neuron signalling. *Nature* 369:744–747
- Pellerin L, Magistretti PJ (1994) Glutamate uptake into astrocytes stimulates aerobic glycolysis: a mechanism coupling neuronal activity to glucose utilization. *Proc Natl Acad Sci U S A* 91(22):10625–10629
- Perea G, Araque A (2007) Astrocytes potentiate transmitter release at single hippocampal synapses. *Science* 317(5841):1083–1086
- Peters O, Schipke CG, Hashimoto Y, Kettenmann H (2003) Different mechanisms promote astrocyte Ca^{2+} waves and spreading depression in the mouse neocortex. *J Neurosci* 23(30):9888–9896
- Pettinen A, Aho T, Smolander O-P, Manninen T, Saarinen A, Taattola K-L, Yli-Harja O, Linne M-L (2005) Simulation tools for biochemical networks: evaluation of performance and usability. *Bioinformatics* 21(3):357–363
- Pinsky PF, Rinzel J (1994) Intrinsic and network rhythmogenesis in a reduced Traub model for CA3 neurons. *J Comput Neurosci* 1(1):39–60
- Piri M, Amiri M, Amiri M (2015) A bio-inspired stimulator to desynchronize epileptic cortical population models: a digital implementation framework. *Neural Netw* 67:74–83
- Porto-Pazos AB, Veiguela N, Mesejo P, Navarrete M, Alvarellos A, Ibáñez O, Pazos A, Araque A (2011) Artificial astrocytes improve neural network performance. *PLoS ONE* 6(4):e19109
- Postnov DE, Ryazanova LS, Sosnovtseva OV (2007) Functional modeling of neural-glial interaction. *BioSystems* 89(1):84–91
- Postnov DE, Ryazanova LS, Brazhe NA, Brazhe AR, Maximov GV, Mosekilde E, Sosnovtseva OV (2008) Giant glial cell: new insight through mechanism-based modeling. *J Biol Phys* 34(3–4):441–457
- Postnov DE, Koreshkov RN, Brazhe NA, Brazhe AR, Sosnovtseva OV (2009) Dynamical patterns of calcium signaling in a functional model of neuron-astrocyte networks. *J Biol Phys* 35(4):425–445
- Ranjbar M, Amiri M (2015) An analog astrocyte-neuron interaction circuit for neuromorphic applications. *J Comput Electron* 14(3):694–706
- Ranjbar M, Amiri M (2016) Analog implementation of neuron-astrocyte interaction in tripartite synapse. *J Comput Electron* 15(1):311–323
- Reato D, Cammarota M, Parra LC, Carmignoto G (2012) Computational model of neuron-astrocyte interactions during focal seizure generation. *Front Comput Neurosci* 6:81
- Riera J, Hatanaka R, Ozaki T, Kawashima R (2011a) Modeling the spontaneous Ca^{2+} oscillations in astrocytes: inconsistencies and usefulness. *J Integr Neurosci* 10(4):439–473

- Riera J, Hatanaka R, Uchida T, Ozaki T, Kawashima R (2011b) Quantifying the uncertainty of spontaneous Ca^{2+} oscillations in astrocytes: particulars of Alzheimer's disease. *Biophys J* 101(3):554–564
- Roth BJ, Yagodin SV, Holtzclaw L, Russell JT (1995) A mathematical model of agonist-induced propagation of calcium waves in astrocytes. *Cell Calcium* 17(1):53–64
- Shigetomi E, Kracun S, Sofroniew MV, Khakh BS (2010) A genetically targeted optical sensor to monitor calcium signals in astrocyte processes. *Nat Neurosci* 13(6):759–766
- Shuai J-W, Jung P (2002) Stochastic properties of Ca^{2+} release of inositol 1, 4, 5-trisphosphate receptor clusters. *Biophys J* 83(1):87–97
- Silchenko AN, Tass PA (2008) Computational modeling of paroxysmal depolarization shifts in neurons induced by the glutamate release from astrocytes. *Biol Cybern* 98(1):61–74
- Skupin A, Kettenmann H, Falcke M (2010) Calcium signals driven by single channel noise. *PLoS Comput Biol* 6(8):e1000870
- Soleimani H, Bavandpour M, Ahmadi A, Abbott D (2015) Digital implementation of a biological astrocyte model and its application. *IEEE Trans Neural Netw Learn Syst* 26(1):127–139
- Somjen GG, Kager H, Wadman WJ (2008) Computer simulations of neuron-glia interactions mediated by ion flux. *J Comput Neurosci* 25(2):349–365
- Stamatakis M, Mantzaris NV (2006) Modeling of ATP-mediated signal transduction and wave propagation in astrocytic cellular networks. *J Theor Biol* 241(3):649–668
- Suffczynski P, Kalitzin S, Lopes Da Silva FH (2004) Dynamics of non-convulsive epileptic phenomena modeled by a bistable neuronal network. *Neuroscience* 126(2):467–484
- Tang J, Luo J-M, Ma J (2013) Information transmission in a neuron-astrocyte coupled model. *PLoS ONE* 8(11):e80324
- Tang J, Liu T-B, Ma J, Luo J-M, Yang X-Q (2016) Effect of calcium channel noise in astrocytes on neuronal transmission. *Commun Nonlinear Sci Numer Simul* 32:262–272
- Tewari S, Majumdar K (2012a) A mathematical model for astrocytes mediated LTP at single hippocampal synapses. *J Comput Neurosci* 33(2):341–370
- Tewari SG, Majumdar KK (2012b) A mathematical model of the tripartite synapse: astrocyte-induced synaptic plasticity. *J Biol Phys* 38(3):465–496
- Tewari S, Parpura V (2013) A possible role of astrocytes in contextual memory retrieval: an analysis obtained using a quantitative framework. *Front Comput Neurosci* 7:145
- Tewari S, Parpura V (2014) Data and model tango to aid the understanding of astrocyte-neuron signaling. *Front Comput Neurosci* 8:3
- Toivari E, Manninen T, Nahata AK, Jalonen TO, Linne M-L (2011) Effects of transmitters and amyloid-beta peptide on calcium signals in rat cortical astrocytes: Fura-2AM measurements and stochastic model simulations. *PLoS ONE* 6(3):e17914
- Topalidou M, Leblois A, Boraud T, Rougier NP (2015) A long journey into reproducible computational neuroscience. *Front Comput Neurosci* 9:30
- Traub RD, Wong RK, Miles R, Michelson H (1991) A model of a CA3 hippocampal pyramidal neuron incorporating voltage-clamp data on intrinsic conductances. *J Neurophysiol* 66(2):635–650
- Tsodyks MV, Markram H (1997) The neural code between neocortical pyramidal neurons depends on neurotransmitter release probability. *Proc Natl Acad Sci U S A* 94(2):719–723
- Ullah G, Jung P, Cornell-Bell AH (2006) Anti-phase calcium oscillations in astrocytes via inositol (1, 4, 5)-trisphosphate regeneration. *Cell Calcium* 39(3):197–208
- Ullah G, Cressman JR Jr, Barreto E, Schiff SJ (2009) The influence of sodium and potassium dynamics on excitability, seizures, and the stability of persistent states: II. Network and glial dynamics. *J Comput Neurosci* 26(2):171–183
- Valenza G, Pioggia G, Armato A, Ferro M, Scilingo EP, De Rossi D (2011) A neuron-astrocyte transistor-like model for neuromorphic dressed neurons. *Neural Netw* 24(7):679–685
- Volman V, Ben-Jacob E, Levine H (2007) The astrocyte as a gatekeeper of synaptic information transfer. *Neural Comput* 19(2):303–326

- Volman V, Bazhenov M, Sejnowski TJ (2012) Computational models of neuron-astrocyte interaction in epilepsy. *Front Comput Neurosci* 6:58
- Volman V, Bazhenov M, Sejnowski TJ (2013) Divide and conquer: functional segregation of synaptic inputs by astrocytic microdomains could alleviate paroxysmal activity following brain trauma. *PLoS Comput Biol* 9(1):e1002856
- Volterra A, Liaudet N, Savtchouk I (2014) Astrocyte Ca^{2+} signalling: an unexpected complexity. *Nat Rev Neurosci* 15(5):327–335
- Wade JJ, McDaid LJ, Harkin J, Crunelli V, Kelso JAS (2011) Bidirectional coupling between astrocytes and neurons mediates learning and dynamic coordination in the brain: a multiple modeling approach. *PLoS ONE* 6(12):e29445
- Wade J, McDaid L, Harkin J, Crunelli V, Kelso S (2012) Self-repair in a bidirectionally coupled astrocyte-neuron (AN) system based on retrograde signaling. *Front Comput Neurosci* 6:76
- Wade J, McDaid L, Harkin J, Crunelli V, Kelso S (2013) Biophysically based computational models of astrocyte neuron coupling and their functional significance. *Front Comput Neurosci* 7:44
- Wallach G, Lallouette J, Herzog N, De Pittà M, Jacob EB, Berry H, Hanein Y (2014) Glutamate mediated astrocytic filtering of neuronal activity. *PLoS Comput Biol* 10(12):e1003964
- Wang X, Lou N, Xu Q, Tian G-F, Peng WG, Han X, Kang J, Takano T, Nedergaard M (2006) Astrocytic Ca^{2+} signaling evoked by sensory stimulation in vivo. *Nat Neurosci* 9(6):816–823
- Wei F, Shuai J (2011) Intercellular calcium waves in glial cells with bistable dynamics. *Phys Biol* 8(2):026009
- Yang Y, Yeo CK (2015) Conceptual network model from sensory neurons to astrocytes of the human nervous system. *IEEE Trans Biomed Eng* 62(7):1843–1852
- Zeng S, Li B, Zeng S, Chen S (2009) Simulation of spontaneous Ca^{2+} oscillations in astrocytes mediated by voltage-gated calcium channels. *Biophys J* 97(9):2429–2437

Chapter 17

GECIquant: Semi-automated Detection and Quantification of Astrocyte Intracellular Ca²⁺ Signals Monitored with GCaMP6f



Sharmila Venugopal, Rahul Srinivasan and Baljit S. Khakh

Abstract Astrocytes display diverse and frequent intracellular Ca²⁺ fluctuations that are separable by virtue of their location within the cells, their magnitude, and their duration. Recently, the study of astrocyte Ca²⁺ signaling has rapidly advanced by the availability of genetically encoded Ca²⁺ indicators (GECIs) such as GCaMP3 and GCaMP6. The systematic use of GECIs is beginning to reveal the rules for astrocyte engagement within neural circuits in brain slices and *in vivo*. However, the richness and high numbers of Ca²⁺ signals that have been observed necessitate their routine detection within the complex morphology of astrocytes. To this end, in this chapter, we describe the development and features of GECIquant software that permits the semi-automated detection and quantification of astrocyte Ca²⁺ signals. Biological insights afforded by the use of GECIs and GECIquant are also described.

Keywords GECI · GCaMP · GECIquant · Calcium · Astrocytes · Imaging
Ca²⁺ microdomains · Local waves · Soma · Territory

Sharmila Venugopal and Rahul Srinivasan contributed equally.

B. S. Khakh (✉)

Department of Physiology, David Geffen School of Medicine, University of California Los Angeles, 10833 Le Conte Avenue, 53-263 CHS, Los Angeles, CA 90095–1751, USA
e-mail: bkhakh@mednet.ucla.edu

B. S. Khakh

Department of Neurobiology, David Geffen School of Medicine,
Los Angeles, CA, USA

S. Venugopal (✉)

Department of Integrative Biology & Physiology, Division of Life Sciences,
University of California Los Angeles, 621 Charles E Young Dr South, Los Angeles, CA 90095-1751, USA
e-mail: vsharmila@ucla.edu

R. Srinivasan (✉)

Department of Neuroscience and Experimental Therapeutics, Texas A&M University College of Medicine, Mail Stop 1359, 8447 Riverside Pkwy, Bryan, TX 77807-3260, USA
e-mail: rahulsrinivasan@medicine.tamhsc.edu

17.1 Introduction

Calcium ions (Ca^{2+}) play numerous fundamental roles in biology (Clapham 2007). In the nervous system, neurons use Ca^{2+} as a key intracellular messenger for a variety of processes including regulation of gene expression, modulation of cellular excitability, neurotransmitter release, and synaptic plasticity (Berridge 1998). In contrast, much less is known about Ca^{2+} signaling in astrocytes, a type of glial cell, even though it is estimated that the adult human brain contains equal numbers of neurons and glia (Bahney and von Bartheld 2014; Azevedo et al. 2009). The discovery of intracellular Ca^{2+} fluctuations within astrocytes in the early 1990s triggered renewed interest in these cells, specifically with regards to the properties of Ca^{2+} signals and their possible functional roles within neural circuits. In landmark papers, the Smith laboratory and others showed that cultured astrocytes responded to extracellular glutamate with rapid and oscillatory elevations of intracellular free Ca^{2+} concentration (Cornell-Bell et al. 1990; Dani et al. 1992; Charles et al. 1991). This breakthrough observation, and thought-provoking essays by Smith on the possible functions of astrocyte Ca^{2+} signals for brain function and information processing (Smith 1992, 1994) ushered in an era of intense research which explored astrocyte Ca^{2+} signals in detail in cell cultures, within brain slices and more recently *in vivo*. However, this halcyon period was followed by intense debate on the physiological function of astrocyte Ca^{2+} signals for the regulation of neurons and blood vessels.

The term Ca^{2+} excitability (Smith 1992, 1994) has been frequently used to refer to the possibility that Ca^{2+} signals within astrocytes may be instructive for the regulation of other cells (e.g., neurons). However, it remains to be determined how universally astrocyte Ca^{2+} signals are physiologically utilized to regulate neurons and other cells in an activity and Ca^{2+} -dependent manner. Notwithstanding, astrocyte Ca^{2+} signals are implicated in diverse processes such as the regulation of neurotransmitter release probability at single synapses (Di Castro et al. 2011; Panatier et al. 2011), modulation of synaptic long-term potentiation (Henneberger et al. 2010; Shigetomi et al. 2013a), regulation of brain blood flow by controlling blood vessel diameter (Attwell et al. 2010), regulation of astrocyte morphology dynamics (Bernardinelli et al. 2014; Molotkov et al. 2013; Perez-Alvarez et al. 2014), control of K^+ buffering (Filosa et al. 2006), modulation of neurotransmitter clearance (Shigetomi et al. 2012), control of neuronal synchronization (Sasaki et al. 2014), cortical UP states (Poskanzer and Yuste 2011), neuronal rhythrogenesis (Morquette 2015), and axonal action potential broadening (Sasaki et al. 2011). Some of these physiological responses are now well accepted, while others represent active areas of ongoing research, and yet others are hotly debated (Khakh and McCarthy 2015). We do not discuss or consider gliotransmission in any mechanistic detail in this chapter, because the evidence for and against has been reviewed extensively several times (Araque et al. 2014; Nedergaard and Verkhratsky 2012), and little new information has emerged to resolve the impasse. Instead, we focus on the properties of astrocyte Ca^{2+} signals, which have been studied using organic Ca^{2+} indicator dyes and genetically encoded Ca^{2+} indicators (GECIs). The relative merits of studying astrocytes with organic Ca^{2+}

indicator dyes and/or GECIs have been reviewed (Khakh and McCarthy 2015; Tong et al. 2013; Volterra et al. 2014; Li et al. 2013). We suggest that GECIs are the current tools of choice (Khakh and Sofroniew 2015).

Intracellular Ca^{2+} fluxes in astrocytes in live brain slices and *in vivo* appear as slow, large events encompassing the soma and primary processes, called global waves, expanding signals within astrocyte territories, called local waves, and fast, small ($\sim 4 \mu\text{m}^2$) highly localized Ca^{2+} transients in astrocyte territories, called microdomains. Such diverse Ca^{2+} signals are observed both in live brain slices and *in vivo* (Srinivasan et al. 2015). Measurement of these diverse Ca^{2+} signals can offer critical insight into the physiological roles of astrocytes in the nervous system. Ca^{2+} signals are particularly informative in electrically non-exitable astrocytes, providing an important readout of their potential signaling in relation to neuronal activity (Khakh and McCarthy 2015). Advances in the detection of Ca^{2+} signals using organic Ca^{2+} indicator dyes and more recently by using genetically encoded Ca^{2+} indicators (GECIs) (Tong et al. 2013) have resulted in high-content information-rich datasets. For example, fast GECIs such as GCaMP6f (Chen et al. 2013) revealed an unexpected diversity and spatiotemporal complexity of Ca^{2+} signals in astrocyte processes (Srinivasan et al. 2015; Shigetomi et al. 2010, 2013b). Detection and analyses of such complex signals are time-consuming and subject to user bias, which necessitates automation of these steps. To address this need, we recently developed a software program GECIquant that formalizes a standard set of image processing steps in the detection of astrocyte Ca^{2+} signals from confocal image stacks. Significant improvements in the spatiotemporal resolution of GECIs to record astrocyte Ca^{2+} signals as well as automation of Ca^{2+} signal detection and analyses together have laid the foundation for developing quantitative methods and mechanistic computational models to understand correlative activity of astrocytes and neurons both *in vitro* and *in vivo* (Khakh and McCarthy 2015; Tong et al. 2013; Khakh and Sofroniew 2015).

In this chapter, we describe semi-automated detection and analyses of GECI-detected astrocyte Ca^{2+} signals and discuss how this approach has been useful in time-efficient classification of spatiotemporal Ca^{2+} signal diversity within single astrocytes. We focus on the details of the program, which has been shared with researchers as part of our published work (Srinivasan et al. 2015) and can be freely downloaded from the World Wide Web to enable wider use and direct comparison of results from other groups, as well as for future improvements.

17.2 Detection and Analyses of Ca^{2+} Fluxes Using GECIquant

The GECIquant program for semi-automated detection of astrocyte Ca^{2+} signals is developed using the open source *ImageJ* image analyses platform (Schneider et al. 2012; Schindelin et al. 2012). It is implemented using *ImageJ* script language and runs as a plugin on *ImageJ* versions greater than 1.48 s with Windows and Macintosh

computers. The input to GECIquant is a confocal fluorescence image stack (8, 16, or 32 bits) of arbitrary frame size with time as the third dimension (t-stack). It allows semi-automatic detection of regions of interest (ROI) containing fluorescence-based Ca^{2+} signals in the confocal image stack. Data outputs of GECIquant include average ROI intensity, ROI areas, and centroid distances of each ROI from a reference ROI. Graphical outputs of GECIquant include ROI intensity kymographs and sub-stacks consisting of wave-like signals.

The average fluorescence signal intensity within a ROI is given by:

$$I(t)_{\text{ROI}} = \frac{\sum_{i=1}^N I_i}{N}$$

where $I(t)_{\text{ROI}}$ is the average of pixel intensities I_i of all the N pixels within that ROI and t is the time index of the image stack. These average ROI intensity values can be exported into analyses software such as Mini Analysis (Synaptosoft, Inc.) or Clampfit (Molecular Devices) as a time series (i.e., $I(t)$ versus t) for further detection and analyses of temporal features of Ca^{2+} signals such as event times, rise and decay rates. A Ca^{2+} event is defined as an all-or-none change in $I(t)_{\text{ROI}}$ above baseline (or a certain intensity threshold) in time. In the following sections, we describe the functional modules of GECIquant.

17.3 Functional Modules of GECIquant

The GECIquant program has three modules: (1) image pre-processing, (2) ROI detection, and (3) ROI feature extraction as shown in Fig. 17.1. Background subtraction is performed as a pre-processing step to improve signal-to-noise ratios and to remove fluorescence that is not of biological relevance. Detection of ROI consists of image segmentation using thresholding and object tracing. Subsequent ROI feature extraction involves measurement of signal intensity, area, and spatial criteria such as centroid distances of the detected ROI from a reference ROI. Each module is described in further detail below.

17.4 Background Subtraction

Background subtraction is an essential pre-processing step to improve signal-to-noise ratios by minimizing standing non-specimen fluorescence. First, the pixel intensities are averaged along the time axis to create a two-dimensional average intensity projection image of the t-stack. Upon visual inspection of the average pixel intensities, the user can then demarcate an area in the projected image that represents observed background intensities $I(x, y)_{\text{bck}}$ as shown in the schematic in Fig. 17.2a. This background area is propagated along each frame of the t-stack, and the average

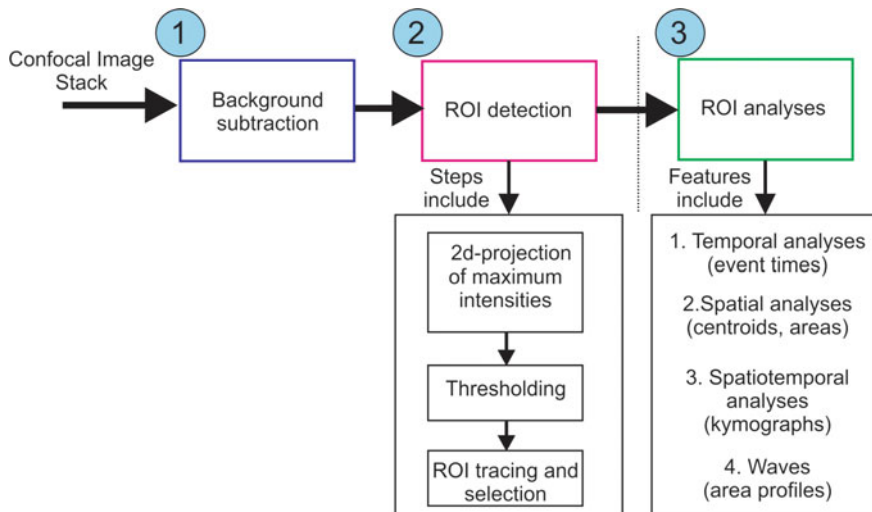


Fig. 17.1 Modules and features of *GECIquant*. Block diagram showing the three modules of the *GECIquant* program. Module 1 involves background subtraction from a confocal image stack. Module 2 involves ROI detection, and the underlying sequential set of steps is shown. Module 3 consists of ROI analyses to extract signal features including ROI time profiles, centroid distances and areas, graphical outputs such as kymographs and area profiles of Ca^{2+} waves

of pixel intensities in this area is calculated as the background value, $I(t)_{\text{avg_bck}}$ for each frame. This value is subtracted from all the pixels of the corresponding frame as given by the equation in Fig. 17.2b (also see legend). The resulting background subtracted image stack is used for ROI detection (see Fig. 17.2c, d for the effect of background subtraction on signal intensity).

17.5 ROI Detection

The key image processing steps involved in ROI detection include object thresholding (Fig. 17.3) and ROI tracing (Fig. 17.4). We implemented the thresholding step by first compressing the stack into a maximum intensity z-projection image. The resulting two-dimensional maximum intensity image is then thresholded using available methods in *ImageJ* to create a binary image that extracts objects (useful signal intensities) from noise/background. The binary information in the thresholded image is used to trace the object boundaries using the particle tracing functionality in *ImageJ*. Finally, an area criterion is applied to create a dataset of spatiotemporally relevant Ca^{2+} signals, which is added to the *ImageJ* ROI manager. In what follows, we describe these steps in further detail.

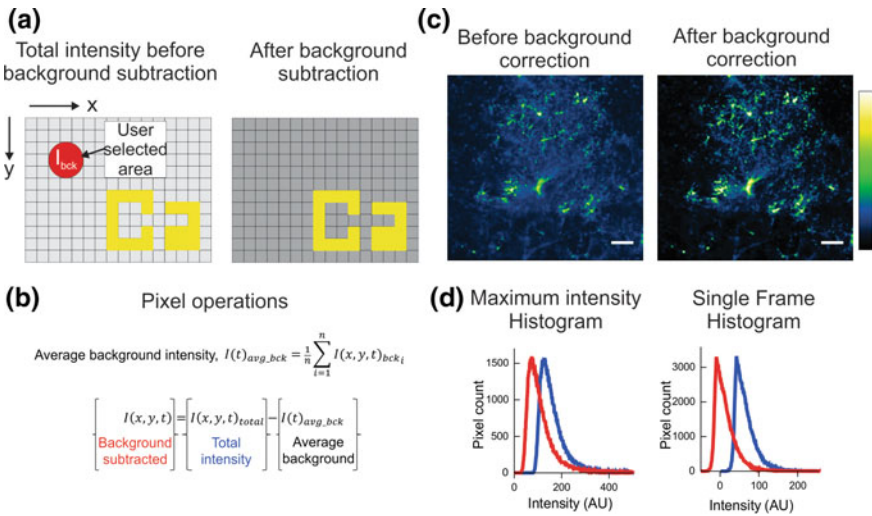


Fig. 17.2 Image background subtraction. **a** Schematic illustrating subtraction of background intensities. An average intensity projection of the t-stack is created in which the user marks a circular area as background with intensities, $I(x, y, t)_{bck}$. The mean of the pixel intensities $I(t)_{avg,bck}$ within this user selected area is subtracted from the total pixel intensity $I(x, y, t)_{total}$ at each time frame as given by the pixel operations in **(b)**. **c** Example showing the maximum intensity projection of an image stack before (*left*) and after (*right*) background subtraction. Scale bars on the image show 10 μm ; intensity calibration shows relative intensities from least intense (blue) to the most intense (white) signals. **d** The intensity histograms of before (*blue*) and after background subtraction (*red*) images are shown for the projection in ‘c’ in the *left* panel and for a single frame of the two images on the *right* panel

2-d projection of maximum intensities: As the first step in ROI detection, the maximum pixel intensities at each x - y coordinate along the time axis are projected on to a two-dimensional grayscale image (schematic in Fig. 17.3a and pixel operations in Fig. 17.3b). Example of maximum image intensities representing peak Ca^{2+} signals at each x - y pixel coordinate along the time axis for an astrocyte t-stack is shown in Fig. 17.3d (panel 1). As a pre-processing step before thresholding, we recommend using a low-pass filter (e.g., linear smoothing method), to smooth the maximum intensity projection. This method is available as a menu-driven function under the process tab in *ImageJ*. We have found this to be a useful step that particularly helps resolve localized Ca^{2+} microdomains from high-frequency noise.

Thresholding: The maximum intensity image of the t-stack is thresholded using a default thresholding method in *ImageJ* that is based on an iterative threshold selection algorithm (Ridler and Calvard 1978). Briefly, the threshold T is set to an initial value (say, 0) and is incremented in an iterative manner (Fig. 17.3c). In each iteration, the input image intensity histogram is divided into two groups containing pixel intensities $> T$ (object) and $\leq T$ (background). Averages of the two groups are calculated as A_O and A_B , respectively. The composite average of A_O and A_B is calculated, and

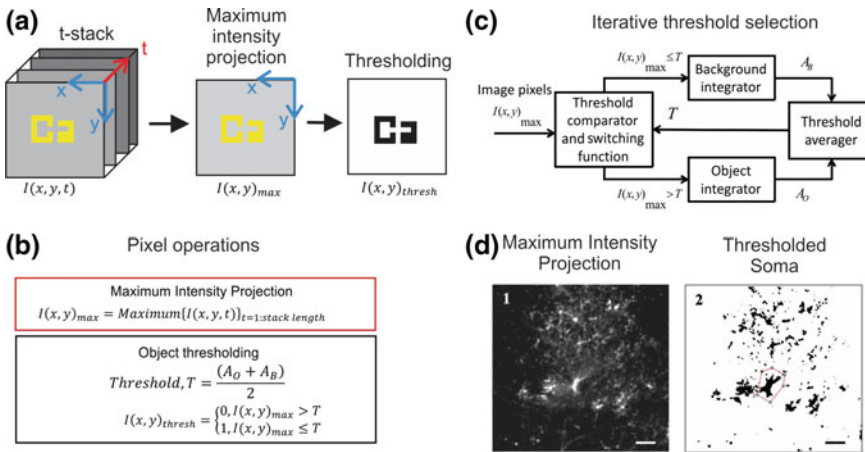


Fig. 17.3 Maximum intensity projection and thresholding. **a** Schematic showing the two-dimensional maximum intensity projection image $I(x, y)_{\max}$ of the image stack at each x - y pixel coordinate of the input image, $I(x, y, t)$. The object intensities $I(x, y)_{\text{thresh}}$ are in black in the thresholded binary image. **b** The pixel operations involved in the above steps are shown. A_o and A_B refer to averages of object and background pixels, respectively, obtained during the thresholding process. **c** The threshold T is estimated using the default algorithm in *ImageJ* that calculates the threshold using an iterative method as shown (also see text). **d** Figure shows an example maximum intensity projection image of an astrocyte t-stack (*left*) and the corresponding thresholded image (*right*) to demarcate astrocyte soma. The red polygon denotes an area drawn by the user to demarcate a region around the soma for thresholding. Scale bars are 10 μm in both panels

the value of T is incremented if it is less than the composite average. The iterations are terminated when $T \geq$ the composite average and the final threshold T is set to this composite average value (Fig. 17.3b). This threshold value can be re-adjusted in a user-interactive manner. However, note that the object intensities are typically limited to upper one-third of the distribution of maximum pixel intensities. A two-dimensional thresholded binary image is thus created with objects in black (pixel value 0) and background in white (pixel value 1). An example thresholded image of an astrocyte is shown in Fig. 17.3d highlighting the somata.

ROI tracing and selection: The binary image from the above step is then used for object tracing. ROIs are traced using the automatic ‘particle analyzer’ functionality in *ImageJ* (see Fig. 17.4a for functions/classes used) (Smith 1992; Di Castro et al. 2011). This built-in functionality implements a combination of computer vision and edge detection algorithms using simple edge description such as an intensity change from 0 to 1. The particle analyzer scans the thresholded image pixels one row at a time until an edge/border is detected. Once an object border is detected, the wand tool in *ImageJ* outlines the object. The object pixels are termed ‘inside,’ and background pixels are termed ‘outside’ pixels (Fig. 17.4b). Object outlining is performed by walking along the border/edge between an inside and outside pixel from one vertex to the next. A vertex is the intersection of four pixels as shown Fig. 17.4c. First, the ‘start’ pixel to

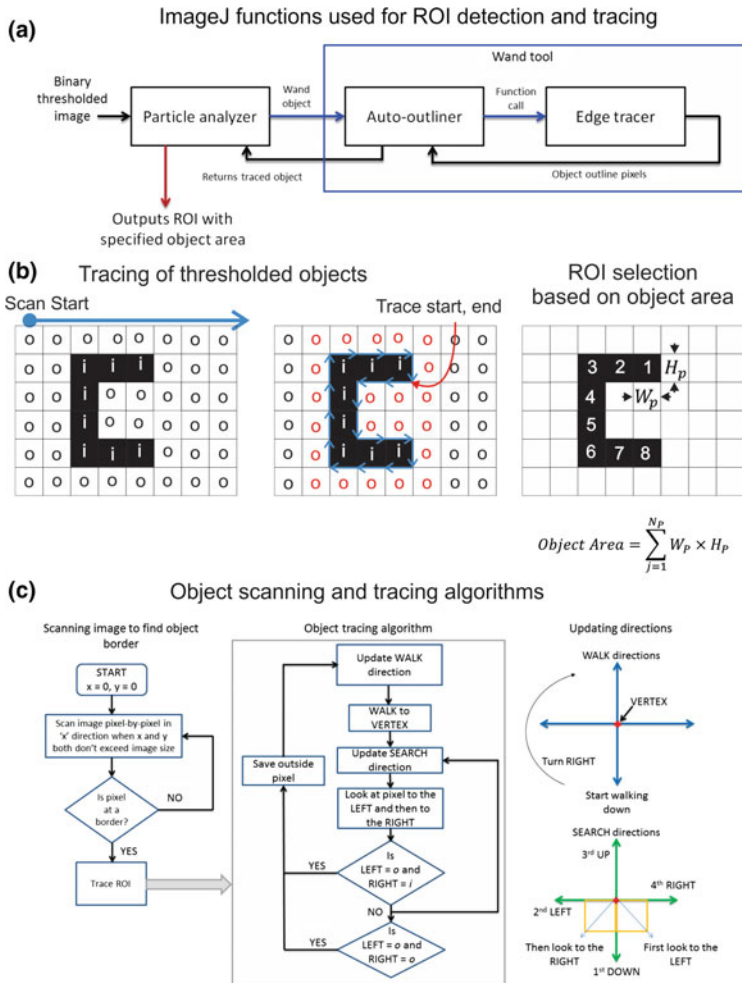


Fig. 17.4 ROI tracing algorithm. **a** Block diagram showing the *ImageJ* functions/classes used in *GECIquant* for object tracing and area-based selection. **b** Schematic showing the steps involved in object tracing. *Left*: The object pixels are marked inside pixels, ‘i’, and the background pixels are marked outside pixels, ‘o’. The pixel scan direction is shown by the blue line starting at the top-left pixel at coordinates (0, 0). *Middle*: The vertex at which tracing begins and ends is highlighted by the red curved arrow. The outline pixels of the traced object in black are marked as ‘o’ in red. *Right*: The resulting object’s area is calculated by summing the pixel areas covered by the detected object as given by the area equation, where W_P is the pixel width, H_P is the pixel height, and N_P represents the total number of pixels in the detected object. If the object area is within the range area set by the user apriori, then the program saves it as a ROI for further analyses. **c** The left panel shows a flow chart of the algorithm used for tracing the objects by the ROI detection and tracing functions in *ImageJ*. On the right, a vertex at which edge search is being performed is highlighted in red. The arrows show ‘walk’ and ‘search directions’. The yellow squares are pixels to the left and right of the vertex at which edge search is being performed

begin object tracing is resolved. To do so, the wand tool continues to scan the inside pixels along a row until it encounters a border pixel with intensity change from 0 to 1. Tracing starts at the vertex at this border pixel. To move from one vertex to the next, the tracer updates the ‘walking’ direction. The walking directions are UP, DOWN, LEFT, and RIGHT. The tracer always walks such that there is an outside pixel to the left and an inside pixel to the right of the walking direction. When at a vertex, there are four search (or pixel) directions similar to the walking directions. The tracer looks at the pixel to the LEFT and then to the RIGHT in the walking direction first. If a border is detected (LEFT = outside and RIGHT = inside), the pixel to the left is saved in the outline pixel array. A flow diagram is shown in Fig. 17.4c (*left panel*). The search continues by suitably updating the walking and searching directions. During a search, if no border is detected, then a clockwise turn is made at the same vertex and the search is continued until a border is detected. Also, if a corner pixel is encountered (i.e., LEFT = RIGHT = outside), the corresponding pixel is saved in the outline pixel array. Tracing ends when a clockwise loop is complete, i.e., when the start and end vertices are the same. The particle analyzer then computes the ROI area by summing the square pixel area covered by each ROI. The user interface of *GECIquant* allows the user to specify an area range for the ROI. Such area criteria are used to distinguish different compartments of an astrocyte/neuron such as somatic versus extra-somatic. The area constraints are passed as arguments to the particle analyzer function that selects only those ROIs that meet the preset area criteria to be included in the *ImageJ* ROI manager for further analyses.

The above technical details of object thresholding and object tracing algorithms are included here for completeness. An end user interested in using these methods for ROI detection may only be concerned with the accuracy of the approach. To address this, we have further tested and verified the resolution and accuracy of the area of detected ROIs using standard specimens such as the quantum blinking dots.

17.6 ROI Analyses

Temporal analyses: For each ROI, the temporal profile of Ca^{2+} signal intensities are calculated at each time frame as the average of pixel intensities that the ROI encompasses and is calculated as follows:

$$\left[\left\{ I(t)_k = \frac{1}{n} \sum_{i=1}^n R(t)_{(x_i, y_i)} \right\}_{t=1 \dots L} \right]_{k=1 \dots N}$$

where $I(t)_k$ is the average intensity of the k^{th} ROI, t is the time index of the image stack, n is the number of pixels in k^{th} ROI, $R(t)_{(x_i, y_i)}$ is the pixel intensity at coordinates (x, y) of the image stack at the t^{th} frame, and i is the index of the pixel in an array of n pixels. The image stack length is L , and the total number of ROI is N . The resultant ROI time profile is updated on the *ImageJ* ‘results’ window.

Spatial analyses: The spatial profiles of ROI in astrocyte processes are characterized by two features, namely ROI area and centroid distances from the somatic ROI.

- (i) ROI area: The area of each ROI in μm^2 is given by the sum of the squared pixels times the pixel calibration in microns.

$$A_{\text{ROI}} = \text{Total number of pixels in the ROI} \times \text{pixel width} \times \text{pixel height}$$

- (ii) Centroids and centroid distances: For each ROI, its centroid is calculated as the average of the (x, y) pixel coordinates as follows:

$$\left[C_k = \left(\frac{1}{m_k} \sum_{i=1}^{m_k} x_i, \frac{1}{m_k} \sum_{i=1}^{m_k} y_i \right) \right]_{k=1..N}$$

where C_k is the centroid of the k^{th} ROI, and m_k is the total number of pixels in the corresponding ROI, (x_i, y_i) are the i^{th} coordinates of the k^{th} ROI and N is the total number of ROI. The Euclidean distances from the reference centroid (e.g., somatic ROI centroid) to every other ROI (e.g., centroids of extra-somatic ROIs) are determined as below:

$$\left[d_k = \sqrt{(X_{\text{soma}} - X_k)^2 + (Y_{\text{soma}} - Y_k)^2} \right]_{k=1..(N-1)}$$

where d_k is the distance of the centroid (X_k, Y_k) of k^{th} ROI from the soma centroid $(X_{\text{soma}}, Y_{\text{soma}})$ and N is the total number of ROI.

17.7 Detection and Analyses of Genetically Encoded Astrocyte Ca^{2+} Signals Using *GECIquant*

1. Diversity of GCaMP6f encoded astrocyte Ca^{2+} signals detected using *GECIquant*

Using *GECIquant*, we were able to detect and discriminate three types of GCaMP6f encoded Ca^{2+} signals in hippocampal CA1 astrocytes *in vitro* (Fig. 17.5) and in cortical astrocytes *in vivo* (Fig. 17.6). Note that the microdomains and waves have non-overlapping and distinct spatial characteristics but occur randomly throughout the astrocyte territory. Detection of each of these three types of signals was enabled by identifying a suitable signal threshold that was approximately near the upper one-third of the intensity values. Often, this criterion can fail to detect considerable numbers and/or the expanse of less

intense microdomain signals since the higher intensity somatic signals predominate the upper one-third intensity values. To enable consistent detection of less intense peripheral Ca^{2+} signals, object thresholding can be performed in separate runs for detection of somatic versus peripheral waves and microdomain ROIs. During the detection of peripheral astrocyte Ca^{2+} signals, the somatic intensities can be set to zero using the ‘set’ function in the ‘process’ tab of *ImageJ*, such that the intensity histogram used for thresholding objects in the periphery would reflect the object intensities specifically in these compartments.

2. ROI intensity kymographs

Although Ca^{2+} signals in the periphery (microdomains and waves) are distinct from somatic Ca^{2+} fluxes, GECIquant creates kymographs for visualization of spatiotemporal correlations between these signals. Using the centroid distances from soma, distance-intensity kymographs can be generated for waves and microdomain signals. Each ROI is represented as a pixel row in the kymograph, and the temporal profile of intensity changes within a ROI is represented as graded colors using standard colormaps available in *ImageJ*. The pixel rows represent ROIs rank ordered based on their distance from a reference ROI (e.g., soma). This distance is calculated as the Euclidean distance from the peripheral ROI centroid to the soma centroid as described earlier. The kymograph in Fig. 17.7a illustrates that waves and microdomains in close proximity to soma show signal intensity similar to the somatic ROI than those farther from the soma. This correlation is further enhanced during bath application of endothelin (200 nM) that enhances somatic signal by Ca^{2+} release from intracellular stores (Srinivasan et al. 2015).

3. Characterization of wave-like expanding signals

ROI area is considered as the distinctive criterion to segregate waves from microdomains during ROI detection (Srinivasan et al. 2015). Additionally, waves also presented spatiotemporal dynamics (wave patterns). To begin characterization of such wave patterns, the *GECIquant* program creates sub-stacks that encompass the temporal sequence of a wave-like pattern. Within the sub-stack, the spatial dynamics of the expansion and contraction of the wave-like pattern can be quantified as changes in ROI area over time. The user interface allows specification of various parameters for sub-ROI detection within the sub-stack including image calibration, sub-stack START and STOP frames with respect to the original stack and an area range for the sub-ROI. The image processing steps involved in the detection of sub-ROI of the expanding signal are the same as described earlier for ROI detection. An example of a wave profile detected using *GECIquant* is shown in Fig. 17.7b, and the corresponding area profile is shown in Fig. 17.7c.

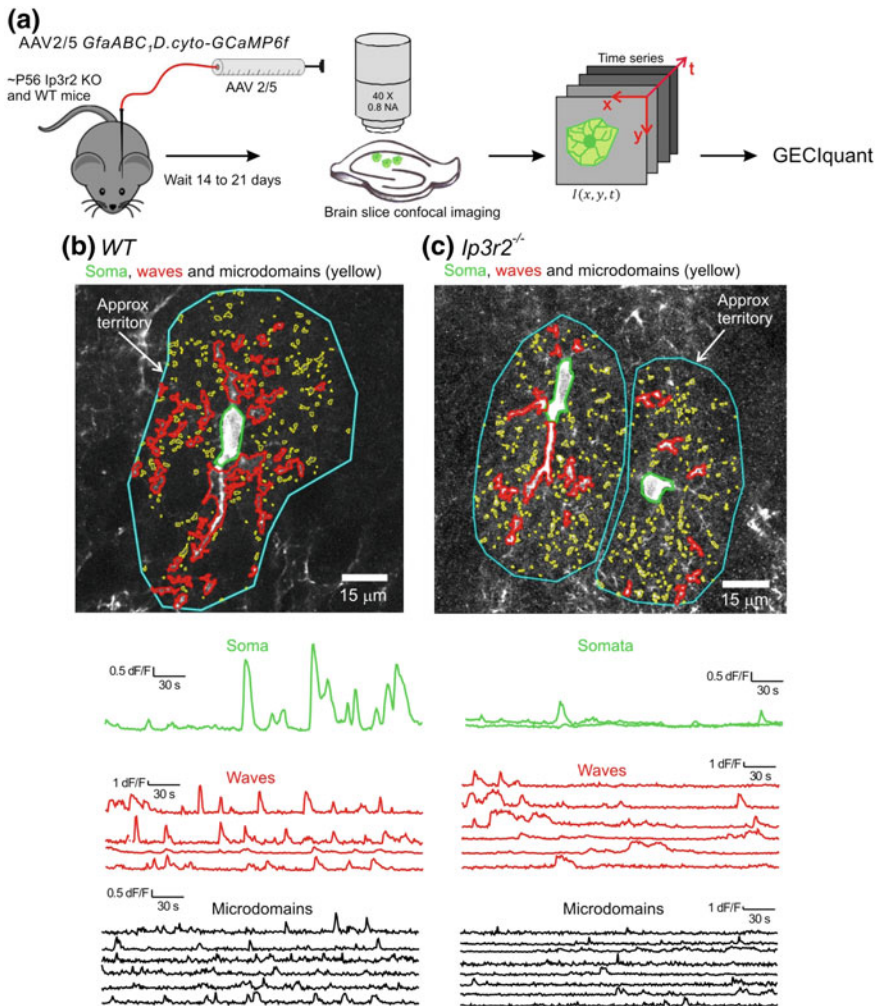


Fig. 17.5 Detection of diverse in vitro Ca^{2+} fluctuations in hippocampal astrocytes from wild-type (WT) and *I�3r2^{-/-}* mice using *GECIquant*. **a** Schematic illustrating the experimental approach. **b** Representative images and traces for Ca^{2+} fluctuations measured in an astrocyte from a WT mouse. Three predominant types of Ca^{2+} events are demarcated: somatic fluctuations (green), waves (red), and microdomains (yellow). Approximate territory boundaries are outlined in blue. **c** As in (b), but for two astrocytes from an *I�3r2^{-/-}* mouse. Figure reproduced from our past work (Srinivasan et al. 2015)

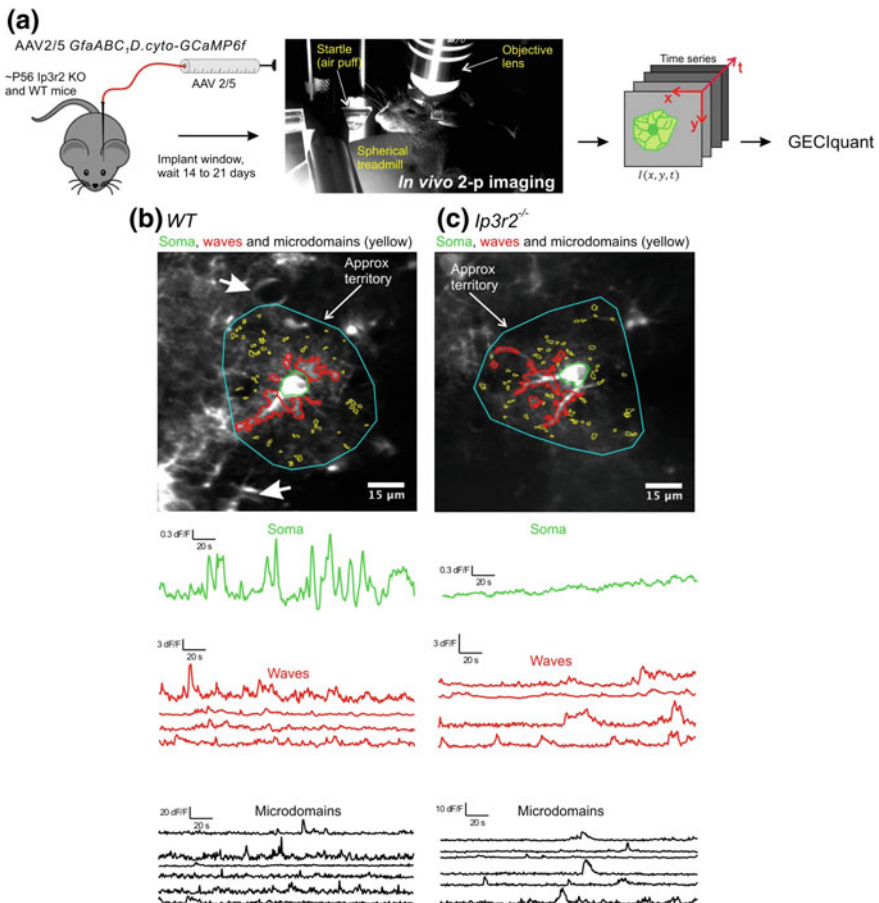


Fig. 17.6 Detection of diverse in vivo Ca^{2+} fluctuations in cortical astrocytes from WT and $I\ddot{\nu}3r2^{-/-}$ mice, using *GECIquant*. **a** Schematic illustrating the experimental approach for in vivo imaging in fully awake mice free to rest or run on a spherical treadmill (with no anesthesia). **b** Representative images and traces for Ca^{2+} fluctuations measured in a cortical astrocyte from a WT mouse. Three predominant types of Ca^{2+} event are shown: somatic, waves, and microdomains. Approximate territory boundaries are outlined in blue. **c** As in (b), but for an astrocyte from an $I\ddot{\nu}3r2^{-/-}$ mouse. Figure reproduced from our past work (Srinivasan et al. 2015)

17.8 Summary and Future Questions

We have summarized the development and main features of GECIquant software. The program which is freely available is published, and its use has already shed new light on aspects of astrocyte biology. Further expansion of GECIquant to incorporate additional features of relevance to astrocyte biology such as detection of coincident events in distinct ROIs or separate astrocytes will further expand its utility. Systematic

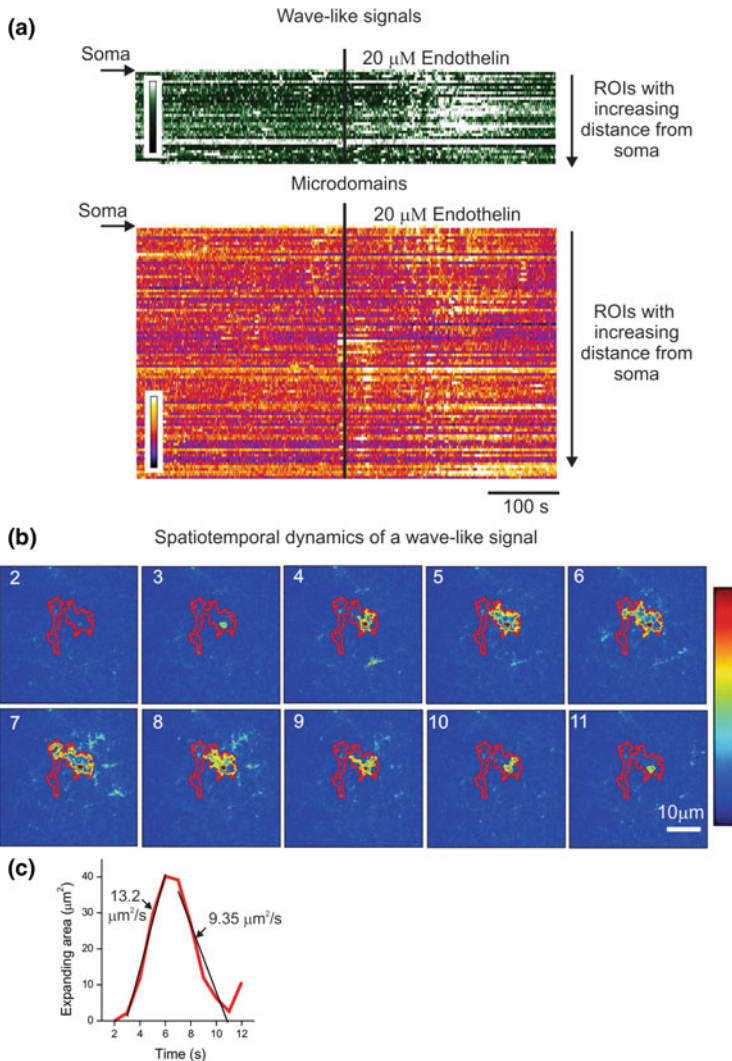


Fig. 17.7 Spatiotemporal analyses of microdomains and waves. **a** Kymographs showing intensity changes over time for each ROI; each pixel row in the graph corresponds to one ROI. Top panel shows wave ROIs, and bottom panel shows microdomain ROIs. In both kymographs, the first pixel row corresponds to the somatic ROI (indicated by the arrow) and each subsequent row corresponds to ROI in the astrocyte processes/branches rank ordered based on their centroid distance from the soma centroid to the ROI centroid. Intensity calibration shows relative intensities from least intense (dark colors) to the most intense (white) signals. **b** Image showing a sequence of time frames (frame numbers at the top-left corner) highlighting overlay of a wave ROI. In red is shown the detected wave ROI, in yellow are shown the changes in area covered by detectable Ca^{2+} signal intensities across ten consecutive frames (frame frequency = 1 Hz) within the image stack during a wave-like activity. Intensity calibration shows relative intensities from least intense (blue) to the most intense (red) signals. **c** Corresponding area changes in time is shown with linear fits indicating the rates of expansion and contraction of the wave-like activity

analyses of astrocyte Ca^{2+} signals promises to provide quantitative data on the basic properties of astrocyte Ca^{2+} signals, which will be required in computational studies of astrocyte Ca^{2+} dynamics and their functions within brain circuits. Many of these topics are covered in other chapters in this book.

Acknowledgements The authors are supported by the NINDS (BSK, SV), NIMH (BSK), and CHDI Foundation (BSK) Awards.

References

- Araque A et al (2014) Gliotransmitters travel in time and space. *Neuron* 81:728–739
- Attwell D et al (2010) Glial and neuronal control of brain blood flow. *Nature* 468:232–243
- Azevedo FA et al (2009) Equal numbers of neuronal and nonneuronal cells make the human brain an isometrically scaled-up primate brain. *J Comp Neurol* 513:532–541
- Bahney J, von Bartheld CS (2014) Validation of the isotropic fractionator: comparison with unbiased stereology and DNA extraction for quantification of glial cells. *J Neurosci Methods* 222:165–174
- Bernardinelli Y et al (2014) Activity-dependent structural plasticity of perisynaptic astrocytic domains promotes excitatory synapse stability. *Curr Biol* 24:1679–1688
- Berridge MJ (1998) Neuronal calcium signaling. *Neuron* 21:13–26
- Charles AC, Merrill JE, Dirksen ER, Sanderson MJ (1991) Intercellular signaling in glial cells: calcium waves and oscillations in response to mechanical stimulation and glutamate. *Neuron* 6:983–992
- Chen TW et al (2013) Ultrasensitive fluorescent proteins for imaging neuronal activity. *Nature* 499:295–300
- Clapham DE (2007) Calcium signaling. *Cell* 131:1047–1058
- Cornell-Bell AH, Finkbeiner SM, Cooper MS, Smith SJ (1990) Glutamate induces calcium waves in cultured astrocytes: long-range glial signaling. *Science* 247:470–473
- Dani JW, Chernjavsky A, Smith SJ (1992) Neuronal activity triggers calcium waves in hippocampal astrocyte networks. *Neuron* 8:429–440
- Di Castro MA et al (2011) Local Ca^{2+} detection and modulation of synaptic release by astrocytes. *Nat Neurosci* 14:1276–1284
- Filosa JA et al (2006) Local potassium signaling couples neuronal activity to vasodilation in the brain. *Nat Neurosci* 9:1397–1403
- Henneberger C, Papouin T, Oliet SH, Rusakov DA (2010) Long-term potentiation depends on release of D-serine from astrocytes. *Nature* 463:232–236
- Khakh BS, McCarthy KD (2015) Astrocyte calcium signaling: from observations to functions and the challenges therein. *Cold Spring Harb Perspect Biol* 7:a020404
- Khakh BS, Sofroniew MV (2015) Diversity of astrocyte functions and phenotypes in neural circuits. *Nat Neurosci* 18:942–952
- Li D, Agulhon C, Schmidt E, Oheim M, Ropert N (2013) New tools for investigating astrocyte-to-neuron communication. *Front Cell Neurosci* 7:193
- Molotkov D, Zobova S, Arcas JM, Khiroug L (2013) Calcium-induced outgrowth of astrocytic peripheral processes requires actin binding by Profilin-1. *Cell Calcium* 53:338–348
- Morquette P et al (2015) An astrocyte-dependent mechanism for neuronal rhythmogenesis. *Nat Neurosci*
- Nedergaard M, Verkhratsky A (2012) Artifact versus reality—how astrocytes contribute to synaptic events. *Glia* 60:1013–1023
- Panatier A et al (2011) Astrocytes are endogenous regulators of basal transmission at central synapses. *Cell* 146:785–798

- Perez-Alvarez A, Navarrete M, Covelo A, Martin ED, Araque A (2014) Structural and functional plasticity of astrocyte processes and dendritic spine interactions. *J Neurosci* 34:12738–12744
- Poskanzer KE, Yuste R (2011) Astrocytic regulation of cortical UP states. *Proc Natl Acad Sci U S A* 108:18453–18458
- Ridler T, Calvard S (1978) Picture thresholding using an iterative selection method. *IEEE Trans Syst Man Cybern SMC-8:630–632*
- Sasaki T, Matsuki N, Ikegaya Y (2011) Action-potential modulation during axonal conduction. *Science* 331:599–601
- Sasaki T et al (2014) Astrocyte calcium signalling orchestrates neuronal synchronization in organotypic hippocampal slices. *J Physiol* 592:2771–2783
- Schindelin J et al (2012) Fiji: an open-source platform for biological image analysis. *Nat Methods* 9:676–682
- Schneider C, Rasband W, Eliceiri K (2012) NIH image to ImageJ: 25 years of image analysis. *Nat Methods* 9:671–675
- Shigetomi E, Kracun S, Sofroniew MV, Khakh BS (2010) A genetically targeted optical sensor to monitor calcium signals in astrocyte processes. *Nat Neurosci* 13:759–766
- Shigetomi E, Tong X, Kwan KY, Corey DP, Khakh BS (2012) TRPA1 channels regulate astrocyte resting calcium and inhibitory synapse efficacy through GAT-3. *Nat Neurosci* 15:70–80
- Shigetomi E, Jackson-Weaver O, Huckstepp RT, O'Dell TJ, Khakh BS (2013a) TRPA1 channels are regulators of astrocyte basal calcium levels and long-term potentiation via constitutive D-serine release. *J Neurosci* 33:10143–10153
- Shigetomi E et al (2013b) Imaging calcium microdomains within entire astrocyte territories and endfeet with GCaMPs expressed using adeno-associated viruses. *J Gen Physiol* 141:633–647
- Smith SJ (1992) Do astrocytes process neural information? *Prog Brain Res* 94:119–136
- Smith S (1994) Neural signalling. Neuromodulatory astrocytes. *Curr Biol* 4:807–810
- Srinivasan R et al (2015) Ca(2+) signaling in astrocytes from *Ip3r2(-/-)* mice in brain slices and during startle responses in vivo. *Nat Neurosci* 18:708–717
- Tong X, Shigetomi E, Looger LL, Khakh BS (2013) Genetically encoded calcium indicators and astrocyte calcium microdomains. *Neuroscientist* 19:274–291
- Volterra A, Liaudet N, Savtchouk I (2014) Astrocyte Ca²⁺ signalling: an unexpected complexity. *Nat Rev Neurosci* 15:327–335

Chapter 18

Modeling Neuron–Glia Interactions with the *Brian 2* Simulator



Marcel Stimberg, Dan F. M. Goodman, Romain Brette
and Maurizio De Pittà

Abstract In spite of compelling evidence that glial cells could crucially regulate neural network activity, the vast majority of available neural simulators ignores the possible contribution of glia to neuronal physiology. Here, we show how to model glial physiology and neuron–glia interactions in the *Brian 2* simulator. *Brian 2* offers facilities to explicitly describe any model in mathematical terms with limited and simple simulator-specific syntax, automatically generating high-performance code from the user-provided descriptions. The flexibility of this approach allows us to model not only networks of neurons, but also individual glial cells, chemical coupling of glial cells, and the interaction between glial cells and synapses. We therefore conclude that *Brian 2* provides an ideal platform to efficiently simulate glial physiology, and specifically, the influence of astrocytes on neural activity.

Keywords *Brian 2* simulator · Neuron–glial interactions · Tripartite synapses · Neuron–glial networks · Astrocyte · Gliotransmission

M. Stimberg (✉) · R. Brette
Sorbonne Université, INSERM, CNRS, Institut de la Vision, Paris, France
e-mail: marcel.stimberg@inserm.fr

D. F. M. Goodman
Department of Electrical and Electronic Engineering,
Imperial College London, London, UK

M. D. Pittà (✉)
BCAM - Basque Center for Applied Mathematics, Bilbao, Spain
e-mail: maurizio.depitta@gmail.com

M. D. Pittà
Department of Statistics and Neurobiology,
The University of Chicago, Chicago, USA

M. D. Pittà
Team BEAGLE, INRIA Rhône-Alpes, Villeurbanne, France

18.1 Introduction

18.1.1 Challenges in Modeling of Neuron–Glia Interactions

Computational modeling is an important part of modern neuroscience research (Abbott 2008). Neuronal models are available at many scales of investigation (Dayan and Abbott 2001): highly detailed multi-compartmental models describe the ion channels that establish the membrane potential and are responsible for action potential generation; simplified models, such as the integrate-and-fire neuron, regard action potentials as stereotypical events that are not described any further; and even more abstract models, such as Poisson neurons, only aim to capture the statistics of timing of action potentials rather than the shape or the biophysical mechanism of their generation. Such neuronal models can be readily simulated by a wide range of simulator packages for neuronal simulations (Brette et al. 2007), given that they are well-established and fairly standardized and thus are often provided by libraries built in these packages (but see Brette 2012).

The same does not hold true for glial cell models (De Pittà et al. 2013). Despite compelling emerging evidence that glial cells could crucially regulate neural network activity (Poskanzer and Yuste 2016) and plasticity (De Pittà et al. 2016), the vast majority of available neuronal models completely ignores the possible contribution of glia to neuronal physiology. Arguably, one of the reasons for this is that standard glia models are yet to be defined (Chap. 1), and thus, simulator packages generally do not provide models of glial cells as part of their libraries.

Although several popular neural simulators, such as NEURON (Carnevale and Hines 2006) or NEST (Gewaltig and Diesmann 2007), allow for extending their built-in library with user-defined glia models, this is generally not straightforward as it requires specific programming skills in a low-level language (Savtchenko et al. 2018). Additionally, it usually involves an additional step of compilation and integration into the simulator every time the library is changed. This may ultimately discourage research that involves adding or modifying a glia model in a simulator, since iterative improvements are very inconvenient. As a consequence, computational studies that model glia either use a standard simulator such as NEURON but are limited in usability by the specific choice made for the glial model which cannot easily be modified by the user (Aleksin et al. 2017), or use custom code written in a general-purpose language such as MATLAB (Wade et al. 2011; De Pittà et al. 2011; Naeem et al. 2015) or lower-level languages such as C/C++ (Volman et al. 2007; Nadkarni et al. 2008), in turn suffering from reduced accessibility to researchers with less technical experience. Overall, both the scenarios raise potential issues in terms of portability, reproducibility, and correctness of the code which are detrimental to model sharing and dissemination (Cannon et al. 2007).

In contrast to most other simulators, the *Brian* simulator (Goodman and Brette 2008; Goodman et al. 2009) was created with the aim to ease definition and portability of new models. In its latest version, *Brian 2*, this flexibility is extended to and combined with a generic approach for code generation that allows high-performance

simulations (Goodman 2010; Stimberg et al. 2014). This chapter explores these aspects, elucidating several advantages that should encourage researchers to use the *Brian 2* simulator to model glia in their work.

18.1.2 *The Brian Simulator*

The *Brian* simulator, created in 2008, is provided as a package for the Python programming language. All aspects of the model can be defined in a single Python script and are made explicit: rather than relying on predefined “black-box” models, models can be readily and flexibly described in mathematical terms by differential equations for continuous dynamics and a series of update statements for discrete events (Brette 2012; Stimberg et al. 2014). This allows high code readability and flexibility as the user can freely change details of the model’s equations which are written in mathematical notation with only very little *Brian*-specific syntax. Furthermore, because the description of the model is explicit, all model details are unambiguously defined and appear in the main simulation description file.

In line with the principle of readability and simplicity, *Brian 2* also comes with a system for the use of physical units. For example, it allows the user to directly specify a parameter in $\mu\text{M}/\text{s}$ units, by multiplying its value by `umolar/second`. *Brian 2* also checks the consistency of all specified units across all assignments, statements, and equations and issues an error if there is a mismatch.

Brian is open source and freely distributed under the GPL-compatible CeCILL v2.1 license. For more information, see <http://briansimulator.org> and <http://brian2.readthedocs.io>.

18.1.3 *Modeling Strategy*

In the following, we focus on astrocytes and their interactions with synapses, but the modeling arguments and code design principles that we present are of general validity and could be used to also model other glial cells, such as microglia, oligodendrocytes, or reactive astrocytes. Computational modeling of neuron–astrocyte signaling has previously been tackled both on the microscopic (molecular) level and the macroscopic (network) scale. On the microscopic level, the MCell simulator (Stiles et al. 2001) has been used to investigate specific astrocytic signals impinging on synaptic elements (Beenhakker and Huguenard 2010). On the network level, the NEURON-based ARACHNE platform to study astrocyte functions in neural network physiology is available but only considers astrocyte-mediated “volume-transmitted” extracellular signaling (Savtchenko and Rusakov 2014; Aleksin et al. 2017).

In the following modeling section, we pursue instead a mixed strategy, considering models of astrocytes and of their interactions with synapses that lump both microscopic and macroscopic aspects. Based on this approach, we show how *Brian 2*

can be used to create a network of neurons and synapses connected with a network of astrocytes that sense synaptic activity and modulate it in turn, starting from a molecular-level description of astrocytic signaling. We do so by first introducing a simple network model of only neurons and synapses (Sects. 18.2.2 and 18.2.3). Then, we present modeling of individual astrocytes that respond to synaptic activation by intracellular calcium signaling (Sect. 18.2.4) and release gliotransmitters that could modulate synaptic transmission (Sects. 18.2.5 and 18.2.6). Next, we discuss signaling between astrocytes in a network (Sect. 18.2.7), and finally, we combine all these aspects in a recurrent network of interacting neurons, synapses, and astrocytes (Sect. 18.2.8).

For the sake of brevity, we only show excerpts of the *Brian 2* code describing the models used in the presented simulations. The full code (see also Appendix 2), including the code for recording and analyzing the results, as well as plotting the figures of this chapter can be downloaded from <https://github.com/mdepitta/comp-glia-book>. It is also part of the *Brian 2* documentation at <http://brian2.readthedocs.io> and it is available as well in ModelDB (McDougal et al. 2017) at <http://modeldb.yale.edu/233393>.

18.2 Modeling of Neuron–Glia Network Interactions with *Brian 2*

18.2.1 General Approach

In *Brian 2*, models of neurons, synapses, and astrocytes are defined by a set of state variables, e.g. the neuron’s membrane potential, the synaptic conductances, or the astrocyte’s intracellular calcium, and a description of their evolution over time. This description takes the form of ordinary differential equations (ODEs) for the continuous temporal dynamics between “events”, e.g. the membrane potential, postsynaptic conductances, or astrocytic intracellular calcium concentration between action potentials. Discontinuities in the dynamics of state variables triggered by events such as the crossing of the firing threshold by a neuron’s membrane potential, or the arrival of an action potential at a presynaptic terminal, are described by a set of statements that update these variables.

Groups of elements that share the same description of their dynamics are represented by a single object. Thus, for example, groups of neurons, synapses, and astrocytes would each be represented by an object. However, these groups can be heterogeneous. For example, neurons or astrocytes in the same group can be stimulated by different synapses, or synapses can be characterized by different cellular parameters. State variables are updated according to the dynamics specified by the user. If the evolution of a state variable is of interest for the purpose of analysis or visualization, the user can record it by a “monitor” object either for all elements of a group or for a subset thereof.

Once all elements of a model have been specified, including initial values, constants, and model parameters, the simulation can be launched. This is done by calling the `run` function with a parameter that specifies the desired total simulated time in biological time units (e.g. second). Upon completion of the `run` call, the user can analyze the simulation results either by accessing the final values of state variables (e.g. to analyze the synaptic weight distribution at the end of a simulated plasticity-inducing protocol), or by accessing values stored in a monitor. All these values are readily accessible as NumPy arrays (van der Walt et al. 2011) and can be stored, analyzed, and displayed by standard tools. Since simulation results are annotated with physical units, plotting them in a specific scale can easily be done by dividing them by those units. For example, when the state variable `v` (“membrane potential”) of a group of neurons has been recorded by `monitor=StateMonitor(neurons, 'v')`, the first neuron’s membrane potential may be shown in mV as function of time in ms using Matplotlib’s `plot` function (Hunter 2007) by `plot(monitor.t/ms, monitor[0].v/mV)`.

18.2.2 Neurons

In *Brian 2*, neurons are represented by objects of the `NeuronGroup` class (Fig. 18.1a). Each `NeuronGroup` object models the activity of a group of neurons with identical dynamics, i.e. neurons whose state variables evolve according to the same differential equations. Consider, for example, the simple model of an integrate-and-fire neuron with conductance-based excitatory (g_e) and inhibitory synapses (g_i) and a constant input current I_{ex} (Dayan and Abbott 2001), whose equations are

$$\frac{dv}{dt} = (g_l(E_l - v) + g_e(E_e - v) + g_i(E_i - v) + I_{ex}) \frac{1}{C_m} \quad (18.1)$$

$$\frac{dg_e}{dt} = -\frac{g_e}{\tau_e} \quad (18.2)$$

$$\frac{dg_i}{dt} = -\frac{g_i}{\tau_i} \quad (18.3)$$

In *Brian 2* we closely follow the above mathematical notation, defining the neuron model by a multi-line string:

```
neuron_eqs = '''
dv/dt = (g_l*(E_l-v) + g_e*(E_e-v) + g_i*(E_i-v) +
          I_ex)/C_m      : volt (unless refractory)
dg_e/dt = -g_e/tau_e : siemens # post-synaptic exc. conductance
dg_i/dt = -g_i/tau_i : siemens # post-synaptic inh. conductance
'''
```

Each line of the `neuron_eqs` string defines a state variable of the model (`v`, `g_e` or `g_i`) and consists of two parts separated by a colon and an optional comment after the ‘#’ sign. The part before the colon specifies the ODE for the dynamics of the state variable. The part that follows the colon specifies the physical units of this state variable

and (optionally) additional information about it. In the case of the neuron's membrane potential v for example, the additional specification `(unless refractory)` states that the differential equation for v is not to be integrated during the refractory period following the firing of an action potential by the neuron, but instead should stay at the post-spike reset value. It should be noted that the stated physical unit after the colon has to be a SI base unit, i.e. a unit such as `volt`, `second`, or `siemens`, and not a scaled unit such as `mV`, `ms`, or `nS`.¹ This is to emphasize that internally all variable values are stored as floating point numbers in the base unit. While users do not have to care about this most of the time—they set values using the unit system in whatever scale they prefer and receive values with the scaling information back—this becomes relevant when the unit information is stripped away, e.g. when quantities are passed through library functions that are not unit-aware.

The implementation of the neuron model in Eqs. 18.1–18.3 refers to model parameters, namely the leak, excitatory, and inhibitory reversal potentials E_l , E_e and E_i ; the constant input current I_{ex} ; the membrane capacitance C_m ; and the time constants of excitatory and inhibitory synaptic inputs, τ_e and τ_i . Here, these parameters are taken to be equal for all simulated neurons and can be defined by standard Python variables (one per parameter) in the script that runs the simulation.² Alternatively, neuron-specific parameters can be defined by appending lines in the form of `<name> : <unit> (constant)` to the model equations.

In the scenario of a network of N_e excitatory and N_i inhibitory neurons (Fig. 18.1b), we can then create a `NeuronGroup` object of $N_e + N_i$ neurons based on the above description, and further define the condition for firing of an action potential (`threshold`), as well as the statement(s) (if any) to be executed after an action potential (`reset`), and finally the refractory period (`refractory`), which in this case we assume to be a constant value τ_r (defined along with the other model parameters):

```
neurons = NeuronGroup(N_e + N_i, model=neuron_eqs,
                      threshold='v>V_th', reset='v=V_r',
                      refractory='tau_r', method='euler')
```

The model's state variables are exposed as attributes of the `neurons` object so that, for example, the membrane potential can be accessed by `neurons.v`, and their initial value can be assigned in the same way. Although all neurons in our example are described by the same equations, the initial values of their variables can be different. Here, we set these latter to random values using string expressions that are executed via the code generation facilities provided by *Brian 2* (Stimberg et al. 2014) and refer to uniformly distributed random numbers between 0 and 1 using the predefined function `rand()`. Finally, we use Python's slicing syntax to separate the group into subgroups of excitatory and inhibitory neurons:

¹Note that `molar` is *not* a SI base unit, because it is defined as $M = \text{mol L}^{-1}$, i.e. referring to L instead of the SI base unit m^3 . Since $1 \text{ mol L}^{-1} = 1000 \text{ mol m}^{-3}$, the base unit to use is $\text{mM}(\text{mmolar})$.

²*Brian 2* also offers an alternative system to specify constants via a `namespace` argument that receives a Python dictionary mapping constant names to their values. Refer to *Brian 2*'s online documentation for details at <http://brian2.readthedocs.io>.

```

neurons.v = 'E_1 + rand()*(V_th-E_1)'
neurons.g_e = 'rand()*w_e'
neurons.g_i = 'rand()*w_i'
exc_neurons = neurons[:N_e]
inh_neurons = neurons[N_e:]

```

18.2.3 Synapses

In most models of neuronal systems, neurons are connected by chemical synapses that are activated by action potentials fired by presynaptic neurons. In the following, we use the phenomenological description of neocortical synapses exhibiting short-term plasticity originally introduced by Tsodyks and Markram (Tsodyks et al. 1998; Tsodyks 2005). According to this description, synaptic release is modeled by the product of two variables u_S and x_S , where u_S loosely relates to the neurotransmitter resources “docked” for release by the Ca^{2+} sensor for synaptic exocytosis of neurotransmitter, and x_S represents the fraction of total neurotransmitter available for release (Fuhrmann et al. 2002; Tsodyks 2005). Between action potentials, u_S decays to 0 at rate Ω_f while x_S recovers to 1 at rate Ω_d , i.e.

$$\frac{du_S}{dt} = -\Omega_f u_S \quad (18.4)$$

$$\frac{dx_S}{dt} = \Omega_d(1 - x_S) \quad (18.5)$$

The arrival of an action potential triggers calcium influx at the presynaptic terminal, which moves a fraction U_0 of the neurotransmitter resources not scheduled for release ($1 - u_S$) to the readily releasable “docked” state (u_S). Subsequently, a fraction u_S of the available neurotransmitter resources is released as r_S while x_S is reduced by the same amount; that is,

$$u_S \leftarrow u_S + U_0(1 - u_S) \quad (18.6)$$

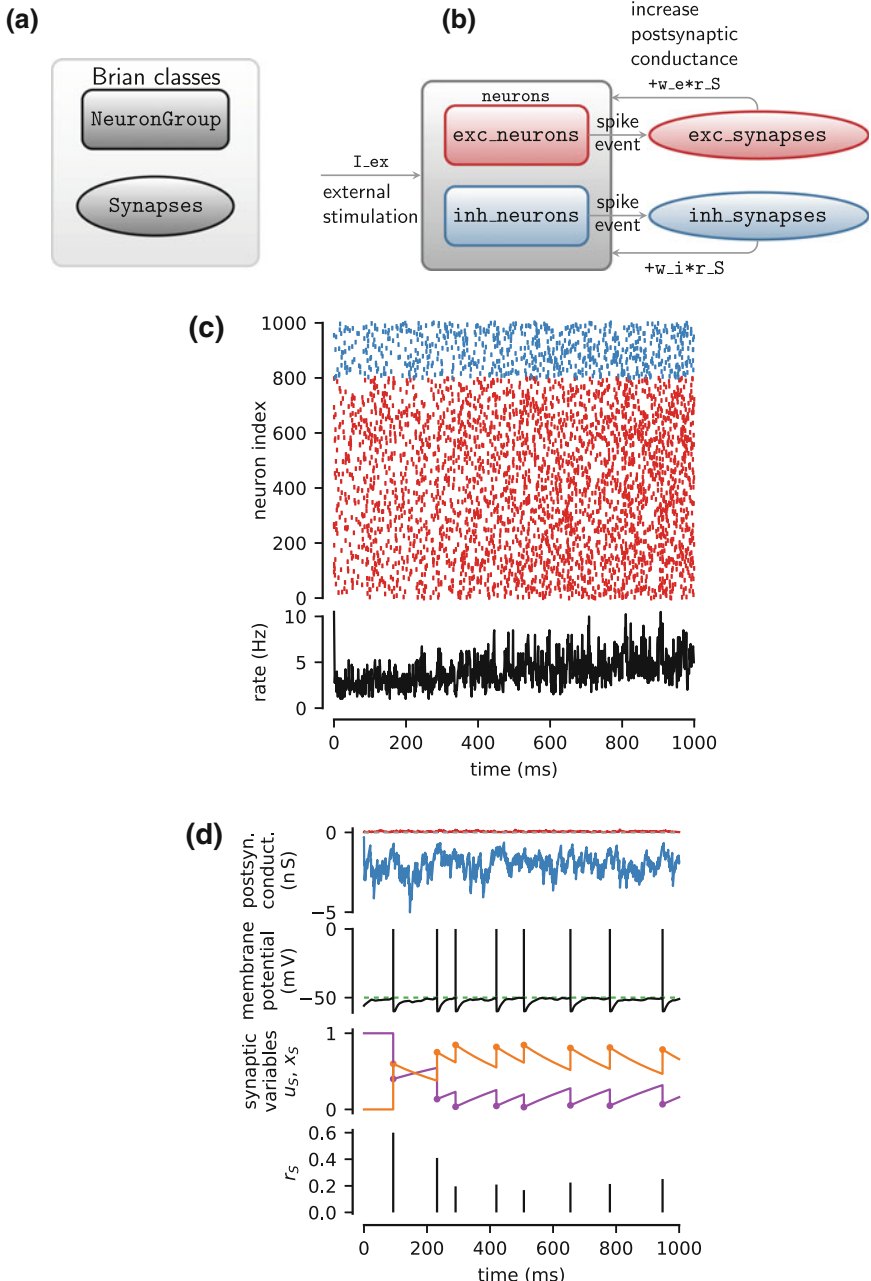
$$r_S \leftarrow u_S x_S \quad (18.7)$$

$$x_S \leftarrow x_S - r_S \quad (18.8)$$

In *Brian 2*, connections between neurons are modeled by objects of the `Synapses` class (Fig. 18.1a). Analogously to neurons of a `NeuronGroup`, we define each synapse’s state variables x_S and u_S by a multi-line string:

```

synapses_eqs = '''
# Usage of releasable neurotransmitter per single action potential:
du_S/dt = -Omega_f * u_S : 1 (event-driven)
# Fraction of synaptic neurotransmitter resources available:
dx_S/dt = Omega_d * (1 - x_S) : 1 (event-driven)
'''
```



◀ **Fig. 18.1** Modeling of neurons and synapses. **a** In *Brian 2*, neurons and synapses are modeled by two distinct classes, `NeuronGroup` and `Synapses`. As a convention, in all the schemes presented in this chapter, `NeuronGroup` objects are shown as *rectangles*, whereas `Synapses` objects are displayed by *ellipses*. **b** In a classic balanced network model (Brunel 2000), neurons are separated into excitatory (`exc_neurons`) and inhibitory ones (`inh_neurons`), being recurrently connected both by excitatory (`exc_synapses`) and by inhibitory synapses (`inh_synapses`). **c** Raster plot of the firing activity of 25% out of all excitatory (red) and inhibitory neurons (blue) of the network in panel (b) and associated network-averaged firing rate (computed in 1 ms time bins). **d** Asynchronous network activity coexists with large fluctuations in postsynaptic excitatory (red traces) and inhibitory conductances (blue traces) and relatively sporadic firing by individual neurons (green dotted line: firing threshold, V_{th}). Timing of incoming presynaptic action potentials also shapes the dynamics of synaptic transmission by short-term synaptic plasticity. Synaptic release of neurotransmitter (r_S) is not fixed, but rather varies at each action potential, depending on the history of synaptic activity reflected in the values of the synaptic state variables u_S (orange) and x_S (purple) at the action potential instant. Postsynaptic conductances and membrane potential are shown for neuron 50 from the raster plot. Displayed synaptic variables are from one excitatory synapse made by this neuron. Model parameters as in Tabel 18.1 and in addition, $I_{ex} = 150 \text{ pA}$

Synaptic equations are specified to be (`event-driven`) because we only need values of synaptic variables when an action potential arrives presynaptically. This tells *Brian 2* to update synaptic variables only at new incoming action potentials using the analytical solution of their differential equations and the time interval since the last update. This is possible because the synapse's Eqs. 18.4 and 18.5 are linear so that their analytical solution is known, allowing to simulate a large number of synapses efficiently. We also note that in our model implementation, synaptic equations do not include postsynaptic conductances as they were previously defined in the neuronal equations. This allows storing and updating synaptic conductances only once per neuron rather than once per synapse and is mathematically equivalent due to the assumed linear summation of postsynaptic conductances.

Discrete changes of synaptic variables on arrival of an action potential can be implemented by a series of statements in a multi-line string such as

```
synapses_action = '''
u_S += U_0 * (1 - u_S)
r_S = u_S * x_S
x_S -= r_S
'''
```

In addition, excitatory (inhibitory) synapses will increase the excitatory (inhibitory) conductance in the postsynaptic cell whenever a presynaptic action potential arrives (Fig. 18.1b), i.e.

$$g_e \leftarrow g_e + w_e r_s \quad (18.9)$$

$$g_i \leftarrow g_i + w_i r_s \quad (18.10)$$

This is done by extending `synapses_action` by an update assignment “`+=`” of the respective postsynaptic conductance, identified by the `post` suffix, i.e. `g_e_post` and `g_i_post`. Combining all of this together, we create two types of synapses, respectively originating from excitatory and inhibitory neurons, i.e.

Table 18.1 Parameters for neurons and synapses

Symbol	Name in code	Description	Value	Units
<i>Neuron parameters</i>				
C_m	C_m	Membrane capacitance	198	pF
E_l	E_l	Leak reversal potential	-60	mV
g_l	g_l	Leak conductance	9.99	nS
I_{ex}	I_ex	External current	†	pA
V_r	V_r	Reset potential	-60	mV
V_θ	V_th	Firing threshold	-50	mV
τ_r	tau_r	Refractory period	5	ms
<i>Synapse parameters</i>				
Ω_d	Omega_d	Synaptic depression rate	2	s ⁻¹
Ω_f	Omega_f	Synaptic facilitation rate	3.33	s ⁻¹
$U_0^* (U_0)$	U_0_star (U_0)	Resting synaptic release probability	0.6	-
Y_T	Y_T	Total vesicular neurotransmitter concentration	500	mM
ρ_c	rho_c	Synaptic vesicle-to-extracellular space volume ratio	0.005	-
Ω_c	Omega_c	Neurotransmitter clearance rate	40	s ⁻¹
w_e	w_e	Excitatory synaptic conductance	50	pS
w_i	w_i	Inhibitory synaptic conductance	1	nS
τ_e	tau_e	Excitatory synaptic time constant	5	ms
τ_i	tau_i	Inhibitory synaptic time constant	10	ms
E_e	E_e	Excitatory synaptic reversal potential	0	mV
E_i	E_i	Inhibitory synaptic reversal potential	-80	mV
<i>Presynaptic receptors</i>				
O_G	O_G	Agonist binding (activating) rate	1.5	μMs ⁻¹
Ω_G	Omega_G	Agonist release (deactivating) rate	0.5	min ⁻¹

Simulation-specific parameters are marked by “†” and are reported in respective figure captions

```
exc_syn = Synapses(exc_neurons, neurons, model=synapses_eqs,
                    on_pre=synapses_action+'g_e_post += w_e*r_S')
inh_syn = Synapses(inh_neurons, neurons, model=synapses_eqs,
                    on_pre=synapses_action+'g_i_post += w_i*r_S')
```

where the `on_pre` keyword argument denotes that the series of statements should be executed on arrival of a presynaptic action potential.

It must be stressed that the above code only defines the synaptic model in *Brian 2*, but not the connectivity. To create synapses, we have to specify what source–target neuron pairs should be connected together out of all the possible pairs specified by the first two input arguments in the `Synapses` initializer. One way to do this is by specifying a logical condition on neuronal connectivity and, optionally, a connection probability, provided as arguments to the `connect` method of the `Synapses` object

(Stimberg et al. 2014). Here, we want to connect all possible neuron pairs with a probability of 20% for each pair for inhibitory neurons, and 5% for excitatory neurons. Thus, we do not set any condition to be fulfilled and only specify a probability for all possible connection pairs:

```
exc_syn.connect(p=0.05)
inh_syn.connect(p=0.2)
```

For parameters values such as those in Table 18.1, simulation of the resulting network reveals the emergence of characteristic asynchronous neuronal firing activity (Brunel 2000), as evidenced in Fig. 18.1c by the *top left* raster plot of the firing activity of 25% of the neurons in the network. The network-averaged firing rate associated with this raster plot indeed presents noisy dynamics (Fig. 18.1c, *bottom panel*) that coexists with large fluctuations of postsynaptic excitatory (*red traces*) and inhibitory conductances (*blue traces*) and sporadic firing of individual neurons (Fig. 18.1d, *top panels*). Consideration of a sample excitatory synapse of the network allows appreciating how synaptic dynamics is modulated by short-term plasticity (Fig. 18.1d, *bottom panels*). The state variables u_s and x_s associated with the sample synapse evolve in a characteristic exponential fashion intermingled with discontinuities triggered by action potentials arriving at the presynaptic terminal. The resulting values define the amount of synaptic neurotransmitter released by the synapse (r_s), setting how effectively each action potential is transmitted to the postsynaptic neuron.

18.2.4 Astrocytes

Intracellular Ca^{2+} concentration is unanimously regarded as a prominent readout signal of astrocyte activity (Zorec et al. 2012). Although astrocytic intracellular Ca^{2+} can be regulated by multiple mechanisms, Ca^{2+} -induced Ca^{2+} release (CICR) from the astrocyte's endoplasmic reticulum (ER) appears to be one of the main mechanisms to regularly occur in the healthy brain (Nimmerjahn 2009). Recall from Chaps. 3 and 5 that astrocytic CICR is triggered by the intracellular second messenger inositol 1,4,5-trisphosphate (IP_3), which is produced upon astrocyte activation, and can be described, in one of its simplest formulation (Falcke 2004; De Pittà et al. 2008), by two ordinary differential equations in the Hodgkin–Huxley form (Li and Rinzel 1994). The first equation is a mass balance for Ca^{2+} (C) in terms of three fluxes J_r , J_l , J_p which, respectively, denote CICR (J_r), Ca^{2+} leak from the ER (J_l), and Ca^{2+} uptake from the cytosol back to the ER by $\text{Ca}^{2+}/\text{ATPase}$ pumps (J_p). The second equation is for the gating variable (h) of de-inactivation of the channels that are responsible for CICR. These channels are inside the astrocyte, on the membrane that separates the ER Ca^{2+} -rich stores from the cell's cytosol and are nonlinearly gated by both IP_3 (I) and Ca^{2+} . This leads to the well-known two-equation model originally introduced by Li and Rinzel (1994):

$$\frac{dC}{dt} = J_r + J_l - J_p \quad (18.11)$$

$$\frac{dh}{dt} = \frac{h_\infty - h}{\tau_h} \quad (18.12)$$

where

$$\begin{aligned} J_r &= \Omega_C m_\infty^3 h^3 (C_T - (1 + \varrho_A)C) & m_\infty &= \mathcal{H}_1(C, d_5) \mathcal{H}_1(I, d_1) \\ J_l &= \Omega_L (C_T - (1 + \varrho_A)C) & h_\infty &= d_2 \frac{I + d_1}{d_2(I + d_1) + (I + d_3)C} \\ J_p &= O_P \mathcal{H}_2(C, K_P) & \tau_h &= \frac{I + d_3}{\Omega_2(I + d_1) + O_2(I + d_3)C} \end{aligned}$$

and \mathcal{H} denotes the sigmoidal (Hill) function with $\mathcal{H}_n(x, K) = x^n / (x^n + K^n)$.

For the sake of completeness, we also want to consider the stochastic opening and closing process of CICR-mediating channels which, as discussed in Chap. 4, can be mimicked by introducing a white noise term $\xi(t)$ into the equation governing the dynamics of the gating variable h , so that Eq. 18.12 becomes (Shuai and Jung 2002):

$$\frac{dh}{dt} = \frac{h_\infty - h}{\tau_h} (1 + \xi(t) \sqrt{\tau_h}) \quad (18.13)$$

Astrocytic IP₃ is regulated by the complex Ca²⁺-modulated interplay of enzymatic production by phospholipase C β (J_β) and C δ (J_δ) and degradation by IP₃ 3-kinase (J_{3K}) and inositol polyphosphatase 5-phosphatase (J_{5P}) (De Pittà et al. 2009a; see also Chap. 5). To reproduce experimental observations, we consider two possible ways to trigger IP₃ production. One is by synaptic stimulation of astrocytic metabotropic receptors which starts phospholipase C β -mediated IP₃ production, modeled by making J_β proportional to the activated fraction of these receptors (denoted hereafter by Γ_A). The other way is to include a further J_{ex} term for constant IP₃ production by an exogenous source of stimulation such as, for example, IP₃ uncaging or intracellular diffusion from subcellular regions far from the CICR site (Goldberg et al. 2010). In conclusion, IP₃ dynamics evolves according to the mass balance equation (De Pittà et al. 2009a)

$$\frac{dI}{dt} = J_\beta(\Gamma_A) + J_\delta - J_{3K} - J_{5P} + J_{ex} \quad (18.14)$$

with

$$\begin{aligned} J_\beta(\Gamma_A) &= O_\beta \Gamma_A & J_\delta &= O_\delta \frac{\kappa_\delta}{\kappa_\delta + I} \mathcal{H}_2(C, K_\delta) \\ J_{3K} &= O_{3K} \mathcal{H}_4(C, K_D) \mathcal{H}_1(I, K_3) & J_{5P} &= \Omega_{5P} I \\ J_{ex} &= -\frac{F_{ex}}{2} \left(1 + \tanh \left(\frac{|\Delta I_{bias}| - I_\theta}{\omega_I} \right) \right) \text{sgn}(\Delta I_{bias}) & \Delta I_{bias} &= I - I_{bias} \end{aligned}$$

where the fraction of activated astrocyte receptors Γ_A depends on the neurotransmitter concentration in the periastrocytic space Y_S and is given by the further equation (Wallach et al. 2014) (Chap. 5)

$$\frac{d\Gamma_A}{dt} = O_N Y_S (1 - \Gamma_A) - \Omega_N (1 + \zeta \cdot \mathcal{H}_1(C, K_{KC})) \Gamma_A \quad (18.15)$$

For a concise description of the meaning of all the model's parameters in the above equations, see Table 18.2.

Dynamics of the astrocyte's state variables Γ_A , I , C , h are governed by ODEs akin to neuronal state variables, although on a longer time scale (De Pittà et al. 2009b). Accordingly, they can be implemented by a `NeuronGroup` object, exactly in the same way as neuronal variables. In this fashion, the following code exemplifies how we can create two astrocytes with dynamics governed by the above equations:

Table 18.2 Parameters for astrocytes and gliotransmission

Symbol	Name in code	Description	Value	Units
<i>Calcium-induced Ca^{2+} release</i>				
C_T	<code>C_T</code>	Total cell free Ca^{2+} content	2	μM
ρ_A	<code>rho_A</code>	ER-to-cytoplasm volume ratio	0.18	–
d_1	<code>d_1</code>	IP_3 dissociation constant	0.13	μM
d_2	<code>d_2</code>	Ca^{2+} inactivation dissociation constant	1.05	μM
d_3	<code>d_3</code>	IP_3 dissociation constant	0.9434	μM
d_5	<code>d_5</code>	Ca^{2+} activation dissociation constant	0.08	μM
O_2	<code>O_2</code>	IP_3R binding rate for Ca^{2+} inhibition	0.2	μMs^{-1}
Ω_C	<code>Omega_C</code>	Maximal rate of Ca^{2+} release by IP_3Rs	6	s^{-1}
Ω_L	<code>Omega_L</code>	Maximal rate of Ca^{2+} leak from the ER	0.1	s^{-1}
O_P	<code>O_P</code>	Maximal Ca^{2+} uptake rate by SERCAs	0.9	μMs^{-1}
K_P	<code>K_P</code>	Ca^{2+} affinity of SERCAs	0.05	μM
<i>IP_3 signaling</i>				
O_β	<code>O_beta</code>	Maximal rate of IP_3 production by $\text{PLC}\beta$	†	μMs^{-1}
O_δ	<code>O_delta</code>	Maximal rate of IP_3 production by $\text{PLC}\delta$	0.6	μMs^{-1}
κ_δ	<code>kappa_delta</code>	Inhibition constant of $\text{PLC}\delta$ by IP_3	1.5	μM
K_δ	<code>K_delta</code>	Ca^{2+} affinity of $\text{PLC}\delta$	0.1	μM
O_{3K}	<code>O_3K</code>	Maximal rate of IP_3 degradation by $\text{IP}_3\text{-3K}$	4.5	μMs^{-1}
K_{3K}	<code>K_3K</code>	IP_3 affinity of $\text{IP}_3\text{-3K}$	1	μM
K_D	<code>K_D</code>	Ca^{2+} affinity of $\text{IP}_3\text{-3K}$	0.7	μM
Ω_{5P}	<code>Omega_5P</code>	Maximal rate of IP_3 degradation by IP 5P	0.05	s^{-1}
<i>Metabotropic receptor kinetics</i>				
O_N	<code>O_N</code>	Agonist binding rate	0.3	μMs^{-1}
Ω_N	<code>Omega_N</code>	Maximal inactivation rate	0.5	s^{-1}
K_{KC}	<code>K_KC</code>	Ca^{2+} affinity of PKC	0.5	μM
ζ	<code>zeta</code>	Maximal reduction of receptor affinity by PKC	10	–

(continued)

Table 18.2 (continued)

Symbol	Name in code	Description	Value	Units
<i>IP₃ stimulation & diffusion</i>				
<i>F_{ex}</i>	<i>F_ex</i>	Maximal exogenous IP ₃ flow	2	μMs^{-1}
<i>I_{bias}</i>	<i>I_bias</i>	External IP ₃ drive	†	μM
<i>F</i>	<i>F</i>	GJC IP ₃ permeability	0.09	μMs^{-1}
<i>I_θ</i>	<i>I_Theta</i>	Threshold gradient for IP ₃ diffusion	0.3	μM
ω_I	<i>omega_I</i>	Scaling factor of diffusion	0.05	μM
<i>Gliotransmission</i>				
<i>C_θ</i>	<i>C_Theta</i>	Ca ²⁺ threshold for exocytosis	0.5	μM
<i>G_T</i>	<i>G_T</i>	Total vesicular gliotransmitter concentration	200	mM
Ω_A	<i>Omega_A</i>	Gliotransmitter recycling rate	0.6	s^{-1}
<i>U_A</i>	<i>U_A</i>	Gliotransmitter release probability	0.6	—
ρ_e	<i>rho_e</i>	Astrocytic vesicle-to-extracellular volume ratio	0.00065	—
Ω_e	<i>Omega_e</i>	Gliotransmitter clearance rate	60	s^{-1}
α	<i>alpha</i>	Gliotransmission nature	0	—

Simulation-specific parameters are marked by “†” and are reported in respective figure captions

```

astro_eqs = '''
# Fraction of activated astrocyte receptors:
dGamma_A/dt = O_N * Y_S * (1 - Gamma_A) -
    Omega_N*(1 + zeta * C/(C + K_KC)) * Gamma_A : 1

# IP_3 dynamics:
dI/dt = J_beta + J_delta - J_3K - J_5P + J_ex : mmolar
J_beta = O_beta * Gamma_A : mmolar/second
J_delta = O_delta/(1 + I/kappa_delta) *
    C**2/(C**2 + K_delta**2) : mmolar/second
J_3K = O_3K * C**4/(C**4 + K_D**4) * I/(I + K_3K) : mmolar/second
J_5P = Omega_5P*I : mmolar/second
delta_I_bias = I - I_bias : mmolar
J_ex = -F_ex/2*(1 + tanh((abs(delta_I_bias) - I_Theta)/omega_I)) *
    sign(delta_I_bias) : mmolar/second
I_bias : mmolar (constant)

# Ca2+-induced Ca2+ release:
dC/dt = J_r + J_l - J_p : mmolar
# IP3R de-inactivation probability
dh/dt = (h_inf - h_clipped)/tau_h *
    (1 + noise*xi*tau_h**0.5) : 1
h_clipped = clip(h,0,1) : 1
J_r = (Omega_C * m_inf***3 * h_clipped***3) *
    (C_T - (1 + rho_A)*C) : mmolar/second
J_l = Omega_L * (C_T - (1 + rho_A)*C) : mmolar/second
J_p = O_P * C**2/(C**2 + K_P**2) : mmolar/second
m_inf = I/(I + d_1) * C/(C + d_5) : 1
h_inf = Q_2/(Q_2 + C) : 1
tau_h = 1/(O_2 * (Q_2 + C)) : second
Q_2 = d_2 * (I + d_1)/(I + d_3) : mmolar

# Neurotransmitter concentration in the extracellular space

```

```

Y_S      : mmolar
# Noise flag
noise   : 1 (constant)
...
# Milstein integration method for the multiplicative noise
astrocytes = NeuronGroup(2, astro_eqs, method='milstein')

```

In the above *Brian 2* code, the multi-line `astro_eqs` string defines our astrocyte model. The white noise term ξ in Eq. 18.13 is implemented by the special symbol `xi` (in units of $s^{-1/2}$) which is a predefined symbol in *Brian 2*. Also note that as a gating variable, h has to be bound between 0 and 1, which is not guaranteed by the (approximated) nature of Eq. 18.13. We therefore restrict h to this interval by replacing it by `h_clipped=clip(h, 0, 1)` on the right-hand side of the ODE for h and in the formula of J_r (Shuai and Jung 2002). The noise term in Eq. 18.13 is multiplicative, since $\xi(t)$ multiplies the gating variable h), we therefore have to use a numerical integration method that can handle multiplicative stochastic differential equations. We do this by specifying `method='milstein'` as an argument to the `NeuronGroup` initializer, leading to the use of the Milstein method for integration, under the Stratonovich representation of Eq. 18.13 (Mil'shtein 1975; Kloeden and Platen 1992; also see details on `example_2_gchi_astrocyte.py` in Appendix 2).

The above model also defines three astrocyte-specific variables that are not defined by equations: `I_bias`, `Y_S`, and `noise`. `I_bias` and `noise` are constant over time, but `Y_S`, the concentration of synaptically released neurotransmitter in the extracellular space around astrocytic receptors, i.e. Y_s in Eq. 18.15, depends on synaptic activity that changes and therefore does not have the `(constant)` flag. We will define how it gets linked to the synaptic activity further below.

In this example, we want to compare two types of astrocytes, a deterministic and a stochastic one. To distinguish them, we have introduced the above-mentioned `noise` constant which scales the strength of the noise term in Eq. 18.13. We can therefore switch the noise term on or off, and we initialize it so that the first astrocyte is deterministic and the second is stochastic:

```
astrocytes.noise = [0, 1]
```

To complete our model, we also need to specify how to calculate Y_s in Eq. 18.15, as it is needed for the integration of the Γ_A state variable. For now, we are only interested in the activity of the astrocyte and how it is stimulated by synaptic neurotransmitter. Therefore, we do not take into account short-term synaptic plasticity, and rather consider a trivial synaptic model stating that Y_s increases by the same amount at every action potential and then decays exponentially (Dayan and Abbott 2001):

```

synapses_eqs = 'dY_S/dt = -Omega_c * Y_S : mmolar (clock-driven)'
synapses_action = 'Y_S += rho_c * Y_T'
synapses = Synapses(source_neurons, target_neurons,
                    model=synapses_eqs, on_pre=synapses_action,
                    method='linear')
synapses.connect()

```

Finally, we have to specify how the synapses stimulate the astrocytes. We do this by introducing a further `Synapses` object that connects our synapses (which thus represent the “presynaptic” source in our object) to the two astrocytes (hence regarded

as “postsynaptic” targets) in an all-to-all fashion, which can be concisely expressed by a call to `connect()` without any arguments. Each astrocyte i senses the sum of Y_S across all \mathcal{S}^i synapses that impinge on it. This can be mathematically expressed as $Y_S^i = \sum_{j \in \mathcal{S}^i} Y_S^{ij}$, and the implementation in *Brian 2* closely follows this formulation, using the flag `(summed)` to denote the summing operation:

```
ecs_syn_to_astro = Synapses(synapses, astrocytes,
                             'Y_S_post = Y_S_pre : mmolar (summed)')
ecs_syn_to_astro.connect()
```

The above definition will update Y_S for each astrocyte at every time step so that the integration of the Γ_A has access to the current value at all times.

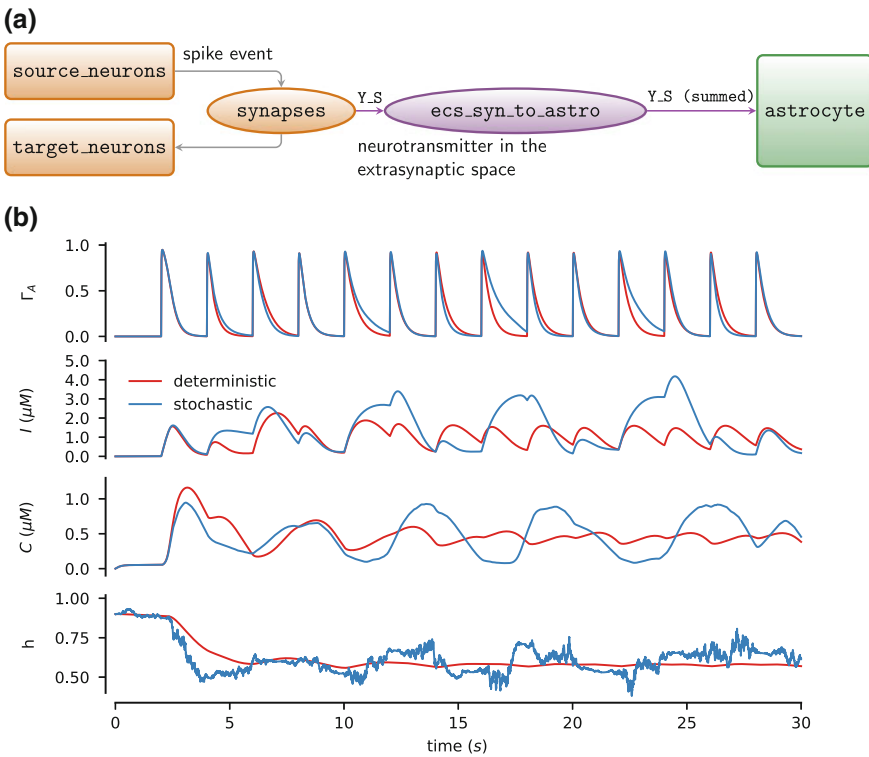


Fig. 18.2 Modeling of synaptically activated astrocytes. **a** Illustration of the design principles to implement an astrocyte stimulated by synaptic inputs in *Brian 2*. The coupling between synapses and the astrocyte is achieved by an additional `Synapses` object, labeled here as `ecs_syn_to_astro`, which feeds into the astrocyte the sums of all individual synaptic inputs. **b** Simulated dynamics of the state variables of two synaptically activated astrocytes, one deterministic (red traces) and one with noise on the gating variable h according to Eq. 18.13 (blue traces). The two astrocytes shared the same synaptic input which was repeatedly triggered by action potentials arriving at a rate of 0.5 Hz. Model parameters as documented in Tables 18.1 and 18.2, with the exception of $\rho_c = 0.001$; $K_P = 0.1 \mu\text{M}$; $O_\beta = 5 \mu\text{Ms}^{-1}$; $O_\delta = 0.2 \mu\text{Ms}^{-1}$; $\Omega_{SP} = 0.1 \text{ s}^{-1}$; $K_D = 0.5 \mu\text{M}$; $F_{ex} = 0.09 \mu\text{M}$; $K_\delta = 0.3 \mu\text{M}$; and $I_{bias} = 0$

Figure 18.2a summarizes the design of the astrocyte model previously described, exemplifying its implementation by *Brian 2* classes originally introduced in Fig. 18.1a. A sample simulation of this model is presented in Fig. 18.2b, which shows the dynamics of the state variables Γ_A , I , C and h for the deterministic (*red traces*) vs. stochastic astrocyte (*blue traces*) in response to synaptic stimulation by periodic action potentials at a rate of 0.5 Hz. It may be appreciated how noisy dynamics of the gating variable h could dramatically alter C and I dynamics compared to the deterministic scenario. This could also impact the activated fraction of astrocytic metabotropic receptors (Γ_A) by the Ca^{2+} -dependent Hill nonlinearity in the right-hand side of Eq. 18.15, although in this example, the effect may be deemed moderate for the specific choice of values for the model’s parameters (Table 18.2).

18.2.5 Gliotransmitter Release and Modulation of Synaptic Release

Astrocytes are not only stimulated by synapses but they can also modulate them by releasing neurotransmitters (also termed “gliotransmitters” for their glial origin; Bezzi and Volterra, 2001) in a Ca^{2+} -dependent fashion. This process generally requires astrocytic intracellular Ca^{2+} concentration to increase beyond a certain threshold, resulting in the release of a quantum of gliotransmitter into the periastrocytic space (De Pittà et al. 2013). In turn, released gliotransmitter molecules diffuse in the extracellular space, ultimately reaching extrasynaptic receptors found on synaptic elements belonging either to the very synapses that stimulate the astrocyte in the so-called closed-loop scenario of gliotransmission, or to other synapses in the case of “open-loop” gliotransmission (Araque et al. 2014). Among these targeted receptors, presynaptically located ones, once bound by gliotransmitters, can ultimately regulate synaptic transmission through modulations of synaptic release probability (Engelman and MacDermott 2004; Pinheiro and Mulle 2008). In the simplest approximation, as elucidated in Chap. 10, this modulation can be modeled by treating the parameter U_0 in the previously introduced Tsodyks–Markram synapse model (Eq. 18.4) no longer as a constant, but rather as linearly dependent on the fraction Γ_S of activated presynaptic receptors (De Pittà et al. 2011):

$$\frac{d\Gamma_S}{dt} = O_G G_A (1 - \Gamma_S) - \Omega_G \Gamma_S \quad (18.16)$$

$$U_0 = (1 - \Gamma_S) U_0^* + \alpha \Gamma_S, \quad (18.17)$$

where G_A denotes the gliotransmitter concentration in the extracellular space, and α dictates whether the effect of gliotransmitters on the synapse is to decrease ($0 \leq \alpha < U_0^*$) or increase neurotransmitter release ($U_0^* < \alpha \leq 1$) (De Pittà et al. 2011). In *Brian 2* syntax, this leads to the following synaptic equations:

```

synapses_eqs = '''
# Neurotransmitter
dY_S/dt = -Omega_c * Y_S : mmolar (clock-driven)
# Fraction of activated presynaptic receptors
dGamma_S/dt = O_G * G_A * (1 - Gamma_S) -
    Omega_G * Gamma_S : 1 (clock-driven)
# Usage of releasable neurotransmitter per single action potential:
du_S/dt = -Omega_f * u_S : 1 (clock-driven)
# Fraction of synaptic neurotransmitter resources available:
dx_S/dt = Omega_d * (1 - x_S) : 1 (clock-driven)
# released synaptic neurotransmitter resources:
r_S : 1
# gliotransmitter concentration in the extracellular space:
G_A : mmolar
'''

```

Because the value of U_0 is only needed at the arrival of an action potential, there is no need to include Eq. 18.17 in the above code. Rather, we update U_0 at the beginning of the statements executed by synapses upon action potential arrival, i.e.

```

synapses_action = '''
U_0 = (1 - Gamma_S) * U_0_star + alpha * Gamma_S
u_S += U_0 * (1 - u_S)
r_S = u_S * x_S
x_S -= r_S
Y_S += rho_c * Y_T * r_S
'''

synapses = Synapses(source_neurons, target_neurons,
    model=synapses_eqs, on_pre=synapses_action,
    method='linear')

```

For the sake of simplicity, we retained two inefficiencies in the above code which should otherwise be avoided in larger, computationally demanding simulations. First, we used the (clock-driven) specification (instead of (event-driven)), even though synaptic state variables need only be updated on action potential arrival (Sect. 18.2.3). This allows us to directly retrieve and plot state variables at each time step without the need to manually interpolate between their values at the timing of action potentials. For the same reason, we also defined r_S (Eq. 18.7) as an additional state variable in the synapse model in `synapses_eqs` rather than using it as an auxiliary temporary variable in the statements of `synapses_action` as we previously did (Sect. 18.2.3). This choice allows us to easily record r_S by a monitor, avoiding the need to recompute it a posteriori based on the values of the other state variables.

Finally, we need to model gliotransmitter release from the astrocyte. For this, we use a similar description to that of synaptic neurotransmitter release (Chap. 10). We thus introduce a new variable x_A which represents the fraction of gliotransmitter resources available for release from the astrocyte and thereby controls the value of G_A . These two state variables decay as (De Pittà et al. 2011)

$$\frac{dx_A}{dt} = \Omega_A(1 - x_A) \quad (18.18)$$

$$\frac{dG_A}{dt} = -\Omega_e G_A, \quad (18.19)$$

while, when gliotransmitter is released, they are updated according to

$$G_A \leftarrow G_A + \rho_e G_T U_A x_A \quad (18.20)$$

$$x_A \leftarrow x_A(1 - U_A) \quad (18.21)$$

As before, we can implement the above by textual equations and statements in *Brian 2*, i.e.

```
astro_eqs = '''
# [...]
# Fraction of gliotransmitter resources available:
dx_A/dt = Omega_A * (1 - x_A) : 1
# gliotransmitter concentration in the extracellular space:
dG_A/dt = -Omega_e*G_A : mmolar
'''

glio_release = '''
G_A += rho_e * G_T * U_A * x_A
x_A -= U_A * x_A
'''
```

We also need to include in the astrocytic model a mechanism to time gliotransmitter release. We do this by imaging that when the astrocyte’s Ca^{2+} concentration increases beyond a threshold C_θ , the astrocyte “fires” a gliotransmitter release event upon which the statements of `glio_release` are executed. In this fashion, we can define in the astrocyte’s `NeuronGroup` a threshold crossing for Ca^{2+} concentration (by the `threshold` keyword), upon which gliotransmitter is released, and specify by the `reset` keyword what to do following firing of a gliotransmitter release event by the astrocyte. Moreover, to avoid the `threshold` condition repeatedly triggering the release in all the time steps where the Ca^{2+} concentration is above the threshold, we use the same condition for the `refractory` keyword, thereby stating that, as long as the Ca^{2+} concentration is above threshold, no new event should be triggered. That is,

```
astrocyte = NeuronGroup(2, astro_eqs,
                       threshold='C>C_Threshold',
                       refractory='C>C_Threshold',
                       reset=glio_release,
                       method='rk4')
```

Finally, to complete our model, we have to define how synapses are modulated by the astrocytes’ gliotransmitter release. We do this defining another `Synapses` object as exemplified in Fig. 18.3a, akin to what we did in the previous section to connect synaptic neurotransmitter release to astrocytes (Fig. 18.2a). However, the connection between synapses and the astrocyte is now in the opposite direction, i.e astrocytic gliotransmission is upstream (namely “presynaptic”) with respect to synapses (which are thus “postsynaptic”). Hence,

```
ecs_astro_to_syn = Synapses(astrocyte, synapses,
                           'G_A_post = G_A_pre : mmolar (summed)')
```

Fig. 18.3b illustrates how gliotransmitter release from the astrocyte could change synaptic neurotransmitter release in our model. The *top panels* show Ca^{2+} traces (C) from two astrocytes that are differently stimulated by exogenous IP_3 production

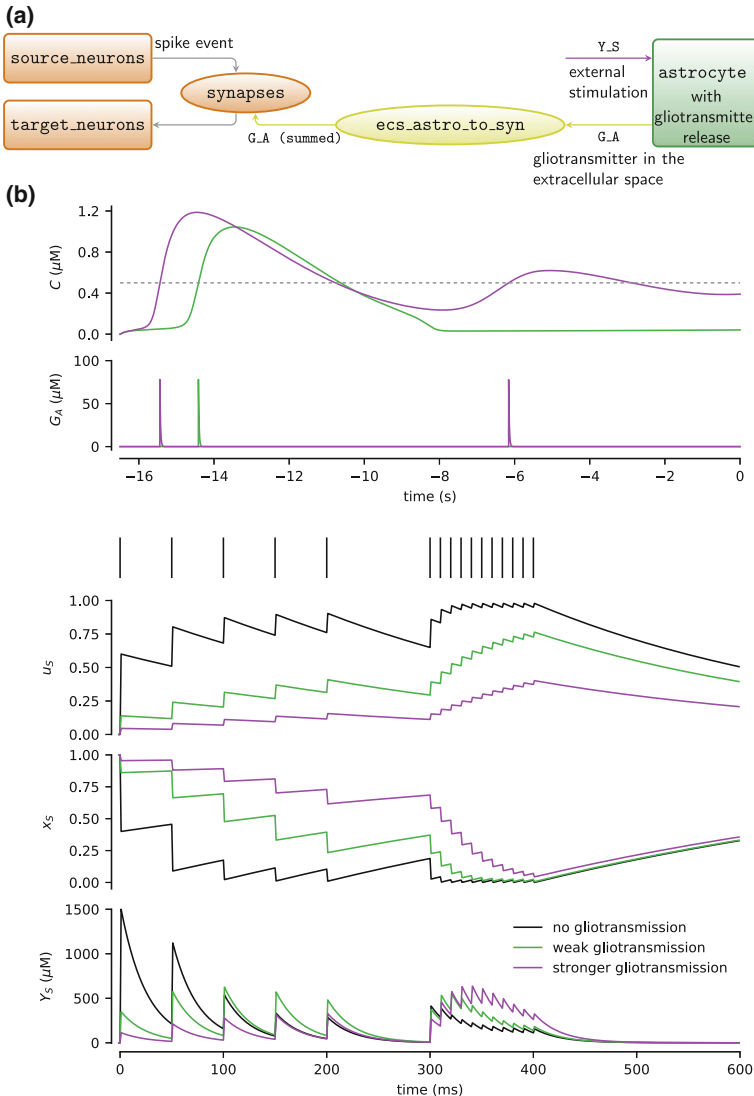


Fig. 18.3 (Previous page.) Modeling of modulation of synaptic release by gliotransmission. **a** The model uses a `Synapses` object `ecs_syn_to_astro` to allow synapses' modulation by perisynaptic gliotransmitters. **b** (*Top panels*) Extracellular gliotransmitter concentration (G_A) resulting from intracellular Ca^{2+} dynamics (C) in two differently activated astrocytes. (*Bottom panels*) Dynamics of synaptic state variables (u_S , x_S) and extracellular neurotransmitter concentration (Y_S) in response to a sequence of action potentials (*top*) for a synapse without (*black*) and with (*green* and *purple*) gliotransmitter-mediated modulation. The two astrocytes were initialized at $t = -17.1$ s at $x_A = 1$, $I = 0.4 \mu\text{M}$, and $h = 0.9$ and were, respectively, stimulated by $I_{bias} = 0.8 \mu\text{M}$ (*weak gliotransmission*) and $I_{bias} = 1.25 \mu\text{M}$ (*stronger gliotransmission*). Other model parameters as in Tables 18.1 and 18.2

(J_{ex} in Eq. 18.14) so that their intracellular Ca^{2+} concentration crosses the threshold for gliotransmitter release (*gray dashed line*) at different times. This results in one astrocyte releasing gliotransmitter in the extracellular space (G_A) only once (*green traces*, “weak gliotransmission”), while the other releases gliotransmitter twice (*purple traces*, “stronger gliotransmission”). The modulation of synaptic release ensuing from these two different timings of gliotransmitter release is illustrated in the *lower panels*, where neurotransmitter release from a synapse stimulated by a sample train of action potentials is monitored first in the absence of gliotransmitter release from the astrocyte and then in the presence of weak vs. stronger gliotransmission. Without gliotransmission, the extracellular neurotransmitter concentration (Y_S) progressively decreases with the incoming action potentials, compatibly with the onset of strong short-term synaptic depression (*black traces*). In the presence of gliotransmission instead, while the amount of released neurotransmitter per action potential is generally lower than in the “naive” synapse (since we assumed $\alpha = 0$ in this example), this amount tends to increase at every action potential with respect to preceding ones, and this increase is larger for stronger gliotransmission. This is consistent with the onset of short-term synaptic facilitation and agrees with the experimental observation and the theoretical argument that gliotransmission could change the synapse’s short-term plasticity (Araque et al. 2014; De Pittà et al. 2016; see also Chaps. 8 and 10).

18.2.6 Closed-Loop Gliotransmission

In the examples discussed so far, we only separately considered one-way interactions between synapses and astrocytes, modeling either modulation of astrocytic activity by synaptic neurotransmitters (Sect. 18.2.4) or modulations of synaptic release by astrocytic gliotransmitters (Sect. 18.2.5). In practice, however, these two pathways may coexist, with gliotransmission feeding back in a closed-loop fashion on the very synapses that stimulate the astrocyte and trigger its gliotransmitter release. This section focuses on such a closed-loop scenario for gliotransmission.

Closed-loop gliotransmission can easily be implemented in *Brian 2* by combining the model of a synaptically activated astrocyte (Fig. 18.2a) with that of open-loop gliotransmission (Fig. 18.3a), resulting in the model scheme shown in Fig. 18.4a. However, it may be noted that in doing so we end up using two independent *Synapses* objects (*ellipses*) to separately describe the extracellular space for synapse-to-astrocyte signaling (`ecs_syn_to_astro`) and the extracellular space for astrocyte-to-synapse gliotransmission (`ecs_astro_to_syn`). In reality, both neurotransmitter and gliotransmitter release could occur in the same extracellular space, and thus only a single *Synapses* object might be considered at the benefit of computational efficiency. Nonetheless, the choice of using two independent objects allows us to take into account the more general scenario of astrocytes that are either sensitive or not to the activity of the same synapses they modulate (Navarrete and Araque 2010; Martín et al. 2015). This is therefore an appropriate choice when dealing with many synapses interacting with astrocytes as in the case of the neuron–glia network discussed at the end of this chapter.

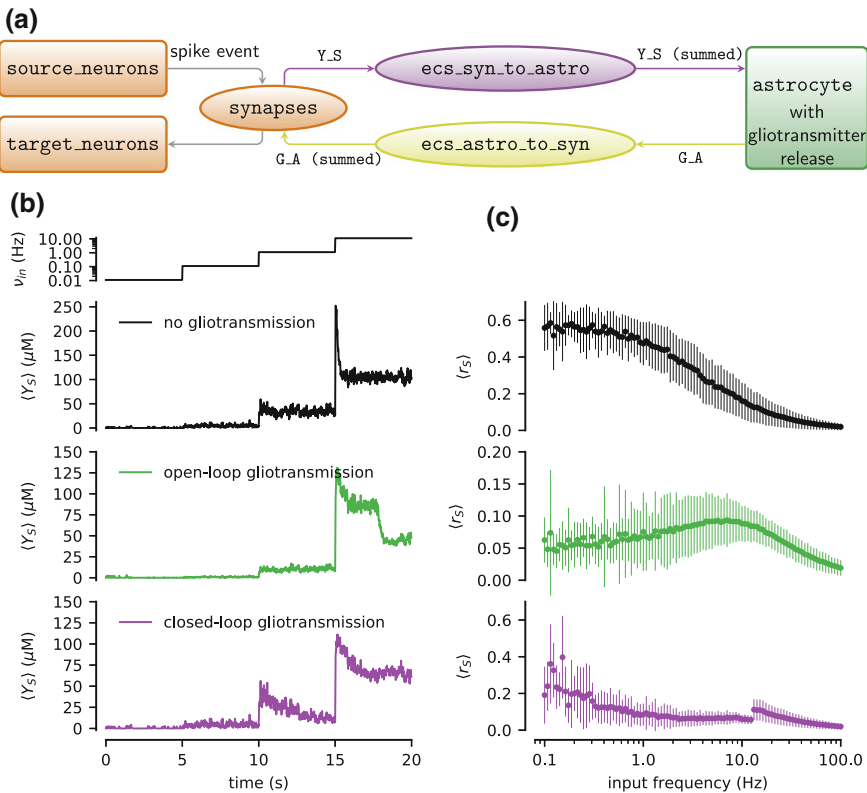


Fig. 18.4 Closed-loop gliotransmission. **a** In the most general design, modeling of closed-loop gliotransmission in *Brian 2* separates between the extracellular space of synapse-to-astrocyte signaling (*ecs_syn_to_astro*) and the extracellular space of astrocyte-to-synapse gliotransmission (*ecs_astro_to_syn*). **b** Average extracellular concentration of synaptically released neurotransmitter ($\langle Y_S \rangle$) for step increases of the mean rate of Poisson-generated incoming action potentials (top panel, $v_{in} = 0.011 \text{ Hz}, 0.11 \text{ Hz}, 1.1 \text{ Hz}, 11 \text{ Hz}$ for 5-s time intervals; traces averaged over 500 identical synapses.) **c** Corresponding average release of synaptic neurotransmitter resources as function of the rate of incoming action potentials (data points and error bars: mean \pm standard deviation for 100 trials.) Parameters as in Tables 18.1 and 18.2 except for $O_\beta = 3.2 \mu\text{M s}^{-1}$; $I_{bias} = 1 \mu\text{M}$ (open-loop gliotransmission); $I_{bias} = 0 \mu\text{M}$ (closed-loop gliotransmission)

To elucidate some of the possible functional implications of closed-loop gliotransmission, we set out to characterize the average synaptic release for $N_{\text{synapses}}=500$ identical synapses for different input stimuli and compare it to the open-loop scenario of gliotransmission as well as to the “naive” scenario without gliotransmission. *Brian 2* is optimized to deal with large objects (see Appendix 1), so rather than simulating one synapse at a time, for 500 times in the three different scenarios (i.e. 1500 simulations in total), we simulate all synapses in all scenarios in one single run. This is achieved by considering 500×3 synapses and an astrocyte group of 500×2 elements. The first 500 synapses are modulated by gliotransmitters from the first 500

astrocytes in a closed-loop fashion, the second group of 500 synapses is modulated by open-loop gliotransmission mediated by the other 500 astrocytes; and finally, the remaining synapses do not consider any gliotransmission. In contrast to previous synaptic connection patterns, here we can directly calculate a target index for each connection, instead of evaluating a logical condition for every possible connection pair. *Brian 2* has a built-in syntax for such descriptions, which offers a much more efficient way of establishing connections. In this syntax, we provide an expression to calculate the target index j based on the source index i and potentially other pre- or postsynaptic properties. To exclude certain potential connections, this expression can be combined with an optional `if` string stating the condition for a connection to exist. Remember that in our example here, the source index i and the target index j each refer either to synapses or astrocytes, depending on the direction of the connection (“synapses to astrocytes” or “astrocytes to synapses”). This leads to the following *Brian 2* code:

```
ecs_syn_to_astro = Synapses(synapses, astrocyte,
                            'Y_S_post = Y_S_pre : mmolar (summed)')
# Connect the first N_synapses synapses--astrocyte pairs
ecs_syn_to_astro.connect(j='i if i < N_synapses')
ecs_astro_to_syn = Synapses(astrocyte, synapses,
                            'G_A_post = G_A_pre : mmolar (summed)')
# Connect the first N_synapses astrocytes--pairs (closed-loop)
ecs_astro_to_syn.connect(j='i if i < N_synapses')
# Connect the second N_synapses astrocyte--synapses pairs (open-loop)
ecs_astro_to_syn.connect(j='i if i >= N_synapses and i < 2*N_synapses')
```

Figure 18.4b shows a reproduction of Fig. 10.2 by our *Brian 2* implementation of closed-loop gliotransmission for the time evolution of the average neurotransmitter concentration in the synaptic cleft ($\langle Y_S \rangle$) in response to step increases in the rate of incoming action potentials (v_{in} , top panel). Gliotransmission dramatically changes synaptic transmission (colored vs. black traces), with the effect of closed-loop gliotransmission (purple trace) being somewhat intermediate between the scenarios of no gliotransmission (black trace) and open-loop gliotransmission (green trace).

This is further elucidated in Fig. 18.4c where the mean neurotransmitter concentration in the extracellular space in the three scenarios is shown for different mean rates of randomly incoming action potentials. In line with what observed in Chap. 10, the low-pass filter characteristics of synapses without gliotransmission (top panel) turns into a bell-shaped, band-pass filter characteristics caused by (release-decreasing) open-loop gliotransmission (middle panel). In the presence of closed-loop gliotransmission, however, the average concentration of synaptically released neurotransmitter is in between those expected in the other two scenarios for low input rate values, and tends to approach the shape of the curve in the open-loop scenario for increasing rates. For high input rates, however, the release-decreasing effect of gliotransmission is such that the synapse is ultimately silenced and cannot sustain further gliotransmitter release. Synaptic transmission then becomes independent of gliotransmission again as if it were in the naive scenario without gliotransmission, which accounts for the jump at $v_{in} > 10$ Hz.

18.2.7 Networks of Astrocytes

Astrocytes are known to arrange in networks of different shape and connectivity depending on the brain region under consideration (Giaume et al. 2010), and to be capable of propagating Ca^{2+} signals through such networks in the form of inter-cellular (regenerating) waves. The mechanisms underlying such propagation can be multiple and varied (Scemes and Giaume 2006). Here, we only focus on the well-characterized mechanism of intracellular IP_3 diffusion through gap junctions channels (GJCs) between neighboring astrocytes.

From a modeling perspective, IP_3 diffusion from one astrocyte j to a neighboring one i can be thought as a flux of IP_3 (J_{ij}) which is some nonlinear (rectifying) function of the IP_3 concentration gradient between cells i and j , i.e. $\Delta_{ij}I = I_i - I_j$, such as, for example (Lallouette et al. 2014; see also Chap. 7)

$$J_{ij} = -\frac{F}{2} \left(1 + \tanh \left(\frac{|\Delta_{ij}I| - I_\theta}{\omega_I} \right) \right) \text{sgn}(\Delta_{ij}) \quad (18.22)$$

Incidentally, we note that the above formula is reminiscent of the expression of the exogenous IP_3 flux (J_{ex}) in Eq. 18.14, insofar as the latter may be regarded as a special case of intercellular IP_3 influx to any astrocyte from a much larger external IP_3 source (i.e. I_{bias} in our notation) (Goldberg et al. 2010). Because J_{ij} is a function of IP_3 concentrations in connected astrocytes (i.e. I_i, I_j) by $\Delta_{ij}I$, it is astrocyte-dependent and not constant. Therefore, once we add J_{ij} to our astrocyte equations in *Brian 2* (denoted in the code below by $J_{coupling}$), we must define it as an astrocytic variable (that is without the (constant) flag), i.e.

```
astro_eqs = ''
dI/dt = J_delta - J_3K - J_5P + J_ex + J_coupling : mmolar
# [...]
# Diffusion between astrocytes
J_coupling : mmolar/second
# [...]
'''
```

Connections between astrocytes by GJCs may conveniently be implemented by a `Synapses` object in *Brian 2*, once we regard J_{ij} as the IP_3 flow from “presynaptic” astrocyte j to “postsynaptic” astrocyte i (Fig. 18.5b). The effective total $J_{coupling}$ to cell i by intercellular IP_3 diffusion is the sum of all IP_3 fluxes incoming to cell i from the \mathcal{A}^i astrocytes connected to this latter by GJCs, i.e. $J_{coupling}^i = \sum_{j \in \mathcal{A}^i} J_{ij}$. In *Brian 2* code, this reads

```
astro_to_astro_eqs = ''
delta_I = I_post - I_pre : mmolar
J_coupling_post = -F/2 * (1 + tanh((abs(delta_I) - I_Theta)/omega_I)) *
                     sign(delta_I) : mmolar/second (summed)
...
astro_to_astro = Synapses(astrocytes, astrocytes,
                         model=astro_to_astro_eqs)
```

The above code bears the caveat of defining GJCs as unidirectional when they may not be so. This caveat can be easily overcome, specifying both a connection

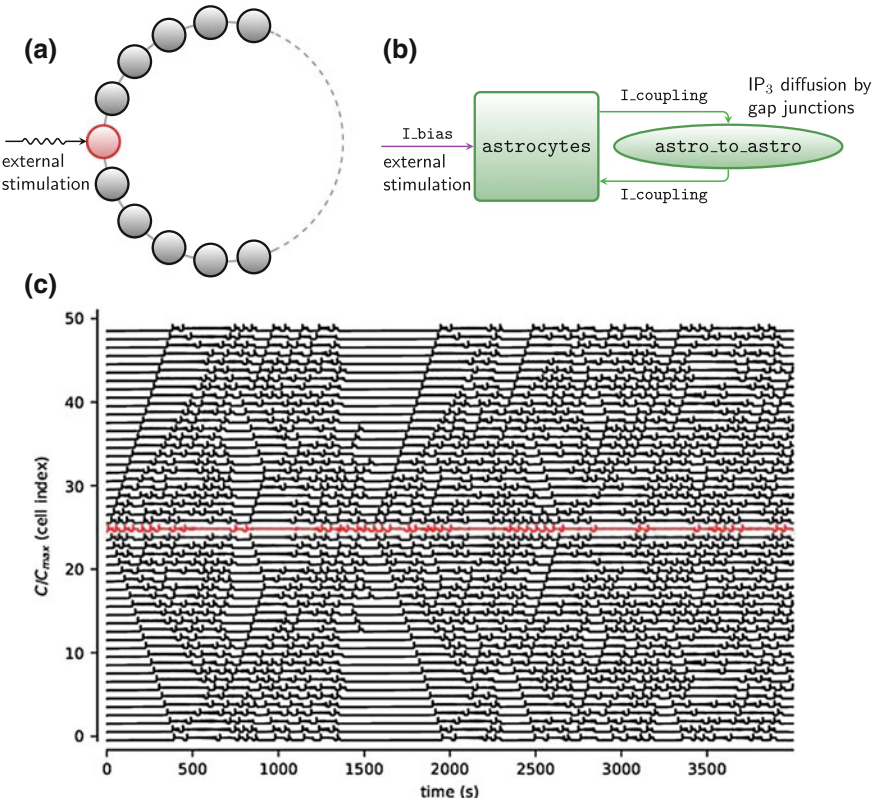


Fig. 18.5 Astrocytes connected in a network. **a** Sample astrocyte network in a ring configuration with only one cell (in red) being exogenously stimulated. Connections between cells are bidirectional, and represent GJC-mediated coupling between neighboring astrocytes. **b** General *Brian 2* modeling principle of astrocytic networks: GJC-mediated connections can be modeled by a *Synapses* object (ellipse). **c** Intercellular Ca²⁺ wave generation and propagation in a ring of 50 identical astrocytes mediated by stimulation of cell 25 (red trace). Parameters as in Table 18.2 with $F_{ex} = 0.09 \mu\text{Ms}^{-1}$; and $I_{bias} = 1 \mu\text{M}$

from astrocyte i to astrocyte j and a connection from j to i , whenever we want to model bidirectional IP₃ diffusion between neighboring astrocytes. For example, to connect astrocytes in a ring, where every astrocyte is connected to its neighbors (Fig. 18.5a), we can make use of the `connect` method of the `astro_to_astro` object, and specify the following condition in terms of *Brian 2* predefined pre- and post-synaptic indexes, i and j , respectively, and the total number of elements in the presynaptic group N_{pre} ³:

```
astro_to_astro.connect('j == (i + 1) % N_pre or '
                      'j == (i + N_pre - 1) % N_pre')
```

³Note that the expression has been split into two strings for better readability. Python automatically merges adjacent strings.

where the `%` operator implements the modulo (remainder) operation.

Figure 18.5c shows a snapshot of Ca^{2+} dynamics of 50 astrocytes connected in a ring, where only the 25th cell is exogenously stimulated (*red trace*). The fact that all cells, for some $t > 0$, display Ca^{2+} fluctuations, is a direct consequence of inclusion of intercellular IP_3 diffusion in our model. Such diffusion allows excess IP_3 from the stimulated cell to be redistributed by GJCs in the ring to other cells where it ultimately triggers CICR. It may also be appreciated how, in this example, bidirectional GJC communication allows for emergence of intercellular Ca^{2+} waves that propagate both from and to the stimulated cell, as evidenced by wavefronts, respectively, oriented like “\” or like “/”.

18.2.8 Coupled Neuron and Astrocyte Networks

The examples discussed so far provide together all the ingredients to model complex networks of interacting neurons and astrocytes (Fig. 18.6a). However, to realistically implement such networks we also need to specify the connections among neurons, synapses and astrocytes in the physical (Euclidean) space. In the following, we show how to include space in such networks, limiting our focus here to planar networks for simplicity, although the outlined procedure can easily be extended to higher dimensions.

We start by adding two cell-specific parameters, x and y , to each neuron which store the cell’s 2D spatial coordinates and initialize them so that neurons are arranged on a grid of `N_rows` rows and `N_cols` columns:

```
neuron_eqs = '''
# [...]
# Neuron position in space
x : meter (constant)
y : meter (constant)
'''

neurons = NeuronGroup(N_e + N_i, model=neuron_eqs,
                      threshold='v>V_th', reset='v=V_r',
                      refractory='tau_r', method='euler')
exc_neurons = neurons[:N_e]
inh_neurons = neurons[N_e:]
# Arrange excitatory neurons in a grid
N_rows = int(sqrt(N_e))
N_cols = N_e/N_rows
grid_dist = (size / N_cols)
exc_neurons.x = '(i / N_rows)*grid_dist - N_rows/2.0*grid_dist'
exc_neurons.y = '(i % N_rows)*grid_dist - N_cols/2.0*grid_dist'
```

Furthermore, we also add a synapse-specific constant `astrocyte_index` to the synapse’s equations, whose value will correspond to the index of the astrocyte that ensheathes a synapse:

```
synapses_eqs = '''
# [...]
# which astrocyte covers this synapse ?
astrocyte_index : integer (constant)
```

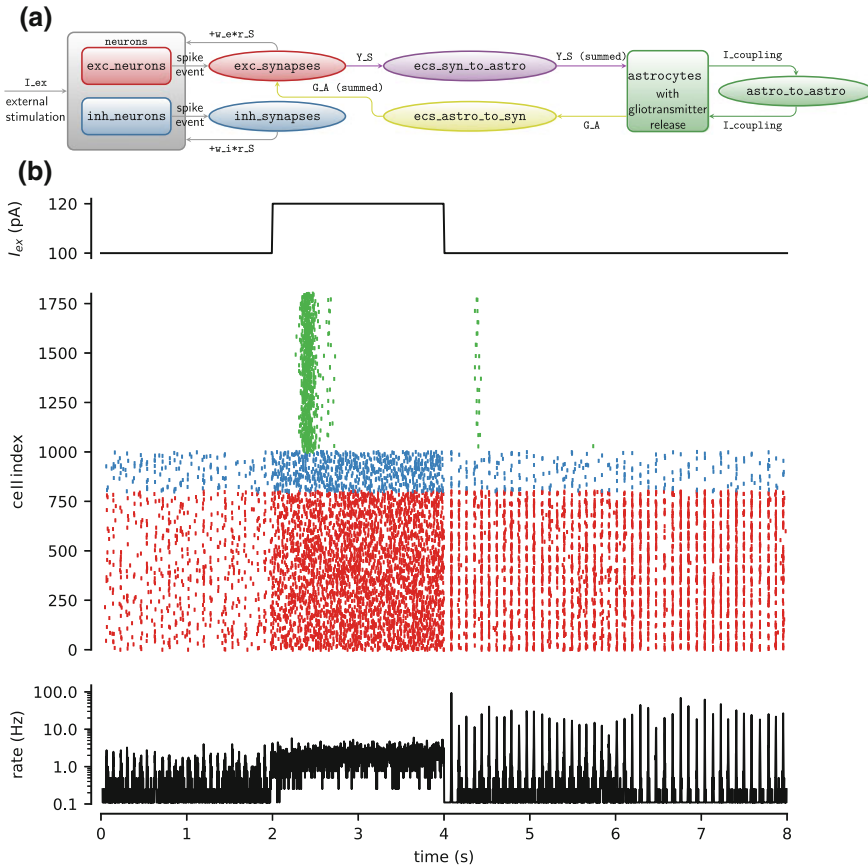


Fig. 18.6 Recurrent neuron–glial network. **a** Neuron–glial network model design in *Brian 2*. **b** Simulations of neuron–glia network for a rectangular-pulse increase of external current (I_{ex} , top panel). The raster plot (middle panel) shows the firing activity of 25% out of all excitatory (red) and inhibitory neurons (blue) of the network, and gliotransmitter release (green) from an equal fraction of astrocytes. The network-averaged firing rate is shown at the bottom. Neural activity dramatically changes from asynchronous low-firing activity to synchronous high-firing activity following gliotransmitter release from astrocytes during the period of high stimulation ($2 \leq t < 4$ s). External current: $I_{ex} = 100 \text{ pA}$ for $t < 2$ s or $t \geq 4$ s; $I_{ex} = 120 \text{ pA}$ for $2 \leq t < 4$ s. Neural and synaptic parameters as those in Fig. 18.1 (see also Table 18.1). Astrocyte parameters as in Table 18.2 except for $O_\beta = 0.5 \mu\text{Ms}^{-1}$; $O_\delta = 1.2 \mu\text{Ms}^{-1}$; and $I_{bias} = 0$

```
...
#   [...]
exc_syn = Synapses(exc_neurons, neurons, model=synapses_eqs,
                    on_pre=synapses_action+'g_e_post += w_e*r_S',
                    method='linear')
```

We finally need to define the effective connections between the different cells of the network. Overall, there are four different types of connections: (i) connections

between neurons which defines the actual synapses; (ii) connections from synapses to astrocytes, as pathways to trigger astrocyte activation; (iii) connections from astrocytes to synapses as routes for gliotransmission and thereby modulation of synaptic release; and ultimately, (iv) connections between astrocytes by GJCs. Here, for simplicity, we assume random connectivity between all neurons, independently of their spatial coordinates (as in Fig. 18.1c). Furthermore, we make the assumption that only excitatory synapses can activate astrocytes and be modulated by them, restricting in this way our focus on the experimentally well-characterized pathway of closed-loop glutamatergic gliotransmission (Perea and Araque 2007; Panatier et al. 2011). In particular, we specify which astrocyte is responsible for which excitatory synapse on the basis of the spatial position of postsynaptic neurons with respect to N_a astrocytes (N_a) which, like neurons, are arranged on a regularly spaced grid of N_{rows} rows (N_{rows_a}) and N_{cols} columns (N_{cols_a}), i.e.

```
N_rows_a = int(sqrt(N_a))
N_cols_a = N_a/N_rows_a
grid_dist = size / N_rows_a
exc_syn.astrocyte_index = ('int(x_post/grid_dist) + '
                           'N_cols_a*int(y_post/grid_dist)')
```

We then define the network of astrocytes:

```
astro_eqs = '''
# [...]
# The astrocyte position in space
x : meter (constant)
y : meter (constant)
'''
# [...]
# Arrange astrocytes in a grid
astrocytes.x = '(i / N_rows_a)*grid_dist - N_rows_a/2.0*grid_dist'
astrocytes.y = '(i % N_rows_a)*grid_dist - N_cols_a/2.0*grid_dist'
```

Next, we connect the astrocytes with those synapses that they are supposed to ensheathe according to `astrocyte_index`, i.e.

```
ecs_astro_to_syn = Synapses(astrocytes, exc_syn,
                            'G_A_post = G_A_pre : mmolar (summed)')
ecs_astro_to_syn.connect('i == astrocyte_index_post')
ecs_syn_to_astro = Synapses(exc_syn, astrocytes,
                            'Y_S_post = Y_S_pre/N_incoming : mmolar
                                         (summed)')
ecs_syn_to_astro.connect('astrocyte_index_pre == j')
```

Finally, we specify the connectivity of the astrocyte network. In this example, we introduce recurrent connections between astrocytes by GJCs, connecting each astrocyte to all other astrocytes found at the boundary of its anatomical domain, in line with the experimental observation that neighboring astrocytes are more likely to be connected than astrocytes that are far apart (Giaume et al. 2010; Pannasch and Rouach 2013). Given that the diameter of astrocyte is between 50–130 μm (Chao et al. 2002), we consider an intermediate value of 75 μm , whereby:

```
astro_to_astro.connect('i != j and '
                      'sqrt((x_pre-x_post)**2 +'
                      '(y_pre-y_post)**2) < 75*um')
```

We present a simulation of our neuron–glia network in Fig. 18.6b, where we show the raster plot of the firing activity of 25% of the excitatory (*red*) and inhibitory neurons (*blue*) of the network along with gliotransmitter release events from an equal fraction of astrocytes (*green*), in response to a transient increase of external stimulation (rectangular pulse in the *top panel*). Up to the onset of stimulation (i.e. $t < 2\text{ s}$) there is no gliotransmitter release from astrocytes, therefore the network behaves as it would be expected for a neuronal network without the astrocyte component. It may be noted in fact how the raster plot of our network, and the ensuing dynamics of the total firing rate (*bottom panel*), show low-frequency population activity, similar to those reported in Fig. 18.1c for our neuronal-only network model introduced in Sects. 18.2.2 and 18.2.3. For $2 \leq t < 4\text{ s}$, the increase of external stimulation correlates with an increase in the firing rate of the whole network, as reflected by a denser raster plot during this period. In particular for $t > 3.5\text{ s}$, the larger neuronal firing triggers gliotransmitter release from astrocytes and thus astrocytic modulation of excitatory synaptic transmission. Because this modulation is slow-decaying (Chaps. 8 and 10), it outlasts the transient increase of external stimulation and changes neural firing once the external stimulation returns to its original value (at $t = 4\text{ s}$). We can indeed clearly see how, for $t > 4\text{ s}$, excitatory neurons are more synchronized in firing than for $t < 2\text{ s}$, as a consequence of gliotransmission from astrocytes. This is just one example of the many possible ways astrocytes could actively shape neural activity, which has also been suggested to participate in the genesis of cortical UP and DOWN states (Fellin et al. 2012).

18.3 Conclusions

Computational approaches to model glial physiology are hampered by the lack of definitive experimental evidence and a missing comprehensive modeling framework that could tackle the many different scales of glial signaling. “Standard” glia models have yet to be identified, and neural simulator packages therefore do not ship such models as part of their pre-built model libraries. While in theory these libraries could be extended by individual researchers to add their preferred glia model, in practice this path is only open to experienced programmers.

In this chapter, we have shown how *Brian 2*’s simple syntax and versatility can offer a solution to these problems, providing an ideal tool to model glial physiology and specifically the influence of astrocytes on neural activity. *Brian 2*’s syntax allows the researcher to flexibly describe models by using conventional mathematical notation instead of low-level programming code (Goodman and Brette 2008; Goodman et al. 2009; Stimberg et al. 2014). Moreover, *Brian 2*’s core data structure `NeuronGroup`, which describes a neuron by a set of ODEs, parameters, and actions that are triggered by conditions, provides a versatile framework that can be borrowed to also describe non-neuronal cell types such as astrocytes. Similarly, the `Synapses` data structure that, in purely neural simulations, represents chemical and electrical synapses that connect neurons, can also be used to model the interactions

between astrocytes and synapses, as well as GJCs between astrocytes. Importantly, this flexibility does not come at the cost of computational efficiency: without any user interaction, *Brian 2* employs a code generation approach that generates highly efficient code based on the user-provided high-level description (Goodman 2010). We hope that these arguments motivate newcomers as well as experienced researchers to experiment with *Brian 2* in the future and use it to model glial physiology in their research, thereby contributing to the growth of this exciting emerging field of computational research.

Acknowledgements This work was supported by Agence Nationale de la Recherche (Axode ANR-14-CE13-0003). MDP acknowledges the support of the Junior Leader Fellowship Program by “la Caixa” Banking Foundation, as well as the support by the Basque Government through the BERC 2018-2021 program and by the Spanish Ministry of Science, Innovation and Universities: BCAM Severo Ochoa accreditation SEV-2017-0718. Writing of this chapter was also partly supported by a Marie Skłodowska-Curie International Outgoing Fellowship to MDP from the European Commission (Project 331486 “Neuron-Astro-Nets”).

Appendix 1 Technical remarks on *Brian 2*

Brian 2 scripts are executed by default in the so-called “runtime mode”. This mode runs the simulation loop over the time steps in Python and executes chunks of target language code that have been generated from the model description provided by the user. The choice of target language depends on the user’s system; *Brian 2* will prefer to use the C++ programming language but, if the user does not have a working C++ compiler, will fall back to a pure Python-based simulation. A Python-based simulation will usually be significantly slower but can give comparable performance for big networks due to the use of vectorized computation (Brette and Goodman 2011). The advantage of the runtime mode is that the user has full control to combine the automatically generated simulation code with arbitrary hand-written Python code. This code could dynamically change aspects of the model during the run, or interact with it in other ways. For example it could read out the model’s state and hand it over to some code for visualization or terminate the simulation based on some criterion. This mode however involves a significant overhead per simulated time step, since the program flow constantly switches between Python and the individually-generated code chunks. For small-to-medium size networks for which computations during a single time step do not take long, this overhead can critically dominate the total runtime and lead to long simulation times.

To avoid this problem and allow more efficient simulations, *Brian 2* also offers an alternative mode called “standalone mode”. In this mode, the complete simulation code, including the main simulation loop, are written as a set of C++ files to disk which can then be compiled and executed as a single program. The resulting files are independent of the Python platform, so that the simulation could also be run on systems where Python may not be available (for example, in robotics). Moreover, if the user code complies to some specific conventions and does not run custom Python

code during a simulation, then switching from runtime to standalone mode only requires the addition of a `set_device('cpp_standalone')` line to the simulation script; *Brian 2* then takes care of the whole process transparently. For further details, the reader is invited to see comments in individual examples files (Appendix 2) and/or refer to the online *Brian 2* documentation.

Appendix 2 Example Files

The code for all the simulations presented in this chapter has been organized in multiple standalone example files as detailed in the following. Unless stated otherwise, all simulations start from zero initial conditions, except for $h(0) = 0.9$ and $x_S(0) = x_A(0) = 1$.

`example_1_COBA.py`

This file implements the simulation of the neuron-only network model of Fig. 18.1. The simulation runs for 1 s with an integration time step of 0.1 ms. Out of all neurons, we distinguish between excitatory (`exc_neurons`) and inhibitory ones (`inh_neurons`), which give rise to excitatory synapses (`exc_syn`) and inhibitory synapses (`inh_syn`), connecting from the respective population to the full population. Because the dynamics of synaptic variables are updated only at incoming action potentials (i.e. (`event-driven`)), we can monitor the value of these variables only at the arrival time of action potentials but not in between. However, we can reconstruct the whole synaptic dynamics by recording synaptic variables immediately after each action potential (i.e. at t_i^+ with $i > 0$), which is achieved by specifying the keyword argument `when='after_synapses'` in the synaptic `StateMonitor`. For $t > t_i$, the solutions of the synapse's Eqs. 18.4 and 18.5 then read (Tsodyks 2005):

$$\begin{aligned} u_S(t) &= u_S(t_i^+) \exp(-\Omega_f(t - t_i)) \\ x_S(t) &= 1 + (x_S(t_i^+) - 1) \exp(-\Omega_d(t - t_i)) \end{aligned}$$

whereas synaptic release by the i th action potential at time t_i is given by $r_S(t_i) = u_S(t_i^+)x_S(t_i^-) = u_S(t_i^+)x_S(t_i^+)/\left(1 - x_S(t_i^+)\right)$.

`example_2_gchi_astrocyte.py`

This code implements the synaptically stimulated astrocyte model and related simulations of Fig. 18.2. The astrocyte's temporal dynamics in response to synaptic activity was simulated for 30 s using the derivative-free Milstein integration method with a time step of 1 ms. In the deterministic limit of $\xi(t) \rightarrow 0$ in Eq. 18.13, the Milstein method reduces to the classical (forward) Euler method which is suitable, at sufficiently small time steps, to numerically solve dynamics of the deterministic astrocyte model too. Synapses are stimulated by a train of periodic action potentials at rate $f_0 = 0.5$ Hz (`f_0`, rate of generation of action potentials by presynaptic neurons) generated by

```
source_neurons = NeuronGroup(1, 'dx/dt = f_0 : 1', threshold='x>1',
                             reset='x=0', method='euler')
```

example_3_io_synapse.py

This file implements the open-loop model of gliotransmission and the simulations shown in Fig. 18.3. The code considers three synaptic connection between one presynaptic `source_neurons` and one postsynaptic `target_neurons`, built by passing `n=3` as an argument to the `synapses.connect` method. We further consider two astrocytes stimulated by different `I_bias` values, and connect them to synapses 2 and 3, respectively, leaving synapse 1 as it is (i.e. without gliotransmission). This is done by:

```
ecs_astro_to_syn.connect(j='i+1')
```

example_4_synrel.py

This code runs the closed-loop model of gliotransmission for simulations in Fig. 18.4b. The code considers `N_synapses` neurons (`source_neurons`), each firing action potentials drawn from an independent, inhomogeneous Poisson process with a stepped rate specified in a `TimedArray`, i.e.

```
rate_in = TimedArray([0.011, 0.11, 1.1, 11] * Hz, dt=5*second)
source_neurons = PoissonGroup(N_synapses, rates='rate_in(t)')
target_neurons = NeuronGroup(N_synapses, '')
```

The `target_neurons` are used to build `N_synapses` multi-synaptic connections from the `source_neurons`, with each connection constituted of three synapses. Out of these three synapses, the first one is connected with its own astrocyte and, in turn, is modulated by gliotransmitters released from this latter (closed-loop scenario); the second one is modulated by gliotransmitters released from another astrocyte (open-loop scenario); the third one is left as it is (scenario without gliotransmission). Since this is repeated for all `N_synapses`, and overall we have `N_astro=2` different scenarios of gliotransmission (open-loop vs. closed-loop), we consider `N_astro*N_synapses` astrocytes in total, and connect them accordingly with `N_synapses*(N_astro+1)` synapses as elucidated in Sect. 18.2.6.

example_4_rsmean.py

The file provides the code to build the synaptic transfer characteristics in Fig. 18.4c in terms of average synaptically-released neurotransmitter resources for different input rates of (presynaptically) incoming action potentials.

example_5_astro_ring.py

This code implements the astrocyte ring model in Fig. 18.5. The simulation runs for 4000 s with a time step of 50 ms. Calcium concentrations shown in Fig. 18.5c were normalized by their maximum.

example_6_COBA_with_astro.py

This file runs the simulation of the recurrent neuron–glial network in Fig. 18.6. To stimulate the network by a time-varying external current, we multiply `I_ex` in

neuron_eqs on page xx by `stimulus = TimedArray([1.0, 1.2, 1.0, 1.0], dt=2*second)`. Neurons are placed on a square lattice of size 3.75×3.75 mm at $50\text{ }\mu\text{m}$ distance from each other. For $t = 0$ we set $C = I = 0.01\text{ }\mu\text{M}$.

References

- Abbott LF (2008) Theoretical neuroscience rising. *Neuron* 60(3):489–495
- Aleksin SG, Zheng K, Rusakov DA, Savchenko LP (2017) ARACHNE: A neural-neuroglial network builder with remotely controlled parallel computing. *PLoS Comput Biol* 13(3):e1005467
- Araque A, Carmignoto G, Haydon PG, Oliet SHR, Robitaille R, Volterra A (2014) Gliotransmitters travel in time and space. *Neuron* 81(4):728–739
- Beenhakker MP, Huguenard JR (2010) Astrocytes as gatekeepers of GABA_B receptor function. *J Neurosci* 30(45):15262–15276
- Bezzi P, Volterra A (2001) A neuron-glia signalling network in the active brain. *Curr Opin Neurobiol* 11:387–394
- Brette R (2012) On the design of script languages for neural simulation. *Network* 23(4):150–156
- Brette R, Goodman DFM (2011) Vectorized algorithms for spiking neural network simulation. *Neural Comput* 23(6):1503–1535
- Brette R, Rudolph M, Carnevale T, Hines M, Beeman D, Bower JM, Diesmann M, Morrison A, Goodman PH, Harris JFC, Zirpe M, Natschläger T, Pecevski D, Ermentrout B, Djurfeldt M, Lansner A, Rochel O, Vieville T, Muller E, Davison AP, El Boustani S, Destexhe A (2007) Simulation of networks of spiking neurons: a review of tools and strategies. *J Comput Neurosci* 23(3):349–398
- Brunel N (2000) Dynamics of sparsely connected networks of excitatory and inhibitory spiking neurons. *J Comput Neurosci* 8(3):183–208
- Cannon RC, Gewaltig M-O, Gleeson P, Bhalla US, Cornelis H, Hines ML, Howell FW, Muller E, Stiles JR, Wils S, Schutter ED (2007) Interoperability of Neuroscience Modeling Software: Current Status and Future Directions. *Neuroinform* 5(2):127–138
- Carnevale NT, Hines ML (2006) The NEURON book. Cambridge University Press
- Chao TI, Rickmann M, Wolff JR (2002) The synapse-astrocyte boundary: an anatomical basis for an integrative role of glia in synaptic transmission. In: Volterra A, Magistretti PJ, Haydon PG (eds) The tripartite synapse: glia in synaptic transmission, chapter 1. Oxford University Press, New York, pp 3–23
- Dayan P, Abbott LF (2001) Theoretical neuroscience, vol 806. MIT Press, Cambridge, MA
- De Pittà M, Brunel N, Volterra A (2016) Astrocytes: orchestrating synaptic plasticity? *Neuroscience* 323:43–61
- De Pittà M, Goldberg M, Volman V, Berry H, Ben-Jacob E (2009a) Glutamate-dependent intracellular calcium and IP_3 oscillating and pulsating dynamics in astrocytes. *J Biol Phys* 35:383–411
- De Pittà M, Volman V, Levine H, Ben-Jacob E (2009b) Multimodal encoding in a simplified model of intracellular calcium signaling. *Cogn Proc* 10(S1):55–70
- De Pittà M, Volman V, Berry H, Ben-Jacob E (2011) A tale of two stories: astrocyte regulation of synaptic depression and facilitation. *PLoS Comput Biol* 7(12):e1002293
- De Pittà M, Volman V, Berry H, Parpura V, Liaudet N, Volterra A, Ben-Jacob E (2013) Computational quest for understanding the role of astrocyte signaling in synaptic transmission and plasticity. *Front Comp Neurosci* 6:98
- De Pittà M, Volman V, Levine H, Pioggia G, De Rossi D, Ben-Jacob E (2008) Coexistence of amplitude and frequency modulations in intracellular calcium dynamics. *Phys Rev E* 77(3):030903(R)
- Engelman HS, MacDermott AB (2004) Presynaptic ionotropic receptors and control of transmitter release. *Nature Rev* 5:135–145

- Falcke M (2004) Reading the patterns in living cells: the physics of Ca^{2+} signaling. *Adv Phys* 53(3):255–440
- Fellin T, Ellenbogen JM, De Pittà M, Ben-Jacob E, Halassa M (2012) Astrocyte regulation of sleep circuits: experimental and modeling perspectives. *Front Comput Neurosci* 6(65)
- Fuhrmann G, Segev I, Markram H, Tsodyks M (2002) Coding of temporal information by activity-dependent synapses. *J Neurophysiol* 87:140–148
- Gewaltig M-O, Diesmann M (2007) NEST (NEural Simulation Tool). *Scholarpedia* 2(4):1430
- Giaume C, Koulakoff A, Roux L, Holcman D, Rouach N (2010) Astroglial networks: a step further in neuroglial and gliovascular interactions. *Nat Rev Neurosci* 11(2):87–99
- Goldberg M, De Pittà M, Volman V, Berry H, Ben-Jacob E (2010) Nonlinear Gap junctions enable long-distance propagation of pulsating calcium waves in astrocyte networks. *PLoS Comput Biol* 6(8):e1000909
- Goodman D, Brette R (2008) Brian: a simulator for spiking neural networks in Python. *Front Neuroinform* 2:5
- Goodman DFM, Brette R (2009) The brian simulator. *Front Neurosci* 3:26
- Goodman DFM (2010) Code generation: A strategy for neural network simulators. *Neuroinform* 8(3):183–196
- Hunter J (2007) Matplotlib: a 2D graphics environment. *Comput Sci Eng* 9(3):90–95
- Kloeden PE, Platen E (1992) Numerical solution of stochastic differential equations
- Lallouette J, De Pittà M, Ben-Jacob E, Berry H (2014) Sparse short-distance connections enhance calcium wave propagation in a 3D model of astrocyte networks. *Front comput neurosci* 8:45
- Li Y, Rinzel J (1994) Equations for InsP_3 receptor-mediated $[\text{Ca}^{2+}]_i$ oscillations derived from a detailed kinetic model: A Hodgkin-Huxley like formalism. *J Theor Biol* 166:461–473
- Martín R, Bajo-Grañeras R, Moratalla R, Perea G, Araque A (2015) Circuit-specific signaling in astrocyte-neuron networks in basal ganglia pathways. *Science* 349(6249):730–734
- McDougal RA, Morse TM, Carnevale T, Marenco L, Wang R, Migliore M, Miller PL, Shepherd GM, Hines ML (2017) Twenty years of ModelDB and beyond: building essential modeling tools for the future of neuroscience. *J Comput Neurosci* 42(1):1–10
- Mil'shtejn G (1975) Approximate integration of stochastic differential equations. *Theory Probab Its Appl* 19(3):557–562
- Nadkarni S, Jung P, Levine H (2008) Astrocytes optimize the synaptic transmission of information. *PLoS Comput Biol* 4(5):e1000088
- Naeem M, McDaid L, Harkim J, Wade JJ, Marsland J (2015) On the role of astroglial syncytia in self-repairing spiking neural networks. *Neural Networks and Learning Systems*, page, IEEE Trans In press
- Navarrete M, Araque A (2010) Endocannabinoids potentiate synaptic transmission through stimulation of astrocytes. *Neuron* 68(1):113–126
- Nimmerjahn A (2009) Astrocytes going live: advances and challenges. *J. Physiol.* 587:1639–1647
- Panatier A, Vallée J, Haber M, Murai K, Lacaille J, Robitaille R (2011) Astrocytes are endogenous regulators of basal transmission at central synapses. *Cell* 146:785–798
- Pannasch U, Rouach N (2013) Emerging role for astroglial networks in information processing: from synapse to behavior. *Trends in Neurosciences* 36(7):405–417
- Perea G, Araque A (2007) Astrocytes potentiate transmitter release at single hippocampal synapses. *Science* 317:1083–1086
- Pinheiro PS, Mulle C (2008) Presynaptic glutamate receptors: physiological functions and mechanisms of action. *Nat Rev Neurosci* 9:423–436
- Poskanzer KE, Yuste R (2016) Astrocytes regulate cortical state switching in vivo. *Proc National Acad Sci* 113(19):E2675–E2684
- Savchenko LP, Rusakov DA (2014) Regulation of rhythm genesis by volume-limited, astroglia-like signals in neural networks. *Phil Trans Royal Soc B biological sciences* 369(1654):20130614
- Savchenko LP, Bard L, Jensen TP, Reynolds JP, Kraev I, Medvedev N, Stewart MG, Henneberger C, Rusakov DA (2018) Disentangling astroglial physiology with a realistic cell model in silico. *Nat Commun* 9(1):3554

- Scemes E, Giaume C (2006) Astrocyte calcium waves: what they are and what they do. *Glia* 54:716–725
- Shuai J-W, Jung P (2002) Stochastic properties of Ca^{2+} release of inositol 1,4,5-trisphosphate receptor clusters. *Biophys J* 83(1):87–97
- Stiles JR, Bartol TM (2001) Monte Carlo methods for simulating realistic synaptic microphysiology using MCell. In: Schutter ED (ed) *Comput Neurosci: Realistic Model Experimentalists*. CRC Press, Boca Raton, FL, pp 87–127
- Stimberg, M., Goodman, D. F. M., Benichoux V, Brette R (2014) Equation-oriented specification of neural models for simulations. *Frontiers in Neuroinformatics*, 8
- Tsodyks M (2005) Activity-dependent transmission in neocortical synapses. In: Chow CC, Gutkin B, Hansel D, Meunier C, Dalibard J (eds) *Methods and Models in Neurophysics*, pp 245–265. Elsevier
- Tsodyks M, Pawelzik K, Markram H (1998) Neural networks with dynamic synapses. *Neural Computation* 10(4):821–835
- van der Walt S, Colbert S, Varoquaux G (2011) The NumPy array: a structure for efficient numerical computation. *Comput Sci Eng* 13(2):22–30
- Volman V, Ben-Jacob E, Levine H (2007) The astrocyte as a gatekeeper of synaptic information transfer. *Neural Comput* 19(2):303–326
- Wade JJ, McDaid LJ, Harkin J, Crunelli V, Kelso JAS (2011) Bidirectional coupling between astrocytes and neurons mediates learning and dynamic coordination in the brain: a multiple modeling approach. *PLoS One* 6(12):e29445
- Wallach G, Lallouette J, Herzog N, De Pittà M, Ben-Jacob E, Berry H, Hanein Y (2014) Glutamate-mediated astrocytic filtering of neuronal activity. *PLoS Comput Biol* 10(12):e1003964
- Zorec R, Araque A, Carmignoto G, Haydon P, Verkhratsky A, Parpura V (2012) Astroglial excitability and gliotransmission: An appraisal of Ca^{2+} as a signaling route. *ASN Neuro* 4(2):e00080